



TECHNISCHE
UNIVERSITÄT
WIEN

PhD-Thesis

Dissertation

Small molecules for the improvement of mechanical properties and degradation of photopolymers

ausgeführt zum Zwecke der Erlangung
des akademischen Grades eines Doktors der technischen Wissenschaften

unter der Leitung von
Univ. Prof. Dipl.-Ing. Dr. techn. Robert Liska
und der Betreuung von
Ass. Prof. Dipl.-Ing. Dr. techn. Stefan Baudis

E163
Institut für Angewandte Synthesechemie

eingereicht an der Technischen Universität Wien
Fakultät für Technische Chemie

von
Dipl.-Ing. Lisa Sinawehl, BSc
01325328

Wien, am 11.4.2023



Danksagung

Zuallererst möchte ich mich bei **Prof. Robert Liska** für die Möglichkeit bedanken, meine Arbeit in dieser einzigartigen Forschungsgruppe durchzuführen. Danke für die Betreuung und die vielen fachkundigen Ratschläge, die mich sowohl in meiner professionellen als auch persönlichen Entwicklung weitergebracht haben. Durch die positive Arbeitsatmosphäre, die du geschaffen hast, bin ich jeden Tag gerne ins Labor gekommen.

Mein besonderer Dank gilt **Prof. Stefan Baudis**. Als mein direkter Betreuer hast du mich ohne zu zögern in das CD Labor aufgenommen und mir ermöglicht an diesem interessanten Forschungsthema zu arbeiten. Danke, dass du dein Vertrauen in mich gesetzt hast und mich stets in allen Belangen unterstützt hast!

Ganz herzlich möchte ich mich auch bei allen **Kooperationspartnern des CD Labors** bedanken, da so eine gute Zusammenarbeit und der viele hilfreiche Input aller Beteiligten nicht selbstverständlich sind.

Danke auch an meine Bachelorstudenten **Philip** und **Alexandra** und an meine Praktikanten **Selina**, **Jan-Luca** und **Jo**, die mit ihrer genauen und engagierten Arbeitsweise zum Gelingen dieser Arbeit beigetragen haben.

Vielen Dank an **Dr. Thomas Koch**, für die Unterstützung bei den unzähligen mechanischen und thermischen Tests, den fachlichen Input und deinen unermüdlichen Einsatz sowohl innerhalb als auch außerhalb „normaler“ Arbeitszeiten.

Dem gesamten Arbeitsbereich für Makromolekulare Chemie, unter der Leitung von **Prof. Simone Knaus**, möchte ich einen riesigen Dank aussprechen. Sowohl den „Alten“, als auch meinen jetzigen Arbeitskollegen, **Tina**, **Miriam**, **Roli**, **Betti**, **Toni**, **Carola**, **Klaus**, **Philip**, **Flo**, **Dani**, **Jelena**, **Jakob** und **Sarah** möchte ich danken, dass ihr mich mit offenen Armen aufgenommen habt und mir stets mit Rat und Tat zur Seite gestanden seid. Besonders möchte ich mich bei **Ricky**, **Fitzi**, **Baumi**, **Ralle**, **David**, **Michi**, **Pontus** und **Florian** für die vielen heiteren Stunden bedanken, die ich mit euch innerhalb und außerhalb des Labors verbringen durfte (und hoffentlich noch weiter verbringen werde!). Danke an euch alle für das tolle Arbeitsklima, die hervorragende Zusammenarbeit und die vielen unterhaltsamen Abende. Ihr habt die letzten drei Jahre hier unvergesslich gemacht!

Auch allen **Institutsangestellten**, ohne die ein reibungsloser Laborbetrieb nicht möglich wäre, möchte ich aufrichtig danken. Vor allem **Walter** für die unzähligen Male, an denen du mein Office aktiviert hast, und alles, mit dem du die gesamte Forschungsgruppe am Laufen gehalten hast.

Ein ganz großes Dankeschön geht an meinen Bench-Nachbarn **Oskar Berk, MSc.** Auch wenn ich am Anfang keine Lust auf den (deutschen) Wahlpraktikanten in meiner Bench hatte, wäre H21 ohne dich und dein Quietschen nicht dasselbe gewesen. Ich bin dankbar, dass wir den manchmal harten Laboralltag gemeinsam gemeistert haben und du nie Staplerfahrer werden musstest. Ich hoffe, dass unsere Freundschaft noch viele Jahre hält – schließlich ist dein Österreichisch ja noch verbesserungswürdig.

Meinen Mädels **Larissa, Anna** und **Babsi** gebührt ein besonderer Dank, da meine Zeit hier ohne euch nicht dieselbe gewesen wäre. Ihr seid mir durch alle Höhen und Tiefen beigestanden und habt es geschafft mich auch in den schwierigsten Zeiten zu motivieren. Durch euch und unsere täglichen Bench-Gespräche wurde meine Dissertation zu einer unvergesslichen Zeit, an die ich immer mit einem Lächeln zurückdenken werde! Vor allem dir, **Babsi**, möchte ich hier noch zusätzlich für deine riesige Unterstützung bei vielen Dingen und Problemen danken. Ich kann mit Sicherheit sagen, dass diese Zeit ohne dich, und die unzähligen Feierabend-Biere mit dir, nie so schön gewesen wäre.

Mein größter Dank geht an meine Familie, insbesondere an meine Eltern, die mir diese Ausbildung erst ermöglicht und mich all die Jahre unterstützt haben. Danke, dass ich mich immer auf euch verlassen konnte und immer noch kann!

Zuletzt möchte ich noch dir danken, **Stefan**. Nicht nur zu Beginn meiner Zeit in H21 hast du mich stets unterstützt, auch jetzt, während der nicht immer leichten Zeit des Fertigwerdens hast du es immer geschafft mich aufzuheitern. Dafür bin ich dir jetzt schon dankbar und freue mich schon sehr auf alle zukünftigen, randomen Erlebnisse mit dir!

DANKE!

Abstract

In case of critical bone loss due to accidents or diseases, the process of bone regeneration cannot be fulfilled, and additional surgical intervention in the form of bone transplants is required. Lithography-based additive manufacturing technologies were shown to be ideal tools for the fabrication of biocompatible and biodegradable, patient-specific regeneration scaffolds used in bone tissue engineering. However, currently employed state-of-the-art photopolymers based on (meth)acrylates, vinyl esters, or vinyl carbonates do not meet the high requirements for implants used *in vivo*, as they display irritancy or even cytotoxicity of residual monomers, undesirable degradation behavior leading to failure or insufficient degradation rates. Additionally, formed materials exhibit high brittleness, shrinkage, and poor strength, further limiting their use for the intended application.

In this thesis, two strategies were investigated involving small molecule building blocks for the generation of photopolymers that combine superior mechanical properties with enhanced degradation compared to state-of-the-art materials. Cyclopolymerizable monomers (CPMs) were investigated as building blocks, comprising advantages such as lower shrinkage and the formation of rigid polymers with cyclic backbone structures while allowing the incorporation of hydrolytically labile groups. As degradable motifs, acetal and carbonate moieties, as well as heteroatoms, including phosphorus, silicon, or boron, forming less stable bonds to oxygen than carbon were used. Several CPMs were successfully synthesized and tested for their cyclopolymerization tendency, which, however, was found to be low with both radical and cationic initiators. Consequently, allyl ether and allyl ester monomers comprising rigid structural elements and heteroatom-oxygen bonds were developed. By employing them in thiol-ene chemistry, homogeneous and tough networks were formed, which could be cleaved at the respective hydrolyzable bonds. Cyclic boronic esters were discovered as efficient degradation enhancers, combining a facile synthesis, significantly lower toxicity compared to (meth)acrylates, reduced shrinkage, and exceptional material properties with accelerated degradation via desired surface erosion under conditions present during bone remodeling. Ultimately, a test structure was successfully 3D-printed, supporting the suitability of these monomers for the production of biocompatible and biodegradable bone regeneration scaffolds.

Kurzfassung

Bei kritischem Knochenverlust aufgrund von Unfällen oder Krankheiten kann der Prozess der Knochenregeneration nicht stattfinden und die chirurgische Behandlung mit Knochen-
transplantaten ist erforderlich. Lithographie-basierte additive Fertigungsmethoden sind ideale
Werkzeuge für die Herstellung biokompatibler und bioabbaubarer, patientenspezifischer
Gerüststrukturen für das Bone Tissue Engineering. Die derzeit verwendeten Photopolymere auf
der Basis von (Meth)acrylaten, Vinylestern oder Vinylcarbonaten erfüllen jedoch nicht die hohen
Anforderungen an *in vivo* anwendbare Implantate, da Restmonomere zu Irritationen oder
Zelltoxizität führen können, und Polymere ein unerwünschtes Abbauverhalten oder
unzureichende Abbauraten aufweisen. Darüber hinaus weisen Materialien oft eine hohe
Sprödigkeit, hohen Schrumpf und geringe Festigkeit auf, was ihre Anwendbarkeit weiter
einschränkt.

In dieser Arbeit wurden zwei Strategien untersucht, bei denen kleine Molekülbausteine
verwendet wurden, um Photopolymere herzustellen, welche gute mechanische Eigenschaften mit
verbessertem Abbauverhalten kombinieren. Einerseits wurden cyclopolymerisierbare Monomere
(CPMs) untersucht, die Vorteile wie einen geringen Schrumpf und die Bildung rigider Polymere mit
zyklischem Rückgrat aufweisen und gleichzeitig den Einbau hydrolytisch labiler Gruppen in die
Monomerstruktur ermöglichen. Als abbaubare Motive wurden Acetal- und Carbonatgruppen
sowie Heteroatome wie Phosphor, Silizium oder Bor verwendet, die weniger stabile Bindungen zu
Sauerstoff im Vergleich zu Kohlenstoff ausbilden. Mehrere CPMs wurden erfolgreich synthetisiert
und auf ihre Cyclopolymerisationstendenz getestet, die jedoch sowohl mit radikalischen als auch
mit kationischen Initiatoren gering war. Folglich wurden Allylether- und Allylestermonomere
entwickelt, welche rigide Strukturelemente sowie Heteroatom-Sauerstoff-Bindungen enthielten.
Durch ihren Einsatz in Verbindung mit Thiol-En-Chemie wurden homogene und zähe Netzwerke
gebildet, die an den jeweiligen hydrolysierbaren Bindungen gespalten werden konnten. Zyklische
Borsäureester wurden als abbauverbessernde Verbindungen festgestellt, und zeichnen sich durch
eine einfache Synthese, deutlich geringere Toxizität im Vergleich zu (Meth)acrylaten und
geringeren Schrumpf aus. Weiters führen sie zu Materialien mit sehr guten mechanischen
Eigenschaften und beschleunigtem Abbau durch Oberflächenerosion bei Bedingungen, bei denen
die Knochenregeneration stattfindet. Letztlich wurde eine Teststruktur erfolgreich mittels 3D-
Druck hergestellt, was die Eignung dieser Monomere für die Herstellung von biokompatiblen und
bioabbaubaren Gerüststrukturen für die Knochenregeneration belegt.

Table of Contents

Introduction		1
Objective		33
General Part		53
Summary		171
Experimental Part		181
	Gen.	Exp.
1. Novel cyclopolymerizable monomers for enhanced mechanical properties and network degradation	53	181
1.1 Cyclopolymerizable model compounds	55	181
1.1.1 Synthesis of carbon-based model compounds	55	181
1.1.2 Synthesis of heteroatom-based model compounds	59	190
1.1.3 Reactivity towards cyclopolymerization	60	191
1.1.3.1 Radical cyclopolymerization	62	193
1.1.3.2 Cationic cyclopolymerization	63	193
1.2 Monomers with improved cyclopolymerization tendency	68	193
1.2.1 Synthesis of carbon-based cyclopolymerizable monomers	68	193
1.2.2 Synthesis of heteroatom-based cyclopolymerizable monomers	71	195
1.3 Resumé	72	
2. New monomers and thiols for enhanced mechanical properties and degradation of thiol-ene networks	73	196
2.1 Selection of monomers for improved network degradation	74	196
2.1.1 Model study of monomer hydrolysis	75	196
2.1.2 Screening of photoinitiator concentration for thiol-ene systems	77	196
2.1.3 Mechanical properties of model networks	78	196
2.1.4 Degradation behavior of model networks	81	197
2.2 Thiols for enhanced mechanical properties	84	198
2.2.1 Screening of thiols for improved mechanical properties	84	198
2.2.2 Syntheses of novel thiols	86	198

2.2.3 Mechanical properties of networks	88	201
2.3 New monomers containing heteroatoms	89	202
2.3.1 Compounds based on phosphorus	90	202
2.3.2 Compounds based on silicon	92	203
2.3.2 Compounds based on boron	93	204
2.4 Characterization of degradable systems	100	212
2.4.1 Reactivity of formulations	101	212
2.4.2 Mechanical properties of polymer networks	104	213
2.4.3 Degradation of polymer networks	108	214
2.5 Optimization of mechanical properties and degradation behavior	113	214
2.5.1 Optimization with a trifunctional crosslinker	115	214
2.5.1.1 <i>Reactivity of formulations with TAI</i>	115	214
2.5.1.2 <i>Mechanical properties of polymer networks with TAI</i>	120	215
2.5.1.3 <i>Degradation of polymer networks with TAI</i>	125	215
2.5.2 Optimization with a difunctional crosslinker	131	215
2.5.2.1 <i>Syntheses of difunctional crosslinkers</i>	133	215
2.5.2.2 <i>Mechanical properties of networks with difunctional crosslinkers</i>	134	217
2.5.2.3 <i>Reactivity of formulations with VSA</i>	135	218
2.5.2.4 <i>Mechanical properties of polymer networks with VSA</i>	141	218
2.5.2.5 <i>Degradation of polymer networks with VSA</i>	146	219
2.6 Influence of toughness enhancers	153	219
2.6.1 Rheological properties of formulations	155	219
2.6.2 Reactivity of formulations	156	220
2.6.3 Mechanical properties of polymer networks	158	220
2.7 3D printing	161	220
2.7.1 Characterization of the printing resin	161	220
2.7.2 Laser-SLA	163	221
2.8 Influence of sterilization on mechanical properties	166	222
2.9 Evaluation of cytotoxicity	169	222

Appendix	225
Materials and methods	256
Abbreviations	260
References	268

Introduction

The Skeletal System

The human skeleton serves as the internal framework of the body and is composed of around 206 bones for a healthy adult, which are connected by joints and assembled by a system of tendons, cartilage, and ligaments.¹ By this elaborate organization, the skeleton provides both structural support and flexibility for movement. Other functions include the protection of vital organs, acting as a mineral repository for calcium and phosphate, and production of hormones responsible for regulation of blood sugar and deposition of fat. Furthermore, the skeleton is the primary site for production of blood and stem cells, which takes place in the bone marrow.²⁻⁴

In general, the bones of the human body can be grouped into two divisions, the axial skeleton comprises 80 bones, which construct the central axis of the body, and the appendicular skeleton contains 126 bones, which are attached to the axial system, as depicted in Figure 1 A.⁵ According to their shape, a further classification into five categories (long, short, flat, irregular or sesamoid) is possible (Figure 1 B).⁶

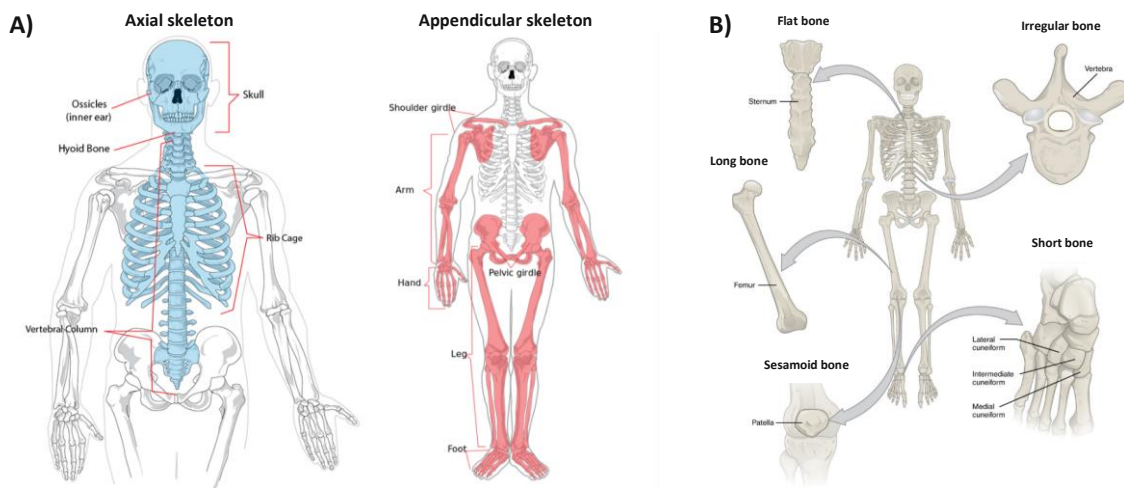


Figure 1: Classification of bones of the skeletal system according to their location into A) axial and appendicular skeleton⁵ and B) according to their shape into long, short, flat, irregular, or sesamoid bones.⁶

Bone as an organ is a highly specialized, micro- and nanocomposite tissue composed of an organic and an inorganic phase. The organic phase (35 % of dry weight) consists mainly of type I collagen (90%), which gives the hard tissue rigidity, viscoelasticity, and toughness. The other organic components are non-collagenous proteins, which can stimulate cellular functions responsible for bone formation and resorption. The mineral phase (65 w% of dry weight) is composed of

hydroxyapatite (HAP) nanocrystals with a hexagonal crystal structure and the chemical composition $\text{Ca}_{10}(\text{PO}_4)_6(\text{OH})_2$, and is responsible for structural reinforcement and stiffness.^{2, 4,7,8}

Bone tissue is organized in a hierarchical structure on numerous levels from the macroscopic down to the sub-nanoscale (Figure 2).⁹ Macroscopically, it consists of a dense outer shell of cortical bone, encompassed by trabecular bone, also referred to as spongy or cancellous bone, at the proximal and distal ends. Trabecular bone is composed of a network of rod and plate-shaped bony struts (*trabeculae*) comprising the bone marrow.^{10,11} While trabecular bone exhibits a porosity of 50-90%, cortical bone displays a denser structure, with a porosity of 3-12%.² On a smaller scale, collagen molecules first organize into triple helices, which are surrounded and infiltrated by HAP crystals and stacked parallel to form fibrils, fibers, and finally, layers, so-called *lamellae*. These *lamellae* wrap concentrically around a central canal (Haversian canal) containing nerve and blood vessels to form so-called osteons.^{11,12}

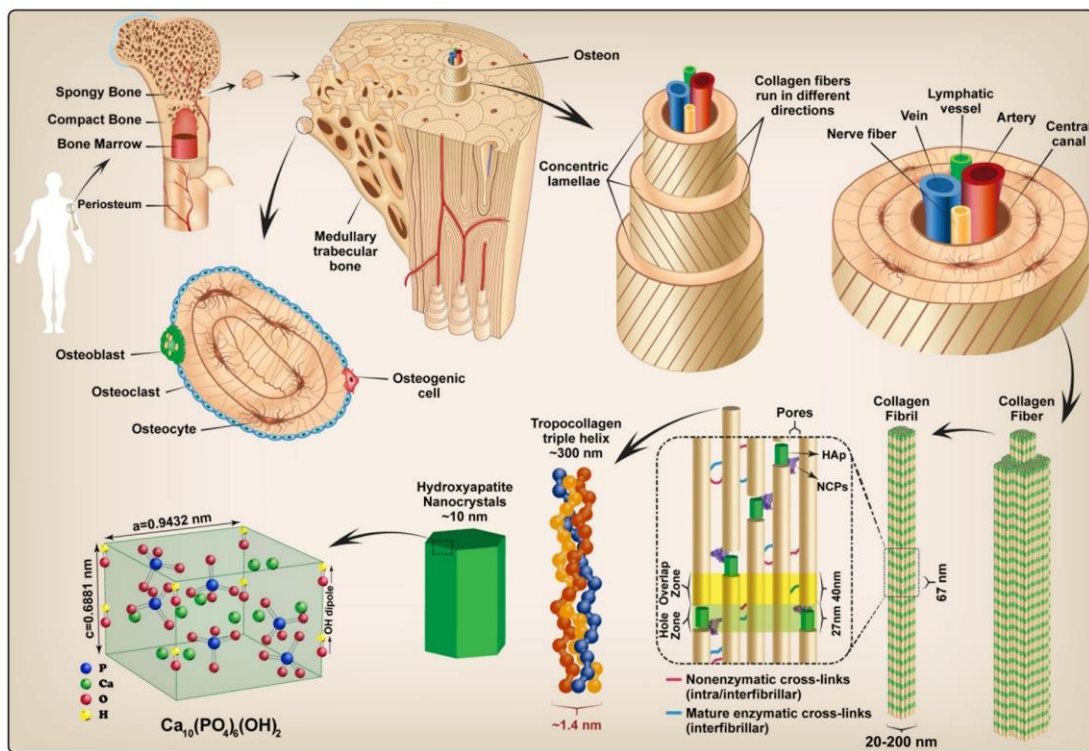


Figure 2: Hierarchical structure of bone from the macroscopic to the sub-nanoscale level.⁹

The mechanical properties of bone depend on the specific composition and the structure (trabecular or cortical bone, etc.).² Approximate values for important properties are summarized in Table 1.

Table 1: Mechanical properties of cortical and trabecular bone.²

Property	Cortical bone	Trabecular bone
Tensile strength [MPa]	50-150	10-20
Strain at break [%]	1-3	5-7
Fracture toughness [MJ/m ³]	2-12	-

Bone is a dynamic tissue continuously being remodeled in response to influences, such as mechanical loading and calcium homeostasis, and it is estimated that 10-15% of human bone is replaced with new bone tissue every year.^{2-4,13} It is populated by four cell types responsible for the bone remodeling process, including bone maintenance, resorption, and re-formation.^{8,14}

Osteoclasts, bone-resorbing cells, originate from hematopoietic stem cells, which fuse to form these multinucleated cell types. For bone resorption, they form a tight junction between the bone surface and small projections (*microvilli*) on their membrane before secreting acid, enzymes (most important among them acid phosphatase), and matrix metalloproteinases, which are able to dissolve collagen, non-collagenous proteins, and HAP. By this, the pH decreases from 7.4 to ~4, and erosive pits are formed on the bone surface, called Howship *lacunae*. Resulting bone fragments are digested within cytoplasmic vacuoles of the osteoclasts, and dissolved mineral ions are released into the bloodstream.^{9,15-19}

Osteoblasts, bone-forming cells, originate from mesenchymal stem cells, which first differentiate into osteogenic and then further to osteoblasts in the tissue covering the outer bone surface (*periosteum*) and the bone marrow cavity (*endosteum*). They produce many different cell products, including alkaline phosphatase, growth factors, hormones such as osteocalcin, and unmineralized type I collagen, called osteoid, which is subsequently mineralized through the accumulation of HAP. Eventually, the osteoblast is entrapped in the growing bone matrix and becomes an osteocyte. These cells form networks connected by channels and act as mechanosensors in the bone, able to regulate osteoblast and osteoclast activity by releasing signaling molecules.^{9,15-18,20-23}

The last cell type, bone lining cells, are modified osteoblasts, which form a protective layer on bone areas, currently not in the state of remodeling and regulate the flux of mineral ions into and out of the bone.^{24,25}

The bone remodeling process, therefore, consists of four phases: activation, resorption, reversal, and formation. In the activation phase, preosteoclasts are recruited to the bone surface, where they form multinucleated osteoclasts. After osteoclastic bone resorption in the resorption phase, the reversal phase occurs, in which the osteoclasts die, and mononuclear cells appear on the surface, which prepare the bone surface for attachment of bone-forming osteoblasts by providing signals for their differentiation and migration. Subsequently, osteoblast progenitors are recruited, and in the formation phase, mature osteoblasts form the osteoid until the old tissue is completely replaced by new bone. The bone surface is then covered by bone lining cells, leading to a resting period until a new bone remodeling cycle begins. This process is highly regulated to guarantee a balance between osteoblast-mediated bone formation and osteoclast-driven bone resorption without a major alteration in net bone mass or mechanical properties. Dysregulation of this essential metabolic function may cause excessive bone resorption causing osteoporosis.¹⁴

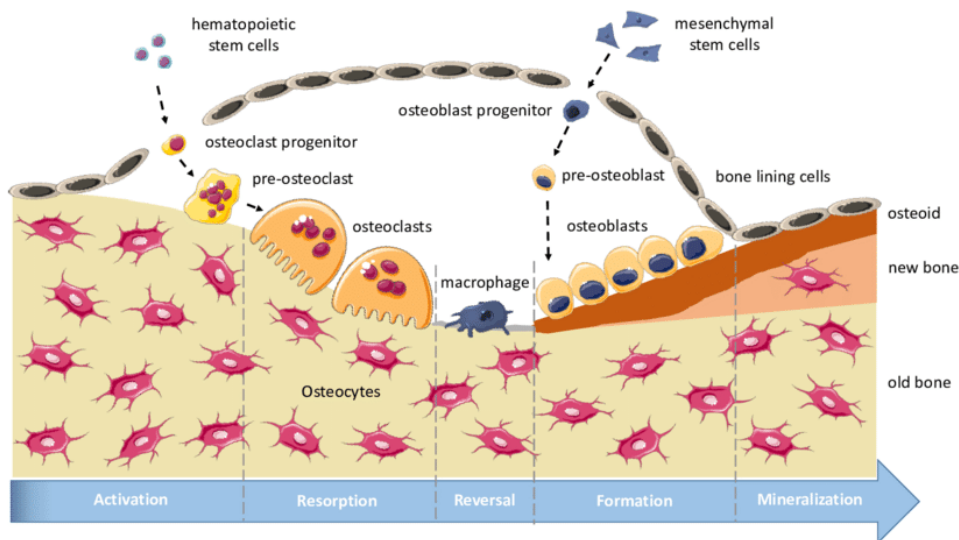


Figure 3: Phases of bone remodeling: activation, resorption, reversal, formation, and mineralization.²⁶

In contrast to other tissues, bone is capable of healing without the formation of scar tissue.² A bone fracture is defined as a disruption of the structural continuity of the bone, with injuries to the surrounding soft tissue.²⁷ Similar to bone remodeling, bone regeneration also consists of four steps. Immediately following the fracture, a hematoma forms (Figure 9 A) due to the rupture of blood vessels supplying the bone, which clots and forms a temporary protective layer. Cytokines are subsequently secreted, attracting cells, which remove damaged tissue and secrete vascular endothelial growth factor (VEGF) to stimulate the healing process at the fracture site. This leads to the formation of new blood vessels, and within the hematoma, granulation tissue is formed. Fibroblasts, chondroblasts, and osteoblasts are recruited to the area and form a soft, collagen-rich fibrocartilaginous network, the so-called soft callus connecting the broken bone ends (Figure 9 B).

Around this callus, a layer of woven bone is deposited. The hyaline cartilage is then resorbed and calcified while more layers of woven bone are laid down, leading to the formation of a hard, bony callus of immature bone (Figure 9 C). This hard callus then undergoes repeated remodeling by action of osteoblasts and osteoclasts, and ultimately, the center is replaced by compact bone, while trabecular bone is formed at the proximal and distal ends (Figure 9 D). This process can last from months to years, ultimately resulting in the formation of bone, which does not differ structurally or mechanically from the surrounding, undamaged tissue.^{2,27-31}

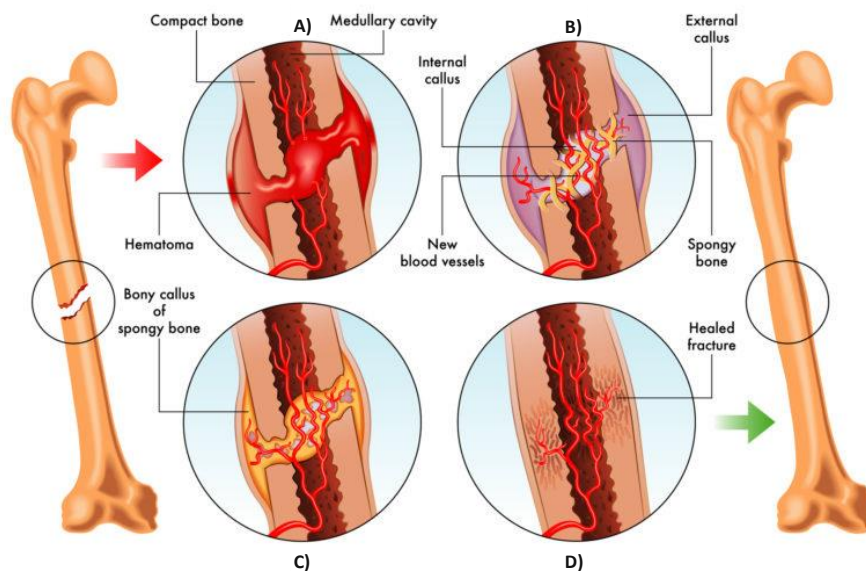


Figure 4: Four stages of bone regeneration; A) Hematoma formation; B) Soft callus formation; C) Bony callus formation; D) Bone remodeling;³²

Fracture Treatment

Despite the tremendous regenerative capacity of bone, this process cannot be accomplished after critical bone loss caused by high-energy trauma, infection requiring extensive debridement, or tumor resection. The critical size of these defects depends on many factors, such as the absolute versus the relative size, the soft tissue environment, the age of the patient, and the presence of chronic disease. For example, due to the favorable soft tissue environment of the femur, spontaneous healing of defects with a size of 6-15 cm has been reported, while lack of spontaneous healing was determined for defects in the tibia, which exceed 1-2 cm.³³ Furthermore, it is estimated that 5-10% of all fractures display delayed healing or even fail to heal completely.²

Therefore, these fractures require further surgical intervention, and bone transplants, so-called bone grafts, remain the conventional therapy. Until today bone is still the second most

transplanted material, with only blood being transplanted more frequently.^{2,30} Autologous bone grafts (autografts) originate from different areas of the skeleton of the same patient, such as the iliac crest or the mandibular symphysis.^{34,35} The treatment of defects with autologous bone is still considered the golden standard, as it combines all the properties desired in a bone graft. It acts as a scaffold for the ingrowth of bone-forming cells (osteoconductive), promotes the proliferation of osteoblasts (osteoinductive), and contains cells that can form new bone tissue (osteogenic). Nevertheless, the amount of autologous graft is limited, an additional surgical procedure is required, and a high risk of donor site morbidity was observed in patients. Allogeneic grafts (allografts) from a donor comprise a high risk of transmission of infections, as well as the risk of lifelong immunosuppression therapies due to incompatibility, which were also reported for xenogenic materials (xenografts), originating from other species.^{2 4}

These limitations of current clinical therapies necessitated the development of alternative approaches using synthetic replacement materials (synthografts), thereby reducing the risk of transmission of diseases, immunogenic reactions, and the number of surgical procedures.²

Tissue Engineering and Regenerative Medicine

Tissue engineering (TE) and its application in regenerative medicine were introduced in 1993 as an interdisciplinary field of science, combining knowledge from chemistry, medicine, and mechanical engineering. From this new field, bone tissue engineering (BTE) emerged as a promising approach to repair bone defects. The “diamond concept” underlying BTE is to generate an osteoconductive three-dimensional scaffold with sufficient mechanical properties that contains osteogenic cells and osteoinductive factors and promotes vascularization (Figure 5).² Despite years of research, apart from autografts, no currently available bone substitute material combines all these properties.

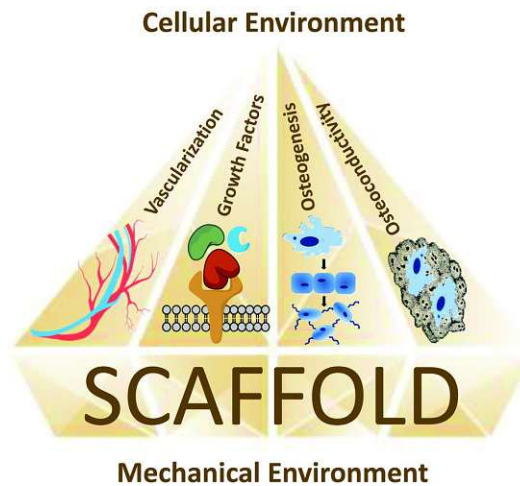


Figure 5: Diamond concept for scaffolds used in bone tissue engineering.³⁶

A reason for that are the highly specific standards demanded for three-dimensional scaffolds in BTE. Regarding the structure, an ideal scaffold should be highly porous with interconnected pores for cell growth and allow the flux of nutrients and metabolic waste. Furthermore, the optimal surface should allow the attachment, migration, proliferation, and differentiation of bone-forming cells and their progenitors. In general, good mechanical properties such as high strength and toughness of the scaffold are required, matching the properties of the replaced bone for good load dissipation and tissue integration. Above all, the material should be biocompatible and not cause an immune response or have toxic effects. As the scaffold is designed as a temporary support, it should also be biodegradable, with degradation rates matching the growth speed of newly formed tissue (Figure 6). Upon degradation, low molecular weight compounds should be formed, which should be non-toxic, easily metabolized, and removed from the body. For metabolization or elimination via the liver or kidneys, a prerequisite is water solubility of the products. In BTE, the desired degradation kinetics depend on the type and location of the replaced bone tissue and are patient-specific, but in general, degradation should be exhibited in the order of 3-12 months to enable tissue remodeling and vascularization.^{2,37-39}

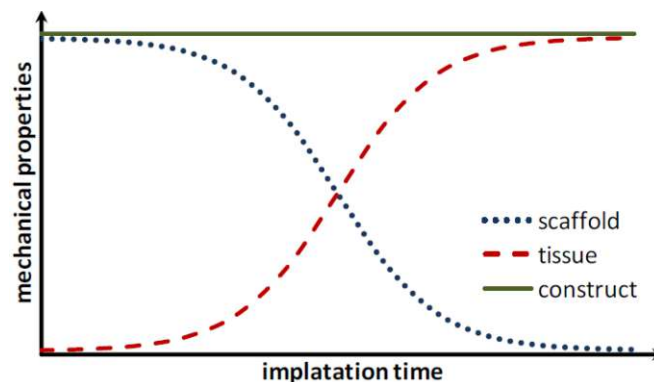


Figure 6: Schematic of the ideal degradation behavior of a biodegradable scaffold at the same rate, at which new tissue regenerates.⁴⁰

Most widely used synthetic bone substitute materials include bioglasses, derived from acidic oxides (aluminum oxide, silicon dioxide)^{41,42}, ceramics composed of HAP or tricalcium phosphate⁴³⁻⁴⁵, metals and alloys⁴⁶⁻⁴⁸ or composites^{9,49}. Additionally, bio-inert synthetic polymers such as poly(ethylene) (PE), especially ultra-high-molecular-weight poly(ethylene) (UHMWPE), poly(urethane) (PU), poly(ether ether ketone) (PEEK), poly(tetrafluoroethylene) (PTFE) or poly(ethylene terephthalate) (PET) are commonly used in orthopedic implants, *i.e.*, as artificial joints, vertebrae or bone plates.⁵⁰ Nevertheless, all of these materials exhibit drawbacks, especially insufficient mechanical properties and degradability, with a good overview given by Bose *et al.*⁴⁹, Henkel *et al.*², and Davison *et al.*⁵¹

Therefore, degradable bone substitute materials are required in BTE. Biodegradability of polymers can either occur via hydrolytic or enzymatic degradation or a combination of both.⁵² In general, the hydrolytic degradation rate is quite complex and dependent on several factors, such as the nature of the labile bond, hydrophilicity of the material defining the extent of water uptake, the accessibility of the cleavable bonds to enzymes and water, as well as other parameters such as morphology, crystallinity and molecular weight.⁵¹

In principle, the erosion of polymers can be classified as a bulk erosion or surface erosion process. Bulk erosion occurs when the rate of water penetration exceeds the rate of hydrolysis, leading to chain scission throughout the specimen. This results in an abrupt decrease in molecular weight and hence mechanical properties, whereas a delayed mass loss is observed, shown in Figure 7 B. The dimensions of the specimens remain virtually unchanged until abrupt disintegration occurs at a critical time point (Figure 8 B). As hydrolysis occurs throughout the specimen, hydrolysis products are unable to diffuse and accumulate in the interior of the material. Hence, in the case of acidic degradation products, this process is further autocatalyzed, resulting in autocatalytic bulk erosion (Figure 8 C).^{51,53} Therefore, bulk erosion is undesired, as an abrupt failure of the implant occurs, and the local decrease in pH can promote inflammatory response and tissue necrosis.

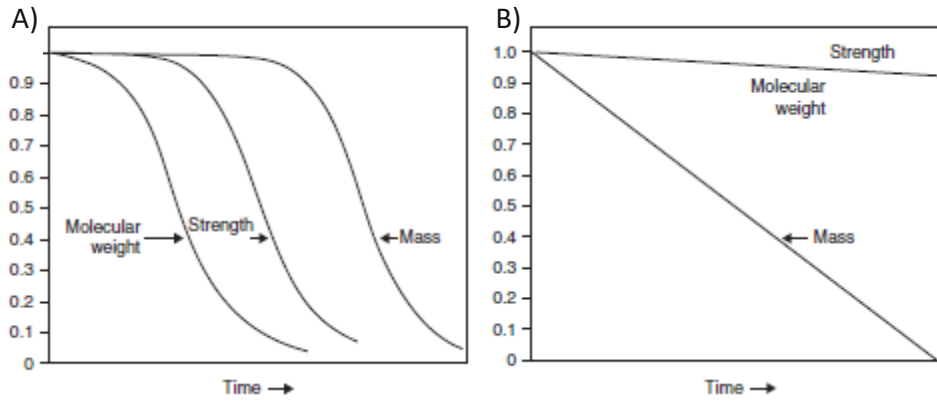


Figure 7: Molecular weight, strength, and mass over time for A) surface erosion, B) and bulk erosion.⁵¹

Preferably, surface erosion of materials should be displayed, during which hydrolysis is faster than the diffusion of water into the bulk polymer. This leads to a loss in both size and mass over time, while the molecular weight and mechanical properties do not change (Figure 7 A). Furthermore, the loss of the material is confined to the surface, and the structural integrity of the specimen is maintained throughout the degradation process (Figure 8 A). For this degradation mechanism, a certain hydrophobicity of the material is required to restrict water penetration. Furthermore, rather labile bonds towards hydrolysis are needed to accelerate hydrolysis rates at the surface, and no acidic hydrolysis products should be formed to prevent autocatalysis.⁵¹

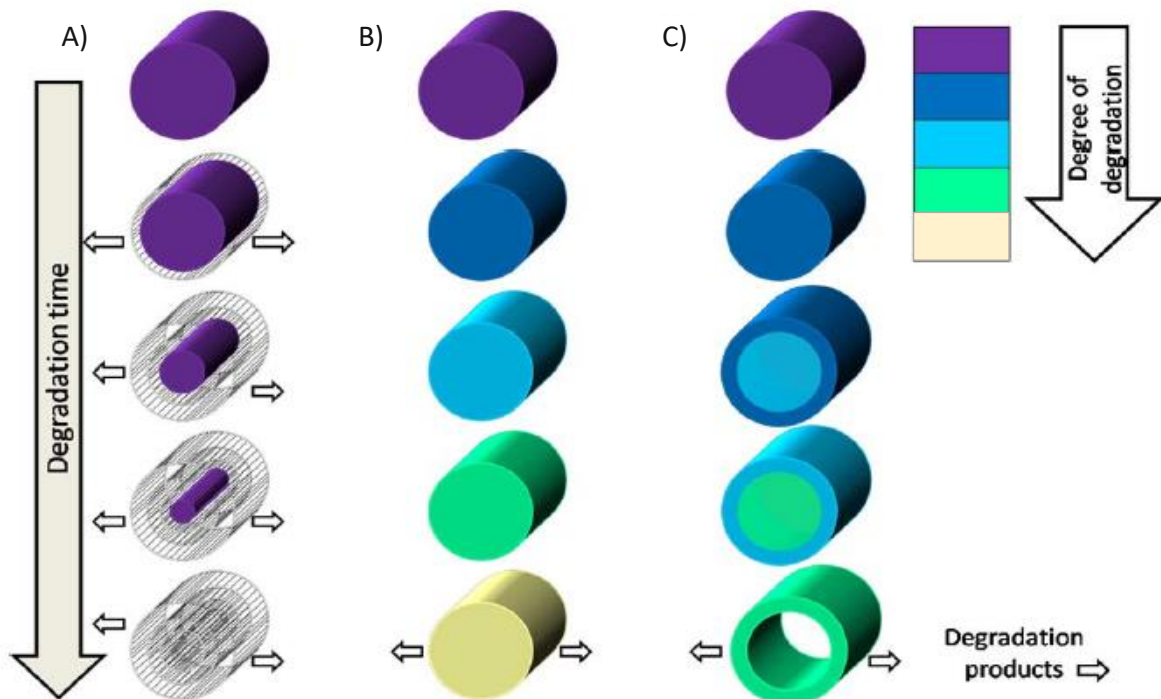


Figure 8: Different degradation mechanisms for polymers: A) Surface erosion, B) bulk degradation, and C) autocatalytic bulk erosion.⁵³

Biodegradable polymers used in TE can be classified as natural biopolymers or synthetic polymers. Biopolymers derived from natural sources, such as proteins and polysaccharides, have been used in biomedical applications for centuries, with a broad spectrum of mechanical properties at hand.^{54,55} They bear the advantage of being similar or identical to substances, which can be recognized, enzymatically degraded, and metabolized by the body, typically evoke little to no immune response, and show high bioactivity by providing selective binding sites for cells. In BTE, used proteins include collagen, the major component of muscles and skin, its degradation product gelatin, studied in the preparation of degradable hydrogels and fibrin, a blood coagulant used for hemostasis and tissue sealants. Prominent examples of polysaccharides are hyaluronic acid, which is abundant in every tissue in vertebrates and plays an important role in wound healing, as well as other glycosaminoglycans such as alginate and chitosan.^{39,56} A major drawback, however, is that the number of these natural polymers and possible modifications to improve or alter their mechanical properties are limited, and pathogenic risks may be associated with materials of animal or human origin. Furthermore, since natural sources are prone to batch-to-batch variability and challenging regarding purification and processability, the quality and specific properties can fluctuate. Furthermore, since degradation depends on the availability of enzymes at the implantation site, the control and prediction of degradation rates *in vivo* are difficult.⁵¹

Compared to biopolymers of natural origin, synthetic polymers comprise the advantage of predictable mechanical properties and degradation rates while being biologically inert with fewer pathogenic risks.⁵¹ Labile bonds employed include esters⁵⁷, orthoesters⁵⁸, anhydrides⁵⁹, carbonates⁵⁹, acetals⁶⁰ and ketals⁶¹. Synthetic, hydrolytically degradable polyesters such as poly(lactic acid) (PLA), poly(glycolic acid) (PGA), and poly(caprolactone) (PCL) are considered the golden standard in tissue engineering (Figure 9), which degrade in the order of years under hydrolytic conditions.^{51,62}

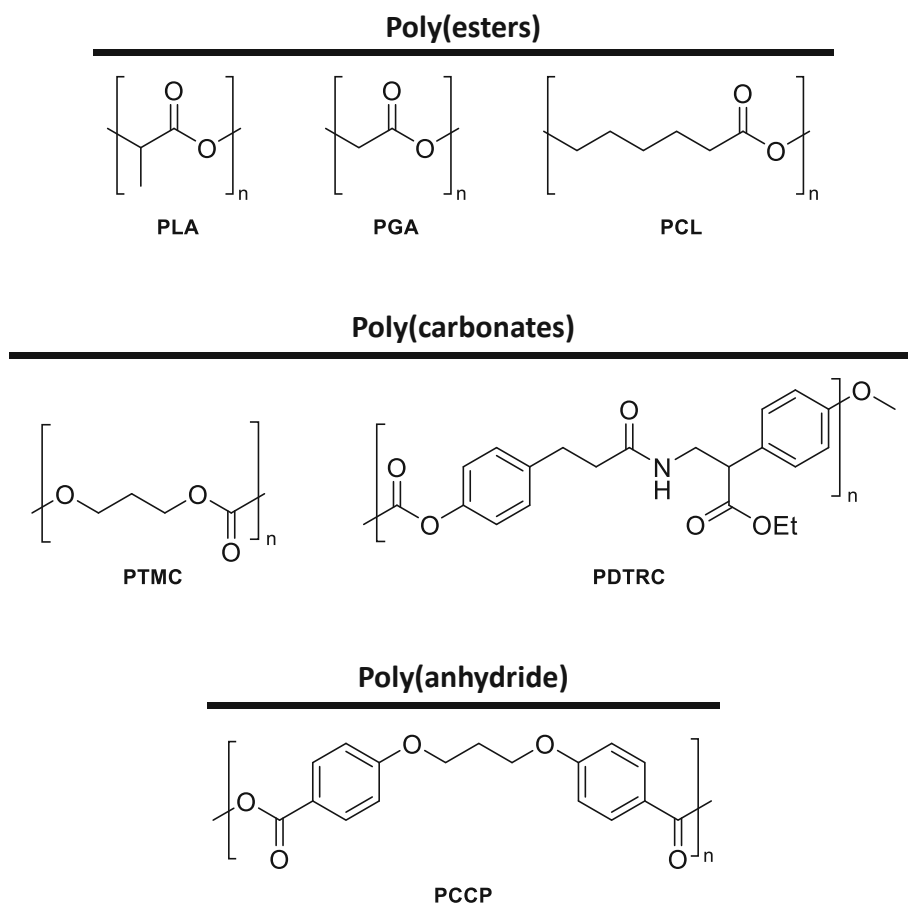


Figure 9: Chemical structures of synthetic biodegradable poly(esters) PLA, PGA, and PCL, poly(carbonates) PTMC and PDTRC, and poly(anhydride) PCCP.

Starting in the 1960s, degradable PGA sutures were used in surgery, and since then, this polymer was also utilized for degradable implants.³⁹ Due to its chiral carbon center, PLA exists in three isomeric forms. As D-lactide cannot be metabolized, only poly(L-lactide) and the copolymer of the racemic mixture of L- and D-lactide are important. While poly(L-lactide) is a semi-crystalline thermoplastic used for load-bearing applications in orthopedics, the copolymer is amorphous with lower strength and typically used in drug delivery applications.⁶³ PCL is obtained by ring-opening polymerization of ϵ -caprolactone, which is abundant and cheap. Due to its hydrophobicity, degradation rates are rather slow, and good drug permeability is provided, making it ideal for long-term drug delivery systems. A major drawback of these polymers is their degradation behavior, which follows an autocatalytic bulk erosion mechanism due to the formation of acidic hydrolysis products, which may also cause a strong inflammatory response or tissue necrosis.^{53,64,65}

Alternatively, poly(anhydrides) and poly(carbonates), containing more labile functionalities, can be used, which leads to materials degrading within minutes to days.⁵⁷ Due to the less stable bonds, these polymers may display preferable degradation via surface erosion. Examples include the

poly(anhydride) poly(carboxy phenoxy propane) (PCCP) and the poly(carbonates) poly(trimethylene carbonate (PTMC) and poly(desaminotyrosyl tyrosine ethyl ester carbonate) (PDTRC) (Figure 9).⁵¹ Recently, the great potential of these materials as bone replacement materials⁶⁶⁻⁷⁰, orthopedic implants^{71,72}, and soft tissue materials⁷³ was demonstrated.

Fabrication Techniques for Porous Bone Scaffolds

According to the requirements for scaffolds used in bone tissue engineering, precise control over the three-dimensional structure is essential. While macroscopically, a good fit of the scaffold in the defect site is required, microscopic structural control is necessary to optimize osteoinduction, osteoconduction, osteogenesis, and vascularization. Even the structure on a nanoscopic level is crucial, as it determines whether protein adsorption and adhesion, differentiation, and proliferation of cells can occur.^{2,74} Based on these requirements, various techniques have been developed in order to produce repeatable scaffolds with a controlled hierarchy of pores.

Conventional means for scaffold fabrication include, among others, solvent-casting and particulate-leaching, gas foaming, phase separation, and freeze-drying, with a schematic overview of each technique given in Figure 10.⁷⁵

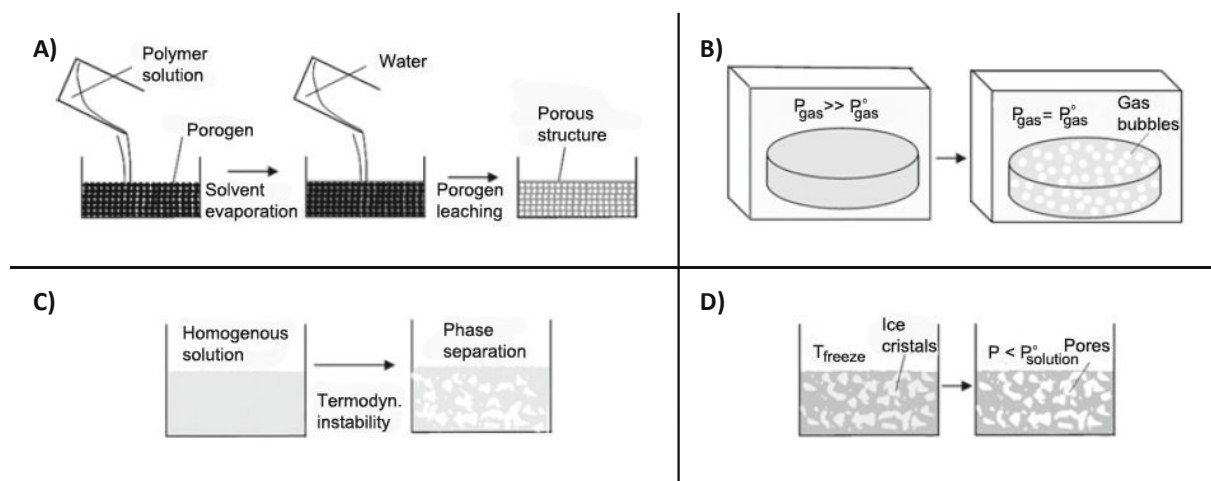


Figure 10: Schematic overview of conventional scaffold fabrication techniques: A) solvent-casting and particulate-leaching, B) gas foaming, C) phase separation, and D) freeze-drying. Adapted from Ning *et al.*⁷⁶

Solvent casting (Figure 10 A) is a simple and established method for the production of polymer scaffolds with interconnected porosity, in which salt particles of the required pore size are uniformly mixed with a polymer solution.⁷⁷ Evaporation of the solvent results in a polymer matrix with embedded salt particles, which are leached out upon immersion in water to produce structures with up to 93% porosity and pore diameters up to 500 μm .⁷⁶ Another method for

scaffold production includes gas foaming (Figure 10 B), during which polymer solutions are pressurized into a solid form with gas-foaming agents such as CO₂, nitrogen, water, or fluoroform until saturated, resulting in the nucleation and growth of gas bubbles upon pressure reduction. By this, pores in the range of 100 to 500 μm can be generated.^{75,78} Phase separation (Figure 10 C) presents another powerful process to manufacture porous implants, in which a homogeneous polymer solution is quenched, resulting in phase separation. Quenching is either obtained by immersion in a non-solvent, referred to as non-solvent induced phase separation (NIPS), or by applying low temperatures, specified as thermally-induced phase separation (TIPS). By this, a polymer-rich and a polymer-poor/solvent-rich phase are formed. The scaffold matrix is created upon solidification of the polymer-rich phase, whereas the polymer-poor phase is removed by extraction, sublimation, or evaporation, leaving behind a highly porous polymer network.^{75,76} Furthermore, freeze drying or lyophilization (Figure 10 D) is considered a conventional technique to obtain porous scaffolds for BTE. In this method, a water-based polymer solution is frozen, leading to the formation of ice crystals, which force polymer aggregation in the interstitial spaces. Upon application of a pressure lower than the equilibrium vapor pressure of the solvent, solvent sublimation occurs, leaving behind a dry scaffold with interconnected pores of different shapes and sizes.^{75,76}

All of these conventional methods comprise the severe drawback of being subtractive in nature and hence incapable of precise control over pore sizes, pore geometries, pore interconnectivity, pore distribution, and the fabrication of internal channels. Additionally, significant amounts of materials are wasted during manufacturing, and organic solvents are often applied, with residues reducing the biocompatibility of the scaffold due to cytotoxic effects exerted on the cells.^{2,74} With the introduction of additive manufacturing technologies (AMTs) in the medical field in the 1990s, most of these restrictions were overcome.

Additive Manufacturing Technologies

In additive manufacturing (AM), three-dimensional objects are generated in a computer-controlled layer-by-layer fabrication process. For this, a computer-aided design (CAD) or a 3D scan of an existing structure is used to create a three-dimensional model (a), which is then virtually sliced into two-dimensional planes (b). Subsequently, the object is produced layer by layer under computational control (c) with temporary support structures for overhanging elements (Figure 11).⁷⁹⁻⁸²

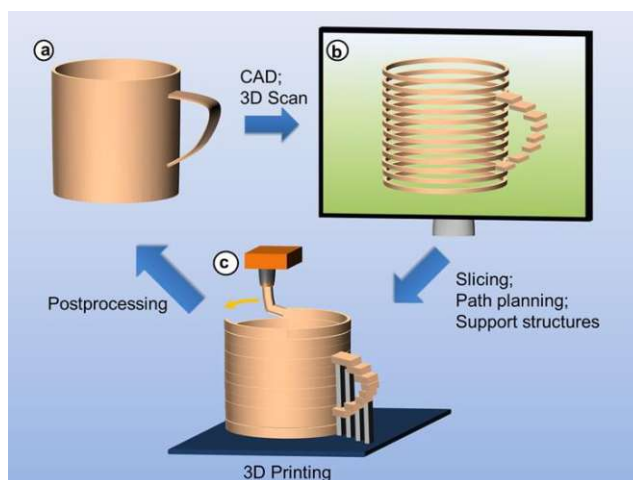


Figure 11: Basic principle of additive manufacturing processes.⁸³

In the medicinal sector, AM was initially only applied in the production of prototypes (rapid prototyping), such as 3D models of bone pathologies in orthopedics and neurosurgery, to plan surgical procedures.² With recent technological advances, such as significantly improved repeatability, accuracy, and material range, AM is used nowadays to produce surgical tools (rapid tooling) and patient-specific implants (rapid manufacturing).⁸²

In BTE, the introduction of AM marked a major breakthrough, and these techniques have now become the new gold standard for the fabrication of scaffolds. Next to freedom in design, they allow for the fabrication of precise, complex structures containing internal substructures such as pores and channels out of metals, ceramics, and polymers. No expensive molds, tools, or machining typical for conventional formative or subtractive fabrication methods are required, and less material is wasted during production.⁷⁹⁻⁸² Furthermore, few process steps and little manual interaction are needed, allowing the economical production of customized, patient-specific tissue engineering scaffolds in hours to days.² Due to recent efforts to increase the production speed, such as the development of continuous liquid interface production (CLIP) by Tumblestone *et al.*⁸⁴, even the limit in the produced number of parts can be overcome.

The overall AM market is currently valued at around 8 billion euros, with a projected growth of 18% until 2026. The polymer-based AM is the most profitable sector, with the aerospace, turbine, and helicopter industry covering the largest share, followed by the medicinal industry.⁸⁵

For AM of polymers, two approaches are distinguishable. The first approach includes methods, in which polymers are processed in the form of powders or filaments. In particle bonding techniques, such as selective laser sintering (SLS), polymer particles are fused by a laser beam scanning the surface of the powder bed. Melt-dissolution deposition systems, such as fused deposition modeling (FDM), form each layer via extrusion of a meltable polymer filament through a heated

nozzle, which is then fused with the previous layer by heat conductivity.^{81,82} This method is especially relevant in TE, as it allows the production of scaffolds with interconnected pores from thermoplastic polymers such as PCL.^{53,86}

The second principle is based on photopolymerization, in which polymers are synthesized *in situ* from liquid resins via irradiation with light. In material jetting (MJ), different photosensitive resins can be dispensed through the nozzles of the printer and subsequently cured via UV light, enabling the fabrication of parts consisting of several materials or dissolvable support structures within printed structures. The other and more significant class of light-based methods is represented by lithography-based AMTs (L-AMTs), such as laser-based stereolithography (Laser-SLA), digital light processing-based stereolithography (DLP-SLA), and two-photon induced polymerization (2PP). In these methods, an initially liquid photopolymerizable resin is located in a vat and selectively exposed to light by a coherent light source. While Laser-SLA and 2PP use lasers, an LED light source with a digital micro mirror device chip is utilized in DLP-SLA. As the polymer is only formed in irradiated areas, superior precision is exhibited compared to methods such as SLS or FDM, and structures with resolutions up to the nanometre scale can be obtained.⁸⁷ Additionally, surface topology and feature sizes of patient-specific implants produced with these methods were found to be highly beneficial for bone regeneration.^{88,89}

Laser-based stereolithography

Introduced in the 1980s, laser-based stereolithography (Laser-SLA) is the oldest lithography-based AMT, in which the photoactive resin is exposed to the light of a laser beam with energies ranging from UV to the visible spectrum of light. The lateral position of the laser is determined by a pair of movable mirrors within a Galvano scanner, which utilize different tilt angles for scanning the beam along the xy-plane. By this, very thin polymer layers are formed, which stack up to create the solid structure.⁸² This can either be performed from the top (bottom-up) or from below through a transparent vat (upside-down or top-down). The conventional top-down approach benefits from larger building volumes and reduced forces on the part during structuring. However, it suffers from high amounts of resin necessary to fill the vat and increased oxygen inhibition during photopolymerization resulting in tacky surfaces of the objects. Both can be prevented by using the upside-down approach depicted in Figure 12. In this process, a layer is polymerized onto the platform via irradiation. Subsequently, the platform moves up along the z-axis, and the part is submerged under fresh resin, from which the next layer is formed. In this approach, adhesion of

the part to the building platform rather than the vat is crucial to prevent detachment during the printing process.⁹⁰⁻⁹³



Figure 12: Principle of upside-down Laser-SLA.⁹⁴

Laser-SLA offers excellent control over the spatial resolution of generated objects. Outstanding lateral resolutions of 0.1-5 μm can be obtained, primarily dependent on the spot size of the laser. The vertical resolution is influenced by the penetration depth of the light source, which depends on the irradiation time and intensity of the laser and can be regulated by the addition of light-absorbing compounds. High curing speeds, smooth surfaces, and high precisions of objects are attainable, which, however, can be limited by shrinkage stress during the curing reaction.^{90,95,96} A downside of this method is the rather limited material portfolio, as state-of-the-art resins are based on (meth)acrylates and epoxides. Due to the high crosslinking density, usage of these resins typically results in very brittle parts, which exhibit poor (thermo)mechanical properties. However, the development of novel monomers yielding polymers with enhanced properties is currently under extensive research.^{70,97-101} Another disadvantage is the high cost of the irradiation system. Nevertheless, Laser-SLA is still considered a benchmark, unparalleled in combining high building speeds with superior resolution.^{81,90}

Digital light processing-based stereolithography

Similar to Laser-SLA, digital light processing-based SLA (DLP-SLA) uses a light source to selectively polymerize resins.¹⁰² However, DLP-SLA utilizes an inexpensive LED light source combined with a digital micromirror device (DMD) chip, with wavelengths ranging from UV- to visible light. The DMD controls which areas are irradiated and one whole layer at a time is cured based on the CAD

model. Similar to Laser-SLA, DLP-SLA either follows a top-down or bottom-up approach for generating the 3D structure, with the latter being illustrated in

Figure 13. Here, a coating blade is used to apply a new layer of unpolymerized resin.^{68,91,103}

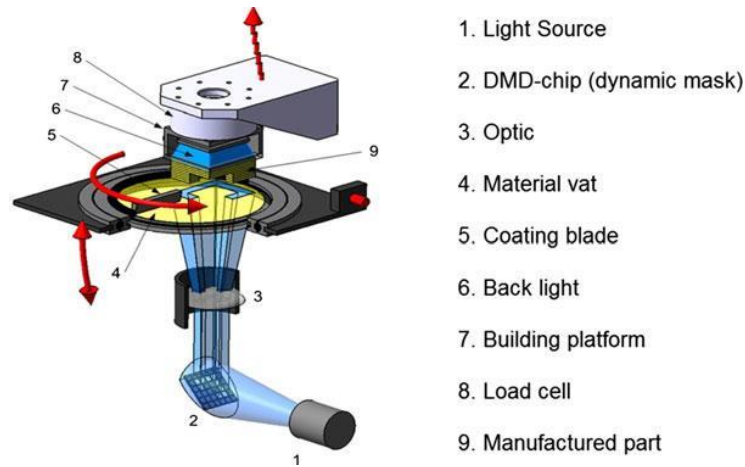


Figure 13: Principle of digital light processing-based stereolithography.¹⁰⁴

In DLP-SLA, the lateral resolution depends on the number and density of mirrors, hence pixels in the DMD, and the optics used for the projection. In general, it is lower compared to Laser-SLA and within the range of 10–50 μm . Nevertheless, the irradiation apparatus is cheaper, and due to the production of one layer at a time, building times for objects are considerably shorter. As in Laser-SLA, a limited number of possible resins is available, and high brittleness of parts is exhibited.^{90,95}

Two-photon polymerization

As the name suggests, two-photon polymerization (2PP), also called multiphoton lithography, is based on the simultaneous absorption of two photons. This is a non-linear process, in which a volume of photosensitive resin is exposed to NIR-femtosecond laser pulses. In the focal point of the laser, two photons are absorbed at once, and the resin solidifies. The principal setup of a 2PP printer is depicted in Figure 14. Femtosecond laser pulses are emitted and tightly focused into a certain resin volume, while a waveplate (WP) combined with a beam splitter (BS) are used as an attenuator and an acusto-optical modulator (AOM) together with an aperture act as a fast shutter. The laser focus is positioned inside the photosensitive resin via a beam expander (BE), and a Galvano scanner (GS), and a camera is used for online monitoring of the process.¹⁰⁵

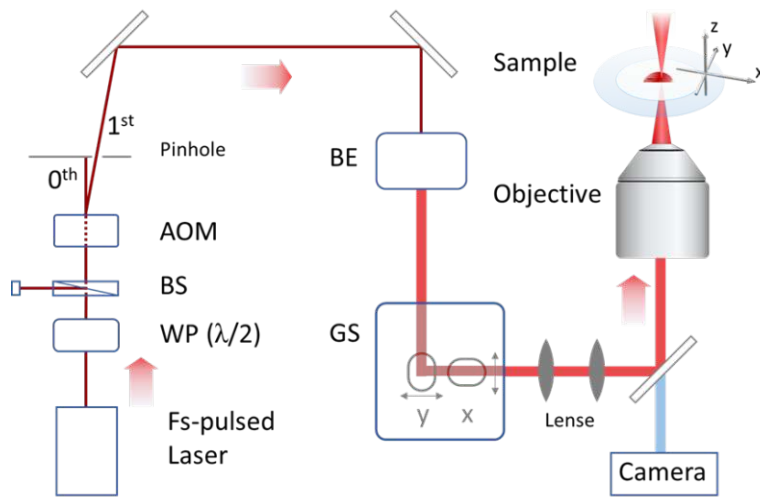


Figure 14: General setup of a 2PP-printer.^{106,107}

Due to this highly localized deposition of light, 3D-micro- and nanostructures can be produced at a resolution of a few hundred nanometers beyond the diffraction limit of the used light. As photopolymerization occurs only in the focal point of the laser, while the rest of the resin remains transparent, no layer-by-layer deposition of material is needed as in conventional AMTs. Therefore, this light-based method is the only true 3D-printing technique, as structures can be produced throughout the whole resin volume. This makes this process attractive in various applications, including the manufacturing of microlenses, photonic crystals, and microscaffolds used for biomedical applications. Drawbacks, however, include the low production speeds and, as a result, the size of printable structures in reasonable time scales, limiting the use of this technique for the production of macroscopic bone replacement materials.^{105,108}

Photopolymerization

In general, photopolymerization is a process that uses electromagnetic irradiation to solidify liquid organic materials consisting of monomers, oligomers, or polymers, typically in combination with a light-sensitive component, the so-called photoinitiator (PI).¹⁰⁴ When exposed to photons with energies confined to the UV-, visible, or Near-IR spectrum of light, excitation of the PI occurs, which then induces the polymerization reaction.^{109,110} Nowadays, photocuring is the most rapidly growing polymerization method in industry due to the vast economic and ecologic advantages compared to conventional thermal curing techniques. It comprises higher spatial resolutions, the absence of solvents, low emission of organic compounds, high curing speeds even at room temperature, low energy consumption, and low costs.^{104,109,111} In addition, LEDs have replaced

traditional mercury lamps, which require even less energy, and for some applications, even conventional lamps or sunlight can be used for curing. Therefore, photopolymerization is often regarded as “green chemistry”.^{99,104,109-111}

When introduced in the 1940s, restriction of the curing depth in the range of millimeters caused by absorption processes of either the photoinitiator, photoinitiator by-products, additives, or the monomer, made these light-activated systems only applicable for protective and decorative coatings of paper, wood, metals or plastics.¹¹² Nevertheless, due to extensive research, curing depths could be successfully improved, resulting in the expansion of applications to dental fillings, optical materials, adhesives, biocompatible and biodegradable polymers used in medical applications and additive manufacturing technologies (AMTs).^{99,104,109-111}

Photosensitive formulations are a mixture of several components to adapt to certain requirements and different applications, while the essential parts are a light source, a polymerizable monomer, and the photoinitiator (PI). For applications in industry, formulations often demand the addition of numerous compounds, such as stabilizers, inhibitors, fillers, plasticizers, pigments, surfactants, regulators, *etc.*, and often a complex mixture of different monomers and initiators is required.^{111,113} Monomers for photopolymerization are molecules containing polymerizable groups with a high amount of trapped chemical energy, such as carbon-carbon double bonds or strained rings, and their structure stands in direct correlation with the final properties of the cured polymer. The photoinitiator is needed, as the direct formation of the reactive species from the monomer is inefficient. Upon irradiation, this compound generates reactive radical or ionic species, which can then initiate free-radical, cationic, or anionic photopolymerization, while radical photopolymerization is by far the most widely used in industry.¹¹⁰

The mechanism of free-radical photopolymerization consists of four steps, which are displayed in Figure 15. First, excitation of the PI occurs via light absorption, causing the formation of radical species R_i^* . These radicals then cause initiation of the polymerization by attacking the reactive group of a monomer (*i.e.*, a double bond), generating the propagating species. During propagation, further monomers are added to the propagating chain end, preferably in a head-to-tail manner (1,3- or anti-Markownikoff addition) until termination occurs, which can either happen via recombination of two radicals or disproportionation. This entire process proceeds very rapidly, and the final molecular weight of the polymer is reached within seconds due to the short lifetime of radicals, in the range of microseconds to seconds.^{114,115}

Radical photopolymerization

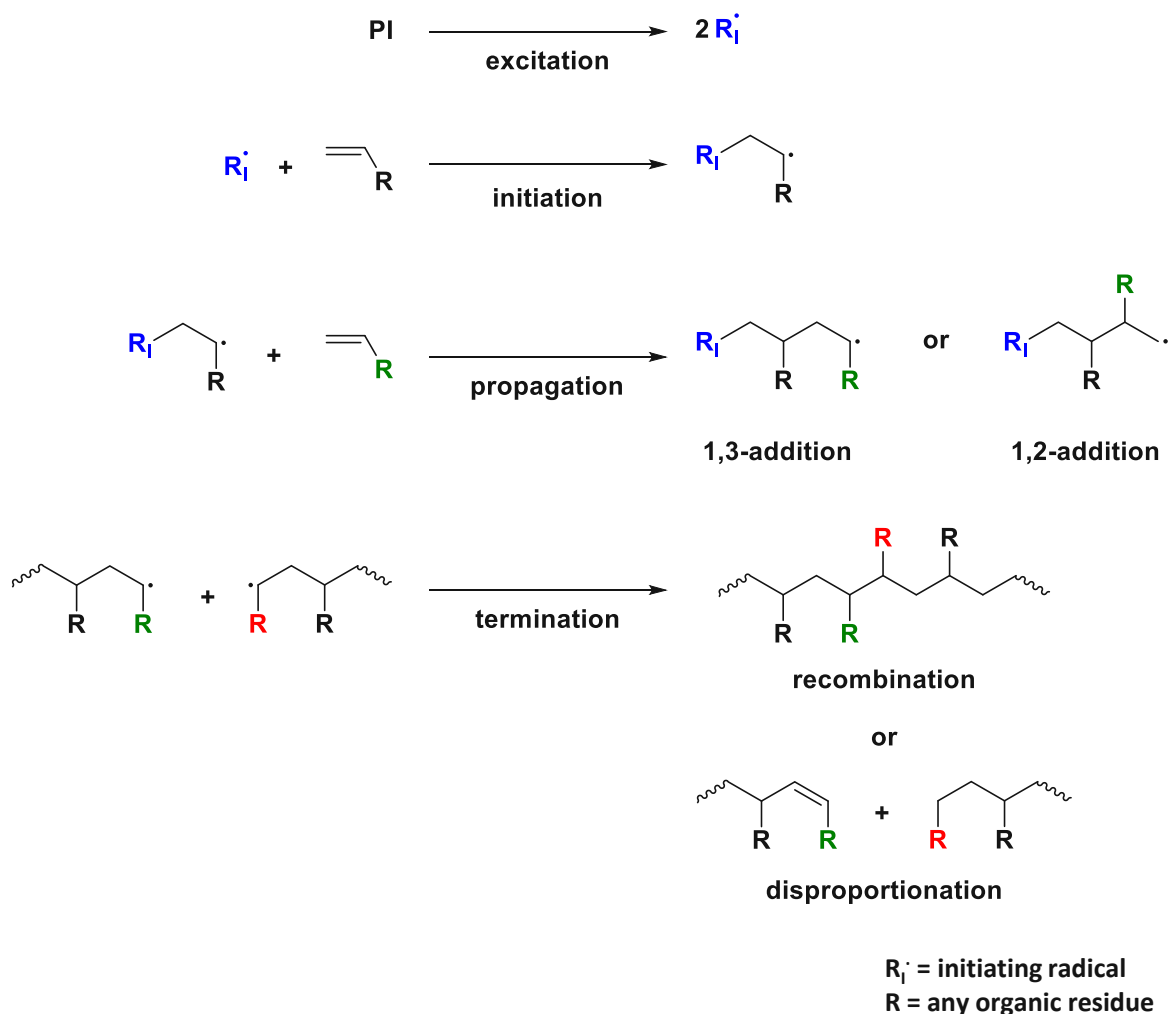


Figure 15: Mechanism of radical polymerization.

Under ambient atmosphere, also recombination with oxygen is possible, as it exists in a biradical state in the atmosphere. This leads to the formation of a non-reactive radical depicted in Figure 16, significantly retarding further polymerization. This so-called oxygen inhibition often leads to tacky surfaces upon polymerization of thin films; hence inert atmosphere or certain additives are needed.¹¹⁶

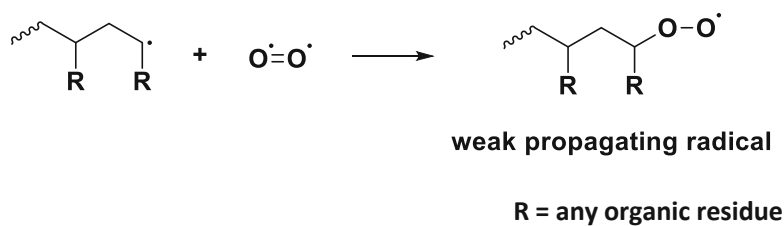


Figure 16: Oxygen inhibition of free-radical polymerization.

Another important component often necessary in formulations include inhibitors, which are molecules capable of scavenging unwanted radical species formed prior to the intended polymerization due to thermal stress onto the monomer or inadequate light protection. The formed radicals can abstract a hydrogen atom from the inhibitor, resulting in a highly resonance stabilized radical that is incapable of further reactions. Figure 17 shows this process with the typically used inhibitor benzene-1,2,3-triol (pyrogallol, PYR).⁸³

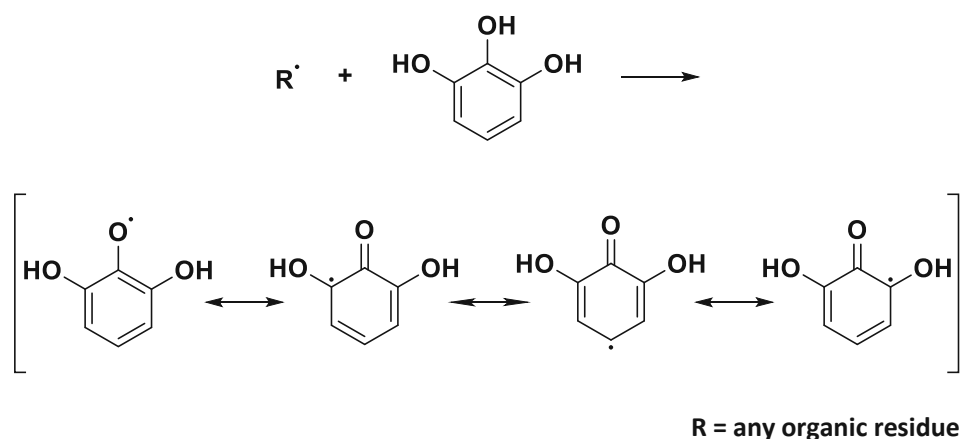


Figure 17: Mechanism of inhibitors for radical photopolymerization.

The used photoinitiator (PI) plays a key role in the photosensitive formulation, influencing curing speeds as well as the absorption wavelength of the system, which is in direct correlation with the resulting curing depth. This component absorbs light and converts it into chemical energy due to a change in the electronical structure of the PI. Light absorption occurs through certain elements in the molecular structure, so-called chromophores containing n or π electrons, which absorb light in the UV-VIS region. In general, electronic transitions can only occur from occupied to unoccupied orbitals. The energy of the highest occupied molecular orbital (HOMO) and the lowest unoccupied molecular orbital (LUMO) define the energy, which needs to be absorbed for the electronic transition and, therefore, the absorption maximum of the PI. For efficient initiation, the emission bands of the light source need to overlap with the absorption maximum of the initiator. In general, higher energies hence lower wavelengths, are necessary to cause π - π^* - compared to n - π^* -transitions of electrons, which is exemplarily shown for the molecular orbital scheme of a carbonyl moiety depicted in Figure 18.¹¹⁷⁻¹²²

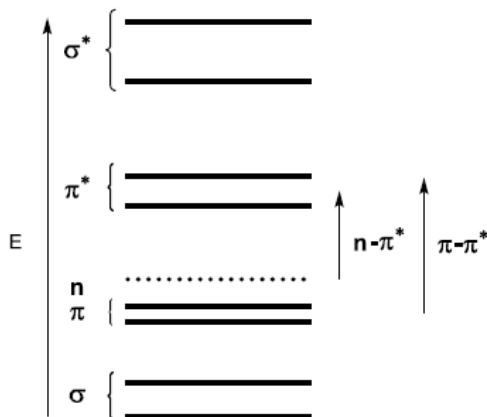


Figure 18: MO-scheme depicting the energy necessary for $n-\pi^*$ - compared to $\pi-\pi^*$ -transitions.¹¹³

The detailed process ultimately leading to the formation of radicals is depicted in Figure 18. Absorption of light causes the excitation of an electron from the ground singlet state (S_0) to an excited singlet state (S_2). Then, either direct emission of photons (fluorescence) can occur or non-radiative processes such as internal conversion (IC) or intersystem-crossing (ISC) into an excited triplet state (T_2). In this state, electrons have the same spin direction, giving the molecule characteristics of a biradical. After relaxation to the excited triplet state T_1 , depending on its stability, radical formation can be induced, which can then initiate the polymerization. This process directly concurs with radiation-less deactivation via cage recombination, emission of photons (phosphorescence), or bimolecular extinction processes.^{117,118,122-124}

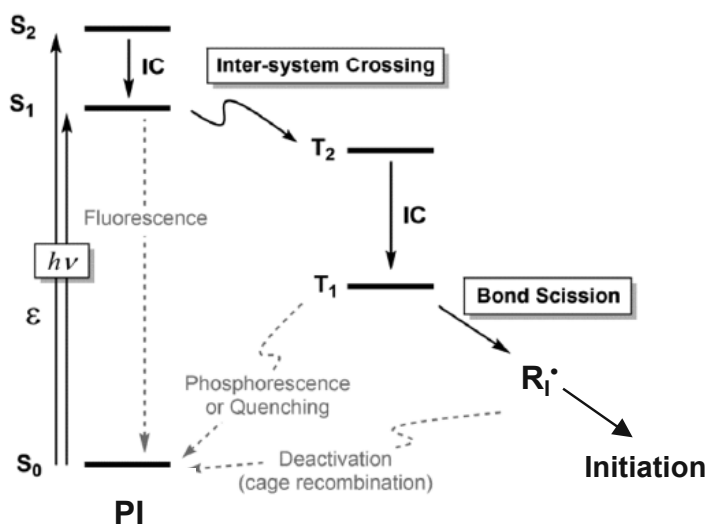
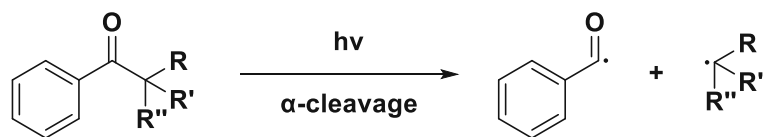


Figure 19: Jablonski diagram demonstrating the photogeneration of radicals (R_i), or different deactivation pathways.¹¹⁸

Depending on the mechanism for radical formation upon irradiation, two types of PIs can be distinguished. Norrish Type I photoinitiators contain cleavable bonds with dissociation energies lower than the energy of the excited state. Hence, upon irradiation, homolytic α -cleavage occurs, which leads to the formation of two radicals (Figure 20).^{109,114,125}



R, R', R'' = any organic residue

Figure 20: Mechanism of α -cleavage in Norrish Type I photoinitiators.

The triplet state of these molecules is short-lived, which makes them less prone to deactivation processes. Furthermore, both resulting radicals can initiate the polymerization reaction, giving them high atom efficiency. Typically, a benzoyl chromophore is attached to a tertiary carbon, and applied initiators include benzil ketals, such as Irgacure 651, hydroxy alkyl acetophenones, such as Darocur 1173, and acyl phosphine oxides, such as BAPO, which are shown in Figure 21 and exhibit typical absorption maxima around 380 nm.^{114,126}

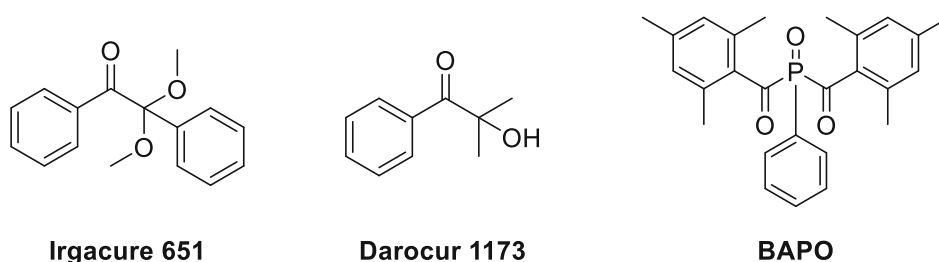


Figure 21: Chemical structure of typical Type I PIs.

To shift the absorption of the system to higher wavelengths, recently heteroatoms such as germanium or tin were introduced into the PI structure.^{127,128} With the germanium-based PI Ivocerin® (bis(4-methoxybenzoyl)diethylgermanium), a bathochromic shift towards 408 nm was observed, leading to higher possible curing depths together with high curing speeds and efficient bleaching, making it ideal for the application in 3D-printing.¹²⁹ Additionally, the biocompatibility of this initiator was confirmed.¹³⁰ The mechanism for its cleavage is depicted in Figure 22.

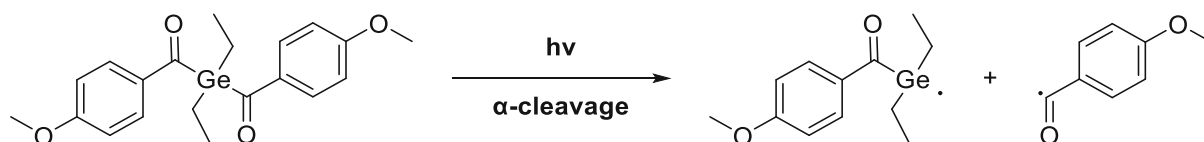


Figure 22: Mechanism of the α -cleavage of the Ge-based PI Ivocerin.

In contrast, Norrish Type II systems consist of a photosensitive component and a co-initiator. After the transition of the initiator into the excited triplet state, no homolytic cleavage occurs, but the PI reacts with the co-initiator in a bimolecular mechanism. Radicals can either form through H-abstraction from a hydrogen donor such as alcohols or ethers (Figure 23 A) or photoinduced electron transfer to an amine and subsequent proton transfer (Figure 23 B). Since the formation of the charge transfer complex and subsequent hydrogen transfer require time and are diffusion- and equilibrium-controlled, Type II systems are generally less reactive than Type I systems. As well, a longer lifetime of the excited state is required, as the encounter with the co-initiator is essential for radical formation, making them prone to deactivation processes. This also leads to lower excitation rates and curing speeds. The most often employed Type II system consists of camphorquinone (CQ) and the tertiary amine ethyl 4-(dimethylamino)benzoate (DMAB) as a co-initiator (Figure 23 B). As well, diaryl ketones, such as benzophenone (BP), are often employed, which form radicals via H-abstraction, displayed in Figure 23 A.^{121,131-133}

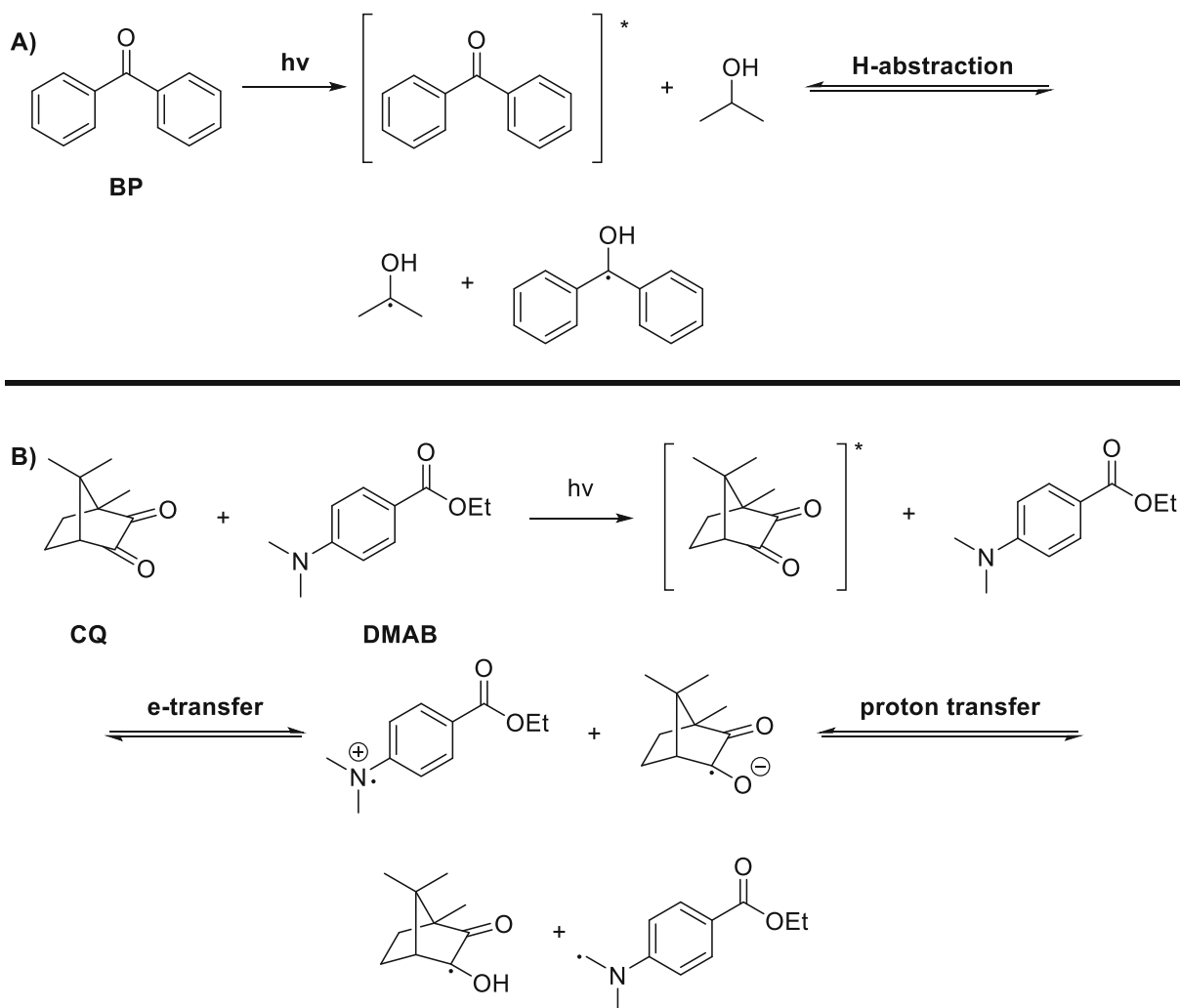


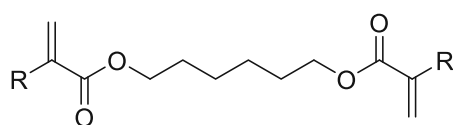
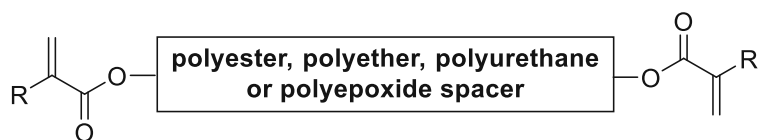
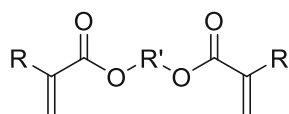
Figure 23: Reaction mechanism of Norrish Type II initiators by A) hydrogen abstraction demonstrated for BP and isopropanol, and B) electron/proton transfer shown for CQ and DMAB.

In industry, resins containing monomers with a molecular weight ranging from 300-5000 g/mol are utilized to obtain high conversions and resistant networks. Foremost, state-of-the-art monomers include acrylates and methacrylates, depicted in Figure 24, which are characterized by high reactivity, efficient curing, and good storage stability.¹³⁴ To adjust important characteristics such as hardness, toughness, flexibility, thermal and chemical resistance, as well as hydrophilicity of resulting polymers, different spacers between the reactive groups can be used, and most employed resins include (meth)acrylated polyesters, polyethers, polyurethanes or polyepoxides (Figure 24). Due to the spacer, higher intermolecular interactions and lower crosslink densities are exhibited by resulting photopolymers, which leads to improved mechanical properties.¹¹² However, also higher viscosity is displayed, limiting resin processability for certain applications. Therefore, compounds, which should reduce the formulation viscosity for enhanced processability and copolymerize with other present monomers, are added, which are referred to as “reactive diluents”. These monomers should ideally exhibit high reactivity, low viscosity, low volatility, low

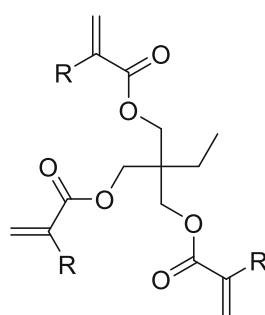
toxicity and good mechanical properties. In general, they can be classified into mono- and multifunctional monomers, while mono- and difunctional compounds are most common due to their lower viscosity. As brittleness increases proportionally to the crosslinking density of the network, monofunctional diluents are advantageous to generate polymers with high toughness.¹³⁵ The most popular reactive diluents include 1,6-hexanediol di(meth)acrylate (HDD(M)A) as well as isobornyl (meth)acrylate (IB(M)A) (Figure 24). Due to the bulky side group, IB(M)A not only effectively reduces formulation viscosity but also results in high glass transition temperatures of resulting materials. If networks with higher crosslinking density are required, monomers with higher functionality, such as trimethylolpropane tri(meth)acrylate (TT(M)A) and pentaerythritol tetra(meth)acrylate (PET(M)A) can be applied (Figure 24).

Besides the outstanding reactivity of state-of-the-art systems containing (meth)acrylates, photopolymers based on these monomers are unsuitable for tissue engineering applications for several reasons. For medical applications, low cytotoxicity of monomers is essential, as residual low molecular weight compounds can be leached out of the network and cause unwanted side reactions.⁶⁴ Especially acrylates display considerable cytotoxicity *in vivo* as they undergo irreversible Michael addition reactions with amine and thiol groups of proteins and DNA. Due to the higher steric hindrance of the double bond in methacrylates caused by the methyl group, they exhibit lower toxicity but are also less reactive. Another problem of polymers formed by acrylates and methacrylates is their degradation behavior (Figure 25 A). Upon degradation, high molecular weight poly((meth)acrylic acids) (P(M)AA) are formed, which cannot be removed from the body and promote inflammation or tissue necrosis. They further cause autocatalytic bulk erosion of the material leading to abrupt implant failure.^{51,52,87,98} Additionally, unreacted monomers may form (meth)acrylic acid in aqueous environments, with high LD₅₀ (lethal dose, which causes the death of 50% of test subjects) of 1.40 mg/kg for acrylic acid and 1.32 mg/kg for methacrylic acid respectively (oral, rat).^{136,137}

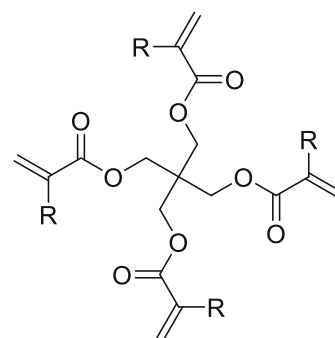
(Meth)acrylates



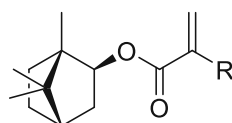
HDD(M)A



TT(M)A



PET(M)A



IB(M)A

R = H...acrylate
 R = CH₃... methacrylate
 R' = any organic residue

Figure 24: (Meth)acrylates used in industry.

Over the last decade, vinyl esters emerged as potent alternatives to (meth)acrylic resins in terms of substantially decreased cytotoxicity.^{59,67,69,70,98,99,112} Furthermore, upon hydrolytic degradation of respective polymers, non-toxic poly(vinyl alcohol) (PVA) is formed, which is approved by the FDA and can be excreted from the body (Figure 25 B). Hydrolysis of the monomer itself leads, for one part, to the formation of acetaldehyde, which can be converted to acetic acid *in vivo* by acetaldehyde dehydrogenase. Nevertheless, also small acid molecules are formed from polymers and the monomer, able to induce autocatalytic bulk erosion of the material. However, due to the small size of these molecules, bulk erosion was found to be far less pronounced compared to polymers based on (meth)acrylates.^{99,112,138} Other recently investigated alternatives to (meth)acrylates include vinyl carbonates, which also display low cytotoxicity, and polymers behave even better upon degradation compared to poly(vinyl esters) since next to PVA, low-molecular weight alcohols and carbon dioxide are formed, resulting in real surface erosion behavior (Figure 25 C).^{69,70,112,139}

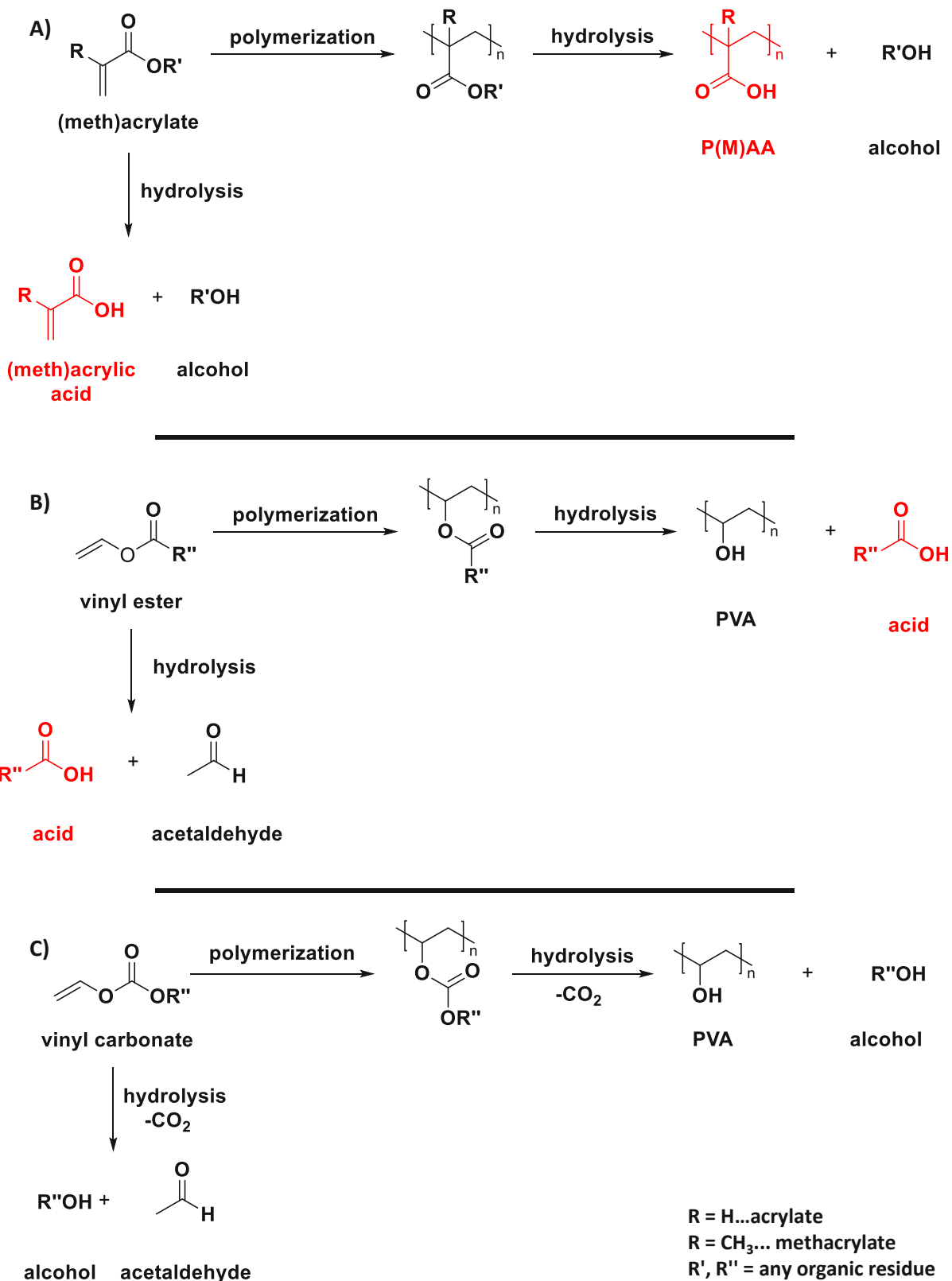


Figure 25: Hydrolysis and formed products of A) poly(meth)acrylates, B) poly(vinyl esters), and C) poly(vinyl carbonates).

For both poly(vinyl esters) and poly(carbonates), first *in vivo* studies confirmed good biocompatibility of the photopolymers and no bulk erosion of implanted scaffolds. Nevertheless, the degradation speed of all polymers was insufficient to match the rate, at which bone tissue

regenerates.^{59,68,98,99} Another major drawback is the low reactivity of these monomers towards radical polymerization compared to (meth)acrylate-based systems, which can be explained by the stability and resulting reactivity of formed radicals. Upon attack of the initiating radical species, in the case of (meth)acrylates, a well resonance stabilized and, therefore stable radical is formed, which results in high reactivity of respective monomers towards radical addition and further propagation with almost no side reactions (Figure 26 A).¹¹² In contrast, vinyl esters, and vinyl carbonates form radicals upon initiation, which lack resonance stabilization and are highly reactive, resulting in low monomer reactivity. Additionally, due to the high radical reactivity, they are prone to side reactions like H-abstractions, which, for example, may occur on ethylene glycol units. The then-formed radicals comprise very low reactivity, which retard further polymerization (Figure 26 B).¹¹²

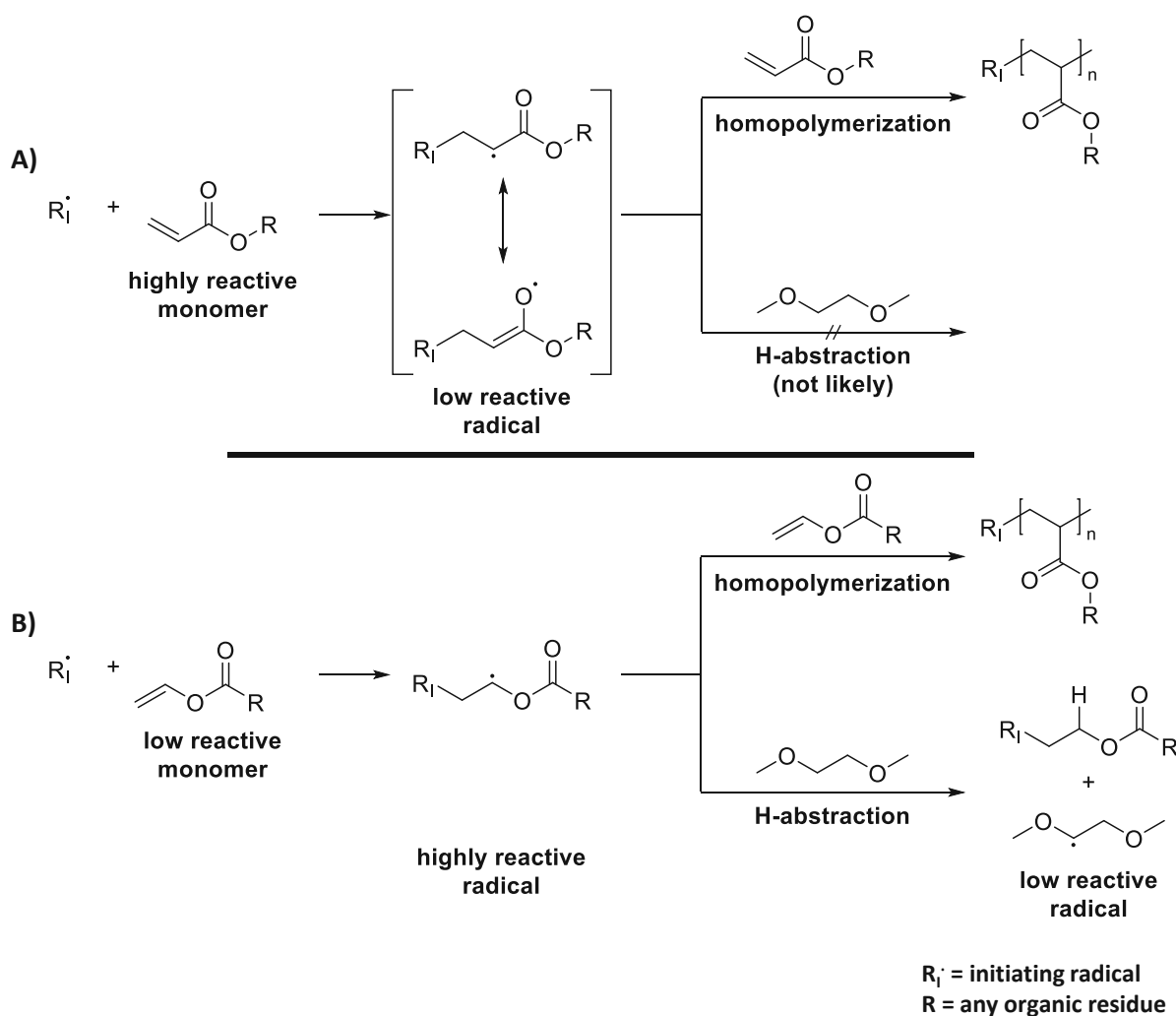


Figure 26: Mechanism of radical polymerization for A) monomers with high reactivity on the example of acrylates, and B) monomers with low reactivity, for example, vinyl esters.

An approach to prevent this terminating effect is the addition of substrates with easily abstractable hydrogens such as thiols. Upon H-abstraction, highly reactive radicals are formed, causing re-initiation of a new polymer chain instead of termination. This so-called thiol-ene chemistry was first described by Posner¹⁴⁰ in 1905 as a general concept of the reaction between reactive double bonds or so-called “enes” and thiols and was further investigated by Cramer, Hoyle, and Bowman.^{141,142} Upon the addition of thiols, the polymerization mechanism is altered from a radical chain growth to a mixed step-growth/chain growth mechanism, in which thiols act as chain transfer agents. Formed initiating radicals preferably abstract hydrogens from the thiol groups, and the highly reactive thiyl radical then reacts in an anti-Markownikov manner with the ene. The radical addition product can undergo chain transfer with a thiol or propagation with further enes (Figure 27). If the ene and the thiol comprise a functionality, higher than two, polymer networks are formed.^{97,141,143-147}

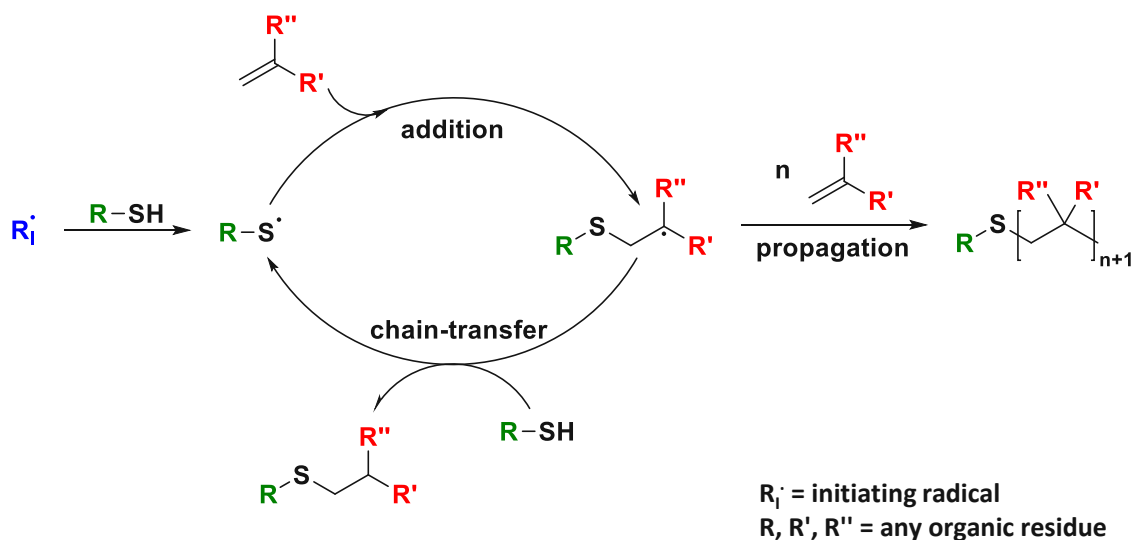


Figure 27: Mechanism of radical polymerization in the presence of thiols.

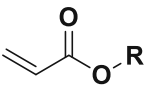
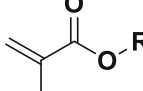
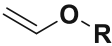
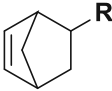
In an ideal thiol-ene reaction, a strict alternation between thiyl radical addition to the ene and the chain-transfer reaction should be observed without any homopolymerization. Therefore, the radical should add to the monomer and the chain transfer agent with the same probability to enable an ideal step-growth reaction without homopolymerization. This probability is defined by the chain transfer constant C_T , which equals the ratio of the rate of chain transfer (k_t) and propagation (k_p) (Equation 1). Hence for ideal reactions, a C_T value close to 1 is exhibited, as chain transfer and propagation should occur with the same probability.¹⁴⁷

$$C_T = \frac{k_t}{k_p}$$

Equation 1: Calculation of the chain transfer constant. C_T ...chain transfer constant; k_{tr} ...rate of chain transfer; k_p ...rate of propagation.

For a given thiol, monomers containing electron-rich double bonds, such as norbornenes or vinyl ethers, display higher reaction rates and C_T than electron-poor enes, such as acrylates and methacrylates, which is shown in Table 2. This, again, can be explained by increased radical stability due to resonance stabilization when polymerizing these monomers. In contrast, in the case of vinyl ethers comprising high electron density, highly reactive radicals are formed, and for norbornenes, alleviation of the ring strain results in high radical reactivity. Therefore, ideal thiol-ene reactions are observed for these monomers without homopolymerization or chain growth, while (meth)acrylate-based monomers display a mixed step growth/chain growth mechanism.^{97,141,147,148}

Table 2: Chain transfer constants for electron-rich and electron-poor enes (R= any organic residue).¹⁴⁸

	electron-poor		electron-rich	
				
	acrylate	methacrylate	vinyl ether	norbornene
C_T [-]	0.08	0.26	0.83	1.00

Formulations for uncontrolled radical polymerization comprise a high density of double bonds and therefore reach the gel point, at which a crosslinked network is formed at rather low conversions. At this point, the network domains lose their mobility, and further polymerization results in the evolution of shrinkage stress (Figure 28 A). As a result, high volumetric shrinkage during polymerization is exhibited, and heterogeneous networks with localized regions of high crosslink density interspersed among regions of lower crosslink density are formed, which display a high and broad glass transition temperature and low impact resistance.^{52,98,113,138,149}

Chain transfer agents such as thiols terminate a growing polymer chain at lower conversions and result in a decrease in the kinetic chain length. This leads to a shift of gelation to higher conversions and, therefore, lower shrinkage stress (Figure 28 B). By this, networks with a uniform architecture exhibiting sharp glass transitions and high impact resistance are formed. Another beneficial effect is the reduction of oxygen inhibition in the presence of thiols, as the formed peroxy radicals can

easily abstract hydrogens from these compounds resulting in reactive thiyl radicals able to reinitiate the polymerization. Due to these advantages, thiol-ene chemistry is patented for several biomedical applications such as dental restoratives¹⁵⁰⁻¹⁵⁴ 155-157 and was also recently used in bone adhesives¹⁵⁸.

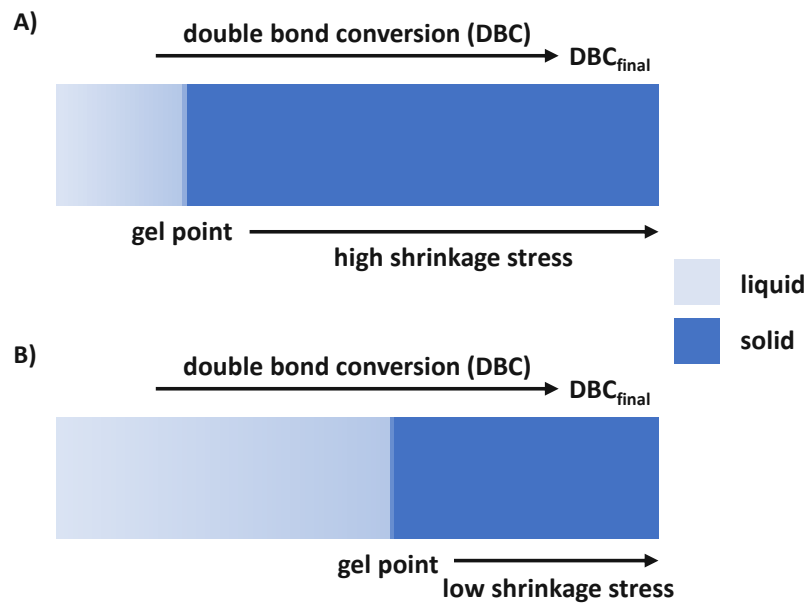


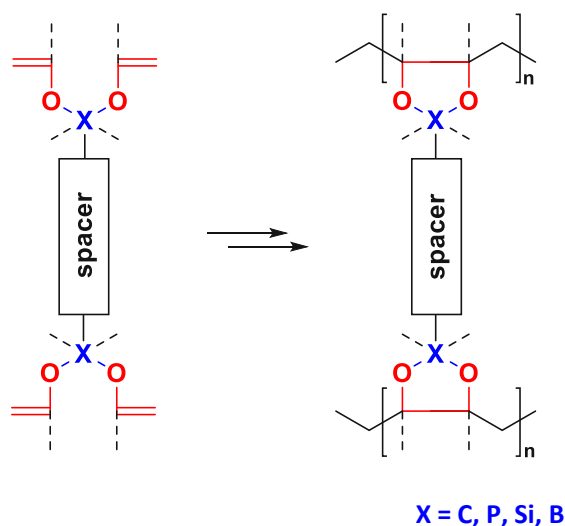
Figure 28: Development of shrinkage stress during A) unregulated polymerization, and B) polymerization regulated with CTAs such as thiols. Adapted from Gauss *et al.*¹¹³

Detrimental effects of thiol-ene chemistry include malodor of many thiols, reduced storage stability of formulations, and low modulus of materials, as flexible thioether bridges may reduce hardness and stiffness.^{113,138}

Objective

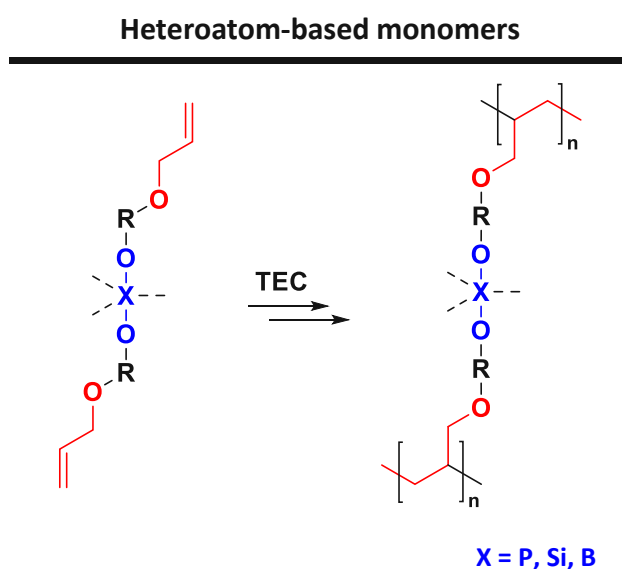
Photopolymerization is widely applied in industry due to its vast economic and ecologic advantages, including high spatial resolutions, absence of solvents, and high curing speeds. While extensively used for coatings and curing of dental restoratives, photopolymerization is now utilized in lithography-based additive manufacturing technologies to produce patient-specific implants. Especially in bone tissue engineering (BTE), achievable surface topology and feature sizes were found to support the bone regeneration process. Currently used photopolymers based on (meth)acrylates, vinyl esters, or vinyl carbonates display poor mechanical properties, such as significant shrinkage during polymerization, high brittleness, and low strength, and suffer from irritancy or even cytotoxicity of monomers, degradation via autocatalytic bulk erosion, acidic degradation products, or insufficient degradation speed *in vivo*. Therefore, despite decades of research, no artificial bone substitute material meets all the needed properties. This thesis investigates novel small molecule building blocks to generate networks that combine superior mechanical properties with enhanced degradation behavior compared to state-of-the-art materials.

Cyclopolymerizable monomers (CPMs)



As a first concept, cyclopolymerizable monomers (CPMs) should be investigated, as they may result in reduced shrinkage and the formation of rigid networks containing cyclic backbone structures. Furthermore, owing to the variability of the center atom, these compounds comprise high flexibility in design and allow for the integration of degradable moieties into the structures for enhanced degradation characteristics. Vinyl ether monomers should be chosen for increased cyclopolymerization tendency, as they are known not to homopolymerize with radical initiators.

As hydrolytically labile groups, for one part, acetals and carbonates should be chosen, as they are known to be cleavable under acidic conditions present during bone remodeling and do not form acidic hydrolysis products, causing inflammation or necrosis. Furthermore, the replacement of the carbon center with heteroatoms should be studied, as they may form less stable bonds to oxygen and thereby facilitate network cleavage. Monomers and polymers containing phosphorus, silicon, and boron were previously shown to be hydrolytically cleavable while forming low-toxic, less acidic degradation products, compared to carbon-based analogs. As a starting point, different divinyl ether CPMs with degradable moieties should be synthesized and investigated for their reactivity as well as their potential for cleavage under acidic conditions. From these carbon- and heteroatom-based CPMs, essential features for efficient cyclopolymerization should be abstracted and used for the generation of monofunctional compounds with improved cyclopolymerization tendency and, ultimately, for the synthesis of higher functional cyclopolymerizable compounds capable of network formation.



As a second approach, novel monomers for enhanced mechanical properties and degradation should be investigated. Similar to the heteroatom-based CPMs, the focus was on compounds containing heteroatom-oxygen bonds. As polymerizable groups, allyl ethers or esters of the respective heteroatom-containing acids should be selected. By employing thiol-ene chemistry, homogeneous and tough networks with improved mechanical properties should be formed due to the quasi-ideal reaction of this polymerizable group with thiols, which may then be cleaved at the respective bonds between the heteroatoms and oxygen. To further provide the networks with important properties, such as high strength, rigid elements, bulky substituents, or cyclic structures should be incorporated into both monomer and thiol structures.

Additionally, to further enhance (thermo)mechanical properties, certain additives, such as toughness enhancers and fillers, should be applied. All resins and resulting polymers should be investigated towards the fulfillment of certain requirements for 3D-printed bone regeneration scaffolds, such as photoreactivity, (thermo)mechanical properties, degradation behavior and rates, and cytotoxicity.

State of the Art

Degradable photopolymers in tissue engineering

Degradable polymers have been widely employed in biomedical applications and are of particular interest for temporary therapeutic applications such as surgical implants (sutures, bone plates, and screws), medical devices, and targeted therapeutic delivery vehicles.^{51,159,160} More recently, effort has been made to use degradable polymers as temporary scaffolds in tissue engineering.¹⁶¹ Especially in bone tissue engineering (BTE), biodegradable regeneration scaffolds as support structures are required, as the body is incapable of repairing larger bone defects caused by trauma or diseases.¹⁶⁰

Biocompatible and biodegradable PGA, PLA, and PCL are state-of-the-art materials and were frequently used to fabricate porous bone regeneration scaffolds, mostly by fiber bonding, solvent casting, particulate leaching, membrane lamination, melt molding or fused deposition modeling.^{2,86,95} However, they suffer from several drawbacks, such as the limited complexity of structures and feature resolutions due to their thermoplastic nature. Additionally, they degrade via undesired bulk erosion in the order of years under physiological conditions, which is too slow for BTE applications.^{51,62}

During the last decade, additive manufacturing technologies (AMTs) gained increasing interest for generating biocompatible and biodegradable, patient-specific scaffolds with defined porosity in a layer-by-layer process.^{68,82} Especially, lithography-based AMTs (L-AMTs), which use selective irradiation of photosensitive resins, achieve feature resolutions down to 10 μm and in case of BTE, surface topology and feature sizes of scaffolds aided the bone regeneration process.^{68,87-89,162}

The simplest approach to generate photopolymerizable precursors for L-AMTs is to attach photoreactive groups to thermoplastic, biodegradable polymers, with a good overview given by Baroli *et al.*¹⁶³ and Ifkovits *et al.*¹⁶⁴ The reactive groups can either be attached to the end groups or placed along the polymer backbone.¹⁶⁵ The most typically applied biopolymer in L-AMTs is poly(ethylene glycol) (PEG) with (meth)acrylate end groups, as it can be subjected to photopolymerization but is also able to form hydrogels. Furthermore, due to its hydrophilicity, it prevents unspecific protein adsorption in aqueous media.^{166,167} In BTE, *in situ* photocurable PEG-hydrogels, encapsulating cells such as osteoblasts¹⁶⁸ or mesenchymal stem cells¹⁶⁹, as well as growth factors such as recombinant human morphogenic protein 2 (rhBMP-2)¹⁷⁰, were used to

successfully restore bone defects *in vivo*. As PEG is non-degradable, it is often copolymerized with D,L-lactide, glycolide, or ϵ -caprolactone to introduce degradable ester bonds into the polymer backbone.^{166,171} Another prominent example is poly(propylene fumarate) (PPF), which can be crosslinked via double bonds along its backbone and was recently used to produce bone regeneration scaffolds.¹⁷² Degradation speed and products can be adjusted by the degree of crosslinking, and the degradation products include non-toxic propylene glycol and fumaric acid as well as excretable molecules related to the cross-linking.¹⁷³ Vehof *et al.* used photo-crosslinked, porous scaffolds to treat cranial defects in rabbits and observed bone formation upon coating with recombinant human transforming growth factor 1 (rhTGF- β 1).¹⁷³ Lee *et al.* fabricated scaffolds with embedded drug-delivery microspheres by Laser-based stereolithography (Laser-SLA), which gradually released BMP-2 and improved proliferation of osteoblasts and bone formation.¹⁷⁴ A drawback, which has to be mentioned, is the poor reactivity of PPF towards radical polymerization, causing expanded times necessary for 3D-printing.¹⁷⁵ Another currently utilized thermoplast is poly(trimethylene carbonate) (PTMC), mostly used in copolymers with PLA or PCL end-capped with (meth)acrylate groups.¹⁷⁶⁻¹⁷⁸ Applications range from drug delivery systems^{179,180} to 3D-printed scaffolds for soft¹⁸¹, vascular¹⁸² or bone tissue engineering¹⁸³. For BTE, Guillaume *et al.* prepared scaffolds of PTMC filled with HAP nanoparticles by Laser-SLA, which significantly improved osteogenesis, osseointegration and bone regeneration in calvarial defects in rabbits.¹⁸³

A drawback of all currently employed state-of-the-art (meth)acrylate-based photopolymers is their adverse effects, such as irritancy or even cytotoxicity of residual photoreactive groups.^{87,99} Additionally, upon degradation, high molecular weight poly((meth)acrylic acids) are formed, which cannot be removed from the body and promote inflammatory response or tissue necrosis and further cause autocatalytic bulk erosion of the material.^{51,52,87,98} Another problem lies in their high reactivity towards uncontrolled homopolymerization, which leads to the formation of heterogeneous networks with high volumetric shrinkage causing cracks in 3D-printed structures.^{52,98} The resulting networks typically exhibit poor mechanical properties, especially high brittleness, which limits their applications in BTE.

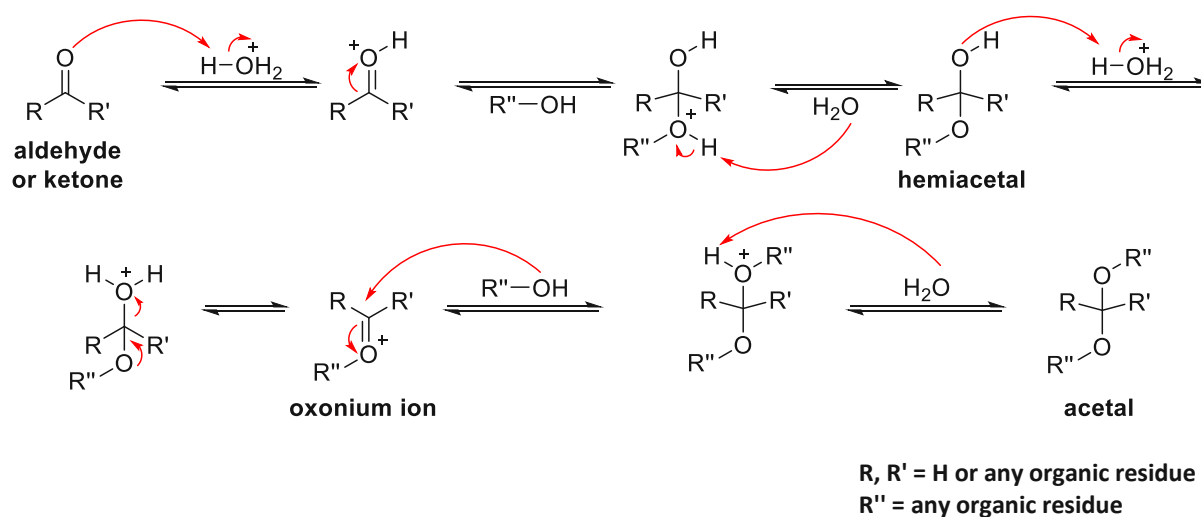
Recently, vinyl esters, vinyl carbonates, and vinyl carbamates were thoroughly investigated as alternatives to (meth)acrylic resins.^{59,67,69,70,98,99,112} Monomers were shown to be one order or even two orders of magnitude less toxic compared to conventional methacrylates or acrylates, respectively, and implanted 3D-printed scaffolds to treat defects of the femoral bone in rabbits displayed good osseointegration, *de novo* bone formation and no signs of inflammation reactions.⁶⁷ Nevertheless, similar to classical (meth)acrylate-based photopolymers, materials

tended to break during polymerization owing to the high brittleness and volumetric shrinkage.⁸⁷ Additionally, although no autocatalytic bulk erosion of implanted scaffolds was observed for these materials, the degradation speed of all polymers was insufficient to match the rate, at which bone tissue regenerates.^{59,68,98,99} Therefore, novel biocompatible monomers are required in BTE, which form polymers with enhanced degradation characteristics *in vivo* and mechanical properties.

Acetals

For the employment of materials as bone replacement materials, dependent on the patient and the location of the implant site, degradation of scaffolds should occur within 3-12 months for efficient bone regeneration and vascularization.^{2,37-39} This degradation can occur under physiological conditions (pH=7.4) but should especially be exhibited under acidic conditions, as a pH below 4.5 is essential for osteoclastic bone resorption.^{60,184}

Instead of photopolymers such as poly(esters) or poly(carbonates), biomaterials based on acetal moieties recently came into focus.¹⁸⁵ The expression “acetal” is nowadays used as a term that encompasses both aldehyde and ketone-derived structures; hence ketals are classified as a subset of acetals.^{186,187} These compounds are formed upon the nucleophilic addition of two alcohol molecules to a ketone or an aldehyde under acidic catalysis with azeotropic removal of the formed water due to the reversibility of the reaction.¹⁸⁸⁻¹⁹⁰ Typically used acids include hydrochloric acid¹⁹¹, sulfonic acid¹⁹² or p-toluenesulfonic acid (pTsOH)¹⁹¹. During the formation, the carbonyl group is protonated by water and thereby activated for nucleophilic addition of the alcohol producing the hemiacetal species. The hemiacetal is then protonated, resulting in an oxonium ion, which can be further attacked by a second alcohol molecule. In the last step, the oxonium ion is deprotonated to form the corresponding acetal (Scheme 1). While prone to hydrolysis under acidic conditions, these compounds are stable towards bases and therefore typically employed as protecting groups for carbonyl compounds in organic synthesis. In general, the stability of an acetal against acids is determined by the stability of the oxonium ion formed in the first stage of the hydrolysis. The more stabilized by electron donating groups, the higher the rate of hydrolysis. Therefore, acetals derived from ketones are more prone to cleavage compared to compounds formed from aldehydes.^{188-190,193} Upon hydrolysis, alcohols and aldehydes or ketones are formed, which do not change the pH of the surrounding medium and in some cases might even be metabolized (*i.e.*, acetaldehyde by the enzyme acetaldehyde dehydrogenase).¹⁹⁴



Scheme 1: Mechanism of the acetal formation of an aldehyde or ketone with an alcohol.

In general, acetals can be classified according to their structure into spiroacetals and linear or cyclic acetals containing five- or six-membered rings (Figure 29).^{60,184}

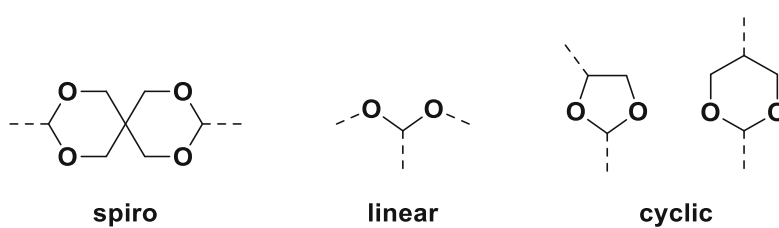


Figure 29: Classification of acetals according to their structure.^{60,184}

Spiroacetals are typically utilized as protecting groups of carbonyl compounds as well as plasticizers and vulcanizers and yield materials with excellent strength.^{191,195,196} Nevertheless, these compounds exhibit high hydrolytic stability under acidic conditions due to the rather hydrophobic environment of the acetal moieties in the structure, impeding their use in biodegradable implants.^{197,198} For example, Lingier *et al.* observed no acidic hydrolysis of polyurethanes containing spiroacetal linkages for one month at elevated temperatures.¹⁹⁹

In contrast, linear and cyclic acetals are cleavable under acidic conditions, while linear acetals are less stable against hydrolysis, as it is more entropically favored.^{188,193} Most publications deal with the use of these compounds to release therapeutic or other bioactive payloads under acidic conditions, particularly in areas of inflammation, in the gastrointestinal tract, or in the environment of tumor cells, which exhibit a lower pH.²⁰⁰⁻²⁰³ However, recently, linear and cyclic acetals end-capped with polymerizable groups were also implemented in tissue engineering applications.^{185,204,205} The most common monomer found is cyclic 5-ethyl-5-(hydroxymethyl)-b,b-dimethyl-1,3-dioxane-2-ethanol diacrylate (EHD, Figure 30), which is either homopolymerized for the production of scaffolds^{204,205} or used in combination with PEG-DA to form hydrogels^{185,206}. Betz

et al. showed that these degradable hydrogels could be used for the encapsulation and osseodifferentiation of bone marrow stromal cells without exerting any cytotoxic effects due to the absence of acidic degradation products.¹⁸⁵ Upon incorporation of hydroxyapatite nanoparticles into these hydrogels enhanced endogenous osteogenic signal expression, and hence, BMSC differentiation was observed by Patel *et al.*²⁰⁶ Moreau *et al.* determined that upon homopolymerization, rigid scaffolds were formed, exhibiting good degradability and cell viability.²⁰⁴ Most remarkably, EHD-scaffolds synthesized by Falco *et al.* allowed the attachment and proliferation of myoblastic cells as well as the release of insulin-like growth factor 1 (IGF-1), making them promising for applications in tissue engineering, especially for skeletal muscle regeneration.²⁰⁵

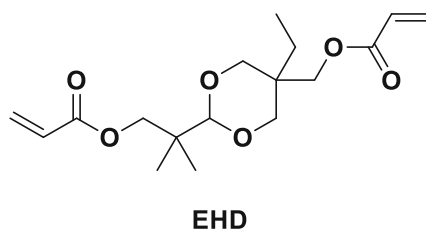


Figure 30: Structure of the monomer EHD.

Heteroatoms

Another appealing approach to obtain polymer networks with enhanced degradation behavior is to replace the carbon atom with heteroatoms. It is well known that the strength of covalent bonds is determined by the overlap between the valence orbitals of the bonded atoms and typically decreases along a period and down a group due to a decrease in shared relative orbital volume. Therefore, particular heteroatoms may form less stable bonds to oxygen than carbon, facilitating network cleavage.^{62,207-212}

Recently, polymers containing bonds between phosphorus and oxygen, so-called poly(phosphoesters) (PPEs, Figure 31), were introduced as biodegradable and biocompatible materials in medical applications, with a good overview given by Bauer *et al.*²⁰⁹ PPEs are omnipresent in living systems in the form of deoxyribonucleic acid (DNA) and ribonucleic acid (RNA) and serve as energy storage in the form of the pyrophosphates ATP and ADP. *In vivo*, enzyme activity in cells is regulated by various phosphatases, able to cleave phosphoester bonds.^{209,211} Therefore, in addition to the potential cleavage of the ester bonds under acidic or basic conditions,

synthetic phosphoesters can also be degraded enzymatically and are, in general, considered to exhibit high biocompatibility and low toxicity. Another major advantage compared to poly(carboxylic ester)s is the penta-valency of phosphorus. Therefore, in addition to the P=O double bond, it is able to form three bonds, enabling main-chain and side-chain modifications, as well as crosslinking between the units, to tune material properties, such as hydrophilicity, mechanics, and degradation.^{190,207-211,213-219} Depending on the side group, PPEs are categorized into poly(phosphites), poly(phosphonates), or poly(phosphates), with their general structure depicted in Figure 31.²⁰⁹ PPEs can be synthesized in a variety of ways, most important being classical polycondensation of phosphoric acid chlorides and diols and anionic, cationic or metal-catalyzed ring-opening polymerization of cyclic phosphonates. Radical polymerization of compounds containing reactive groups, such as double bonds, is also frequently reported.²⁰⁹

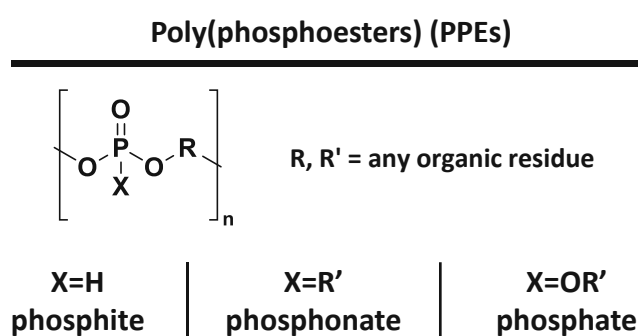


Figure 31: General structure of poly(phosphoesters), and classification into poly(phosphites), poly(phosphonates), and poly(phosphates).

Due to their intumescent flame retardance, PPEs are typically used in industry as flame retardant additives, plastics, or coatings.²¹¹ Recently, applications in drug and gene delivery and tissue engineering were reported.^{220,221 222,223} Wen *et al.* synthesized copolymers of D,L-lactide, and the cyclic phosphate ethyl ethylene phosphate (EEP, Figure 32) by ring-opening polymerization, which displayed accelerated degradation, high biocompatibility, and constant release profiles of a model protein.²²⁴ In the field of tissue engineering, PPEs were used to fabricate guide conduits for nerve regeneration, which triggered the formation of fibroblasts in defects of the sciatic nerve of rats.²²¹ More recently, the focus was laid on photo-crosslinked hydrogels as injectable, degradable scaffolds used for bone regeneration, as an inherent adhesion to bone²¹³ and osteoinductive effects of PPEs were confirmed^{223,225}, and it was presumed that produced phosphoric acid can capture calcium ions, and thereby facilitates the deposition of HAP. Du *et al.* utilized the cyclic phosphoester monomer 2-(2-oxo-1,3,2-dioxaphospholoyloxy) ethyl methacrylate (OPEMA, Figure 32) in combination with PEG to form linear macromers, which were crosslinked to hydrogels by

photopolymerization. These hydrogels were shown to be biocompatible and able to encapsulate osteoblasts without any toxic effects.²²⁶ Furthermore, Li *et al.* demonstrated excellent biocompatibility with another photo-crosslinked hydrogel, which did not exert toxic effects on bone marrow-derived mesenchymal stem cells from goats and displayed signs of mineralization upon culture in an osteogenic medium.²²⁷ Very recently, scaffolds with mechanical properties sufficient for the replacement of human bone were reported.^{112,228} Mautner *et al.* synthesized the monofunctional and trifunctional vinyl phosphates (diethyl vinyl phosphoformate, DEVPF, and trivinyl phosphate, TVP, Figure 32), and complete network degradation via surface erosion was confirmed.¹¹² Zhang *et al.* fabricated composites of unsaturated PPEs with β -tricalcium phosphate (β -TCP) particles, which were *in situ* crosslinked and may be used as injectable and biodegradable substitutes for alveolar bone.²²⁸

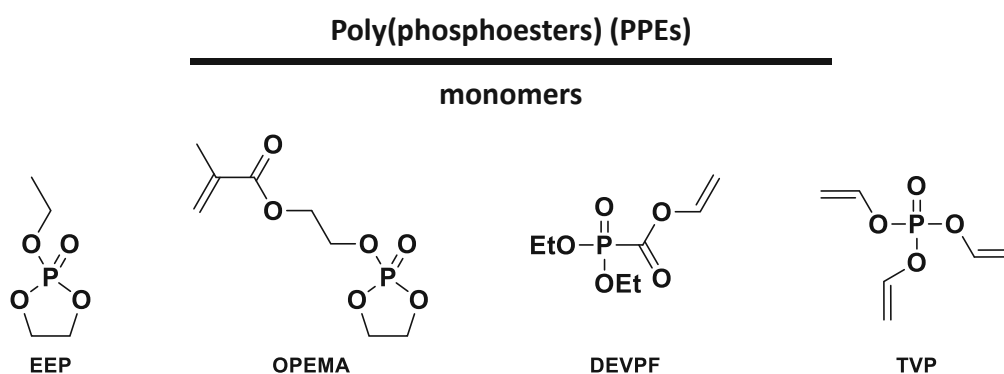


Figure 32: Structure of monomers used in literature for the formation of PPEs.^{112,224,226}

In addition to phosphoesters, silyl ethers (SE), with the general structure $(R'O)_nSiR_{4-n}$, recently gained attention for the production of biocompatible and biodegradable materials.^{62,229-233} These compounds are commonly utilized for the protection of alcohols and are readily hydrolyzed to a silanol and an alcohol, both of which are not considered inherently toxic or cause changes in the pH of the surrounding medium.⁶² Various studies showed that degradation of SE-based polymers occurs under mild acidic conditions, and degradation rates are tunable over several orders of magnitude dependent on the substituents on the Si-atom.²³¹ For example, Wang *et al.* used silyl ether bonds as acid-cleavable links in antibody-drug conjugates for the delivery of cytotoxins to cancer cells.²³² Parrott *et al.* reported the synthesis of difunctional silyl ether crosslinkers with acrylate groups, which were molded by a soft lithography technique to obtain degradable Trojan horse particles for targeted drug release as well as sutures and stents for general surgery.²²⁹ Very recently, Bunton *et al.* prepared degradable crosslinked networks by base-catalyzed addition of SE-containing acrylates and thiols. Additionally, the controlled release of an encapsulated

fluorescein dye as a drug surrogate was possible by varying the substituent attached to the Si-atom.²³³ The only known thiol-ene photopolymerization of SEs was conducted by Ware *et al.*, which synthesized several silyl ether-containing monomers and thiols, displayed in Figure 33. From these compounds, networks were generated, which exhibited rapid hydrolytic degradation without swelling. Additionally, they showed that these materials can be applied in photolithography to fabricate biodegradable cortical electrodes.⁶²

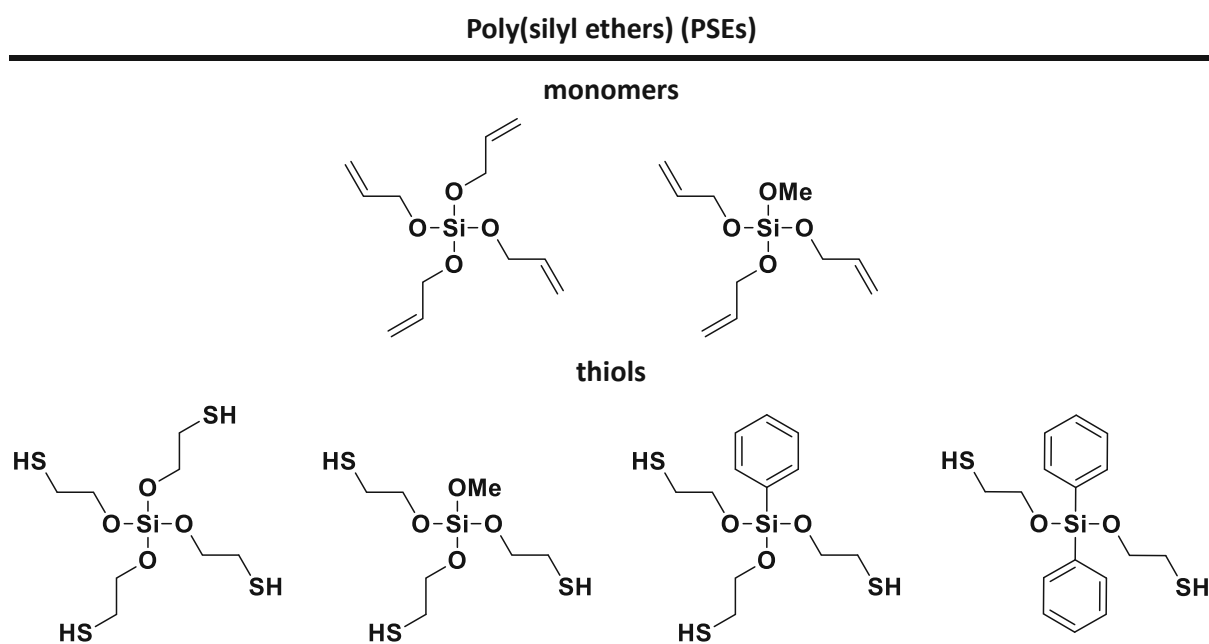
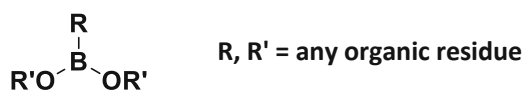


Figure 33: Structure of SE-based monomers, and thiols used by Ware *et al.*⁶²

Another heteroatom, known for its labile bond with oxygen, is boron.²¹² Hence boronic esters (BE), with the general structure depicted in Figure 34, are highly interesting for generating hydrolytically labile networks. These compounds can be easily prepared by the condensation of boronic acids and diols and removal of the formed water. As the esterification is reversible, they are known to be readily hydrolyzed.^{234,235} This can be explained by the electron deficiency of the sp^2 -hybridized boron in the structure, which only holds six valence electrons. Hence, the empty p-orbital orthogonal to the three substituents is easily attacked by nucleophiles such as water.²¹² Typically, boronic esters are used as low-cost reagents for Suzuki-Miyaura couplings and are generally considered to comprise low cytotoxicity.^{212,236} Furthermore, hydrolysis of these compounds, next to alcohols, yields boronic acids, which are mild Lewis acids with low toxicity and do not lead to significant changes in the pH of the surrounding medium.^{62,212,236,237}

Boronic esters (BEs)



monomers and thiols

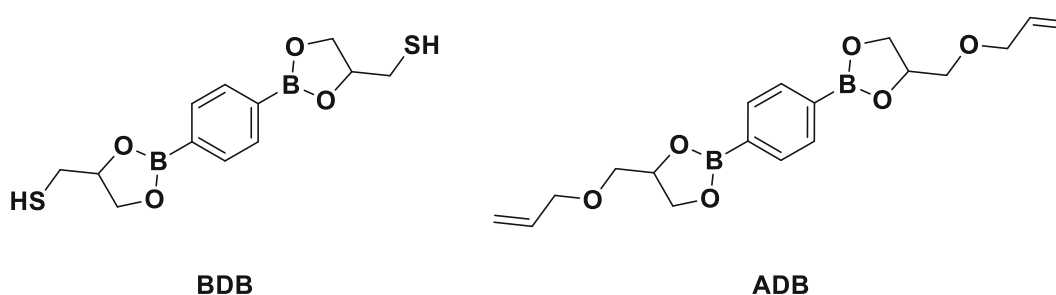


Figure 34: General structure of boronic esters, and the literature-known BE-based monomers and thiols BDB, and ADB.

Next to being hydrolyzable, the boronic ester moiety allows for catalyst-free transesterification reactions, and therefore, these compounds were frequently used in solution-based systems with dynamic properties, such as molecular sensors and drug delivery systems.²³⁸⁻²⁴² Recently, associative exchange reactions enabling network rearrangement in bulk polymers were reported by Röttger *et al.*²⁴³ and Cromwell *et al.*²⁴⁴, leading to the development of BE-based materials capable of self-healing, reshaping, and recycling.^{235,237,239,244-251} Chen *et al.* prepared crosslinked self-healable, malleable, and re-processable rubbers by thermally initiated thiol-ene polymerization of a butadiene rubber with the BE-containing thiol 12,2'-(1,4-phenylene)-bis(4-mercaptan-1,3,2-dioxaborolane) (BDB, Figure 34).^{234,235} Cash *et al.* synthesized crosslinked boronic ester networks via radical-initiated thiol-ene polymerization, which displayed intrinsic self-healing under ambient conditions.^{249,251} Recently, boronic esters were applied in 3D printing to prepare self-healable hydrogels via extrusion, with possible applications in drug release and tissue engineering.²⁵²⁻²⁵⁵ For example, Shi *et al.* fabricated hydrogels from boronic acid-modified hyaluronic acid and PVA, which could be used for drug delivery and encapsulation and protection of neural progenitor cells without exerting toxic effects. DLP-printing of self-healable materials containing boronic ester bonds was first reported by Robinson *et al.*²⁵⁶, which utilized the BE-based monomer 1,4-bis(4-((allyloxy)methyl)-1,3,2-dioxaborolan-2-yl)benzene (ADB, Figure 34) in thiol-ene photo-polymerizations. However, due to the low glass transition temperature of formed polymers, the addition of a crosslinker without boronic ester bonds was necessary to prevent

creep and failure during printing.^{245,257,258} Up to date, there are no reports on the usage of boronic esters to obtain biodegradable polymers used for bone tissue engineering.

Thiol-ene chemistry

Bone regeneration scaffolds require certain mechanical properties for good load dissipation and tissue integration.⁸⁷ To improve the mechanical properties of state-of-the-art photopolymers, especially toughness, several strategies can be found, which have been extensively reviewed in recent years.^{98,143,146,259} A potent approach is the employment of chain-transfer agents such as thiols, resulting in more homogeneous networks with sharpened glass transition temperatures, lower shrinkage stress, and high fracture toughness.^{97,141,147,260} Additionally, for monomers with poor homopolymerizability, such as vinyl esters, vinyl carbonates, and vinyl carbamates, thiol addition leads to an increase in monomer reactivity as it suppresses intermolecular H-abstraction and reduces oxygen inhibition.⁶⁹ Thiol-ene chemistry (TEC) has been frequently employed in the biomedical sector and has found widespread application in low-shrinkage dental restoratives.^{150-154 155-157} Additionally, TEC was used in the fabrication of degradable hydrogels, mostly PEG, end-capped with acrylates, norbornenes or allyl ethers, which were employed as drug-delivery vehicles²⁶¹⁻²⁶⁵ or applications in tissue engineering.^{266,267} Most remarkably, Aimetti *et al.* reported the synthesis of human neutrophil elastase- (HNE) responsive hydrogels functionalized with norbornene groups, which were crosslinked via thiol-ene reaction and physically entrapped drugs. These hydrogels exhibited surface erosion upon exposure to HNE, an enzyme released by neutrophils at sites of inflammation.²⁶¹ Very recently, inspired by dental resin composites, Granskog *et al.* applied TEC in bone adhesives. Combined with a fiber-reinforced adhesive patch, these systems exhibited unprecedented shear bond strength, good adhesion on rat femoral fractures, and good biocompatibility without inflammatory responses.¹⁵⁸ A big issue with thiol-ene-based photopolymers is the glass transition temperature of final materials, which is typically low due to the formation of flexible thioether bridges, and limits the use of TEC in BTE applications. Nevertheless, literature offers several strategies to circumvent these problems, *i.e.*, the incorporation of functionalized nanoparticles proposed by Polizzotti²⁶⁷ and Schreck *et al.*²⁶⁸

Cyclopolymerization

Another approach to generate photopolymers with superior mechanical properties is the concept of cyclopolymerization, which was discovered in the 1950s by Butler *et al.*, who surprisingly obtained water-soluble polymers upon radical polymerization of difunctional, non-conjugated 1,5- and 1,6-dienes, such as quaternary diallyl ammonium salts.²⁶⁹ As it was believed that these monomers would either yield cross-linked, insoluble and saturated polymers or linear, soluble polymers containing one residual double bond per unit, a novel alternating intra-intermolecular propagation mechanism was proposed, yielding ring structures along the polymer backbone. This type of polymerization is now known as cyclopolymerization.^{270,271} Since then, quantitative cyclopolymerization with a variety of symmetrical dienes, such as dimethacrylamides (DMAA)²⁷², methacrylic anhydride (MAA)²⁷³, or activated diallylamines (DAA)²⁷⁴ was reported, which are shown in Figure 35. While cyclopolymerization based on a radical propagation mechanism is most thoroughly studied, nowadays also ionic and transition metal-catalyzed propagation mechanisms are reported in literature, with a comprehensive overview given by Pasini *et al.*²⁷⁵. While ionic and metal-mediated cyclopolymerization require certain conditions, such as inert atmosphere, absence of nucleophiles such as water, low initial monomer concentrations to suppress homopolymerization or living initiator systems, radical cyclopolymerization may proceed in bulk at ambient conditions under the formation of high molecular weight polymers, making it still by far most abundant.²⁷⁶⁻²⁷⁸

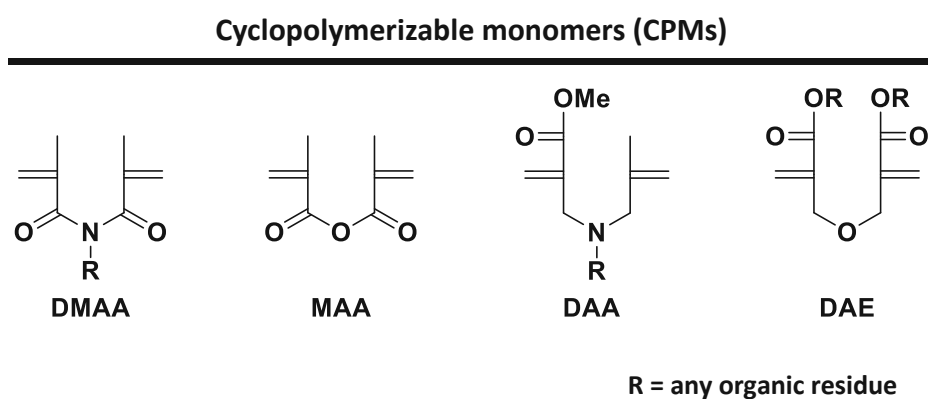


Figure 35: Structure of different CPMs used in literature.

The mechanism of radical cyclopolymerization was first elucidated by Hall *et al.* and is depicted in Figure 36.²⁷⁹ Most typically, cyclopolymerizable monomers (CPMs) are α,ω -unsaturated, 7-atom centered molecules containing either carbon, oxygen, or nitrogen as a center atom, which cyclize to form five-, (Figure 36 A), six- (Figure 36 B) or seven-membered (Figure 36 C) rings. As the formation of a primary radical is not favored, seven-membered rings are least likely to form. Upon

ring closure to five- or six-membered rings, either an unfavored primary radical (Figure 36 B) or a more stable secondary radical is formed (Figure 36 C). Still, monomers preferentially forming both 5- or 6-membered rings are abundant, confirming that the preferred pathway is determined by both thermodynamic and kinetic influences.²⁷⁹

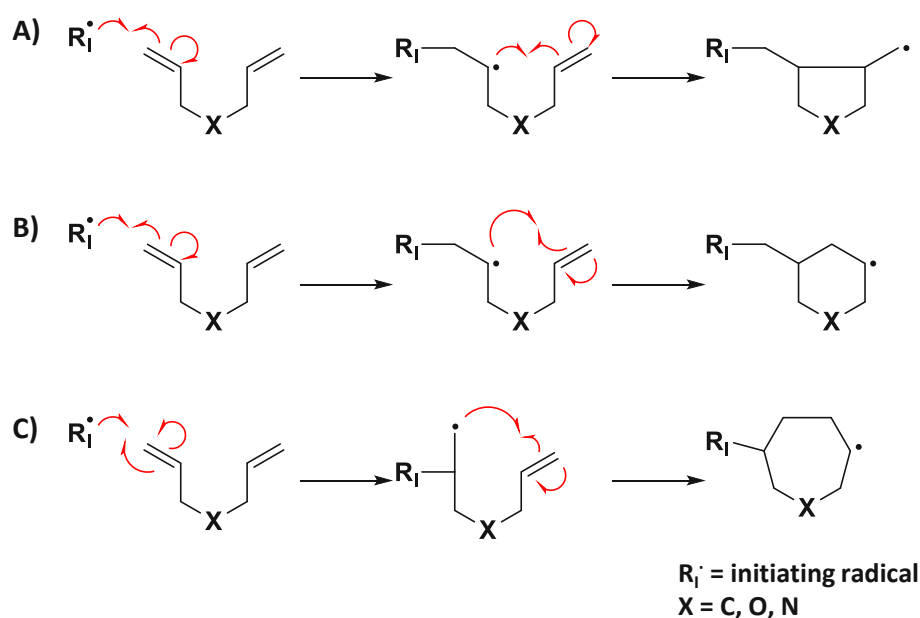


Figure 36: Mechanism of cyclopolymerization to form five- (A), six- (B), or seven- (C) membered rings.

Due to the formation of cyclic structures along the polymer backbone, exceptionally high glass transition temperatures were reported for cyclopolymers, making it ideal for generating polymers with enhanced mechanical properties.²⁷⁶ Additionally, due to the intramolecular propagation mechanism, resulting in decreased crosslinking density, CPMs were recently proposed as reactive diluents with low viscosity and volatility.¹⁰¹

Kodaira *et al.* thoroughly investigated the structure of CPMs necessary for efficient cyclopolymerization.²⁸⁰ On the one hand, monomers should undergo intramolecular instead of intermolecular propagation, equal to a low tendency towards homopolymerization. For these monomers, according to the Gibbs-Helmholtz equation (Equation 2), intermolecular propagations exhibit a loss of entropy (ΔS), which is not compensated by the low reaction enthalpy (ΔH). In contrast, a lower entropy loss is displayed for the intramolecular mechanism of cyclopolymerization, resulting in energetically favored polymerizations. Therefore, a low tendency towards homopolymerization is essential for efficient cyclopolymerization.²⁸⁰ For low homopolymerizability, the double bond can be activated by electron-withdrawing groups, such as ester groups, and activation can occur from the inside of the double bond, as in DMAA or MAA or outside, as in DAA (Figure 35).

$$\Delta G = \Delta H - T\Delta S$$

Equation 2: Gibbs-Helmholtz equation; G...Gibbs free energy; H...enthalpy; T...absolute temperature; S...entropy.

The second principle includes steric considerations, particularly the introduction of bulky substituents to bring the double bonds in close proximity for efficient ring closure, shown for various ether dimers substituted with ester groups (DAE, Figure 35). These CPMs find application in dental materials comprising low shrinkage, as shown by Stansbury *et al.*^{157,281} Other than that, no actual biomedical applications of cyclopolymers were reported yet, and CPMs were never used in bone tissue engineering.

For the formation of three-dimensional networks, difunctional diallyl amides (Figure 37, left) or respective salts containing two cyclopolymerizable motifs were proposed by Hall *et al.* to enhance the polymerization efficiency.²⁸² Subsequently, Ruppitsch *et al.* studied dimethacrylamides (Figure 37, right) as crosslinking-CPMs with low volumetric shrinkage.²⁸³ These compounds allow tuning of the resulting material properties by variations in the spacer bridging the cyclopolymerizable groups. Other than that, the topic of higher functional CPMs as crosslinking monomers has not been extensively studied.

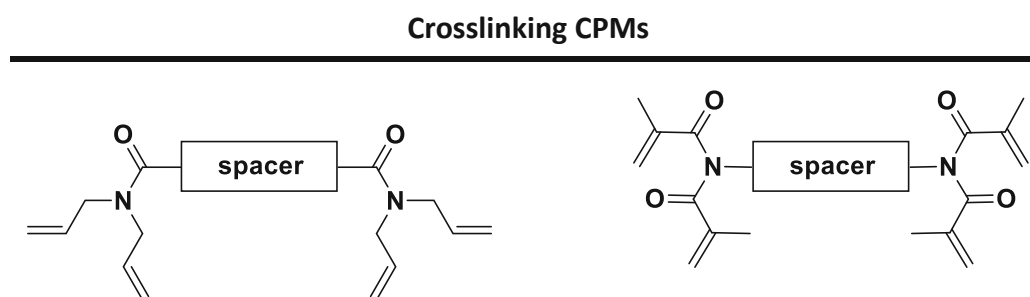


Figure 37: Schematic representation of crosslinking cyclopolymerizable monomers (CPMs) diallyl amides (left)²⁸², or dimethacrylamides (right)²⁸³ with a spacer unit bridging the cyclopolymerizable groups.

Due to the possible variability of the center atom, CPMs can also be designed to contain degradable features within the structure to possibly enable biomedical applications with enhanced degradation characteristics to conventional poly(esters) or poly((meth)acrylates). Arbuzova *et al.* were the first to investigate cyclopolymerization of divinyl acetals using the monomers divinyl formal (DVF), divinyl ethanal (DVE), and divinyl benzal (DVB) shown in Figure 38. Upon photopolymerization in bulk, soluble polymers with slight residual unsaturation were formed, which could be hydrolyzed to FDA-approved PVA-like structures and aldehydes under acidic conditions (Figure 38).²⁸⁴ These compounds were then further extensively investigated by Matsoyan *et al.*, which polymerized a broad variety of aliphatic and aromatic divinyl acetals and

ketals with radical initiators such as AIBN in bulk and solution and showed that polymerization occurred exclusively via cyclopolymerization mechanism.²⁸⁵⁻²⁸⁸ Tsukino *et al.* demonstrated that the overall rate of radical cyclopolymerization decreases with increasing methyl substitution at the center acetal carbon.²⁸⁹ Corfield *et al.* also investigated the ionic cyclopolymerization of several divinyl acetals.²⁷⁰ While aromatic compounds yielded saturated, linear polymers containing no residual unsaturation, crosslinked networks were formed in the case of aliphatic acetals, such as DVF.²⁷⁰

In recent years, cyclopolymerization of divinyl acetals was only reported by metal-mediated insertion polymerization. For example, Jian *et al.* performed a Pd-catalyzed cyclopolymerization of ethylene and divinyl formal, resulting in novel poly(ethylenes) containing cyclic dioxolane and dioxane units.²⁹⁰

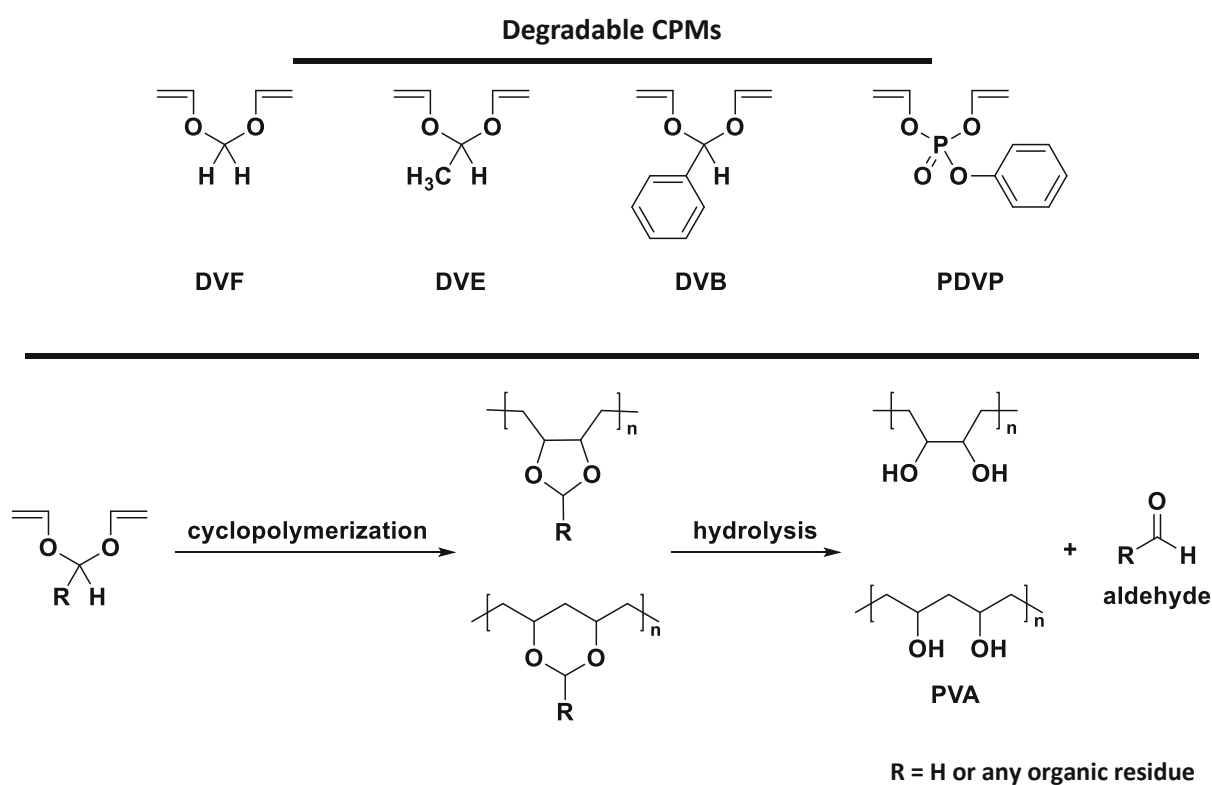


Figure 38: Structure of literature-known CPMs containing degradable motifs such as acetals (DVF, DVE, DVB)²⁸⁴ or phosphoesters (PDVP)²⁹¹. Acidic degradation of cyclopolymers formed by divinyl acetals under the formation of PVA or PVA-like structures, and aldehydes reported by Arbuzova *et al.*²⁸⁴

Hardly any CPMs with heteroatoms as center atoms are literature-known. In the late 1970s, radical cyclopolymerization of the phosphorous-based CPM phenyl divinyl phosphate (PDVP, Figure 38) was studied by Hayashi *et al.*, which mainly observed crosslinking instead of cyclopolymerization.²⁹¹ Nevertheless, the soluble fraction, containing mainly five-membered cyclized units, was shown to be degradable under hydrolytic conditions.

To summarize, various photopolymers are currently being investigated as biocompatible and biodegradable bone replacement materials. However, due to drawbacks of state-of-the-art materials such as cytotoxicity of residual monomers, poor mechanical properties, and/or undesirable degradation of resulting materials, only a few are currently investigated in animal models, and no reports on applications in humans have been published, so far. Therefore, the aim of this work is to find novel small molecule building blocks to generate networks that combine superior mechanical properties with enhanced degradation behavior compared to state-of-the-art materials.

General Part

1. Novel cyclopolymerizable monomers for enhanced mechanical properties and network degradation

3D-printed scaffolds used in bone tissue engineering face certain challenges, above all, poor mechanical properties and insufficient degradation speed of materials. Cyclopolymerizable monomers (CPMs) are an intriguing approach to generate polymers with reduced shrinkage and superior mechanical properties owing to the formation of cyclic backbone structures. Furthermore, due to the variability of the center atom, these compounds allow for the integration of degradable moieties into the structures for enhanced degradation characteristics. As high cyclopolymerization efficiency is achievable with monomers exhibiting a low tendency towards homopolymerization, vinyl ether moieties were chosen as polymerizable groups, which are known not to homopolymerize with radical initiators.²⁸⁰

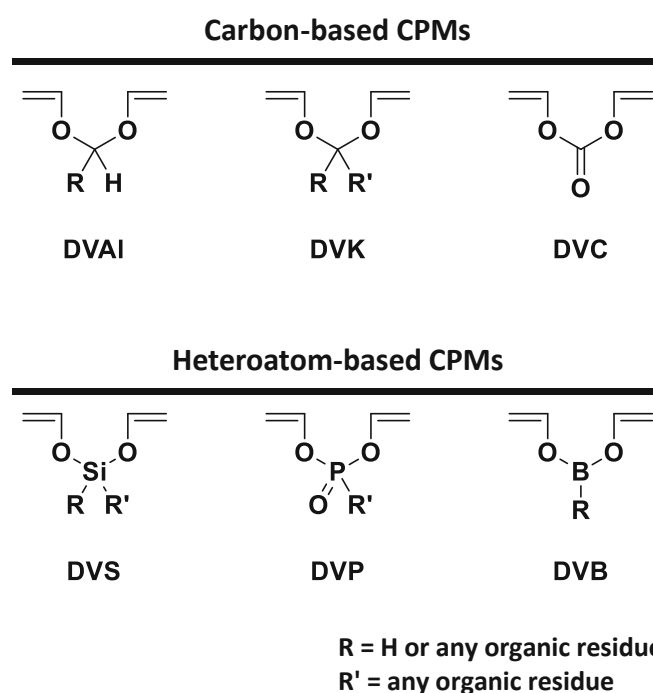


Figure 39: General target structures of CPMs containing degradable motifs: carbon-based CPMs with acetal (DVAI), ketal (DVK), and carbonate moieties (DVC), and heteroatom-based CPMs with silicon (DVS), phosphorus (DVP), and boron (DVB) as the center atom.

As hydrolyzable motifs, acetals, ketals, and carbonates, for one part, were selected, which are known to be cleavable under acidic conditions present during bone remodeling and do not form acidic hydrolysis products, potentially causing inflammation or necrosis. Several divinyl alkanals (DVAI), divinyl ketals (DVK), and divinyl carbonate (DVC), with their general structure depicted in

Figure 39, were already studied for their cyclopolymerization tendency. While most recent literature only reports the ionic²⁷⁰ or metal-mediated cyclopolymerization of these compounds,²⁹⁰ Arbuzova *et al.*²⁸⁴ and Matsuyan *et al.*^{285-288,292} extensively investigated the radical cyclopolymerization of several divinyl alkanals and ketals in bulk and in solution in the 1960s, including the monomers divinyl formal (DVF), divinyl ethanal (DVE), divinyl benzal (DVB), and divinyl acetal (DVAc) shown in Figure 40, and confirmed that polymerization of these compounds occurred exclusively via a cyclopolymerization mechanism. Furthermore, the formation of soluble polymers was determined, which were hydrolyzed to PVA-like structures and aldehydes under acidic conditions. Murahashi *et al.* examined the radical polymerization of divinyl carbonate (DVC, Figure 40) in bulk and reported the formation of cyclic backbone structures, although due to the high degree of residual unsaturation, cyclopolymerization was not presumed the predominant propagation mechanism.²⁹³

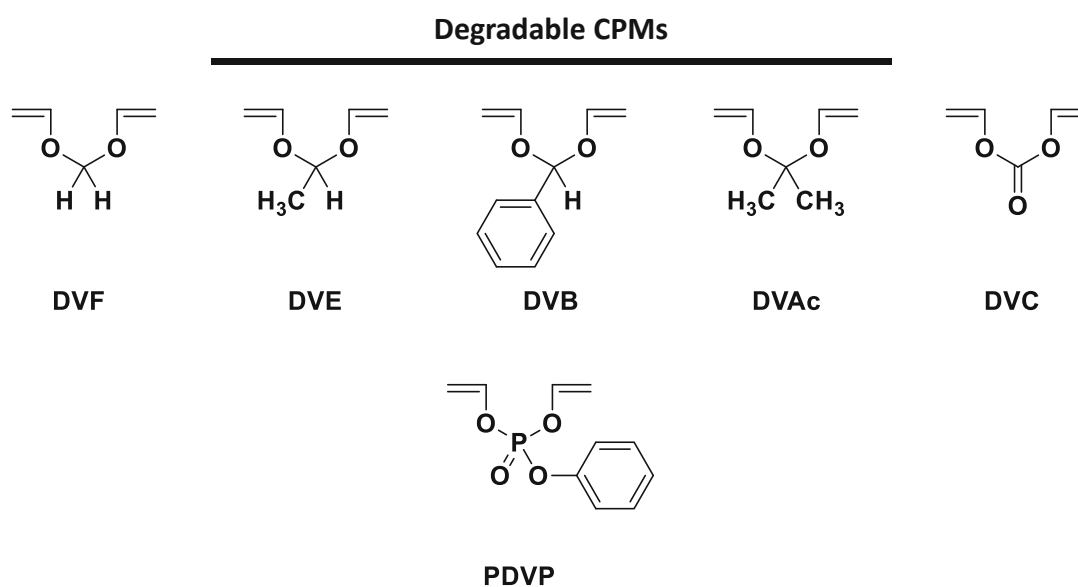


Figure 40: Structure of literature-known CPMs containing degradable motifs, including the divinyl alkanals DVF, DVE, and DVB, the divinyl ketal DVAc²⁸⁴, divinyl carbonate (DVC)²⁹³, and the divinyl phosphate PDVP²⁹¹.

Another strategy to improve polymer degradation is to replace the center carbon of the CPMs with heteroatoms, such as phosphorus, silicon, or boron, due to a less stable bond to oxygen than carbon.^{62,207-212} Polymers formed from the resulting heteroatom-based CPMs (DVS, DVP, and DVB) depicted in Figure 39 would hydrolyze under the formation of non-toxic and less acidic phosphonic acids, silanols, or boronic acids.^{62,209-212,233} Almost no literature reports the cyclopolymerization of vinyl ether compounds containing these degradable motifs. Hayashi *et al.* examined the radical polymerization and copolymerization of vinyl phosphates, including phenyl divinyl phosphate (PDVP), shown in Figure 40 but mainly observed crosslinking instead of cyclopolymerization, although the soluble fraction containing five-membered rings was degradable under hydrolytic

conditions.²⁹¹ In contrast, cyclopolymerization of Si- and B-containing vinyl ethers is unstudied entirely.

As a result, carbon- and heteroatom-based CPMs, comprising the structural elements summarized in Figure 39, were selected as target structures and synthesized. Subsequently, the tendency of these monofunctional model compounds towards cyclopolymerization was tested. To further improve cyclopolymerizability, also CPMs containing features for efficient cyclopolymerization were synthesized. As the final objective was the formation of polymer networks, the essential structural elements for efficient cyclopolymerization and degradation should be determined from these compounds and used for the design and synthesis of di- or higher-functional CPMs, enabling the formation of degradable networks with cyclic backbone structures.

1.1 Cyclopolymerizable model compounds

Based on these target structures, the first goal was the synthesis of monofunctional carbon- and heteroatom-based model compounds and subsequent investigation of their potential towards cyclopolymerization.

1.1.1 Synthesis of carbon-based model compounds

First, different monofunctional carbon-based CPMs, including divinyl alkanals (DVAI), divinyl ketals (DVK) as well as divinyl carbonate (DVC), were synthesized.

Divinyl alkanals and ketals can be easily prepared in a two-step reaction, with general procedures described by Jian *et al.*²⁹⁰, Matsuyan *et al.*^{285,287,292}, and Lorette *et al.*²⁹⁴ For the first step, two procedures are possible (Figure 41 A and B). Pathway A involves the acid-catalyzed acetalization of the respective aldehyde or ketone (0.7-1 equivalents, eq.) with a slight excess of 2-chloroethanol (2.2 eq.) to the bis(2-chloro)ethylacetal species.^{285,287,290,292} As the formation of an acetal is unfavorable with regards to entropy, another method is to perform the first step by acetal exchange using an acetal-type reagent, such as an orthoester, which avoids the entropic cost, as shown for pathway B).²⁹⁴ As catalysts for both reactions, sulfuric acid (0.08 eq.)²⁹⁰ and *p*-toluenesulfonic acid (pTsOH, 0.01 eq.)²⁸⁷ are reported, and the reaction is performed in solvents such as chloroform, toluene, or benzene, which are used to remove water or in case of pathway B) the formed alcohol by azeotropic distillation, to prevent reformation of the starting materials.

The desired divinyl alkanal or ketal can then be formed in the second step by double elimination of HCl under strongly alkaline conditions, with an excess of KOH (6-12 eq.) under high temperatures (190-240 °C), dependent on the boiling point of the final product.^{285,287,290,292,294}

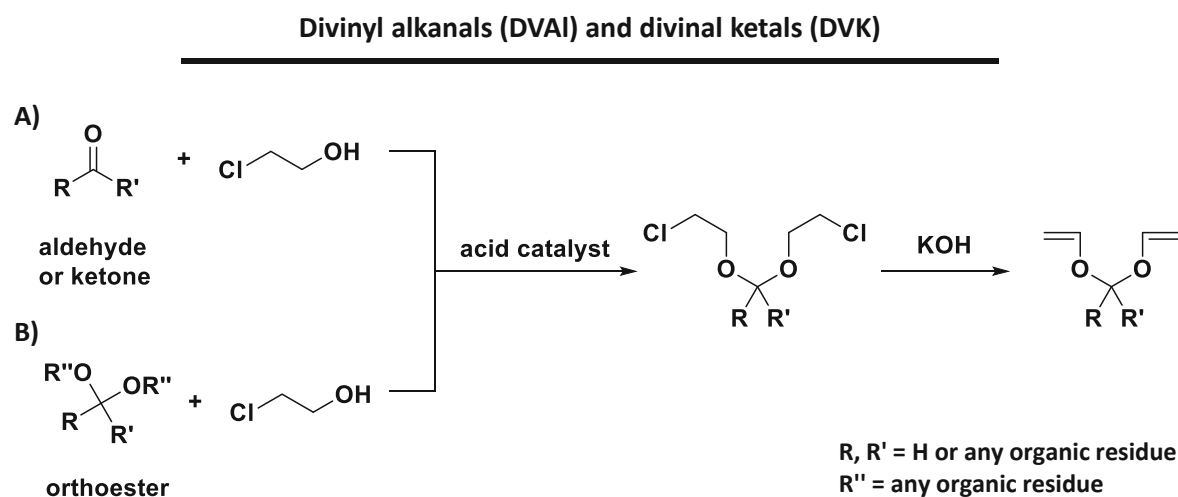
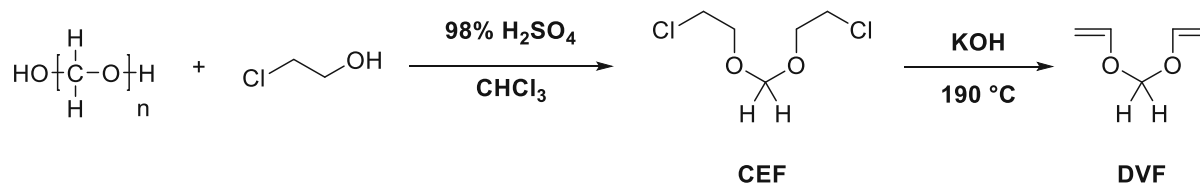


Figure 41: General procedures for the synthesis of divinyl alkanals and divinyl ketals by acid-catalyzed A) acetalization of the respective aldehyde or ketone, or B) acetal exchange from the orthoester. The second step involves the base-catalyzed elimination of HCl to form the product.^{285,287,290,292,294}

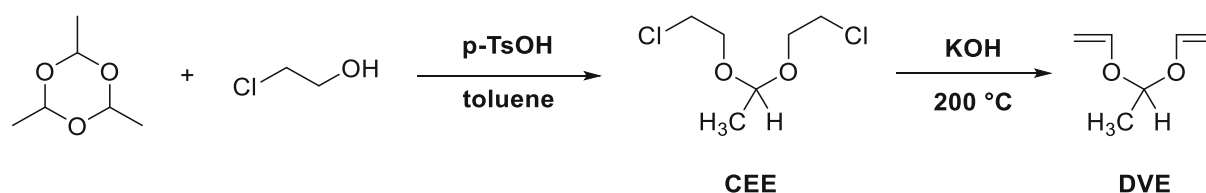
The simplest divinyl alkanal species, divinyl formal (DVF), with two hydrogen atoms attached to the center carbon atom, was synthesized as the first model compound. The synthesis was carried out according to Jian *et al.*²⁹⁰ via pathway A).



For the synthesis of the intermediate bis(2-chloroethyl)formal (CEF), 0.08 eq. of 98% sulfuric acid, 0.7 eq. of paraformaldehyde, and 2.2 eq. of 2-chloroethanol were dissolved in chloroform and heated for 48 h until the evolution of water ceased. The crude product was purified by distillation to afford CEF as a colorless liquid in a yield of 40 %. The final product DVF was prepared from 1 eq. of and 12 eq. of KOH, which were heated for 8 h. After extraction and solvent removal, a mixture containing ~40% of DVF and ~60% of the side product 2-chloroethyl vinyl formal was obtained, which was redistilled to yield the desired product DVF as a colorless liquid in a yield of 21%.

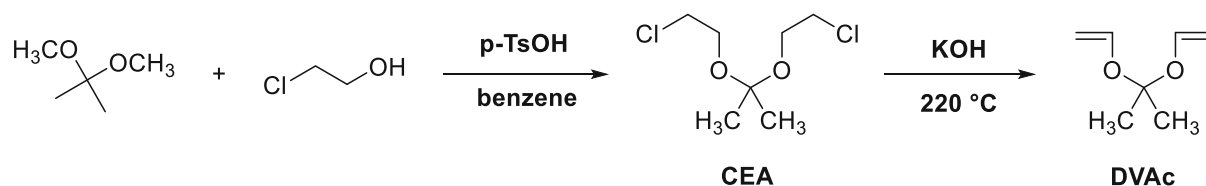
As the final goal was to synthesize difunctional CPMs to form degradable networks, acetal compounds substituted at the central atom were also synthesized. Here, the simplest compound is divinyl ethanal (DVE), containing a methyl group attached to the central atom. As hydrolysis

rates of acetals are influenced by substituents at the carbon atom, this may also impact the degradation behavior of the resulting networks.¹⁸⁸ The synthesis was conducted similarly to DVF, according to Matsoyan *et al.*²⁸⁷.



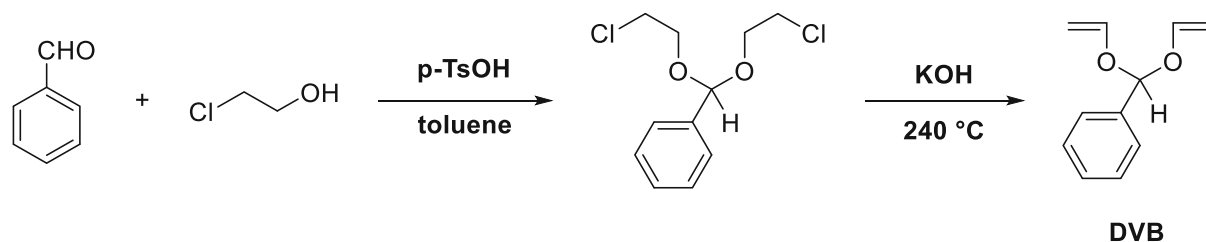
For the synthesis of the intermediate bis(2-chloroethyl)ethanal (CEE), 1 eq. of paraldehyde, 6.8 eq. of 2-chloroethanol, 0.01 eq. of pTsOH were dissolved in toluene and heated until the evolution of water ceased, resulting in a yield of 63%. To synthesize the desired product, 1 eq. of CEE and 10 eq. of KOH were utilized and heated for 8 h to obtain the product in a yield of 25%.

Next, a compound with a fully substituted central atom was synthesized, and the monomer divinyl acetal (DVAc) with two methyl groups was selected. The synthesis was done according to Lorette *et al.*²⁹⁴ following pathway B) using the orthoester dimethoxypropane as a starting material.



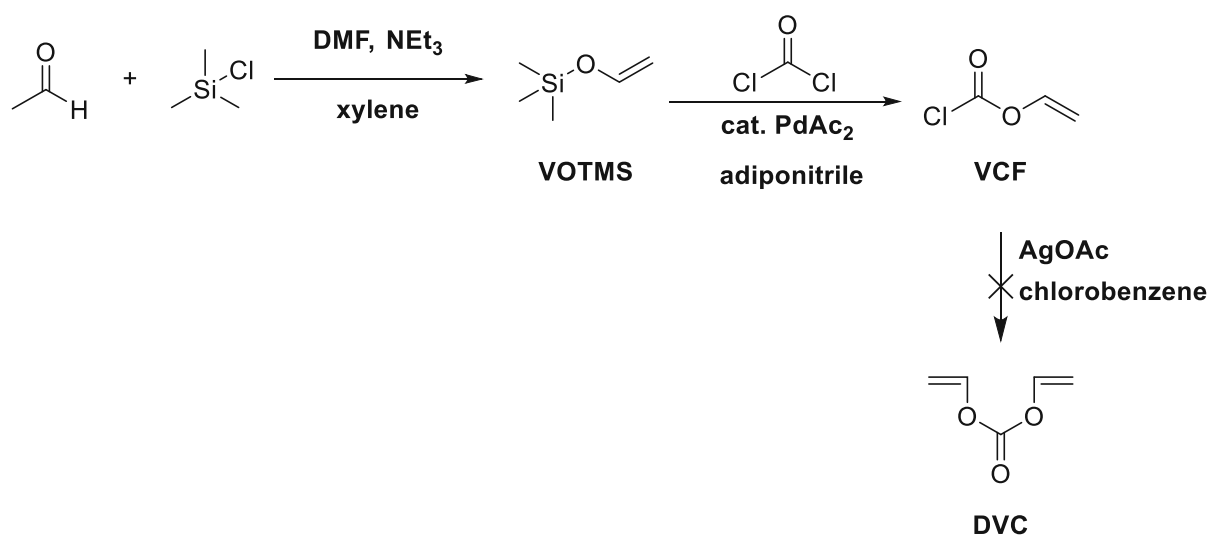
For the synthesis of the intermediate bis(2-chloroethyl)acetal (CEA), 1 eq. of 2,2-dimethoxypropane, 2.2 eq. of 2-chloroethanol, 0.01 eq. of pTsOH were dissolved in benzene and heated until the evolution of methanol ceased to obtain a yield of 27%. For the next step, 1 eq. of CEA and 10 eq. of KOH were heated for 8 h, and the product was afforded in a yield of 13%.

As good mechanical properties, such as high strength and stiffness, are required for the final material used in BTE, aromatic substituents at the center carbon were also envisioned. An influence of the aromatic moieties on network degradation was also expected. Hence, the synthesis of divinyl benzal (DVB), containing a phenyl moiety at the center atom, was done according to Matsoyan *et al.*²⁸⁶.



For the synthesis of the intermediate bis(2-chloroethyl)benzal (CEB), 1 eq. of benzaldehyde, 2 eq. of chloroethanol, 0.01 eq. of pTsOH were dissolved in toluene and heated until the evolution of water ceased to obtain a yield of 44%. For the second step, 1 eq. of CEB and 6 eq. of KOH were heated for 8 h to afford the product in a yield of 16%.

To determine the influence of electron-withdrawing groups on the cyclopolymerization tendency of divinyl ethers, divinyl carbonate (DVC) was chosen as a model compound. Although no higher functional CPMs containing carbonate moieties are obtainable, due to the full substitution of the center carbon, DVC might be used as a reactive diluent in combination with other higher functional CPMs. Additionally, the bulky and electron-withdrawing carbonate group may improve cyclopolymerization tendency due to a more favorable double bond orientation for ring formation. The synthesis of DVC was conducted via a three-step procedure. The first two steps were done according to Hofecker *et al.*²⁹⁵, and the last step was conducted according to Beak *et al.*²⁹⁶



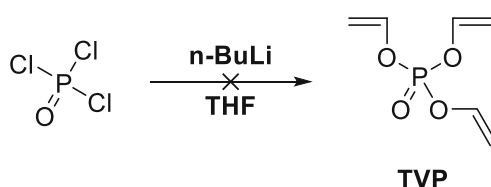
In the first step, vinyloxy trimethylsilane (VOTMS) was synthesized using 1.25 eq. triethylamine (NEt_3), 1 eq. trimethylsilyl chloride, and 2.5 eq. acetaldehyde dissolved in DMF, which were stirred at rt for 1 week, and the product was obtained in a yield of 46%. In the next step, DVC was synthesized using 1 eq. of VOTMS, 0.01 eq. of palladium(II) acetate (PdAc_2) as a catalyst, and phosgene (20 w% solution in toluene), which were subsequently stirred at rt for 72 h. To determine if any phosgene was left in the mixture, phosgene test strips were prepared. After complete removal of phosgene, the mixture was distilled to yield the product vinyl chloroformate (VCF) in a yield of 46% as a solution in toluene. Toluene and the product could not be separated due to their similar boiling points. For the third step, 1 eq. of vinyl chloroformate (23% solution in

toluene) was added to 0.8 eq. of silver acetate in chlorobenzene. After 1 week, still, no product was formed, according to NMR. This is most probably due to the usage of VCF as a solution in toluene, which might interfere with the formation of the desired product.

1.1.2 Synthesis of heteroatom-based model compounds

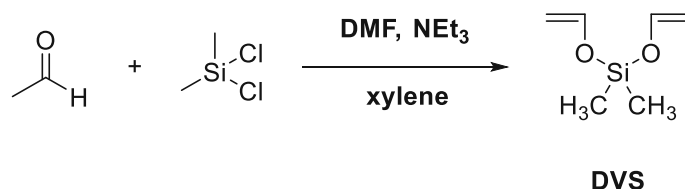
Due to their less stable bonds formed with oxygen compared to carbon, heteroatoms, such as phosphorus, silicon, and boron, were incorporated into the CPM structure by replacement of the central carbon atom. Monomers and polymers containing these bonds were studied by several groups, which showed that they are hydrolyzable under certain conditions and form less acidic and non-toxic degradation products^{62,190,207-211,213,217,218,229-235,256}. Nevertheless, radical cyclopolymerization of divinyl ether compounds containing these degradable motifs was only studied for the compound PDVP, depicted in Figure 40, so far. Therefore, these compounds are highly interesting for the field of BTE and might offer the solution for a biocompatible material that both exhibits sufficient mechanical properties while also being degradable without forming toxic or irritant products. As no vinyl ethers of boronic acids were found in literature, the focus was especially on compounds containing phosphorus and silicon.

First, the phosphorus-based compound trivinyl phosphate (TVP) was synthesized according to Dworak *et al.*²⁹⁷



For the synthesis, first, the cycloreversion of THF was performed to form the necessary Li-enolate.²⁹⁷ For this, 2.9 eq. of n-BuLi were added to 56 eq. of THF and then stirred for 30 min at 0 °C and another 16 h at rt. Subsequently, the solution was added to 1 eq. of phosphoryl chloride, followed by stirring for 1 h at -78 °C and rt overnight. Unfortunately, no product was obtained after removal of the precipitate and solvent evaporation.

As an analog to divinyl acetal, the Si-based compound bis 2-(vinylloxy)-dimethylsilane (DVS), with two methyl groups attached to center atom, was synthesized in accordance with Hofecker *et al.*²⁹⁵



For the preparation, 2.5 eq. NEt_3 , 1 eq. dichlorodimethylsilane and 5 eq. acetaldehyde were dissolved in DMF and stirred at rt for 1 week to yield the product in a yield of 26%.

1.1.3 Reactivity towards cyclopolymerization

After the successful synthesis of five carbon- and heteroatom-based model compounds summarized in Figure 42, next, the tendency of these monomers for radical cyclopolymerization was investigated. As vinyl ethers are typical monomers for cationic photopolymerization, cationic photoinitiators (PIs) were applied to study the possibility of cationic cyclopolymerization. Hence, after irradiation, it was determined whether soluble polymer chains with cyclic structures within the backbone, instead of crosslinked networks, were formed upon polymerization.

Due to the high volatility of all compounds, except DVB, no photo-DSC measurements could be performed, as substantial evaporation of the samples in the crucibles was observed, even when using a glass lid. Therefore, RT-NIR photorheology measurements were conducted, during which a significant reduction of sample evaporation was achieved due to the small gap size.

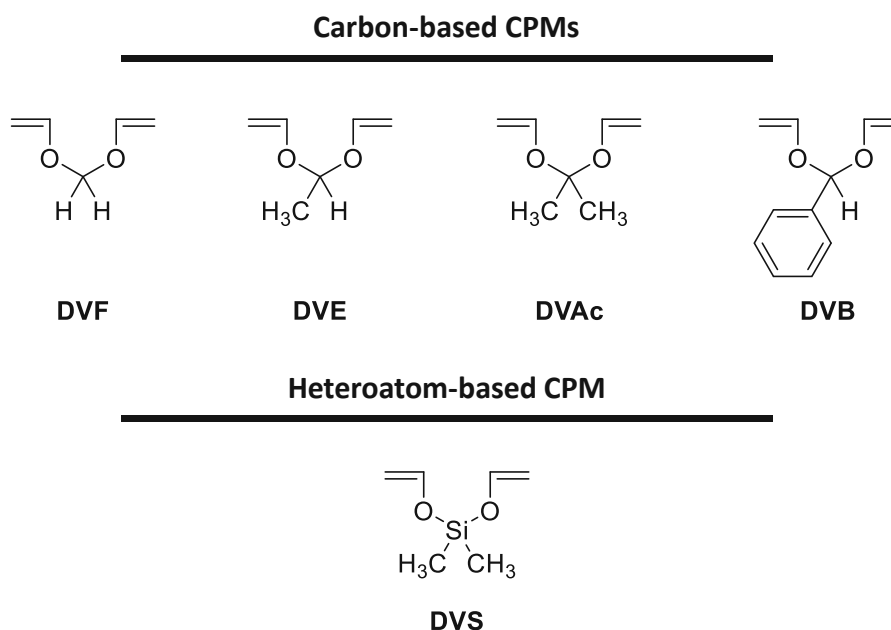


Figure 42: Synthesized carbon-based and heteroatom-based CPMs.

This method is a powerful tool to simultaneously determine rheological and kinetic data during polymerization. For this, a defined amount of resin is applied onto a glass plate, and rheology data is collected via oscillatory shearing with a plate-plate rheometer (PP25). The formulation containing monomer and photoinitiator (PI) is irradiated from below with UV light, and the double bond conversion (DBC) is followed via a NIR beam, which is guided through the resin and reflected by the plate of the rheometer (Figure 43).

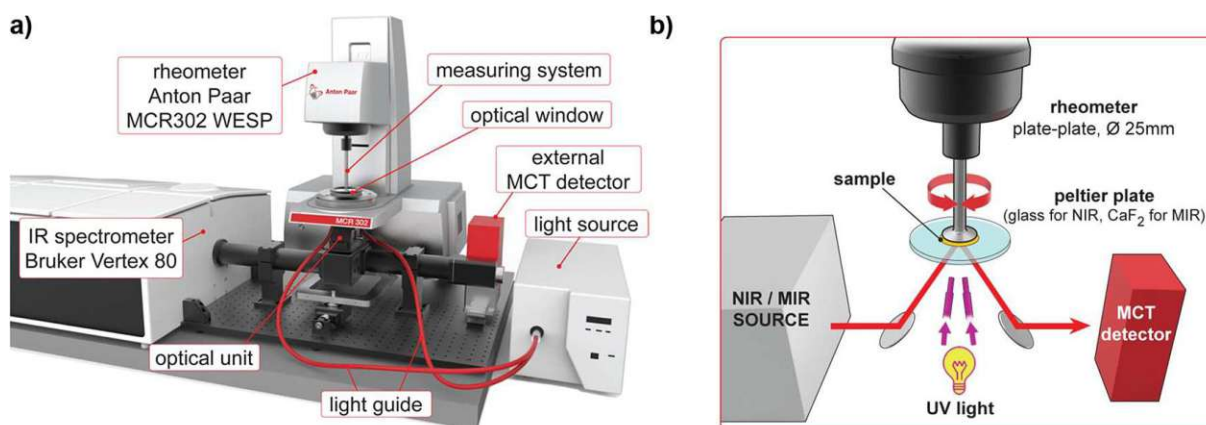


Figure 43: a) General setup of the RT-NIR photorheometer; b) Schematic illustration of the IR-beam path.²⁹⁸

Important mechanical data, which can be determined from the rheological data, includes the storage modulus G' and the loss modulus G'' over the course of the polymerization and the final storage modulus G'_{final} of the material. Furthermore, the time when the gel point is reached (t_{gel}) can be calculated, corresponding to the time of intersection of the storage and loss modulus curves. When polymerization starts, the gel point marks the time, at which a gel is formed in the

liquid monomeric formulation, reflected in a loss in fluidity and the formation of a 3D network, which results in an abrupt change in viscosity. From the IR data, the double bond conversion at the gel point (DBC_{gel}), final double bond conversion (DBC_{final}), and time when 95 % of DBC is reached (t_{95}) can be calculated. Lastly, the occurring shrinkage stress can be determined, which correlates with the maximum normal force ($F_{N,max}$) during the measurement.²⁹⁸

For the experiments, filtered light from a broadband Hg lamp (320-500 nm) was used. 150-180 μ L of sample volume was applied to the glass plate, which was covered with a PE tape, and each formulation was irradiated for 540 s with a 200 μ m gap between the measuring system and the glass plate. It is important to note that irradiation was induced 65 s after the start of each measurement. The light intensity at the surface of the samples was adjusted to 30 mW/cm². The measurements were performed in triplicates at 25 °C with a closed furnace. The DBC over time was determined by integration of the double bond signal at ~ 6170 cm⁻¹ and related to the integral at t_0 .

All samples obtained after the measurements were treated with CDCl₃ for NMR measurements to determine the double bond conversion (DBC_{NMR}) and THF for gel permeation chromatography (GPC) to investigate the molecular weight of the received polymers. The double bond conversion could be determined for all monomers via the signal of the double bond, while the -H at the center carbon for DVF, the -CH₃ at the center carbon for DVE, DVAc, and DVS and the aromatic -H at the phenyl group for DVB were used as internal standards.

1.1.3.1 Radical cyclopolymerization

To determine the reactivity of the synthesized monomers towards radical cyclopolymerization, RT-NIR-photorheology measurements were conducted with formulations prepared from each monomer and 1 w% of the photoinitiator bis(4-methoxybenzoyl)diethylgermanium (Ivocerin®), which was already confirmed to be biocompatible by the company Ivoclar GmbH.¹³⁰

Table 3: Detailed results of RT-NIR-photorheology, GPC, and NMR measurements of formulations containing each monomer with 1 w% Ivocerin. *No gelation occurred. °No polymer detected.

monomer	t_{gel} [s]	DBC_{gel} [%]	t_{95} [s]	DBC_{final} [%]	G'_{final} [kPa]	$F_{N,max}$ [N]	M_n [kDa]	PDI [-]	DBC_{NMR} [%]
DVF	-*	-*	317.5 ± 32.5	14.6 ± 8.4	-*	-*	-°	-°	0
DVE	-*	-*	392.5 ± 47.5	14.9 ± 1.3	-*	-*	0.43	1.08	7
DVAc	-*	-*	285.0 ± 68.0	10.4 ± 0.2	-*	-*	1.86	1.90	3
DVB	-*	-*	54.0 ± 21.0	13.1 ± 0.1	-*	-*	3.20	3.49	6
DVS	-*	-*	219.5 ± 141.5	13.1 ± 1.0	-*	-*	-°	-°	0

Table 3 shows that upon radical polymerization, no gelation occurred for all monomers, as expected in the case of complete cyclopolymerization. However, no solid specimens were obtained, and all samples remained liquid. Additionally, a maximum double bond conversion of 15% for all formulations was determined, which could also be an artifact of the evaporation of the volatile compounds.

All samples dissolved readily in $CDCl_3$ and THF. Results in Table 3 confirmed that no double bond conversion was detected via NMR for DVF and DVS, and only slight conversions were shown for the other monomers (3-7%). This supports the results of the photorheology measurements, in which slightly higher but still very low DBC values, up to 14%, were observed. The NMR spectra additionally showed the formation of slight amounts of oligomeric substances for the polymerization of DVE, DVAc, and DVB. GPC confirmed that soluble oligomers were formed for these photopolymerizations, with the highest molecular weight determined for DVB with 3.2 kDa. This shows that although the tendency of these compounds for homopolymerization and hence crosslinking is low, radical cyclopolymerization also does not occur, or occurs only to a small extent as only soluble oligomers with a very low chain length are formed for DVE, DVAc, and DVB.

1.1.3.2 Cationic cyclopolymerization

Next, measurements were done with formulations containing each monomer and 1 w% of the cationic initiator I-Al (Figure 44) to get insights if cationic cyclopolymerization is possible. In general, due to the high reactivity of vinyl ethers towards cationic initiation, no cyclopolymerization, but crosslinking of vinyl ethers with cationic initiators was expected. The mechanism of the photoinitiated cationic polymerization of vinyl ethers with diaryliodonium salts as initiators is depicted in Figure 44. Briefly, photoexcitation of the diaryliodonium salt occurs, leading to both heterolytic and homolytic cleavage of the carbon iodonium bond. The generated aryl cations and aryl cation radicals then react with present solvents, monomers, or impurities to

yield the protonic superacid HMtX_n , which then initiates the photopolymerization by addition to the vinyl ether double bond, followed by propagation with further monomers.²⁹⁹

Cationic photopolymerization

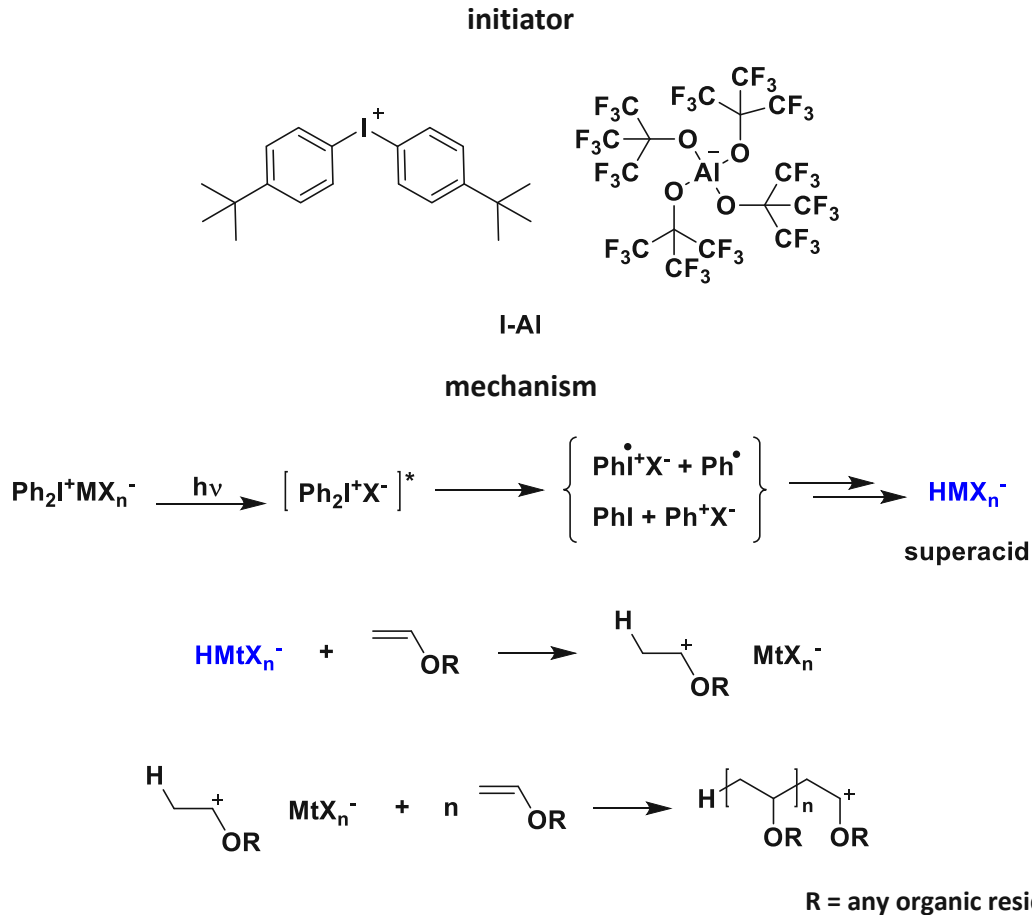


Figure 44: Structure of the cationic photoinitiator I-Al and mechanism of cationic photopolymerization of vinyl ether monomers.

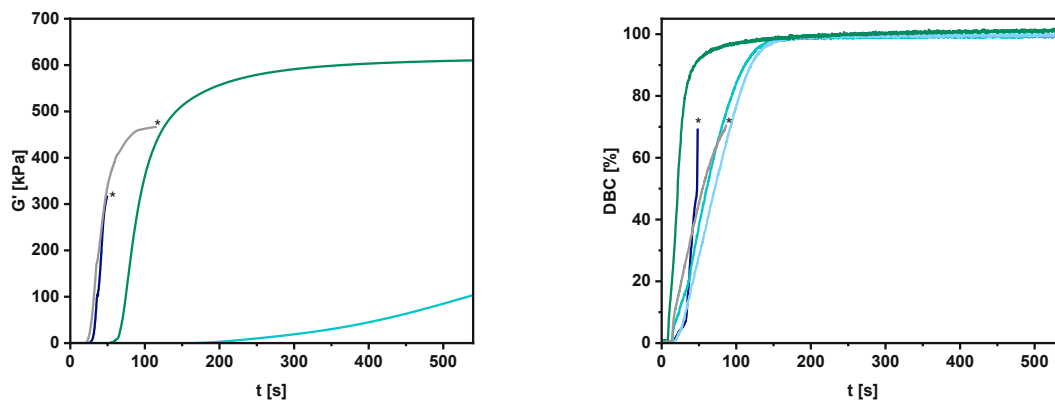


Figure 45: Storage Modulus (G' , left) and DBC (right) over time for DVF (—), DVE (—), DVAc (—), DVB (—), and DVS (—). *Detachment from stamp occurred.

The rheological data (Figure 45, left) shows that gelation was observed for all monomers except for DVAc, which did not display any increase in storage modulus and resulted in a highly viscous

liquid after irradiation for 540 s. Crosslinking was shown for all monomers, DVF, DVE, DVB, and DVS, indicating a greater tendency to homopolymerize than for cyclopolymerization. With DVF, DVB, and DVS, brittle sample platelets were obtained, while polymerization of DVE resulted in a rather soft platelet. DVF and DVS show relatively fast gelation with crosslinking observed after ~ 20 s. Additionally, detachment of the solid polymers from the stamp was observed for these formulations due to the high shrinkage of these networks (~ 40 N); hence, the curing process could only be monitored for < 100 s. This further supports that homopolymerization occurred, as cyclopolymerization should lead to reduced shrinkage during curing.²⁸³ A significantly retarded polymerization was shown with DVB and was even more substantial for the formulation containing DVE. This may be due to the electron-donating effect or steric effects of the phenyl and the methyl group on the acetal moiety, retarding cationic polymerization. The IR data (Figure 45, right) confirmed that high conversions were observed, even for the sample containing DVAc, with conversions $> 99\%$ for DVE-, DVAc-, and DVB-based formulations. Since no gelation occurred for the sample containing DVAc, this indicates that cyclopolymerization might have occurred. For the formulations containing DVF and DVS, the conversion could only be monitored until detachment from the stamp and is hence seemingly lower compared to the other monomers.

Cationic photopolymerization uses an initiator, which forms a superacid initiating species upon irradiation with light. As acetals can be hydrolyzed under acidic conditions, cleavage of the monomers and the formed polymer network was expected and was evident in many ways. For the slower polymerizing monomers DVE and DVB, this effect appears to be more significant, as upon closer look at the DBC curves over time (Figure 45, right), a kink at around 20% conversion was observed. Additionally, t_{95} values were lower than the time for gelation, and a DBC_{gel} of almost 100% was attained in the polymerization of these monomers. Therefore, cleavage of the acetal moiety of the monomers and the formed network by the acid must occur, which directly competes with the formation of a crosslinked network. This leads to the observed retardation and results in an apparent but “false” increase in DBC, as aldehydes or ketones are formed from the double bond-containing species during this process. This also might explain the high DBC observed for the polymerization of DVAc, which does not display network formation. For the monomers DVF and DVS, with faster polymerization kinetics, significantly accelerated gelation, and lower DBC_{gel} values of 4-11% were shown. This indicates that the cationic polymerization is significantly faster than the cleavage of the acetal groups, which might indicate higher stability of these monomers towards the acid-initiating species. In general, the stability of an acetal or ketal against acids is determined by the stability of the oxonium ion formed in the first stage of the hydrolysis, depicted

in Figure 46. The more stabilized by electron-donating groups, the higher the rate of hydrolysis.¹⁸⁸ The resulting order of stability for the synthesized monomers is shown in Figure 46, which further confirms the results, as the fastest crosslinking was observed with the most stable compound DVF, while slower crosslinking was shown for less stable DVE and DVB, with increased extent of monomer and polymer cleavage. For DVAc, stability might even be so low that cleavage occurs faster than polymerization. The detailed results of the measurements are given in Table 4.

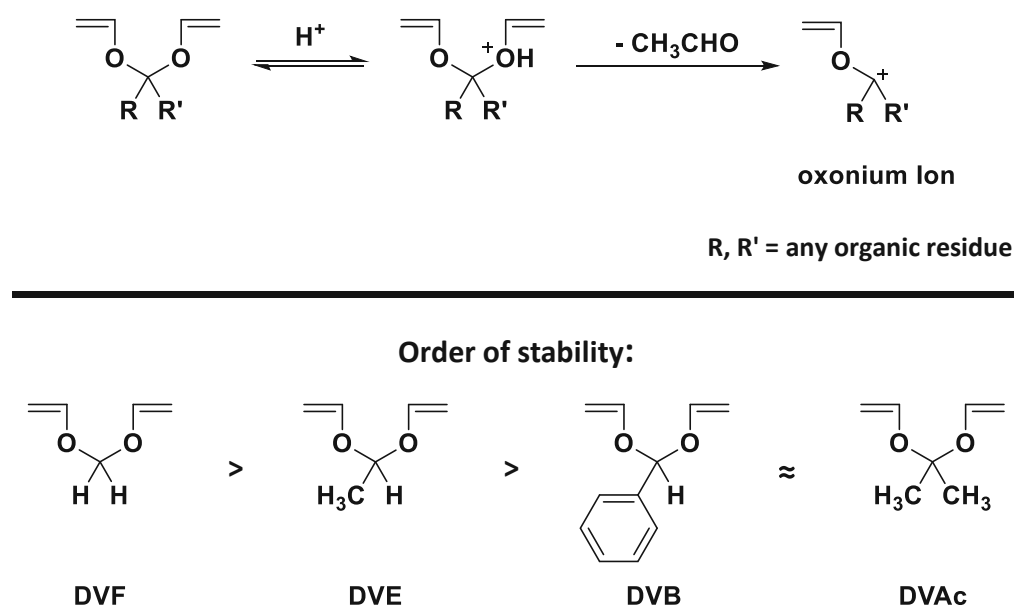


Figure 46: Acidic hydrolysis of acetals or ketals under the formation of an oxonium ion as an intermediate and resulting order in the stability of carbon-based CPDs.

Table 4: Detailed results of RT-NIR-photorheology measurements. °No gelation occurred. *Detachment from stamp was observed.

monomer	t_{gel} [s]	DBC _{gel} [%]	t_{95} [s]	DBC _{final} [%]	G'_{max} [kPa]	$F_{N,max}$ [N]
DVF	25.1 ± 1.9	4.4 ± 0.5*	47.6 ± 0.3*	69.5 ± 2.6*	315.2 ± 3.9*	-38.4 ± 3.9*
DVE	175.0 ± 2.0	98.5 ± 0.2	125.5 ± 2.5	99.1 ± 0.1	115.0 ± 1.9	-7.6 ± 0.2
DVAc	°	°	135.5 ± 0.5	>99.9	0.0 ± 0.0	-0.1 ± 0.1
DVB	83.2 ± 0.6	96.5 ± 0.3	66.0 ± 0.1	99.8 ± 0.1	615.9 ± 5.1	-8.1 ± 0.1
DVS	18.8 ± 0.1	10.9 ± 0.4*	78.2 ± 1.1*	70.7 ± 2.1*	445.5 ± 21.11*	-44.7 ± 3.6*

Table 5: Detailed results of GPC and NMR measurements of monomers with 1 w% I-AI. °No polymer detected. *No residual double bonds.

monomer	M_n [kDa]	PDI [-]	DBC _{NMR} [%]
DVF	°	°	*°
DVE	0.43	1.02	*°
DVAc	0.94	1.75	*°
DVB	1.01	1.49	*°
DVS	°	°	*°

No dissolution of the samples containing DVF, DVE, and DVS occurred, which shows that crosslinking instead of cyclopolymerization took place. GPC data in Table 5 confirmed that no oligomeric or polymeric soluble substances were detected for DVF and DVS, while oligomers with an extremely low molecular weight of 0.4 kDa were observed for DVE, which supports that almost fully crosslinked networks were formed. For DVAc and DVB, dissolution of the samples occurred in both CDCl_3 and THF, which indicates that cyclopolymerization might have happened. Nevertheless, oligomers with low molecular weights (0.9-1.0 kDa) were also formed. This shows that for all monomers, cyclopolymerization efficiency to form polymers with high molecular weight is extremely low. NMR data in Table 5 shows that no monomer was present after polymerization as no double bonds were detected after polymerization, and no conversion could be determined due to the lack of internal reference peaks. Nevertheless, spectra confirm that this is due to monomer and network cleavage, as peaks for the respective aldehydes or ketones are visible in all spectra of carbon-based CPMs. For DVS, no peaks of the cleaved products are present, which indicates higher stability of the Si-O-bond towards acidic conditions, and, therefore, supports the high gelation rates observed in photorheology.

To conclude, polymerization of the synthesized compounds with cationic initiators leads to full crosslinking instead of cyclopolymerization for all monomers except DVAc and DVB. Although solubility in different solvents could be confirmed for these samples, only very low molecular weights were determined (<1.1 kDa), which shows that although cyclopolymerization might have occurred, only small oligomers, instead of polymers with high chain length, were formed. Additionally, it was shown that cleavage of the monomers takes place upon irradiation due to the formation of the acidic initiating species. Therefore, these compounds are not suitable for cationic photopolymerization. The results are also supported by literature, which states that for efficient cationic cyclopolymerizations, high monomer dilutions and living initiator systems (ZnCl_2/HCl) are essential to suppress homopolymerization.^{276-278,300} Therefore, cationic cyclopolymerization by photoinitiation in bulk seems impossible and was hence not pursued further.

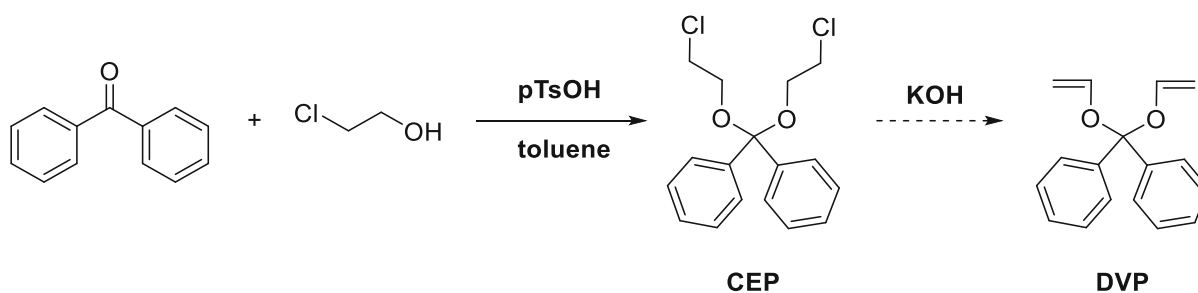
1.2 Monomers with improved cyclopolymerization tendency

Since preliminary attempts for cyclopolymerization with the synthesized CPMs were unsuccessful, and no significant cyclopolymer formation was observed with both radical and cationic photoinitiators, a new monomer design was pursued. As described in the State of the Art, two principles can be employed for efficient cyclopolymerization. The first principle comprises the introduction of bulky substituents into the structure to orient the double bonds in close proximity for ring closure. These bulky substituents may, for example, be attached to the center atom of the CPMs. Secondly, a low tendency towards homopolymerization was found beneficial, which can be achieved by activating the double bond with electron-withdrawing groups from inside or outside of the double bond with typically applied groups, including ester moieties.²⁸⁰ Therefore, the synthesis of novel compounds was conducted, and both approaches of enhancing cyclopolymerization tendency via sterically hindered moieties attached to the central carbon and activation of the double bond by electron-withdrawing groups were used to generate new target structures.

1.2.1 Synthesis of carbon-based cyclopolymerizable monomers

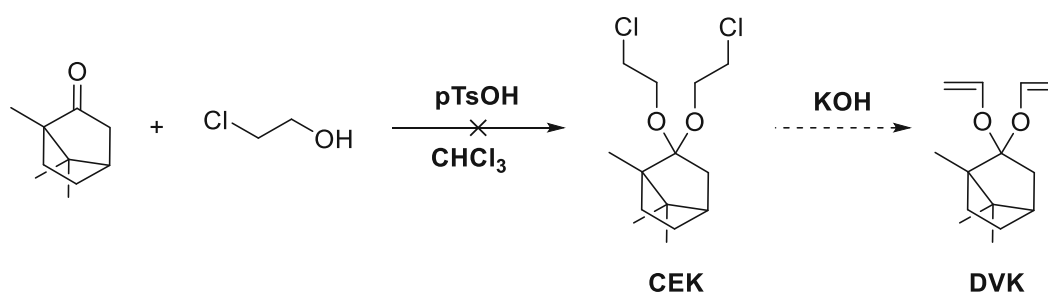
First, several compounds with bulky substituents at the central carbon atom were synthesized. For this, the same procedure as for divinyl alkanals and ketals described in 1.1.1 was used. However, as ketalization with sterically demanding substituents is less favored, higher amounts of 2-chloroethanol (2.5-4 eq.) and pTsOH (0.04 eq.) for some reactions were employed to shift the equilibrium towards the ketal product.

Especially benzophenone was found to be an interesting starting compound, as ketalization would result in the formation of a sterically-hindered center atom attached to two phenyl moieties. Hence, the synthesis of diphenyl-bis(vinyloxy)methane (DVP) was conducted according to Matsoyan *et al.*^{285,292}



The intermediate bis(2-chloroethoxy)diphenylmethane (CEP) was synthesized with 1 eq. of benzophenone, 2.5 eq. of chloroethanol, and 0.01 eq. of pTsOH, which were dissolved in toluene and heated until the evolution of water ceased. NMR showed that the solid consisted mainly of benzophenone and ~12% of the desired product. This indicates that the high steric hindrance at the center carbon results in an equilibrium shift towards the starting materials instead of the desired ketal. Distillation under vacuum was attempted but was unsuccessful, and column chromatography was not possible due to the high similarity in R_f values of benzophenone and the desired product. Therefore, the product could not be isolated.

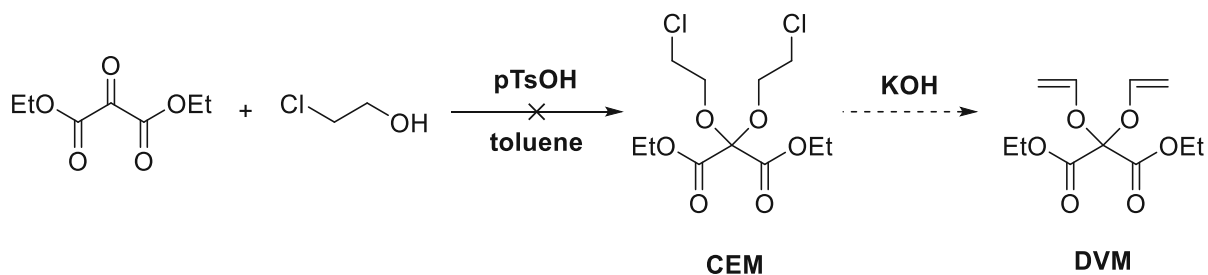
Another interesting naturally occurring compound for ketalization is camphor, as it would lead to a strongly sterically-hindered center carbon. Liu *et al.*³⁰¹ published the synthesis of a cyclic acetal of camphor with glycerin; however, literature gives no results for linear acetals of this compound. Nevertheless, the synthesis of 1,7,7-trimethyl-2,2-bis(vinyloxy)bicyclo[2.2.1]heptane (DVK) was conducted according to Matsoyan *et al.*^{285,292}



For the first step of the synthesis of 2,2-bis(2-chloroethoxy)-1,7,7-trimethylbicyclo[2.2.1]heptane (CEK), 1 eq. of (+/-)-camphor, 3 eq. of chloroethanol, 0.01 eq. of pTsOH were dissolved in chloroform and heated to reflux. No water formation was observed, and NMR confirmed that no product was formed. Therefore, toluene and benzene were also tested as solvents in combination with higher concentrations of pTsOH (0.04 eq.) and chloroethanol (4 eq.). However, still, no product formation was observed. Most probably, the steric hindrance at the center carbon is too high for the formation of the product, and only the formation of cyclic acetals described in literature³⁰¹ is thermodynamically favored.

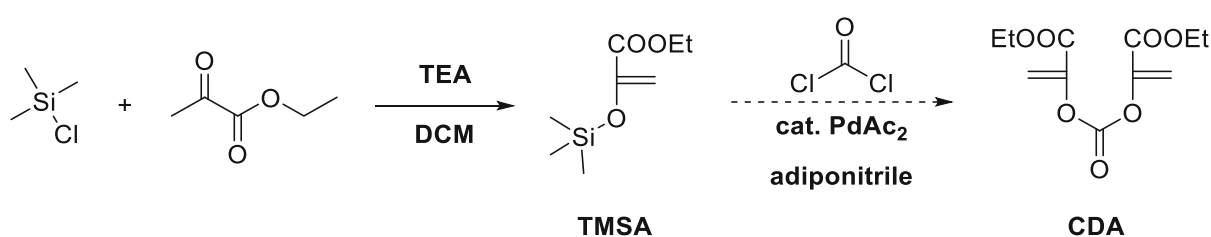
To enhance the electrophilicity of the center carbon, and hence the attack of the alcohol during the first step of ketalization, diethyl ketomalonate, containing two ester groups next to the carbonyl group, was used as the next precursor. Similar to camphor, for this compound, a cyclic ketal formation was published with chloroethanol under basic conditions by Wang *et al.*³⁰² The

synthesis of diethyl 2,2-bis(vinylloxy)malonate (DVM) was conducted according to Matsuyan *et al.*^{285,292}



For the synthesis of diethyl 2,2-bis(2-chloroethoxy)malonate (CEM), 1 eq. of diethyl ketomalonate, 4 eq. of chloroethanol, and 0.04 eq. of pTsOH were dissolved in toluene and heated to reflux. Again, no water formation was observed, and according to NMR, not the desired product was formed, but the side-product from the transesterification of diethyl ketomalonate with chloroethanol. This again supports that the steric hindrance might be too high and only cyclic acetals of the starting material are thermodynamically favored.

To determine whether cyclopolymerization tendency is increased by activation of the double bond with electron-withdrawing groups, the synthesis of the new carbonate-based compound diethyl 2,2'-(carbonylbis(oxy)) diacrylate (CDA) was attempted via a two-step procedure according to Barton *et al.*³⁰³ This compound displays the advantage that upon cleavage of the carbonate moiety, ethyl pyruvate is formed, a non-toxic substance with a high LD₅₀ (lethal dose, which causes the death of 50% of test subjects) reported for rats (LD_{50,oral,rat}=5 g/kg).¹²⁸



In the first step, trimethylsilyloxy ethyl acrylate (TMSA) was synthesized as described by Barton *et al.*³⁰³ For the synthesis, 1 eq. of ethyl pyruvate was enolized by 1.1 eq. of NEt₃ at 0 °C, and then, 1.1 eq. trimethylsilyl chloride were added, after which the mixture was stirred at rt for 1 h. The product was purified by distillation, yielding the product, which started to polymerize spontaneously during the process. This instability was already reported by Gauss *et al.*¹¹³, who observed polymerization of the product during distillation or upon storage in the freezer and the formation of high molecular weight polymers (>100 kDa) with a low PDI (<2). Subsequently, inhibition of the polymerization was attempted by addition of various radical and cationic

stabilizers, such as BHT, phenothiazine, and NEt_3 (1000 ppm). Nevertheless, polymerization during distillation still occurred. Another possibility would be group transfer polymerization of TMSA in the presence of nucleophiles, depicted in Figure 47. Therefore, also the acid stabilizer (2-((2-(ethoxycarbonyl)allyl)oxy)ethyl) phosphonic acid (MA154), shown in Figure 48, was added, but still, polymerization was observed, and the product could not be isolated.



Figure 47: Group transfer polymerization of TMSA.

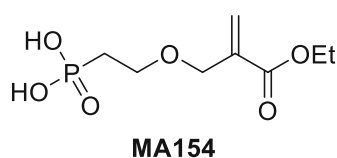
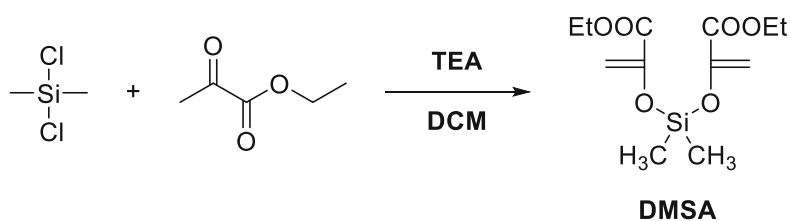


Figure 48: Chemical structure of the acid stabilizer MA154.

1.2.2 Synthesis of heteroatom-based cyclopolymerizable monomers

As the synthesis of novel carbon-based compounds with both bulky substituents or electron withdrawing groups was unsuccessful, the synthesis of heteroatom-based CPMs comprising these principles was attempted. As a result, the synthesis of the silicon-based compound diethyl 2,2'-((dimethylsilanediy)bis(oxy))diacrylate (DMSA), containing electron-withdrawing and sterically demanding ester groups attached to the double bonds, was conducted analogously to TMSA, as described by Barton *et al.*³⁰³



For the synthesis, 2 eq. of ethyl pyruvate, 2.2 eq. of NEt_3 , and 1.1 eq. dichlorodimethylsilane dissolved in DCM were used, which were stirred at rt for 1 h. Similar to TMSA, the product polymerized spontaneously during solvent evaporation, suggesting a similar polymerization mechanism. Again, stabilization with various stabilizers (1000 ppm of BHT, phenothiazine, NEt_3 , or

MA154) was unsuccessful. Slight amounts of unpolymerized solid could be removed from the flask and analyzed, showing a high melting point of 165 °C. Therefore, this compound is unsuitable as a cyclopolymerizable monomer, which generally should display low melting points or even be liquid at rt, and the synthesis was not pursued further.

1.3 Resumé

A library of different carbon- and heteroatom-based divinyl ether monomers containing cleavable bonds at the center atom and tested for their tendency towards both radical and cationic cyclopolymerization. It was shown that cyclopolymerization efficiency is very low with a radical initiator, with the formation of soluble oligomers with low molecular weight (<3.2 kDa) for some of the monomers. Upon the addition of a cationic initiator, crosslinking instead of cyclopolymerization occurred for most monomers. GPC showed that only oligomeric structures with even lower molecular weights (<1.1 kDa) were formed for the compounds that did not display gelation. Furthermore, it was shown that upon irradiation, monomers and the forming polymer network were cleaved, by the acidic initiating species. Therefore, novel target structures with increased cyclopolymerization tendency were envisioned, containing either bulky substituents at the center carbon or electron-withdrawing groups attached to the double bonds. Unfortunately, all the synthetic attempts were unsuccessful. This was due to the spontaneous polymerization of some compounds or high steric hindrance at the center carbon resulting in an equilibrium shift towards the starting materials, impeding product formation. Therefore, the first approach, to use di- or higher functional CPMs containing degradable motifs at the center atom for the generation of cleavable, rigid networks comprising cyclic structures, was unsuccessful, and the second approach to generate polymers with good (thermo)mechanical properties and enhanced degradation behavior, described in 1, was pursued.

2. New monomers and thiols for enhanced mechanical properties and degradation of thiol-ene networks

State-of-the-art photopolymers used for the production of 3D-printed scaffolds, next to poor mechanical properties, tend to exhibit unfavorable degradation behavior or insufficient degradation speed *in vivo*.^{59,68,98,99} Accordingly, novel biocompatible monomers are required, which form polymers with accelerated degradation *in vivo*. As the synthesis of CPMs containing degradable motifs with a sufficient tendency towards cyclopolymerization was unsuccessful, another approach was considered to enhance both mechanical properties and network degradation. Therefore, this work aimed to develop and characterize novel monomers with possible application in lithography-based additive manufacturing technologies (L-AMTs) for the fabrication of biocompatible and biodegradable scaffolds for bone tissue engineering (BTE). For this, the focus was especially on compounds containing bonds between oxygen and the heteroatoms phosphorus, silicon, or boron. As described in the State of the Art, poly(phosphoesters) (PPEs) and poly(silylethers) (PSEs) are highly interesting, as these polymers exhibit hydrolytic degradation, high biocompatibility and low toxicity.^{207,209,211} Above all, PPEs are most intriguing, as good adhesion to bone,²¹³ osteoinductive effects^{223,225} and degradation of bulk materials via surface erosion¹¹² were shown. For PSEs, biocompatible and biodegradable soft tissue implants were reported,^{62,233} making them highly attractive for subsequent studies. Boron as a heteroatom was selected, as boronic esters (BEs) are known for their facile hydrolysis and dynamic transesterification reactions. Although never studied as degradation enhancers, BEs were thoroughly investigated for materials capable of self-healing, reshaping, and recycling.^{235,237,239,244-251} Nevertheless, until now, there are no reports on the usage of compounds based on phosphorus, silicon, or boron in 3D-printed biodegradable scaffolds with mechanical properties sufficient for the replacement of human bone.

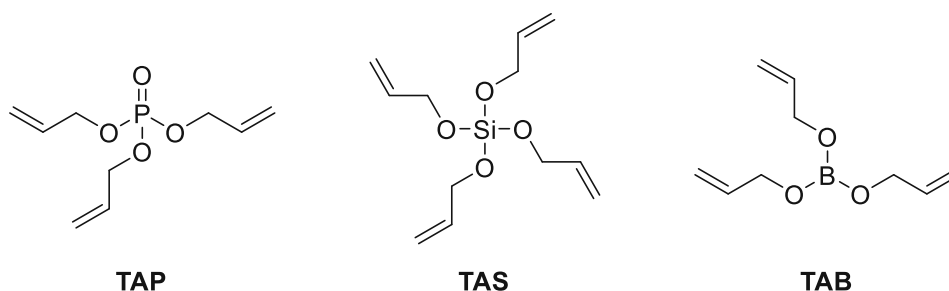
Starting point of these studies was the investigation of monomers and polymers containing bonds between oxygen and phosphorus, silicon or boron by comparing their hydrolysis and degradation to carbon-based analogs. To synthesize materials with good (thermo)mechanical properties, the aim was to apply these monomers in thiol-ene photopolymerization, which results in reduced oxygen inhibition, and the formation of homogeneous and tough networks.^{97,194} For quasi-ideal thiol-ene reactions, allyl ethers, and esters were selected as a polymerizable group, resulting in equimolar consumptions of double bonds and thiol groups during photopolymerization.^{141,147} As a next step, rigid elements such as bulky substituents or cyclic structures were incorporated into

monomer and thiol structures to provide the networks with other properties essential for bone regeneration scaffolds, such as high stiffness and strength. Additionally, to further enhance (thermo)mechanical properties, also additives were introduced. All resins and resulting polymers were then investigated towards the fulfilment of certain requirements for 3D-printed bone regeneration scaffolds, such as photoreactivity, (thermo)mechanical properties, degradation behavior and rates, sterilization, and cytotoxicity.

2.1 Selection of monomers for improved network degradation

To determine, which heteroatoms can be used for improved degradation under hydrolytic conditions, first, simple allyl ester monomers containing phosphorus, silicon, and boron were selected. Therefore, P-based triallyl phosphate (TAP), Si-based tetraallyl ortho silicate (TAS), and B-based triallyl borate (TAB) were chosen (Figure 49), for which thiol-ene polymerization is already described in literature. P-based TAP was applied in thiol-ene photopolymerization for the production of phosphorus-nitrogen-containing flame-retardant wood coatings by Wang *et al.*, but only temperature degradation was studied, and no hydrolytic degradation was reported.³⁰⁴ The thiol-ene photopolymerization of the Si-based compound TAS was used by Ware *et al.*, to synthesize hydrolytically degradable networks to fabricate biodegradable cortical electrodes. Only one patent from Skarja *et al.*³⁰⁵ deals with the thiol-ene polymerization of the monomer TAB, proposing its use for producing porous chromatography membranes, which, however, were not intended to be degradable. As a reference, a C-based allyl ester was used, namely citric acid triallyl ester (CTAE, Figure 49), for which thiol-ene polymerization is only reported for the fabrication of non-degradable anti-fogging coatings³⁰⁶ and transparent, self-healable coatings.³⁰⁷ Its hydrolysis product, citric acid, is known to be biocompatible, as it takes part in the Krebs cycle *in vivo* to release energy.³⁰⁸

Heteroatom-based allyl esters



Carbon-based reference

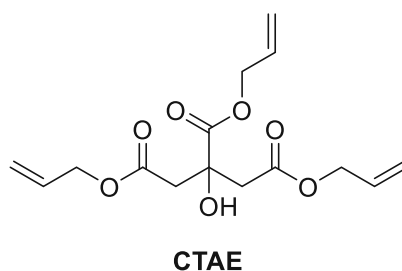


Figure 49: Structure of the heteroatom-based allyl esters triallyl phosphate (TAP), tetraallyl ortho silicate (TAS), and triallyl borate (TAB), and the carbon-based reference citric acid triallyl ester (CTAE).

2.1.1 Model study of monomer hydrolysis

First, a model study was conducted to determine the rate of hydrolysis of each heteroatom-containing monomer and compare it to the carbon-based allyl ester CTAE. For this, an NMR study was done, in which the monomers were dissolved in D₂O/CD₃CN solutions (1:1). Subsequently, the formation of the hydrolysis product allyl alcohol was monitored over time. The studies were conducted under neutral conditions. Furthermore, acidic conditions (addition of 0.01 M DCl) with a pH of ~4 were used to mimic the conditions during bone regeneration, as an acidic pH below 4.5 is essential for osteoclast-driven bone resorption.⁶⁰ Lastly, basic conditions with a pH of ~10 (addition of 0.01 M NaOD) were applied to determine possible differences to the behavior of the monomer in neutral and acidic conditions. The amount of formed allyl alcohol, which is equal to the amount of hydrolyzed monomer, was determined by integration of the double bond signal of allyl alcohol at 4.55 ppm.

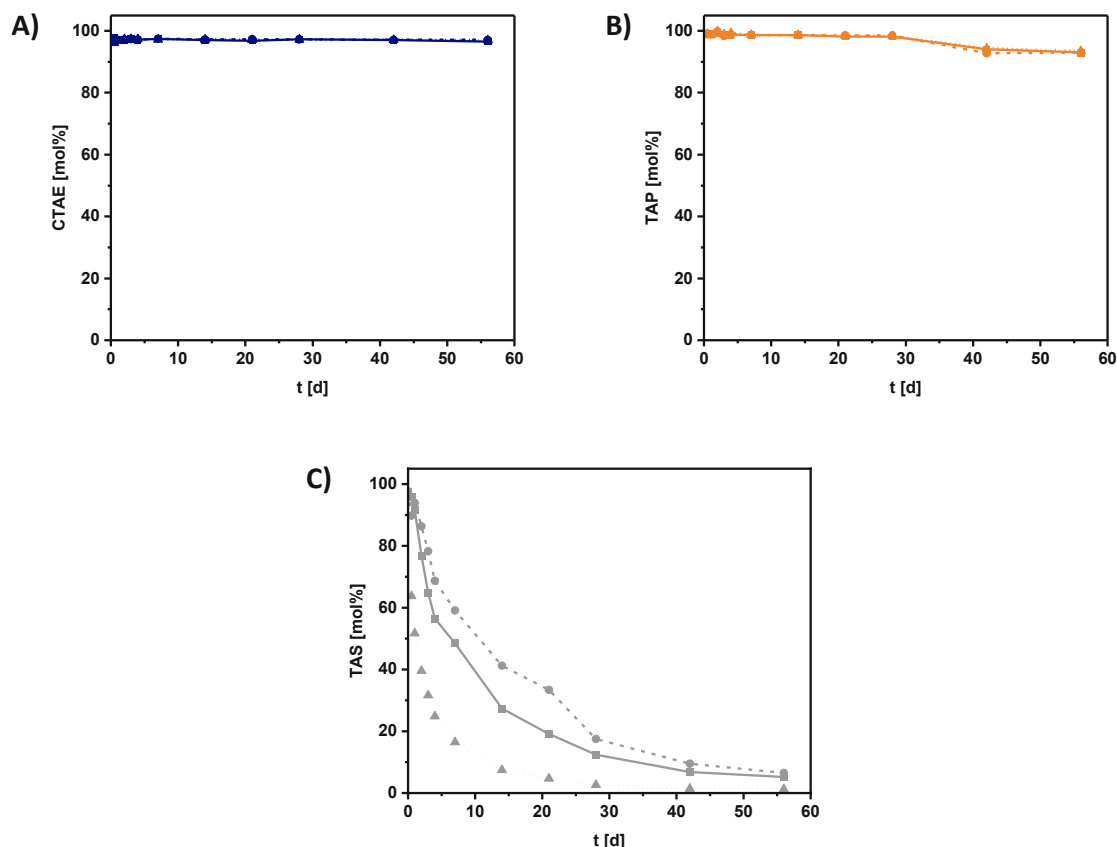


Figure 50: NMR hydrolysis study in D_2O/CD_3CN at pH of ~ 7.0 , 4.0 and 10.0 for different monomers: A) CTAE; B) TAP, and C) TAS under neutral (—■—), acidic (---●---) and basic (····▲····) conditions.

The results in Figure 50 display that for the carbon-based allyl ester reference CTAE only slight monomer hydrolysis of 3% after 56 d was determined under all conditions. Therefore, the ester group is stable at pH levels ranging from 4 to 10. For P-based TAP after 56 d, only 6-7% of the monomer was hydrolyzed under all conditions, confirming that the P-O bond is not prone to hydrolysis under hydrolytic conditions. In the case of the silicon-based TAS, hydrolysis was observed under all conditions, with 93-99% of the monomer hydrolyzed after 56 d, while basic hydrolysis was shown to be accelerated compared to neutral and acidic conditions. This indicates that the Si-O bond is labile enough for hydrolytic cleavage. For the B-based compound TAB, full hydrolysis of the monomer was shown directly after addition to the D_2O/CD_3CN solution; hence no results are shown for this monomer in Figure 50. This proves that the B-O bond is most prone to cleavage by water. This study, therefore, indicates that monomers based on silicon and boron are most promising for enhanced network degradation.

2.1.2 Screening of photoinitiator concentration for thiol-ene systems

To prepare homogeneous polymer networks, the allyl ester monomers should be polymerized with a thiol in an equimolar ratio of double bonds to thiol groups. Difunctional 2,2'-(ethylenedioxy)diethanethiol (EDDT, Figure 51) was chosen for the first studies, as it does not contain any ester groups, which might influence the degradation behavior. As a PI, the radical initiator Ivocerin® was selected, as it displays high curing speeds and a high maximum absorption wavelength of 408 nm, resulting in improved curing depths compared to other typically employed commercial initiators, making it ideal for the subsequent application in 3D-printing.¹²⁹ Additionally, Ivocerin was already confirmed to be biocompatible.¹³⁰ For stabilization of the thiol-ene formulations, 0.02 w% of the stabilizer pyrogallol (PYR, Figure 51) were added, as described by Orman *et al.*¹⁹⁴, which led to improved stability of formulations (see Appendix, chapter 1).

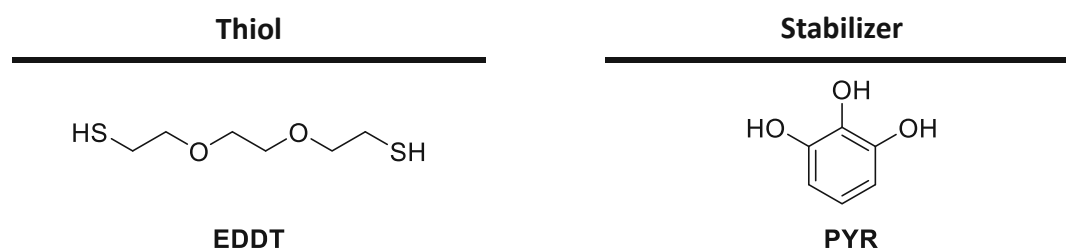


Figure 51: Structure of the difunctional thiol 2,2'-(ethylenedioxy)diethanethiol (EDDT) and the stabilizer pyrogallol (PYR).

First, the optimum PI concentration for photopolymerization of the thiol-ene systems was determined via RT-NIR photorheology measurements described in 1.1.3. For the experiments, a broadband Hg lamp equipped with a 400-500 nm filter was used, with a set intensity of 1 W/cm² at the end of the light guide, which translates to an intensity of 20 mW/cm² at the surface of the samples. 140 μ L of sample volume was applied to the glass plate, which was kept at 25 °C, and the samples were irradiated for 320 s.

The measurements were conducted with the reference compound CTAE, the thiol EDDT and different Ivocerin concentrations of 0.125 w%, 0.250 w%, 0.500 w%, and 1.00 w%.

Table 6: Detailed results of the RT-NIR photorheology measurements.

w% PI	t_{gel} [s]	DBC _{gel} [%]	t_{95} [s]	DBC _{final} [%]	G' _{final} [kPa]	F _{N,max} [N]
0.125	28.0 \pm 3.5	40.1 \pm 3.1	97.6 \pm 5.8	56.3 \pm 1.1	268 \pm 10.4	-5.1 \pm 1.7
0.250	22.0 \pm 3.6	46.4 \pm 0.4	88.7 \pm 7.9	68.5 \pm 2.3	324 \pm 32.7	-9.1 \pm 2.2
0.500	18.0 \pm 0.0	51.3 \pm 1.2	68.1 \pm 1.9	87.7 \pm 0.4	402 \pm 4.00	-13.9 \pm 1.5
1.00	8.0 \pm 0.0	35.0 \pm 2.3	45.3 \pm 3.2	88.1 \pm 1.3	408 \pm 5.00	-15.0 \pm 1.2

The results in Table 6 show that PI concentrations of 0.125 w%, 0.25 w%, and 0.5 w% are too low for efficient photopolymerization of the thiol-ene systems, leading to a significantly retarded crosslinking and curing behavior, lower conversions, and deteriorated mechanical properties. With 1 w% of PI significantly faster crosslinking was observed with a decrease in t_{gel} by 10 s compared to formulations containing 0.5 w% PI. When analyzing the t_{95} values, it was determined that curing of the network is accelerated by 23 s when increasing the PI concentration from 0.5 w% to 1 w%. Therefore, a PI concentration of 1 w% was used for the following studies.

2.1.3 Mechanical properties of model networks

Scaffolds used in tissue engineering require mechanical properties that match the properties of the replaced tissue. For bone regeneration scaffolds, high strength and toughness for good load dissipation and tissue integration are crucial.⁸⁷

To determine the thermomechanical properties of materials, DMTA measurements can be conducted. This method allows for the determination of the time-resolved strain-rate dependent viscoelastic properties of the materials, such as the glass transition temperature (T_g), as well as the temperature dependence of the dynamic storage modulus G' and loss modulus G'' . The glass transition can be observed in amorphous and semi-crystalline polymers and is described as a reversible transition from a hard and “glassy” state into a viscous or rubbery state. The storage modulus G' correlates with the elastic, while the loss modulus G'' correlates with the viscous response of the material. From the ratio of G''/G' , the loss factor $\tan\delta$ can be determined. Due to non-linear or abrupt changes in moduli occurring close to the T_g , $\tan\delta$ increases until a maximum is reached at the glass transition temperature of the material. Depending on the application, either a high T_g , when a hard, unyielding material is required or a low T_g , when a soft, elastic polymer is needed, should be exhibited. For bone replacement materials, a high T_g significantly above body temperature is required for good load dissipation. Additionally, from the shape of the storage modulus curves, information about crosslinking density, degree of crystallinity, and molecular weight can be obtained, which is shown in Figure 52.³⁰⁹

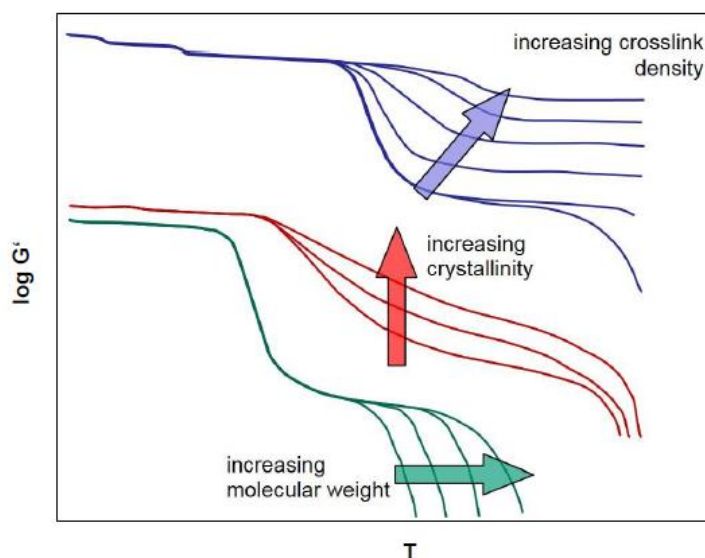


Figure 52: Scheme of storage modulus curves of polymers with different crosslinking densities, degree of crystallinity, and molecular weight.^{309,310}

Other important parameters that can be determined are the storage modulus at 25 °C $G'_{25^{\circ}\text{C}}$ and the storage modulus at body temperature $G'_{37^{\circ}\text{C}}$, which should be high as they correlate with the stiffness of the material at the respective temperature. The storage modulus at the rubber plateau G'_R , reveals the degree of network crosslinking. Lastly, the full width at half maximum of the $\tan\delta$ curve (fwhm) is an indicator for the homogeneity of a network, as these materials display very sharp glass transitions.³⁰⁹

For the measurements, formulations were prepared from each allyl ester monomer and the thiol EDDT. For initiation, the optimum PI concentration of 1 w% was added. Due to the autopolymerization of all formulations in the dark, 0.02 w% of PYR were added. The curing of DMTA specimens with a shape of $5 \times 2 \times 40 \text{ mm}^3$ was conducted in transparent silicone molds. For formulations containing CTAE, TAP, and TAS, photopolymerization was done in a Lumamat 100 visible light oven. Each sample was irradiated for 10 min on both sides. For the formulation containing TAB, sticky specimens were received after curing in the Lumamat light oven. Therefore, curing was conducted in an Intelli-Ray 600 broadband UV oven (2x10 min), which significantly reduced surface stickiness of the samples.

From this point forward, formed copolymer networks between a respective monomer and a thiol in an equimolar ratio for means of simplicity will be referred to as p(monomer), *i.e.*, pCTAE. DMTA measurements of the formed networks were performed in torsion mode from $-100 \text{ }^{\circ}\text{C}$ to $+200 \text{ }^{\circ}\text{C}$ with a heating rate of 2 K/min, a torsion strain of 0.1%, and a frequency of 1 Hz. Due to the high reproducibility of this method, specimens were tested once. As samples were very soft but brittle

at room temperature, they were clamped into the measuring device at $-100\text{ }^{\circ}\text{C}$ to avoid constrictions.

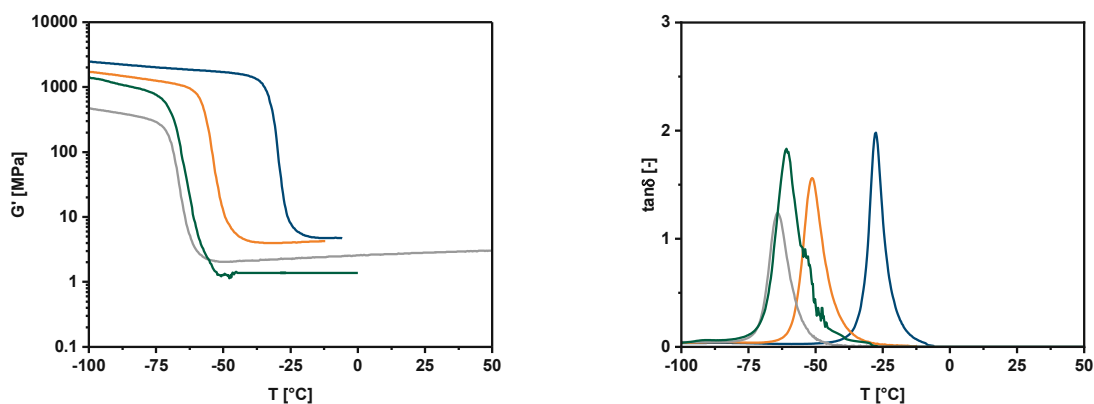


Figure 53: G' (left) and $\tan\delta$ (right) over temperature for the networks formed from the carbon-based reference CTAE or the heteroatom-based allyl esters TAP, TAS, or TAB with the thiol EDDT. pCTAE (—); pTAP (—); pTAS (—); pTAB (—). Due to high brittleness, all samples broke at some point after the glass transition; hence, values for G' and $\tan\delta$ were only determined until this point.

The curves of storage modulus over temperature in Figure 53 (left) show that all samples broke at some point after the glass transition, as softening of the samples together with a slight expansion during heating occurred. This ultimately caused failure at the sites of clamping. Therefore, $G'_{25^{\circ}\text{C}}$ could not be determined for some networks.

Figure 53 (right) depicts that all specimens display T_g values significantly below room and body temperature. This is due to the monomers and the thiols being rather flexible and further loosening of resulting the network caused by the flexible thioether bridges. Therefore, soft and rather brittle materials were formed at the cost of hardness and stiffness. Furthermore, it was shown that heteroatoms in the network seem to further lower the T_g , with T_g values ranging from -50 to $-65\text{ }^{\circ}\text{C}$ compared to the material formed from the carbon-based allyl ester, with a slightly higher T_g of $-28\text{ }^{\circ}\text{C}$. G'_R values confirm that the crosslinking density of all formed networks is low, with values ranging from 3-5 MPa for pCTAE, pTAP, and pTAS. The lowest crosslinking density was observed with pTAB ($G'_R \sim 1\text{ MPa}$). This is probably due to the high moisture sensitivity of the monomer determined in the previous study, which causes cleavage of the network even due to air humidity and lower crosslinking density. Also, some disturbance was observed during the measurements, which might also be explained by the moisture sensitivity of the material.

Lastly, it was shown that the addition of the thiol leads to very sharp glass transitions with full width at half maxima (fwhm) ranging from 6-10 $^{\circ}\text{C}$. Therefore, this study showed that the difunctional thiol EDDT leads to a very low crosslinking density of the networks and low T_g values

due to the rather flexible structure of both monomers and the thiol. Hence, these materials are not yet suitable as bone replacement materials, but this study gave a good first insight about the behavior of networks containing heteroatoms, which were formed from quasi-ideal thiol-ene reactions. The summarized results are given in Table 7.

Table 7: Detailed results of the DMTA measurements. *Sample ruptured before reaching G' at the respective temperature.

thiol	monomer	T_g [°C]	$G'_{25^\circ\text{C}}$ [MPa]	$G'_{37^\circ\text{C}}$ [MPa]	fwhm [°C]	G'_R [MPa]
EDDT	CTAE	-28	-*	-*	6	5
	TAP	-51	-*	-*	8	4
	TAS	-64	3	3	8	3
	TAB	-61	-*	-*	10	1

2.1.4 Degradation behavior of model networks

(Meth)acrylate-based photopolymers currently employed in TE display an unfavorable degradation behavior, as high molecular weight poly((meth)acrylic acids) are formed upon hydrolysis. These compounds cannot be removed from the body and may promote inflammation or tissue necrosis. Additionally, they cause autocatalytic bulk erosion of the material with an abrupt loss of mechanical strength.^{51,52,87,98} For a material used for bone regeneration scaffolds, ideally, the degradation should occur via surface erosion, during which no acidic products are formed, resulting in negligible swelling. Additionally, the loss of the material is confined to the surface, which prevents premature implant failure.^{51,57}

To determine, which heteroatoms enhance the hydrolytic degradation of the formed thiol-ene networks compared to networks based on (meth)acrylates, next degradation studies were conducted. For these studies, cylindrically-shaped specimens ($d=5$ mm, $h=2$ mm) were prepared analogously to the DMTA samples described in 2.1.3.

Degradation of these samples was studied under physiological conditions present in the body (phosphate-buffered saline, PBS, $\text{pH}=7.4$). Furthermore, acidic conditions (acetate buffer, $\text{pH}=4$) were used to mimic the conditions during bone remodeling, as an acidic pH below 4.5 is exhibited during osteoclast-driven bone resorption.⁶⁰ Basic conditions (carbonate-bicarbonate buffer, $\text{pH}=10$) were also tested to determine possible differences between the networks stored under neutral and acidic conditions. The studies were conducted at body temperature (37°C) in triplicates. The samples were weighed and then immersed in the respective buffer medium. After certain time points, three samples of each material and condition were removed, blotted dry, and

weighed to determine the swelling of the samples, with Equation 1. The sample was then put back into the empty vial and dried to constant weight at 50 °C. The mass loss was calculated with Equation 2.

$$\text{swelling} [\%] = \frac{m_t - m_{\text{dry}}}{m_{\text{dry}}} \cdot 100$$

Equation 3: Calculation of swelling; m_{dry} ... mass of the dry sample; m_t ...mass of the blot-dried sample at the time t .

$$\text{mass loss} [\%] = \frac{m_{\text{dry}} - m_0}{m_0} \cdot 100$$

Equation 4: Calculation of mass loss; m_0 ...initial mass of sample; m_{dry} ...mass of the dry sample.

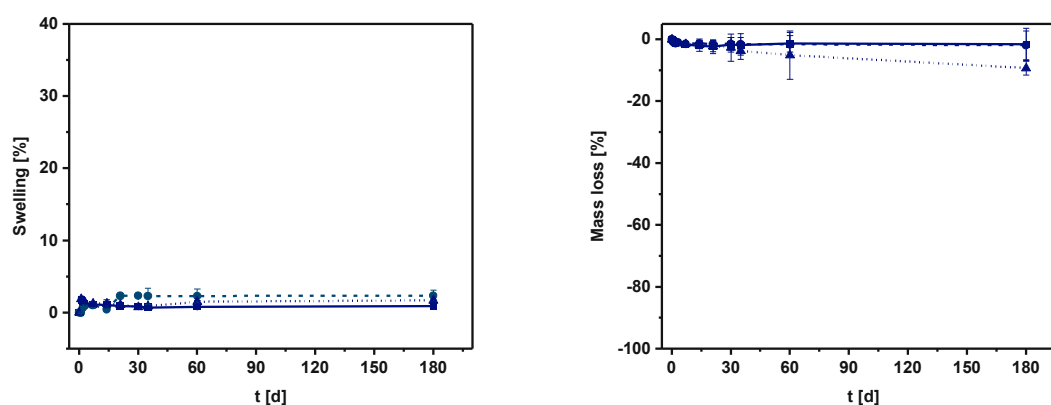


Figure 54: Results of the degradation studies for the C-based reference network pCTAE; left: swelling over time; right: mass loss over time; pH 7.4 (—■—); pH 4 (-◆-), pH 10 (···▲···).

The network containing the carbon-based reference ester CTAE displays a slight amount of swelling under all conditions (1-2% after 6 months), as well as a slight mass loss (2%) in the neutral and acidic buffer solutions, which is displayed in Figure 54 (left). Under basic conditions, a slightly higher mass loss of 9% was shown, which was expected, as ester groups are prone to cleavage with bases (Figure 54, right). This confirms that the network does not display sufficient degradability under hydrolytic conditions, which is consistent with the poor degradability of networks formed from vinyl esters and vinyl carbonates reported by Mautner *et al.*¹¹²

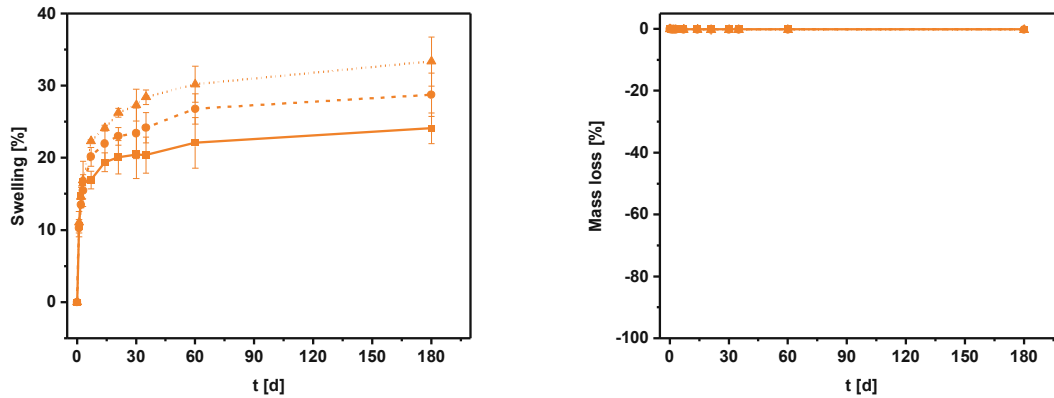


Figure 55: Results of the degradation studies for the P-based network pTAP; left: swelling over time; right: mass loss over time; pH 7.4 (—■—); pH 4 (-◆-), pH 10 (···▲···).

In the case of the P-based polymer pTAP, a different behavior was observed in Figure 55, as significant swelling (24-33% after 6 months) occurred under all conditions, while almost no mass loss (-0.1-0.3%) was shown. Therefore, this network is more hydrophilic, which causes water uptake, but the P-O bond of this specific network is too stable for cleavage under hydrolytic conditions.

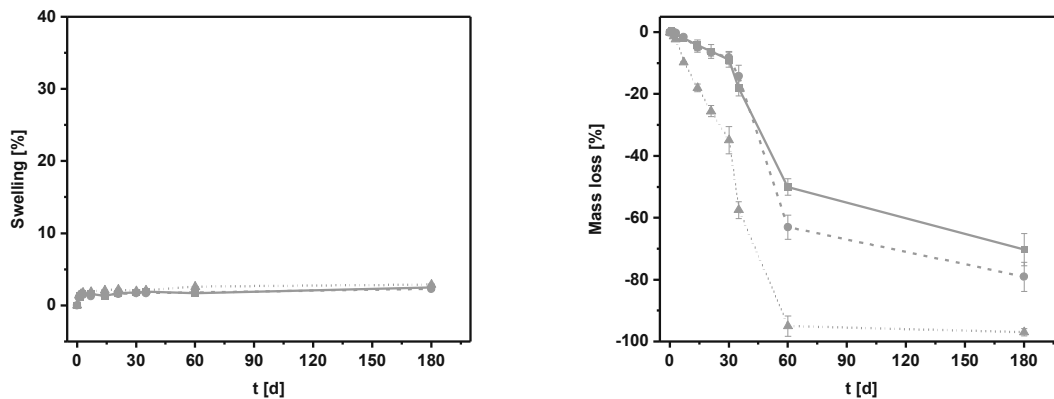


Figure 56: Results of the degradation studies for the Si-based network pTAS; left: swelling over time; right: mass loss over time; pH 7.4 (—■—); pH 4 (-◆-), pH 10 (···▲···).

For the Si-based network pTAS only slight swelling (2-3% after 6 months) occurred (Figure 56, left). Furthermore, an almost linear mass loss was shown under all conditions, accelerated under basic conditions. After 6 months 70-79% of the total mass was lost at pH 7.4 and 4, respectively, while almost full network degradation (97%) occurred at pH 10. Hence, the Si-O bond seems to be labile enough for hydrolytic network degradation, and the samples display the desired degradation behavior of surface erosion without significant swelling.

For the polymer containing TAB, full dissolution of samples was shown after 24 h under all conditions. Therefore, no results are shown for this network. As a result, the B-O bond is the most labile bond compared to the other heteroatoms.

To conclude, the best degradation behavior was observed with the Si-based material TAS, which displayed negligible swelling combined with a fast mass loss over 6 months under physiological and acidic conditions. Additionally, the fastest network degradation was observed with the network based on the boronic ester monomer TAB with full dissolution of networks after 24 h. Therefore, orthosilicic and boronic ester monomers can improve network degradation compared to carbon-based allyl esters.

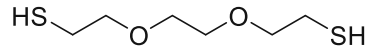
2.2 Thiols for enhanced mechanical properties

2.2.1 Screening of thiols for improved mechanical properties

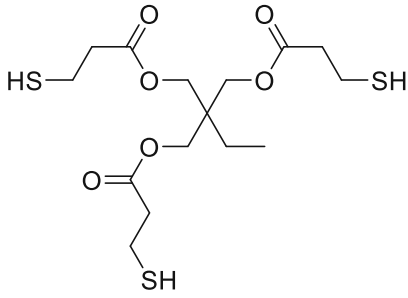
It was shown that Si- and B-based monomers lead to accelerated network degradation compared to carbon-based esters. Nevertheless, all tested systems containing heteroatoms or carboxylic esters and the thiol EDDT exhibited glass transition temperatures significantly below body temperature (-28 to -64 °C), which limits their use in bone replacement materials. As this is probably due to the rather flexible structure and low functionality of EDDT, a screening for thiols for enhanced mechanical properties was conducted. Different thiols were selected, such as trifunctional trimethylolpropane tris(3-mercaptopropionate) (TMPMP), trifunctional tris[2-(3-mercaptopropionyloxy)-ethyl] isocyanurate (TEMPIC) and dipentaerythritol hexa(3-mercaptopropionate) (diPETMP) containing six thiol groups (Figure 57).

As a fast screening for resulting thermomechanical properties, DMTA measurements were conducted as described in 2.1.3. For these tests, the reference compound CTAE was chosen as a monomer, and samples were again prepared with each thiol in an equimolar ratio of double bonds to thiol groups.

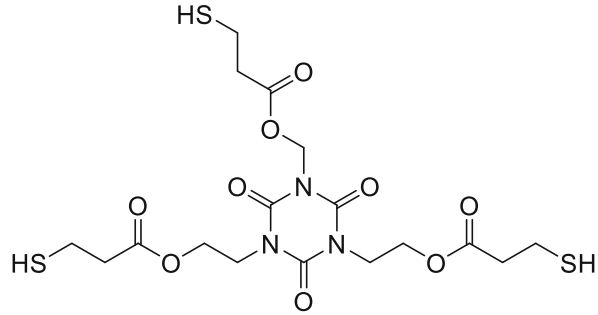
Thiols



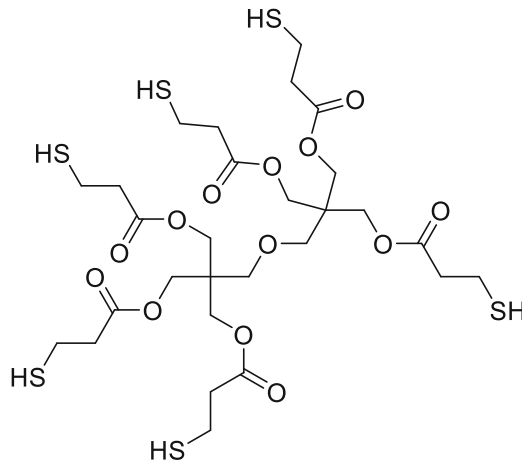
EDDT



TMPMP



TEMPIC



diPETMP

Figure 57: Structures of the thiols EDDT, TMPMP, TEMPIC, and diPETMP.

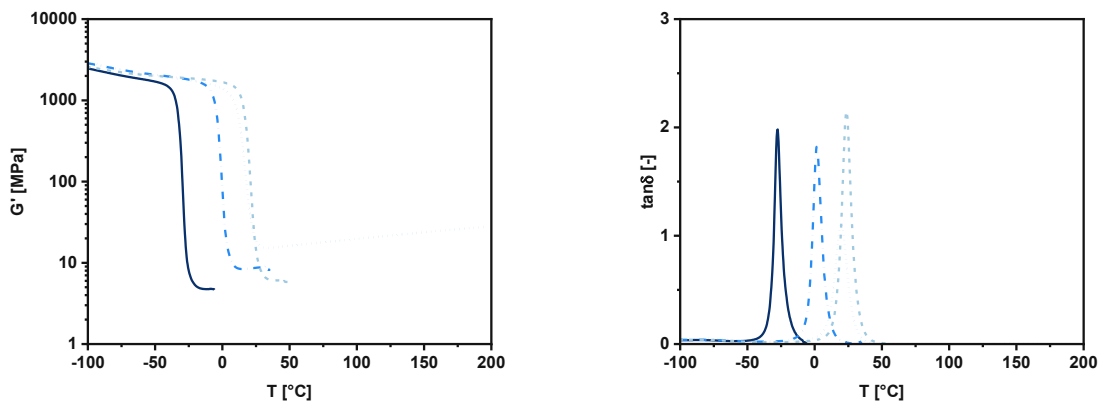


Figure 58: G' (left) and $\tan\delta$ (right) over temperature for the networks formed from carbon-based reference CTAE and the different thiols. pEDDT (—); pTMPMP (- · - ·); pTEMPIC (·····); diPETMP (- - - -). The samples containing EDDT, TMPMP, and diPETMP ruptured after the glass transition.

Figure 58 (left) shows a significant enhancement in material stiffness for all materials upon the addition of tri- or higher functional thiols, with a significant increase in G' at 25 °C and 37 °C, compared to the network formed with difunctional EDDT. Additionally, $\tan\delta$ curves (Figure 58, right) display that all thiols lead to the formation of very homogeneous networks, reflected in the low fwhm values (6-10 °C) for all materials. With the thiols TEMPIC and diPETMP, the highest T_g values around 20 °C were obtained, while a lower T_g was observed with TMPMP (1 °C). This is due to its more flexible structure compared to TEMPIC and lower functionality than diPETMP. Noteworthy, the highest $G'_{37^\circ\text{C}}$ and crosslinking density were observed with trifunctional TEMPIC. Therefore, it was shown that a trifunctional rigid thiol is necessary to generate materials with the best thermomechanical properties. The collected data of the DMTA measurements is presented in Table 8.

Table 8: Detailed results of the DMTA measurements. *Sample ruptured before reaching G' at the respective temperature.

monomer	thiol	T_g [°C]	$G'_{25^\circ\text{C}}$ [MPa]	$G'_{37^\circ\text{C}}$ [MPa]	fwhm [°C]	G'_R [MPa]
CTAE	EDDT	-28	-*	-*	6	5
	TMPMP	1	10	0.3	9	9
	TEMPIC	20	19	15	10	28
	diPETMP	24	15	6	8	6

2.2.2 Syntheses of novel thiols

Previous results showed that TEMPIC, a trifunctional thiol with a rigid core, results in the best thermomechanical properties of the thiol-ene materials. However, like most commercial thiols, TEMPIC contains ester groups, which might influence the degradation properties of formed polymers and, upon cleavage, form acids, which may cause inflammation or necrosis. Therefore, novel trifunctional and rigid thiols without any ester groups were synthesized, namely benzene-1,3,5-triyltrimethanethiol (TMB) and 1,3,5-tris(3-mercaptopropyl)-1,3,5-triazine-2,4,6-trione (TMT). TMT is known from literature, as a low-odor thiol used in dental applications.^{311,312} The two target structures are shown in Figure 59. To also incorporate degradable groups into the network via the thiol, the synthesis of a thiol-containing cleavable boronic ester bonds and thioacids containing hydrolyzable thioester groups was conducted, which is described in detail in chapters 4 and 5 of the Appendix, respectively.

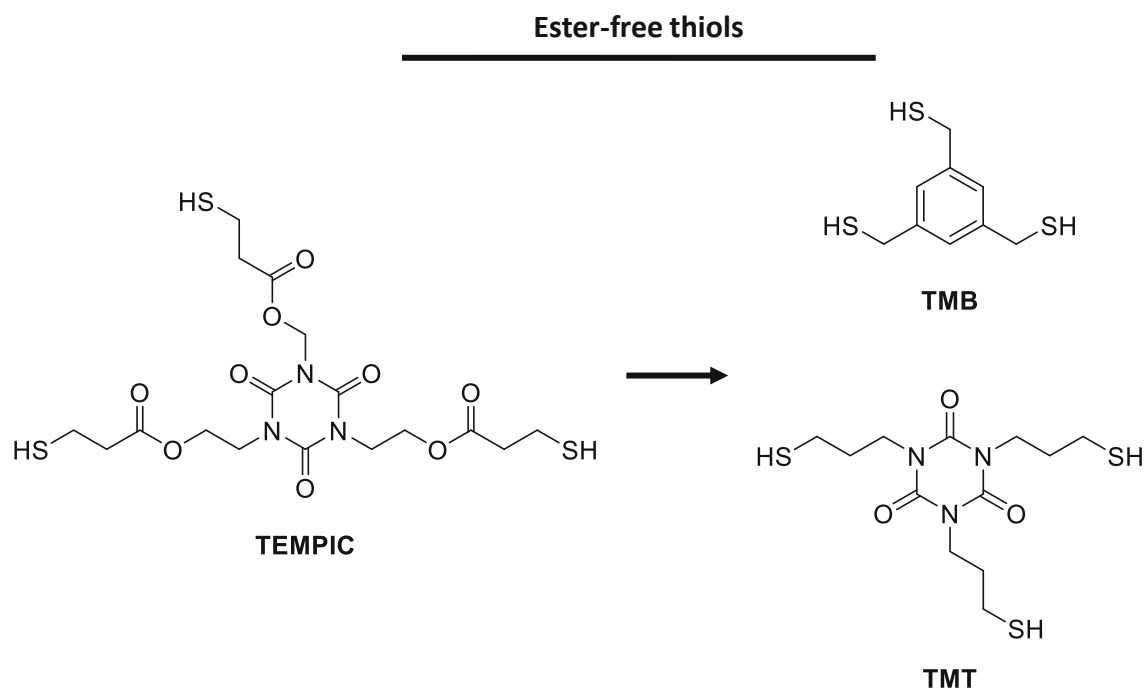
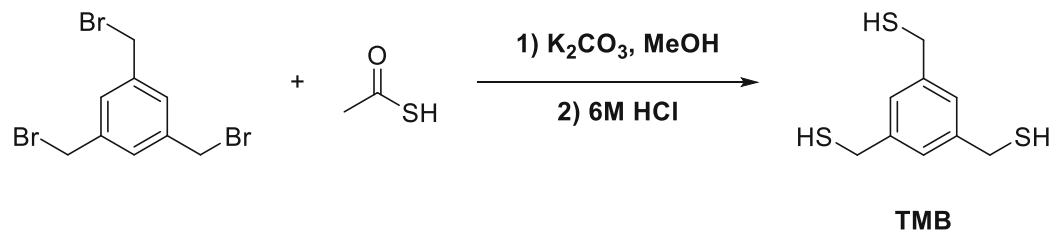


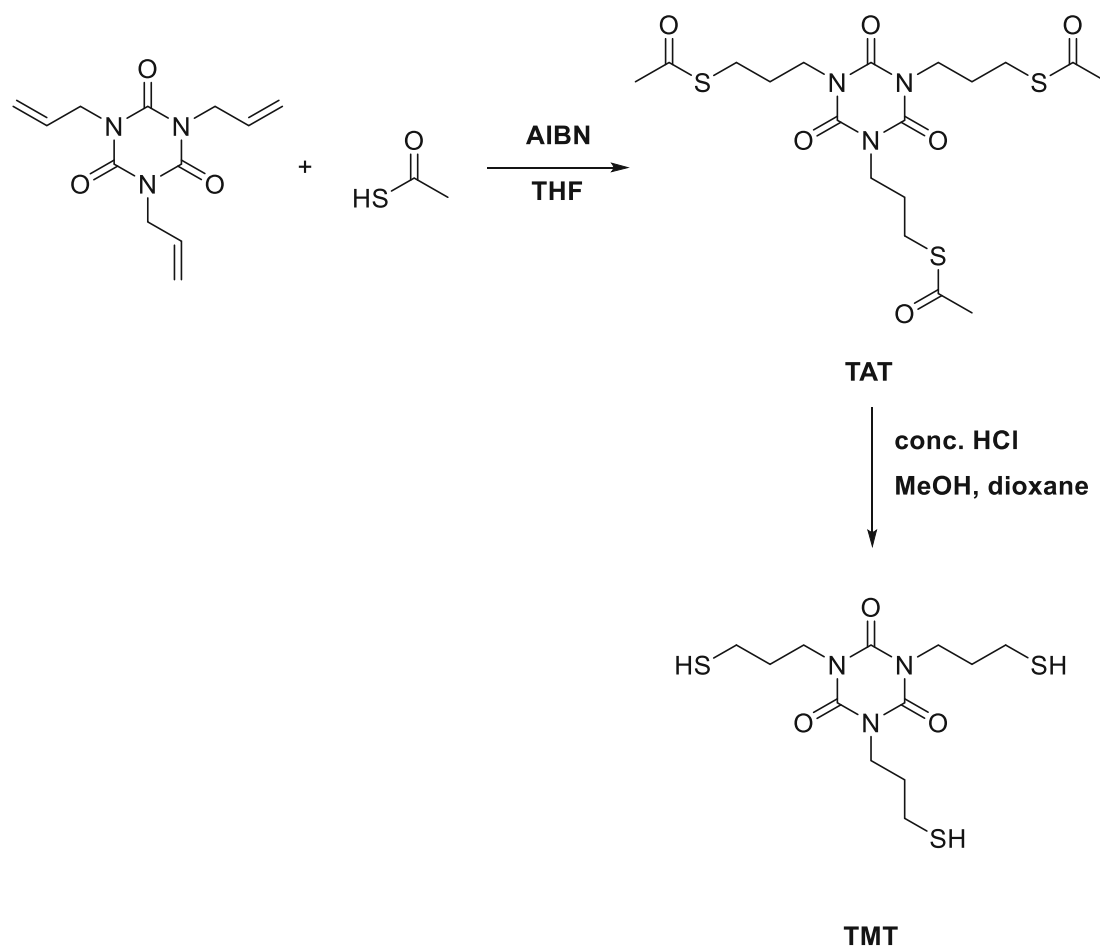
Figure 59: Structures of the ester-free thiols TMB and TMT.

The synthesis of the thiol benzene-1,3,5-triyltrimethanethiol (TMB) was attempted in a one-step process adapted from Morrison *et al.*³¹³ and Li *et al.*³¹⁴



For the synthesis, 1 eq. 1,3,5-tris(bromomethyl)benzene, 4.5 eq. thioacetic acid and 4.5 eq. K_2CO_3 in MeOH were stirred at rt for 2 h to yield the crude product benzene-1,3,5-triyltrimethanethiol (TMB) as a white to transparent paste. Unfortunately, purification by column chromatography was unsuccessful, and the product could only be obtained in crude form with ~10% of unknown impurities, according to NMR.

The synthesis of the ester-free thiol 1,3,5-tris(3-mercaptopropyl)-1,3,5-triazine-2,4,6-trione (TMT) was conducted according to Reinelt *et al.*^{311,312} in a two-step procedure by radical addition of thioacetic acid and subsequent hydrolysis to the product under acidic conditions.



In the first step of the synthesis, 1 eq. of 1,3,5-triallyl-1,3,5-triazine-2,4,6-trione (TAI), 3.6 eq. of thioacetic acid, and 0.15 eq. of 2,2'-azobis(2-methylpropanionitrile) (AIBN) dissolved in dry THF were used. To ensure a proper radical addition reaction, all traces of oxygen were removed by purging the mixture with argon before heating to 65 °C for 24 h. The obtained crude product was then recrystallized from methanol to yield the product 1,3,5-tris(3-acetylmercaptopropyl)-1,3,5-triazine-2,4,6-trione (TAT) as a white solid (62%). In the second step, 1 eq. of TAT and 3.2 eq. of HCl (37 w%) dissolved in a mixture of methanol and 1,4-dioxane were heated for 24 h to yield the product as a colorless liquid in a yield of 93%.

2.2.3 Mechanical properties of networks

After successful synthesis of the trifunctional, rigid thiol TMT as a fast screening, the thermomechanical properties of the material containing the reference compound CTAE and the novel thiol TMT in an equimolar ratio of double bonds to thiol groups were determined with DMTA

measurements described in 2.1.3. Curing of the specimen was performed at 25 °C. As a reference, the specimens derived from the thiols EDDT and TEMPIC were used.

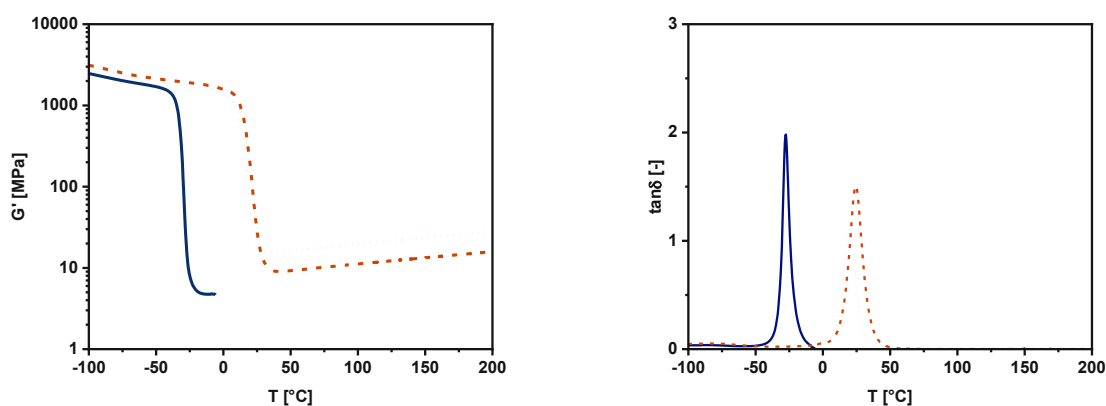


Figure 60: G' (left) and $\tan\delta$ (right) over temperature for the networks formed from carbon-based reference CTAE and the thiols EDDT, TEMPIC, or TMT. pEDDT (—); pTEMPIC (.....); pTMT (- - -). The sample pEDDT ruptured after the glass transition.

Figure 60 shows that a significant increase in T_g by 53 °C is possible with the thiol TMT compared to difunctional EDDT. Additionally, enhanced thermomechanical properties, compared to the network containing trifunctional and rigid TEMPIC with an increase in T_g of 5 °C, were observed, although a slightly lower crosslinking density was determined. The material containing the novel thiol also displays a homogeneous network structure as it exhibits low fwhm (11 °C). Nevertheless, a T_g value at rt, which is still below body temperature, was shown. Hence, this indicates that next to rigid trifunctional thiols, also structures of the allyl ether or ester monomers need to be optimized. The collected results of the DMTA measurements are displayed in Table 9.

Table 9: Detailed results of the DMTA measurements. *Sample ruptured before reaching G' at the respective temperature.

monomer	thiol	T_g [°C]	$G'_{25^\circ\text{C}}$ [MPa]	$G'_{37^\circ\text{C}}$ [MPa]	fwhm [°C]	G'_R [MPa]
CTAE	EDDT	-28	-*	-*	6	5
	TEMPIC	20	19	15	10	28
	TMT	25	29	9	11	16

2.3 New monomers containing heteroatoms

Preliminary studies showed that next to rigid thiols, also monomer structures need to be optimized to synthesize materials with the desired properties for bone replacement materials. To generate high stiffness and strength of networks, rigid elements, such as sterically demanding, bulky substituents, or cyclic structures, can be incorporated into the monomer structure. The target elements for this are depicted in Figure 61. Next to cleavable oxygen-heteroatom bonds,

allyl ether or ester monomers should exhibit a functionality ≥ 2 for the formation of degradable networks. As bulky substituents, aromatic moieties were envisioned. Furthermore, two different 5-membered ring structures containing heteroatom-oxygen bonds were selected, with the allyl ether or ester bond either directly incorporated into the ring or attached to it via a methylene bridge. Based on these elements, an extensive literature search was performed, and several new compounds based on phosphorus, silicon, and boron were subsequently synthesized.

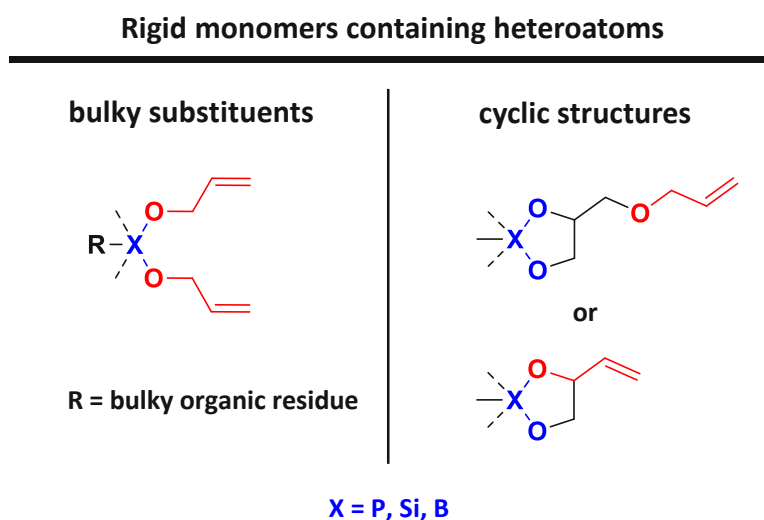
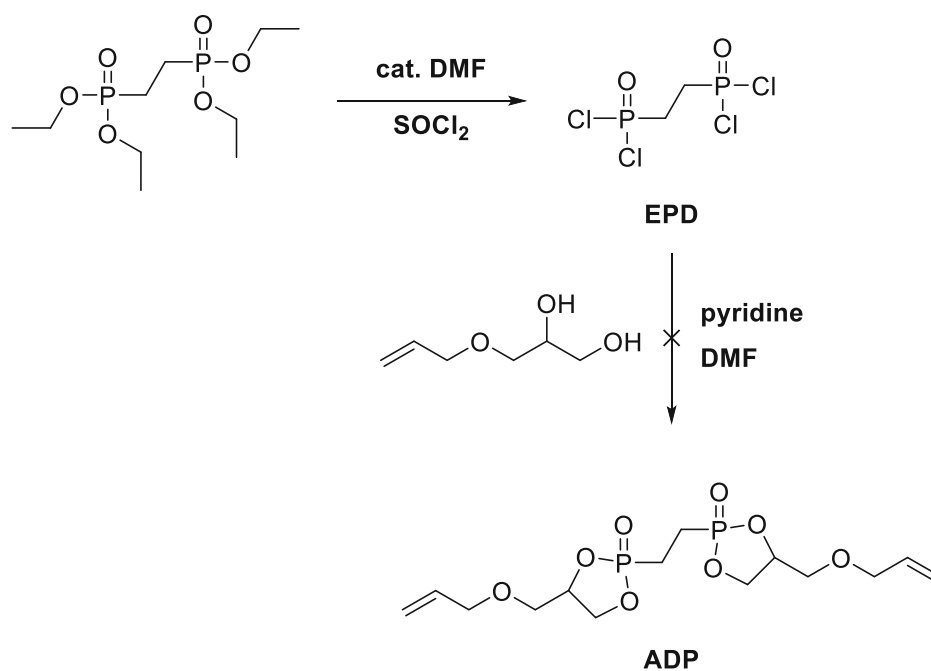


Figure 61: General structure of target elements for designing rigid monomers containing heteroatoms using either bulky substituents or cyclic structures.

2.3.1 Compounds based on phosphorus

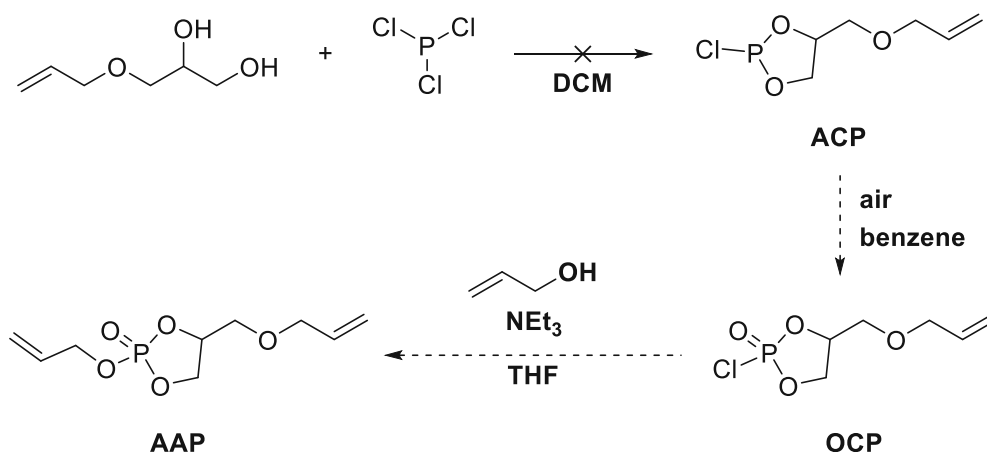
Although no degradation was observed under hydrolytic conditions with the material containing the monomer TAP, P-based monomers are still of interest, as improved degradation is expected *in vivo*, where enzymes such as phosphatases, able to cleave P-O bonds, are present. Furthermore, a literature search showed that linear poly(phosphoesters) synthesized from cyclic phosphonates by the group of Wurm *et al.*^{190,207-211,214,216,218} and Zhang *et al.*³¹⁵ were degradable under hydrolytic conditions. Therefore, several compounds containing cyclic phosphonate groups were synthesized to generate degradable and rigid networks with cyclic structures.

First, the synthesis of 2,2'-(ethane-1,2-diyl)bis(4-((allyloxy)methyl)-1,3,2-dioxaphospholane-2-oxide) (ADP) was done in accordance with a two-step protocol published by Wolf *et al.*²⁰⁸



In the first step, ethylene phosphonic dichloride (EPD) was synthesized. For the synthesis, 1 eq. of tetraethyl ethylene diphosphonate, 0.013 eq. DMF as a catalyst and 5 eq. of thionyl chloride (SOCl_2) were heated for 4 h, resulting in an off-white solid in a yield of 92% was obtained. This solid, however, showed poor solubility in benzene, which is reported as a solvent for EPD in literature.³¹⁶ Nevertheless, ^1H and ^{31}P -NMR showed no impurities, and the product was used directly for the next step. For this, the solid EPD, 2 eq. of 3-allyloxy-1,2-propanediol, and 4 eq. of pyridine in THF were used and stirred at rt overnight. NMR showed complete consumption of the starting material but also the formation of many side products, with some of them containing P-O-P-bonds indicated by duplets in the ^{31}P -NMR spectrum. This is probably due to the steric hindrance of the cyclic structures at the phosphorus atom, which causes a considerable amount of uncyclized products, which are only cyclized on one side, and condensation products with P-O-P bonds. Therefore, the desired product could not be isolated.

Another interesting difunctional monomer containing allyl ether and allyl ester bonds found in literature, containing these cyclic units, was 2-(allyloxy)-4-((allyloxy)methyl)-1,3,2-dioxaphospholane 2-oxide (AAP), which was synthesized similar to a three-step protocol developed by Zhang *et al.*³¹⁵ The group prepared a cyclic phosphonate with ethylene glycol, which was used for the ring-opening synthesis of phosphoryl-choline-capped poly(caprolactone)-poly(ethyleneoxide)-copolymers, able to prevented fibrinogen adsorption of polyurethane films.



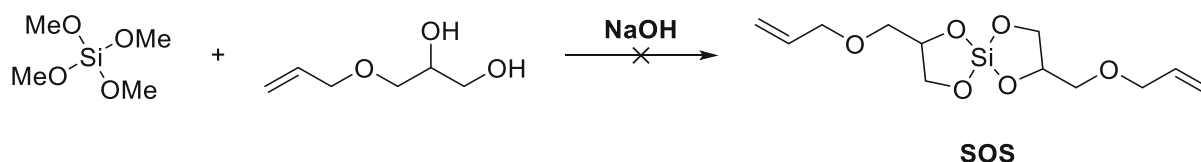
In the first step 4-((allyloxy)methyl)-2-chloro-1,3,2-dioxaphospholane (ACP) was synthesized using 1 eq. of phosphorus trichloride and 1 eq. of 3-allyloxy-1,2-propanediol dissolved in DCM and stirred at rt overnight. After solvent removal, ^{31}P -NMR showed the formation of two different phosphorus compounds in a ratio of $\sim 1:2.5$, in which the phosphorus was attached to one chlorine atom. Separation of the compounds by distillation failed. Therefore, the product could not be obtained, and the second step for the synthesis of 4-((allyloxy)methyl)-2-chloro-1,3,2-dioxaphospholane 2-oxide (OCP), as well as the third step for the formation of the product, were not conducted.

Therefore, it was shown that the synthesis of difunctional compounds containing cyclic phosphonate groups was unsuccessful, which is probably due to the high steric hindrance of the cyclic structures at the phosphorus atom, causing the considerable formation of side-products, such as uncyclized or partially cyclized compounds. Hence, the synthesis of these monomers was not further pursued.

2.3.2 Compounds based on silicon

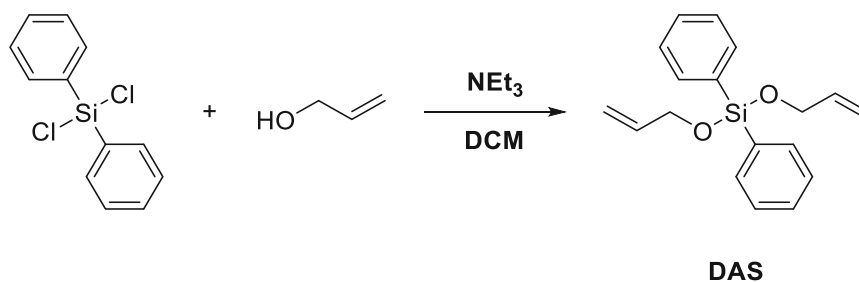
Studies showed that polymers derived from the Si-based monomer TAS exhibited a linear mass loss in degradation studies. Nevertheless, networks were formed with a T_g below body temperature, which limits the use of these compounds in bone replacement materials. Therefore, novel monomers containing the previously mentioned rigid structural elements were synthesized.

First, the synthesis of the spiroorthosilicate 2,7-bis((allyloxy)methyl)-1,4,6,9-tetraoxa-5-silaspiro[4.4]-nonane (SOS), containing two cyclic rings directly attached to the silicon atom, was conducted according to Shan *et al.*³¹⁷



For the synthesis, 1 eq. of tetramethyl silicate, 1.8 eq. of 3-allyloxy-1,2-propanediol, and 0.1 eq. of NaOH were heated to 70 °C for several hours. After a certain amount of MeOH was formed, polymerization occurred. The reaction was done again with the addition phenothiazine as inhibitor, but, still, polymerization occurred. Therefore, most probably, condensation of formed silanols to a polysiloxane took place instead of the formation of the desired product. A literature search regarding spirocyclic esters of orthosilicic acid revealed that these compounds are readily hydrolyzed, even by moisture present in air.³¹⁸ Furthermore, even upon water exclusion, these monomers readily polymerize during storage to form polysiloxanes by reversible ring-opening polymerization due to an equilibrium between the cyclized and open form.^{319,320} Additionally, only a few 5-membered spirocyclic silicates are reported due to high ring strain, and all known spiroorthosilicates are solids at rt.³²¹⁻³²³ Therefore, these compounds were not further pursued.

As spirocyclic compounds were not accessible, the synthesis of compounds containing bulky substituents was pursued, and bis(allyloxy)diphenylsilane (DAS) containing two phenyl moieties was synthesized according to Hoyer *et al.*³²⁴



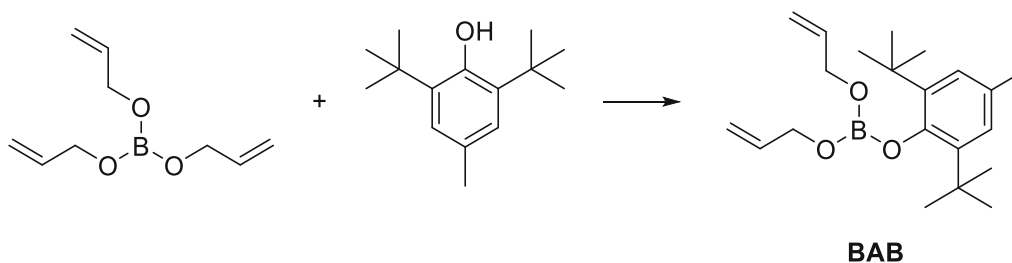
For the synthesis, 1 eq. of diphenyldichlorosilane and 2 eq. of triethylamine were dissolved in DCM and stirred at rt for 1 h. The crude liquid was subjected to distillation to obtain the pure product in a yield of 92%.

2.3.2 Compounds based on boron

Previous studies demonstrated that the B-based compound TAB exhibits the most labile heteroatom-oxygen bond of all tested monomers, with full network degradation after 24 h. Therefore, boronic esters are suitable substances to enhance the degradation of bone

replacement materials, but better mechanical properties are required. Additionally, higher stability of compounds towards hydrolysis would be beneficial. The low stability of aliphatic boronic esters is due to the electron deficiency of boron, described in the State of the Art, which is, therefore, easily attacked by nucleophiles such as water.²¹² Therefore, the introduction of bulky substituents and cyclic structures should also impede or retard network hydrolysis by partial blockage of the empty p-orbital.

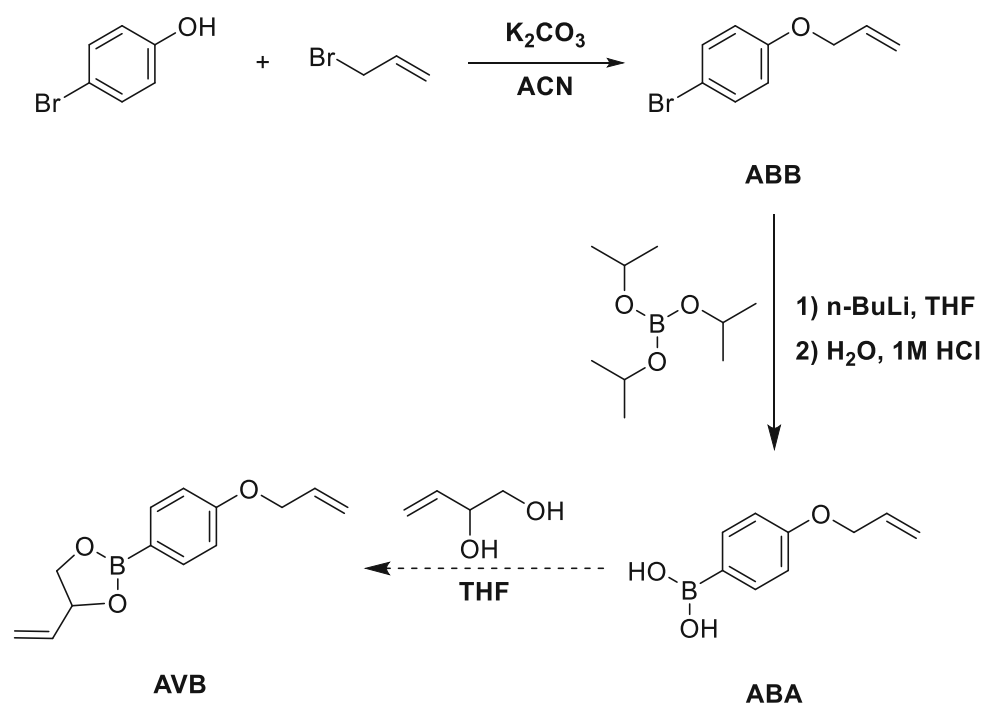
A literature search showed that borate esters containing bulky 2,6-ditertbutyl groups, synthesized by Washburn *et al.*³²⁵, are hydrolytically more stable than aliphatic boronic esters due to the steric hindrance of the residues. Therefore, 2,6-ditertbutylphenyl diallyl borate (BAB) was envisioned as another potential heteroatom-based monomer for the generation of stiff networks and synthesized according to Washburn *et al.*³²⁵



For the synthesis, 3 eq. of triallyl borate and 1 eq. of BHT were heated to 100 °C for 3 d, and the formed allyl alcohol was distilled off. The residual mixture was distilled *in vacuo*, but decomposition of the product occurred. Therefore, the reaction was repeated, and instead of the final vacuum-distillation step, the crude product was purified by extraction. NMR showed ~5% of BHT as an impurity. Unfortunately, the pure product could not be obtained, as the formed ester was unstable towards column chromatography on silica and alumina.

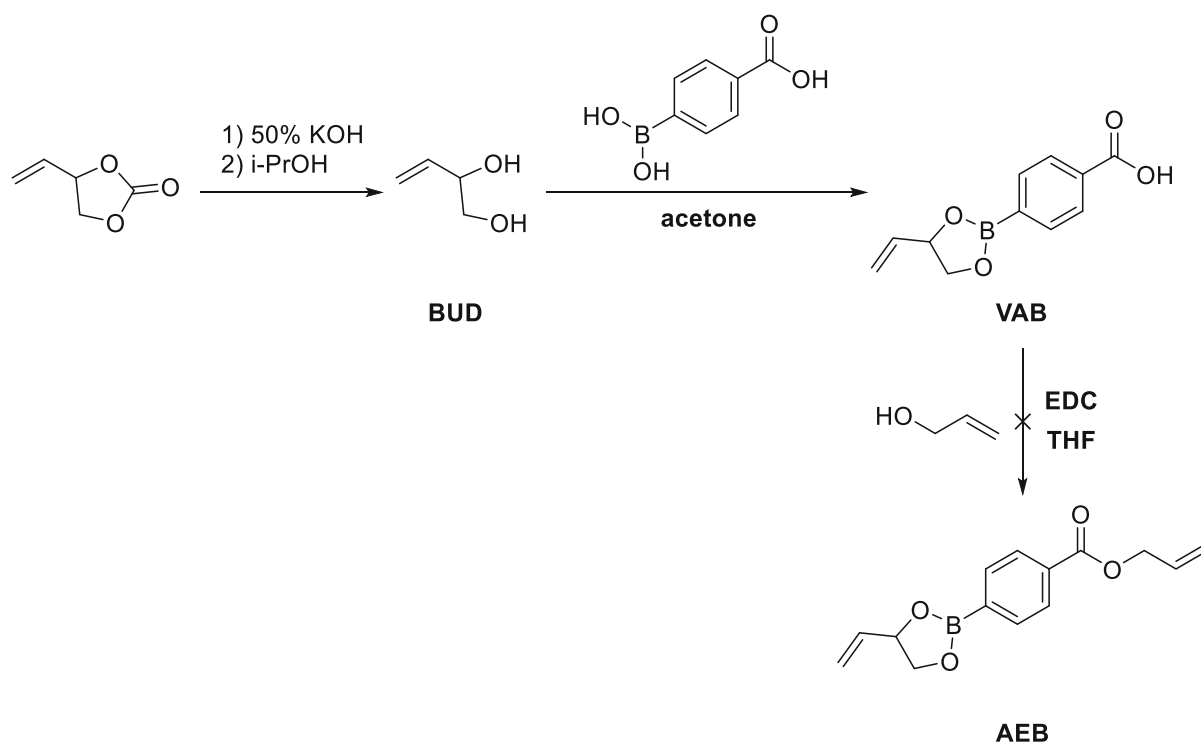
Next to providing the resulting network with high strength and stiffness, literature showed that boronic esters containing cyclic structures attached to the boron exhibit superior stability compared to linear compounds, as they hinder the attack of water at the empty p-orbital.^{212,326} Therefore, several substances containing these cyclic features were synthesized as well.

First, the synthesis of the compound 2-(4-(allyloxy)phenyl)-4-vinyl-1,3,2-dioxaborolane (AVB), containing one cyclic structure, was attempted in a three-step procedure. This monomer contains a cyclic boronic ester group and a rigid aromatic moiety. As difunctional compounds were required, the phenyl ring was also attached to an allyl ether group. The first two steps were conducted according to Chardin *et al.*³²⁷, and the third step was done analogously to Chen *et al.*²³⁵



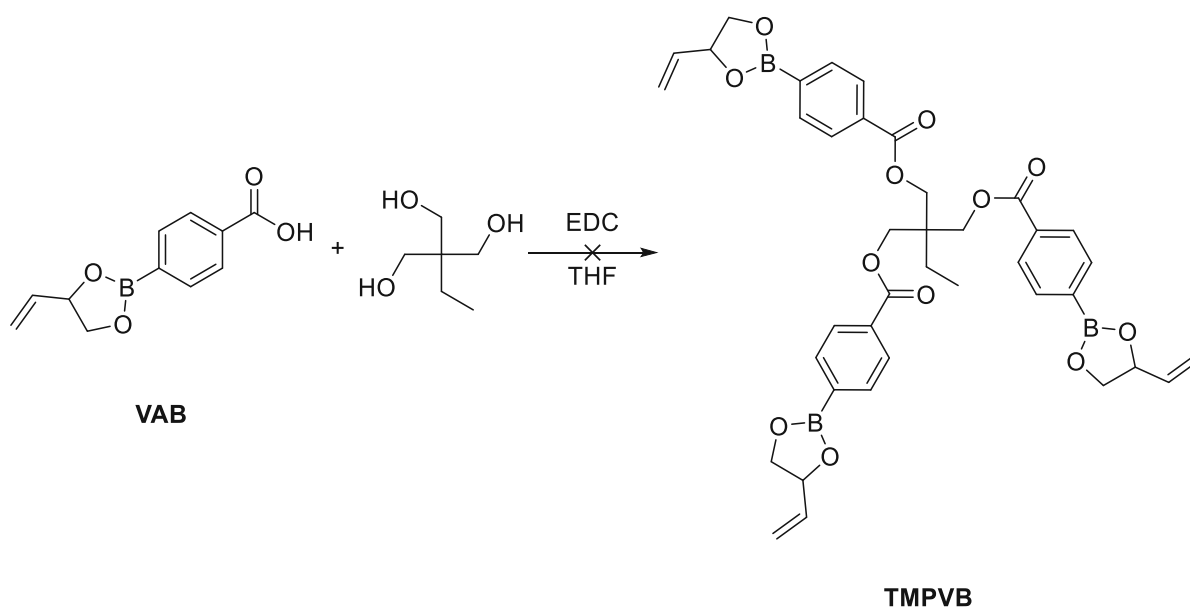
In the first step 1-(allyloxy)-4-bromobenzene (ABB) was synthesized. For this, 1 eq. of 4-bromophenol, 2.5 eq. of K_2CO_3 , and 2 eq. of allyl bromide were dissolved in acetonitrile (ACN) and heated to reflux for 72 h to yield the product as a slightly yellow oil in a yield of 94%. In the second step, 1 eq. of ABB, 1.2 eq. of $n\text{-BuLi}$ (2.5 M in hexane), and 1.5 eq. of triisopropyl borate were in THF were used and stirred for 30 min at $-78\text{ }^\circ\text{C}$ and at rt overnight, affording the crude product (4-(allyloxy)phenyl)boronic acid (ABA). Purification with flash and column chromatography was unsuccessful, as ~5-7% of impurities remained in the product. Therefore, the pure compound could not be obtained.

Next, the synthesis of a similar compound to AVB was conducted. The monomer allyl 4-(4-vinyl-1,3,2-dioxaborolan-2-yl)benzoate (AEB), containing an allyl ester group attached to the aromatic moiety was synthesized via a three-step synthesis. The first step was done in accordance with Boaz *et al.*³²⁸ The second and third steps were conducted as described by Schörpf *et al.*³²⁶ and Schnöll *et al.*³²⁹



In the first step, the alcohol but-3-ene-1,2-diol (BUD) was synthesized by hydrolysis of 1 eq. of 4-vinyl-1,3-dioxolan-2-one with 1.2 eq. of 50 wt% aqueous KOH. The mixture was heated to 60 °C for 16 h affording the product as a colorless liquid in a yield of 75 %. In the second step, 4-(4-vinyl-1,3,2-dioxaborolan-2-yl)benzoic acid (VAB) was synthesized using 1 eq. of carboxy phenyl boronic acid, 1 eq. of BUD, and 11.2 eq. of Na₂SO₄ in acetone at rt to yield the target compound after 24 h as a white solid in a yield of 90%. In the next step, the synthesis of AEB was attempted via a modified Steglich esterification. For the synthesis, 1 eq. of AEB, 4 eq. of allyl alcohol, 1 eq. of 1-ethyl-3-(3-dimethyl aminopropyl) carbodiimide (EDC), and 0.3 eq. of DMAP as a catalyst in THF were used due to poor solubility of AEB in DCM, described as a solvent by Schörpf *et al.*³²⁶ EDC was used instead of DCC, because the resulting urea compound is soluble in water and can easily be separated from the product. The mixture was stirred for 2 h at 0 °C and at rt for 1 week, but NMR showed that a compound with only one double bond, which was not the desired product or the starting material, was formed. Therefore, the product could not be obtained.

Subsequently, also the synthesis of a trifunctional boronic ester containing cyclic structures was attempted, and 2-ethyl-2-(((4-(4-vinyl-1,3,2-dioxaborolan-2-yl)-benzoyl)oxy)methyl)-propane-1,3-diyl bis(4-(4-vinyl-1,3,2-dioxaborolan-2-yl)-benzoate) (TMPVB) was synthesized in accordance with Schnöll *et al.*³²⁹



For the synthesis, 3 eq. of previously synthesized VAB, 1 eq. of trimethylol propane, 3 eq. of EDC, and 0.3 eq. of DMAP as a catalyst in THF were used. The mixture was stirred for 2 h at 0 °C and at rt for 1 week. Then, different work-up strategies were attempted by extraction with Et₂O or DCM. Unfortunately, NMR showed that only a mixture of many different byproducts, neither being the desired compound, could be obtained.

It is well known in literature that neighboring groups greatly affect the equilibrium constants for transesterification reactions of boronic esters. Cromwell *et al.*²⁴⁴ showed that the neighboring-group assisted acceleration in transesterification kinetics by Lewis bases such as nitrogen could be used to tune the malleability and healing efficiency of bulk networks. In such polymers, boronic esters can form adducts with N-donor ligands through Lewis acid-base interactions leading to a more stable tetrahedral boronate ester (sp³-hybridized boron) with accelerated transesterification rates but higher hydrolytic stability, compared to trigonal planar boronic esters (sp²-hybridized boron) (Figure 62). These networks containing B-N dative bonds did not show any loss in mass or mechanical strength on overnight immersion in water, indicating that this approach might be highly promising.

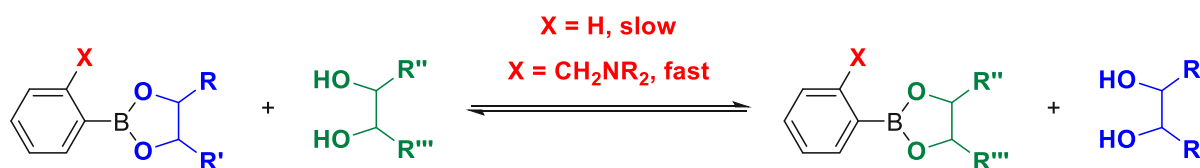
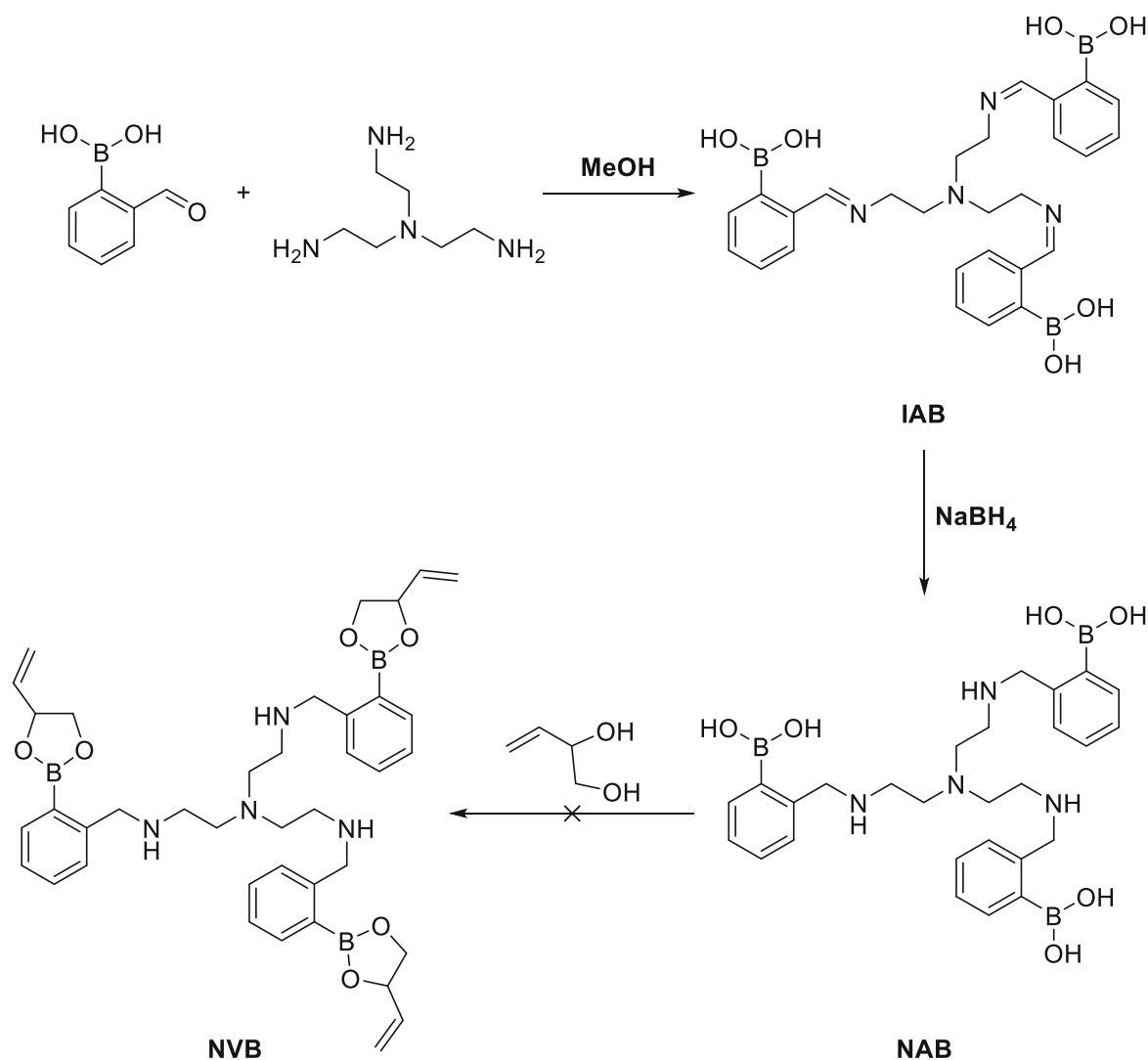


Figure 62: Neighboring group affecting the transesterification kinetics of boronic esters.²⁴⁴

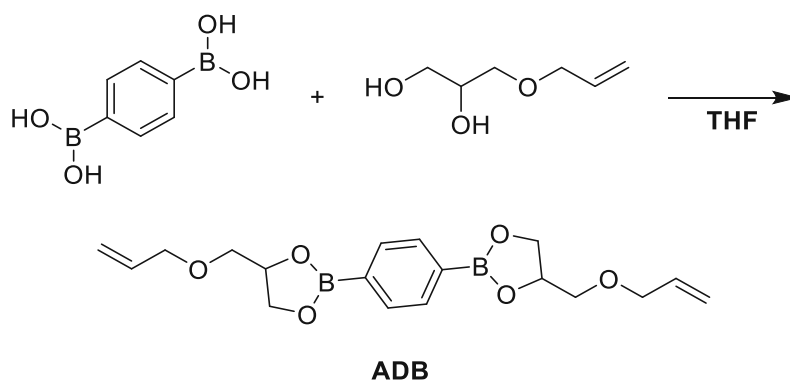
As a consequence, the synthesis of the boronic ester N1-(2-(4-vinyl-1,3,2-dioxaborolan-2-yl)benzyl)-N2,N2-bis(2-((2-(4-vinyl-1,3,2-dioxaborolan-2-yl)benzyl)amino)ethyl)ethane-1,2-diamine (NVB), containing N-atoms at strategically good positions for dative interactions with boron, was attempted in a three-step procedure. Step one and two of the synthesis were conducted according to Leed *et al.*³³⁰ and Gray *et al.*³³¹ The last step was done analogously to Chen *et al.*²³⁵ and Schnöll *et al.*³²⁹



For the synthesis of the triimine (2-((E)-((2-(bis(2-((Z)-2-boronobenzylidene)amino)ethyl)amino)-ethyl)imino)methyl)phenyl)boronic acid (IAB), 3 eq. of 2-formylphenylboronic acid and 1 eq. tris(2-ethylamino)amine) in MeOH were heated to 60 °C for 1 d for a reductive amination reaction. The resulting solution was directly used for the reduction to the amine, for which 3.6 eq. of NaBH₄ were added at 0 °C, and the mixture was subsequently stirred for 16 h at rt. The product (((nitriлотris(ethane-2,1-diyl))tris(azanediyl))tris(methylene))tris(benzene-2,1-diyl))triboronic acid (NAB) could be obtained as a white solid in a yield of 73%. In the last step, dissolution of NAB was

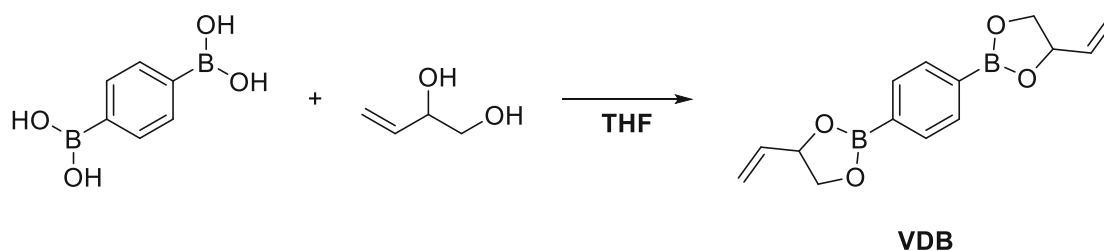
attempted in acetone, DCM, DMF, DMSO and THF, but the compound could not be fully dissolved. Nevertheless, 1 eq. of but-3-ene-1,2-diol and 11.2 eq. of Na_2SO_4 were added, and the mixture was stirred for 1 week at rt. NMR showed that no product was formed, probably due to the poor solubility of NAB in the different solvents. Therefore, the desired compound NVB could not be obtained.

Next, the synthesis of the literature-known boronic ester monomer with cyclic structures, 1,4-bis(4-((allyloxy)methyl)-1,3,2-dioxaborolan-2-yl)benzene (ADB), was conducted. This monomer was recently described to undergo thiol-ene photopolymerization under the formation of polymers used for self-healing, reprocessing, and shape memory.^{256,332} Nevertheless, it has never been applied in terms of improving network degradation. This compound contains a methylene bridge between the cyclic boronic ester and the allyl ether group. Studies from Schörpf *et al.*³²⁶ showed that the group attached to the ring affects the cleavage of the boronic ester. A methylene group attached to the cyclic structure led to a slower exchange rate with other alcohols in NMR experiments. Furthermore, for these compounds, an equilibrium state of initial to exchanged state of 50% was determined, whereas no methylene group attached to the cyclic ester led to almost full exchange after 5 min. Therefore, it was assumed that networks containing ADB might display slower hydrolysis compared to TAB. The synthesis of ADB was conducted analogously to Chen *et al.*^{234,235} and Robinson *et al.*²⁵⁶ in a one-step procedure.



For the synthesis, 1 eq. of benzene-1,4-diboronic acid, 2.05 eq. of 3-allyloxy-1,2-propan-diols, and 2.3 eq. of Na_2SO_4 were added to THF and stirred at rt for 24 h to yield the product as a slightly yellow oil, which crystallized in the freezer to yield a white solid in a yield of 95%.

Simultaneously to the compound ADB, the monomer with the allyl group incorporated into the ring structure and hence even higher rigidity, 1,4-bis(4-vinyl-1,3,2-dioxaborolan-2-yl)benzene (VDB) was synthesized according to Chen *et al.*^{234,235} and Robinson *et al.*²⁵⁶



For the synthesis, 1 eq. of benzene-1,4-diboronic acid, 2.05 eq. of previously synthesized but-3-ene-1,2-diol, and 2.3 eq. of Na_2SO_4 were added to THF and stirred at rt for 24 h to obtain the solid product in a yield of 90%.

2.4 Characterization of degradable systems

After the successful synthesis of several compounds containing heteroatoms, next, formulations of all non-rigid and rigid monomers and the novel ester-free thiol TMT were characterized. As high photocuring rates are a prerequisite for successful 3D structuring, formulations were analyzed regarding their photoreactivity. For the use as bone replacement materials, high stiffness, strength, and toughness are crucial. Hence, the mechanical properties of resulting bulk networks were investigated as well. Lastly, the degradation behavior under hydrolytic conditions was determined to establish whether network cleavage can be improved by incorporating heteroatoms into the networks and whether surface erosion is exhibited by the materials. All the compounds used in subsequent studies are shown in Figure 63.

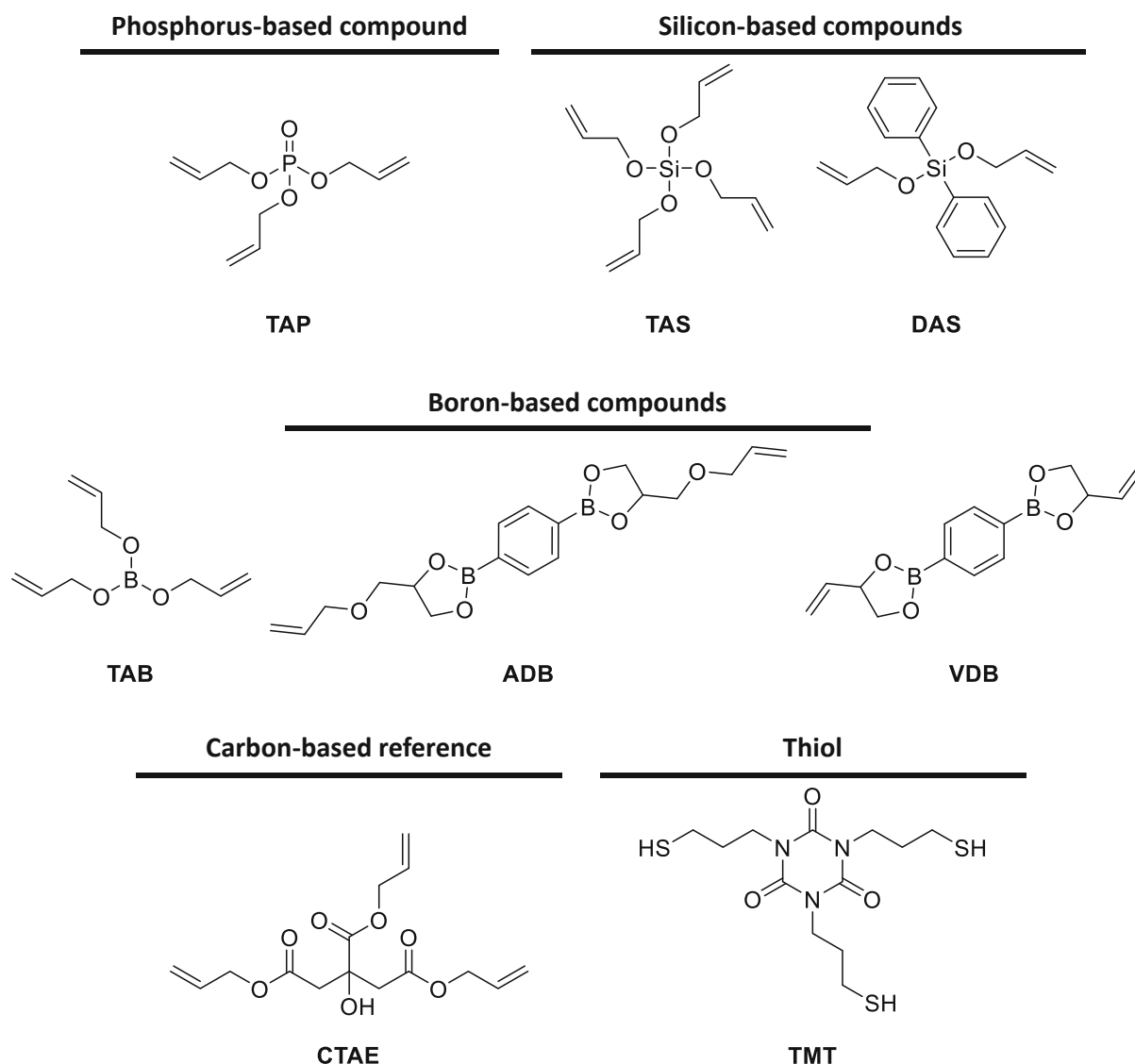


Figure 63: Heteroatom-based allyl ester monomers and non-degradable reference compounds, and the thiol TMT used in the studies.

2.4.1 Reactivity of formulations

For the intended application of the formulations in 3D printing, parameters such as the reactivity and chemical conversion during photopolymerization are important. These crucial values can be determined with RT-NIR photorheology described in 1.1.3. T_{gel} should be as low as possible, as it determines the minimum irradiation time required to generate one object layer. Furthermore, high DBC_{final} are necessary to achieve good mechanical properties of resulting objects. A low t_{95} is favorable for building objects with sufficient speed since the previous layer needs a certain stability before the next layer can be deposited to avoid failure during printing. Lastly, the

occurring shrinkage stress, which correlates with $F_{N,max}$ should be as low as possible to avoid residual internal stress or cracks within the printed structures.^{87,298}

For the experiments, formulations containing each monomer and the thiol TMT in an equimolar ratio of double bonds to thiol groups were prepared. A broadband Hg lamp (400-500 nm) was used. 150-180 μL of sample volume were applied to the glass plate and irradiated for 320 s. The light intensity at the surface of the samples was adjusted to 20 mW/cm^2 .

Due to the non-miscibility of Si-based TAS and B-based TAB with the thiol at rt, due to phase separation, measurements were performed at 100 °C, at which homogeneous solutions were obtained. Due to the rather high melting point of VDB (75-76°C) and reprecipitation after dissolution under heating in the thiol, formulations were homogenized by heating to 110 °C for 10 min. It was determined that the formulation does not phase separate when stored at a minimum temperature of 55 °C. Nevertheless, for means of consistency, measurements were performed simultaneously to TAS- and TAB-based formulations at 100 °C. Since homogeneous formulations containing P-based TAP, Si-based DAS, B-based ADB, or the reference compound CTAE and the thiol were obtained at rt, these measurements were performed at 25 °C.

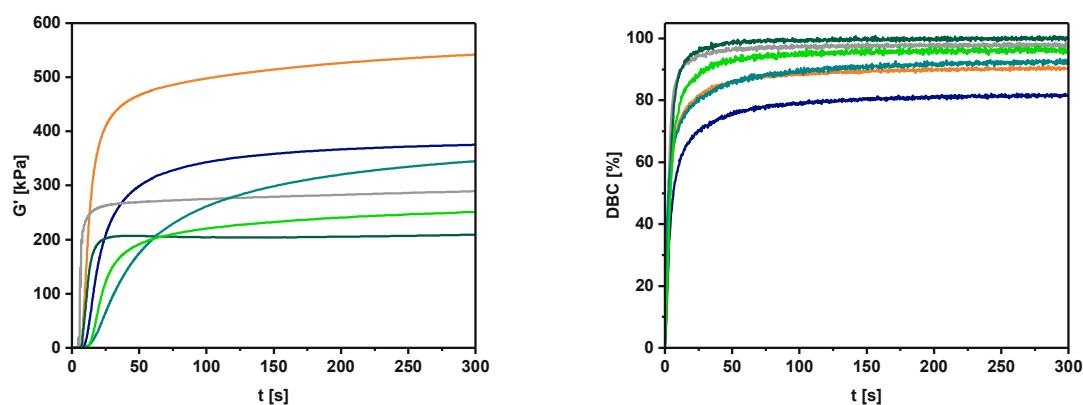


Figure 64: Storage Modulus (G' , left) and DBC (right) over time for CTAE (—), TAP (—), TAS (—), TAB (—), ADB (—), and VDB (—).

No network formation was observed for the formulation containing the Si-based monomer DAS, and a liquid sample was obtained after the measurement. Therefore, no results are shown for this compound. This might be caused by the hyperconjugation of the silicon atom with the two aromatic rings impeding radical polymerization.³³³

The rheological data in Figure 64 (left) shows that the monomers CTAE, TAP, and TAS display fast gelation with the thiol TMT. Gelation of the formulations containing the boronic esters is slightly delayed, with t_{gel} values ranging from 14-34 s. Nevertheless, this should be sufficiently fast for 3D

printing. This is also supported by t_{95} values, which show that all materials are fully cured after 65 s. Higher final storage moduli were determined for CTAE, TAP, and ADB. This is due to the fact that polymerization of these monomers was conducted at 25 °C, while the other monomers were polymerized at 100 °C.

The IR data in Figure 64 (right) shows fast monomer conversion over time and significantly higher DBC_{final} (>90%) for systems containing heteroatom-based monomers compared to the carbon-based reference CTAE (82%). Hence, a low residual amount of monomer remains in these systems after polymerization, which limits the risks of cytotoxic responses *in vivo*.

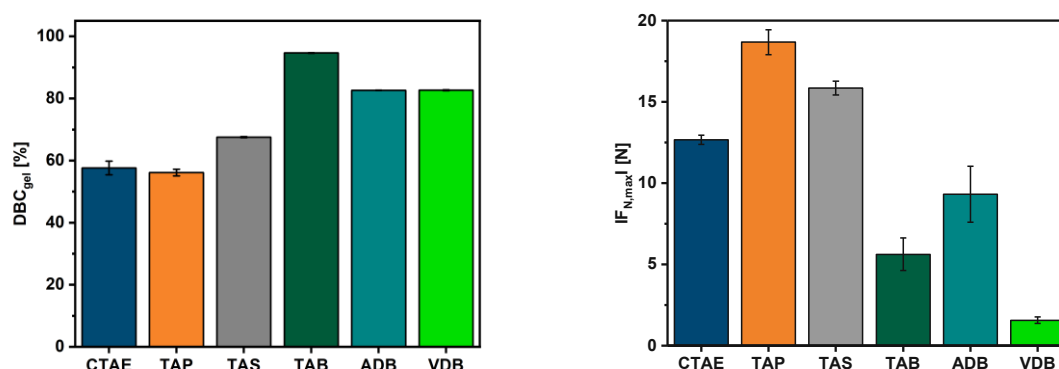


Figure 65: DBC_{gel} (left) and $IF_{N,\text{max}}$ (right) for CTAE (■), TAP (■), TAS (■), TAB (■), ADB (■), and VDB (■) polymerized with the thiol TMT.

DBC_{gel} values in Figure 65 (left) are quite high for all monomers (>50%). This is due to the quasi-ideal reaction of the allyl ester monomers with the thiol in contrast to non-regulated radical chain growth reactions.¹¹³ Exceptionally high values were shown for the formulations containing boronic esters. For TAB, a DBC_{gel} of 95% was determined, which is most likely due to the facile hydrolysis of the aliphatic monomer due to the easy accessibility of the empty p-orbital by donor molecules, such as water. Therefore, upon exposure to ambient conditions, monomers in the formulation are hydrolyzed, which causes the formation of boronic acid and mono- and difunctional boronic ester molecules. These molecules serve as reactive diluents, which results in high DBC_{gel} values. For B-based formulations containing VDB and ADB, a DBC_{gel} of 83% was determined. As access to the empty p-orbital in these compounds is slightly restricted by the cyclic structures, another explanation for these high values is the reversibility of the formation of cyclic boronic ester bonds, which gives the materials a dynamic character. These bonds are able to reopen and close during the network formation via transesterification reactions enabling network mobility up to high conversions. This high mobility is also corroborated by the retarded gelation shown in the rheology data. Furthermore, the formulation containing ADB exhibited significantly lower $IF_{N,\text{max}}$ during

crosslinking compared to the other samples cured at 25 °C, shown in Figure 65 (right). Exceptionally low shrinkage of -1.6 N was observed for the VDB-based formulation, which is significantly lower than TAS, which was also polymerized at 100 °C. Therefore, these compounds also serve as potent shrinkage-reducing agents. Table 10 shows the cumulative data for the RT-NIR photorheology measurements.

Table 10: Detailed results of the RT-NIR photorheology measurements. ¹Curing was conducted at 100 °C; ²No gelation occurred.

atom	monomer	t_{gel} [s]	DBC_{gel} [%]	t_{95} [s]	DBC_{final} [%]	G'_{final} [kPa]	$F_{N,max}$ [N]
C	CTAE	9.3 ± 1.1	57.6 ± 2.2	63.5 ± 3.1	81.6 ± 0.1	422 ± 41.9	-12.7 ± 0.3
P	TAP	5.0 ± 0.0	56.1 ± 1.1	49.3 ± 2.4	90.5 ± 0.1	475 ± 95.9	-18.7 ± 0.8
Si	TAS ¹	4.0 ± 0.0	67.6 ± 0.2	19.5 ± 1.1	98.0 ± 0.3	287 ± 1.80	-15.9 ± 0.4
	DAS	²	²	118.5 ± 6.1	1.3 ± 0.2	²	²
B	TAB ¹	17.0 ± 0.0	94.7 ± 0.2	17.9 ± 3.2	99.7 ± 1.9	175 ± 40.8	-5.6 ± 1.0
	ADB	33.7 ± 1.2	82.6 ± 0.1	65.0 ± 2.0	92.4 ± 0.2	332 ± 23.8	-9.3 ± 1.7
	VDB ¹	14.0 ± 0.0	83.0 ± 0.3	35.4 ± 2.1	96.5 ± 0.4	252 ± 4.40	-1.6 ± 0.2

2.4.2 Mechanical properties of polymer networks

Since high photoreactivity and fast curing were observed for all heteroatom-containing systems, the mechanical properties of resulting polymers were determined.

The thermomechanical properties of the materials containing CTAE, TAP, TAS, TAB, ADB, or VDB and the thiol TMT were determined with DMTA measurements described in 2.1.3. Curing of formulations containing CTAE, TAP, or ADB was conducted at rt, while formulations containing TAB, TAS, or VDB were cured at elevated temperature using a preheated silicon mold and a photocuring program at ~104 °C. This was done due to miscibility issues of the monomers with the thiol TMT, described in chapter 2.4.1.

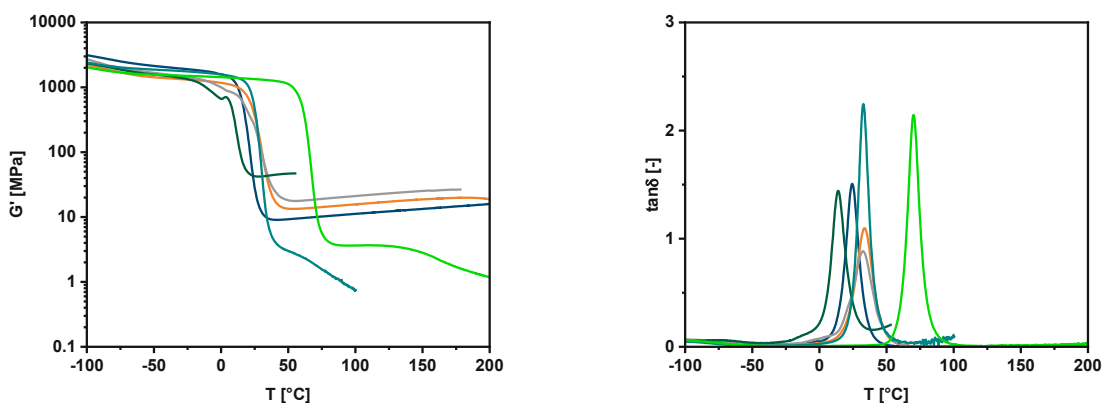


Figure 66: G' (left) and $\tan\delta$ (right) over temperature of the different networks formed from carbon-based reference CTAE or the heteroatom-based allyl esters TAP, TAS, TAB, ADB or VDB with the thiol TMT. pCTAE (—); pTAP (—); pTAS (—); pTAB (—), pADB (—), and pVDB (—).

The results in Figure 66 (left) show that all materials derived from non-rigid allyl ester monomers such as CTAE, TAP, TAS, or TAB display low $G'_{37^\circ\text{C}}$. Furthermore, these materials exhibit a T_g at or slightly above rt but still below body temperature (Figure 66, right). Although the highest crosslinking density was observed for the B-based material pTAB, it also displayed the lowest T_g . Poor mechanical properties were also observed in the cured specimens, which exhibited a sticky surface and creep upon storage, which again can be explained by the facile hydrolysis of the monomer even from moisture present in air. A T_g below body temperature was also shown for the polymer containing the boronic ester ADB due to the rather flexible and long side chain resulting in reduced crosslinking density. Nevertheless, homogeneous networks are formed with all monomers and the thiol TMT with sharp glass transitions, reflected in the low fwhm values ranging from 9-17 °C. In contrast, the rigid monomer VDB leads to a substantial increase in material T_g significantly above body temperature (70 °C) and high $G'_{37^\circ\text{C}}$ (1280 MPa). Noteworthy, both materials containing the boronic esters ADB and VDB display a thermoplastic flow instead of a rubber plateau, which can also be explained by the reversible dynamic boronic ester bonds within the network enabling high network mobility, especially at elevated temperatures.

Hence, these studies proved that next to rigid trifunctional thiols, rigid allyl ester monomers are important for the generation of stiff materials, with a T_g significantly above body temperature and high stiffness observed for the specimen containing the novel boronic ester VDB. The collected results of these measurements can be found in Table 11.

Table 11: Detailed results of the DMTA measurements. *No rubber plateau observed.

atom	monomer	T _g [°C]	G' _{25°C} [MPa]	G' _{37°C} [MPa]	fwhm [°C]	G' _R [MPa]
C	CTAE	25	29	9	11	16
P	TAP	34	297	24	15	19
Si	TAS	32	214	33	17	27
B	TAB	14	43	44	12	47
	ADB	33	447	5	9	-*
	VDB	70	1340	1280	10	-*

To determine other important mechanical parameters, such as strength, which is defined as the ability of a material to withstand plastic and irreversible deformation, and toughness, tensile tests were conducted with the materials. These tests are a shock-free, quasi-static destructive method with a slow strain rate. Uniaxial loading is applied on the sample and steadily increased until the specimen ruptures. The resulting strain is monitored with increasing stress to obtain stress-strain curves.³⁰⁹ The tensile stress σ [MPa] is calculated with Equation 5, while the strain ϵ [%] can be determined with Equation 6.

$$\sigma = \frac{F}{A_0}$$

Equation 5: Calculation of the stress in tensile testing. σ ... tensile stress [MPa]; F...tensile force [N]; A₀...initial cross section [mm²].

$$\epsilon = \frac{\Delta L}{L_0} \cdot 100 \%$$

Equation 6: Calculation of the strain in tensile testing. ϵ ... tensile strain [%]; ΔL ...elongation [mm]; L₀...initial length [mm].

The most important parameters obtained from stress-strain plots are the tensile strength σ_B [MPa], strain or elongation at break ϵ_B [%], and maximum strength σ_M [MPa]. Furthermore, tensile toughness or deformation energy U_T [MJ/m³], defined as the energy of mechanical deformation per unit volume prior to fracture, can be determined via the integration of the stress-strain curve.

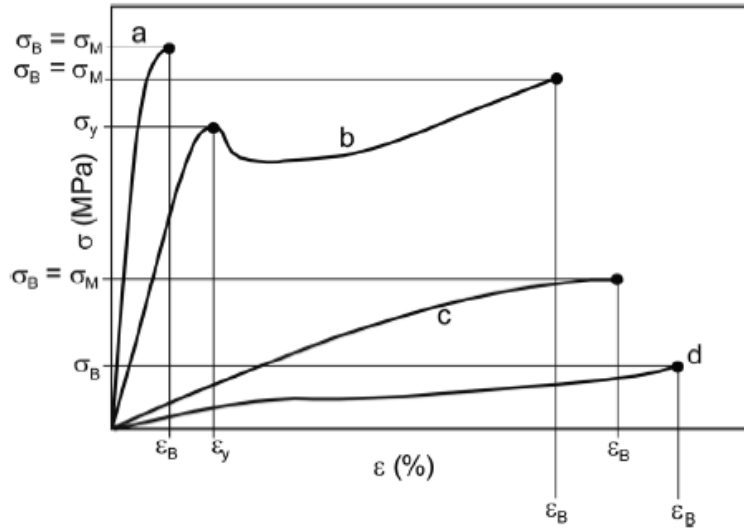


Figure 67: Exemplary stress-strain curves for various polymers.³⁰⁹

Figure 67 shows typical stress-strain curves of different materials. Initially, for all polymers, a linear behavior is observed. With increasing stress, a non-linear regime is exhibited, and a different behaviors occurs. Highly crosslinked networks are very brittle and display very low ϵ_B and high σ_M (a). Furthermore, no yield point with a yield strength σ_y , as in curve b, is observed. If the crosslinking density is low, for example, in elastomers, high ϵ_B and low σ_M are exhibited (d). When toughening agents such as thiols or high molecular weight additives are present, curves b or c are typically observed, combining high strengths and strains.³⁰⁹

For the tests, tensile test specimens of shape 5B of materials were prepared analogously to the DMTA specimens under the same curing conditions. Testing was performed according to ISO 527 with a traverse speed of 5 mm/min.

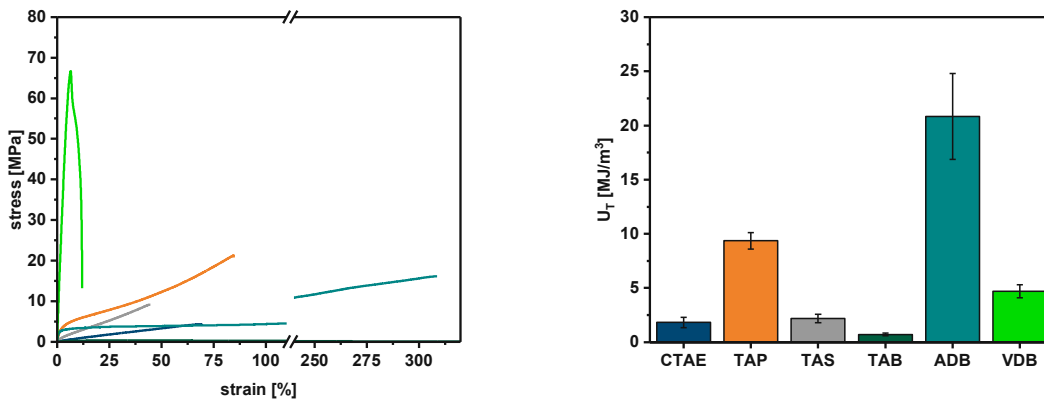


Figure 68: Stress-strain curves (left) for pCTAE (—); pTAP (—); pTAS (—); pTAB (—), pADB (—) and pVDB (—). Tensile toughness (right) for pCTAE (■), pTAP (■), pTAS (■), pTAB (■), pADB (■), and pVDB (■).

Figure 68 (left) shows that low strengths were exhibited by materials derived from the non-rigid monomers CTAE, TAP, TAB, and TAS with $\sigma_M < 22$ MPa. For pTAP and pADB, high elongations at

break of 84% and 323%, respectively were determined. The network pTAB displayed an extreme viscoplastic behavior, with almost no strength (0.4 MPa) but high elongations at break (585%). Furthermore, high deviations in ϵ_B were observed, due to the moisture sensitivity of these samples, making the fabrication of reproducible specimens difficult. In contrast, the B-based monomer VDB led to a drastic increase in network strength (67 MPa), while a good elongation at break (11%) was exhibited. This further demonstrates the importance of a rigid monomer structure on the good mechanical properties of resulting materials. Additionally, good tensile toughness (4.7 MJ/m³) was confirmed for this material (Figure 68, right). The highest tensile toughness values were shown for pTAP and pADB, which, however, are due to the high elongations at break, as the materials exhibited low strengths.

To conclude, the material formed from the rigid boronic ester VDB in combination with the rigid thiol TMT displayed excellent (thermo)mechanical properties, with a high T_g significantly above body temperature, high storage modulus at 37 °C, high strength, and good elongation at break, as well as good tensile toughness. Hence, this material seems ideal for use in artificial bone substitutes, which require these properties for good load dissipation and tissue integration. The cumulated results are summarized in Table 12.

Table 12: Detailed results of the tensile tests.

atom	monomer	σ_M [MPa]	ϵ_B [%]	U_T [MJ/m ³]
C	CTAE	4.8 ± 0.9	69.8 ± 7.1	1.8 ± 0.5
P	TAP	21.1 ± 1.0	84.3 ± 1.3	9.4 ± 0.8
Si	TAS	9.2 ± 1.2	44.3 ± 1.6	2.2 ± 0.4
B	TAB	0.4 ± 0.1	585 ± 272	0.7 ± 0.1
	ADB	14.6 ± 2.3	313 ± 30.4	20.8 ± 4.0
	VDB	67.0 ± 0.1	11.0 ± 1.1	4.7 ± 0.6

2.4.3 Degradation of polymer networks

To determine the degradation of the formed polymer networks under hydrolytic conditions, studies were conducted with cylindrically-shaped specimens (d= 5 mm, h = 2 mm), which were prepared analogously to the DMTA samples under the same curing conditions. Degradation was studied under physiological conditions (pH= 7.4), acidic (pH=4), and basic conditions (pH=10), as described in 2.1.4.

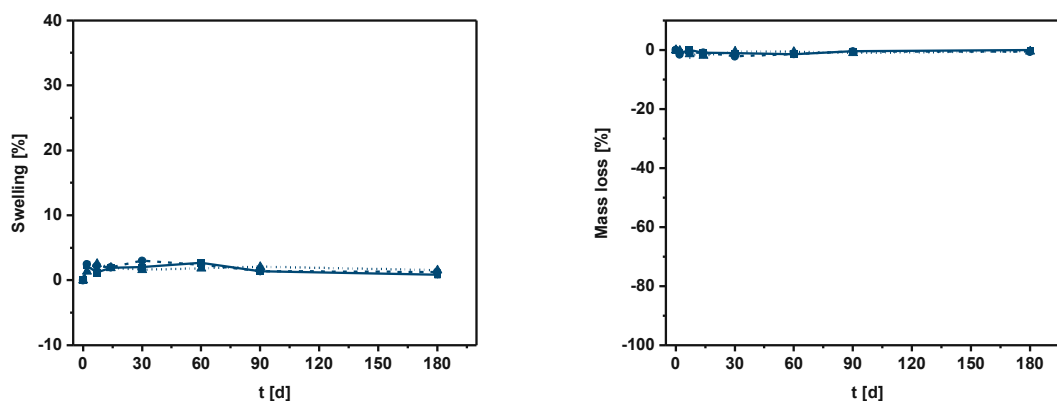


Figure 69: Degradation studies for the C-based reference network pCTAE prepared with the thiol TMT; left: swelling over time; right: mass loss over time; pH 7.4 (—■—); pH 4 (-●-), pH 10 (···▲···).

Figure 69 displays the degradation behavior for the carbon-based reference network formed from CTAE. Although only a slight amount of swelling (~2-3%) was determined throughout the experiment under all conditions, a maximum mass loss of <1% was shown under acidic conditions. Again, no significant mass loss of the network occurred under basic conditions, indicating high stability of the carboxylic ester bond of the network, even after 6 M. This confirms the results by Mautner *et al.*¹¹² that carbon-based esters are not suitable compounds to generate materials with sufficient degradability under hydrolytic conditions.

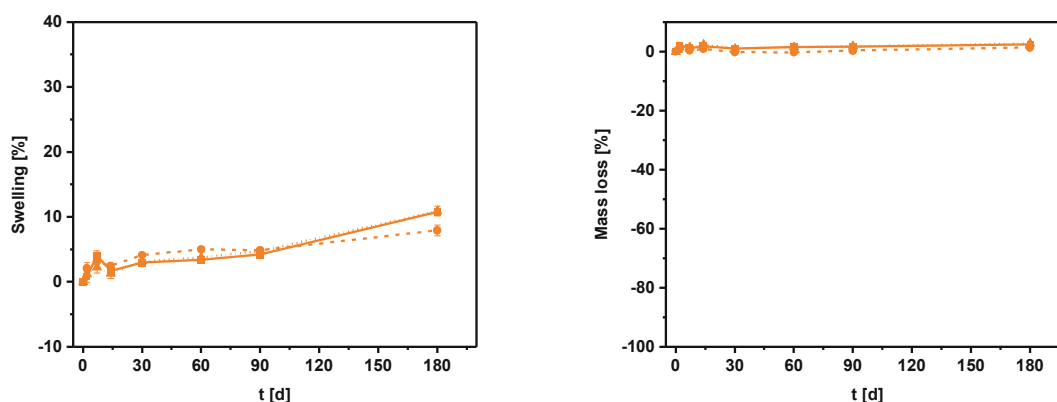


Figure 70: Degradation studies for the P-based network pTAP prepared with the thiol TMT; left: swelling over time; right: mass loss over time; pH 7.4 (—■—); pH 4 (-●-), pH 10 (···▲···).

For P-based material containing TAP, slight swelling (8-11%) was observed after 6 M (Figure 70, left). Nevertheless, no significant cleavage of the P-O-bonds occurred under hydrolytic conditions, with a maximum mass loss of <1% determined under basic conditions (Figure 70, right). Therefore, P-based materials are less promising, although a different behavior is expected in further *in vitro* and *in vivo* studies, in which phosphatases are present, as these enzymes are able to cleave the bonds between the heteroatom and oxygen.

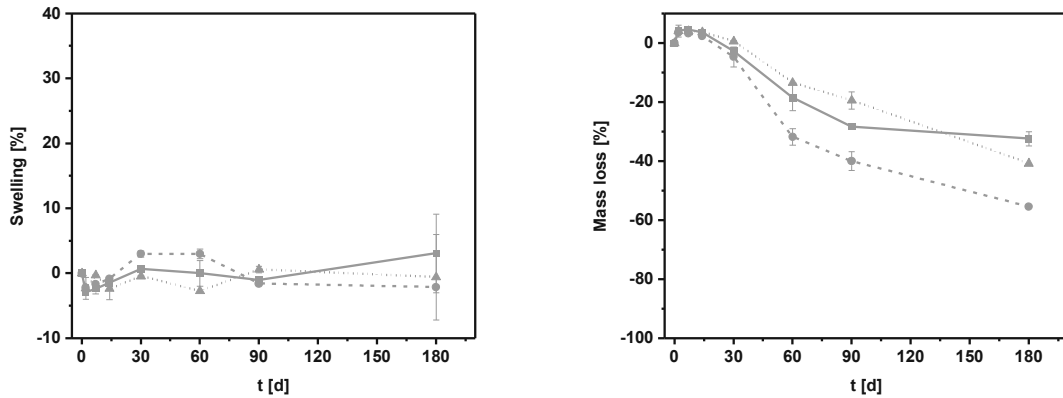


Figure 71: Degradation studies for the Si-based network pTAS prepared with the thiol TMT; left: swelling over time; right: mass loss over time; pH 7.4 (—■—); pH 4 (-◆-), pH 10 (…▲…).

Only slight swelling was shown for the material derived from Si-based TAS shown in Figure 71 (left). Furthermore, a linear mass loss with an onset after 30 d was determined, with the highest mass loss of 55% observed under acidic and basic conditions. This shows that enhanced degradation is possible with polymers containing Si-O bonds compared to the carbon-based reference network. However, the mechanical properties of the network determined in the previous chapter were shown to be insufficient for the desired application in bone replacement materials, making further optimization necessary.

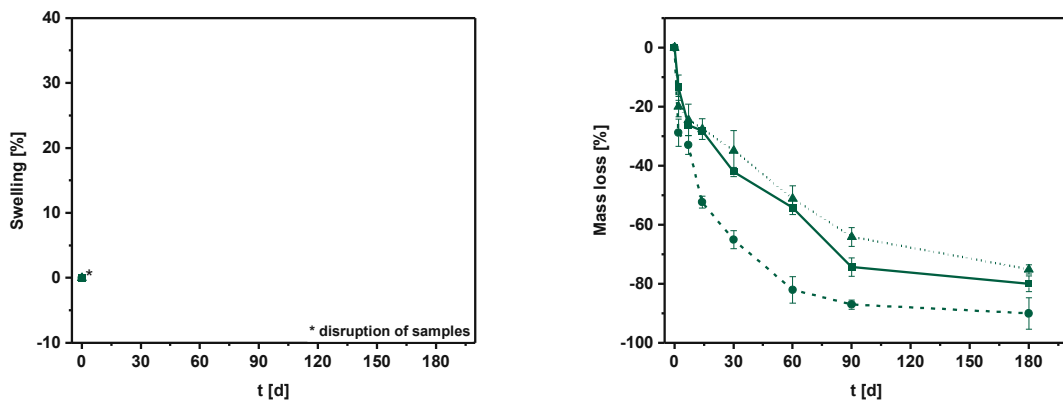


Figure 72: Degradation studies for the B-based network pTAB prepared with the thiol TMT; left: swelling over time; right: mass loss over time; pH 7.4 (—■—); pH 4 (-◆-), pH 10 (…▲…).

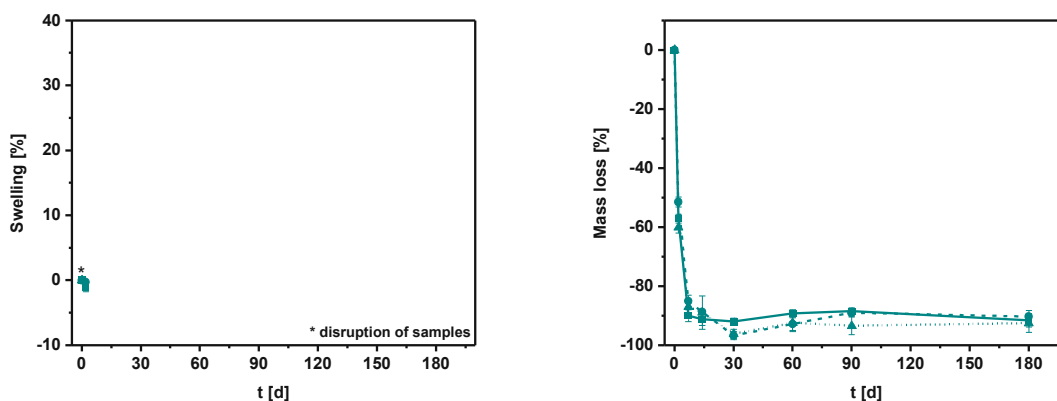


Figure 73: Degradation studies for the B-based network pADB prepared with the thiol TMT; left: swelling over time; right: mass loss over time; pH 7.4 (—■—); pH 4 (-●-), pH 10 (···▲···).

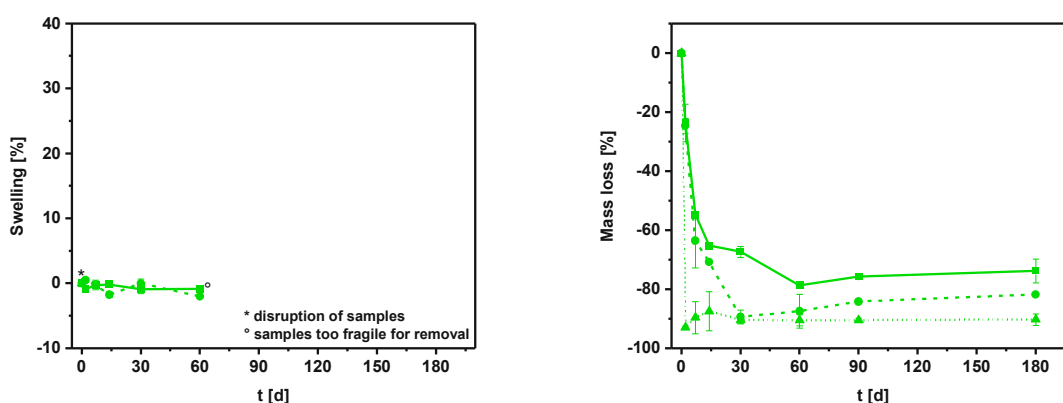


Figure 74: Degradation studies for the B-based network pVDB prepared with the thiol TMT; left: swelling over time; right: mass loss over time; pH 7.4 (—■—); pH 4 (-●-), pH 10 (···▲···).

Degradation studies of networks based on boronic esters are displayed in Figure 72 to Figure 74. For the polymers derived from B-based TAB and ADB, which were shown to exhibit T_g values below body temperature, the same degradation behavior was observed (Figure 72 and Figure 73). Swelling of the samples could not be determined after 48 h, as disruption of the samples occurred under all conditions. This was also shown in the mass loss curves, which display a rapid mass loss over time. This trend is even slightly accelerated for the network containing ADB, with erosion of 85-90% after 7 days and only a slight further reduction (88-96%) for the remaining testing period. This shows that the cleavage of aliphatic boronic ester bonds in TAB and the cyclic boronic ester bonds with an attached methylene group present in ADB proceeds too fast for the desired application. A possible explanation for this behavior is the low T_g of the networks containing TAB and ADB, which exhibit values of 14 °C and 33 °C, respectively. Hence, upon storage in the buffer media at 37 °C, high network flexibility is exhibited, enabling water penetration and facilitating the cleavage of the network boronic ester bonds. Hence, these systems are more suitable for

applications requiring low T_g values and fast degradation rates within 2 days, such as drug delivery vehicles.

For the network containing VDB, disruption of the samples occurred under basic conditions after 48 h, demonstrating the high instability of the B-O bond towards bases. Under physiological and acidic conditions, a different behavior was observed without significant swelling throughout the experiment. Additionally, an immediate onset of degradation was shown, followed by an exponential decay of the mass, with a mass loss of 79% and 87% after 60 days under neutral and acidic conditions, respectively. After 90 days, no samples could be removed for determination of the swelling, as only very thin and fragile samples were observed at the bottom of the vials. Figure 75 provides insight into the degradation mechanism of networks based on VDB under neutral and acidic conditions. It is shown that a general retention of the shape occurs, which decreases in size as a function of degradation time. This is characteristic of a surface erosion process and shows the importance of the high T_g and tensile strength of this material, as this results in reduced chain mobility at the degradation temperature. This, in turn, prevents the diffusion of water into the samples and confines hydrolysis to the surface.

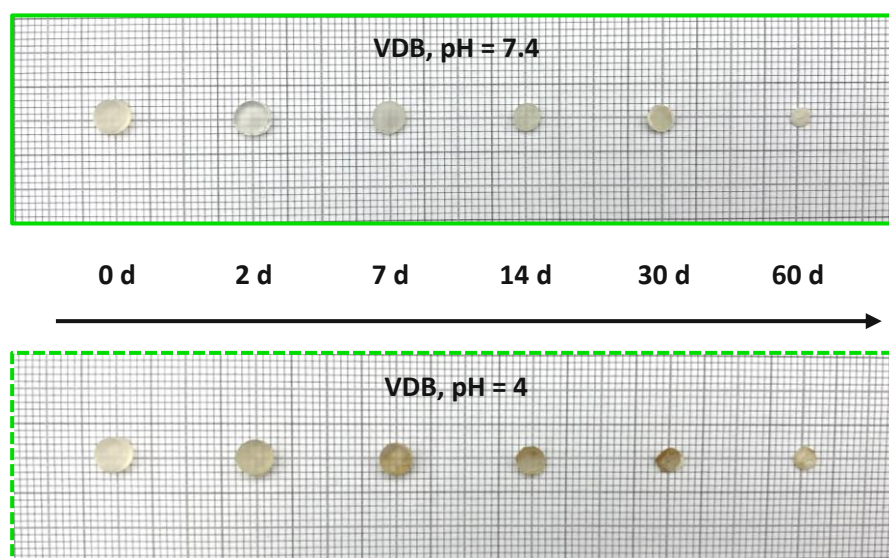


Figure 75: Photographs of the VDB-based network at different degradation times under physiological conditions (PBS, pH = 7.4, upper photograph) and acidic conditions (acetate buffer, pH = 4, lower photograph) depicting the surface erosion degradation behavior.

As cleavable bonds reside at every crosslinking point, ideally, total material dissolution was expected. Nevertheless, no total degradation of the polymers was determined for any material during the testing period. Instead, slight traces of solid residues were observed at the bottom of the vials after drying to constant weight, attributed to slight traces of hydrolysis products, residual material, and buffer salts in the testing vials.

A slight decrease in swelling was observed for some materials (*i.e.*, pVDB) throughout the experiment. These results can be explained by residual salt traces of the buffer solutions in the vials, which were weighed in combination with the dried sample to determine the dry weight. This was done for consistency as some samples were disrupted during the experiment or became too fragile for removal due to the small sample sizes used (~50 mg). Negative values can be additionally explained by the irreversible water uptake of some of the networks (*i.e.*, pTAS).

To conclude, enhanced degradation compared to the carbon-based reference network was shown with the polymer containing Si-based TAS. However, this material is unsuitable for bone scaffolds, as rather poor mechanical properties are exhibited. Furthermore, the results demonstrate that a combination of excellent mechanical properties such as low shrinkage, high glass transition temperature, strength, toughness, and degradation behavior, as well as accelerated degradation via surface erosion under physiological and acidic conditions, are possible with the material containing the novel boronic ester VDB in combination with the rigid thiol TMT.

2.5 Optimization of mechanical properties and degradation behavior

It was shown that degradation could be significantly enhanced by using allyl esters containing silicic and boronic ester bonds, compared to networks with carboxylic ester bonds. Furthermore, due to the quasi-ideal reaction of these compounds with thiols, unprecedented high network homogeneity was determined for these materials, unlike for state-of-the-art vinyl esters and vinyl carbonates, which also display a significant amount of homopolymerization.^{67,69,98,112}

Nevertheless, certain disadvantages of formulation and material properties were observed. High processing temperatures were necessary to obtain homogeneous formulations containing the B-based VDB or Si-based TAS. This limits their use in 3D-printing methods, in which objects are generated by photopolymerization of layers at rt. For materials containing TAS and B-based ADB, rather poor (thermo)mechanical properties with a T_g below body temperature and low tensile strength were determined, due to the rather flexible monomer structures, making applications in bone replacement materials impossible. Lastly, due to the low network T_g , rapid material disintegration under hydrolytic conditions occurred for pADB instead of the desired surface erosion behavior. Therefore, optimization of these properties was conducted.

The aliphatic boronic ester TAB was not used in subsequent studies, as high sensitivity of this monomer to air moisture was observed, leading to samples with a sticky surface and making the

fabrication of reproducible specimens difficult. Furthermore, the worst mechanical properties were shown for this material, with extremely low strengths and high elongations at break, rendering it unsuitable as a monomer used to fabricate bone regeneration scaffolds.

2.5.1 Optimization with a trifunctional crosslinker

To optimize formulation and mechanical properties, a monomer, which in the best case is liquid at rt was envisioned to lower the processing temperature of the formulations by improvement of the solubility of the compounds in the thiol TMT. To not spoil the mechanical properties of the materials, this monomer should further contain rigid structures. As the best mechanical properties were shown with trifunctional thiols in previous studies, a trifunctional monomer, triallyl isocyanurate (TAI), depicted in Figure 76, was chosen. This rigid monomer does not contain any degradable motifs, which might influence the degradation behavior of the network. All compounds used for this study are depicted in Figure 76 as well. Parallel to optimizing the mechanical properties with this trifunctional crosslinker, the influence of adding the filler hydroxyapatite (HAP) to these systems was studied, which is described in detail in chapter 2 of the Appendix.

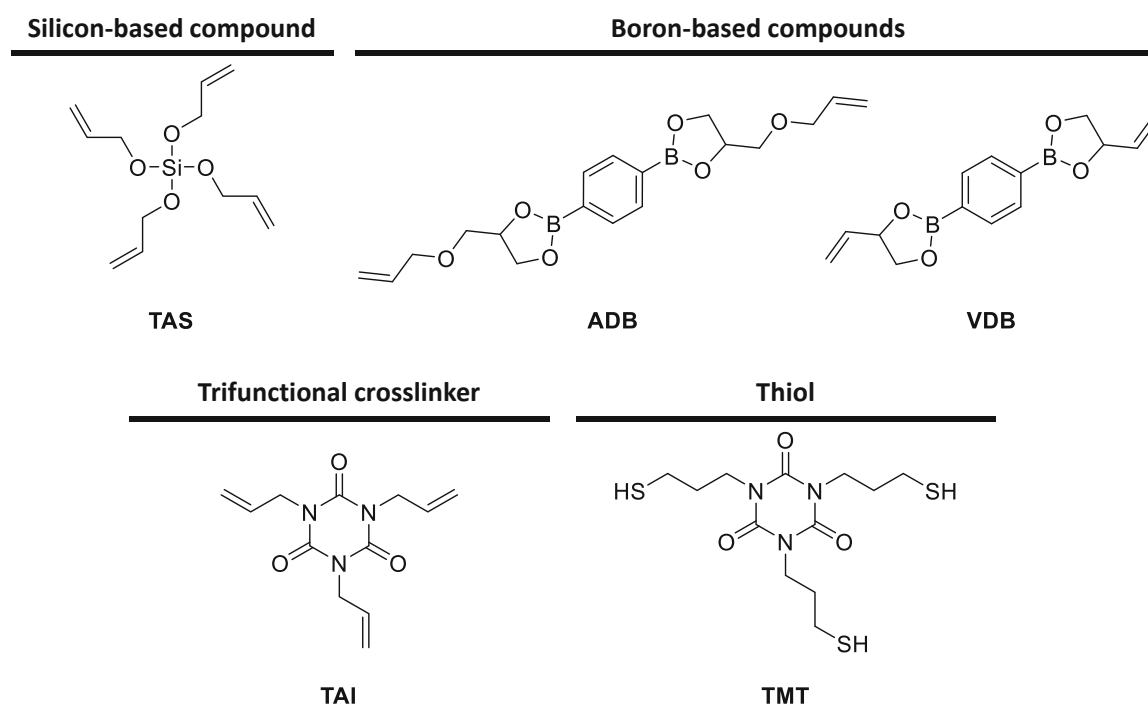


Figure 76: Structure of the compounds used for the optimization studies.

First, formulations were prepared, in which each degradable monomer was partially substituted by TAI. Different molar ratios of 40 mol%, 60 mol%, or 80 mol% of each degradable monomer (x_{deg})

with respect to TAI were chosen for the studies. TMT was used as a thiol, and formulations were prepared in an equimolar ratio of overall double bonds to thiol groups. To calculate the molar amount of TAI, Equation 7 was used.

$$n_{\text{TAI}} = \frac{n_{\text{deg}}}{x_{\text{deg}}} \cdot (100 - x_{\text{deg}})$$

Equation 7: Calculation of molar amount of TAI; n_{TAI} ...molar amount of TAI; n_{deg} ...molar amount of degradable monomer; x_{deg} ...mol% of degradable monomer.

Formulations containing 40-80 mol% of each degradable monomer with respect to TAI and the thiol TMT in an equimolar ratio of double bonds to thiol groups were prepared. For initiation, 1 w% of Ivocerin, and for stabilization 0.02 w% of PYR were used. As references, formulations containing 0 mol% of degradable monomer (equivalent to 100 mol% TAI) and 100 mol% of each degradable monomer were used. The formulations were homogenized by careful heating and mixing. Then, they were stored at rt for 2 d to determine the time, after which phase separation or precipitation of compounds occurred. All formulations containing 40 mol% and 60 mol% of each degradable monomer with respect to TAI were stable for more than 48 h at rt. Additionally, a homogeneous formulation was obtained with 80 mol% ADB. For formulations containing 80 mol% TAS and VDB, phase separation or precipitation were determined at rt, which was also observed for the 100 mol% formulations in previous studies. Therefore, these formulations were processed at 100 °C, while all other systems were processable and curable at rt.

2.5.1.1 Reactivity of formulations with TAI

To determine whether high photocuring rates are maintained upon the addition of the trifunctional crosslinker, RT-NIR photorheology measurements were conducted as described in 1.1.3. For the experiments, a broadband Hg lamp (400-500 nm) was used. 150-180 μL of sample volume were applied to the glass plate and irradiated for 320 s. The light intensity at the surface of the samples was adjusted to 20 mW/cm^2 . Measurements were performed at 25 °C for formulations stable at rt. For the formulations containing 80 mol% or 100 mol% TAS or VDB, a temperature of 100 °C was used since homogeneous formulations were only obtained upon heating to this temperature.

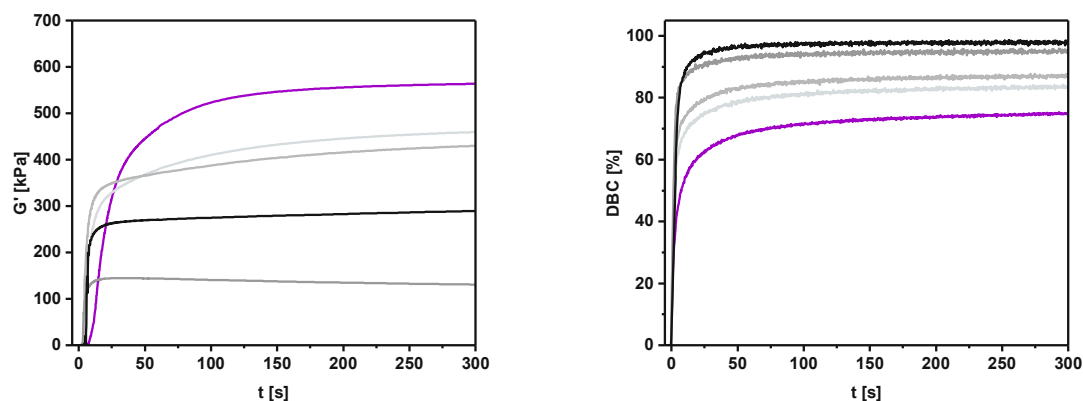


Figure 77: Storage Modulus (G' , left) and DBC over time (right) for formulations containing 0 mol% (—), 40 mol% (—), 60 mol% (—), 80 mol%* (—), and 100 mol% (—) TAS*. *Curing at 100 °C.

First, the influence of the addition of TAI on the photocuring rates of the thiol-ene system containing the degradable Si-based monomer TAS was determined. Figure 77 (left) shows that gelation for the formulation containing 0 mol% TAS (100 mol% TAI) is slightly retarded compared to 40-80 mol% TAS, which display fast crosslinking. As well, significantly lower final double bond conversions were observed with this sample (75%) (Figure 77, right), although the highest final storage modulus (533 kPa) was determined, making this monomer highly promising for the enhancement of mechanical properties of Si-based polymers. All formulations containing TAS exhibit low t_{gel} and t_{95} values and high conversions, while the fastest crosslinking and curing was observed for the formulations containing 80 mol% and 100 mol% TAS, which were cured at 100 °C. Due to the curing conducted at elevated temperatures, formed networks also display significantly lower final storage moduli, while the lowest value (123 kPa) was obtained with 80 mol% TAS, probably due to the lower final conversion of this system.

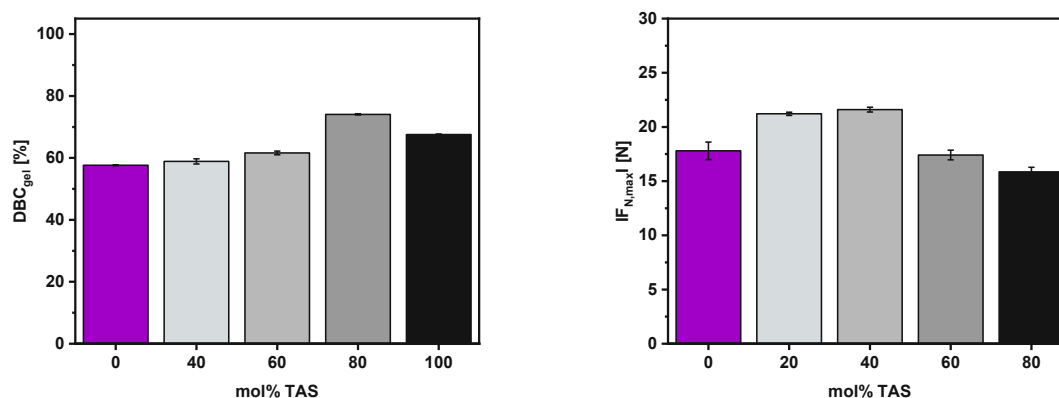


Figure 78: DBC_{gel} (left) and $F_{N,max}$ (right) for formulations containing 0 mol% (■), 40 mol% (■), 60 mol% (■), 80 mol% (■), and 100 mol% (■) TAS.

High $DBC_{gel} > 58\%$ were observed for all formulations, with the highest value for 80 mol% TAS and 100 mol% TAS, due to the curing at elevated temperature resulting in higher network mobility

during curing (Figure 78, left). Similar $F_{N,max}$ were shown for all formulations (Figure 78, right), with slightly lower values exhibited by the formulations cured at 100 °C. Therefore, partial substitution of the degradable monomer TAS with TAI does not significantly impact the curing process, and high photocuring rates of the Si-based systems are maintained.

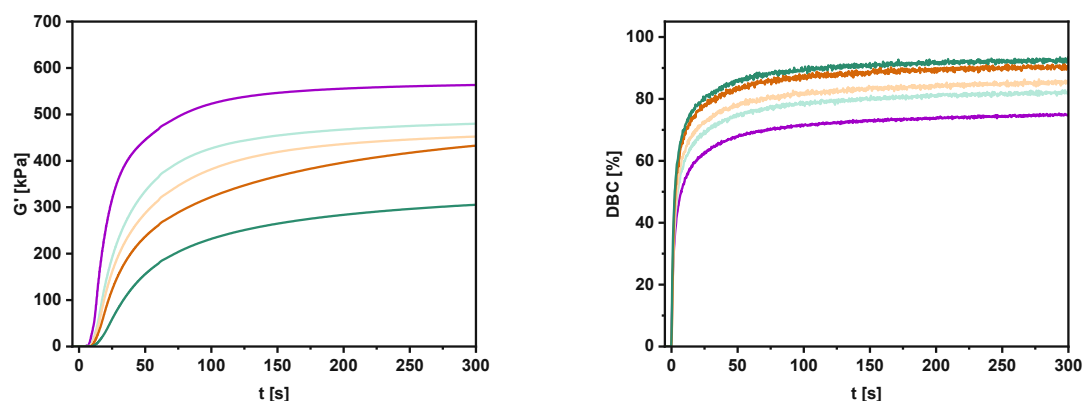


Figure 79: Storage Modulus (G' , left) and DBC over time (right) for formulations containing 0 mol% (—), 40 mol% (—), 60 mol% (—), 80 mol% (—), and 100 mol% (—) ADB.

Next, the influence of TAI addition on the photorheological behavior of the B-based formulation containing ADB was investigated. Figure 79 (left) displays the influence on the gelation of formulations containing ADB. Increased polymerization rates and higher final storage moduli were observed with increasing TAI concentration. Therefore, TAI is a promising molecule for enhancing the mechanical properties of ADB-based materials. Conversion curves over time (Figure 79, right) show a decrease in final double bond conversions with increasing TAI content. Nevertheless, high values $>82\%$ were attained for all systems.

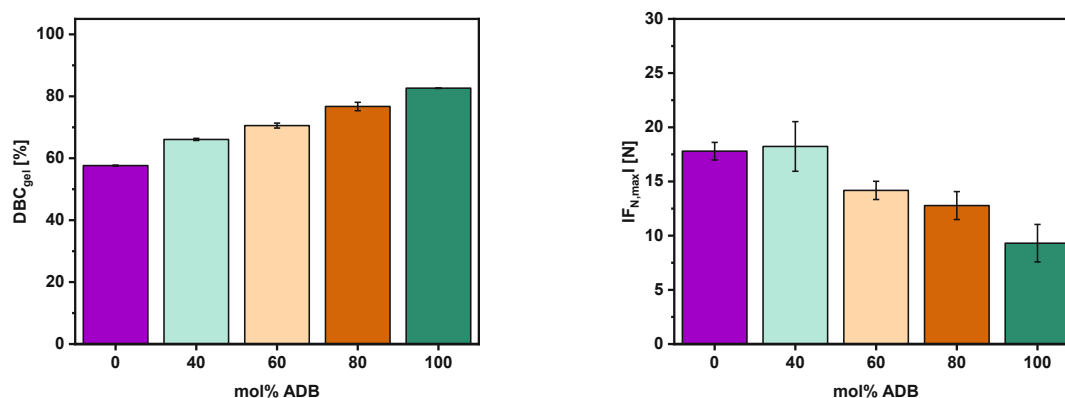


Figure 80: DBC_{gel} (left) and $F_{N,max}$ (right) for formulations containing 0 mol% (■), 40 mol% (■), 60 mol% (■), 80 mol% (■), and 100 mol% (■) ADB.

Figure 80 depicts that DBC_{gel} increases with the rising concentration of the boronic ester. An explanation for this is the dynamic character of the cyclic boronic ester bonds, which can reversibly

reopen during crosslinking, enabling network mobility up to high conversions. This high mobility is also corroborated by the retarded gelation compared to 100 mol% TAI shown in the rheology data.

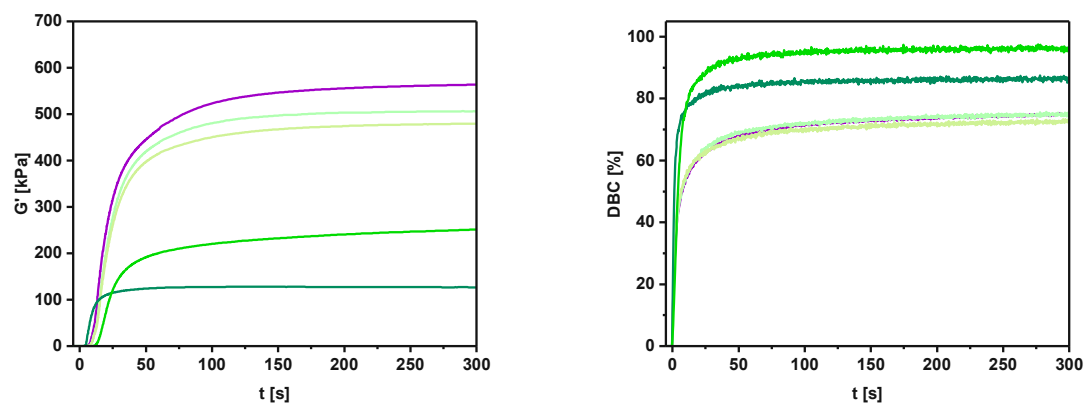


Figure 81: Storage Modulus (G' , left) and DBC over time (right) for formulations containing 0 mol% (—), 40 mol% (—), 60 mol% (—), 80 mol%* (—), and 100 mol% (—) VDB*. *Curing at 100 °C.

Lastly, the photocuring rates and rheological behavior of the B-based thiol-ene formulation containing VDB were determined. Figure 81 (left) shows that similar polymerization rates are obtained with all samples except 80 mol% VDB, which displays an accelerated crosslinking of the network. Nevertheless, also the lowest final storage modulus was observed for this formulation, followed by 100 mol% VDB, which is due to the curing conducted at 100 °C. Similar, high storage moduli were determined for the 0-60 mol% formulations, which again shows the positive impact of rigid TAI on the mechanical properties of resulting networks. Conversion over time curves (Figure 81, right) show that curing at elevated temperatures significantly increases final conversions. Additionally, increasing the concentration of TAI results in lower final conversions, which, however, still exceed 72% for all formulations.

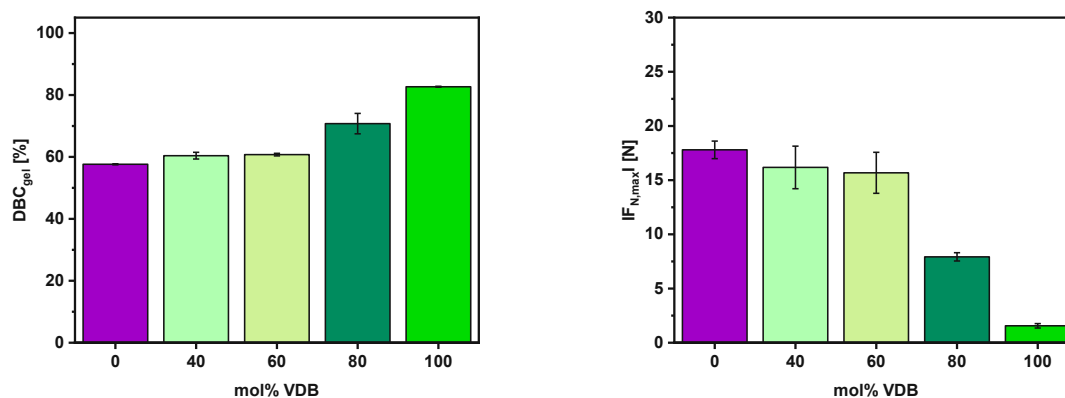


Figure 82: DBC_{gel} (left) and F_{N,max} (right) for formulations containing 0 mol% (■), 40 mol% (■), 60 mol% (■), 80 mol% (■)*, and 100 mol% (■) VDB*. *Curing at 100 °C.

Figure 82 (left) shows the same trends for rising DBC_{gel} with increasing boronic ester concentrations, which were also observed for systems containing ADB. Exceptionally high values were shown for 80 mol% and 100 mol% VDB due to the dynamic character of the B-O bonds, already described in 2.4.1. This is also shown for F_{N,max}, which decreases with an increasing amount of boronic ester due to the potential for network rearrangement, resulting in enhanced network mobility during curing.

To conclude, all formulations containing TAI display sufficiently fast crosslinking and curing for 3D printing. It was shown that an increasing amount of TAI results in a decrease in final double bond conversion for all systems, as they become less flexible during curing. Nevertheless, conversions >72% were shown for all formulations, which should be high enough for successful structuring. Lastly, the addition of TAI leads to higher final storage moduli, showing the potential of this monomer for enhanced mechanical properties of resulting networks. The cumulated data of these measurements is given in Table 13.

Table 13: Detailed results of the RT-NIR photorheology measurements. *Curing at 100 °C.

atom	monomer	x_{deg} [mol%]	t_{gel} [s]	DBC_{gel} [%]	t_{95} [s]	DBC_{final} [%]	G'_{final} [kPa]	$F_{N,max}$ [N]
C	TAI	0	15.0 ± 0.0	57.6 ± 0.2	90.3 ± 3.3	75.0 ± 0.1	533 ± 31.9	-17.8 ± 0.8
Si	TAS	40	3.7 ± 0.6	58.9 ± 0.8	57.5 ± 5.4	82.7 ± 1.8	453 ± 20.1	-21.2 ± 0.2
		60	3.0 ± 0.0	61.6 ± 0.6	46.8 ± 1.4	87.3 ± 0.0	420 ± 16.6	-21.6 ± 0.2
		80*	3.0 ± 0.0	74.1 ± 0.2	20.0 ± 2.7	93.6 ± 3.2	123 ± 13.8	-17.4 ± 0.5
		100*	4.0 ± 0.0	67.6 ± 0.2	19.5 ± 1.1	98.0 ± 0.3	287 ± 1.80	-15.9 ± 0.4
B	VDB	40	18.3 ± 0.6	60.4 ± 1.5	78.0 ± 3.6	74.6 ± 1.7	517 ± 15.5	-16.2 ± 2.0
		60	19.0 ± 0.0	60.8 ± 0.4	63.6 ± 4.5	72.3 ± 0.4	506 ± 23.9	-15.7 ± 1.9
		80*	5.0 ± 0.0	70.8 ± 3.3	27.3 ± 2.7	86.3 ± 4.2	128 ± 1.00	-7.9 ± 0.4
		100*	14.0 ± 0.0	83.0 ± 0.3	35.4 ± 2.1	96.5 ± 0.4	252 ± 4.40	-1.6 ± 0.2
B	ADB	40	17.0 ± 1.7	66.1 ± 0.3	76.7 ± 5.9	82.4 ± 0.7	480 ± 29.4	-18.2 ± 2.3
		60	19.0 ± 0.0	70.5 ± 0.8	77.4 ± 5.4	85.5 ± 0.1	446 ± 45.9	-14.2 ± 0.8
		80	22.0 ± 0.0	76.7 ± 1.4	69.4 ± 2.0	90.6 ± 0.3	434 ± 10.9	-12.8 ± 1.3
		100	33.7 ± 1.2	82.6 ± 0.1	65.0 ± 2.0	92.4 ± 0.2	332 ± 23.8	-9.3 ± 1.7

2.5.1.2 Mechanical properties of polymer networks with TAI

After high photoreactivity and fast curing were confirmed for all formulations optimized with the trifunctional crosslinker TAI, next, the mechanical properties of resulting polymers were determined.

The thermomechanical properties of the materials were determined with DMTA measurements described in 2.1.3. DMTA specimens were cured in a Lumamat 100 light oven. Polymerization of formulations was conducted at rt, except for 80 mol% or 100 mol% TAS or VDB, which were cured at elevated temperatures using a preheated silicon mold and a photocuring program at ~104 °C. This was done due to miscibility issues of the monomers with the thiol TMT, described in 2.5.1.

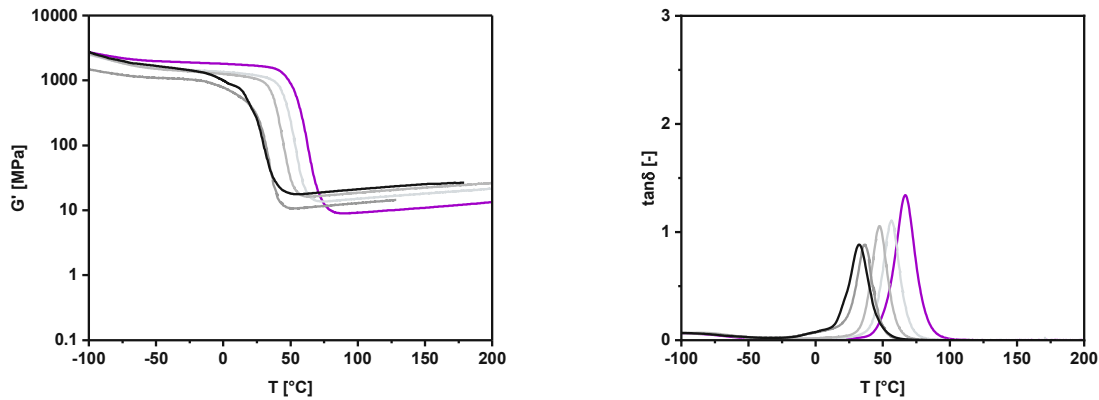


Figure 83: G' (left) and $\tan\delta$ (right) over temperature of the different networks formed from formulations 0 mol% (—), 40 mol% (—), 60 mol% (—), 80 mol% (—), and 100 mol% (—) TAS.

First, the influence of TAI addition on the thermomechanical properties of the Si-based materials containing TAS was determined. Storage modulus and $\tan\delta$ curves of polymers derived from 40-80 mol% Si-based TAS in Figure 83 show that adding rigid TAI to the formulations containing the rather flexible monomer increases T_g and storage modulus at 37 °C with increasing TAI concentration. While the sample containing 80 mol% TAS exhibits a T_g located exactly at body temperature, a T_g exceeding 37 °C was determined for the specimens containing higher TAI amounts. Therefore, the addition of the trifunctional, rigid crosslinker significantly enhanced the thermomechanical properties. High crosslinking density was shown for the polymers containing TAS, with higher network density for increasing concentration of this monomer due to its higher functionality compared to TAI. Interestingly, the lowest crosslinking density of polymers containing TAS was observed with 80 mol% TAS, which was also shown in the G' curves of the photorheology measurements (2.5.1.1).

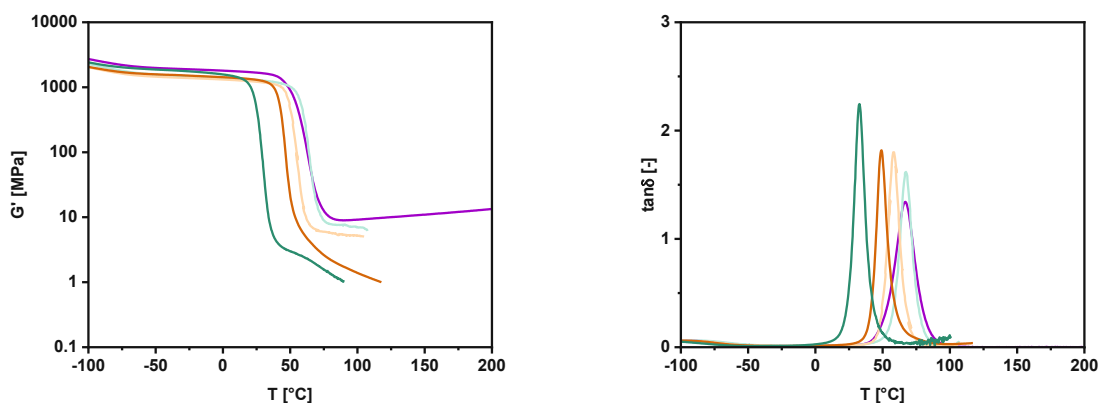


Figure 84: G' (left) and $\tan\delta$ (right) over temperature of the different networks formed from formulations 0 mol% (—), 40 mol% (—), 60 mol% (—), 80 mol% (—), and 100 mol% (—) ADB.

Next, the thermomechanical properties of the B-based materials containing ADB were investigated. The same trends for the Si-based specimens were observed with samples containing

40-80 mol% ADB (Figure 84), with a significant enhancement of all thermomechanical properties upon TAI addition. Most importantly, all specimens exhibited a T_g significantly above body temperature. A significantly lower crosslinking density and a thermoplastic flow were observed for ADB-containing materials, which is explained by the lower functionality compared to TAS and TAI, as well as the dynamic character of these networks, due to the reversible boronic ester bonds.

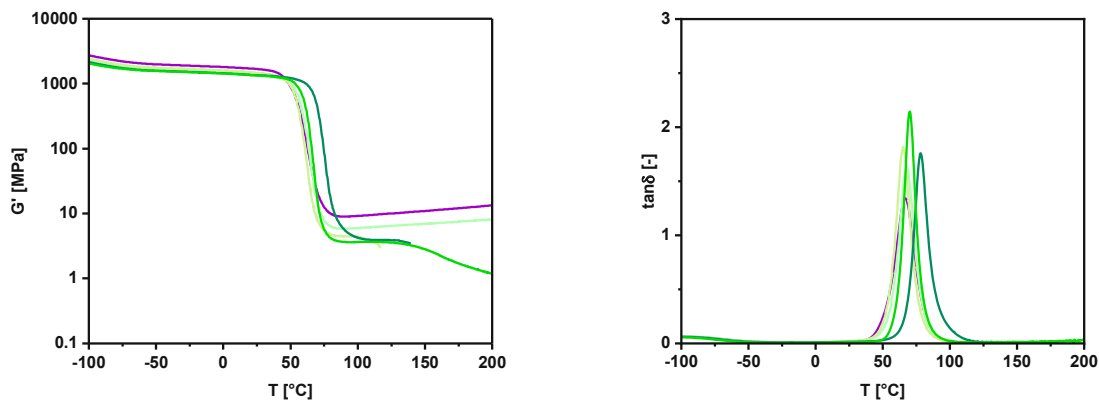


Figure 85: G' (left) and $\tan\delta$ (right) over temperature of the different networks formed from formulations 0 mol% (—), 40 mol% (—), 60 mol% (—), 80 mol% (—), and 100 mol% (—) VDB.

Subsequently, the thermomechanical properties of the materials containing the boronic ester VDB were determined. Figure 85 shows that high storage moduli at body temperature (>1280 MPa) and T_g values >65 °C were determined for all specimens containing B-based, rigid VDB. This shows that the addition of TAI does not lead to a deterioration of the excellent thermomechanical properties. Hence, these materials seem most promising for the desired application in bone regeneration scaffolds. Interestingly, all polymers except the network containing 40 mol% VDB display a thermoplastic flow at elevated temperatures. Presumably, at a concentration of 40 mol% VDB, a network with a rather static character is formed due to the high amount of TAI present, which forms permanent crosslinks. The summarized results are given in Table 14.

Table 14: Detailed results of DMTA measurements. *No rubber plateau observed.

atom	monomer	x_{deg} [mol%]	T_g [°C]	$G'_{25^\circ C}$ [MPa]	$G'_{37^\circ C}$ [MPa]	fwhm [°C]	G'_R [MPa]
C	TAI	0	67	1680	1550	17	13
Si	TAS	40	56	1190	996	14	21
		60	47	1050	572	14	26
		80	37	287	32	14	14
		100	32	214	33	17	27
B	ADB	40	67	1300	1210	10	*
		60	58	1220	1120	10	*
		80	49	1300	1030	9	*
		100	33	447	5	9	*
B	VDB	40	68	1380	1290	13	8
		60	65	1470	1360	12	*
		80	78	1350	1310	12	*
		100	70	1340	1280	10	*

Also, tensile test specimens of shape 5B of all described formulations were prepared under the same curing conditions as DMTA specimens, and testing was performed as described in 2.4.2.

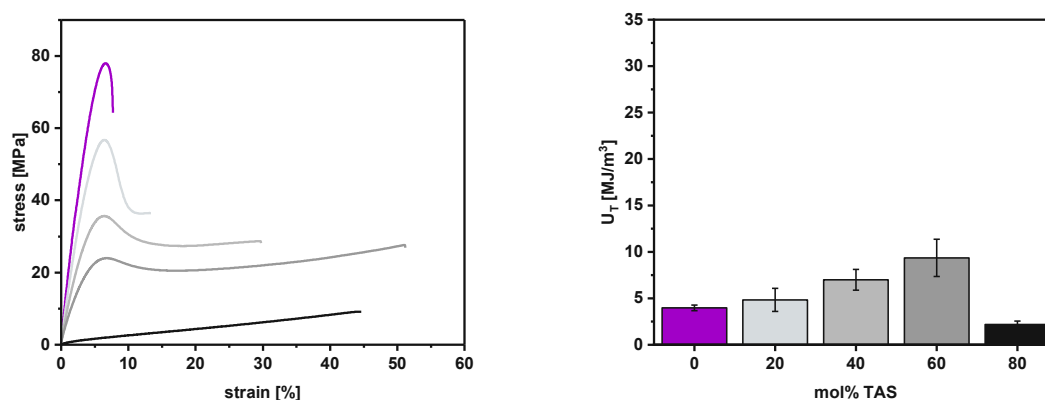


Figure 86: Stress-strain curves (left) for polymers containing 0 mol% (—), 40 mol% (—), 60 mol% (—), 80 mol% (—), and 100 mol% (—) TAS. Tensile toughness (right) for polymers containing 0 mol% (■), 40 mol% (■), 60 mol% (■), 80 mol% (■), and 100 mol% (■) TAS.

For the polymers containing the rather flexible silicone-based monomer TAS, the stress-strain curves in Figure 86 (left) confirmed that an increasing amount of TAI leads to an enhancement of mechanical properties with a significant increase in σ_M and good elongations at break maintained for all materials containing 40-80 mol% of the monomer. Additionally, tensile toughness could be improved by a factor of 2, 3, and even 4 for materials containing 40 mol%, 60 mol%, and 80 mol%, respectively, compared to the network without TAI Figure 86 (right).

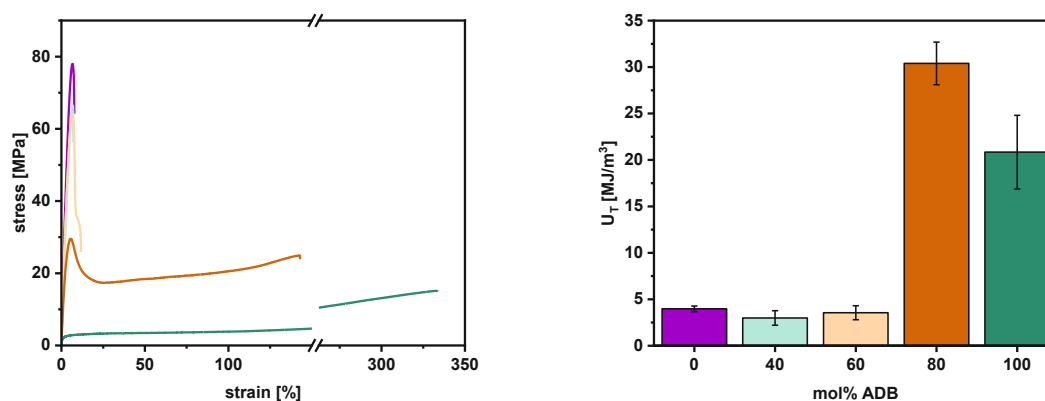


Figure 87: Stress-strain curves (left) for polymers containing 0 mol% (—), 40 mol% (—), 60 mol% (—), 80 mol% (—), and 100 mol% (—) ADB. Tensile toughness (right) for polymers containing 0 mol% (■), 40 mol% (■), 60 mol% (■), 80 mol% (■), and 100 mol% (■) ADB.

The same trends as for networks containing the flexible monomer TAS were observed for materials derived from B-based and rather flexible ADB, with a significant increase in tensile strength observed for all polymers containing 40-80 mol% of the monomer with respect to TAI (Figure 87, left), while good elongations (7-148%) were maintained. Furthermore, all samples display high tensile toughness (Figure 87, right), with an exceptional value >30 MJ/m³ obtained for p(80 mol% ADB), which is due to its relatively good strength (29 MPa) combined with high elongation at break (148%).

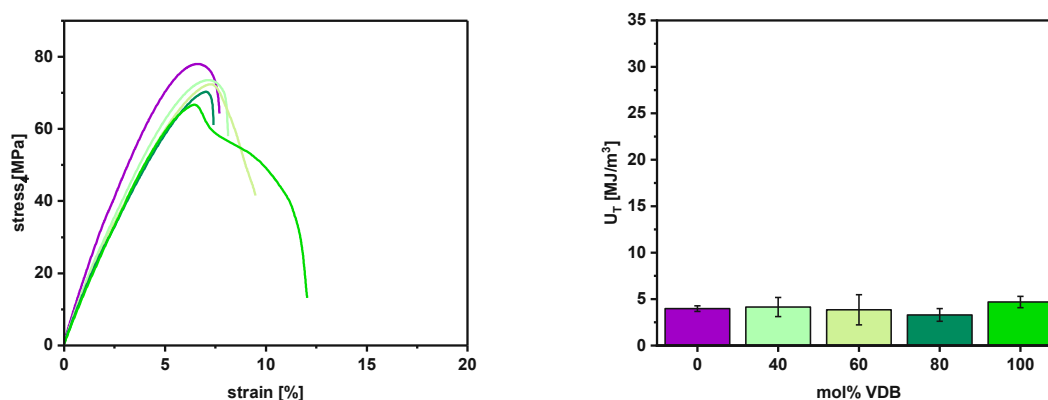


Figure 88: Stress-strain curves (left) for polymers containing 0 mol% (—), 40 mol% (—), 60 mol% (—), 80 mol% (—), and 100 mol% (—) VDB. Tensile toughness (right) for polymers containing 0 mol% (■), 40 mol% (■), 60 mol% (■), 80 mol% (■), and 100 mol% (■) VDB.

Lastly, the mechanical properties of the materials containing the B-based, rigid VDB were determined. Figure 88 depicts that all materials comprised of 40-80 mol% VDB display high strengths (67-73 MPa), good elongations (7-11%), and tensile toughness (3-4 MJ/m³). Therefore, the substitution of VDB with TAI does not spoil the good mechanical properties obtained for samples containing only the boronic ester.

To conclude, the addition of TAI leads to stiff materials with higher glass transition temperatures, high strength, and good elongation at break for polymers containing non-rigid Si-based TAS and B-based ADB. Therefore, (thermo)mechanical properties for these networks could be successfully enhanced with this trifunctional, rigid monomer. For materials containing B-based VDB, the previously shown good mechanical properties, with high strength and stiffness, were not negatively influenced by TAI. The collected data is given in Table 15.

Table 15: Detailed results of the tensile tests.

atom	monomer	x_{deg} [mol%]	σ_M [MPa]	ϵ_B [%]	U_T [MJ/m ³]
C	TAI	0	77.9 ± 0.6	7.7 ± 0.4	4.0 ± 0.3
		40	56.0 ± 1.0	12.5 ± 3.4	4.8 ± 1.2
Si	TAS	60	38.3 ± 5.6	25.4 ± 5.7	7.0 ± 1.1
		80	26.5 ± 1.0	43.5 ± 9.5	9.4 ± 2.0
		100	9.2 ± 1.2	44.3 ± 1.6	2.2 ± 0.4
		40	65.8 ± 3.4	7.2 ± 1.3	3.0 ± 0.8
B	ADB	60	64.7 ± 1.3	9.1 ± 1.7	3.6 ± 0.8
		80	28.9 ± 2.1	148 ± 10.2	30.4 ± 2.3
		100	14.6 ± 2.3	313 ± 30.4	20.8 ± 4.0
		40	73.0 ± 1.2	8.8 ± 2.0	4.1 ± 1.0
B	VDB	60	73.3 ± 1.3	9.4 ± 0.9	3.9 ± 1.6
		80	69.6 ± 3.6	7.5 ± 1.1	3.3 ± 0.7
		100	67.0 ± 0.1	11.0 ± 1.1	4.7 ± 0.6

2.5.1.3 Degradation of polymer networks with TAI

As optimization of the mechanical properties with the trifunctional, rigid monomer TAI was successful, next degradation of the materials was studied under hydrolytic conditions. Studies were conducted with cylindrically-shaped specimens ($d = 5$ mm, $h = 2$ mm), prepared analogously to the DMTA and tensile test specimens described in 2.5.1.2. Degradation was studied under physiological conditions ($pH = 7.4$), acidic ($pH = 4$), and basic conditions ($pH = 10$), as described in 2.1.4.

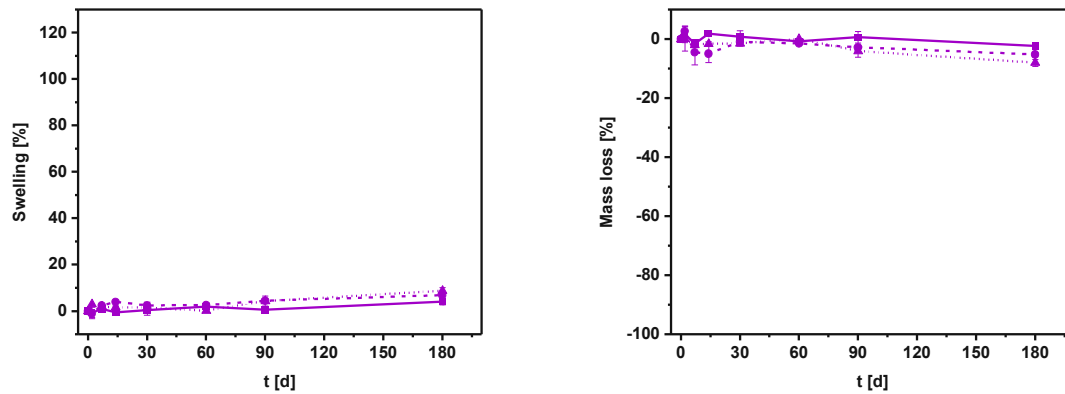


Figure 89: Degradation studies for the reference network containing 0 mol% of degradable monomer (equal to 100 mol% TAI); left: swelling over time; right: mass loss over time; pH 7.4 (—■—); pH 4 (-●-), pH 10 (···▲···).

First, the degradation of the rigid reference network containing 100 mol% TAI was studied. Figure 89 shows that a slight amount of swelling ($\sim 4\text{-}9\%$) occurred under all conditions, indicating that the formed network is rather hydrophilic. Additionally, a negligible mass loss of 2-8% was shown, with the highest values obtained under basic conditions, which proves that a high network stability is exhibited by this material.

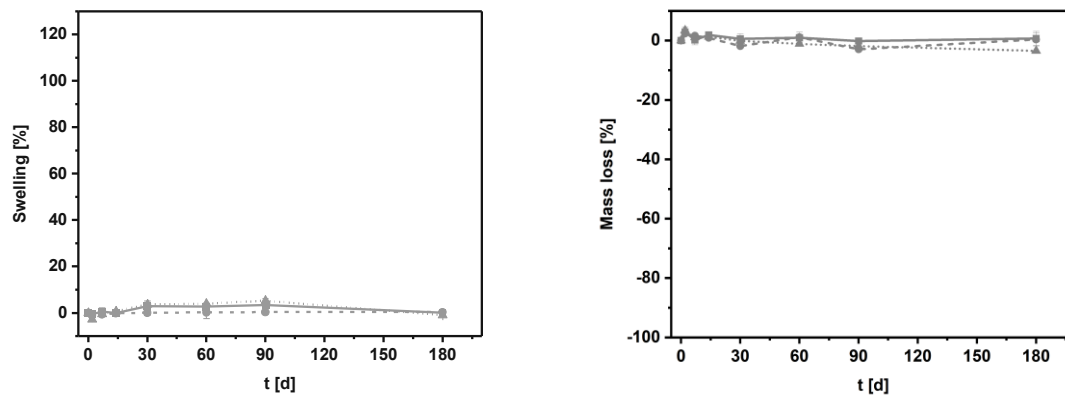


Figure 90: Degradation studies for the Si-based network containing 40 mol% TAS; left: swelling over time; right: mass loss over time; pH 7.4 (—■—); pH 4 (-●-), pH 10 (···▲···).

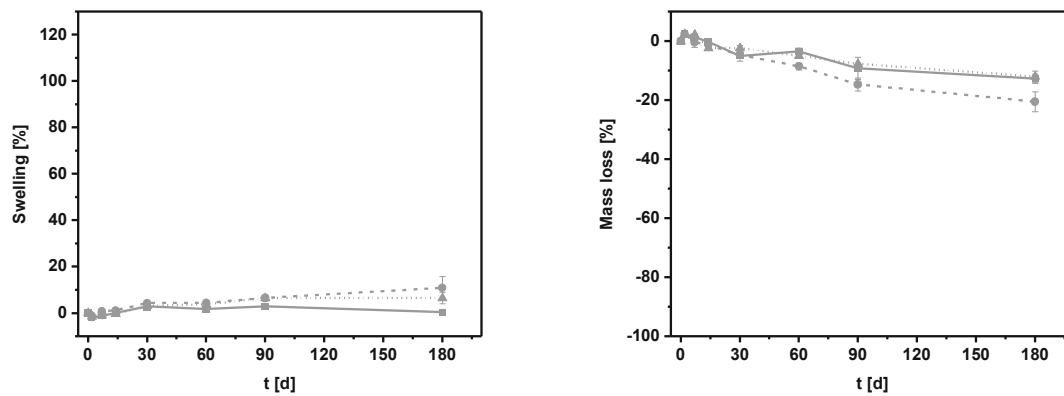


Figure 91: Degradation studies for the Si-based network containing 60 mol% TAS; left: swelling over time; right: mass loss over time; pH 7.4 (—■—); pH 4 (-●-), pH 10 (···▲···).

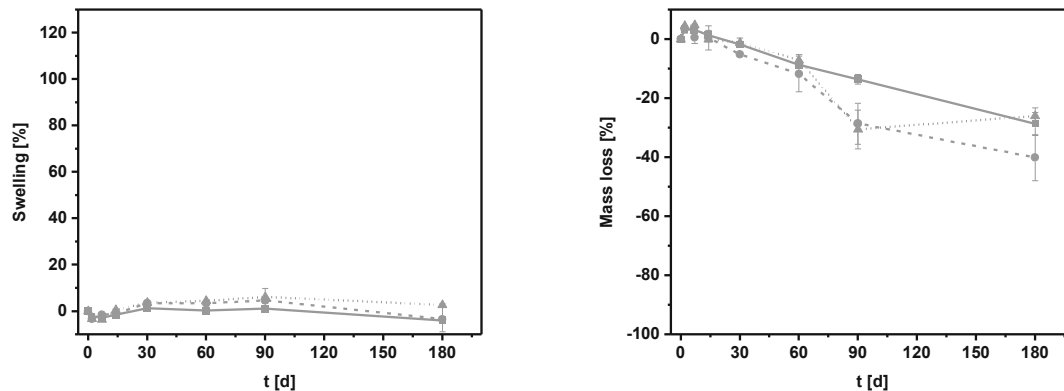


Figure 92: Degradation studies for the Si-based network containing 80 mol% TAS; left: swelling over time; right: mass loss over time; pH 7.4 (—■—); pH 4 (-●-), pH 10 (···▲···).

Next, the influence of TAI addition on the degradation behavior of the Si-based materials containing TAS was determined. Results in Figure 90 to Figure 92 show that slight swelling of 0–11% is observed for all networks containing 40 mol%, 60 mol%, or 80 mol% of TAS while swelling increases with increasing concentration of the degradable monomer. This indicates that the network becomes slightly more hydrophilic with rising amounts of TAS. As expected, mass loss increases with increasing TAS concentration due to the higher amount of degradable bonds within the network. A negligible maximum mass loss of 3% was observed for the material containing 40 mol% TAS, while higher network erosion with a maximum loss of 21% and 40% was determined for polymers derived from 60 mol% and 80 mol% TAS, respectively. The fastest degradation was observed under acidic conditions, which are present during bone remodeling. This shows that 40 mol% TAS is insufficient in these systems to generate degradable implants, while in systems containing higher amounts of this monomer, successful tuning of the network degradation is possible by the addition of TAI and variation of its content, making these systems adaptable for each patient and application.

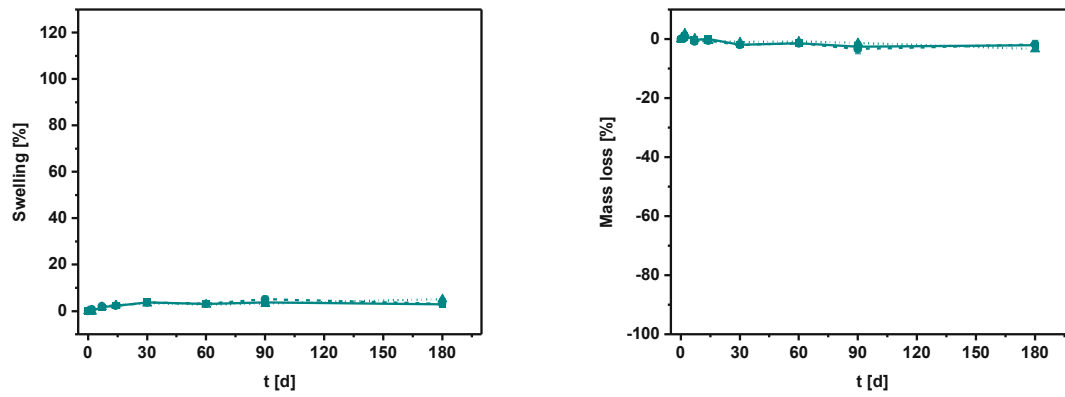


Figure 93: Degradation studies for the B-based network containing 40 mol% ADB; left: swelling over time; right: mass loss over time; pH 7.4 (—■—); pH 4 (-●-), pH 10 (···▲···).

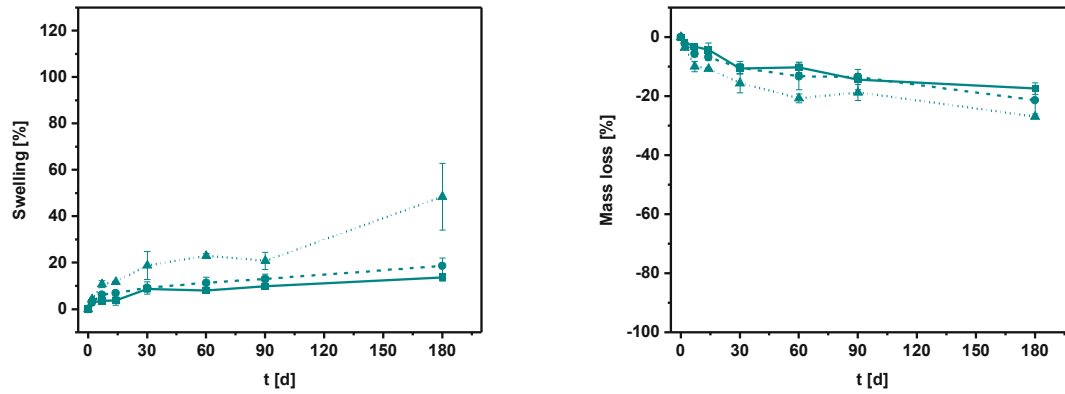


Figure 94: Degradation studies for the B-based network containing 60 mol% ADB; left: swelling over time; right: mass loss over time; pH 7.4 (—■—); pH 4 (-●-), pH 10 (···▲···).

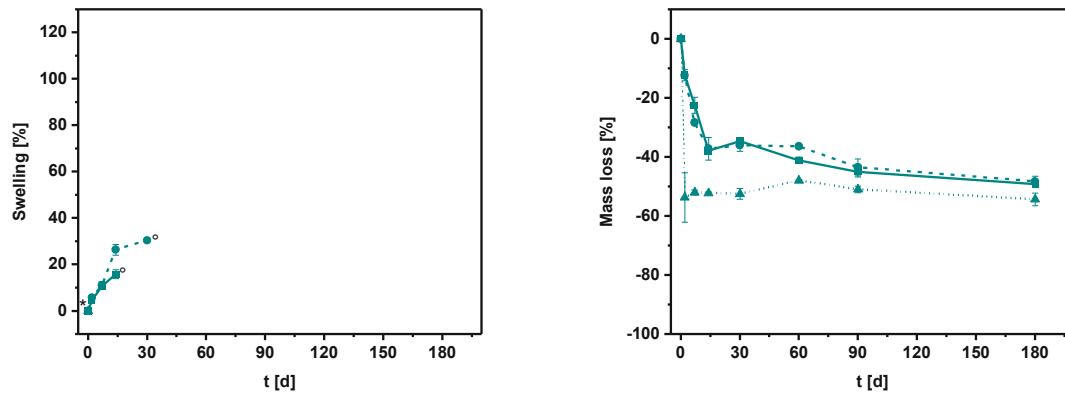


Figure 95: Degradation studies for the B-based network containing 80 mol% ADB; left: swelling over time; right: mass loss over time; pH 7.4 (—■—); pH 4 (-●-), pH 10 (···▲···). *Disruption of specimens. °Drastic shape change.

Subsequently, the degradation behavior of the materials containing the more flexible boronic ester ADB in combination with the non-degradable reference TAI was studied. The results for the networks containing 40-80 mol% ADB are given in Figure 93 to Figure 95. Negligible swelling (3-

5%) and mass loss (2-3%) were determined for the material containing 40 mol% ADB after 6 M, proving that the degradable monomer content is too low for the generation of materials prone to hydrolytic cleavage. Significant swelling of the samples was observed for the polymers containing higher concentrations of ADB. With 60 mol% ADB, swelling of 14-49% was shown, with a mass loss of 21% under acidic conditions. For the material containing 80 mol% of the degradable monomer, significant swelling, a substantial change of shape, and surface stickiness were observed for all samples. Therefore, no samples could be removed after 1 M under these conditions, as the samples were stuck to the bottom of the vials. Simultaneously, a higher network erosion of 48% under acidic conditions was determined due to the higher concentration of degradable bonds. This rather unfavorable swelling and creep during the experiment is probably due to the T_g of this network (49 °C), which is close to the conditions of the degradation studies. This results in a rather flexible network, which can be penetrated by water and cleaved throughout the specimen. By this, a looser network structure is formed, which is prone to creep. Therefore, these systems are not promising for use as bone replacement materials, and this again proves the importance of a high network T_g significantly above body temperature for enhanced degradation behavior.

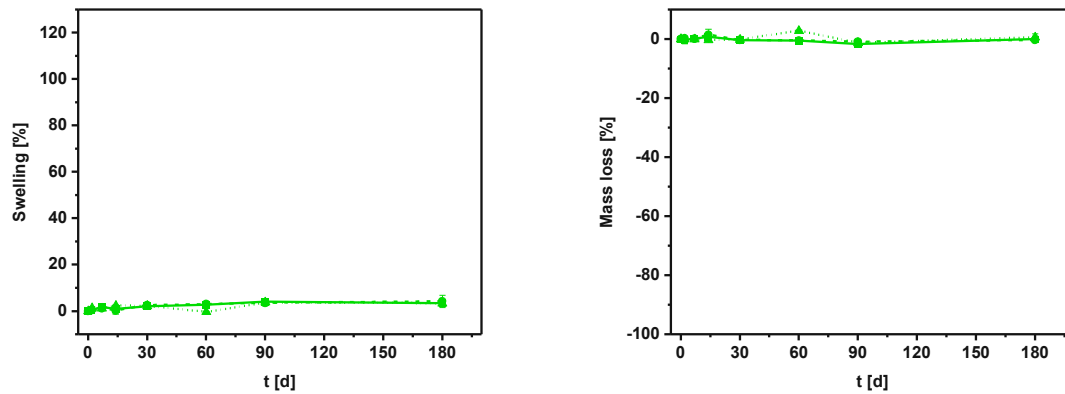


Figure 96: Degradation studies for the B-based network containing 40 mol% VDB; left: swelling over time; right: mass loss over time; pH 7.4 (—■—); pH 4 (-●-), pH 10 (···▲···).

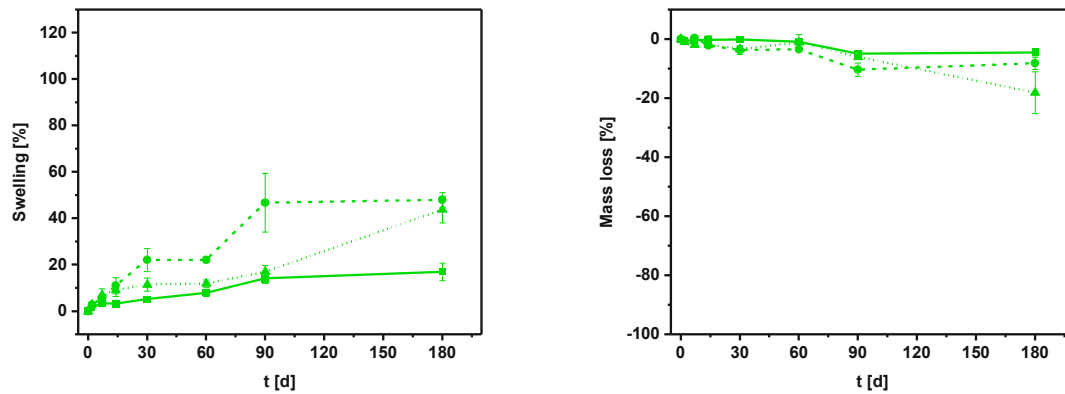


Figure 97: Degradation studies for the B-based network containing 60 mol% VDB; left: swelling over time; right: mass loss over time; pH 7.4 (—■—); pH 4 (-●-), pH 10 (···▲···).

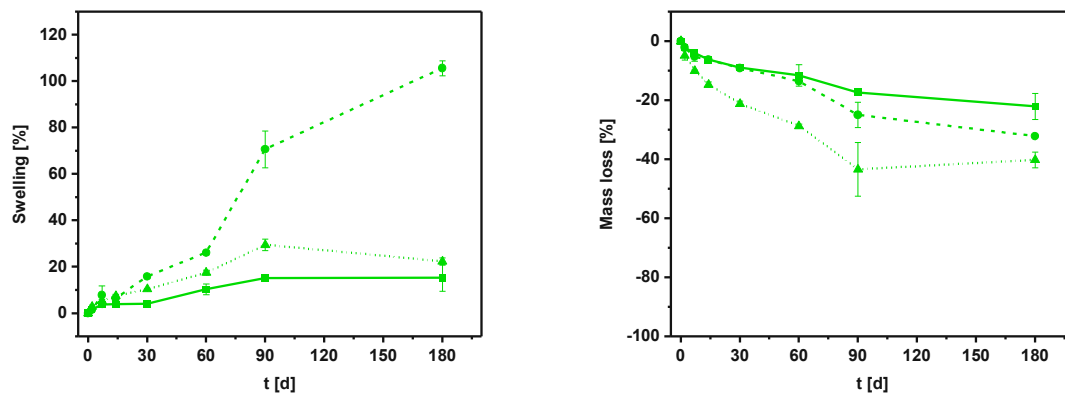


Figure 98: Degradation studies for the B-based network containing 80 mol% VDB; left: swelling over time; right: mass loss over time; pH 7.4 (—■—); pH 4 (-●-), pH 10 (···▲···).

Lastly, also the degradation under hydrolytic conditions was investigated for the materials containing the more rigid boronic ester VDB. Figure 96 shows that at a content of 40 mol% of this monomer, negligible swelling (3%) and mass loss (0-1%) were determined under all conditions after 6 M. This shows that similar to ADB- and TAS-containing systems, the content of degradable

monomer is too low for sufficient erosion. The same trends were observed for the materials containing higher concentrations of VDB. While intermediate swelling of 17-44% and 15-22% was shown for the materials containing 60 mol% or 80 mol% of the boronic ester under neutral and basic conditions, respectively, increased swelling of 48% and 106% occurred under acidic conditions for these networks (Figure 97 and Figure 98). Additionally, a maximum mass loss of 18% (60 mol% VDB) and 40% (80 mol% VDB) was determined for these materials after 6 M. Due to the high $T_g > 64$ °C of these polymers, the water uptake cannot be explained by the high network flexibility at the degradation temperature, which is also supported by the fact that no shape change or creep was observed. Hence, another explanation for the swelling of these networks might be that continuous non-degradable subnetworks are formed by TAI with the thiol TMT due to its higher functionality than VDB. Hence, after cleavage of the boronic ester bonds, a looser but non-degradable network remains, which can be penetrated but not cleaved by water. Therefore, a difunctional non-degradable monomer instead of TAI might reduce the possibility of the formation of these subnetworks and lead to enhanced degradation with reduced swelling, especially under acidic conditions present during bone remodeling.

To conclude this chapter, processing temperatures for all Si- and B-based formulations could be reduced by partially substituting the monomers with trifunctional, rigid TAI, except for 80 mol% TAS or VDB, which still require curing at 100 °C. Additionally, (thermo)mechanical properties could be successfully enhanced for all degradable materials. Nevertheless, a deteriorated degradation behavior with significant swelling was observed for the materials, which can be explained by a non-degradable subnetwork formed by trifunctional TAI and the trifunctional thiol TMT. Therefore, a reduction of the functionality of the non-degradable monomer might prevent the formation of these subnetworks.

2.5.2 Optimization with a difunctional crosslinker

To avoid the possibility of the formation of non-degradable subnetworks, a difunctional monomer instead of trifunctional TAI should be used to enhance both mechanical properties and degradation of resulting networks. Therefore, a literature search was conducted for difunctional, non-degradable allyl or vinyl ethers, as monomers should perform ideal step-growth reactions with thiols such as TMT (Figure 99) for homogeneous network formation. As another criterion, only compounds with rigid elements within the structure, such as cycloaliphatic, aromatic rings, and spirocyclic elements, were considered to obtain materials with good (thermo)mechanical

properties. As a result, six different target compounds were chosen, which are depicted in Figure 99.

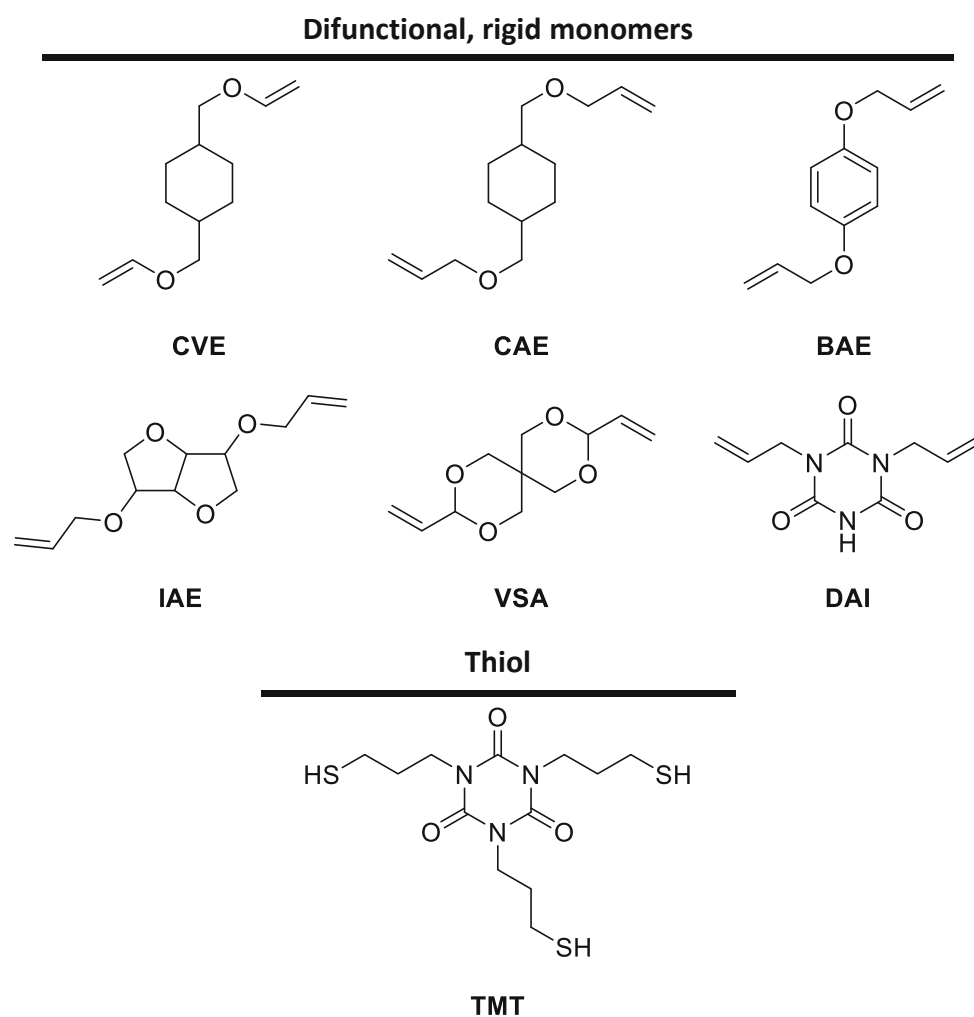


Figure 99: Structures of difunctional vinyl ether and allyl ether monomers containing rigid elements within the structure and the thiol TMT used for subsequent studies.

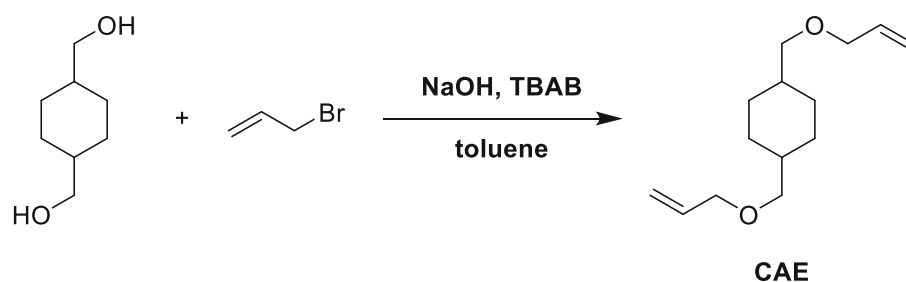
The envisioned monomers include 1,4-cyclohexanedimethanol divinyl ether (CVE), 1,4-cyclohexanedimethanol diallyl ether (CAE) and 1,4-diallyloxybenzene (BAE), diallyl isosorbide (IAE), 3,9-divinyl-2,4,8,10-tetraoxaspiro(5.5)undecane (VSA) and diallyl isocyanurate (DAI). Due to the limited commercial availability of difunctional monomers, CAE and BAE had to be synthesized.

For all of these compounds, except CAE and DAI, radical-initiated thiol-ene polymerization was frequently reported. CVE was predominantly used in oxygen-insensitive, photopatternable thiol-ene resins either applied in photolithography to produce submicrometer patterns,³³⁴ or for the fabrication of dielectrics for organic field-effect transistors.^{335,336} IAE, a biobased building block derived from corn starch, was often applied in thiol-ene photopolymerization in combination with terpenes,³³⁷ fluorinated phosphonium salts,³³⁸ or silver nanoparticles³³⁹ to produce environmentally friendly, antibacterial coatings. Childress *et al.* utilized BAE and VSA in

combination with thiols containing alkyl chains of different lengths to synthesize semicrystalline, recyclable thermoplastics with tunable optical, thermal, and mechanical properties.³⁴⁰ VSA was further applied in ternary thiol-ene systems by Sycks *et al.* to generate semicrystalline polymers with tunable crystallinity and mechanical properties,³⁴¹ which were also used in 3D printing.³⁴² The group determined that the incorporation of the spiroacetal moieties significantly improved the mechanical properties, especially the toughness, of printed parts, making this compound particularly interesting for subsequent studies.

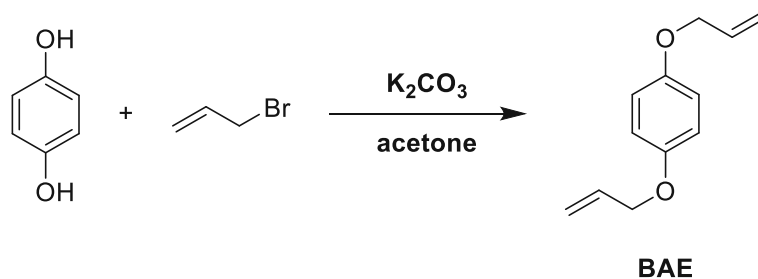
2.5.2.1 Syntheses of difunctional crosslinkers

1,4-Bis(2-propenyloxy)methylcyclohexane (CAE) was synthesized according to Lohse *et al.*³⁴³ via a one-step procedure.



For the synthesis, 1 eq. 1,4-cyclohexanedimethanol, 3.5 eq. allyl bromide, 0.13 eq. of tetra-*n*-butylammonium bromide (TBAB) as a phase transfer catalyst, and 2.9 eq. of NaOH were dissolved in toluene and stirred at 40 °C for 8 h and at 80 °C for 10 h. The crude product, a mixture of mono- and disubstituted compounds, was purified via column chromatography to yield the product as a colorless liquid in a yield of 70%.

Next, the synthesis of 1,4-bis(allyloxy)benzene was performed according to a combined procedure by Kotha *et al.*³⁴⁴ and Childress *et al.*³⁴⁰ in a one-step procedure.



For the synthesis, 1 eq. of hydroquinone, 1.4 eq. of K₂CO₃, and 2.2 eq. of allyl bromide in acetone were utilized. The mixture was heated to a maximum of 45 °C for 3 d to avoid Claisen

rearrangement of the product. The crude product was purified by column chromatography to yield the pure product as white crystals in a yield of 69%.

2.5.2.2 Mechanical properties of networks with difunctional crosslinkers

To readily exclude difunctional monomers resulting in polymers with poor thermomechanical properties, DMTA measurements described in 2.1.3 were performed as a fast screening method.

Formulations were prepared with all difunctional monomers and the thiol TMT in an equimolar ratio of double bonds to thiol groups. Due to the insolubility of DAI in the thiol due to its high melting point of 148 °C, no polymerization was conducted with this monomer. For all other compounds, homogeneous formulations were obtained at 25 °C, and specimens were cured at rt in a Lumamat 100 light oven.

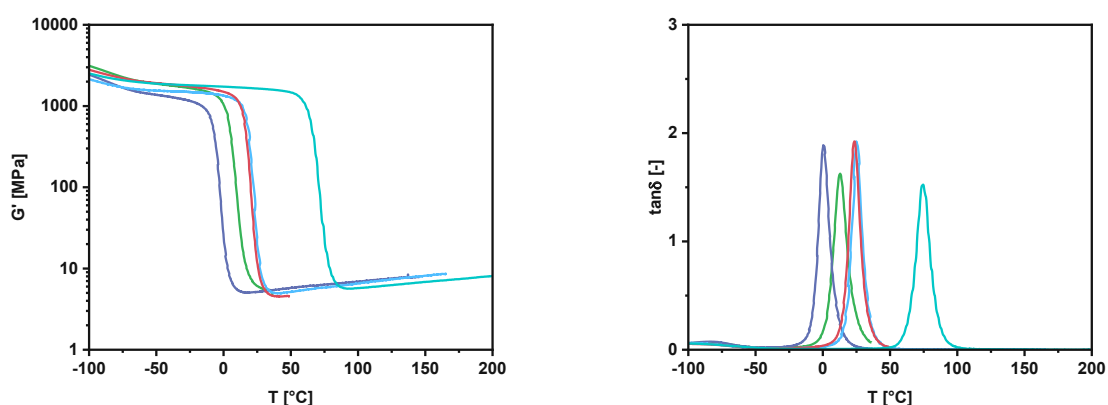


Figure 100: G' (left) and $\tan\delta$ (right) over temperature for the networks formed from the difunctional monomers CVE (—), CAE (—), BAE (—), IAE (—), or VSA (—) and the thiol TMT. The samples containing CVE, CAE, BAE, or IAE ruptured at some point during the measurement.

Curves in Figure 100 show that materials derived from the vinyl and allyl ethers CVE, CAE, BAE, or IAE display low T_g values below body temperature, while the lowest values were observed for the cycloaliphatic compounds. When comparing CVE and CAE, it is shown that T_g can be increased by 10 °C with a slightly shorter side chain. For materials derived from aromatic BAE and the isosorbide-based compound IAE, a higher T_g around rt was observed due to the rigidity of the monomer cores. Nevertheless, an even higher T_g was expected for pBAE, which should be capable of π -stacking of the benzene moieties. An explanation for this was found in literature by Childress *et al.*³⁴⁰, which found the π -stacking of BAE to be very sensitive to the spacer length of a linear thiol. Hence, the specific structure of TMT seems to inhibit these aromatic interactions, and a thiol with a slightly longer or slightly shorter spacer length or different functionality might be beneficial in combination with this monomer.

In contrast, the network containing the spirocyclic acetal VSA displays the best thermomechanical properties with a high network T_g significantly exceeding body temperature as well as high storage modulus at 37 °C. Although it contains an acetal moiety, this compound is literature-known as non-degradable and is patented for biomedical applications, such as in photopolymerized orthopedic implants³⁴⁵, cosmetics³⁴⁵, dental applications³⁴⁶, or sealants³⁴⁶. In addition, the SDS for this compound reports a high LD_{50} for rats ($LD_{50,oral, rat}=3.25$ g/kg⁴⁰), which corresponds to a low acute toxicity of this compound.

To conclude, VSA was chosen as a difunctional, non-degradable monomer in future studies, as it leads to enhanced thermomechanical properties of networks with TMT. All other tested vinyl and allyl ethers were excluded from further tests due to low network $T_g < 30$ °C obtained in combination with the thiol. The cumulated data is given in Table 16.

Table 16: Detailed results of the DMTA measurements. *Sample ruptured during the measurement.

thiol	monomer	T_g [°C]	$G'_{25^\circ C}$ [MPa]	$G'_{37^\circ C}$ [MPa]	fwhm [°C]	G'_R [MPa]
TMT	CVE	13	6	0.3	11	-*
	CAE	0.3	5	5	9	8
	BAE	25	20	5	8	9
	IAE	24	11	5	9	5
	VSA	74	1640	1590	12	8

2.5.2.3 Reactivity of formulations with VSA

As studies with TAI showed that non-degradable subnetworks were formed, a literature search was performed regarding the percolation threshold of networks containing “dynamic”, hence hydrolyzable and permanent crosslinks. Li *et al.*²⁵⁸ calculated the critical fraction of permanent crosslinks for the formation of a percolated permanent network for a network formed by a difunctional monomer with dynamic bonds, a difunctional monomer with static bonds, and a trifunctional static crosslinker. For such a system, the theoretical critical fraction of static difunctional monomer was found to be <50 mol%. This theory was confirmed for networks containing boronic esters by Robinson *et al.*²⁵⁶

Due to these findings, similar to 2.5.1, formulations were prepared, in which each degradable monomer was partially substituted by VSA. To maintain the same concentration of degradable bonds within the networks, the same molar ratios as previously described for TAI, of 40 mol%, 60 mol% or 80 mol% of the degradable monomers TAS, ADB or VDB (x_{deg}) with respect to the difunctional monomer, were chosen for the studies, to possibly see the transition from a static, hence non-degradable to a dynamic, hence degradable network. TMT was used as a thiol, and

formulations were prepared in an equimolar ratio of overall double bonds to thiol groups. As references, formulations containing 0 mol% of degradable monomer (equivalent to 100 mol% VSA) and 100 mol% of each degradable monomer were used. To calculate the molar amount of VSA, Equation 8 was used.

$$n_{\text{VSA}} = \frac{n_{\text{deg}}}{x_{\text{deg}}} \cdot (100 - x_{\text{deg}})$$

Equation 8: Calculation of molar amount of VSA; n_{VSA} ...molar amount of VSA; n_{deg} ...molar amount of degradable monomer; x_{deg} ...mol% of degradable monomer.

The formulations were prepared with 1 w% Ivocerin and 0.02 w% of PYR and homogenized by careful heating and mixing. Then, they were stored at rt for 2 d to determine the time, after which phase separation or precipitation of compounds occurred.

It was determined that all formulations, except 80 mol% TAS, can be processed and cured at 25 °C, as no phase separation or precipitation was observed for several hours or days. Compared to studies with TAI (2.5.1), a higher concentration of 80 mol% of B-based, rigid VDB can be added to formulations without precipitation of the monomer. For curing of 80 mol% TAS 100 °C will be used. This shows that although VSA is solid at rt, it enhances the solubility of the degradable monomers compared to trifunctional TAI.

To determine the photoreactivity of the formulations, RT-NIR photorheology measurements were conducted as described in 1.1.3. For the experiments, filtered light from a broadband Hg lamp (400-500 nm) was used. 150-180 μL of sample volume were applied to the glass plate and irradiated for 320 s. The light intensity at the surface of the samples was adjusted to 20 mW/cm^2 . Measurements were performed at 25 °C for formulations stable at rt. For the formulations containing 80 mol% TAS or 100 mol% TAS or VDB, a temperature of 100 °C was used due to the miscibility issues described above.

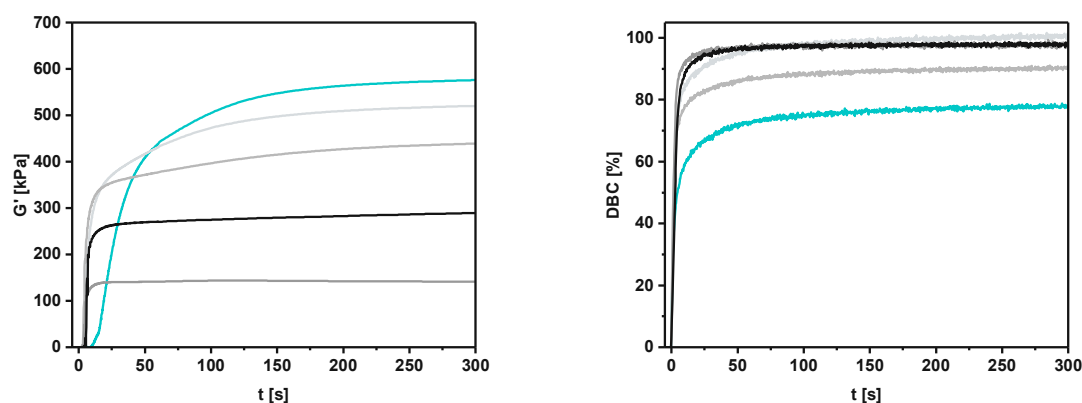


Figure 101: Storage Modulus (G' , left) and DBC over time (right) for formulations containing 0 mol% (—), 40 mol% (—), 60 mol% (—), 80 mol%* (—), and 100 mol% (—) TAS*. *Curing at 100 °C.

First, the influence of VSA addition on the photorheological properties of formulations containing the Si-based monomer TAS was determined. Figure 101 compares the rheological (left) and the IR data (right) of systems containing 0-100 mol% TAS. It is shown that the formulations with the Si-based monomer exhibit a significantly accelerated crosslinking of the networks compared to the slightly retarded photopolymerization of 100 mol% VSA, with gelation occurring within 5 s. Also, accelerated curing ($t_{95} < 48$ s) and higher final double bond conversions were observed ($> 90\%$). The highest G'_{final} was obtained with the reference formulations, which proves its potential as a comonomer resulting in enhanced mechanical properties of formed polymers. High storage moduli were also shown for 40 mol% and 60 mol% TAS, while significantly lower values were obtained for 80 mol% TAS and 100 mol% TAS due to the curing at 100 °C.

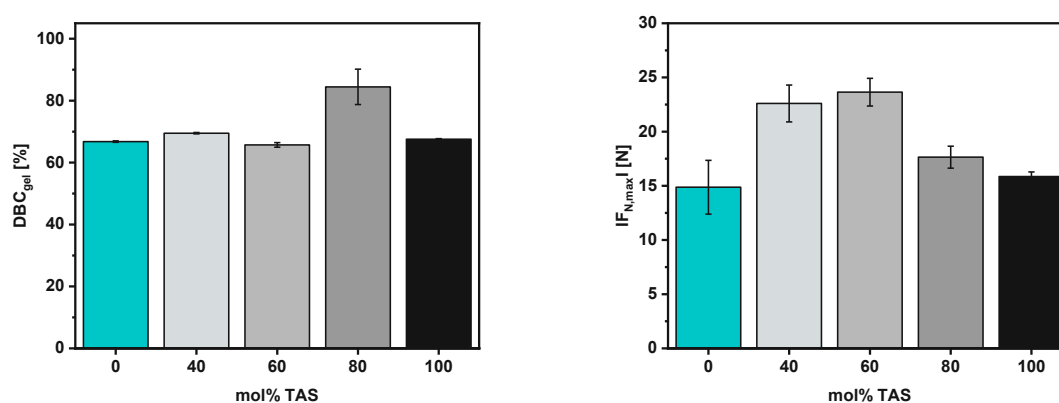


Figure 102: DBC_{gel} (left) and $F_{N,\text{max}}$ (right) for formulations containing 0 mol% (■), 40 mol% (■), 60 mol% (■), 80 mol% (■), and 100 mol% (■) TAS.

DBC_{gel} values (Figure 102, left) for all samples are quite high and in the same range as for the reference formulation (66-68%). Significantly higher DBC_{gel} were observed with 80 mol% TAS (85%) due to curing conducted at elevated temperatures, enhancing monomer and thiol mobility during network formation. Figure 102 (right) shows that high shrinkage during polymerization is

exhibited when VSA is substituted by 40 mol% or 60 mol% TAS due to the higher functionality of the Si-based monomer resulting in higher crosslinking density. As a result of the curing at 100 °C, significantly lower shrinkage is exhibited by the 80 mol% and 100 mol% systems.

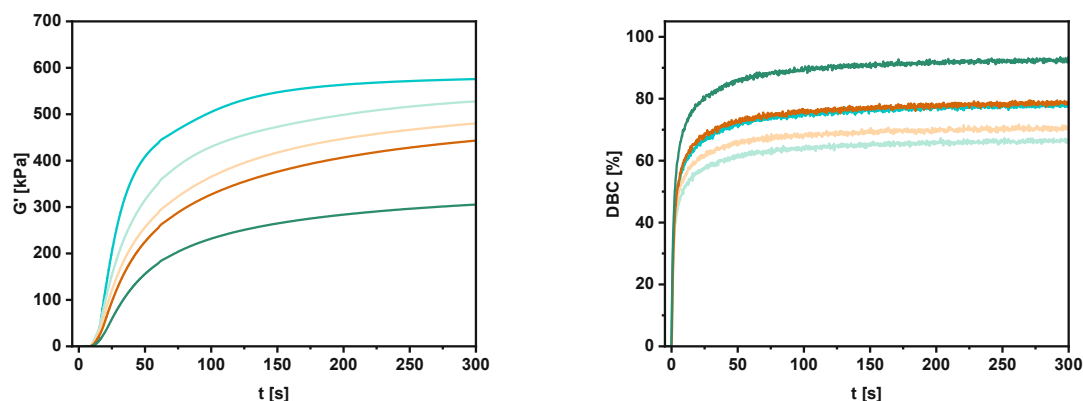


Figure 103: Storage Modulus (G' , left) and DBC over time (right) for formulations containing 0 mol% (—), 40 mol% (—), 60 mol% (—), 80 mol% (—), and 100 mol% (—) ADB.

Next, the photocuring behavior of the formulations containing the flexible boronic ester ADB was investigated. Storage modulus over time curves in Figure 103 (left) show that increasing concentration of ADB results in a delayed crosslinking from 25 s for 40 mol% ADB to 34 s for 100 mol% ADB. Nevertheless, a similar time for network curing was observed for all formulations. The IR data in Figure 103 (right) depict that an increasing amount of ADB significantly increases the final conversions from 67% to 92%. This shows that higher boronic ester concentration leads to enhanced mobility during curing and hence final conversion. Due to the rather flexible monomer structure of ADB, with long side chains, an increase in G'_{final} was observed upon partial substitution with rigid VSA.

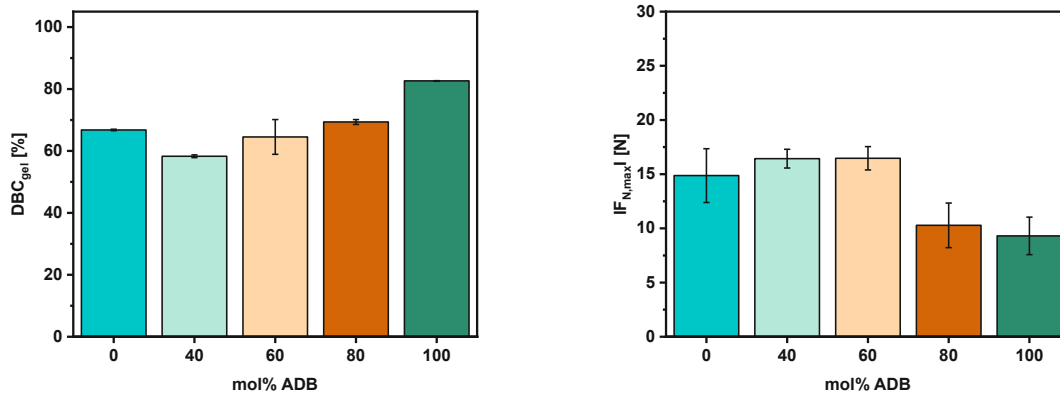


Figure 104: DBC_{gel} (left) and $F_{N,max}$ (right) for formulations containing 0 mol% (■), 40 mol% (■), 60 mol% (■), 80 mol% (■), and 100 mol% (■) ADB.

Figure 104 (left) shows that similar DBC_{gel} are exhibited for 0-80 mol% formulations, while the highest values were obtained with the reference formulation 100 mol% ADB, which can again be explained by the dynamic boronic ester bonds causing network reconfiguration during the curing process. This is also reflected in the significantly decreased shrinkage during polymerization observed for 80 mol% and 100 mol% ADB (Figure 104, right).

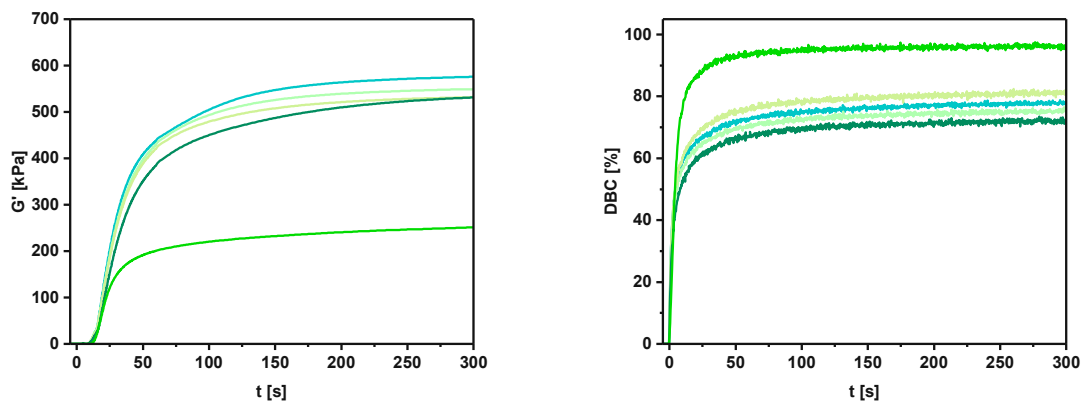


Figure 105: Storage Modulus (G' , left) and DBC over time (right) for formulations containing 0 mol% (—), 40 mol% (—), 60 mol% (—), 80 mol% (—), and 100 mol% (—) VDB*. *Curing at 100 °C.

Lastly, the influence of VSA addition on the photocuring behavior of the formulations containing the rigid boron-based VDB was studied. Similar gelation, curing speed, and final conversions were obtained for formulations containing 0-80 mol% VDB (Figure 105). Due to the curing of 100 mol% VDB conducted at 100 °C, significantly faster crosslinking and network curing were observed and higher DBC_{final}. High final storage moduli were shown for the 0-80 mol% systems, while a lower G' _{final} was determined for the formulation cured at elevated temperatures.

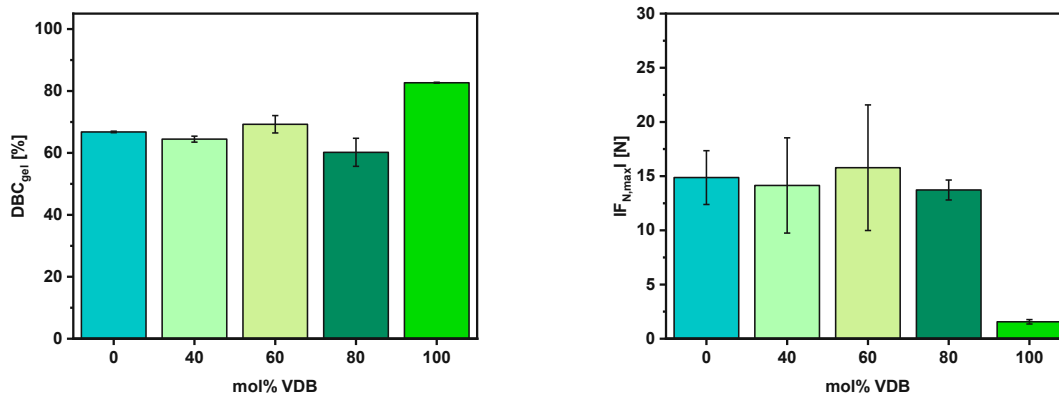


Figure 106: DBC_{gel} (left) and IF_{N,max} (right) for formulations containing 0 mol% (■), 40 mol% (■), 60 mol% (■), 80 mol% (■), and 100 mol% (■) VDB.

For VDB-containing systems, the same trends for DBC_{gel} (Figure 106, left) as for ADB, with similar DBC_{gel} for 0-80 mol% formulations and significantly higher network mobility shown, resulting in an increase in DBC_{gel}, which can again be explained by the dynamic boronic ester bonds causing network reconfiguration during the curing process. Similar and low shrinkage was observed for systems containing 0-80 mol% VDB, with a drastic decrease for 100 mol% VDB, due to the curing at 100 °C (Figure 106, right).

To summarize, fast crosslinking, curing, and high conversions were shown with all Si-based formulations with VSA as a comonomer, while slightly delayed network formation was observed with B-based systems. Nevertheless, the photopolymerization of all systems should be sufficiently fast for the 3D-printing process. Most importantly, high G'_{final} values >400 kPa were obtained for all 40-80 mol% systems cured at rt, which proves that partial substitution with this rigid, difunctional monomer does not spoil but enhances the mechanical properties of the degradable materials. The collected data from all measurements is given in Table 17.

Table 17: Detailed results of the RT-NIR photorheology measurements.

atom	monomer	x_{deg} [mol%]	t_{gel} [s]	DBC_{gel} [%]	t_{95} [s]	DBC_{final} [%]	G'_{final} [kPa]	$F_{N,max}$ [N]
C	VSA	0	25.3 ± 0.6	66.8 ± 0.2	74.8 ± 3.9	77.9 ± 0.3	547 ± 39.9	-14.9 ± 2.5
Si	TAS	40	3.0 ± 0.0	69.5 ± 0.2	47.5 ± 1.4	99.9 ± 0.1	526 ± 33.2	-22.6 ± 1.7
		60	3.0 ± 0.0	65.7 ± 0.7	43.1 ± 1.1	90.3 ± 0.3	442 ± 10.6	-23.6 ± 1.3
		80*	4.0 ± 0.0	84.5 ± 5.7	9.6 ± 3.4	97.4 ± 3.5	147 ± 15.0	-17.6 ± 1.0
		100*	4.0 ± 0.0	67.6 ± 0.2	19.5 ± 1.1	98.0 ± 0.3	287 ± 1.80	-15.9 ± 0.4
B	VDB	40	27.7 ± 0.6	64.4 ± 1.0	70.4 ± 3.0	75.1 ± 0.4	550 ± 20.4	-14.1 ± 4.4
		60	27.0 ± 1.7	69.3 ± 2.8	61.8 ± 9.4	79.4 ± 3.1	509 ± 67.3	-15.8 ± 5.8
		80	28.3 ± 0.6	60.2 ± 4.5	70.1 ± 2.4	70.0 ± 4.6	508 ± 41.1	-13.7 ± 0.9
		100*	14.0 ± 0.0	83.0 ± 0.3	35.4 ± 2.1	96.5 ± 0.4	252 ± 4.40	-1.6 ± 0.2
B	ADB	40	25.0 ± 0.0	58.3 ± 0.4	69.4 ± 3.8	66.5 ± 0.4	496 ± 43.7	-16.4 ± 0.9
		60	25.3 ± 0.6	64.5 ± 5.6	53.1 ± 8.3	72.5 ± 4.4	480 ± 1.60	-16.5 ± 1.1
		80	29.0 ± 0.0	69.4 ± 0.8	62.6 ± 4.0	78.7 ± 0.2	438 ± 9.80	-10.3 ± 2.1
		100	33.7 ± 1.2	82.6 ± 0.1	65.0 ± 2.0	92.4 ± 0.2	332 ± 23.8	-9.3 ± 1.7

2.5.2.4 Mechanical properties of polymer networks with VSA

To determine whether the addition of the difunctional, rigid monomer indeed results in enhanced mechanical properties of the degradable polymers, DMTA measurements and tensile tests were conducted.

DMTA measurements were done according to 2.1.3. DMTA specimens were cured in a Lumamat 100 light oven. Polymerization of formulations was conducted at rt, except for 80 mol% TAS and 100 mol% TAS or VDB, which were cured at elevated temperatures using a preheated silicon mold and a photocuring program at ~104 °C. This was done due to miscibility issues of the monomers with the thiol TMT, described in 2.5.2.3.

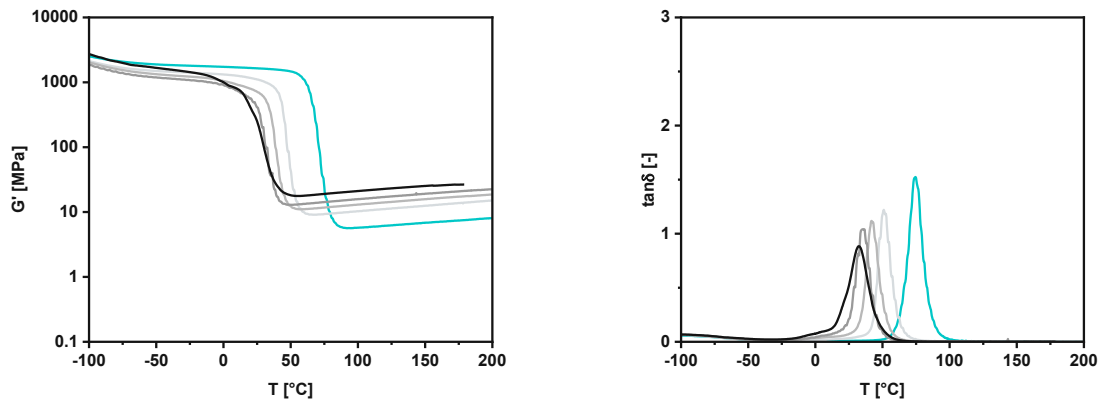


Figure 107: G' (left) and $\tan\delta$ (right) over temperature of the different networks formed from formulations 0 mol% (—), 40 mol% (—), 60 mol% (—), 80 mol% (—), and 100 mol% (—) TAS.

First, the influence of VSA addition on the thermomechanical properties of the silicon-based systems containing TAS was determined. Storage modulus and $\tan\delta$ curves of systems containing 40-80 mol% Si-based TAS in Figure 107 show that the addition of VSA leads to an increase in T_g and storage modulus at 37 °C with increasing concentration of the difunctional, rigid monomer. Additionally, for all specimens, except for p(80 mol% TAS), a T_g exceeding 37 °C was determined. This system also displays a rather low storage modulus at body temperature; hence, it is not suited for the desired application as an artificial bone graft. For all other specimens containing 0-60 mol% TAS, a significantly increased $G'_{37^\circ\text{C}}$ was determined. Compared to the reference formulation containing 100 mol% VSA, higher crosslinking density was shown for the polymers containing the Si-based monomer, with the highest values obtained at the highest concentration, due to its higher functionality than VSA.

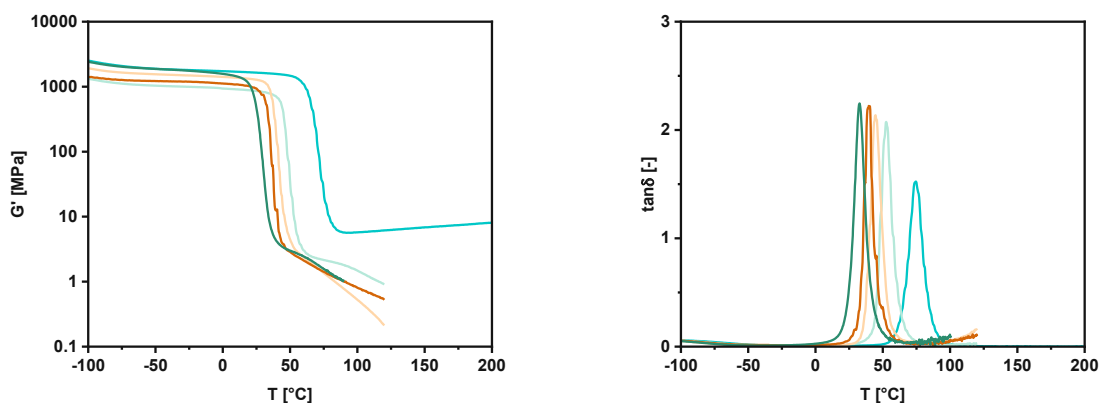


Figure 108: G' (left) and $\tan\delta$ (right) over temperature of the different networks formed from formulations 0 mol% (—), 40 mol% (—), 60 mol% (—), 80 mol% (—), and 100 mol% (—) ADB.

Subsequently, the thermomechanical properties of materials containing the flexible boronic ester ADB were investigated. Figure 108 shows that the same trends as for the Si-based materials were observed with samples containing 40-80 mol% of the boronic ester ADB, with enhanced

thermomechanical properties caused by partial substitution with VSA. In contrast to Si-based polymers, all specimens exhibit a T_g above body temperature and significantly increased storage moduli at 37 °C. Similar to specimens optimized with TAI described in 2.5.1.2, a thermoplastic flow was observed for all ADB-containing materials due to the dynamic character of these networks caused by the reversible boronic ester bonds.

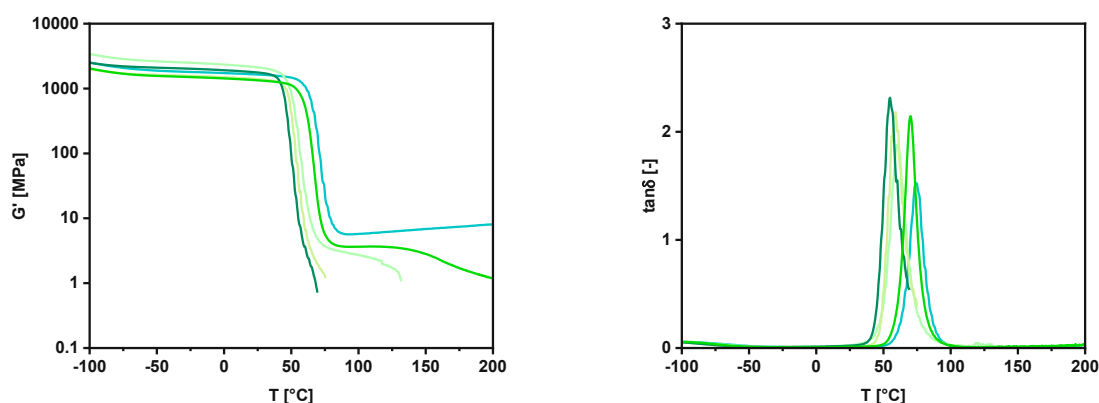


Figure 109: G' (left) and $\tan\delta$ (right) over temperature of the different networks formed from formulations 0 mol% (—), 40 mol% (—), 60 mol% (—), 80 mol% (—), and 100 mol% (—) VDB.

Lastly, the influence of VSA addition on the thermomechanical behavior of materials containing the rigid, boron-based VDB was also determined. For all polymers containing VDB, high storage moduli at body temperature and T_g values >56 °C were determined (Figure 109). Furthermore, compared to the reference without VSA, a further increase in storage modulus at 37 °C was obtained for all materials upon partial substitution with this rigid monomer. This shows that the addition of VSA results in excellent thermomechanical properties for all VDB-based polymers, and similar to TAI-containing systems, these materials are highly promising. Again, a thermoplastic flow was observed for all specimens containing VDB at elevated temperatures, confirming that all networks are rather dynamic at these temperatures. The summarized results of all measurements are given in Table 18.

Table 18: Detailed results of DMTA measurements. *No rubber plateau observed.

atom	monomer	x _{deg} [mol%]	T _g [°C]	G' _{25°C} [MPa]	G' _{37°C} [MPa]	fwhm [°C]	G' _R [MPa]
C	VSA	0	74	1640	1590	12	8
Si	TAS	40	51	1110	852	10	15
		60	42	715	158	11	19
		80	35	384	24	11	22
		100	32	214	33	17	27
B	ADB	40	53	860	762	10	*
		60	44	1280	462	9	*
		80	40	922	64	7	*
		100	33	447	5	9	*
B	VDB	40	60	2120	1930	14	*
		60	58	1390	1310	13	*
		80	56	1760	1600	12	*
		100	70	1340	1280	10	*

To determine other important mechanical properties, such as strength and toughness, tensile tests were conducted with specimens of shape 5B of all described formulations. Samples were prepared under the same curing conditions as DMTA specimens, and testing was performed as described in 2.4.2.

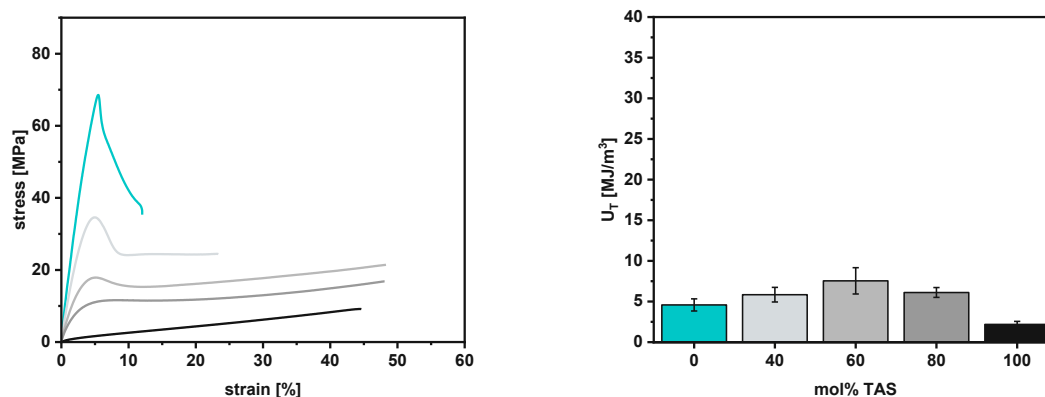


Figure 110: Stress-strain curves (left) for polymers containing 0 mol% (—), 40 mol% (—), 60 mol% (—), 80 mol% (—), and 100 mol% (—) TAS. Tensile toughness (right) for polymers containing 0 mol% (■), 40 mol% (■), 60 mol% (■), 80 mol% (■), and 100 mol% (■) TAS.

First, materials containing the Si-based monomer TAS and VSA were investigated. Figure 110 (left) depicts that increasing concentration of VSA leads to a significant increase in strength while high strain at break is maintained for polymers containing 40-80 mol% TAS. This is also reflected in the tensile toughness (Figure 110, right). Similar tensile toughness values (6-8 MJ/m³) were observed with the 40-80 mol% polymers, while a toughness decreased by a factor of 3 was shown for the polymer formed from 60 mol% TAS, compared to the reference material without VSA.

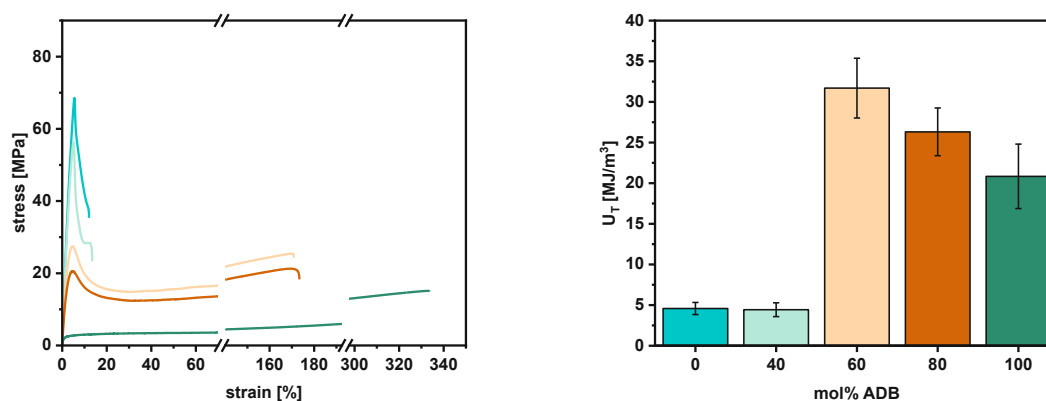


Figure 111: Stress-strain curves (left) for polymers containing 0 mol% (—), 40 mol% (—), 60 mol% (—), 80 mol% (—), and 100 mol% (—) ADB. Tensile toughness (right) for polymers containing 0 mol% (■), 40 mol% (■), 60 mol% (■), 80 mol% (■), and 100 mol% (■) ADB.

The same trends for systems containing flexible TAS were observed for the materials derived from 40-80 mol% of the boronic ester ADB, with increased tensile strength and decreased elongation at break with increasing VSA concentration (Figure 111, left). Noteworthy, exceptionally high elongations combined with good strength were observed for materials containing 60 mol% and 80 mol% ADB, which leads to an unprecedented tensile toughness of 32 MJ/m³ and 26 MJ/m³ (Figure 111, right).

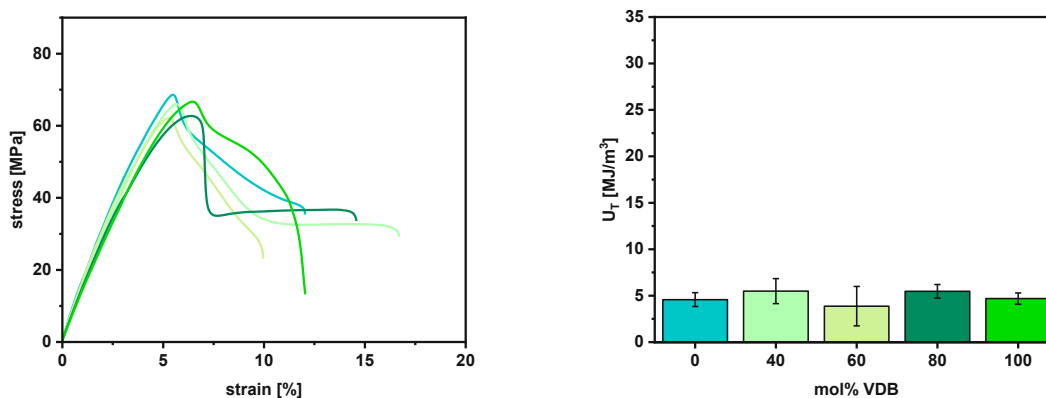


Figure 112: Stress-strain curves (left) for polymers containing 0 mol% (—), 40 mol% (—), 60 mol% (—), 80 mol% (—), and 100 mol% (—) VDB. Tensile toughness (right) for polymers containing 0 mol% (■), 40 mol% (■), 60 mol% (■), 80 mol% (■), and 100 mol% (■) VDB.

Finally, the influence of VSA addition on the mechanical properties of materials containing the rigid boronic ester VDB was determined. Figure 112 shows that similar strength, strain at break, and tensile toughness were observed for all materials containing VDB. Therefore, the addition of rigid difunctional VSA does not negatively influence the good mechanical properties of materials containing rigid difunctional but degradable VDB.

To sum up, the addition of VSA results in materials combining high strength and toughness, while good elongation at break is maintained for all polymers. Therefore, for materials containing non-rigid TAS and ADB, mechanical properties could be successfully enhanced with this difunctional, rigid monomer. For polymers containing B-based VDB, the previously shown mechanical properties with high strength and stiffness were not influenced by DVSA. The collected data from these tests is given in Table 19.

Table 19: Detailed results of the tensile tests.

atom	monomer	x_{deg} [mol%]	σ_M [MPa]	ϵ_B [%]	U_T [MJ/m ³]
C	VSA	0	65.9 ± 6.2	10.5 ± 1.4	4.6 ± 0.7
Si	TAS	40	33.8 ± 1.4	24.3 ± 4.1	5.8 ± 0.9
		60	18.1 ± 2.0	43.8 ± 7.4	7.5 ± 1.6
		80	17.3 ± 0.8	48.9 ± 4.3	6.1 ± 0.6
		100	9.2 ± 1.2	44.3 ± 1.6	2.2 ± 0.4
B	ADB	40	56.6 ± 1.7	13.4 ± 2.3	4.4 ± 0.8
		60	28.3 ± 2.1	165 ± 16.5	31.7 ± 3.7
		80	21.7 ± 2.1	170 ± 10.9	26.3 ± 2.9
		100	14.6 ± 2.3	313 ± 30.4	20.8 ± 4.0
B	VDB	40	64.0 ± 1.6	14.3 ± 3.3	5.5 ± 1.3
		60	60.8 ± 1.9	9.5 ± 0.4	3.9 ± 2.1
		80	63.0 ± 0.6	13.8 ± 1.8	5.5 ± 0.7
		100	67.0 ± 0.1	11.0 ± 1.1	4.7 ± 0.6

2.5.2.5 Degradation of polymer networks with VSA

Next, the degradation behavior of the materials was studied under hydrolytic conditions to determine whether a difunctional instead of a trifunctional crosslinker indeed results in networks with enhanced cleavage without significant swelling and the formation of non-degradable subnetworks. Studies were conducted with cylindrically-shaped specimens ($d = 5$ mm, $h = 2$ mm), which were prepared analogously to the DMTA and tensile test specimens described in 2.5.2.4. Degradation was studied under physiological conditions ($pH = 7.4$), acidic ($pH = 4$) and basic conditions ($pH = 10$), as described in 2.1.4.

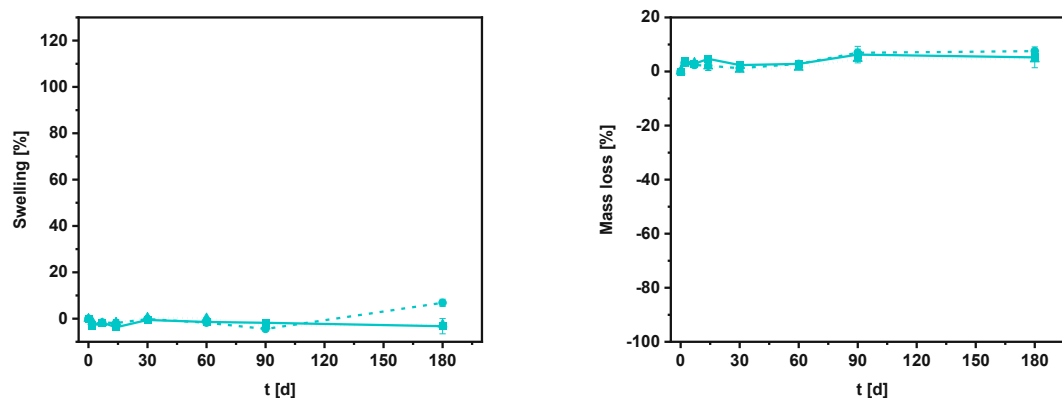


Figure 113: Degradation studies for the reference network containing 0 mol% of degradable monomer with respect to VSA (equal to 100 mol% VSA); left: swelling over time; right: mass loss over time; pH 7.4 (—■—); pH 4 (- -● -), pH 10 (···▲···).

First, the degradation properties of the reference material containing DVSA was studied. Figure 113 shows that for the reference material p(100 mol% DVSA) after 6 M, only slight swelling was observed. A slight increase in mass of (5-7%) was also determined, indicating a hydrophilic network, causing a slight, irreversible water uptake. This proves that compared to the network formed from the trifunctional reference TAI (2.5.1.3), which displayed a slight mass loss of 2-8%, increased stability is exhibited by this polymer. Therefore, it was confirmed that no degradation of this network occurs under hydrolytic conditions, even though it contains a spiroacetal moiety.

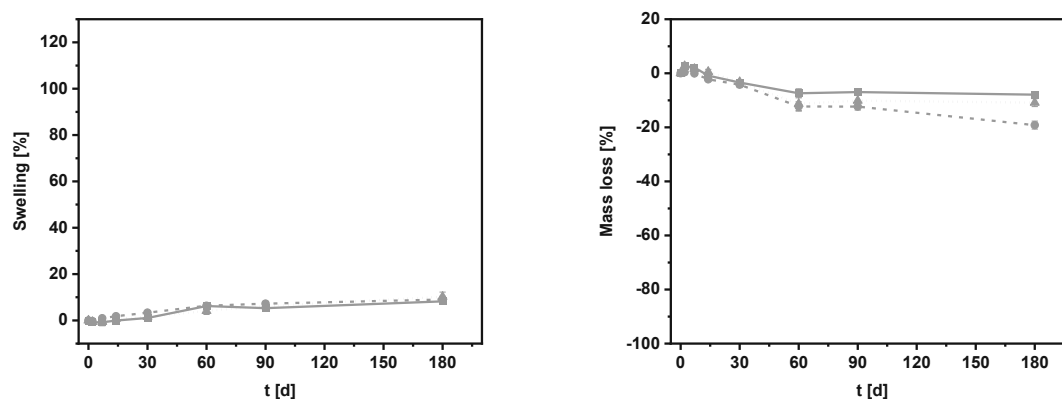


Figure 114: Degradation studies for the Si-based network containing 40 mol% TAS; right: mass loss over time; pH 7.4 (—■—); pH 4 (- -● -), pH 10 (···▲···).

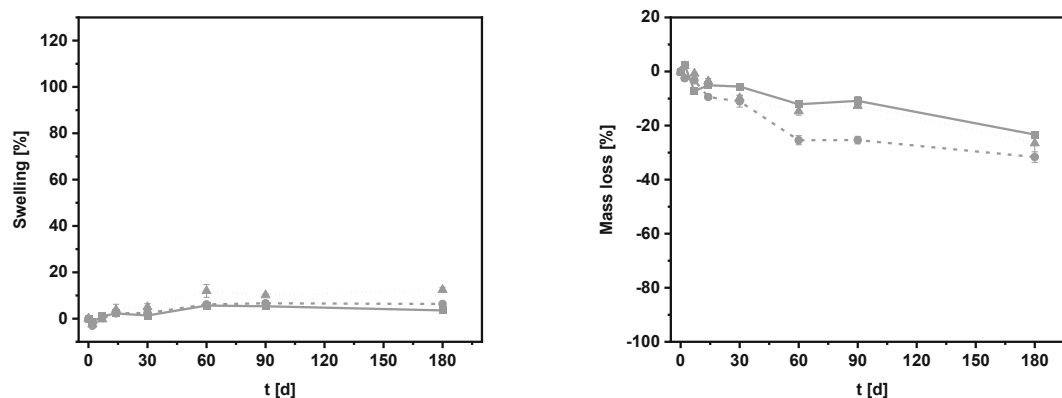


Figure 115: Degradation studies for the Si-based network containing 60 mol% TAS; left: swelling over time; right: mass loss over time; pH 7.4 (—■—); pH 4 (-◆-), pH 10 (···▲···).

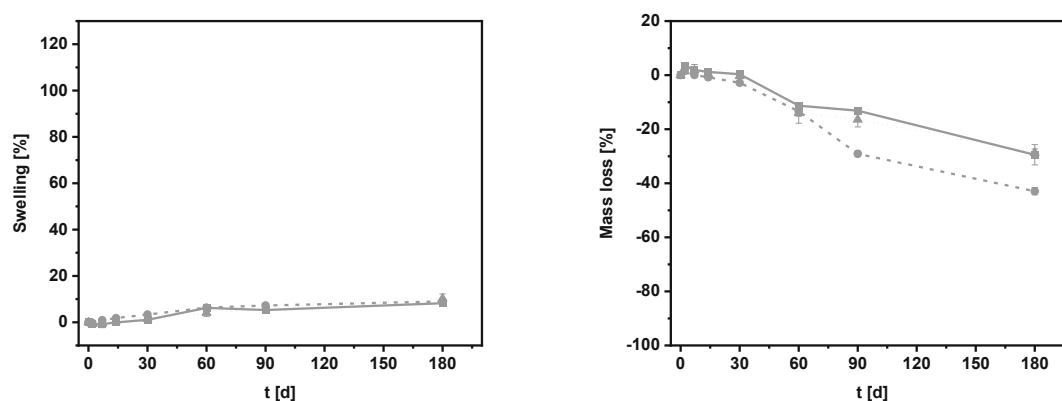


Figure 116: Degradation studies for the Si-based network containing 80 mol% TAS; left: swelling over time; right: mass loss over time; pH 7.4 (—■—); pH 4 (-◆-), pH 10 (···▲···).

Next, also the degradation behavior of the materials containing the Si-based monomer TAS was investigated. Figure 114 to Figure 116 show that for all materials containing 40-80 mol% TAS, slight swelling was observed after 6 M, with a maximum value of 12%. Similar to networks containing TAI, an increase in swelling was determined with increasing concentration of Si-O bonds within the network. In contrast to the TAI-materials, a slightly higher mass loss was confirmed for all 40-80 mol% specimens, with a maximum mass loss of 19% for p(40 mol% TAS), 32% for p(60 mol% TAS) and 43% for p(80 mol% TAS). Again, the fastest and highest mass erosion was observed under acidic conditions. Hence, degradation can be efficiently tuned by varying the content of degradable to non-degradable monomers in these thiol-ene networks. Additionally, even though T_g of the materials containing 60 mol% TAS only slightly exceeded body temperature, and was even lower than 37 °C for the polymer containing 80 mol% TAS, no shape deformation or creep of the samples was observed at 37 °C.

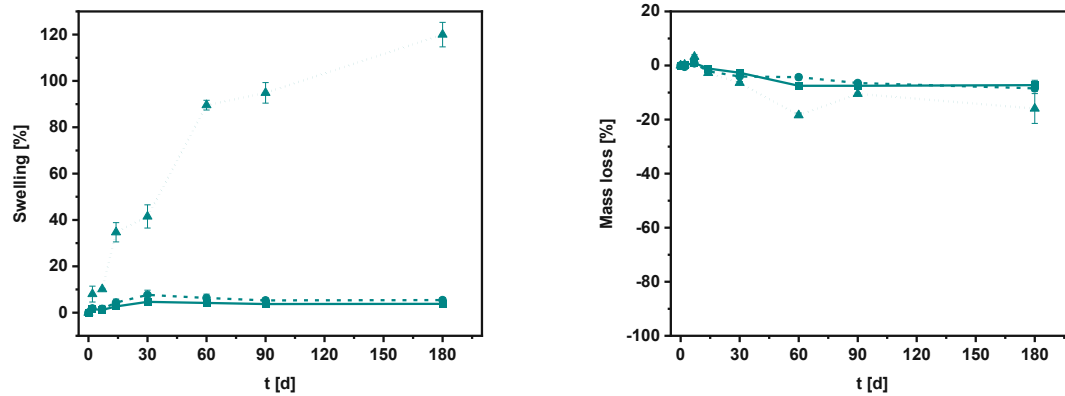


Figure 117: Degradation studies for the B-based network containing 40 mol% ADB; left: swelling over time; right: mass loss over time; pH 7.4 (—■—); pH 4 (-◆-), pH 10 (···▲···).

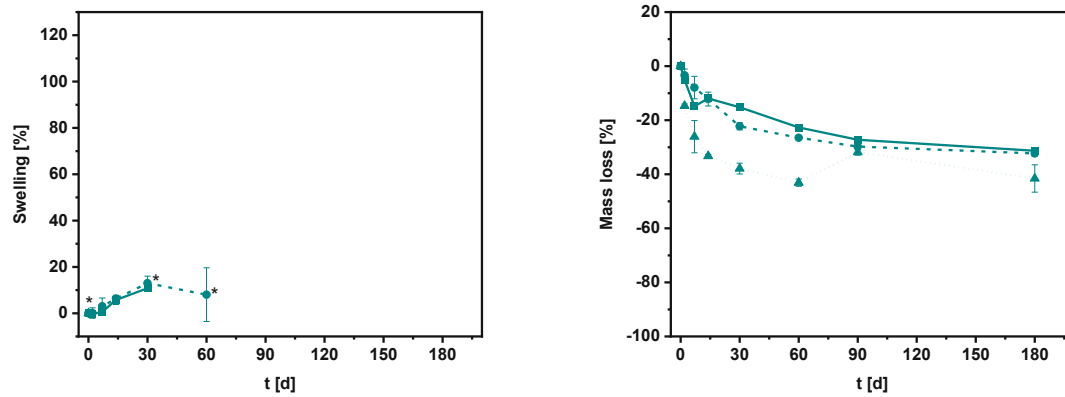


Figure 118: Degradation studies for the B-based network containing 60 mol% ADB; left: swelling over time; right: mass loss over time; pH 7.4 (—■—); pH 4 (-◆-), pH 10 (···▲···). *Disruption of samples occurred.

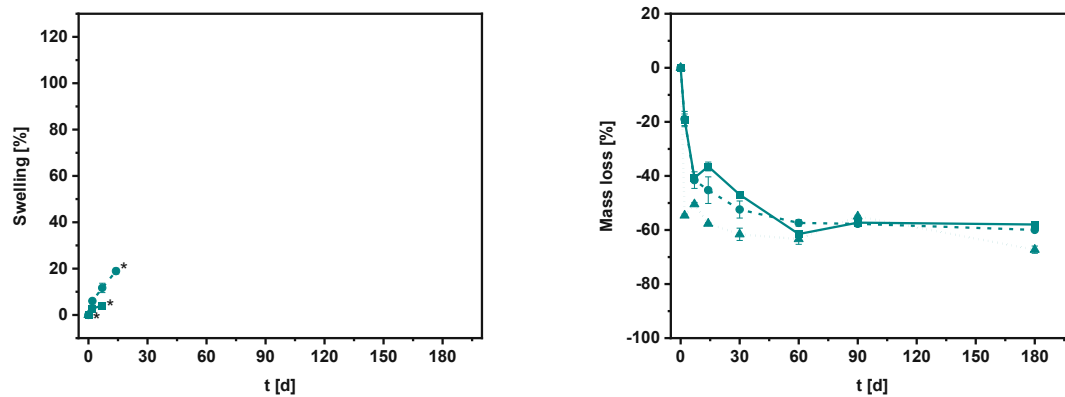


Figure 119: Degradation studies for the B-based network containing 80 mol% ADB; left: swelling over time; right: mass loss over time; pH 7.4 (—■—); pH 4 (-◆-), pH 10 (···▲···). *Disruption of samples occurred.

Subsequently, the degradation of the materials containing 40-80 mol% of the more flexible boronic ester ADB was determined, which is displayed in Figure 117 to Figure 119. Negligible swelling (4-5%) was shown for the material containing 40 mol% ADB in physiological and acidic conditions, while significant swelling of 120% was observed in basic conditions. Furthermore, a

slight mass loss of 7-8% was determined at pH values 7.4 and 4, and a slightly increased erosion of 16% was exhibited at pH 10. This confirms the assumption that at a concentration of 40 mol% of boronic ester, the percolation threshold for a non-degradable subnetwork of VSA is already reached, causing significant network swelling under basic conditions while simultaneously poor network erosion was shown. For the 60 mol% and 80 mol% materials, higher maximum mass loss of 42% and 67%, respectively, was observed after 6 M. Nevertheless, for these materials, disruption of samples occurred at some point during the studies, as well as significant creep at 37 °C. This shows that no continuous VSA network was formed for these materials due to the higher concentration of degradable monomer. The shape change and creep might be explained by the slightly lower T_g of the polymers formed with VSA compared to TAI, which leads to a more flexible network at the degradation temperature and, therefore, more facile penetration by water. Other explanations are the lower crosslinking density due to the lower monomer functionality and increased network hydrophilicity, which was determined for the reference material containing 100 mol% VSA. Therefore, these B-based systems are not promising for further experiments, as they are unsuitable as bone replacement materials.

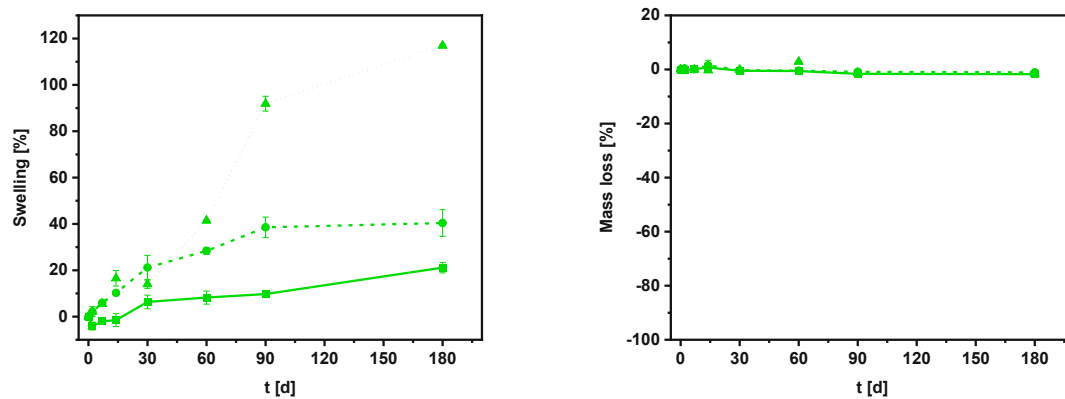


Figure 120: Degradation studies for the B-based network containing 40 mol% VDB; left: swelling over time; right: mass loss over time; pH 7.4 (—■—); pH 4 (-◆-), pH 10 (···▲···).

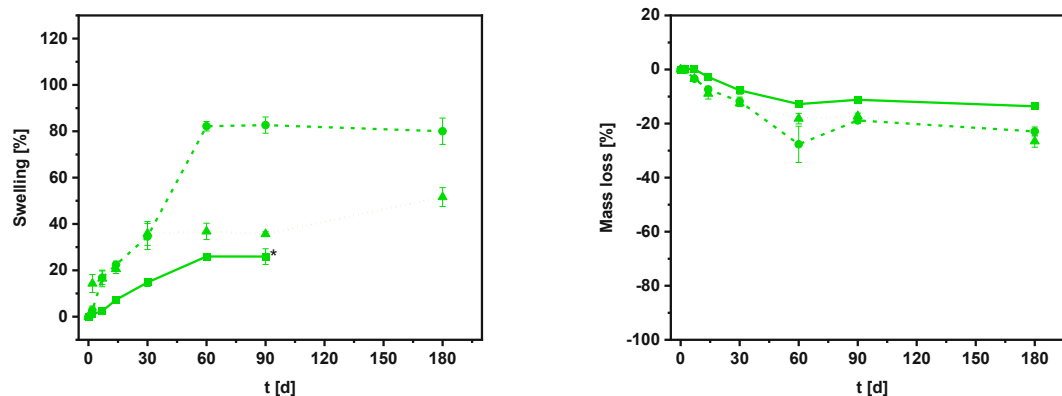


Figure 121: Degradation studies for the B-based network containing 60 mol% VDB; left: swelling over time; right: mass loss over time; pH 7.4 (—■—); pH 4 (-●-), pH 10 (···▲···). *Samples too fragile for removal.

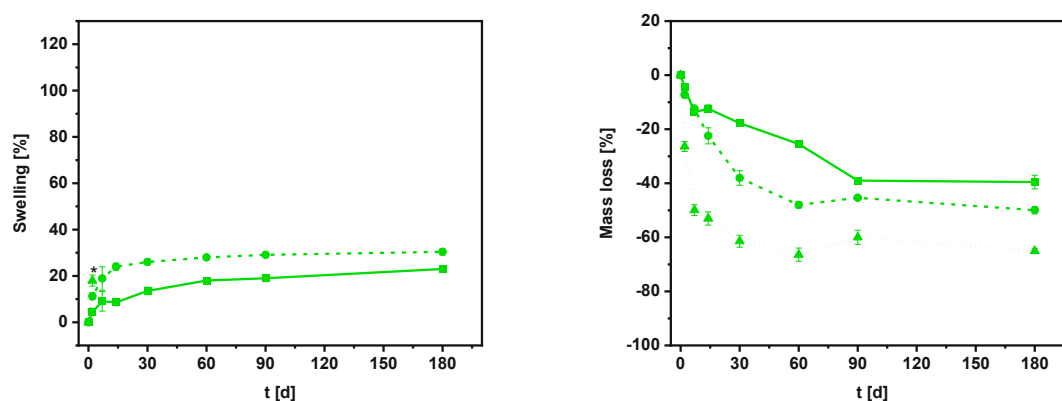


Figure 122: Degradation studies for the B-based network containing 80 mol% VDB; left: swelling over time; right: mass loss over time; pH 7.4 (—■—); pH 4 (-●-), pH 10 (···▲···). *Samples too fragile for removal.

Lastly, the degradation behavior of the materials containing the rigid boronic ester VDB was investigated. Figure 120 shows that similar to the material containing 40 mol% ADB, pronounced swelling was observed for the network containing 40 mol% VDB under basic conditions. In contrast, slightly higher swelling of 21% and 40% was also determined under physiological and acidic conditions, indicating higher network hydrophilicity. As well, negligible mass loss was shown after 6 M, which proves that the percolation threshold for the formation of a non-degradable DVSA network is already reached. With the network containing 60 mol% VDB (Figure 121), significant swelling 50-80% was also determined after 6 M, accompanied by a mass loss of 14% at pH 7.4 and 23-27% in acidic and basic conditions. Due to this high swelling, this degradation behavior is still unfavorable and indicates degradation via bulk rather than surface erosion. Therefore, for this system, even higher concentrations of this boronic ester than described by Robinson *et al.*²⁵⁶ are necessary to prevent the formation of a continuous subnetwork causing substantial swelling of the samples. An explanation is that this theory is described for networks with low T_g values, which exhibit high network mobility and exchange rates at rt. This assumption

was proven with the material p(80 mol% VDB), which shows a different degradation behavior, depicted in Figure 122. Significantly decreased swelling after 6 M of 23% under physiological and 30% under acidic conditions was determined. Under basic conditions, no specimens could be removed from the buffer due to their high fragility after 7 d. Most importantly, an erosion of 40% in PBS, 50% in the acidic buffer, and 65% in basic solution was confirmed after 6 M. This shows that significantly improved degradation was obtained for this material compared to the network containing 80 mol% VDB with respect to TAI, for which significantly increased swelling and lower mass loss was determined at the end of the studies (2.5.1.3).

To summarize this chapter, processing temperatures for all Si- and B-based formulations could be reduced by the addition of difunctional VSA, except for 80 mol% TAS, which still requires curing at 100 °C. Furthermore, with this monomer, enhancement of (thermo)mechanical properties for the materials containing the rather flexible monomer TAS or ADB was successful, while the highest strength, stiffness, and good toughness were still observed for the networks containing the rigid boronic ester VDB. Most importantly, also degradation properties could be enhanced for systems containing TAS and VDB. No favorable degradation was observed for polymers containing the boronic ester ADB, as creep and even sample disruption occurred for materials exhibiting a significant mass loss. Therefore, these materials are not promising to be further studied. For Si-based systems, the best results were obtained with p(80 mol% TAS), with a slight swelling of 10% and a maximum mass loss of 43% under acidic conditions. Nevertheless, besides the high required curing temperature, a T_g below body temperature was shown for this polymer, which is too low for the desired application. For networks containing the rigid boronic ester VDB, good degradation behavior was shown for p(80 mol% VDB), with swelling of 20-30% under neutral and acidic conditions. However, compared to the Si-based system, an improved mass loss of 50% under acidic conditions was determined. As a result, the material containing 80 mol% VDB combines a low processing temperature, the best mechanical properties, and the highest erosion after 6 M and is most promising for use in bone replacement materials.

Therefore, although still swelling of the samples is observed, networks formed with difunctional and rigid VSA seem to combine good hydrophilicity, a network density that is neither too high nor too low, and enhanced mechanical properties at the degradation temperature. Additionally, tuning the degradation behavior of Si- and B-based polymers is possible by partial substitution with this difunctional monomer, and the formation of non-degradable subnetworks is less likely compared to trifunctional TAI.

To conclude, the best results were obtained with the network containing 100 mol% of VDB, which, although requiring higher processing temperatures, still displayed excellent (thermo)mechanical properties and the best degradation behavior observed for all materials. Most importantly, it did not exhibit any swelling and an obvious degradation via surface erosion, with the highest mass loss of 73-90% after 6 M.

2.6 Influence of toughness enhancers

As shown in 2.4, the material formed from the novel, rigid boronic ester VDB and the thiol TMT results in networks with high homogeneity, combines excellent mechanical properties such as low shrinkage, high glass transition temperature, stiffness, and strength, with accelerated degradation via surface erosion and the highest mass loss observed after 6 M in physiological and acidic conditions.

Good mechanical properties are crucial for scaffolds used in tissue engineering in order to provide good load dissipation and tissue integration. Especially high toughness is a common obstacle for photopolymers, which tend to behave very brittle.⁸⁷ In addition to thiol–ene chemistry, several other approaches can be found in literature to improve the toughness of photopolymers.^{98,143,146,259} Among others, high molecular weight substances can be added prior to photopolymerization, which by just physical interactions and reduced crosslinking density, can enable enhanced dissipation of employed stress.⁸⁷

Poly(caprolactone) (PCL, Figure 123) is a well-established thermoplast with good biocompatibility and is used in several biomedical applications, including scaffolds for tissue engineering.^{53,86} Orman *et al.*^{87,194} demonstrated that functionalization with co-polymerizable end groups, such as vinyl carbonate groups (VC-PCL, Figure 121), enables chemical interaction with the polymer network and by covalent incorporation of the toughness enhancer a further improvement of toughness by a factor of 6 was possible. Dellago *et al.*³⁴⁷ modified PCL with norbornene, vinyl ester, and allyl ester groups and showed that the toughness of 3D-printed polymers could be tripled upon addition of these compounds to the formulations.

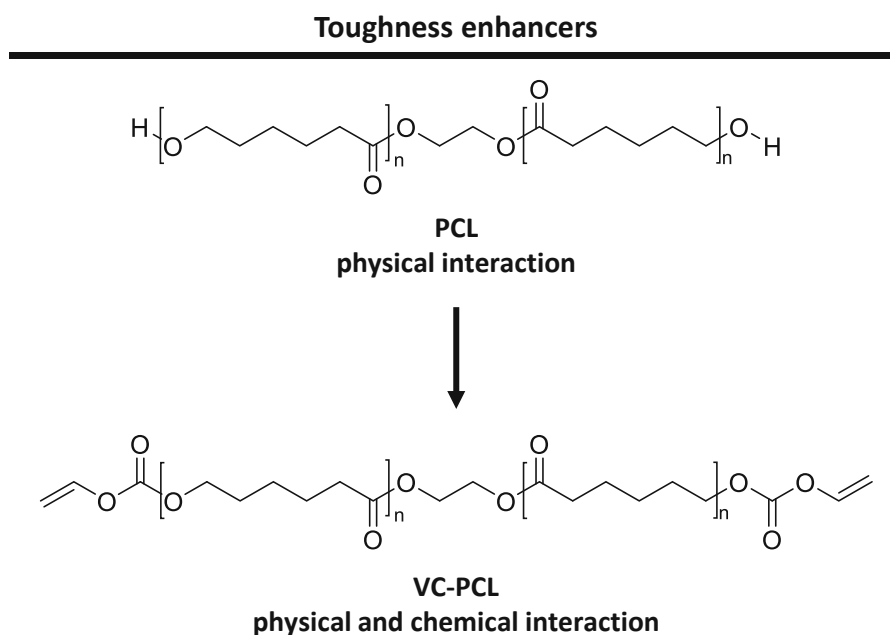


Figure 123: Structure of the toughness enhancers PCL and VC-PCL used by Orman *et al.*⁸⁷

Therefore, the influence of the addition of toughness enhancers on photoreactivity and (thermo)mechanical properties of the material containing the boronic ester monomer VDB and the thiol TMT, which are both displayed in Figure 124, was studied to determine whether the good elongation at break (11%) could be further improved upon integration of a high molecular weight additive into the degradable, rigid network. As a toughness additive, PCL with a molecular weight of 45 kDa was chosen, which was functionalized with norbornene end groups by Dellago *et al.*³⁴⁷. The structure of this toughness enhancer is depicted in Figure 124. To ensure that all high molecular additives are covalently connected via both end groups to the thiol-ene matrix, norbornene was selected as a polymerizable end group, as it displays higher reaction rates with thiols compared to allyl esters, which was demonstratively shown by Steinbauer *et al.*³⁴⁸ This should lead to full covalent incorporation of the toughness enhancer into the network and, therefore, higher toughness of resulting polymers.

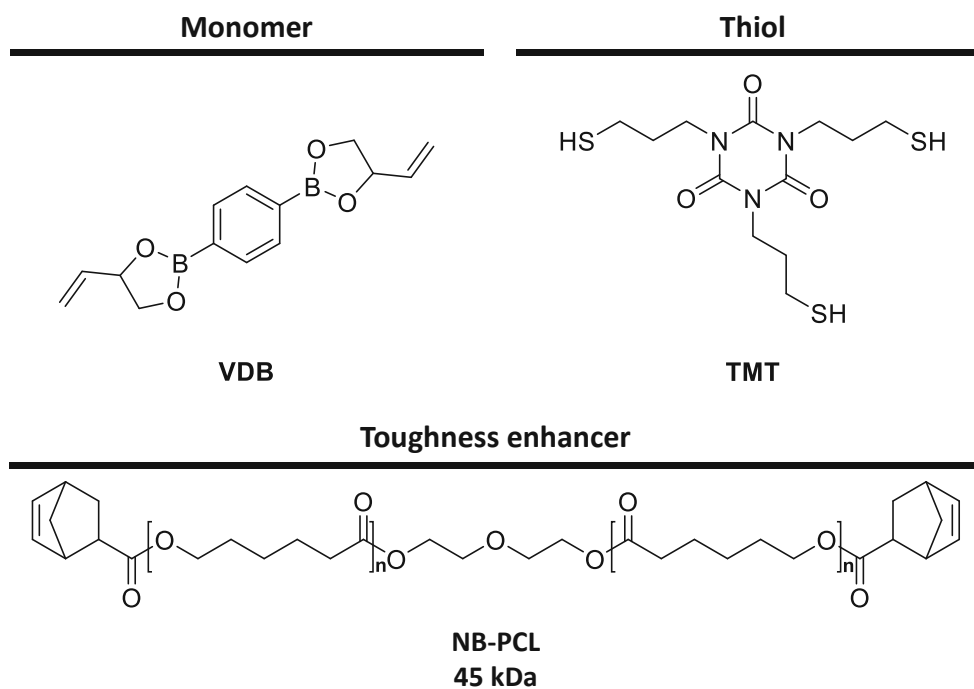


Figure 124: Structure the boronic ester monomer VDB, the thiol TMT of the toughness enhancer NB-PCL.

Hence, 5 w%, 10 w%, 15 w%, 20 w%, or 25 w% ($x_{\text{NB-PCL}}$) of NB-PCL were added to the monomer and the thiol (Figure 124), while the amount of TMT was adjusted to obtain an equimolar ratio of double bonds to thiol groups. For initiation, 1 w% of Ivocerin and for stabilization, 0.02 w% of PYR were added. All formulations were homogenized by heating to 110 °C for 20 min to fully dissolve the toughness modifier. Due to the precipitation of VDB in the formulations at rt, all formulations had to be processed at 100 °C.

2.6.1 Rheological properties of formulations

The addition of high molecular weight compounds might lead to a significant increase in formulation viscosity, which must not exceed 20 Pa·s for 3D printing, to guarantee good processability of the resin on the printer.³⁴⁹ To determine the influence of the toughness enhancer NB-PCL on this property, viscosity measurements of all formulations described in 2.6 were conducted at 100 °C, as homogeneous formulations were only obtained upon heating to this temperature. The viscosity (η) of the samples was determined at a constant shear rate of 100 s⁻¹. As a reference, the formulation without the toughness enhancer was used.

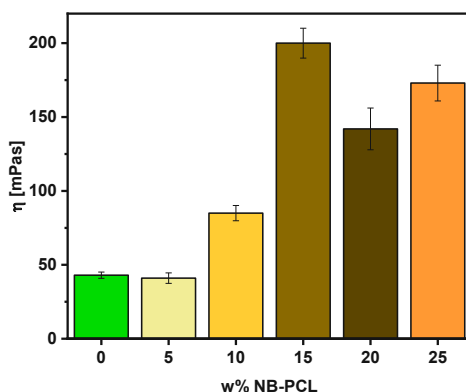


Figure 125: Viscosity of formulations of the monomer VDB with 0 w% (■), 5 w% (■), 10 w% (■), 15 w% (■), 20 w% (■), or 25 w% (■) NB-PCL determined at 100 °C.

Results in Figure 125 show that all formulations exhibit very low viscosities <220 mPa·s at 100 °C, which is significantly lower than the maximum processing viscosity of 20 Pa·s. Starting at a concentration of 10 w% of the toughness enhancer, a significant viscosity increase was observed, with the highest increase by a factor of 5 for the formulation containing 15 w% of the additive, compared to the reference formulation. Nevertheless, these values are sufficiently low for facile processability of the formulations at 100 °C. The detailed data is given in Table 20.

Table 20: Detailed results of the viscosity measurements.

monomer	x _{NB-PCL} [w%]	η [mPa·s]
VDB	0	43 ± 2
	5	41 ± 4
	10	85 ± 5
	15	200 ± 10
	20	142 ± 14
	25	173 ± 12

2.6.2 Reactivity of formulations

To determine whether the addition of the toughness enhancer negatively impacts photoreactivity of the system containing VDB and the thiol TMT, RT-NIR photorheology measurements were conducted as described in 1.1.3 with formulations containing 5-25 w% NB-PCL (described in 2.6). As a reference, the formulation without the toughness enhancer was selected. For the experiments, filtered light from a broadband Hg lamp (400-500 nm) was used. 150-180 μL of sample volume were applied to the glass plate and irradiated for 320 s. The light intensity at the surface of the samples was adjusted to 20 mW/cm². All experiments were conducted at 100 °C due to miscibility issues described in 2.6.

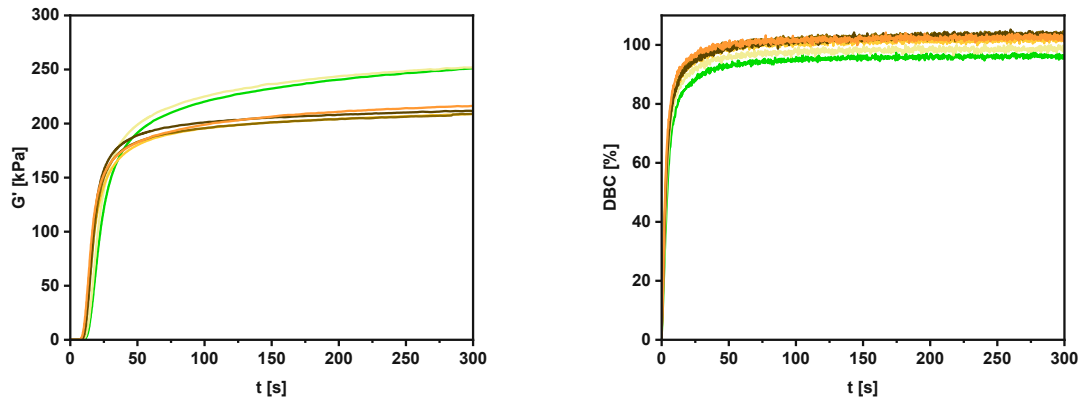


Figure 126: Storage modulus (G' , left) and DBC (right) over time for formulations of the monomer VDB with 0 w% (—), 5 w% (—), 10 w% (—), 15 w% (—), 20 w% (—), or 25 w% (—) NB-PCL.

Storage modulus curves over time in Figure 126 (left) depict the influence of the addition of the high molecular weight additive on gelation and curing. It was shown that an increasing concentration of NB-PCL results in slightly faster gelation and curing of the polymer network. This is due to the increase of formulation viscosity upon the addition of the high molecular weight toughness enhancer, which leads to lower mobility of the reactive chain ends and in turn, less occurring termination reactions. G'_{final} values show a slight softening effect starting at a concentration of 10 w% NB-PCL, which was expected due to the high molecular weight of this linear compound. The IR data in Figure 126 (right) showed that the Trommsdorff effect also affords slightly higher conversions (>98%) than for the reference formulation without the toughness enhancer.

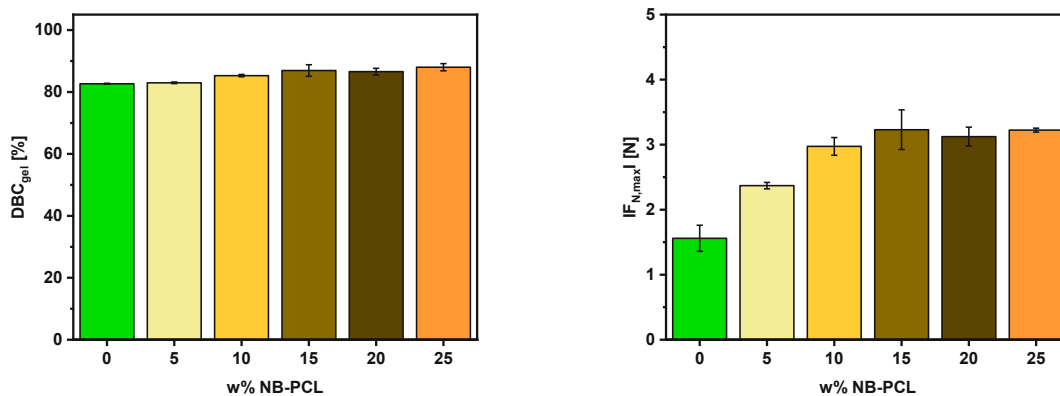


Figure 127: DBC_{gel} (left) and $F_{N,\text{max}}$ (right) for formulations of the monomer VDB with 0 w% (■), 5 w% (■), 10 w% (■), 15 w% (■), 20 w% (■), or 25 w% (■) NB-PCL.

Similar to the formulation without toughness enhancer, high DBC_{gel} were observed for all samples (Figure 127, left), due to the reversible dynamic boronic ester bonds of VDB, enabling a high mobile network up to high conversions. Slightly higher shrinkage was observed for the formulations containing the toughness enhancer (Figure 127, right), which, however, is still very

low compared to all other tested formulations. These higher values can be explained by the dilution of the dynamic boronic ester bonds caused by the addition of the high molecular weight additive, which slightly impedes the transesterification reactions between the chains.

To sum up, all formulations containing NB-PCL show excellent curing rates and high final conversions. Again, high DBC_{gel} values were observed, demonstrating that the combination of dynamic boronic ester bonds, thiol-ene chemistry, and toughness enhancers leads to high network mobility and monomer conversions. The cumulated data of all measurements is given in Table 21.

Table 21: Detailed results of the RT-NIR photorheology measurements.

monomer	X_{NB-PCL} [w%]	t_{gel} [s]	DBC_{gel} [%]	t_{95} [s]	DBC_{final} [%]	G'_{final} [kPa]	$F_{N,max}$ [N]
VDB	0	14.0 ± 0.0	83.0 ± 0.3	35.4 ± 2.1	96.5 ± 0.4	252 ± 4.40	-1.6 ± 0.2
	5	11.3 ± 0.6	83.0 ± 0.3	31.2 ± 1.2	98.4 ± 0.6	248 ± 7.50	-2.4 ± 0.1
	10	11.0 ± 0.0	85.3 ± 0.4	30.6 ± 2.4	>99.9	211 ± 3.30	-3.0 ± 0.1
	15	11.3 ± 0.6	87.0 ± 1.9	31.5 ± 4.3	>99.9	203 ± 10.4	-3.3 ± 0.3
	20	11.0 ± 0.0	86.6 ± 1.1	22.8 ± 3.5	>99.9	210 ± 6.30	-3.1 ± 0.2
	25	10.3 ± 0.6	88.0 ± 1.2	20.0 ± 1.2	>99.9	216 ± 2.80	-3.2 ± 0.0

2.6.3 Mechanical properties of polymer networks

After confirming that even upon the addition of 25 w% NB-PCL, fast crosslinking, and curing were observed, the mechanical properties of resulting polymers were determined with DMTA measurements and tensile tests.

The thermomechanical properties of the materials were determined with DMTA measurements described in 2.1.3. All formulations were cured in a Lumamat 100 light oven at elevated temperature using a preheated silicon mold and a photocuring program at ~104 °C. This was done due to miscibility issues of the monomer VDB with the thiol TMT, described in 2.6. As a reference, the sample without the toughness enhancer was used.

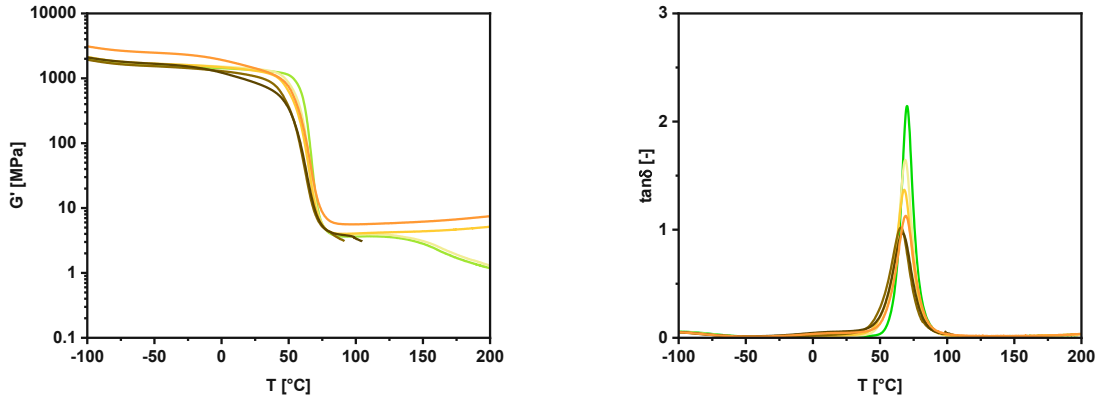


Figure 128: G' (left) and $\tan\delta$ (right) over temperature of the different networks formed from formulations of VDB with 0 w% (—), 5 w% (—), 10 w% (—), 15 w% (—), 20 w% (—), and 25 w% (—) NB-PCL.

The results in Figure 128 show that all samples containing NB-PCL exhibit high storage moduli at 37 °C and a T_g significantly above body temperature. A slight decrease of T_g was observed compared to the reference polymer without toughness enhancer, with a maximum decrease of 5 °C determined for the network containing 15 w% NB-PCL. Also, slightly lower network homogeneity was shown for the polymers containing toughness enhancers, with a slight broadening of $\tan\delta$ curves, which might benefit the toughness of the specimens. As expected, increasing concentration of the flexible, high molecular weight additive leads to a decrease in $G'_{37^\circ\text{C}}$ for all formed polymers, except for the sample containing 20 w% of toughness enhancer. This network showed unprecedented thermomechanical properties, with a T_g as high as for the reference material but the highest modulus of all samples observed at rt. Therefore, 20 w% of NB-PCL seems to be an optimum concentration for this particular system. Significant network softening was shown for the sample containing 25 w% of additive, with a decrease of $G'_{37^\circ\text{C}}$ by a factor of 2 compared to the reference polymer. Therefore, higher concentrations of toughness enhancer would cause the network to be too soft for the application as a bone replacement material. The summarized results are shown in Table 22.

Table 22: Detailed results of DMTA measurements. *No rubber plateau was observed.

monomer	$x_{\text{NB-PCL}}$ [w%]	T_g [°C]	$G'_{25^\circ\text{C}}$ [MPa]	$G'_{37^\circ\text{C}}$ [MPa]	fwhm [°C]	G'_R [MPa]
VDB	0	70	1340	1280	10	—*
	5	69	1390	1290	12	—*
	10	68	1310	1150	14	5
	15	65	1070	860	18	—*
	20	69	1430	1180	16	7
	25	67	857	668	17	—*

Also, tensile test specimens of shape 5B of all described formulations were prepared under the same curing conditions as DMTA specimens, and testing was performed as described in 2.4.2.

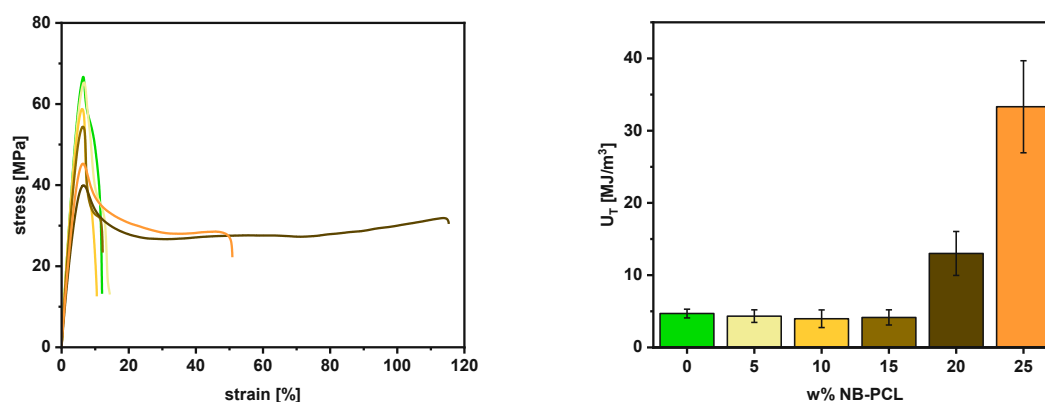


Figure 129: Stress-strain curves (left) for polymers formed from formulations of the monomer VDB containing 0 w% (—), 5 w% (—), 10 w% (—), 15 w% (—), 20 w% (—) and 25 w% (—) NB-PCL. Tensile toughness (right) for polymers containing 0 w% (■), 5 w% (■), 10 w% (■), 15 w% (■), 20 w% (■), and 25 w% (■) NB-PCL.

The stress-strain curves of all materials displayed in Figure 129 show that the tensile strength slightly decreases with an increasing amount of NB-PCL, ranging from 70 MPa for reference material to 39 MPa for the specimen containing 25 w% of toughness enhancer. Nevertheless, this value is still significantly higher than the previously investigated non-rigid systems described in 2.4.2. Most remarkably, a significant increase in ϵ_B was determined, starting at a concentration of 20 w% of NB-PCL addition (46%), which is further elevated with 25 w% of the toughness enhancer to a value of 117%. Good tensile toughness was determined for all materials (Figure 129, right), with exceptionally high values obtained for the network containing 20 w% or 25 w% of NB-PCL, confirming that toughness can be efficiently enhanced by a factor of 3 or even 7, respectively, which is even higher compared to the factor of 6 reported by Orman *et al.* Most remarkably, the tensile toughness of 33 MJ/m³ determined for the latter polymer is the highest value obtained for all materials containing monomer and the thiol TMT.

Therefore, by combining the concepts of rigid monomers containing dynamic covalent bonds and rigid thiols with the covalent incorporation of toughness enhancers into the network, materials can be obtained with superior mechanical properties combining high T_g , strength, stiffness, and strain at break, as well as exceptionally high tensile toughness, while best results were obtained at concentrations of 20 w% or 25 w% of NB-PCL. The summarized data for all tensile tests is given in Table 23.

Table 23: Detailed results of the tensile tests.

monomer	$x_{\text{NB-PCL}}$ [w%]	σ_{M} [MPa]	ϵ_{B} [%]	U_{T} [MJ/m ³]
VDB	0	67.0 ± 0.1	11.0 ± 1.1	4.7 ± 0.6
	5	65.1 ± 3.5	11.1 ± 1.9	4.3 ± 0.9
	10	60.7 ± 1.3	10.6 ± 3.3	4.0 ± 1.2
	15	57.1 ± 2.0	11.3 ± 3.0	4.2 ± 1.1
	20	45.3 ± 1.2	45.9 ± 8.5	13.0 ± 3.1
	25	39.2 ± 1.0	117 ± 20.9	33.3 ± 6.4

2.7 3D printing

As the polymer containing the boronic ester VDB not only displayed excellent mechanical properties but also enhanced degradation via desired surface erosion behavior, 3D structuring of the formulation was conducted to confirm its applicability in the production of patient-specific implants. Very recently, Robinson *et al.*²⁵⁶ reported the first DLP-printing of dynamic networks based on boronic esters capable of self-healing. However, due to the low glass transition temperature of the polymers, the addition of a static crosslinker was necessary to prevent creep and failure during printing.^{245,257,258}

As described in 2.4.1, a homogeneous formulation of the monomer VDB and TMT could only be maintained at elevated temperatures, with a minimum of 55 °C required to hinder reprecipitation of the monomer in the thiol. Therefore, in order to avoid the addition of a static crosslinker as described by Robinson *et al.*²⁵⁶, and to maintain dimensional stability during printing, structuring below the network T_{g} would be beneficial. Hence, printing should be conducted at a temperature of 55 °C below the T_{g} of 70 °C of the material.

2.7.1 Characterization of the printing resin

As a result, the formulation containing the boronic ester VDB used for printing was characterized at the respective printing temperature of 55 °C. To enhance the printing resolution, 0.1 w% of the absorber Quinoline Yellow (QY) was added to the formulation, which was also used by Orman *et al.*¹⁹⁴ and led to objects with high precision. For this absorber, it was further shown by Hofecker *et al.*³⁵⁰ that increasing concentration not only led to enhanced control over the curing depth but also increased mechanical properties of layers when applied in thiol-ene systems.

To apply a resin in 3D printing, formulations should exhibit certain properties. To ensure processing during the printing process and to avoid the formation of bubbles within printed parts, a maximum viscosity of 20 Pa·s should be displayed for Laser-SLA.³⁵¹ Additionally, at the processing temperature, the resin should remain stable throughout the printing process, which can take up to several hours, and should not show any notable change in viscosity or gelation in the vat.

Therefore, viscosity measurements over time of the formulation containing the boronic ester VDB and the thiol TMT in an equimolar ratio of double bonds to thiol groups, as well as 1 w% Ivocerin for initiation, 0.1 w% of the absorber QY and 0.02 w% of PYR for stabilization were conducted at 55 °C for 8 h, which is the average duration of a printing process.

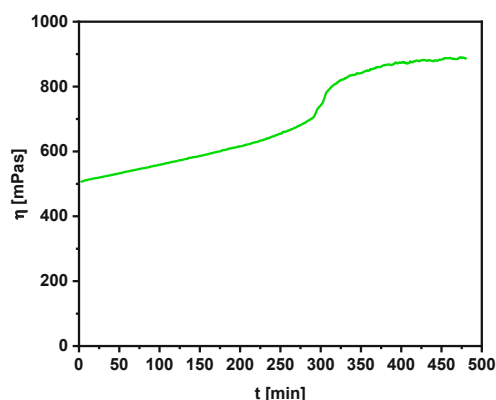


Figure 130: Viscosity over time for the printing formulation containing the boronic ester VDB at the respective printing temperature of 55 °C.

The results in Figure 130 show that the resin exhibits a very low viscosity of 506 mPa·s at the printing temperature, which is far below the maximum processing viscosity of 20 Pa·s. A slight linear increase in viscosity was observed within the first 5 h, which was slightly accelerated for the last 3 h of the studies. After 8 h, viscosity was increased by 75% to 886 mPa·s. Nevertheless, although a certain amount of oligomerization might occur after 4 h at the printing temperature, resin viscosity remains extremely low after 8 h. Most importantly, no gelation with a notable increase in viscosity of the formulation occurs. Therefore, the resin can be applied in 3D printing, but the time for printing should be kept below 4 h to ensure the same reactivity of the formulation at the beginning and the end of the printing process and to avoid a gradient in the mechanical properties of printed parts.

For the intended application of the formulation in 3D printing, the photoreactivity of the resin is important. For printing, low t_{gel} , t_{95} , and $F_{N,\text{max}}$ as well as high $\text{DBC}_{\text{final}}$ are crucial to build stable objects with sufficient speed and with a low amount of internal stress, which was described in detail in 2.4.1.^{87,298} All of the parameters mentioned above were determined for the printing resin

with RT-NIR photorheology described in 1.1.3. For the experiments, filtered light from a broadband Hg lamp (400-500 nm) was used. 150-180 μL of sample volume were applied to the glass plate and irradiated for 320 s. The light intensity at the surface of the samples was adjusted to 20 mW/cm^2 and the experiments were conducted at 55 °C.

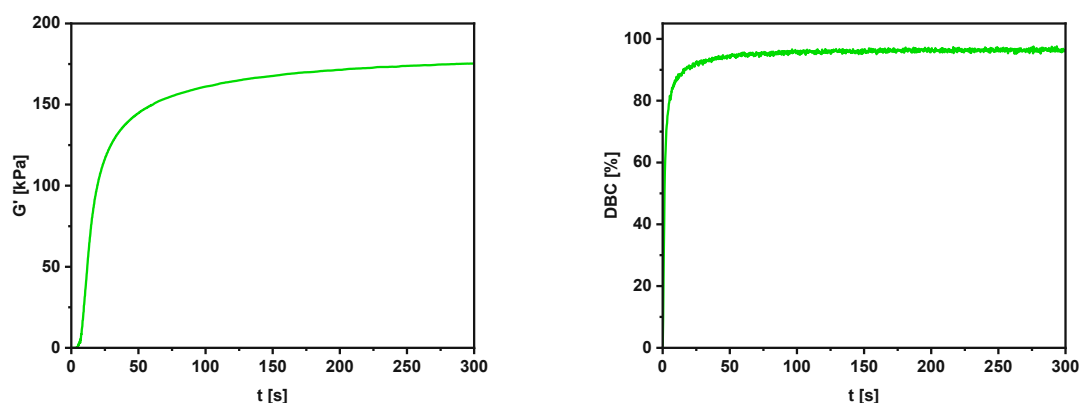


Figure 131: Storage modulus (G' , left) and DBC (right) over time for the printing formulation containing VDB at 55 °C.

Figure 131 shows that fast gelation and curing were attained for the formulation containing VDB and TMT at the printing temperature. Furthermore, high double bond conversions were observed, guaranteeing a low amount of residual low molecular weight components inside the polymer networks. Additionally, a high DBC_{gel} and low shrinkage during the polymerization process were determined due to transesterification reactions of the boronic ester bonds at the printing temperature of 55 °C, which leads to network rearrangement during curing. Therefore, this system displays sufficient photoreactivity for use as a printing resin. The cumulated data is shown in Table 24.

Table 24: Detailed results of the RT-NIR photorheology measurements.

monomer	t_{gel} [s]	DBC_{gel} [%]	t_{95} [s]	$\text{DBC}_{\text{final}}$ [%]	G'_{final} [kPa]	$F_{N,\text{max}}$ [N]
VDB	11.0 ± 0.0	87.1 ± 0.7	21.9 ± 1.8	96.4 ± 0.3	170 ± 11.3	-7.3 ± 0.5

2.7.2 Laser-SLA

As high photoreactivity of the printing resin was confirmed, next, 3D printing was conducted on a Caligma 200 UV prototype. The vat and the building platform of this printer can be heated to temperatures up to 120 °C, which enables the processing of the formulation. This printer uses a laser light source with a wavelength of 375 nm and a power of 70 mW/mm^2 .

For Laser-SLA, first light exposure tests of the printing formulation were done to determine whether and how fast photopolymerization occurs upon laser irradiation. Laser exposures of circular areas ($d=0.5$ cm) were conducted at the vat, which was heated to 55 °C, with different writing speeds of 1000 mm/s, 500 mm/s, 200 mm/s, and 100 mm/s, to determine the necessary writing speed for the formation of a solid specimen, as well as the thickness of the resulting platelet. A layer height of 100 μm was chosen for subsequent 3D printing jobs, as this value combines sufficiently fast building of objects with high resolution. For printing objects with this layer thickness, polymerized samples should display a layer thickness between 250 μm and 300 μm , as this will ensure good layer-to-layer adhesion and sufficient reactive groups remaining on the surface for the next layer to be polymerized on, which avoids delamination between the layers.

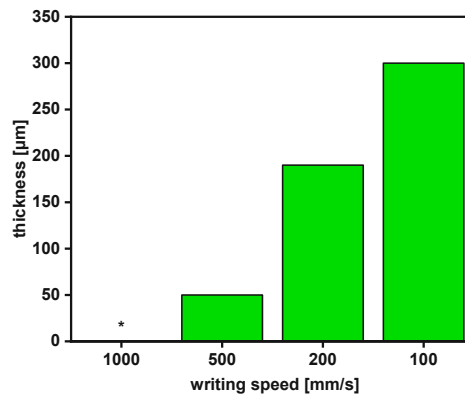


Figure 132: Laser exposure tests of the printing formulation at different writing speeds of 1000 mm/s, 500 mm/s, 200 mm/s, and 100 mm/s and the resulting thickness of the formed platelet at 55 °C. *No solid specimen was formed.

Figure 132 shows that the best curing depth of 300 μm was obtained for a writing speed of 100 mm/s, while no platelet or platelets with insufficient curing depth were formed with writing speeds ranging from 1000 mm/s to 200 mm/s. Therefore 100 mm/s is the optimum writing speed for 3D printing of this particular system. The obtained sample platelet with this writing speed is displayed in Figure 133 and confirms that by the addition of QY, no diffusional or light-induced overpolymerization was observed.

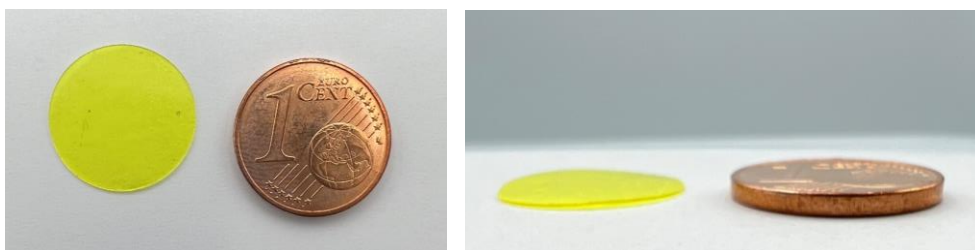


Figure 133: Sample platelet (left: top-view; right: side-view) with a thickness of 300 μm obtained at a writing speed of 100 mm/s.

To confirm the applicability of the formulation in stereolithography, a pyramid object with a square base of 7.3 mm² was printed on the Caligma 200 UV prototype with the previously determined writing speed of 100 mm/s and a layer height of 100 μm . For structuring, the vat and the building platform of the printer were heated to 55 °C during the printing process, as precipitation of the monomer VDB in the thiol occurred at lower temperatures. Due to the high adhesion of the material to the vat, the vat was covered with a PE tape during the printing process, which led to improved adhesion on the building platform.

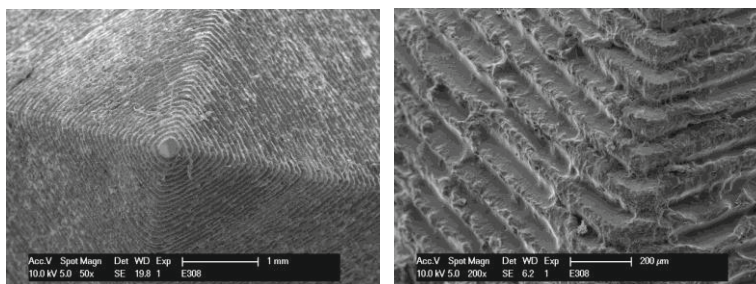
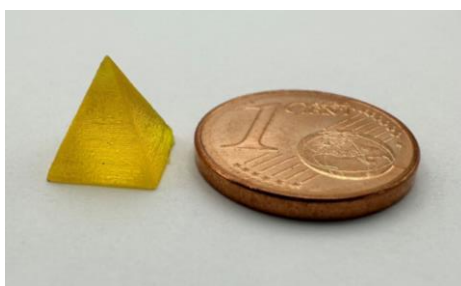


Figure 134: Top: photograph of the 3D-printed pyramid from the VDB-based formulation. Bottom: SEM imaging of the printed structure.

Figure 134 (top) shows the printed structure, which displays a high resolution due to the manufacturing in this layer-by-layer process. SEM images in Figure 134 (bottom) further confirm the spatiotemporal selectivity of the photocuring reaction due to a lack of light-induced or diffusional over-polymerization during structuring. This, therefore, confirms the applicability of this degradable thiol-ene system in 3D printing and the future fabrication of more complex structures with internal pores. Most importantly, due to the exceptional mechanical properties and the high T_g of the formed polymers, no creep or disruption of the structure was observed during the printing process. Hence, no addition of a static crosslinker such as VSA or TAI was

necessary, as previously reported for the 3D printing of resins containing boronic esters by Robinson *et al.*²⁵⁶ With this, as a first group, we demonstrated that this novel boronic ester monomer could be applied in Laser-SLA-printing to print degradable, patient-specific bone regeneration scaffolds in the near future.

2.8 Influence of sterilization on mechanical properties

Good mechanical properties, excellent degradation behavior, and 3D printing were demonstrated for the polymer formed from VDB and TMT. Nevertheless, for this material to be applied *in vivo*, guaranteed sterility of the implant is a crucial premise to minimize the risk of infection or immune response. In general, several sterilization methods are known for medical materials, including exposure to heat (120-190 °C), gaseous or liquid chemicals, or radiation.³⁵²⁻³⁵⁴

As the glass transition temperature of the network is located at 70 °C, heat sterilization cannot be employed. Due to the hydrolyzable boronic ester bonds of the network, also liquid chemical sterilization with substances such as peracetic acid was deemed unsuitable, as these solvents might cause network cleavage. Therefore, gas sterilization and radiation sterilization were chosen to obtain sterilized materials. As a gaseous sterilant, ethylene oxide (EO) was selected, which is the most common way to sterilize medical devices as it has the unique ability to penetrate polymers without damaging them.^{352,353} For radiation sterilization, γ -rays were chosen, as they combine advantages such as high penetration depth at low dose rates, better certainty of sterility, and high effectiveness independent of temperature and pressure.³⁵⁵ Still, drawbacks of these methods have to be mentioned. Due to the rather slow diffusion of EO, long desorption times are required to guarantee that no toxic and carcinogenic gas residues remain in the material, which is especially important in the case of highly porous scaffolds. Besides high costs, high energy γ -radiation might induce irreversible structural changes in the polymer network, as it is able to ionize the polymer chain, leading to further crosslinking or scission via a free radical mechanism. This might lead to an increase in the brittleness of the polymer or strain within the material.³⁵⁶

To investigate the influence of the different sterilization methods on the mechanical properties of the material formed from VDB and the thiol TMT, DMTA, and tensile test specimens were sent to KLS-Martin for sterilization in three batches. The first batch (EO) was sterilized with EO according to DIN EN ISO 11135-1 (6% EO, 55 °C, 2 h). The second batch (low γ) of samples was subjected to the lowest possible dosage of γ -radiation (~18 kGy, 5 h), which is still considered sufficient for

sterilization of medical implants, according to DIN EN ISO 9001, DIN EN ISO 13485 and DIN EN ISO 11137-1. For the third batch (high γ), a higher dose of γ -radiation (~ 31 kGy, 5 h) was employed following the same protocol, as higher doses ensure sterility of implants but might more likely lead to premature network cleavage. Then, the mechanical properties of the three groups were determined with DMTA measurements described in 2.1.3 and tensile tests specified in 2.4.2. As a reference, the non-sterilized material was used (Ref.).

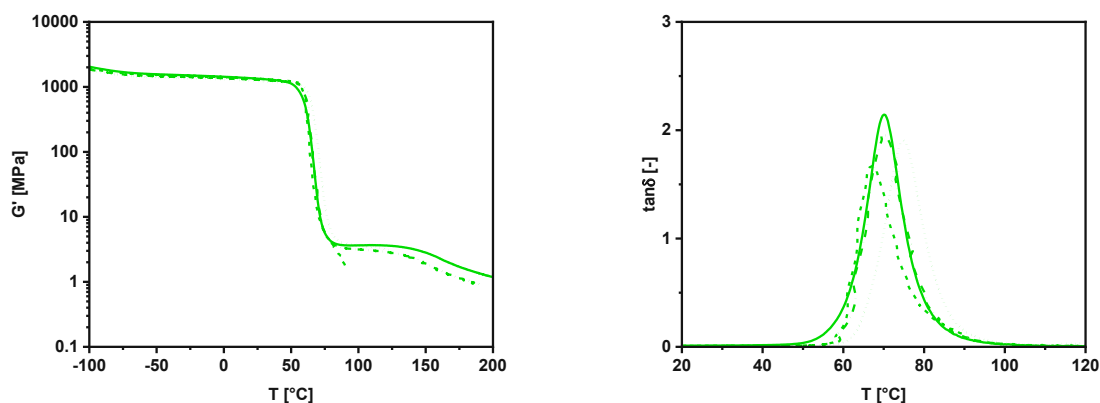


Figure 135: G' (left) and $\tan\delta$ (right) over temperature for the specimens subjected to the different sterilization methods; Ref. (—); EO (---); low γ (.....); high γ (-.-.);

The storage modulus curves over temperature (Figure 135, left) show that similar curve progression and storage moduli at body temperature compared to the non-sterilized sample were determined for all specimens. Furthermore, a similar T_g was shown for all materials, with a maximum decrease of 3 °C observed for the sample subjected to EO and even a slight increase of 5 °C for the sample irradiated with low gamma doses (Figure 135, right). Most importantly, no premature network cleavage due to sterilization was observed, as no significant decrease in storage moduli occurred for all materials. Hence, sterilization does not significantly alter the thermomechanical properties. The collected data of the measurements is given in Table 25.

Table 25: Detailed results of DMTA measurements. *No rubber plateau was observed.

monomer	sterilization	T_g [°C]	$G'_{25^\circ\text{C}}$ [MPa]	$G'_{37^\circ\text{C}}$ [MPa]	fwhm [°C]	G'_R [MPa]
VDB	Ref.	70	1340	1280	10	-*
	EO	67	1340	1290	10	-*
	low γ	75	1230	1190	11	-*
	high γ	70	1290	1240	11	-*

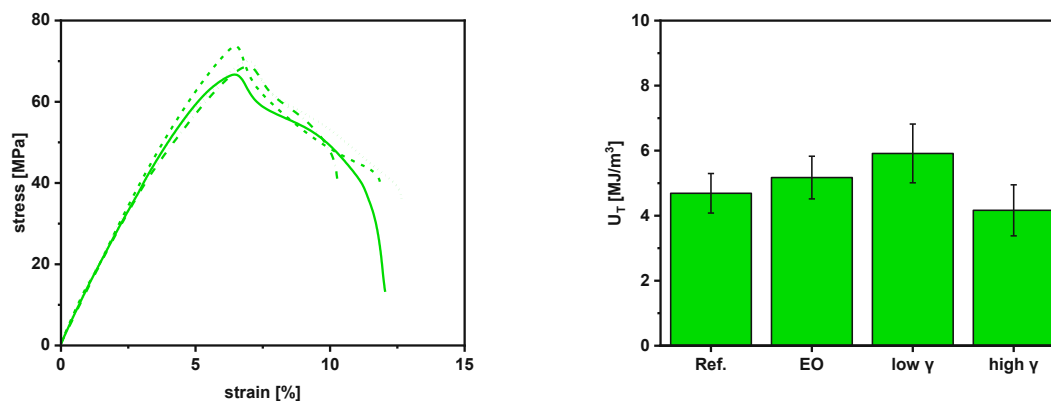


Figure 136: Stress-strain curves (left) for the specimens subjected to the different sterilization methods; Ref. (—); EO (---); low γ (.....); high γ (-.-.). Tensile toughness for Ref., EO, low γ , and high γ ;

Tensile tests of the materials confirmed that for all samples, high tensile strengths (67–72 MPa) and good strains at break (9–13%) were exhibited (Figure 136, left). Slightly higher strength, elongation at break, and tensile toughness were shown for the material sterilized with EO and low gamma doses. For high gamma doses, a minor decrease of strain at break of 2% was observed, while even slightly higher strength was shown. Again, this proves that the excellent mechanical properties are not negatively influenced by any applied sterilization method. The summarized data can be found in Table 26.

Table 26: Detailed results of the tensile tests.

monomer	sterilization	σ_M [MPa]	ϵ_B [%]	U_T [MJ/m³]
VDB	Ref.	67.0 ± 0.1	11.0 ± 1.1	4.7 ± 0.6
	EO	71.7 ± 1.8	11.2 ± 1.2	5.2 ± 0.7
	low γ	71.1 ± 1.0	12.6 ± 1.7	5.9 ± 0.9
	high γ	68.1 ± 0.8	9.4 ± 1.2	4.0 ± 1.2

These studies showed that sterilization of the material containing the novel boronic ester and the thiol TMT via all applied gaseous or radiation techniques does not significantly influence the mechanical properties of the materials, and high glass transition temperatures, strengths and toughness of the network was maintained after sterilization, even with high doses of gamma irradiation. These results are highly promising, as sterilization of scaffolds is crucial before applications of this material *in vivo*.

2.9 Evaluation of cytotoxicity

Photopolymers, which should be used *in vivo*, comprise the risk of releasing unreacted monomers into their surrounding media. Therefore, it is of significant interest how the network building blocks influence cell viability, proliferation, and differentiation.^{69,70,112} Literature showed good biocompatibility of polymers containing phosphoesters, silyl ethers, or boronic esters^{57,62,209-212,233} To finally confirm these reports, the *in-vitro* cytotoxicity of the most important monomers and the thiol TMT was tested in NCTC Clone 929 fibroblast cell culture using a Presto[®] Blue Assay at Vienna Medical University.

For this assay, substances that should be subjected to the test are dissolved in DMSO to obtain solutions with concentrations of 10 mM, 7.5 mM, 5 mM, and 2.5 mM. The cells are then treated with each solution and are incubated at 37 °C for 24 h. The supernatant solution is removed, and blue-colored and non-fluorescent resazurin is added to the cells. This compound is taken up by healthy cells and reduced intracellularly to bright red and fluorescent resorufin (Figure 137). The fluorescence intensity is then determined by fluorometry, and the concentration, at which 50% of the cells are still viable after the incubation time (EC_{50}) is used to evaluate the cytotoxicity of the compounds. The photoinitiator Ivocerin used in the studies was not tested, as non-cytotoxicity was already confirmed by Ivoclar Vivadent.¹³⁰ Low cytotoxicity of the absorber QY used for 3D - printing was confirmed by Orman *et al.*¹⁹⁴

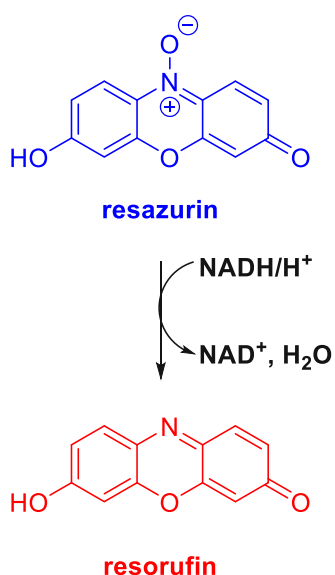


Figure 137: Principle of the Presto[®] Blue Assay.

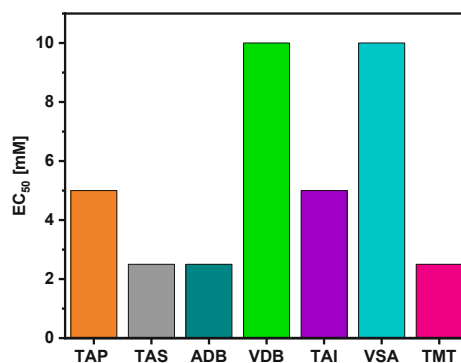


Figure 138: EC₅₀ for the compounds TAP (orange), TAS (grey), ADB (teal), VDB (green), TAI (purple), VSA (cyan), and TMT (pink) after incubation of cells for 24 h at 37 °C.

Figure 138 shows that all compounds exhibit EC₅₀ values from 2.5 to 10 mM. Therefore, compared to low molecular weight (meth)acrylates, *i.e.*, 1,4-butane-diol diacrylate and 1,4-butanediol dimethacrylate with reported EC₅₀ of <0.16 mM and 1.3 mM⁵⁹, all tested compounds demonstrated significantly better tolerance by the cells. This clearly shows that all monomers and thiols used within these studies exert sufficiently low toxic effects on the fibroblast cells, and residual monomers within the networks should not pose a problem *in vivo*. Noteworthy, the novel boronic ester VDB is less toxic than the methacrylate reference by a factor of 8 and even two orders of magnitude less toxic than 1,4-butanediol diacrylate. Furthermore, its EC₅₀ is as high as for the reference VSA (10 mM), which further supports the excellent biocompatibility of this compound, as VSA is patented for several biomedical applications.^{197,198}

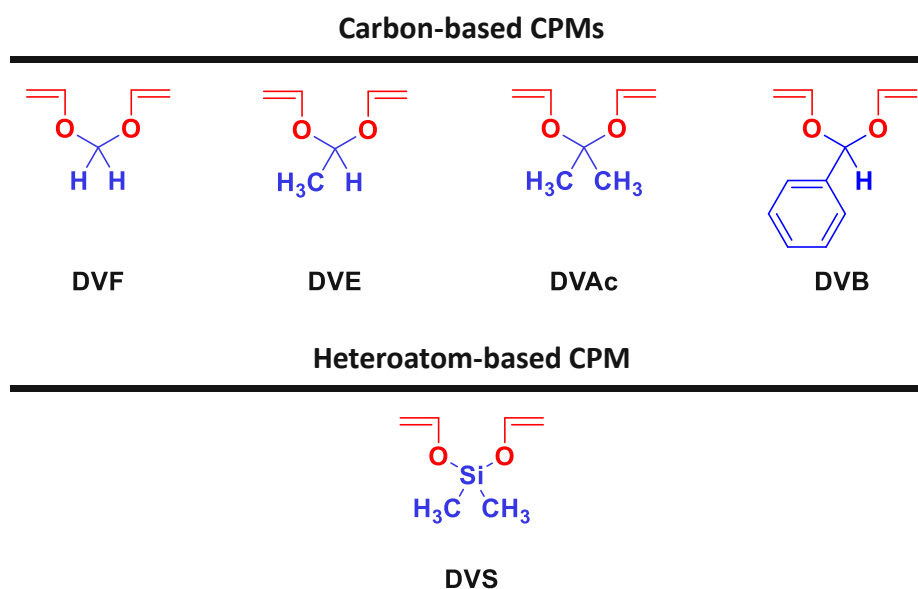
Summary

Bone fractures comprise a global health issue, with 178 million new fractures reported worldwide in 2019, which translates to an increase of 33% since 1990.³⁵⁷ In the case of bone defects exceeding a critical size caused by trauma, infection, or tumors, the process of bone regeneration cannot be accomplished, and additional support structures in the form of three-dimensional scaffolds are required, serving as an osteoinductive, osteoconductive and osteogenic platform, while also displaying sufficient mechanical properties for good tissue integration. Additionally, biodegradability of the temporary support is needed, with degradation rates matching the speed at which bone regenerates and degradation occurring via surface erosion to prevent abrupt implant failure. Formed cleavage products should be low molecular weight compounds that are non-toxic, easily metabolized, and excreted from the body. During the last decades, lithography-based additive manufacturing technologies (L-AMTs) have emerged as a potent strategy for producing 3D-cellular biocompatible and biodegradable scaffolds in bone tissue engineering (BTE), as feature sizes and surface topology of printed constructs were shown to be beneficial for the bone regeneration process. Nevertheless, state-of-the-art photopolymers derived from (meth)acrylates display certain disadvantages, such as significant cytotoxicity of residual monomers and undesirable degradation leading to implant disintegration and the release of high molecular weight acids causing inflammation or even necrosis. Our group has since developed a broad range of new monomers based on vinyl esters, vinyl carbamates, and vinyl carbonates with significantly reduced cytotoxicity. However, while good biocompatibility and no autocatalytic bulk erosion of implanted scaffolds were determined in *in vivo* studies, the degradation speed of all photopolymers was insufficient to match the rate at which bone tissue regenerates. Additionally, printed structures exhibited poor mechanical properties, such as high shrinkage, brittleness, and low strength, further limiting their use as bone replacement materials. Therefore, despite almost three decades of research, only a few materials have made it into animal studies, and no human applications have been reported so far.

The aim of this thesis was the development of novel small molecule building blocks for the generation of polymer networks that combine superior mechanical properties with improved degradation behavior compared to state-of-the-art materials. This was tried by using two general strategies:

- 1) Novel cyclopolymerizable monomers containing degradable motifs
- 2) New monomers and thiols containing heteroatoms

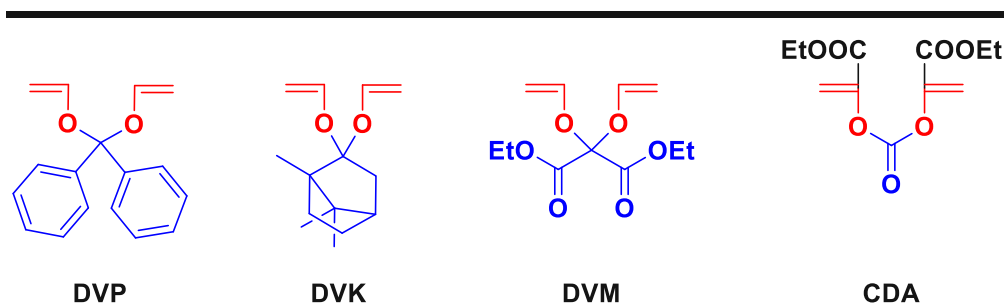
In the **first chapter**, cyclopolymerizable monomers (CPMs) were extensively studied. Due to the intra-intermolecular propagation mechanism resulting in the formation of cyclic structures along the polymer backbone, cyclopolymerization of di- or higher-functional CPMs presents an intriguing approach for generating networks with superior mechanical properties. Additionally, owing to the variability of the center atom, these compounds allow for the integration of degradable motifs into the structures for enhanced degradation characteristics. As a polymerizable motif of target CPMs, non-homopolymerizable vinyl ether groups were selected for increased cyclopolymerization tendency. As hydrolytically labile groups, acetals and carbonates were chosen, which are cleavable under acidic conditions present during bone remodeling without forming acidic hydrolysis products. As a second approach to improve network degradation, the replacement of the center carbon with heteroatoms, including phosphorus, silicon, and boron, was studied. This strategy was selected due to the possible formation of less stable bonds to oxygen compared to carbon. Additionally, low-toxic and less acidic degradation products, in the form of phosphoric acids, silanols, and boronic acids, should be formed upon hydrolysis. As a starting point, a library of different carbon- and heteroatom-based CPMs with degradable moieties was synthesized, and their tendency towards both radical and cationic cyclopolymerization was determined in order to abstract the essential features necessary for efficient cyclopolymerization.



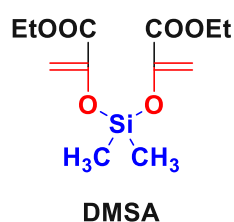
It was shown that cyclopolymerization efficiency was very low with radical initiators, and although no gelation was observed for all formulations, only soluble oligomers with low molecular weight (<3.2 kDa) were formed. With cationic initiators, crosslinking instead of cyclopolymerization was shown for most compounds due to the high reactivity of vinyl ethers towards cationic

homopolymerization. For the few compounds that did not display gelation, oligomeric structures of even lower molecular weight (<1.1 kDa) were formed. Additionally, upon irradiation, monomers and the forming polymer network were cleaved by the acidic initiating species. Therefore, cationic cyclopolymerization of compounds containing these degradable moieties was not pursued further, and the synthesis of novel target structures with increased radical cyclopolymerization tendency was conducted. For this, the envisioned CPMs contained either bulky substituents at the center carbon or electron-withdrawing groups attached to the double bonds.

Carbon-based CPMs



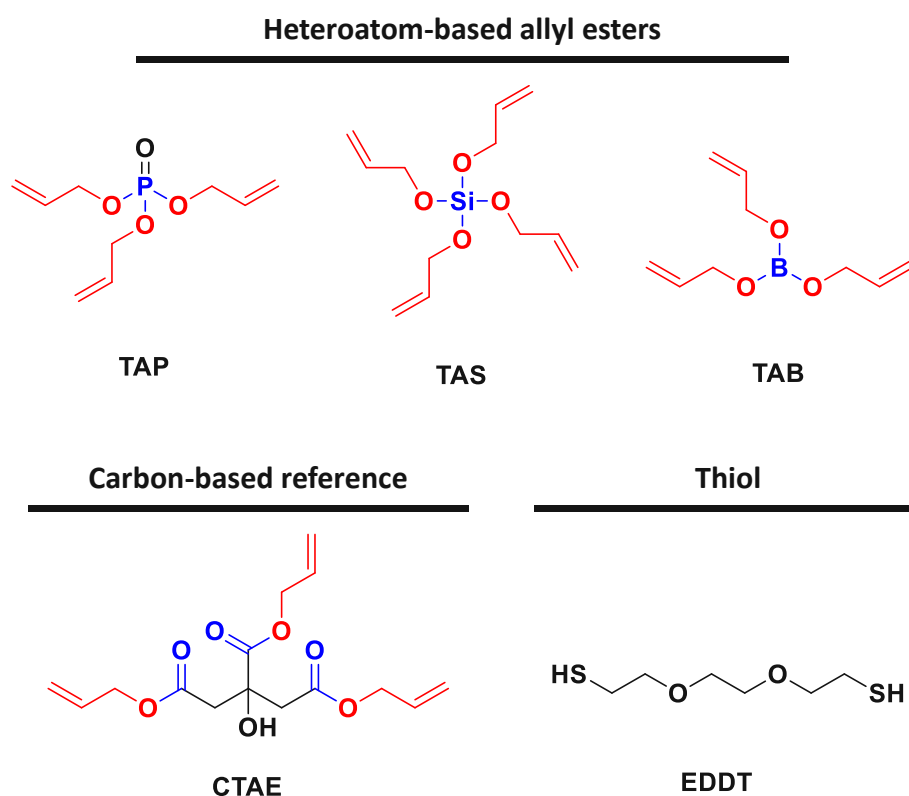
Heteroatom-based CPM



Unfortunately, all the synthetic attempts failed due to the spontaneous polymerization of compounds, possibly by a group transfer mechanism or too high steric hindrance at the center carbon, causing an equilibrium shift towards the starting materials. Therefore, this approach, to use di- or higher functional CPMs containing degradable motifs at the center atom to generate cleavable, rigid networks comprising cyclic structures, was not pursued further.

In the **second chapter**, novel monomers for the generation of networks with improved mechanical properties and degradation were investigated. As state-of-the-art monomers, such as vinyl esters, typically contain ester groups that form undesirable acidic hydrolysis products, the focus again was on compounds containing previously used heteroatom-oxygen bonds. As polymerizable groups, allyl ethers or esters of the respective heteroatom-containing acids were chosen, which should be subjected to thiol-ene photopolymerization in order to form homogeneous and tough networks due to the quasi-ideal reaction with thiols. As a starting point, the simplest, commercially

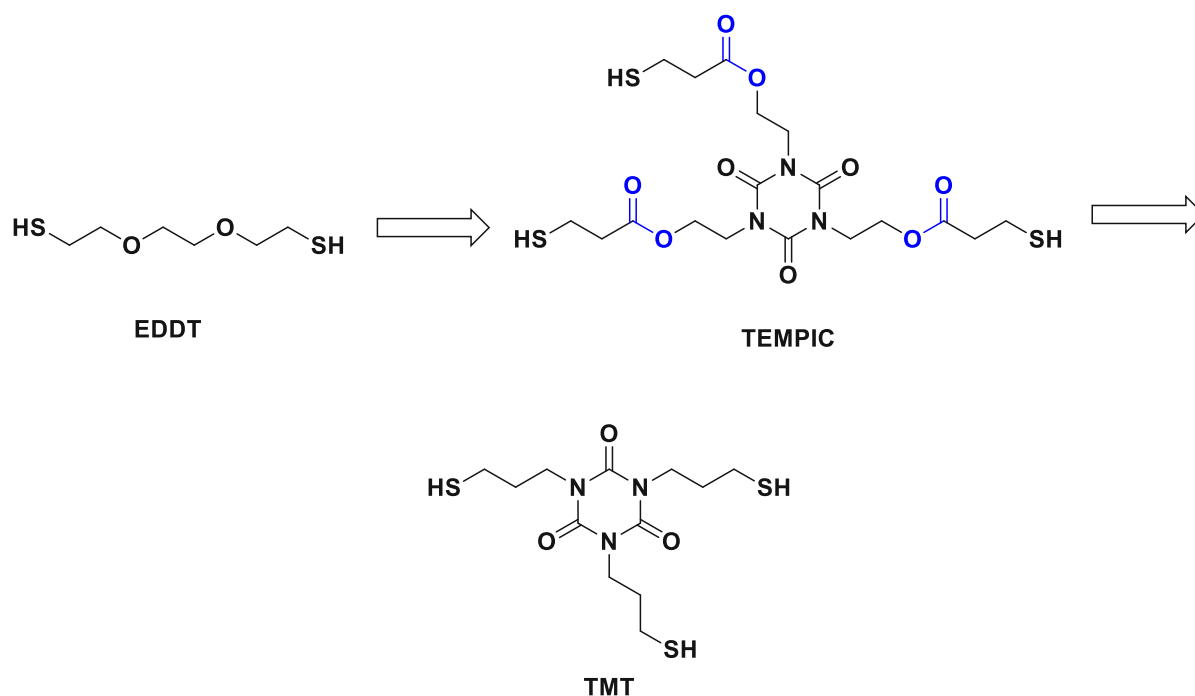
available allyl esters of phosphoric (triallyl phosphate, TAP), orthosilicic (tetraallyl orthosilicate, TAS), and boronic acid (triallyl borate, TAB) were chosen, and the tendency of these monomers and resulting polymer networks, formed with the non-degradable thiol 2,2'-(ethylenedioxy)diethanethiol (EDDT), towards hydrolysis was investigated via NMR and degradation studies under physiological (pH=7.4), acidic (pH=4) and basic conditions (pH=10) and compared to a carbon-based reference compound (citric acid triallyl ester, CTAE) and its respective networks.



For the P- and C-based networks, no degradation under these hydrolytic conditions was determined, showing that these bonds are too stable to accelerate network cleavage. The fastest degradation was observed with the material based on the boronic ester monomer TAB with full dissolution after 24 h. Furthermore, with the network based on the orthosilicate TAS, negligible swelling combined with a fast mass loss over 6 months was determined. Therefore, orthosilicic and boronic ester monomers improved network degradation compared to carbon-based allyl esters.

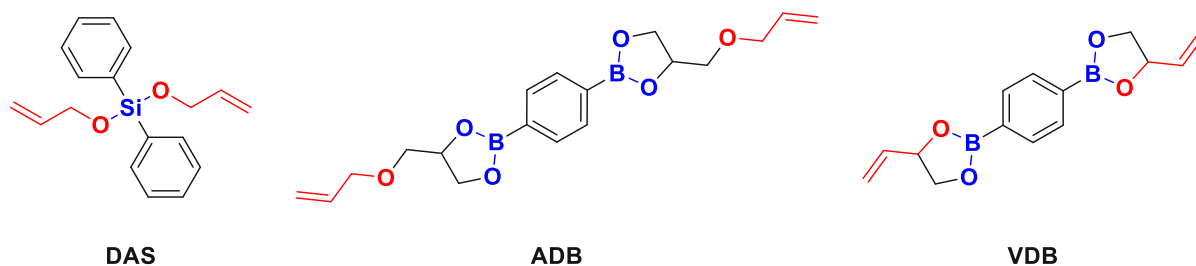
Nevertheless, all tested networks derived from these monomers and the thiol EDDT exhibited rather poor mechanical properties, including glass transition temperatures significantly below body temperature (-28 to -64 °C), limiting their use in bone replacement materials. Therefore, optimization of the thiol structure was conducted, which showed that a trifunctional thiol with a

rigid core, such as tris[2-(3-mercaptopropionyloxy)-ethyl] isocyanurate (TEMPIC) results in the best thermomechanical properties of resulting materials. As TEMPIC, like most commercial thiols, contains undesired ester groups, which may form acidic cleavage products, the trifunctional and rigid thiol 1,3,5-tris(3-mercaptopropyl)-1,3,5-triazine-2,4,6-trione (TMT) was successfully synthesized, resulting in a significant improvement of the thermomechanical properties of all materials, with an average increase in glass transition temperature by 77 °C.



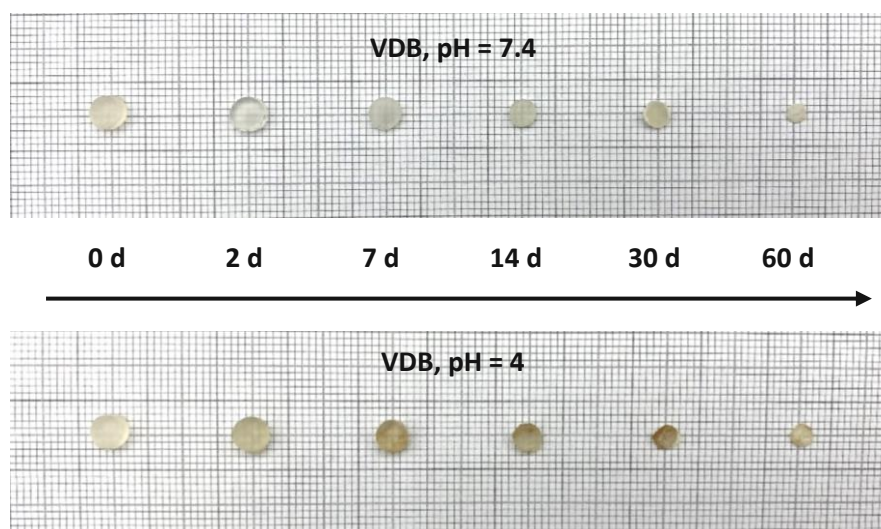
To further increase important properties, such as strength and stiffness, also heteroatom-based monomers containing rigid elements, such as bulky substituents or (spiro)cyclic structures, were synthesized. While the synthesis of cyclic P- and Si-based compounds was unsuccessful due to the high steric hindrance at the heteroatom, causing the considerable formation of side-products or premature polymerization of the monomers during synthesis or storage, compounds containing silicon- or boron-oxygen bonds with bulky substituents and in the case of boron also cyclic monomers could successfully be obtained. Synthesized compounds included, among others, the Si-based monomer bis(allyloxy)diphenylsilane (DAS). Additionally, the more flexible boronic ester 1,4-bis(4-((allyloxy)methyl)-1,3,2-dioxaborolan-2-yl)benzene (ADB), was synthesized, known from literature to undergo thiol-ene photopolymerization and formation of polymers capable of self-healing, reprocessing, and shape memory, but never applied in terms of improving network degradation. Inspired by this compound, the more rigid and previously unknown boronic ester 1,4-bis(4-vinyl-1,3,2-dioxaborolan-2-yl)benzene (VDB) was also synthesized. Remarkably, these monomers can be obtained in near quantitative yields in economically-friendly solvents, such as THF, under mild conditions (24 h stirring at rt).

Rigid monomers containing heteroatoms



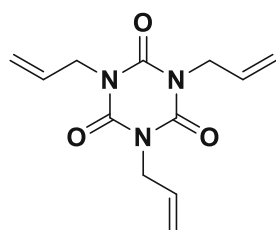
All formulations were subsequently investigated for their photoreactivity by RT-NIR photorheology studies in combination with the thiol TMT, revealing high crosslinking and curing speeds for all samples, except for the formulation containing DAS, which did not polymerize, probably due to hyperconjugation of the silicon atom with the aromatic rings. Therefore, this compound was not studied further. Especially for the formulations containing the boronic esters, exceptionally low shrinkage (-2 to -9 N) was observed due to the reversible boronic ester bonds that reopen and close during the network formation, enabling their use as potent shrinkage-reducing agents. The resulting polymer networks were then examined for their (thermo)mechanical properties. Due to the quasi-ideal reaction of these compounds with thiols, unprecedented high network homogeneity (fwhm: 9-17 °C) was determined for all materials, unlike for state-of-the-art vinyl esters and vinyl carbonates, which also display a significant amount of homopolymerization. Furthermore, the importance of highly rigid monomer structures to produce networks with mechanical properties sufficient for the replacement of human bone was demonstrated. With rather flexible monomers, such as CTAE, TAP, TAS, and ADB, networks with low glass transition temperature, strength, and high strain at break were obtained, while only with rigid VDB superior mechanical properties were shown, combining high glass transition temperature (70 °C), storage modulus ($G'_{25^\circ\text{C}} = 1340 \text{ MPa}$), tensile strength (67 MPa) and toughness (5 MJ/m³).

Degradation studies revealed that for this material also, the best degradation behavior was observed, as no significant swelling and an immediate onset of degradation was shown under physiological and acidic conditions, with an exponential decay in mass and an erosion of 80-90% after 2 M. Furthermore, the samples displayed a general retention of the shape, decreasing in size as a function of time, which is characteristic of the desired surface erosion process. This demonstrated the importance of the good mechanical properties of this material for enhanced degradation behavior, preventing creep of the material, and the diffusion of water into the samples, which confines hydrolysis to the surface.

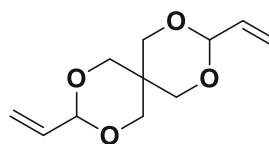


To further optimize processing and curing temperatures of the formulation containing VDB, which required a temperature of 100 °C, and (thermo)mechanical properties of the polymer networks containing flexible TAS and ADB, triallyl isocyanurate (TAI) was added as a rigid, trifunctional crosslinker and formulations were prepared, with molar ratios of 40 mol%, 60 mol%, or 80 mol% of each degradable monomer with respect to TAI, and the thiol TMT in an equimolar ratio of double bonds to thiol groups. Formulations containing up to 60 mol% of VDB could then be processed at room temperature, and for networks derived from the flexible monomers TAS or ADB, a significant improvement of the (thermo)mechanical properties was observed upon TAI addition. Unfortunately, a deteriorated degradation behavior with significant swelling (up to >100%) was determined for all materials due to the formation of a non-degradable subnetwork by trifunctional TAI and the trifunctional thiol TMT. To prevent the formation of these subnetworks, the functionality of the non-degradable monomer was reduced, and the rigid, difunctional crosslinker 3,9-divinyl-2,4,8,10-tetraoxaspiro(5.5)undecane (VSA) was utilized to optimize the materials further. To maintain an equal concentration of degradable bonds within the formed networks, again molar ratios of 40 mol%, 60 mol%, or 80 mol% of degradable monomer with respect to VSA were chosen for these studies, which led to improved processing temperatures of formulations and significantly increased glass transition temperatures, strength and stiffness for all materials. Additionally, degradation studies revealed that the formation of non-degradable subnetworks could be largely avoided, and the best results were obtained with the network formed from 80 mol% VDB, which combined a low processing temperature (room temperature), the best mechanical properties, reduced swelling (23-30%) and the highest erosion (40-65%) of the optimized systems after 6 M.

Rigid non-degradable crosslinkers



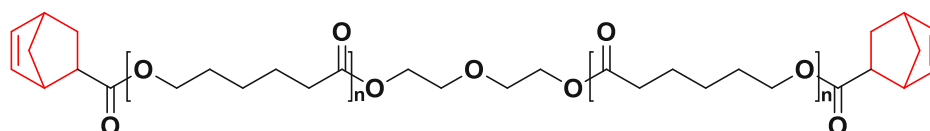
TAI



VSA

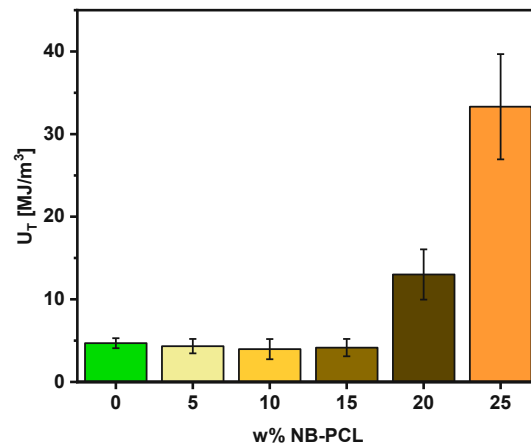
As the best symbiosis of mechanical properties and degradation characteristics was obtained with polymer networks derived from the boronic ester VDB in combination with TMT, without the formation of any subnetworks, a high molecular weight additive was introduced into this formulation to further improve toughness and stress dissipation of resulting materials. As covalent interactions of toughness enhancers with the polymer matrix were previously shown to result in the highest obtainable toughness, the additive poly(caprolactone) (NB-PCL), with a molecular weight of 45 kDa, modified with polymerizable end groups was selected. As polymerizable groups, norbornene moieties were chosen, as they display higher reaction rates with thiols than allyl esters, which should result in better incorporation into the network and, therefore, higher toughness of resulting polymers.

Toughness enhancer

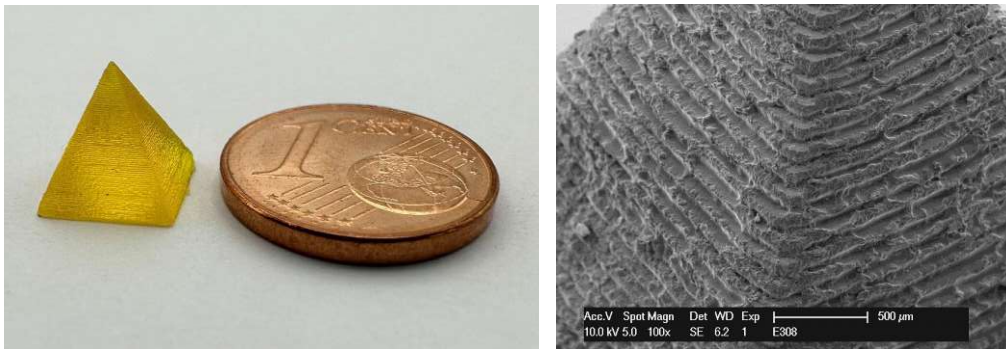


NB-PCL
45 kDa
5-25 w%

5-25 w% of toughness enhancer were added to the formulation, and rheology studies of all resulting formulations revealed that viscosities below 20 Pa·s necessary for 3D-printing were maintained. Most importantly, upon the addition of up to 25 w% of this additive, sufficiently high glass transition temperatures, strengths, and stiffness for the use as bone replacement materials were sustained, while elongations at break could be substantially increased. Therefore, an exceptional increase in tensile toughness was determined for the materials containing 20 w% and 25 w% of the toughness enhancer, which was higher by a factor of 3 or even 7 compared to the material without additive, respectively.



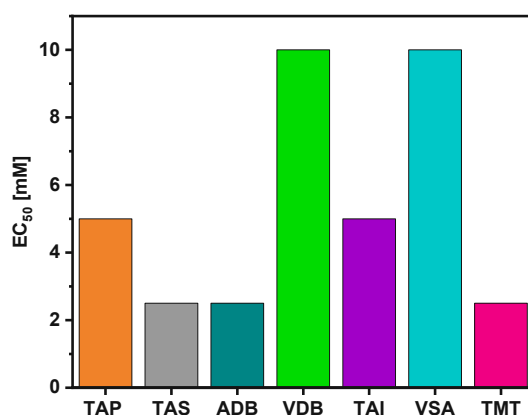
As a proof of concept and to confirm the applicability of this degradable system in the production of patient-specific implants, 3D structuring of the formulation containing VDB and the thiol TMT was conducted below the T_g (at 55 °C). High resolutions of the printed structure due to the spatiotemporal selectivity of the photocuring reaction and lack of light-induced or diffusional over-polymerization were confirmed by SEM measurements. Most importantly, due to the exceptional mechanical properties, especially the high T_g of the formed polymer, no creep or disruption of the structure during the printing process was determined. Therefore, no addition of a static crosslinker for dimensional stability was necessary, as previously reported for the 3D printing of resins containing boronic esters. Hence, as a first group, we could apply a pure thiol-boronic ester-resin in Laser-SLA, which showed the great potential of this degradable thiol-ene system in the future fabrication of patient-specific, biodegradable scaffolds.



As sterilization of scaffolds is crucial before applications *in vivo*, samples were sterilized by KLS Martin via radiation curing with high (~31 kGy) and low gamma doses (~18 kGy) and by subjection to gaseous ethylene oxide (55 °C, 2 h). It was shown that the polymer network was not influenced by any sterilization method, as no significant impact on glass transition temperature, storage modulus, tensile strength or strain at break was determined. For the sterilization with ethylene oxide, even a slight improvement of (thermo)mechanical properties was observed (*i.e.*, T_g

increased by 5 °C), explained by a certain network rearrangement at the sterilization temperature of 55 °C, reducing material flaws and internal stress. This showed that sterilization does not influence the mechanical properties of the materials, and even high doses of gamma irradiation can be applied; hence full sterility of implants can be guaranteed for future applications.

Lastly, to confirm the low cytotoxicity of the most promising compounds, the *in-vitro* cytotoxicity was tested in NCTC Clone 929 fibroblast cell culture using a Presto® Blue Assay at the Vienna Medical University. All compounds exhibited significantly higher concentrations, at which 50% of the cells are still viable after the incubation time (EC_{50}) compared to (meth)acrylates, such as 1,4-butane-diol diacrylate and 1,4-butanediol dimethacrylate ($EC_{50} = <0.16$ mM and 1.3 mM⁵⁹). Noteworthy, the highest cell tolerance was determined for the novel boronic ester VDB ($EC_{50} = 10$ mM), which was less toxic by a factor of 8 and even two orders of magnitude less toxic than these compounds. Additionally, it displayed an EC_{50} as high as the reference VSA, which is already patented for several biomedical applications. This clearly shows the high biocompatibility of this compound, and that residual monomers should not pose a problem in future *in vivo* applications.



To conclude, thiol-ene photopolymerization of boronic ester monomers presents a powerful strategy to include hydrolyzable crosslinks into polymer networks. Besides easy synthesis of these compounds, they display significantly lower cytotoxicity compared to (meth)acrylates and sufficiently high photoreactivity for 3D printing. Compared to state-of-the-art methacrylate-based systems, a combination of improved mechanical properties such as low shrinkage, high strength, toughness, and degradation behavior is achievable with boron-oxygen bonds and careful monomer design. Especially rigid boronic ester monomers, such as the newly-synthesized VDB, are suitable degradation-enhancers, with derived networks displaying accelerated degradation via surface erosion under physiological and acidic conditions present during bone remodeling.

Experimental Part

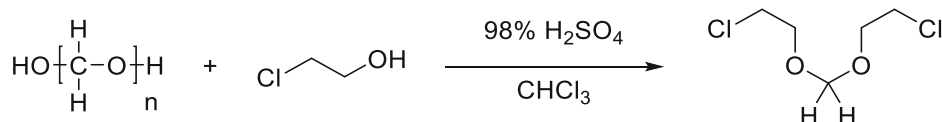
1. Novel cyclopolymerizable monomers for enhanced mechanical properties and network degradation

1.1 Cyclopolymerizable model compounds

1.1.1 Synthesis of carbon-based model compounds

1.1.1.1 Synthesis of divinyl formal (DVF)²⁹⁰

1.1.1.1.1 Synthesis of bis(2-chloroethyl)formal (CEF)



chemicals	M [g/mol]	eq.	n [mmol]	m [g]	V [mL]
paraformaldehyde	30.03	0.7	500	15.0	
2-chloroethanol	80.51	2.2	1571	88.6	
98% H ₂ SO ₄	98.08	0.08	57	5.7	
CHCl ₃					100

The synthesis of bis(2-chloroethyl)formal (CEF) was carried out according to Jian *et al.*²⁹⁰ Therefore, 98 % sulfuric acid was added to a flask containing a mixture of paraformaldehyde, 2-chloroethanol, and distilled chloroform as a solvent at rt. A water separator and a reflux condenser were attached to the flask, and the reaction mixture was heated and stirred until the evolution of water ceased (48 h). The resulting darkened brown solution was cooled to rt and washed two times with 300 mL of water containing 10 g of Na₂CO₃. The organic layer was separated and dried with anhydrous Na₂SO₄. Chloroform was removed, and the remaining yellow to brown liquid was distilled under vacuum (85 °C/10 mbar) to afford bis(2-chloroethyl)formal (CEF) as a colorless liquid in a yield of 40 %.

Yield: 101.5 g colorless liquid (40% theoretical yield)

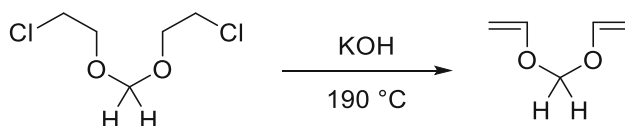
b.p.: 85 °C/10 mbar (Lit.: 60 °C/1.9 mbar²⁹⁰)

RI: 1.4558 (Lit.²⁸⁴ 1.4558)

^1H NMR (400 MHz, CD_2Cl_2): δ 4.79 (s, 2H, OCH_2O), 3.93 – 3.78 (m, 4H, $\text{OCH}_2\text{CH}_2\text{Cl}$). 3.78 – 3.59 (m, 4H, $\text{OCH}_2\text{CH}_2\text{Cl}$).

^{13}C NMR-APT (101 MHz, CD_2Cl_2): 95.70 (OCH_2O), 68.31 ($\text{OCH}_2\text{CH}_2\text{Cl}$), 43.26 ($\text{OCH}_2\text{CH}_2\text{Cl}$).

1.1.1.1.2 Synthesis of divinyl formal (DVF)



chemicals	M [g/mol]	eq.	n [mmol]	m [g]	V [mL]
bis(2-chloroethyl)formal	173.03	1.0	116	20.0	-
KOH	56.11	12.0	1387	77.8	-

The synthesis of divinyl formal (DVF) was carried out according to Jian *et al.*²⁹⁰ For this, bis(2-chloroethyl)formal) was added to a flask containing finely ground potassium hydroxide at rt. A 20 cm Vigreux column was attached to it, and the mixture was stirred and heated to 190 °C for 8 h. Divinyl formal, the side product 2-chloroethyl vinyl formal, and water were distilled off spontaneously from the reaction mixture with a vapor temperature ranging from 60-150 °C. The mixture was extracted with 3x100 mL diethyl ether, dried over anhydrous Na_2SO_4 , and the solvent was removed up to a pressure of 500 mbar. According to NMR, about 40 % of DVF and 60 % of CEVF were formed. DVF was redistilled through a Vigreux column at 82 °C and 800 mbar as a colorless liquid.

Yield: 2.54 g colorless liquid (21% theoretical yield)

b.p.: 82 °C/800 mbar (Lit.²⁹⁰ 90 °C/atm. pressure)

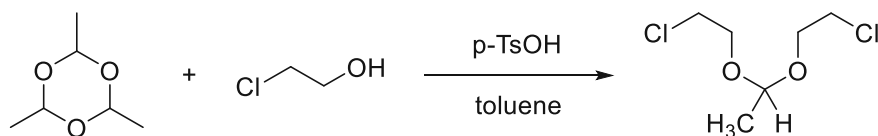
RI: 1.4157 (Lit.²⁸⁷ 1.4158)

^1H NMR (400 MHz, CD_2Cl_2): δ 6.40 (dd, $J = 14.1, 6.6$ Hz, 2H, $\text{OCH}=\text{CH}_2$), 5.10 (s, 2H, OCH_2O), 4.49 (ddd, $J = 14.1, 1.9, 0.5$ Hz, 2H, $\text{OCH}=\text{CH}_2$), 4.19 (ddd, $J = 6.6, 1.9, 0.5$ Hz, 2H, $\text{OCH}=\text{CH}_2$).

^{13}C NMR-APT (101 MHz, CD_2Cl_2): δ 149.84 ($\text{CH}_2=\text{CHO}$), 92.93 (OCH_2O), 91.98 ($\text{CH}_2=\text{CHO}$).

1.1.1.2 Synthesis of divinyl ethanal (DVE)²⁸⁷

1.1.1.2.1 Synthesis of bis(2-chloroethyl)ethanal (CEE)



chemicals	M [g/mol]	eq.	n [mmol]	m [g]	V [mL]
paraldehyde	132.16	1.0	250	33.0	
2-chloroethanol	80.51	6.8	1710	137.7	
pTsOH	190.22	0.01	2.5	0.5	
toluene					300

The synthesis of bis(2-chloroethyl)ethanal (CEE) was carried out according to Matsuyan *et al.*²⁸⁷ Therefore, pTsOH was added to a flask containing a mixture of paraldehyde, 2-chloroethanol, and toluene as a solvent at rt. The flask was equipped with a water separator and a reflux condenser attached to a cryostat containing a 1:1 mixture of ethylene glycol and water, resulting in a temperature of -15 °C. The reaction mixture was heated to 110 °C and stirred for 7 days until the evolution of water ceased. The resulting darkened brown solution was cooled to rt and washed two times with 300 mL of water containing 10 g of Na₂CO₃. The organic layer was separated and dried with anhydrous Na₂SO₄. The solvent was removed, and the remaining dark brown liquid was distilled under vacuum (98 °C/12 mbar) to afford bis(2-chloroethyl)ethanal as a colorless liquid.

Yield: 42.53 g colorless liquid (63% theoretical yield)

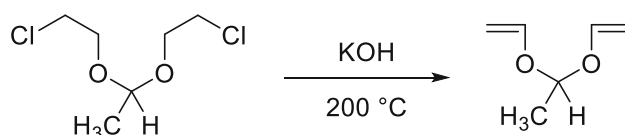
b.p.: 98 °C/12 mbar (Lit.²⁹⁰100-102 °C/14 mbar)

RI: 1.4157 (Lit.²⁸⁷ 1.4158)

¹H NMR (400 MHz, CD₂Cl₂): δ 4.86 (q, J = 5.4 Hz, 1H, OCH₂CH₃O), 3.99 – 3.59 (m, 8H, OCH₂CH₂Cl), 1.37 (d, J = 5.4 Hz, 3H, OCHCH₃O).

¹³C NMR-APT (101 MHz, CD₂Cl₂): δ 100.00 (OCHCH₃O), 65.24 (OCH₂CH₂Cl), 43.40 (OCH₂CH₂Cl), 19.47 (CH₃).

1.1.1.2.2 Synthesis of divinyl ethanal (DVE)



chemicals	M [g/mol]	eq.	n [mmol]	m [g]	V [mL]
bis(2-chloroethyl)formal	187.06	1	185	34.6	-
KOH	56.11	10	1850	103.8	-

The synthesis of divinyl ethanal (DVE) was carried out according to Matsuyan *et al.*²⁸⁷ Therefore, bis(2-chloroethyl)formal was added to a flask containing finely ground potassium hydroxide at rt. A Vigreux column was attached, and the mixture was stirred and heated to 200 °C for 8 h. The distillate was collected with a vapor temperature ranging from 75-150 °C and was then extracted with 3x100 mL diethyl ether, dried over anhydrous Na₂SO₄, and the solvent was removed to yield the pure product directly, without further purification necessary.

Yield: 10.5 g colorless liquid (25% theoretical yield)

b.p.: 98 °C/800 mbar (Lit.²⁹⁰100-102 °C/atm. pressure)

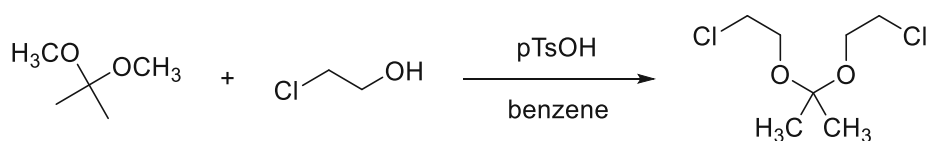
RI: 1.4178 (Lit.²⁸⁷ 1.4180)

¹H NMR (400 MHz, CD₂Cl₂): δ 6.42 (dd, J = 14.0, 6.5 Hz, 2H, OCH=CH₂), 5.36 – 5.15 (m, 1H, OCHCH₃O), 4.45 (ddd, J = 14.0, 1.5, 0.4 Hz, 2H, OCH=CH₂), 4.23 – 4.06 (m, 2H, OCH=CH₂), 1.49 – 1.32 (m, 3H, OCHCH₃O).

¹³C NMR-APT (101 MHz, CD₂Cl₂): δ 147.46 (CH₂=CHO), 99.14 (OCHCH₃O), 92.34 (CH₂=CHO), 20.04 (CH₃).

1.1.1.3 Synthesis of divinyl acetal (DVAc)²⁹⁴

1.1.1.3.1 Synthesis of bis(2-chloroethyl)acetal (CEA)



chemicals	M [g/mol]	eq.	n [mmol]	m [g]	V [mL]
2.2-dimethoxypropane	132.16	1	113	15.0	
2-chloroethanol	80.51	2.2	250	20.1	
pTsOH	190.22	0.01	1.4	0.3	
benzene					50

The synthesis of bis(2-chloroethyl)acetal (CEA) was carried out according to Lorette *et al.*²⁹⁴ Therefore, pTsOH was added to a flask containing a mixture of 2,2-dimethoxypropane, 2-chloroethanol, and benzene at rt. The reaction mixture was heated, and methanol and benzene were distilled off (about 25 mL in total with a boiling point not exceeding 57-60°C). The resulting solution was cooled to rt and 0.08 eq. NaOMe in 25 mL methanol were added rapidly for neutralization. Methanol was distilled off *in vacuo*, and the remaining red to brown liquid was distilled at 11 mbar to yield bis(2-chloroethyl)acetal at 100-102 °C.

Yield: 7.6 g colorless liquid (27% theoretical yield).

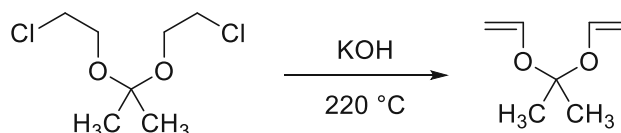
b.p.: 100-102 °C/11 mbar (Lit.²⁹⁴ 75 °C/3 mbar)

RI: 1.4512 (Lit.²⁹⁴ 1.4513)

¹H NMR (400 MHz, CD₂Cl₂): δ 3.77 – 3.69 (m, 4H, OCH₂CH₂Cl), 3.63 (dd, J = 5.2, 1.1 Hz, 4H, OCH₂CH₂Cl). 1.40 (s, 6H, CH₃).

¹³C NMR-APT (101 MHz, CD₂Cl₂): δ 61.67 (OCH₂CH₂Cl), 43.63 (OCH₂CH₂Cl), 25.00 (CH₃).

1.1.1.3.2 Synthesis of divinyl acetal (DVAc)



chemicals	M [g/mol]	eq.	n [mmol]	m [g]	V [mL]
bis(2-chloroethyl)acetal	201.09	1	75	15.0	-
KOH	56.11	10	747	41.9	-

The synthesis of divinyl acetal (DVAc) was carried out according to Lorette *et al.*²⁹⁴ For this, KOH was added to 1 eq. of bis(2-chloroethyl)acetal in a flask. A Vigreux column was attached to it, and the mixture was stirred and heated to 220 °C for 8 h. The resulting distillate was extracted with 3x100 mL diethyl ether, dried over anhydrous Na₂SO₄, and distilled *in vacuo* to remove the solvent. The remaining liquid was distilled at 400 mbar to afford divinyl acetal at 79-80 °C in a yield of 13 %.

Yield: 1.28 g colorless liquid (13 % theoretical yield)

b.p.: 79-80 °C/400 mbar (Lit.²⁸⁵ 101-104 °C/900 mbar)

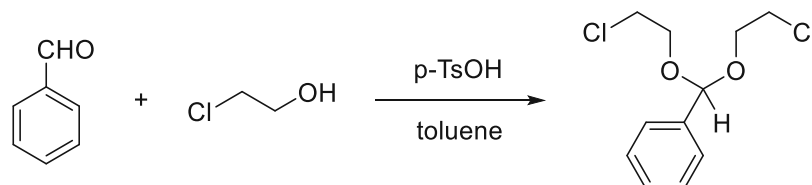
RI: 1.4199 (Lit.²⁸⁵ 1.4200)

$^1\text{H NMR}$ (400 MHz, CD_2Cl_2): δ 6.51 (dd, $J = 13.9, 6.3$ Hz, 2H, $\text{OCH}=\text{CH}_2$). 4.54 (dd, $J = 13.9, 1.0$ Hz, 2H, $\text{OCH}=\text{CH}_2$), 4.21 (dd, $J = 6.3, 1.0$ Hz, 2H, $\text{OCH}=\text{CH}_2$), 1.48 (s, 6H, CH_3).

$^{13}\text{C NMR-APT}$ (101 MHz, CD_2Cl_2): δ 144.51 ($\text{CH}_2=\text{CHO}$), 93.57 ($\text{CH}_2=\text{CHO}$), 25.68 (CH_3).

1.1.1.4 Synthesis of divinyl benzal (DVB)²⁸⁶

1.1.1.4.1 Synthesis of bis(2-chloroethyl)benzal (CEB)



chemicals	M [g/mol]	eq.	n [mmol]	m [g]	V [mL]
benzaldehyde	106.12	1.0	250	26.5	
2-chloroethanol	80.51	2.0	500	40.3	
pTsOH	190.22	0.01	4.0	0.6	
toluene					70

The synthesis of bis(2-chloroethyl)benzal (CEB) was carried out according to Matsuyan *et al.*²⁸⁶ First, for purification, prior to the synthesis, benzaldehyde was distilled at 58-62 °C and 13 mbar. pTsOH was added to a flask containing benzaldehyde, chloroethanol, and toluene. The flask was equipped with a water separator and a condenser, and the mixture was heated to 110 °C for 3 d. Toluene was removed, and the residue was treated with 25 mL 30% NaOH solution, washed with water (3x50 mL), extracted with diethyl ether (3x100 mL), dried over Na_2SO_4 , and the solvent was removed *in vacuo*. The remaining liquid was distilled to yield the product bis(2-chloroethylbenzal) (CEB) at 125-127 °C and 0.08 mbar.

Yield: 27.2 g colorless liquid (44% theoretical yield)

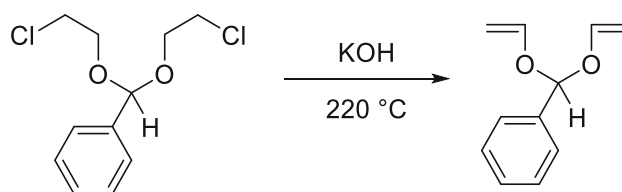
b.p.: 125-127 °C/0.08 mbar (Lit.²⁸⁶ 120-122 °C/1 mbar)

RI: 1.5131 (Lit.²⁸⁶ 1.5133)

$^1\text{H NMR}$ (400 MHz, CD_2Cl_2): δ 8.02 – 6.65 (m, 5H, Ar-H). 5.72 (s, 1H, OCHArO). 3.95 – 3.59 (m, 8H, $\text{OCH}_2\text{CH}_2\text{Cl}$).

$^{13}\text{C NMR-APT}$ (101 MHz, CD_2Cl_2): δ 101.53 ($\text{OC}_{\text{Ar}}\text{HO}$), 65.46 ($\text{OCH}_2\text{CH}_2\text{Cl}$), 43.31 ($\text{OCH}_2\text{CH}_2\text{Cl}$), 128.92 (C_{Ar}), 128.49 ($\text{C}_{\text{Ar}}\text{-H}$), 126.84 ($\text{C}_{\text{Ar}}\text{-H}$).

1.1.1.4.2 Synthesis of divinyl benzal (DVB)



chemicals	M [g/mol]	eq.	n [mmol]	m [g]	V [mL]
bis(2-chloroethyl)benzal	249.13	1	80	20.0	-
KOH	56.11	6	481	27.0	-

The synthesis of divinyl benzal (DVB) was carried out according to Matsuyan *et al.*²⁸⁶ For the synthesis, finely ground KOH was added to a flask containing bis(2-chloroethyl)benzal. A Vigreux column was attached to it, and the mixture was stirred and heated to 220 °C. The resulting distillate was collected over 8 h and then further extracted with diethyl ether (3x100 mL), dried over anhydrous Na₂SO₄, and the solvent was removed. The remaining liquid was distilled *in vacuo* to afford divinyl benzal at 54-56 °C and 0.05 mbar.

Yield: 2.25 g colorless liquid (16 % theoretical yield)

b.p.: 54-56 °C/0.05 mbar (Lit.²⁸⁶ 95-96 °C/13 mbar)

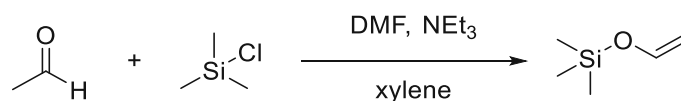
RI: 1.5141 (Lit.²⁸⁴ 1.5143)

¹H NMR (400 MHz, CD₂Cl₂): δ 7.60 – 7.33 (m, 5H, Ar-H). 6.48 (dd, J = 14.0, 6.5 Hz, 2H, OCH=CH₂), 6.06 (s, 1H, OCHArO), 4.60 (dd, J = 14.0, 1.7 Hz, 2H, OCH=CH₂), 4.24 (dd, J = 6.5, 1.7 Hz, 2H, OCH=CH₂).

¹³C NMR-APT (101 MHz, CD₂Cl₂): 147.53 (CH=), 129.31 (C_{Ar}), 128.63 (C_{Ar}-H), 126.74 (C_{Ar}-H), 100.47 (OCHArO), 93.00 (CH₂=).

1.1.1.5 Synthesis of divinyl carbonate (DVC)^{295,296}

1.1.1.5.1 Synthesis of vinyloxy trimethylsilan (VOTMS)



EXPERIMENTAL PART

chemicals	M [g/mol]	eq.	n [mmol]	m [g]	V [mL]
trimethylsilyl chloride	108.64	1	401	43.6	
acetaldehyde	44.10	2.5	995	43.9	
triethylamine	101.19	1.25	505	51.1	
DMF					100

The synthesis of vinyloxy trimethylsilan (VOTMS) was carried out according to Hofecker *et al.*²⁹⁵ For this, all used glassware was dried in an oven, evacuated, and flushed with argon several times. A three-necked flask was equipped with a condenser attached to a cryostat containing a 1:1 mixture of ethylene glycol and water. The cryostat temperature was set to -15 °C. The flask was topped with an argon pressure-leak system, a septum cap, and a dropping funnel and was successively charged with 100 mL dry DMF, NEt₃ (stored over a molecular sieve), and distilled trimethylsilyl chloride. Then cool acetaldehyde, which had previously been stored in the freezer, was slowly added over a period of 1.5 h to the mixture via a dropping funnel. After stirring for 1 week at ambient temperature, 50 mL of distilled xylene were added to the brown reaction slurry. At a pressure of 800 mbar, about 100 mL of the reaction mixture were distilled off with a boiling point ranging from 25-90 °C, while the bottom temperature was allowed to warm to a maximum of 135 °C. The distillate was diluted with 100 mL of xylene and washed with 100 mL of water three times. For neutralization of NEt₃, the organic phase was washed three times with 50 mL saturated NH₄Cl and twice with 50 mL saturated NaHCO₃. After drying over Na₂SO₄, the solution was distilled over a Vigreux column. The product was distilled at 60-69 °C and 830 mbar.

Yield: 21.43 g colorless oil (46 % theoretical yield)

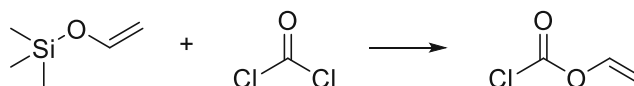
RI: 1.3889 (Lit.³⁵⁸ 1.3385)

b.p.: 60-69 °C/830 mbar (Lit.³⁵⁹ 71-73 °C/760 mbar)

¹H NMR (400 MHz, CDCl₃): δ (ppm) = 6.43 (1H, dd, J = 13.7, 5.9 Hz, CH₂=CH), 4.43 (1H, d, J = 13.7 Hz, CH₂=), 4.12 (1H, d, J = 5.9 Hz, CH₂=), 0.19 (9 H, s, (CH₃)₃).

¹³C NMR-APT (101 MHz, CDCl₃): δ (ppm) = 146.35 (CH₂=CHO), 95.18 (CH₂=CHO), 2.42 (CH₃).

1.1.1.5.2 Synthesis of vinyl chloroformate (VCF)



chemicals	M [g/mol]	eq.	n [mmol]	m [g]	V [mL]
VOTMS	116.24	1	122	14.3	
phosgene (20 w% solution in toluene)	98.91	1	122	12.1	
adiponitrile					60

The synthesis of vinyl chloroformate (VCF) was carried out according to Hofecker *et al.*²⁹⁵ For this, adiponitrile was distilled *in vacuo* (b.p. 103 °C/0.04 mbar) for purification. To a dried three-neck round bottom flask equipped with a condenser (cryostat adjusted to -15 °C), magnetic stirring, and a dropping funnel, VOTMS and adiponitrile were added. Afterward, PdAc₂ was added to the reaction mixture. The reaction apparatus was purged with argon, and the mixture was cooled to -4 °C with an ice bath containing NaCl. After 30 min of stirring at that temperature, phosgene was added as a 20 w% solution in toluene to the dropping funnel, which was prefilled with 40 mL adiponitrile. The solution was added dropwise over a period of 1 h. After complete addition, the cooling bath was removed, allowing the reaction mixture to warm to rt. After 72 h of stirring, the reaction mixture was purged with argon to remove residual phosgene. To determine if any phosgene was left in the mixture, test strips were prepared as described in 1.1.1.5.3. After the complete removal of phosgene, the mixture containing the catalyst was transferred to a one-necked flask and the product in a toluene solution was distilled over a 20 cm Vigreux column, with a boiling point of the distillate ranging from 50-80 °C.

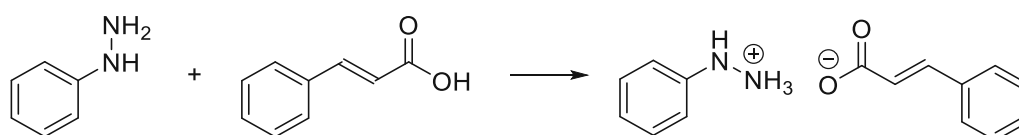
Yield: 27.5 g of 23% vinyl chloroformate in toluene solution (55% theoretical yield)

b.p.: 50-80 °C/atm. pressure (Lit.²⁹⁶ 66-68 °C/760 mbar)

¹H NMR (400 MHz, CDCl₃): δ (ppm) = 7.08 (1 H, dd, J = 6.05 Hz, J = 13.74 Hz, CH₂=CH), 5.07 (1 H, dd, J = 2.70 Hz, J = 13.74 Hz, trans-CH₂=), 4.77 (1 H, dd, J = 2.70 Hz, J = 6.05 Hz, 2x cis-CH₂=).

¹³C NMR-APT (101 MHz, CDCl₃): δ (ppm) = 148.34 (C=O), 142.63 (CH₂=CH), 100.87 (CH₂).

1.1.1.5.3 Phosgene test strips



chemicals	M [g/mol]	eq.	n [mmol]	m [g]	V [mL]
phenylhydrazine	108.14	1	50	5.0	
acetaldehyde	148.16	1	50	6.9	
toluene					50

The synthesis of the phosgene test strips was conducted as described by Schnöll *et al.*³²⁹ Therefore, phenyl hydrazine and cinnamic acid were each dissolved in toluene. The immediately formed off-white solid was washed with PE, recrystallized from toluene, and dried *in vacuo*. To determine whether phosgene was still present in reaction mixtures, a filter paper was drenched in 1 w% solution of CuSO₄ and dried. The white salt of phenylhydrazine and cinnamic acid was rubbed onto the paper, and after removal of excess of the solid, the reaction mixture was applied. After the solvent of the reaction solution was evaporated, a slight amount of water was added. If phosgene is present a reddish-to-violet spot forms on the filter paper.

1.1.2 Synthesis of heteroatom-based model compounds

1.1.2.1 Synthesis of bis 2-(vinylloxy)dimethylsilane (DMSA)²⁹⁵



chemicals	M [g/mol]	eq.	n [mmol]	m [g]	V [mL]
dichlorodimethylsilane	129.06	1	400	51.6	
acetaldehyde	44.10	5	1990	87.8	
triethylamine	101.19	2.5	1010	102.2	
DMF					200

The synthesis of bis 2-(vinylloxy)dimethylsilane (DMSA) was carried out according to Hofecker *et al.*²⁹⁵ For the synthesis, a 1000 mL three-necked flask was equipped with a condenser connected to a cryostat (adjusted to -15°C), a septum cap, and a dropping funnel. The flask was successively charged with 200 mL dry DMF, NEt₃ (stored over a molecular sieve), and distilled dichlorodimethylsilane. Then acetaldehyde was slowly added to the mixture over a period of 1.5 h via dropping funnel, which had previously been stored in the freezer. After stirring for 1 week at ambient temperature, 100 mL of distilled xylene was added to the brown reaction slurry. At a pressure of 400 mbar about 200 mL of the reaction mixture were distilled off with a boiling point ranging from 25-140 °C. The distillate was diluted with 50 mL of xylene and washed thrice with

200 mL of water. For neutralization of NEt_3 , the organic phase was washed three times with 100 mL saturated NH_4Cl solution and twice with 100 mL saturated NaHCO_3 solution. After drying over Na_2SO_4 , the solution was distilled over a Vigreux column. The product **was** distilled at 75-93 °C and 400 mbar. NMR showed that xylene was still present in the distillate; hence the product was redistilled to yield the pure product at 78-80 °C and 400 mbar.

Yield: 25 g of colorless liquid (26% theoretical yield).

b.p.: 78-80 °C/400 mbar (Lit.³⁶⁰ 109-110 °C/atm.pressure)

RI: 1.4064 (Lit.³⁶⁰ 1.4063)

R_f: 0.7 (PE:EE=4:1)

¹H NMR (400 MHz, CDCl_3): δ 6.45 (dd, $J = 13.7, 5.9$ Hz, 2H, $\text{CH}_2=\underline{\text{CH}}$), 4.55 (dd, $J = 13.7, 1.1$ Hz, 2H, $\text{CH}_2=$), 4.25 (dd, $J = 5.9, 1.1$ Hz, 2H, $\underline{\text{CH}}_2=$), 0.29 (s, 6H, $\underline{\text{CH}}_3$).

¹³C NMR-APT (101 MHz, CDCl_3): 144.87 ($\text{CH}_2=\underline{\text{C}}\text{HO}$), 96.33, ($\underline{\text{C}}\text{H}_2=\text{CHO}$), -3.00 ($\underline{\text{C}}\text{H}_3$).

1.1.3 Reactivity towards cyclopolymerization

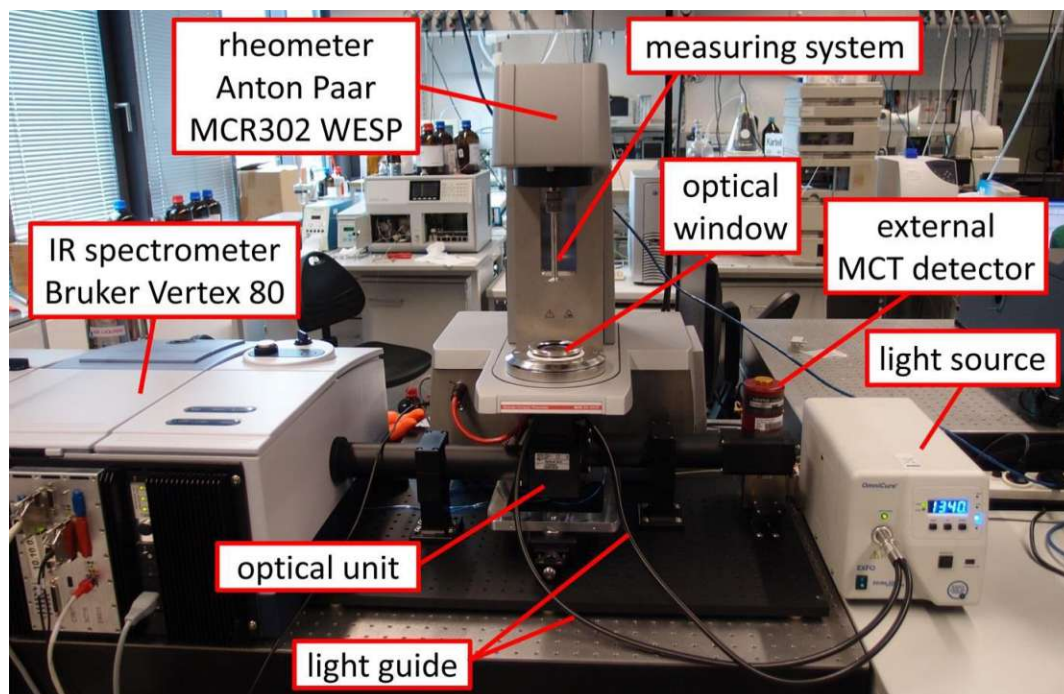


Figure 139: Setup of the RT-NIR photorheometer.

Formulations were prepared from each of the synthesized monomers by the addition of 1 w% of the respective photoinitiator. The samples were then stored in an ultrasound bath for 30 min to

achieve complete dissolution of the PIs. Photorheology measurements were performed with a real time-near infrared photorheometer consisting of an Anton Paar MCR 302 WESP with a P-PTD 200/GL Peltier glass plate and a PP25 measuring system coupled with a Bruker Vertex 80 FTIR spectrometer (Figure 139). An external mirror was used to guide the IR beam from the spectrometer through the glass plate and the sample to the rheology plate, which reflected the beam. The beam was detected with an external MCT detector. 140 μl of all tested monomer formulations were placed at the center of the glass plate, and the measurements were conducted at 25 $^{\circ}\text{C}$ with an Anton Paar H-PTD 200 furnace and a gap of 200 μm . The samples were sheered with a strain of 1% and a frequency of 1 Hz. During the measurement, storage modulus, and loss modulus were recorded. To start the photopolymerization, irradiation was conducted for 520 s with a waveguide from below the glass plate using an Exfo OmniCureTM 2000 with a broadband Hg lamp (320-500 nm). An intensity of 3 W/cm^2 was used at the tip of the light guide, which corresponds to an intensity of 30 mW/cm^2 at the surface of the samples. It is important to note that irradiation was induced 65 s after the start of each measurement. The IR chamber was continuously purged with dry air. The measurements were performed in triplicates with a closed furnace. The double bond conversion (DBC) over time was determined by recording IR spectra every 0.2 s and then integrating the respective double bond bands at $\sim 6170\text{ cm}^{-1}$. The double bond peak area ratio at the start and end of the measurement yielded the DBC.

After each measurement, one part of the obtained sample was mixed with deuterated chloroform ($\sim 10\text{ mg}$ sample with 0.7 mL of CDCl_3) for $^1\text{H-NMR}$ measurements. These measurements were conducted with a Bruker Avance 400 MHz NMR device (64 scans). The DBC could be determined via the signal of the double bond (around 6.4 ppm for all monomers), while either the acetal -H for DVF (5.1 ppm), the $-\text{CH}_3$ for DVAc (1.48 ppm) and DVE (1.49 – 1.32 ppm) and the phenyl group for DVB (7.60 – 7.33 ppm) was used as an internal standard for the determination.

Another part of the sample was treated with THF containing BHT as a flow marker to obtain a concentration of 1-3 mg/mL in THF for gel permeation chromatography (GPC). The THF solutions were then transferred to a GPC vial via a syringe filter. For the measurements, a Waters GPC with three columns connected in series (Styragel HR 0.5, Styragel HR 3 and a Styragel HR 4) and a Waters 2410 RI detector were used. The temperature of the columns was maintained at 40 $^{\circ}\text{C}$, and a flow rate of 1.0 mL min^{-1} was set. For calibration, polystyrene standards (890-177 000 Da) in THF were used, and the recorded data was analyzed with the software tool OmniSEC 4.5.

1.1.3.1 Radical cyclopolymerization

For radical polymerization, formulations were prepared with 1 w% of the PI Ivocerin®, and measurements and analyses were conducted as described in 1.1.3.

1.1.3.2 Cationic cyclopolymerization

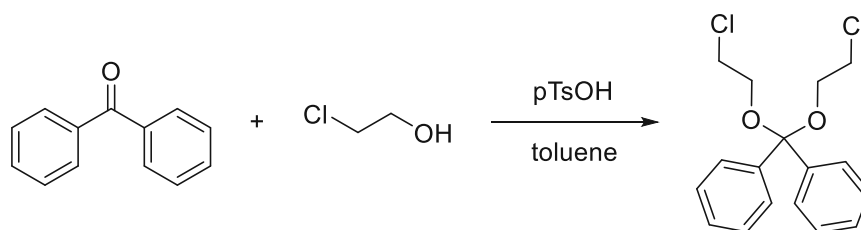
For cationic polymerization, formulations were prepared with 1 w% of the PI I-AI, and measurements and analyses were conducted as described in 1.1.3.

1.2 Monomers with improved cyclopolymerization tendency

1.2.1 Synthesis of carbon-based cyclopolymerizable monomers

1.2.1.1 Synthesis of diphenylbis(vinyloxy)methane (DVP)^{285,292}

1.2.1.1.1 Synthesis of bis(2-chloroethoxy)diphenylmethane (CEP)

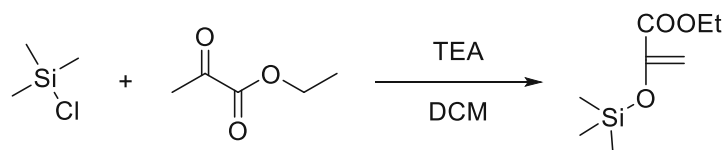


chemicals	M [g/mol]	eq.	n [mmol]	m [g]	V [mL]
benzophenone	182.22	1.0	100	18.2	
2-chloroethanol	80.51	2.5	250	20.1	
pTsOH	190.22	0.01	0.1	0.3	
toluene					100

The synthesis of bis(2-chloroethoxy)diphenylmethane (CEP) was conducted according to Matsuyan *et al.*^{285,292} Therefore, benzophenone, 2-chloroethanol, pTsOH, and toluene were added to a flask, and heated to reflux. After the evolution of water had ceased, the reaction product was treated with 30 mL 30% NaOH, extracted with Et₂O (3x100 mL), and dried over Na₂SO₄. The solvent was removed, which led to the formation of a white solid. NMR showed that the solid was mainly benzophenone, with ~12% of the desired product. Neither vacuum distillation nor column chromatography were possible for further purification; hence no product could be obtained.

1.2.1.2 Synthesis of diethyl 2,2'-(carbonylbis(oxy))diacrylate (CDA)³⁰³

1.2.1.2.1 Synthesis of trimethylsilanoxy ethyl acrylate (TMSA)



chemicals	M [g/mol]	eq.	n [mmol]	m [g]	V [mL]
ethyl pyruvate	116.12	1.0	120	13.9	
triethylamine	101.19	1.1	132	13.4	
trimethylsilyl chloride	108.64	1.1	132	14.3	
DCM					150

The synthesis of trimethylsilanoxy ethyl acrylate (TMSA) was conducted according to Barton *et al.*³⁰³ For the synthesis, ethyl pyruvate was dissolved in 120 mL DCM under argon atmosphere, and the solution was cooled to 0 °C. Subsequently, triethylamine was added dropwise. Freshly distilled trimethylsilyl chloride (b.p.: 57 °C at atm. pressure) was dissolved 30 mL DCM and added dropwise to the mixture. The mixture was allowed to warm to rt and stirred for 1 h. After filtration of the formed salt, the solvent was removed *in vacuo*. Distillation at 50 °C and 7 mbar yielded the product as a colorless liquid, which, however, first partly and then fully polymerized during distillation. For the subsequent syntheses, 1000 ppm of various stabilizers were added to the product flasks, such as BHT, phenothiazine, NEt₃, and MA154, but polymerization was still observed. Therefore, the product could not be obtained.

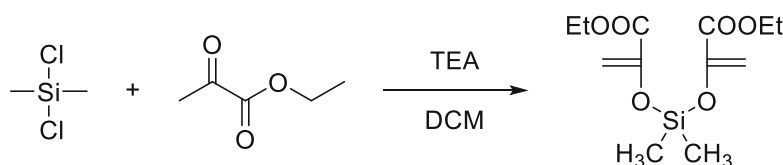
Yield: colorless liquid (yield could not be determined due to spontaneous polymerization).

b.p.: 50 °C/7 mbar (Lit.³⁶¹ 90-92 °C/50 mbar)

¹H NMR (400 MHz, CDCl₃): δ 5.27 (s, 1H, C=CH₂), 4.63 (s, 1H, C=CH₂), 3.97 (q, J = 7.0 Hz, 2H, -CH₂-), 3.55 (t, J = 7.2 Hz, 3H, CH₂-CH₃), 0.00 (s, 9H, Si-CH₃).

¹³C NMR-APT (101 MHz, CDCl₃): 164.31 (C=O), 147.23 (C=CH₂), 103.70 (C=CH₂), 61.15 (-CH₂-), 14.21 (CH₂-CH₃), -0.23 (Si-CH₃).

1.2.2 Synthesis of heteroatom-based cyclopolymerizable monomers

1.2.2.1 Synthesis of diethyl 2,2'-((dimethylsilanediyl)bis(oxy))diacrylate) (DMSA)³⁰³

chemicals	M [g/mol]	eq.	n [mmol]	m [g]	V [mL]
ethyl pyruvate	116.12	2.0	220	25.6	
triethylamine	101.19	2.1	242	24.5	
dichlorodimethylsilane	129.06	1.1	110	14.2	
DCM					250

The synthesis of diethyl 2,2'-((dimethylsilanediyl)bis(oxy))diacrylate) (DMSA) was conducted according to Barton *et al.*³⁰³ Therefore, ethyl pyruvate was dissolved in dichloromethane under argon atmosphere, and the solution was cooled to 0 °C. Then, triethylamine was added dropwise. After complete addition, freshly distilled dichlorodimethylsilane (b.p. 70 °C at atm. pressure) was added dropwise to the mixture. After warming up to rt, the mixture was stirred for 1 h. The formed salt was filtered off and the solvent was removed under reduced pressure, yielding a solid product. The product polymerized spontaneously during the evaporation of the solvent. Subsequently, 1000 ppm of several stabilizers, such as BHT, phenothiazine, NEt₃, and MA154 were added to the flask before the removal of the solvent, but polymerization was still observed. Nevertheless, a small amount of crystalline product could be obtained from the flask and was analyzed.

Yield: off-white solid (yield could not be determined due to spontaneous polymerization).

m.p.: 165 °C

R_f: 0.4 (PE:EE 4:1)

HR-MS (ACN, ESI+, m/z): calcd.: 311.0927 [M+Na]⁺; found, 311.0921 [M+Na]⁺

¹H NMR (400 MHz, CDCl₃): δ 5.56 (d, J = 1.2 Hz, 2H, C=CH₂), 5.07 (d, J = 1.2 Hz, 2H, C=CH₂), 4.24 (q, J = 7.2 Hz, 4H, -CH₂-), 1.37 (dt, J = 20.6, 7.2 Hz, 6H, CH₂-CH₃), 0.37 (s, 6H, Si-CH₃).

¹³C NMR-APT (101 MHz, CDCl₃): 164.33 (C=O), 150.17 (C=CH₂), 103.7 (C=CH₂), 61.15 (-CH₂-), 14.21 (CH₂-CH₃), -1.18 (Si-CH₃).

2. New monomers and thiols for enhanced mechanical properties and degradation of thiol-ene networks

2.1 Selection of monomers for improved network degradation

2.1.1 Model study of monomer hydrolysis

NMR hydrolysis studies of the monomers CTAE, TAS, TAP, and TAB were conducted by dissolving ~10 mg of each compound in 0.35 mL D₂O and 0.35 mL CD₃CN. For acidic conditions, a 0.01 M DCl solution in D₂O was prepared. 7 μL of this solution were added to the beforementioned NMR solvent for a pH of ~4. For basic conditions, a 0.01 M NaOD solution in D₂O was prepared, and 7 μL of this solution were added for a pH of ~10. ¹H-NMR spectra were recorded at t₀ and subsequently after 24 h, 48 h, 72 h, 96 h, 1 week, and subsequently once a week up to 8 weeks. The amount of allyl alcohol, equal to the amount of hydrolyzed monomer, was calculated via the integral of the double bond signal of allyl alcohol at 4.55 ppm. The -CH₂- signal of the double bond of each respective monomer located at ~4.8-5.0 ppm was used as a reference signal.

2.1.2 Screening of photoinitiator concentration of thiol-ene systems

Formulations for RT-NIR photorheology measurements were prepared from CTAE and the thiol EDDT in an equimolar ratio of double bonds to thiol groups. Different concentrations of the PI Ivocerin were used for each formulation, namely 0.125 w%, 0.250 w%, 0.500 w%, and 1.00 w%. 0.02 w% of PYR were added for stabilization.

RT-NIR photorheology measurements were conducted as described in 1.1.3. Samples were irradiated for 320 s with a waveguide from below the glass plate using an Exfo OmniCure™ 2000 with a broadband Hg lamp equipped with a 400-500 nm filter. An intensity of 1 W/cm² was used at the tip of the light guide, corresponding to an intensity of 20 mW/cm² at the surface of the samples. All measurements were conducted at rt.

2.1.3 Mechanical properties of model networks

Specimens for DMTA measurements were prepared from formulations containing each allyl ester-based monomer (CTAE, TAP, TAS, or TAB) and the thiol EDDT in an equimolar ratio of double bonds

to thiol groups. 1 w% Ivocerin for initiation and 0.02 w% PYR for stabilization were added. For the DMTA measurements, polymer specimens were fabricated in a transparent silicon mold with a shape of $5 \times 2 \times 40 \text{ mm}^3$.

Curing of the samples was conducted in a Lumamat 100 light oven, provided by Ivoclar Vivadent AG, with 6 Osram Dulux L Blue 18 W lamps. Samples were irradiated on both sides for 10 min. The emitted wavelength spectrum of this oven ranges from 400-580 nm at a measured total intensity of $\sim 20 \text{ mW/cm}^2$. As the specimens containing the B-based ester TAB remained sticky after curing in the Lumamat Light oven, an Intelli-Ray 600 broadband UV oven from Uvitron (irradiation power 600 W, UV-A: 124 mW/cm^2 , VIS: 125 mW/cm^2) was used, which led to significantly decreased surface stickiness. For this sample, Teflon spray was applied on the mold before curing to enable detachment from the mold. Curing of all samples was conducted at rt without a lid. After curing, the samples were sanded to remove imperfections and were subsequently stored under argon atmosphere.

DMTA measurements were performed with an Anton Paar MCR 302e device with a CTD 450 oven and an SRF 12 measuring system. The fabricated specimens were tested in torsion mode with a frequency of 1 Hz and a torsion strain of 0.1%. The temperature was increased from $-100 \text{ }^\circ\text{C}$ to $+200 \text{ }^\circ\text{C}$ with a heating rate of 2 K/min. The storage modulus and the loss factor of the polymer samples were recorded with the software RheoCompass 1.24 from Anton Paar.

2.1.4 Degradation behavior of model networks

For the degradation studies, cylindrically-shaped specimens with dimensions of $d = 6 \text{ mm}$ and $h = 2 \text{ mm}$ and a mass of approximately 50 mg were prepared analogously to the DMTA specimens described in 2.1.3. Degradation studies were conducted in buffered conditions under acidic (acetate buffer, $\text{pH}=4$) and basic (carbonate-bicarbonate buffer) conditions, as well as conditions present in the body (phosphate-buffered saline, PBS, $\text{pH}= 7.4$). The PBS solution was fabricated with 8.0 g NaCl, 0.2 g KCl, 1.44 g Na_2HPO_4 , and 0.24 g KH_2PO_4 in 1 L of distilled water. The acetate buffer was prepared with 5.77 g sodium acetate and 1.78 g acetic acid dissolved in 1 L of distilled water. The carbonate-bicarbonate buffer was fabricated with 3.88 g NaHCO_3 and 6.71 g Na_2CO_3 dissolved in 1 L of distilled water. The initial mass of the samples was measured with a balance of 0.01 mg precision. Each sample was immersed in 15 mL of the respective buffer medium and stored in a climate chamber at $37 \text{ }^\circ\text{C}$. After 1 d, 2 d, 3 d, 7 d, 14 d, 21 d, 30 d, 35 d, 60 d, and 180 d,

three samples of each material and each condition were removed from the buffer solution, the surface of the polymer was gently dried using an absorbent wipe, and each sample was weighed directly for determination of the swelling, which is calculated as the mass change from swollen mass to degraded mass after drying, normalized to the degraded mass after drying. The removed samples were washed with deionized water and then put back into the empty, washed vial, which was washed with deionized water. The samples were dried to a constant weight in a drying oven at 50 °C. For consistency, all dried samples were weighed with the vial, as some were disrupted during the experiment or became too fragile for removal. The mass loss was calculated as the mass change from the original mass to degraded mass after drying, normalized to the degraded mass. The determined data represent the average of 3 samples at each time point. At regular intervals, the pH of the buffer medium was checked to ensure constant degradation conditions.

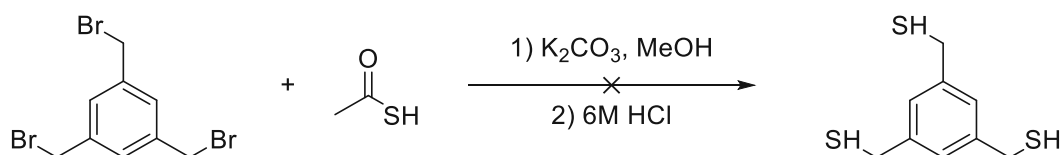
2.2 Thiols for enhanced mechanical properties

2.2.1 Screening of thiols for improved mechanical properties

Specimens for DMTA measurements were prepared from formulations containing the reference compound CTAE and the thiols EDDT, TMPMP, TEMPIC, or diPETMP in an equimolar ratio of double bonds to thiol groups. 1 w% Ivocerin for initiation and 0.02 w% PYR for stabilization were added. Specimens for DMTA measurements were prepared in a Lumamat 100 light oven, and DMTA measurements were performed as described in 2.1.3.

2.2.2 Syntheses of novel thiols

2.2.2.1 Synthesis of benzene-1,3,5-triyltrimethanethiol (TMB)^{313,314}



chemicals	M [g/mol]	eq.	n [mmol]	m [g]	V [mL]
1,3,5-tris(bromomethyl)benzene	356.88	1.0	8.4	3.0	
thioacetic acid	76.11	4.5	37.8	2.9	
K₂CO₃	138.21	4.5	37.8	5.2	
MeOH					50

The synthesis of benzene-1,3,5-triyltrimethanethiol (TMB) was conducted according to Morrisson *et al.*³¹³ and Li *et al.*³⁶² Therefore, 1,3,5-tris(bromomethyl)benzene, thioacetic acid, and half the amount of K_2CO_3 were added to 50 mL MeOH in a 250 mL three-neck flask. The mixture was stirred at ambient temperature for 1 h. Then, the other portion of K_2CO_3 was added, and the mixture was stirred for 1 h before acidification with 6 M HCl to a pH of 4 (~10 mL). The mixture was diluted with 50 mL water and extracted with $CHCl_3$ (3x50 mL). The combined organic layers were dried with Na_2SO_4 , and the solvent was removed to yield the crude product. Unfortunately, purification of the product by column chromatography with hexane:EE (1:1) was unsuccessful, and NMR showed ~10% of unknown impurities in the product.

Yield: white oil (crude yield: 88%)

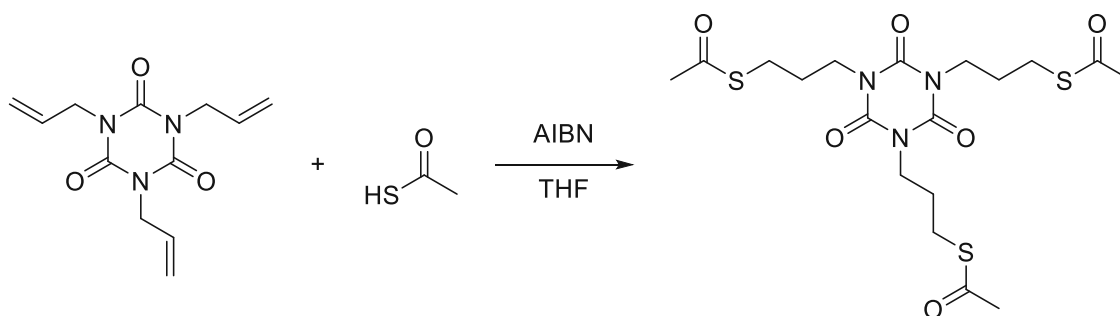
R_f = 0.8 (hexane:EE 1:1)

¹H NMR (400 MHz, CDCl₃): δ 7.17 (s, 3H, -C-H_{Ar}), 3.72 (dd, *J* = 7.6, 4.0 Hz, 6H, -CH₂-), 1.79 (td, *J* = 7.6, 3.2 Hz, 3H, -SH).

¹³C NMR-APT (101 MHz, CDCl₃): 142.05 (-C_{Ar}), 126.53 (-C-H_{Ar}), 28.71 (-CH₂-).

2.2.2.2 Synthesis of 1,3,5-tris(3-mercaptopropyl)-1,3,5-triazine-2,4,6-trione (TMT)^{311,312}

2.2.2.2.1 Synthesis of 1,3,5-tris(3-acetylmercaptopropyl)-1,3,5-triazine-2,4,6 (TAT)



chemicals	M [g/mol]	eq.	n [mmol]	m [g]	V [mL]
1,3,5-triallyl-1,3,5-triazine-2,4,6-trione	249.27	1.0	150	37.4	
AIBN	164.21	0.2	225	4.0	
thioacetic acid	76.12	3.6	540	41.1	
THF					250

The synthesis of 1,3,5-tris(3-mercaptopropyl)-1,3,5-triazine-2,4,6-trione (TMT) was conducted according to Reinelt *et al.*^{311,312} Therefore, in a 500 mL three-neck round-bottom flask, 1,3,5-triallyl-1,3,5-triazine-2,4,6-trione, thioacetic acid, and AIBN were added to THF. The reaction

mixture was purged with argon for 30 min at rt and then heated to 65 °C for 24 h. After cooling to 0 °C, 100 mL of 1 N Na₂CO₃ were added, and the mixture was extracted three times with dichloromethane (300/100/100 mL). The combined organic extracts were washed with 80 mL of 1 N sodium hydroxide solution and 80 mL brine, dried over Na₂SO₄, filtered, and concentrated under reduced pressure to obtain a dark brown oil, which was dried *in vacuo* for 24 h to obtain a dark yellow solid. The residual crude product was recrystallized from 200 mL of methanol three times to yield the solid white product.

Yield: white solid (72% theoretical yield).

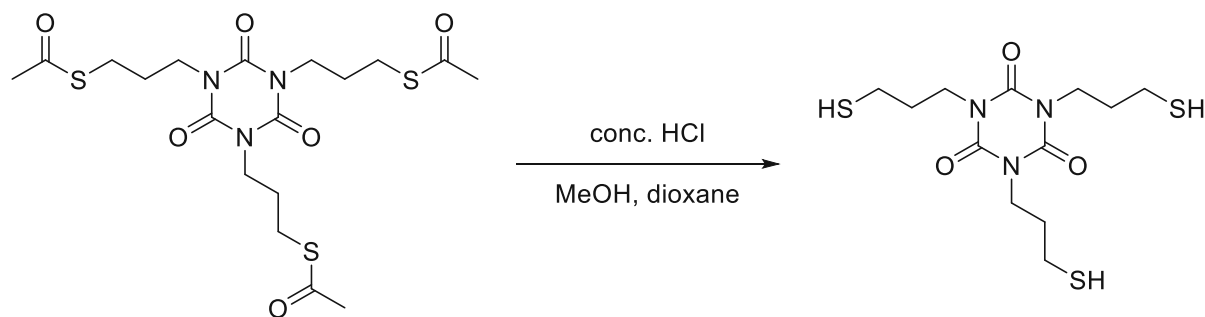
m.p.: 65-68 °C (Lit.³¹² 66-67 °C)

R_f = 0.7 (PE:EE 1:1)

¹H NMR (400 MHz, CDCl₃): 3.89 (t, 7.1 Hz, 6H, -N-CH₂-), 2.83 (t, 3 J = 7.1 Hz, 6H, -CH₂S-), 2.26 (s, 9H, -CH₃), 1.87 (quin., J = 7.1 Hz, 6H, -CH₂-).

¹³C NMR (101 MHz, CDCl₃): δ 195.45 (-S(C=O)CH₃), 149.03 (-C=O), 42.07 (-N-CH₂-), 30.68 (-CH₃), 28.03 (-CH₂-), 26.27 (-CH₂-S-).

2.2.2.2.2 Synthesis of 1,3,5-tris(3-mercaptopropyl)-1,3,5-triazine-2,4,6-trione (TMT)



chemicals	M [g/mol]	eq.	n [mmol]	m [g]	V [mL]
TAT	477.63	1.0	47	37.4	
HCl (37%)	36.46	3.2	150	14.7	
MeOH					95
dioxane					30

The synthesis of 1,3,5-tris(3-mercaptopropyl)-1,3,5-triazine-2,4,6-trione (TMT) was conducted according to Reinelt *et al.*^{311,312} For this, in a 250 mL three-neck round-bottom flask, 1,3,5-tris(3-acetylmercaptopropyl)-1,3,5-triazine-2,4,6-trione (TAT) and aqueous concentrated hydrochloric acid were dissolved in a mixture of methanol (95 mL) and 1,4-dioxane (30 mL). The resulting

solution was purged with argon for 30 min and then heated to 60 °C for 24 h. After cooling to ambient temperature, 200 mL of deionized water were added, and the mixture was extracted three times with DCM (300/150/150 mL). The combined organic extracts were washed two times with 100 mL saturated NaHCO₃ and brine, dried over Na₂SO₄, filtered, and concentrated under reduced pressure. After drying, the product was obtained as a colorless liquid.

Yield: colorless liquid (93% theoretical yield).

R_f = 0.3 (PE:EE 1:1)

RI: 1.5678

¹H NMR (400 MHz, CDCl₃): δ 4.01 (t, J = 7.0 Hz, 6H, -N-CH₂-), 2.56 (dt, J = 6.9, 8.0 Hz, 6H, -CH₂S-), 1.97 (quin., J = 7.0 Hz, 6H, -CH₂-), 1.54 (t, 3 J = 8.0 Hz, 3H, -CH₂-SH).

¹³C NMR (101 MHz, CDCl₃): δ 149.10 (-C=O), 41.91 (-N-CH₂-), 31.94 (-CH₂-), 22.03 (-CH₂-SH).

2.2.2.3 Mechanical properties of networks

Specimens for DMTA measurements were prepared from formulations containing the monomer CTAE and the thiols EDDT, TEMPIC, or TMT in an equimolar ratio of double bonds to thiol groups. 1 w% Ivocerin for initiation and 0.02 w% PYR for stabilization were added. DMTA specimens were prepared in a Lumamat 100 light oven at rt. DMTA measurements were performed as described in 2.1.3.

2.3 New monomers containing heteroatoms

2.3.1 Compounds based on phosphorus

2.3.1.1 Synthesis of 2,2'-(ethane-1,2-diyl)bis(4-((allyloxy)methyl)-1,3,2-dioxaphospholane-2-oxide) (ADP)²⁰⁸

2.3.1.1.1 Synthesis of ethylene phosphonic dichloride (EPD)



chemicals	M [g/mol]	eq.	n [mmol]	m [g]	V [mL]
tetraethyl ethylene diphosphonate	302.24	1.0	14	4.2	
thionyl chloride	118.97	5.0	70	8.3	
DMF	73.09	0.01	0.2	0.01	

The synthesis of ethylene phosphonic dichloride (EPD) was conducted according to Wolf *et al.*²⁰⁸ For the synthesis, all reactants were dried over a molecular sieve (3 Å), and Karl-Fischer titrated to determine their water content, which should be <50 ppm. In a flame-dried three-neck flask, tetraethyl ethylene diphosphonate and DMF as a catalyst were added dropwise to refluxing thionyl chloride at 75 °C, which led to a strong gas evolution. After 4 h, the gas evolution ceased, and a yellowish solid appeared in the flask, which was dissolved in dry chloroform and filtered. After evaporation of the solvent, the product was yielded as an off-white solid, which, however, showed poor solubility in benzene, which is reported as a solvent in the literature.³¹⁶ Nevertheless, NMR showed the formation of the product, which was used directly for the next step of the synthesis.

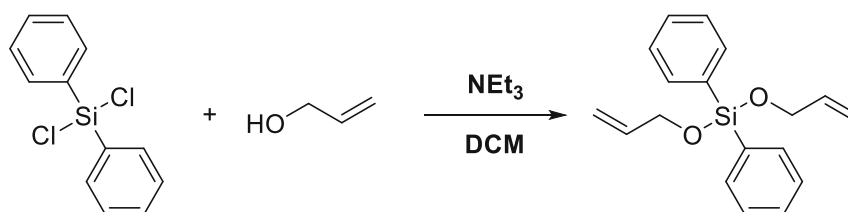
Yield: off-white solid (98% theoretical yield).

¹H NMR (400 MHz, CDCl₃): δ 3.04 (m, -CH₂-)

¹³C NMR-APT (101 MHz, CDCl₃): δ 30.10 (-CH₂-), 29.34 (-CH₂-).

³¹P (162 MHz, CDCl₃): δ 42.53.

2.3.2 Compounds based on silicon

2.3.2.1 Synthesis of bis(allyloxy)diphenylsilane (DAS)³²⁴

chemicals	M [g/mol]	eq.	n [mmol]	m [g]	V [mL]
dichlorodiphenylsilane	253.19	1.0	100	25.3	
allyl alcohol	58.08	2.0	200	11.6	
triethylamine	101.19	2.0	200	20.2	
DCM					200

The synthesis of bis(allyloxy)diphenylsilane (DAS) was conducted according to Hoye *et al.*³²⁴ For the synthesis, dichlorodiphenylsilane and triethylamine were added to a 500 mL three-necked flask containing dichloromethane under inert atmosphere. The mixture was cooled to 0 °C, and allyl alcohol was slowly added dropwise within 0.5 h. After complete addition, the reaction was warmed to rt and stirred for another hour, during which a white solid was formed. The solid was filtered off under reduced pressure, and the filtrate was washed with ice water (3x100 mL). The aqueous phase was extracted with dichloromethane (3x250 mL), the combined organic extracts were dried with Na₂SO₄, and the solvent was removed. The crude mixture was distilled *in vacuo* to yield the product at 140 °C and 5 mbar.

Yield: colorless oil (92% theoretical yield).

RI: 1.5423 (Lit.³⁶³ 1.5424)

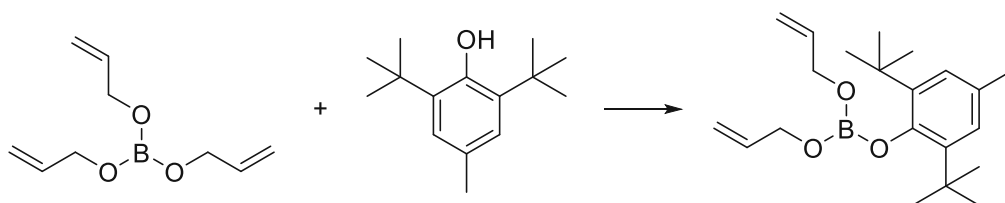
R_f = 0.4 (PE)

b.p.: 140 °C/5 mbar (Lit.³⁶³ 158-160 °C/8 mbar)

¹H-NMR (400 MHz, CDCl₃): δ 7.74 – 7.63 (m, 4H, C-H_{Ar}), 7.47 – 7.34 (m, 6H, C-H_{Ar}), 5.96 (ddt, J = 17.1, 10.4, 4.7 Hz, 2H, CH=CH₂), 5.35 (dq, J = 17.1, 1.9 Hz, 2H, CH=CH₂), 5.13 (dq, J = 10.4, 1.7 Hz, 2H, CH=CH₂), 4.34 (dt, J = 4.8, 1.7 Hz, 4H, -O-CH₂-).

¹³C-NMR (101 MHz, CDCl₃): δ 136.66 (CH=CH₂), 135.04 (C-H_{Ar}), 132.67 (C_{Ar}), 130.52 (C-H_{Ar}), 128.02 (C-H_{Ar}), 114.84 (CH=CH₂), 76.84 (-O-CH₂-).

2.3.3 Compounds based on boron

2.3.3.1 Synthesis of 2,6-ditertbutylphenyl diallyl borate (BAB)³²⁵

chemicals	M [g/mol]	eq.	n [mmol]	m [g]	V [mL]
BHT	220.36	1.0	30	6.6	
triallyl borate	182.03	3.0	90	16.4	

The synthesis of 2,6-ditertbutylphenyl diallyl borate (BAB) was conducted according to Washburn *et al.*³²⁴ Therefore, triallyl borate and BHT were added to a 50 mL flask under argon. The mixture was heated to 100 °C under a vacuum of 600 mbar. Within 3 d, allyl alcohol was distilled off completely, and the solution was distilled *in vacuo*. NMR showed that decomposition of the formed ester occurred during distillation. Therefore, the reaction was done again, and after allyl alcohol was distilled off, the crude product was extracted with DCM (3x100 mL). The combined organic extracts were dried with Na₂SO₄, and the solvent was removed. NMR of the crude liquid showed that the product was formed with ~5% of BHT as an impurity. Column chromatography of the product could not be conducted, as the formed ester was unstable on silica gel and AlOx. Hence, the product could not be obtained due to the instability of the compound.

Yield: slightly yellow oil (10% theoretical yield).

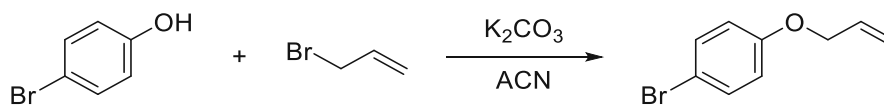
b.p.: 100-115 °C/0.5 mbar (Lit.³⁶⁴ 104-110 °C/0.3 mbar)

¹H NMR (400 MHz, CDCl₃): δ 7.01-7.03 (m, 2H, -C-H_{Ar}), 5.92 (ddt, J = 17.2, 10.3, 5.1 Hz, 2H, -CH=CH₂), 5.38-4.98 (m, 2H, -CH=CH₂), 5.29 (dq, J = 10.5, 1.4 Hz, 1H, -CH=CH₂), 4.47 (dt, J = 5.1, 1.7 Hz, 4H, -O-CH₂-), 2.29 (s, 3H, -CH_{3,Ar}), 1.35 (s, 18H, -C-(CH₃)₃).

¹³C NMR-APT (101 MHz, CDCl₃): 153.20 (-C_{Ar}-O.), 137.52 (-C_{Ar}-C-(CH₃)₃), 134.12 (-CH=CH₂), 130.25 (-C_{Ar}-CH₃), 126.12 (-C_{Ar}-H), 117.65 (-CH=CH₂), 116.57 (-CH=CH₂), 66.08 (-O-CH₂-), 35.87 (-C-(CH₃)₃), 31.21 (-C-(CH₃)₃), 21.25 (-CH_{3,Ar}).

2.3.3.2 Synthesis of 2-(4-(allyloxy)phenyl)-4-vinyl-1,3,2-dioxaborolane (AVB)³²⁷

2.3.3.2.1 Synthesis of 1-(allyloxy)-4-bromobenzene (ABB)



chemicals	M [g/mol]	eq.	n [mol]	m [g]	V [mL]
4-bromophenol	173.01	1.0	173	30.0	
allyl bromide	120.99	2.0	347	42.0	
K ₂ CO ₃	138.21	2.5	434	59.9	
ACN					450

The synthesis of 1-(allyloxy)-4-bromobenzene (ABB) was conducted according to Chardin *et al.*³²⁷ For the synthesis, 4-bromophenol, and K₂CO₃ were added to ACN in a 1 L three-neck flask equipped with a condenser, which resulted in a suspension. Then allyl bromide was added. The mixture was refluxed at 80 °C for 72 h. After cooling to rt, the solvent was removed under reduced pressure, and the resulting residue was partitioned between 300 mL DCM and 200 mL water. The aqueous phase was extracted with DCM (3x300 mL), and the combined organic extracts were washed with 100 mL water, dried with Na₂SO₄, and concentrated *in vacuo* to yield the product.

Yield: slightly yellow oil (94% theoretical yield).

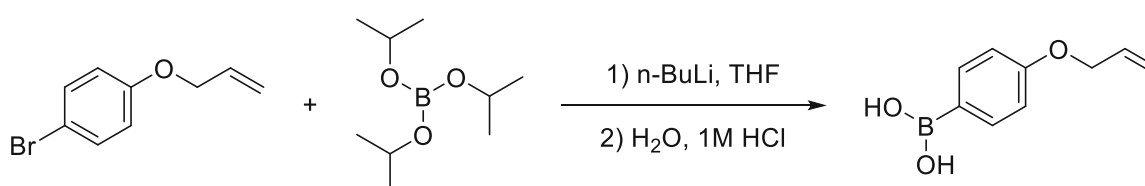
RI: 1.5579 (Lit.³⁶⁵ 1.5583)

R_f: 0.4 (cyclohexane:EE=3:1)

¹H NMR (400 MHz, CDCl₃): δ 7.43 – 7.31 (m, 2H, -C-H_{Ar}), 6.86 – 6.74 (m, 2H, -C-H_{Ar}), 6.03 (ddt, J = 17.3, 10.5, 5.3 Hz, 1H, -CH=CH₂), 5.40 (dq, J = 17.3, 1.6 Hz, 1H, -CH=CH₂), 5.29 (dq, J = 10.5, 1.4 Hz, 1H, -CH=CH₂), 4.51 (dt, J = 5.3, 1.5 Hz, 2H, -O-CH₂-).

¹³C NMR-APT (101 MHz, CDCl₃): 157.70 (-C_{Ar}), 132.87 (-CH=CH₂), 132.25 (-C-H_{Ar}), 117.93 (-CH=CH₂), 116.57 (-CH=CH₂), 69.01 (-O-CH₂-).

2.3.3.2.2 Synthesis of (4-(allyloxy)phenyl)boronic acid (ABA)



EXPERIMENTAL PART

chemicals	M [g/mol]	eq.	n [mol]	m [g]	V [mL]
1-(allyloxy)-4-bromobenzene	213.07	1.0	62.5	13.3	
triisopropyl borate	188.07	1.5	93.8	17.6	
n-BuLi (2.5 M in hexane)	64.05	1.2	75.0	4.8	30
THF					100

The synthesis of (4-(allyloxy)phenyl)boronic acid (ABA) was conducted according to Chardin *et al.*³²⁷ Therefore, a 500 mL three-neck round bottom flask equipped with a thermometer, condenser, and a dropping funnel, was purged with argon. Then, ABB was dissolved in dry THF, and the mixture was cooled to -78 °C with an acetone/liquid N₂ bath. After cooling for 30 min, n-BuLi (2.5 M in hexane) was added dropwise, resulting in an orange solution. After complete addition, the reaction mixture was stirred for 1 h, and subsequently, triisopropyl borate was added dropwise. The mixture was allowed to slowly warm up to rt overnight, which resulted in the formation of a salt. 35 mL of water were slowly added, which led to the precipitation of a white solid. This mixture was then acidified with 100 mL of 1 M HCl. Upon the addition of HCl, the precipitate was dissolved, and two phases were separated. After stirring for 1 h, the reaction mixture was extracted with 3x200 mL diethyl ether, and the combined organic layers were washed with water and dried over Na₂SO₄. Evaporation of the solvent under reduced pressure afforded the crude product as a pink solid, which was purified by flash chromatography on silica gel with cyclohexane:EE (7:3) to yield the product as a white solid. NMR showed that ~7% of impurities were still present. Therefore, column chromatography with pure PE was attempted but was unsuccessful as well, as ~5% of impurities remained in the product. Therefore, the pure compound could not be obtained.

Yield: white solid (crude yield: 62%)

R_f: 0.7 (PE)

m.p.: 102-108 °C (Lit.³²⁷ 106 °C)

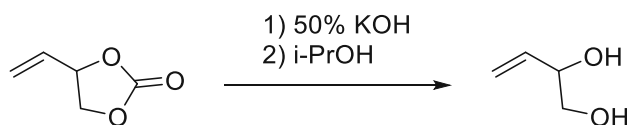
¹H NMR (400 MHz, CDCl₃): δ 8.20 – 8.12 (m, 2H, -C-H_{Ar}), 7.07 – 6.99 (m, 2H, -C-H_{Ar}), 6.10 (ddt, J = 17.3, 10.6, 5.3 Hz, 1H, -CH=CH₂), 5.46 (dq, J = 17.3, 1.6 Hz, 1H, -CH=CH₂), 5.33 (dq, J = 10.5, 1.4 Hz, 1H, -CH=CH₂), 4.63 (dt, J = 5.3, 1.5 Hz, 2H, -O-CH₂-).

¹³C NMR-APT (101 MHz, CDCl₃): δ 162.24 (-C_{Ar}), 137.50 (-C-H_{Ar}), 132.98 (-CH=CH₂), 117.96 (-CH=CH₂), 114.25 (-CH=CH₂), 68.64 (-O-CH₂-).

¹¹B-NMR (128 MHz, CDCl₃): δ 28.07

2.3.3.3 Synthesis of allyl 4-(4-vinyl-1,3,2-dioxaborolan-2-yl)benzoate (AEB)^{326,328,329}

2.3.3.3.1 Synthesis of but-3-ene-1,2-diol (BUD)



chemicals	M [g/mol]	eq.	n [mol]	m [g]	V [mL]
4-vinyl-1,3-dioxolan-2-one	114.10	1.0	69.2	79.0	
KOH	56.11	1.2	79.6	44.7	
iPrOH					370

The synthesis of but-3-ene-1,2-diol (BUD) was conducted according to Boaz *et al.*³²⁸ Therefore, 4-vinyl-1,3-dioxolan-2-one was added to a 1 L flask and cooled to 0 °C with an ice bath. A 50 wt% solution of aqueous KOH was added dropwise over a period of 35 min. Then, the ice bath was removed, and the mixture was heated to 60 °C for 16 h. After cooling to ambient temperature, 370 mL of i-PrOH were added, and the mixture was stirred for 1 h. The inorganic salt precipitate was removed by filtration and washed with 50 mL of i-PrOH. The combined organic layers were concentrated, and the remaining liquid was distilled at 90 °C and 10 mbar to yield the product.

Yield: colorless liquid (80% theoretical yield).

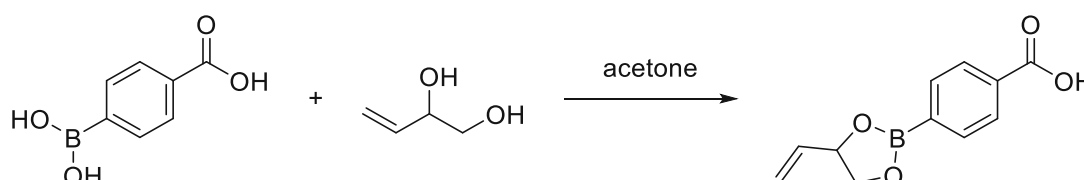
RI: 1.4615 (Lit.³⁶⁶ 1.461).

b.p.: 90 °C/10 mbar (Lit.³⁶⁷ 85 °C/20 mbar).

¹H NMR (400 MHz, CDCl₃): δ 5.84 (ddd, J = 17.3, 10.6, 5.6 Hz, 1H, -CH=CH₂), 5.35 (dt, J = 17.3, 1.5 Hz, 1H, -CH=CH₂), 5.21 (dt, J = 10.6, 1.4 Hz, 1H, -CH=CH₂), 4.25 (ddtq, J = 7.5, 4.3, 3.2, 1.5 Hz, 1H, -CH(OH)-CH₂OH), 3.66 (ddd, J = 11.3, 6.8, 3.4 Hz, 1H, -CH₂OH), 3.49 (ddd, J = 11.3, 7.5, 4.9 Hz, 1H, -CH₂OH), 3.01 (d, J = 4.3 Hz, 1H, -OH), 2.84 (dd, J = 6.8, 5.0 Hz, 1H, -OH).

¹³C NMR-APT (101 MHz, CDCl₃): 136.71 (-CH=CH₂), 116.75 (-CH=CH₂), 73.32 (-CH(OH)-CH₂OH), 66.25 (-CH₂OH).

2.3.3.3.2 Synthesis of 4-(4-vinyl-1,3,2-dioxaborolan-2-yl)benzoic acid (VAB)



EXPERIMENTAL PART

chemicals	M [g/mol]	eq.	n [mol]	m [g]	V [mL]
4-carboxyphenyl boronic acid	165.94	1.0	50	8.3	
but-3-ene-1,2-diol	88.11	1.0	50	4.4	
Na ₂ SO ₄	142.04	11.3	560	80.0	
acetone					700

The synthesis of but-3-ene-1,2-diol (BUD) was conducted according to Schörpf *et al.*³²⁶ and Schnöll *et al.*³²⁹ For the synthesis, 4-carboxyphenyl boronic acid and acetone were added to a 1 L round bottom flask equipped with a reflux condenser under inert atmosphere. The apparatus was purged with argon, and then but-3-ene-1,2-diol was added, upon which complete dissolution of the boronic acid occurred. The reaction was stirred for 30 min at rt, and Na₂SO₄ was added stepwise until no more lumps indicating water were visible. Afterward, the solution was stirred for 36 h. The mixture was then filtrated, washed with acetone and the solvent was removed under reduced pressure to obtain the product.

Yield: white solid (90% theoretical yield).

Melting point: 191 °C

HR-MS (ACN, ESI+, m/z): calcd.: 218.0750 [M]; found, 218.0781 [M]

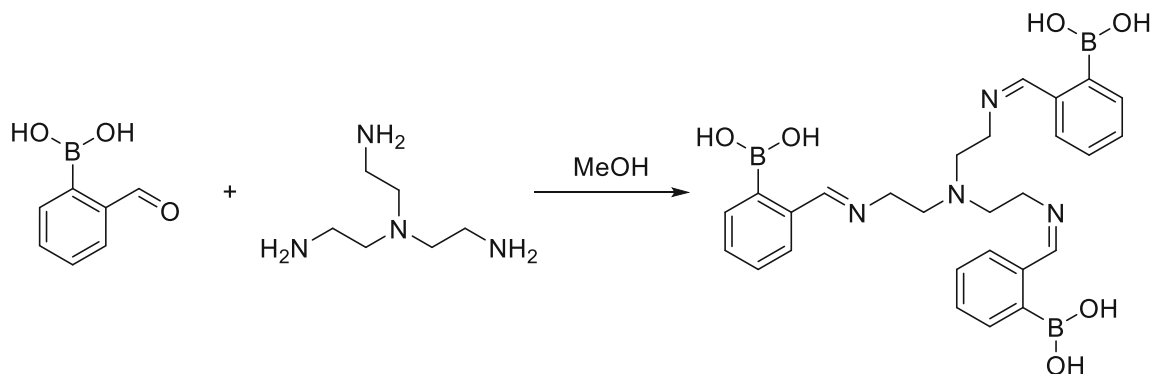
¹H NMR (400 MHz, CDCl₃): δ 8.16 – 8.09 (m, 2H, -C-H_{Ar}), 7.98 – 7.89 (m, 2H, -C-H_{Ar}), 5.97 (ddd, J = 17.1, 10.3, 6.6 Hz, 1H, -CH=CH₂), 5.42 (dt, J = 17.1, 1.3 Hz, 1H, -CH=CH₂), 5.30 (dt, J = 10.3, 1.2 Hz, 1H, -CH=CH₂), 5.11 – 5.00 (m, 1H, -O-CH-CH=CH₂), 4.54 (dd, J = 9.0, 8.2 Hz, 1H, -O-CH₂-), 4.08 (dd, J = 9.0, 7.5 Hz, 1H, -O-CH₂-).

¹³C NMR-APT (101 MHz, CDCl₃): δ 172.23 (-C=O), 137.20 (-CH=CH₂), 135.39 (-C-H_{Ar}), 132.15 (-C_{Ar}-B), 129.80 (-C-H_{Ar}), 118.14 (-CH=CH₂), 78.99 (-O-CH-CH=CH₂), 71.64 (-O-CH₂-).

¹¹B-NMR (128 MHz, CDCl₃): δ 32.42.

2.3.3.5 Synthesis of N1-(2-(4-vinyl-1,3,2-dioxaborolan-2-yl)benzyl)-N2,N2-bis(2-((2-(4-vinyl-1,3,2-dioxaborolan-2-yl)benzyl)amino)ethyl)ethane-1,2-diamine (NVB)^{326,329-331}

2.3.3.5.1 Synthesis of (2-((E)-((2-(bis(2-((Z)-2-boronobenzylidene)amino)ethyl)amino)ethyl)-imino)methyl)phenyl)boronic acid (IAB)



chemicals	M [g/mol]	eq.	n [mol]	m [g]	V [mL]
tris(aminoethyl)amine	146.24	1.0	10	1.5	
2-formylphenylboronic acid	149.94	3.0	30	4.5	
MeOH, abs.					50

The synthesis of (2-((E)-((2-(bis(2-((Z)-2-boronobenzylidene)amino)ethyl)amino)ethyl)-imino)methyl)phenyl)boronic acid (IAB) was conducted according to Leed *et al.*³³⁰ and Gray *et al.*³³¹ Therefore, 2-formylphenylboronic acid was added to a solution of tris(2-ethylamino)amine in anhydrous methanol. The solution was stirred under heating to 60 °C for 1 d. Then, a fraction of 10 mL was removed and the solvent was evaporated resulting in a yellow solid, used for characterization of IAB. A total yield of 80% was calculated from the 10 mL removed.

Yield: yellow solid (80% theoretical yield).

m.p.: 182-184 °C

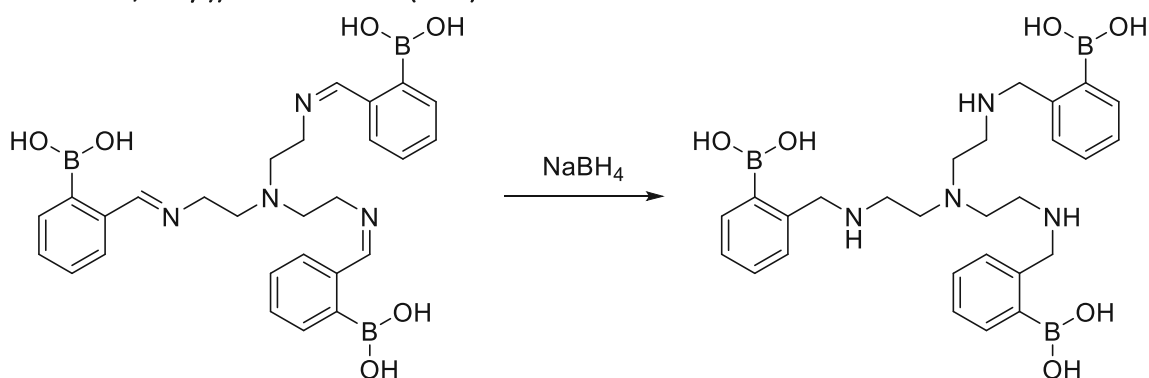
HR-MS (MeOH, ESI+, m/z): calcd.: 543.2758 [M+H]⁺; found, 543.2765 [M+H]⁺

¹H NMR (400 MHz, CD₃OD): δ 8.41 (s, 3H, -CH=N), 7.65 – 7.59 (m, 3H; -C-H_{Ar}), 7.56 (td, J = 7.2, 1.1 Hz, 3H, -C-H_{Ar}), 7.18 (td, J = 7.5, 1.3 Hz, 3H, -C-H_{Ar}), 6.10 (dt, J = 7.5, 1.0 Hz, 3H, -OH), 3.81 (t, J = 5.6 Hz, 6H, -CH=N-CH₂-), 3.04 – 2.97 (m, 6H, -N-CH₂-CH₂-).

¹³C NMR-APT (101 MHz, CD₃OD): 172.45 (-CH=N), 138.97 (-C_{Ar}), 133.90 (-C-H_{Ar}), 131.31 (-C-H_{Ar}), 128.72 (-C-H_{Ar}), 128.40 (-C-H_{Ar}), 52.38 (-N-CH₂-CH₂-), 48.01 (-CH=N-CH₂-).

¹¹B-NMR (128 MHz, CD₃OD): δ 9.43.

2.3.3.5.2 Synthesis of (((nitrilotris(ethane-2,1-diyl))tris(azanediy))tris(methylene))tris(benzene-2,1-diyl)triboronic acid (NAB)



chemicals	M [g/mol]	eq.	n [mol]	m [g]	V [mL]
IAB	542.01	1.0	10	5.4	
NaBH ₄	37.83	3.6	36	1.4	
MeOH, abs.					50

The synthesis of (((nitrilotris(ethane-2,1-diyl))tris(azanediy))tris(methylene))tris(benzene-2,1-diyl)triboronic acid (NAB) was conducted according to Leed *et al.*³³⁰ and Gray *et al.*³³¹ After full conversion to IAB was confirmed with NMR, the reaction solution was cooled to 0 °C, and NaBH₄ was added in small portions. After the evolution of H₂ gas was complete, the solution was warmed to rt and stirred for 16 h. The solvent was evaporated, and the resulting residue was redissolved in DCM to leave NaBH₄ as a white powder. The mixture was vacuum filtrated, and the filtrate was subsequently concentrated. The residue was then redissolved in a small amount of DCM (~5 mL), and hexane was added dropwise until the white precipitate of the product NVB was observed.

Yield: white solid (73% theoretical yield).

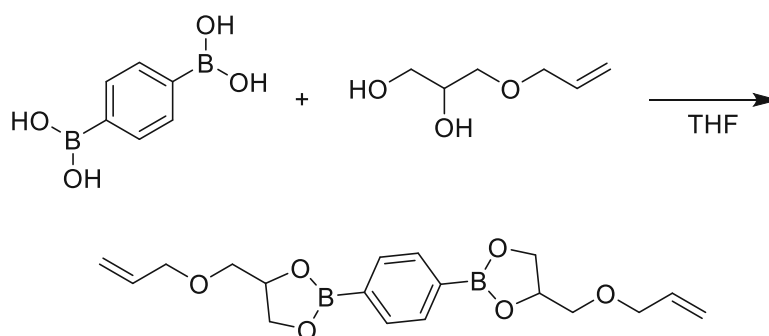
Melting point: 210-211 °C

HR-MS (MeOH, ESI+, m/z): calcd.: 549.3227 [M+H]⁺; found, 549.3241 [M+H]⁺

¹H NMR (400 MHz, CD₃OD): δ 7.46 (dd, J = 5.5, 3.1 Hz, 3H, -C-H_{Ar}), 7.17 (ddd, J = 12.1, 6.9, 3.7 Hz, 9H, -C-H_{Ar}), 4.06 (s, 6H, NH-CH₂-C_{Ar}-), 3.03 (d, J = 6.5 Hz, 6H, -N-CH₂-CH₂-), 2.92 (t, J = 6.4 Hz, 6H, -N-CH₂-CH₂-).

¹³C NMR-APT (101 MHz, CD₃OD): δ 128.34 (-C-H_{Ar}), 127.62 (-C-H_{Ar}), 55.46 (-N-CH₂-CH₂-), 51.63 (NH-CH₂-C_{Ar}-), 46.17 (-N-CH₂-CH₂-)

¹¹B-NMR (128 MHz, CD₃OD): δ 9.25.

2.3.3.6 Synthesis of 1,4-bis(4-((allyloxy)methyl)-1,3,2-dioxaborolan-2-yl)benzene (ADB)^{234,235,256}

chemicals	M [g/mol]	eq.	n [mol]	m [g]	V [mL]
benzene-1,4-diboronic acid	165.75	1.0	70	11.6	
3-allyloxy-1,2-propanediol	132.16	2.1	144	19.0	
Na ₂ SO ₄	142.04	2.3	160	22.7	
THF					450

The synthesis of 1,4-bis(4-((allyloxy)methyl)-1,3,2-dioxaborolan-2-yl)benzene (ADB) was conducted according to Chen *et al.*^{234,235} and Robinson *et al.*²⁵⁶ For the synthesis, first, 3-allyloxy-1,2-propanediol was distilled for purification (b.p. 105 °C/3 mbar). Then, benzene-1,4-diboronic acid was added to a 1 L three-neck round bottom flask equipped with a condenser and purged with argon. Next, THF and 3-allyloxy-1,2-propanediol were added, and the mixture was stirred until complete dissolution of all compounds occurred. Then, Na₂SO₄ was added stepwise to the mixture until no more lumps were observed. After stirring at rt for 24 h, Na₂SO₄ was filtered off (suction filter: P4), washed with THF, and the filtrate was concentrated *in vacuo* to yield the product.

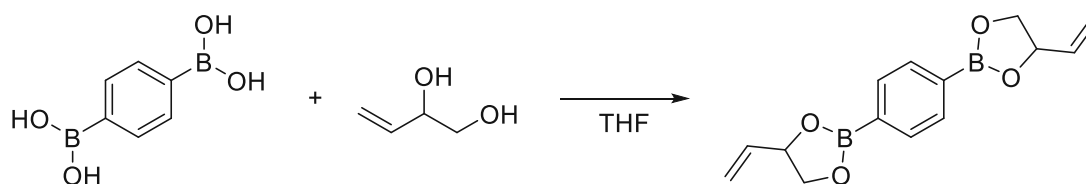
Yield: white solid (95% theoretical yield).

m.p.: 42-43 °C

¹H NMR (400 MHz, CDCl₃): δ 7.83 (s, 4H, -C-H_{Ar}), 5.89 (ddt, *J* = 17.2, 10.4, 5.6 Hz, 2H, -CH=CH₂), 5.28 (dq, *J* = 17.2, 1.6 Hz, 2H, -CH=CH₂), 5.19 (dq, *J* = 10.4, 1.4 Hz, 2H, -CH=CH₂), 4.74 (ddt, *J* = 8.1, 6.6, 5.1 Hz, 2H, -O-CH-CH₂-), 4.43 (dd, *J* = 9.1, 8.2 Hz, 2H, -O-CH-CH₂-), 4.19 (dd, *J* = 9.1, 6.6 Hz, 2H, -CH₂-CH=CH₂), 4.07 (dq, *J* = 5.6, 1.4 Hz, 4H, -O-CH₂-CH), 3.64 (dd, *J* = 10.2, 5.1 Hz, 2H, -O-CH₂-CH=CH₂), 3.57 (dd, *J* = 10.2, 5.1 Hz, 2H, -O-CH-CH₂-O-).

¹³C NMR-APT (101 MHz, CDCl₃): δ 136.95 (-C_{Ar}), 134.36 (-CH=CH₂), 134.11 (-C-H_{Ar}), 117.47 (-CH=CH₂), 76.22 (-O-CH-CH₂-), 72.58 (-O-CH₂-CH=CH₂), 71.91 (-O-CH-CH₂-O-), 68.51 (-O-CH₂-CH).

¹¹B-NMR (128 MHz, CDCl₃): δ 31.5

2.3.3.7 Synthesis of 1,4-bis(4-vinyl-1,3,2-dioxaborolan-2-yl)benzene (VDB)^{234,235,256}

chemicals	M [g/mol]	eq.	n [mol]	m [g]	V [mL]
benzene-1,4-diboronic acid	165.75	1.0	36	6.0	
but-3-ene-1,2-diol	88.11	2.1	74	6.5	
Na ₂ SO ₄	142.04	2.3	83	11.8	
THF					160

The synthesis of 1,4-bis(4-vinyl-1,3,2-dioxaborolan-2-yl)benzene (VDB) was conducted according to Chen *et al.*^{234,235} and Robinson *et al.*²⁵⁶ Therefore, benzene-1,4-diboronic acid, and but-3-ene-1,2-diol were dissolved in THF under inert atmosphere. Then Na₂SO₄ was carefully added stepwise. After stirring at rt for 24 h, the mixture was filtered under reduced pressure (suction filter: P4), the solid was washed with THF, and the filtrate was concentrated to obtain the solid, pure product.

Yield: off-white solid (90% theoretical yield).

Melting point: 73-74.9 °C.

¹H NMR (400 MHz, CDCl₃): δ 7.85 (s, 4H, -C-H_{Ar}), 5.96 (ddd, J = 17.0, 10.4, 6.6 Hz, 2H, -CH=CH₂), 5.41 (dt, J = 17.1, 1.3 Hz, 2H, -CH=CH₂), 5.27 (dt, J = 10.3, 1.2 Hz, 2H, -CH=CH₂), 5.02 (dddt, J = 8.5, 7.7, 6.6, 1.2 Hz, 2H, -O-CH-CH=CH₂), 4.51 (dd, J = 9.1, 8.2 Hz, 2H, -O-CH₂-), 4.05 (dd, J = 9.0, 7.4 Hz, 2H, -O-CH₂-).

¹³C NMR-APT (101 MHz, CDCl₃): δ 136.97 (-CH=CH₂), 134.15 (-C-H_{Ar}), 117.47 (-C-B-), 78.34 (-O-CH-CH=CH₂), 71.05 (-O-CH₂-).

¹¹B-NMR (128 MHz, CDCl₃): δ 32.08.

2.4 Characterization of degradable systems

2.4.1 Reactivity of formulations

Formulations for RT-NIR photorheology measurements were prepared from each monomer (CTAE, TAP, TAS; DAS, TAB, ADB, or VDB) and the thiol TMT in an equimolar ratio of double bonds

to thiol groups. 1 w% of Ivocerin were added for photoinitiation. As autopolymerization of all formulations occurred within 24 h at rt, 0.02 w% of PYR were added for stabilization. The formulations were homogenized with a vortex under slight heating until the complete dissolution of the PI and monomers. Samples containing TAS, TAB, or VDB were homogenized by storage in an oven at 110 °C for 10 min. Due to phase separation of TAS or TAB with TMT at rt, measurements were performed at 100 °C as homogeneous formulations were obtained at this temperature. Due to the high melting point of VDB (74 °C) and the formation of homogeneous solutions only at elevated temperatures, measurements were performed at 100 °C as well. Measurements with formulations containing CTAE, TAP, and ADB were performed at 25 °C.

RT-NIR photorheology measurements were conducted as described in 1.1.3. Samples were irradiated for 320 s with a waveguide from below the glass plate using an Exfo OmniCure™ 2000 with a broadband Hg lamp equipped with a 400-500 nm filter. An intensity of 1 W/cm² was used at the tip of the light guide, corresponding to an intensity of 20 mW/cm² at the surface of the samples.

2.4.2 Mechanical properties of polymer networks

For the DMTA measurements, specimens were fabricated from the formulations described in 2.4.1. Curing of all samples was conducted in a Lumamat 100 light oven. For curing of VDB, TAS, and TAB, the silicon mold was preheated in an oven at 110 °C and a special curing program was used, during which the samples were heated to ~104 °C. Samples were cured on both sides for 10 min. Curing was conducted without a lid, and the resulting samples were sanded to remove surface imperfections and subsequently stored under dry conditions and argon atmosphere. DMTA measurements were performed as described in 2.1.3.

Tensile test specimens of 5B shape were prepared analogously to DMTA specimens. Tensile tests were conducted on a Zwick Z050 tensile testing machine equipped with a 1 kN load sensor. The crosshead speed was set to 5 mm/min, and the strain was measured using a mechanical extensometer. Analysis of the samples was done using TestXpert II testing software.

2.4.3 Degradation of polymer networks

For the degradation studies, cylindrically-shaped specimens with dimensions of $d = 6$ mm and $h = 2$ mm and a mass of approximately 50 mg were prepared, analogously to the DMTA specimens described in 2.4.2. Degradation studies were conducted as described in 2.1.4, with three samples of each material and each condition removed from the buffer solution after 2 d, 7 d, 14 d, 30 d, 60 d, 90 d, and 180 d.

2.5 Optimization of mechanical properties and degradation behavior

Formulations containing different molar ratios of 40 mol%, 60 mol%, or 80 mol% of each degradable monomer (TAP, TAS, VDB, and ADB) with respect to TAI were prepared with the thiol TMT in an equimolar ratio of double bonds to thiol groups. 1 w% of Ivocerin for initiation and 0.02 w% of PYR for stabilization were added. The formulations were homogenized with a vortex under slight heating until complete dissolution of the PI and monomers. Samples containing TAS, ADB, or VDB were homogenized by storage in an oven at 110 °C for 10 min. After homogenization, formulations were stored at rt for 2 d to test if phase separation or precipitation occurred at rt. As references, formulations containing 0 mol% of degradable monomer (100 mol% TAI) and 100 mol% of each degradable monomer were used.

2.5.1 Optimization with a trifunctional crosslinker

2.5.1.1 Reactivity of formulations with TAI

RT-NIR photorheology measurements were conducted as described in 1.1.3 with formulations described in 2.5. Samples were irradiated for 320 s with a waveguide from below the glass plate using an Exfo OmniCure™ 2000 with a broadband Hg lamp equipped with a 400-500 nm filter. An intensity of 1 W/cm² was used at the tip of the light guide, corresponding to an intensity of 20 mW/cm² at the surface of the samples. Measurements were performed at 25 °C for all formulations, except 80 mol% or 100 mol% TAS or VDB. These systems were tested at 100 °C since homogeneous formulations were obtained at this temperature.

2.5.1.2 Mechanical properties of polymer networks with TAI

For the DMTA measurements, specimens were fabricated from the formulations described in 2.5. Curing of all samples was conducted in a Lumamat 100 light oven. For the curing of 80 mol% or 100 mol% TAS or VDB, the silicon mold used was preheated in an oven at 110 °C, and a special curing program was used, during which the samples were heated to ~104 °C. Curing was conducted without a lid, and the resulting samples were sanded to remove surface imperfections and subsequently stored under dry conditions and argon atmosphere. DMTA measurements were performed as described in 2.1.3.

Tensile test specimens of 5B shape were prepared analogously to DMTA specimens. Tensile tests were conducted as described in 2.1.3.

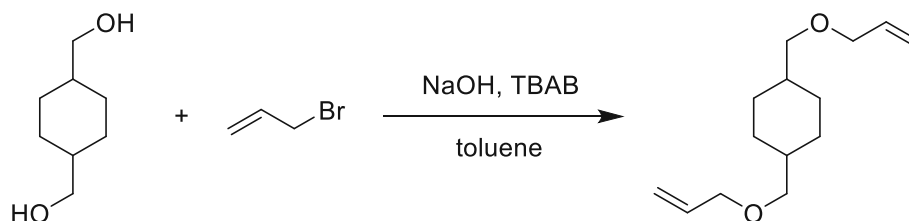
2.5.1.3 Degradation of polymer networks with TAI

For the degradation studies, cylindrically-shaped specimens with dimensions of $d = 6$ mm and $h = 2$ mm and a mass of approximately 50 mg were prepared analogously to the DMTA specimens described in 2.5.1.2. Degradation studies were conducted as described in 2.1.4, with three samples of each material and each condition, and were removed from the buffer solution after 2 d, 7 d, 14 d, 30 d, 60 d, 90 d, and 180 d.

2.5.2 Optimization with a difunctional crosslinker

2.5.2.1 Syntheses of difunctional crosslinkers

2.5.2.1.1 Synthesis of 1,4-bis(2-propenyloxy)methylcyclohexane (CAE)³⁴³



chemicals	M [g/mol]	eq.	n [mol]	m [g]	V [mL]
1,4-cyclohexanedimethanol	144.21	1.0	163	23.4	
allyl bromide	120.99	3.5	569	68.8	
NaOH	40.00	2.9	470	18.8	
tetra-n-butylammonium bromide	322.38	0.13	21	6.9	
toluene					105

The synthesis of 1,4-bis(2-propenyloxy)methylcyclohexane (CAE) was conducted according to Lohse *et al.*³⁴³ For the synthesis, 1,4-cyclohexanedimethanol, allyl bromide, tetra-n-butylammonium bromide, NaOH, and toluene were added to a 250 mL round-bottom three-neck flask equipped with a mechanical stirrer, reflux condenser and an Ar-inlet under inert atmosphere. The reaction mixture was stirred at 40 °C for 8 h and at 80 °C for 10 h. After cooling to rt, the reaction mixture was poured into 250 mL of water, the layers were separated, and the aqueous layer was extracted with 3x50 mL toluene. The toluene solutions were combined and washed with water until pH ~7. The organic phase was dried over Na₂SO₄, and the solvent was removed to yield the crude product as a colorless liquid. As stated in literature, bulb tube distillation was attempted for purification (0.04 mbar, 100 °C), but the separation of the mono- and disubstituted compound was unsuccessful. Column chromatography of the crude mixture (95% PE, 5% EE), yielded the desired product.

Yield: colorless liquid (70%).

R_f: 0.32 (PE:EE=20:1)

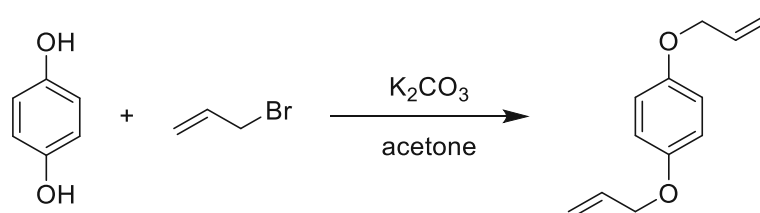
RI: 1.4664 (Lit.³⁶⁸ 1.4662)

b.p.: 100 °C/0.04 mbar (Lit.³⁶⁸ 94-95 °C/1 mbar)

¹H NMR (400 MHz, CDCl₃): δ 5.98 – 5.84 (m, 2H, -CH=CH₂), 5.26 (dp, J = 17.2, 1.7 Hz, 2H, -CH=CH₂), 5.16 (dp, J = 10.4, 1.5 Hz, 2H, -CH=CH₂), 3.95 (ddt, J = 5.6, 4.3, 1.5 Hz, 4H, -O-CH₂-CH=CH₂), 3.33 (d, J = 7.0 Hz, 1H, -O-CH₂-CH-), 3.24 (d, J = 6.5 Hz, 3H, -O-CH₂-CH-), 1.89 – 1.76 (m, 3fH, -O-CH₂-CH- and -CH_{2,cyclic}-), 1.60 – 1.46 (m, 3H, , -O-CH₂-CH- and -CH_{2,cyclic}-), 1.40 (tdd, J = 12.7, 8.6, 4.6 Hz, 1H, -CH_{2,cyclic}-), 1.04 – 0.88 (m, 3H, -CH_{2,cyclic}-).

¹³C NMR-APT (101 MHz, CDCl₃): δ 134.12 (-CH=CH₂), 118.15 (-CH=CH₂), 73.13 (-O-CH₂-CH=CH₂), 69.67 (-O-CH₂-CH=), 36.78 (C_{cyclic}), 28.21 (-CH_{2,cyclic}-).

2.5.2.1.2 Synthesis of 1,4-bis(allyloxy)benzene (BAE)^{340,344}



chemicals	M [g/mol]	eq.	n [mol]	m [g]	V [mL]
hydroquinone	110.11	1.0	163	18.0	
allyl bromide	120.99	2.2	360	43.5	
K ₂ CO ₃	138.21	1.4	229	31.6	
acetone					200

The synthesis of 1,4-bis(allyloxy)benzene (BAE) was conducted according to Kohta *et al.*³⁴⁴ and Childress *et al.*³⁴⁰ For the synthesis, the reaction apparatus consisted of a 500 mL three-neck round bottom flask equipped with a reflux condenser, septum, and an Ar-inlet. Hydroquinone and K₂CO₃ were dispersed in 200 mL of dry acetone under inert atmosphere. The reaction mixture was heated to 45 °C and stirred for 10 min. Then allyl bromide was added. The reaction mixture was then stirred at 45 °C for 3 d. The solid residue was subsequently filtered off, and the filtrate was concentrated to yield the crude product. For purification, recrystallization from hexane at -20 °C was attempted as described by Kotha *et al.*³⁴⁴, however, was not possible as the melting point of the product mixture was too low. Hence, column chromatography (5% EE in PE), as described by Childress *et al.*³⁴⁰ was performed to yield the pure product as white crystals.

Yield: white crystals (69%).

R_f: 0.30 (PE:EE=20:1)

m.p.: 33-34 °C (Lit.³⁶⁹ 33-35°C)

¹H NMR (400 MHz, CDCl₃): δ 6.85 (s, 4H, -C-H_{Ar}), 6.05 (ddt, J = 17.3, 10.6, 5.3 Hz, 2H, -CH=CH₂), 5.40 (dq, J = 17.2, 1.6 Hz, 2H, -CH=CH₂), 5.27 (dq, J = 10.5, 1.5 Hz, 2H, -CH=CH₂), 4.49 (dt, J = 5.3, 1.6 Hz, 4H, -O-CH₂-).

¹³C NMR-APT (101 MHz, CDCl₃): δ 153.0 (-C_{Ar}-O-), 133.7 (-CH=CH₂), 117.6 (-CH=CH₂), 115.8 (C-H_{Ar}), 69.6 (-O-CH₂-).

2.5.2.2 Mechanical properties with difunctional crosslinkers

Formulations were prepared with the difunctional monomers CVE, CAE, IAE, DAI, or VSA and the thiol TMT in an equimolar ratio of double bonds to thiol groups, as well as 1 w% of Ivocerin and 0.02 w% of PYR. For homogenization, formulations were carefully heated and vortexed. For the monomer DAI, no dissolution in the thiol could be achieved, even after heating the sample for 20 min to 110 °C. Also, heating above its melting point of DAI (148 °C) was unsuccessful, as instant

precipitation during mixing occurred. For all other monomers, homogeneous formulations were obtained at 25 °C.

For the measurements, DMTA specimens were prepared from the formulations, and curing was conducted at rt in a Lumamat 100 light oven. Samples were cured on both sides for 10 min. Curing was conducted without a lid, and the resulting samples were sanded to remove surface imperfections and subsequently stored under dry conditions and argon atmosphere before the measurements. DMTA measurements were performed as described in 2.1.3.

2.5.2.3 Reactivity of formulations with VSA

Formulations containing different molar ratios of 40 mol%, 60 mol%, or 80 mol% of each degradable monomer (TAP, TAS, VDB, and ADB) with respect to VSA were prepared with the thiol TMT in an equimolar ratio of double bonds to thiol groups. 1 w% of Ivocerin for initiation and 0.02 w% of PYR for stabilization were added. The formulations were homogenized with a vortex under slight heating until complete dissolution of the PI and monomers. Samples containing TAS, ADB, or VDB were homogenized by storage in an oven at 110 °C for 10 min. After homogenization, formulations were stored at rt for 2 d to test if phase separation or precipitation occurred at rt. As references, formulations containing 0 mol% of degradable monomer (100 mol% VSA) and 100 mol% of each degradable monomer were used.

With these formulations, RT-NIR photorheology measurements were conducted as described in 1.1.3. Samples were irradiated for 320 s with a waveguide from below the glass plate using an Exfo OmniCure™ 2000 with a broadband Hg lamp equipped with a 400-500 nm filter. An intensity of 1 W/cm² was used at the tip of the light guide, corresponding to an intensity of 20 mW/cm² at the surface of the samples. Measurements were performed at 25 °C for all formulations, except for 80 mol% TAS and 100 mol% TAS or VDB. These systems were tested at 100 °C since homogeneous formulations were obtained at this temperature.

2.5.2.4 Mechanical properties of polymer networks with VSA

For the DMTA measurements, specimens were fabricated from the formulations described in 2.5.2.3. Curing of all samples was conducted in a Lumamat 100 light oven. For curing of 80 mol% TAS and 100 mol% TAS or VDB, the silicon mold used was preheated in an oven at 110 °C, and a special curing program was used, during which the samples were heated to ~104 °C. Curing was

conducted without a lid, and the resulting samples were sanded to remove surface imperfections and subsequently stored under dry conditions and argon atmosphere. DMTA measurements were performed as described in 2.1.3.

Tensile test specimens of 5B shape were prepared analogously to DMTA specimens. Tensile tests were conducted as described in 2.1.3.

2.5.2.5 Degradation of polymer networks with VSA

For the degradation studies, cylindrically-shaped specimens with dimensions of $d = 6$ mm and $h = 2$ mm and a mass of approximately 50 mg were prepared analogously to the DMTA specimens described in 2.5.2.4. Degradation studies were conducted as described in 2.1.4, with three samples of each material and each condition, and were removed from the buffer solution after 2 d, 7 d, 14 d, 30 d, 60 d, 90 d, and 180 d.

2.6 Influence of toughness enhancers

NB-PCL was synthesized by Dellago *et al.*³⁴⁷ Formulations were prepared by addition of 5 w%, 10 w%, 15 w%, 20 w%, and 25 w% of NB-PCL to VDB, while the amount of the thiol TMT was adjusted to obtain an equimolar ratio of double bonds to thiol groups. 1 w% of Ivocerin for initiation and 0.02 w% of PYR for stabilization were added. The formulations were homogenized by storage in an oven at 110 °C for 20 min. The formulation containing only VDB and TMT in an equimolar ratio of double bonds to thiol groups was used as a reference.

2.6.1 Rheological properties of formulations

Rheology measurements of formulations described in 2.6 were conducted on a modular compact rheometer MCR 300 by Physica Anton Paar. After 5 min of acclimatization time, the viscosity of the formulations was measured at 100 °C with a CP-25 measuring system (diameter 25 mm), a gap of 48 μm , and a constant shear rate of 100 s^{-1} .

2.6.2 Reactivity of formulations

RT-NIR photorheology measurements were conducted as described in 1.1.3 with formulations described in 2.6. Samples were irradiated for 320 s with a waveguide from below the glass plate using an Exfo OmniCure™ 2000 with a broadband Hg lamp equipped with a 400-500 nm filter. An intensity of 1 W/cm² was used at the tip of the light guide, corresponding to an intensity of 20 mW/cm² at the surface of the samples. Measurements were performed at 100 °C for all formulations since homogeneous formulations were obtained at this temperature.

2.6.3 Mechanical properties of polymer networks

For the DMTA measurements, polymer specimens were fabricated from the formulations described in 2.6. Curing of all samples was conducted in a Lumamat 100 light oven. For the curing of all formulations, the silicon mold used was preheated in an oven at 110 °C, and a special curing program was used, during which the samples were heated to ~104 °C. Samples were cured on both sides for 10 min. Curing was conducted without a lid, and the resulting samples were sanded to remove surface imperfections and subsequently stored under dry conditions and argon atmosphere. DMTA measurements were performed as described in 2.1.3.

Tensile test specimens of 5B shape were prepared analogously to DMTA specimens. Tensile tests were conducted as described in 2.1.3.

2.7 3D printing

2.7.1 Characterization of the printing resin

The printing formulation was prepared from the monomer VDB and the thiol TMT in an equimolar ratio of double bonds to thiol groups. 1 w% of Ivocerin for initiation and 0.02 w% of PYR for stabilization were added. For sufficient resolution during printing, 0.1 w% of the absorber QY were added. The formulation was homogenized by storage in an oven at 110 °C for 30 min for full dissolution of QY and was subsequently stored in an oven at 55 °C, which was determined to be the minimum temperature to obtain a homogeneous formulation without reprecipitation of VDB in the thiol.

The rheology of the formulation was determined with a modular compact rheometer MCR 300 by Physica Anton Paar at 55 °C. After 5 min of acclimatization time, the viscosity of the formulations was measured with a CP-25 measuring system (diameter 25 mm), a gap of 48 µm, and a constant shear rate of 100 s⁻¹ for 8 h.

RT-NIR photorheology measurements of the printing resin were conducted as described in 1.1.3. Samples were irradiated for 320 s with a waveguide from below the glass plate using an Exfo OmniCureTM 2000 with a broadband Hg lamp equipped with a 400-500 nm filter. An intensity of 1 W/cm² was used at the tip of the light guide, corresponding to an intensity of 20 mW/cm² at the surface of the samples. Measurements were performed at 55 °C.

2.7.2 Laser-SLA

Laser exposure tests and 3D printing of the printing formulation described in 2.7.1 were conducted on a Caligma 200 UV prototype developed by Cubicure GmbH. Irradiation of samples was conducted by scanning a laser beam over a 2-dimensional plane using a Galvano scanner. An irradiation wavelength of 375 nm and a power of 70 mW/mm² were used. The diameter of the laser spot during the exposure tests was 25 µm. For light exposure tests, the vat temperature was set to 55 °C, and writing speeds were varied from 1000 mm/s, 500 mm/s, 200 mm/s, and 100 mm/s. The geometry irradiated was a circle with a diameter of 1.5 cm. The structured test platelets were detached from the vat, and their thickness was assessed with a measuring gauge. A schematic view of the printer is depicted in Figure 140.

For 3D printing, the vat and the building platform of the printer were heated to 55 °C during the printing process. A writing speed of 100 mm/s and a layer thickness of 100 µm were applied. Due to the high adhesion of the printed structure on the surface of the vat, the vat was covered with a transparent PE tape, used for RT-NIR-photorheology measurements during the printing process. After ~10 printed layers the tape a new tape had to be attached.

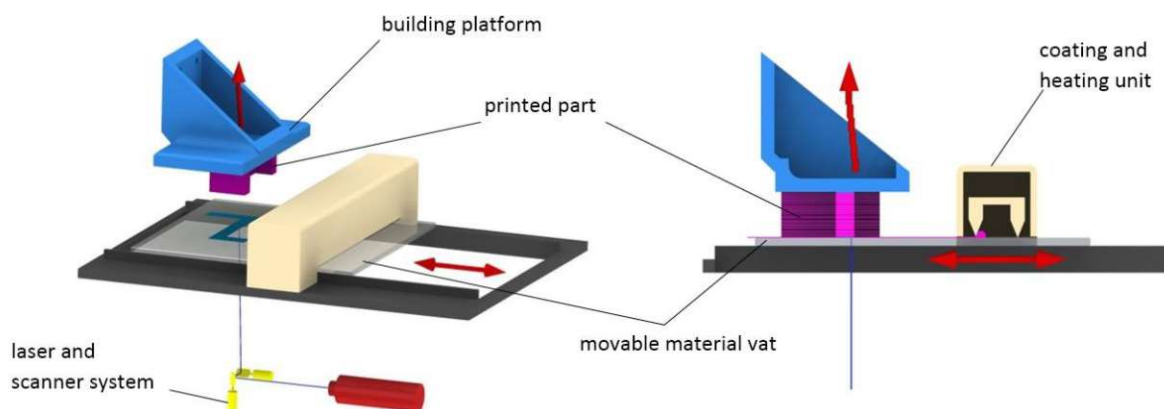


Figure 140: General setup of a Hot Lithography printer.⁴⁹

2.8 Influence of sterilization on mechanical properties

For sterilization studies, six tensile test specimens (shape 5B) and two DMTA samples (5×2×40 mm) of the material containing VDB and the thiol TMT in an equimolar ratio of double bonds to thiol groups as well as 1 w% Ivocerin and 0.02 w% PYR were prepared. Curing of all samples was conducted in a Lumamat 100 light oven with a special curing program, during which the samples were heated to ~104 °C. Samples were cured on both sides for 10 min. Curing was conducted without a lid, and the resulting samples were sanded to remove surface imperfections and stored under dry conditions and argon atmosphere.

Sterilization of all samples was conducted by KLS Martin. Sterilization with EO was conducted according to DIN EN ISO 11135-1 with a concentration of 6% EO in CO₂ for 2 h at 55 °C, followed by a 6 h desorption phase. Sterilization with γ -radiation was applied using a Co⁶⁰-radiation source for 5 h with a radiation dose of 18.6 kGy for low doses and 30.5 kGy for high doses according to DIN EN ISO 9001, DIN EN ISO 13485, and DIN EN ISO 11137-1

DMTA measurements were performed as described in 2.1.3, and tensile tests were conducted as described in 2.4.2.

2.9 Evaluation of cytotoxicity

In-vitro cytotoxicity of the compounds TAP, TAS, ADB, VDB, TAI, VSA, and TMT was tested in NCTC Clone 929 fibroblast cell culture using a Presto[®] Blue Assay. The cells were cultured in Dulbecco's modified eagle medium (DMEM) supplemented with 10% fetal bovine serum (FBS) and penicillin-

streptomycin (100 U/mL penicillin and 100 µg/mL streptomycin) in 96-well plates at a density of 1×10^4 cells per well for 24 h in humidified air with 95% relative humidity and with 5% CO₂ at 37 °C. The tested substances were dissolved in DMSO to obtain 1 M solutions. These solutions were diluted with DMEM, 10% FBS, 100 U/mL penicillin, and 100 µg/mL streptomycin to produce solutions with different concentrations (10 mM, 7.5 mM, 5 mM, and 2.5 mM). After 24 h, the cells were treated with 100 µL of each solution in triplicates and incubated at 37 °C for 24 h. Qualitative screening of morphological changes was conducted under the microscope according to ISO 10993-5. For quantitative screening of cell viability, the supernatant solution was removed, and 10 µL of resazurin were added to the cells. After 1 h at 37 °C, the fluorescence intensity was measured at 570 nm. As control values, cells treated with 1% DMSO solution, a blank value, and PBS buffer were used. The results represent the mean of the triplicate measurements. The concentration at which 50% of the cells are still viable after 1 d was used to determine the cytotoxicity.

Appendix

1. Density, rheology, and stability of formulations

The density of all formulations processable at rt was determined with a 1 mL pycnometer at 25 °C. As well, viscosity at the respective processing temperature T was determined for all formulations at a constant shear rate of 100 s⁻¹. Finally, stability at rt over time was assessed for these formulations and different time points t₀, t_{1d}, t_{3d}, t_{5d}, t_{7d}, and t_{10d}. Studies were stopped before 10 d if either gelation occurred or the viscosity increase was ≥100% with regards to η_{t0}. The results are shown in Table 27 to Table 37

Table 27: Density of formulations processable at rt containing each monomer and the thiol TMT in an equimolar ratio of double bonds to thiol groups, with 1 w% Ivocerin and 0.02 w% PYR.

thiol	monomer	ρ [mg/mL]
TMT	CTAE	1299.89
	TAB	1241.42
	TAP	1295.43
	ADB	1182.37
	DAS	1210.12
	TAI	1324.21
	VSA	1183.07

Table 28: Viscosity at the temperature T of formulations containing each monomer and the thiol and the thiol TMT in an equimolar ratio of double bonds to thiol groups, with 1 w% Ivocerin and 0.02 w% PYR.

thiol	monomer	T [°C]	η [Pa·s]
TMT	CTAE	25	0.187
	TAB	25	1.050
	TAP	100	0.005
	ADB	25	0.073
	DAS	100	0.043
	TAI	25	0.646
	VSA	25	0.525

Table 29: Stability studies of formulations containing each monomer and the thiol and the thiol TMT in an equimolar ratio of double bonds to thiol groups via viscosity measurements at the respective temperature T at t_0 , t_{1d} , t_{2d} , t_{4d} , t_{5d} , and t_{7d} . *Gelation occurred.

thiol	monomer	T [°C]	η_{t0} [Pa·s]	η_{t1d} [Pa·s]	η_{t3d} [Pa·s]	η_{7d} [Pa·s]	η_{t10d} [Pa·s]
TMT	CTAE	25	0.187	0.183	0.187	0.222*	*
	TAB	25	1.050	1.050	1.040	1.500*	*
	TAP	100	0.006	0.006	0.007*	*	*
	ADB	25	0.073	0.061	0.072	0.109*	*
	DAS	100	0.043	0.082	*	*	*
	TAI	25	0.646	0.811	16.3*	*	*
	VSA	*	*	*	*	*	*

Table 30: Density of formulations processable at rt containing 40-80 mol% TAS, VDB, or ADB with respect to non-degradable TAI and the thiol TMT in an equimolar ratio of double bonds to thiol groups, with 1 w% Ivocerin and 0.02 w% PYR.

thiol	comonomer	monomer	x_{deg} [mol%]	ρ [mg/mL]
TMT	TAI	TAS	40	1185.00
			60	1191.23
		VDB	40	1191.89
			60	1198.82
		ADB	40	1167.36
			60	1226.20
			80	1178.92
			100	1182.24

Table 31: Viscosity of formulations processable at rt containing 40-80 mol% TAS, VDB, or ADB with respect to non-degradable TAI and the thiol TMT in an equimolar ratio of double bonds to thiol groups, with 1 w% Ivocerin and 0.02 w% PYR.

thiol	comonomer	monomer	T [°C]	x_{deg} [mol%]	η [Pa·s]
TMT	TAI	TAS	25	40	0.172
			25	60	0.104
			100	80	0.005
			100	100	0.005
		VDB	25	40	1.111
			25	60	1.078
			100	80	0.849
			100	100	0.043
		ADB	25	40	0.975
			25	60	0.825
			25	80	0.825
			25	100	0.646

Table 32: Stability of formulations containing 40-80 mol% TAS, VDB, or ADB with respect to non-degradable TAI and the thiol TMT in an equimolar ratio of double bonds to thiol groups, with 1 w% Ivocerin and 0.02 w% PYR via viscosity measurements at the respective temperature T at t_0 , t_{1d} , t_{2d} , t_{4d} , t_{5d} , and t_{7d} . *Gelation occurred.

thiol	comonomer	monomer	T [°C]	x_{deg} [mol%]	η_0 [Pa·s]	η_{t1d} [Pa·s]	η_{t2d} [Pa·s]	η_{t4d} [Pa·s]	η_{t5d} [Pa·s]	η_{t7d} [Pa·s]
TMT	TAI	TAS	25	40	0.172	0.175	0.173	0.280*	*	*
			25	60	0.104	0.104	0.105	0.150*	*	*
			100	80	0.005	0.010*	*	*	*	*
			100	100	0.005	0.007*	*	*	*	*
		VDB	25	40	1.111	1.822*	*	*	*	*
			25	60	1.078	1.923*	*	*	*	*
			100	80	0.849	4.921*	*	*	*	*
			100	100	0.043	0.084*	*	*	*	*
		ADB	25	40	0.975	0.978	0.969	0.973	0.979	0.972
			25	60	0.825	0.826	0.825	0.828	0.930*	*
			25	80	0.825	0.827	0.823	0.828	0.953*	*
			25	100	0.646	0.123*	*	*	*	*

Table 33: Density of formulations processable at rt containing 40-80 mol% TAS, VDB, or ADB with respect to non-degradable VSA and the thiol TMT in an equimolar ratio of double bonds to thiol groups, with 1 w% Ivocerin and 0.02 w% PYR.

thiol	comonomer	monomer	x_{deg} [mol%]	ρ [mg/mL]
TMT	VSA	TAS	40	1165.20
			60	1177.47
		VDB	40	1226.85
			60	1180.35
			80	1215.91
		ADB	40	1167.36
			60	1195.10
			80	1166.52
			100	1182.37

Table 34: Viscosity of formulations processable at rt containing 40-80 mol% TAS, VDB, or ADB with respect to non-degradable VSA and the thiol TMT in an equimolar ratio of double bonds to thiol groups, with 1 w% Ivocerin and 0.02 w% PYR.

thiol	comonomer	monomer	T [°C]	x _{deg} [mol%]	η [Pa·s]
TMT	VSA	TAS	25	40	0.094
			25	60	0.071
			100	80	0.004
			100	100	0.005
		VDB	25	40	1.525
			25	60	1.633
			100	80	2.145
			100	100	0.043
		ADB	25	40	0.528
			25	60	0.552
			25	80	0.612
			25	100	0.646

Table 35: Stability of formulations containing 40-80 mol% TAS, VDB, or ADB with respect to non-degradable VSA and the thiol TMT in an equimolar ratio of double bonds to thiol groups, with 1 w% Ivocerin and 0.02 w% PYR via viscosity measurements at the respective temperature T at t₀, t_{1d}, t_{2d}, t_{4d}, t_{5d}, and t_{7d}. *Gelation occurred.

thiol	comonomer	monomer	T [°C]	x _{deg} [mol%]	η ₀ [Pa·s]	η _{t1d} [Pa·s]	η _{t2d} [Pa·s]	η _{t4d} [Pa·s]	η _{t5d} [Pa·s]	η _{t7d} [Pa·s]
TMT	VSA	TAS	25	40	0.094	0.094	0.093	0.114*	*	*
			25	60	0.071	0.072	0.072	0.075*	*	*
			100	80	0.004	0.005	0.005	0.005	0.005	0.005
			100	100	0.005	0.006	0.007	0.007	0.007	0.007
		VDB	25	40	1.525	1.992*	*	*	*	*
			25	60	1.633	2.938*	*	*	*	*
			100	80	2.145	5.257*	*	*	*	*
			100	100	0.043	0.082*	*	*	*	*
		ADB	25	40	0.528	0.441	0.521	0.510	0.525	0.510
			25	60	0.552	0.523	0.534	0.555	0.582	0.596*
			25	80	0.612	0.636	0.600	0.580	0.680*	*
			25	100	0.646	0.811*	16.30*	*	*	*

Table 36: Viscosity at the temperature T of formulations containing VDB, 0-25 w% of NB-PCL, and the thiol TMT in an equimolar ratio of double bonds to thiol groups, with 1 w% Ivocerin and 0.02 w% PYR.

thiol	monomer	T [°C]	x _{NB-PCL} [w%]	η [mPa·s]
TMT	VDB	100	0	43
			5	41
			10	85
			15	200
			20	142
			25	173

Table 37: Stability studies of formulations containing VDB, 0-25 w% of NB-PCL, and the thiol TMT in an equimolar ratio of double bonds to thiol groups via viscosity measurements at the respective temperature T at t_0 , t_{1d} , t_{2d} , t_{4d} , t_{5d} , and t_{7d} . *gelation occurred.

thiol	monomer	X_{NB-PCL} [w%]	T [°C]	η_{t0} [Pa·s]	η_{t1d} [Pa·s]	η_{t3d} [Pa·s]	η_{7d} [Pa·s]	η_{t10d} [Pa·s]
TMT	VDB	0	100	0.043	0.082*	*	*	*
		5	100	0.041	0.068*	*	*	*
		10	100	0.085	0.136*	*	*	*
		15	100	0.200	0.183	0.222	0.535*	*
		20	100	0.142	0.302*	*	*	*
		25	100	0.173	0.273*	*	*	*

2. Filling with hydroxyapatite

Human bone is a hard but lightweight nanocomposite tissue and is composed of an inorganic (40 vol%), organic (35 vol%), and water fraction (25 vol%). The inorganic phase is mainly composed of the mineral hydroxyapatite (HAP), while the organic fraction consists mainly of type-I collagen (90%) and 10% of non-collagenous proteins (NPC) and polysaccharides. In this composite structure, the inorganic phase acts as a structural reinforcement, while the organic phase provides toughness.^{112,370} Addition of hydroxyapatite to degradable scaffolds is highly intriguing, as during bone regeneration, the polymer matrix can degrade to release the inorganic particles, which can then be taken up by the regenerating tissue and help the formation of new bone.

Therefore, the degradable polymer system containing the boronic ester VDB was filled with the inorganic mineral hydroxyapatite (HAP), and the influence on formulation viscosity and (thermo)mechanical properties was studied. The filler was kindly provided by Lithoz GmbH®. These studies aimed to obtain highly filled systems, as the average content of inorganic fraction in human bone equals ~40 vol%.

As the addition of HAP to the formulations containing >50 mol% VDB with respect to the non-degradable monomer TAI caused precipitation of the monomer in the slurry, the formulation containing 50 mol% of VDB with respect to TAI and the thiol TMT in an equimolar ratio of double bonds to thiol groups was chosen for subsequent studies.

For this, first, the density of the formulation was determined with a 1 mL pycnometer. The density of HAP was derived from the SDS provided by Lithoz®. The result is given in Table 38.

Table 38: Density of the formulation containing 50 mol% VDB with respect to non-degradable TAI and the thiol TMT in an equimolar ratio of double bonds to thiol groups, with 1 w% Ivocerin and 0.02 w% PYR.

	ρ [mg/mL]
50 mol% VDB	1318.18
HAP	3200.00

This formulation was then filled with different ratios of HAP, namely 10 vol%, 20 vol%, 30 vol%, and 40 vol%. Homogenization of the formulation was conducted by repeated heating and vortexing. The w% of HAP $w\%_{\text{HAP}}$ and the organic phase $w\%_{\text{org. phase}}$ was calculated for each formulation and is given in Table 39. For these first studies, no additives or dispersing agents to prevent segregation and deagglomerate the filler were added.

Table 39: Calculation of resulting w% of HAP and organic phase from vol% HAP.

thiol	comonomer	monomer	vol% HAP	$w\%_{\text{HAP}}$ [%]	$w\%_{\text{org. phase}}$ [%]
TMT	TAI	VDB	10	21.2	78.8
			20	37.8	62.2
			30	51.0	49.0
			40	61.8	38.2

2.1 Rheology measurements

To determine the influence of the filler HAP on rheological properties, rheology measurements were conducted of the formulation filled with 10 vol%, 20 vol%, 30 vol%, or 40 vol% HAP at 25 °C. The measurements were performed with a logarithmical increase in shear rate from 0.1 to 100 s⁻¹, and the viscosity was determined at a shear rate of 30 s⁻¹ ($\eta_{25^\circ\text{C},30\text{s}^{-1}}$), as this is the shear rate typically exerted onto the formulation by a coating unit of a Lithoz printer. The results are given in Table 41.

Table 40: Viscosity of the formulation containing 50 mol% VDB with respect to non-degradable TAI and the thiol TMT in an equimolar ratio of double bonds to thiol groups, which was filled with 10-40 vol% HAP.

thiol	comonomer	monomer	vol% HAP	$\eta_{25^\circ\text{C},30\text{s}^{-1}}$ [Pa·s]
TMT	TAI	VDB	10	6.91
			20	10.85
			30	42.32
			40	188.98

Low viscosities $\eta_{25^{\circ}\text{C},30\text{s}-1} < 20 \text{ Pa}\cdot\text{s}$ were shown for the formulations containing 10 vol% and 20 vol% HAP, while a significant increase was observed at 30 vol% HAP. Therefore, formulations containing higher HAP concentrations need to be processed at elevating printing temperatures.

2.2 DMTA measurements

To determine the thermomechanical properties, DMTA specimens with a shape of 5×2×40 mm were prepared from the 10-40 vol% HAP formulations. 1 w% of Ivocerin and 0.02 w% of PYR were added, and curing was conducted in a Lumamat 100 light oven at rt. Samples were cured on both sides for 10 min. DMTA measurements were performed as described in 2.1.3. The resulting specimens are shown in Figure 141.



Figure 141: from left to right: DMTA specimens of polymerized formulations filled with 10 vol%, 20 vol%, 30 vol%, and 40 vol% of HAP.

The specimens obtained for 10-30 vol% HAP displayed good quality without visible bubbles, while the sample containing 40 vol% HAP contained many bubbles. This was due to the high viscosity of this formulation which made processing very difficult. Nevertheless, this specimen was also tested to get insight into the influence of HAP-filling on mechanical properties. The results of the DMTA measurements are depicted in Figure 142.

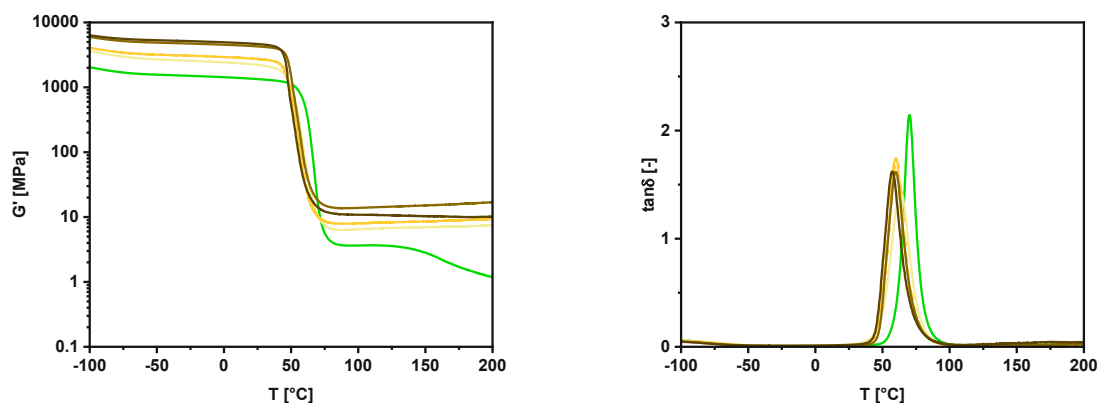


Figure 142: G' (left) and $\tan\delta$ (right) over temperature of the different networks formed from formulations of containing 50 mol% VDB filled 0 vol% (—), 10 vol% (—), 20 vol% (—), 30 vol% (—) or 40 vol% (—) HAP.

Figure 142 (left) shows that the addition of HAP slightly decreases the T_g of the material upon increasing amount, with a maximum decrease of 10 °C for 40 vol% compared to the unfilled system. This might be due to decreased interchain interactions resulting from the HAP particles present in the network. However, T_g values well above body temperature are maintained for all materials. The most drastic effect of the filler is the enormous increase in storage modulus. This effect is most prominent for high filler contents, with an increase in $G'_{25^\circ\text{C}}$ of 138% and 159% for 30 vol% and 40 vol%, respectively. Therefore, significantly higher stiffness is exhibited upon the addition of the filler HAP, while high T_g values are maintained. Hence, filling of the polymer significantly enhances the thermomechanical properties of the materials. The detailed results are given in Table 41.

Table 41: Detailed results of DMTA measurements.

thiol	comonomer	monomer	vol% HAP	T_g [°C]	$G'_{25^\circ\text{C}}$ [MPa]	$G'_{37^\circ\text{C}}$ [MPa]	fwhm [°C]	G'_R [MPa]
TMT	TAI	VDB	0	67	1790	1700	14	6
			10	63	2220	2000	16	8
			20	60	2730	2530	13	9
			30	60	4280	4040	14	17
			40	57	4650	4320	14	10

3. Post-polymerization modification

It is well known in literature that various post-polymerization modification (PPM) techniques of polymer networks can be employed to obtain specific material properties that would be difficult or impossible to achieve through conventional monomer polymerization. Podgórski *et al.*³⁷¹ showed that polysulfide networks, with thicknesses up to 500 μm can be fully converted into polysulfones by treatment with H_2O_2 for 24 h while preserving the primary structure of the thiol-ene network. By this, substantially increased T_g of the polysulfone networks were observed, with an increase of more than 100 $^\circ\text{C}$ for some polymers. It was presumed that this reinforcing effect is due to the strong electrostatic interactions of the polar sulfone groups, leading to high-performance materials with this convenient, clean, and efficient method.

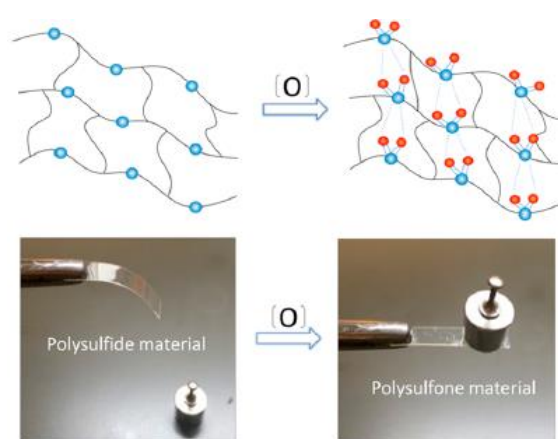


Figure 143: Post-polymerization modification by oxidation of polysulfide materials to polysulfone materials with H_2O_2 .³⁷¹

Therefore, this approach was also attempted for a degradable material and a non-degradable reference material to possibly obtain enhanced thermomechanical properties of the networks.

First, the H_2O_2 concentration was determined to ensure controlled oxidation conditions according to a protocol from Solvay for H_2O_2 solutions with concentrations from 20-70%.³⁷² This method relies on the quantitative oxidation of hydrogen peroxide with a potassium permanganate solution of known strength. By this, a H_2O_2 concentration of $30.73 \pm 0.03 \%$ was determined.

For the oxidation studies, the formulation containing 50 mol% B-based VDB or Si-based TAS with respect to the non-degradable monomer TAI and the thiol TMT in an equimolar ratio of double bonds to thiol groups was chosen. As a reference, the formulation containing only non-degradable TAI and the thiol TMT was chosen (double bonds:thiol groups=1:1). DMTA specimens were prepared from these formulations in the Lumamat 100 light oven with a shape of $5 \times 2 \times 40$ mm. Samples were cured at rt. Furthermore, disc-shaped samples with a diameter of 50 mm and a

height of 50 μm were cured on the RT-NIR photorheometer for transmission-IR and ATR-IR measurements to monitor the appearance of the sulfone band at $\sim 1100\text{ cm}^{-1}$.

The materials were then immersed in $\sim 50\text{ mL}$ 30% H_2O_2 solution for 24 h in a closed container at rt. Furthermore, control samples were immersed in $\sim 50\text{ mL}$ of distilled water to determine the influence of the solvent and to differentiate between actual oxidation and other network-altering effects. After oxidation for 24 h, the samples were washed with distilled water, blot-dried, and weighed to determine the swelling. Then, the samples were dried *in vacuo* for 7 d to constant weight to determine the actual decrease or increase in mass Δm for the sample immersed in H_2O , which will be referred to as $X_{\text{Ref. H}_2\text{O}}$ and the specimen immersed in H_2O_2 referred to as $X_{\text{H}_2\text{O}_2}$ (X =monomer).

The first results were already obtained upon removal of the samples from the H_2O_2 solution and the control samples from distilled water after 24 h. The control samples did not display any changes in dimensions or color. In the case of the oxidized samples, the reference system did not exhibit a change in sample dimensions and resulted in a uniform and geometrically flawless material. In contrast, for the specimens containing the boronic ester VDB, disruption of the material occurred after immersion in H_2O_2 (Figure 144), due to a combination of acidic and oxidative conditions, with a reported pH of 4³⁷³, leading to cleavage of the boronic ester bonds. For the network containing the orthosilicic ester TAS full dissolution of the specimens was observed due to the too labile Si-O bond under these oxidizing and acidic conditions. Therefore, polysulfides containing boronic ester or siloxane bonds cannot be oxidized to polysulfones by this method, and only the reference system containing non-degradable TAI was subjected to further tests.



Figure 144: DMTA specimen before (above) and after (below) oxidation for the sample containing 50 mol% VDB with respect to TAI and the thiol TMT in an equimolar ratio of double bonds to thiol groups.

An increase in weight was expected for the oxidized sample containing TAI and TMT due to the addition of two oxygen atoms to each sulfur atom in the network. The theoretical mass increase

of the DMTA specimen $\Delta m_{\text{theoretical}}$ was used to determine the sulfide oxidation extent SOE. The results are shown in Table 42.

Table 42: Theoretical mass increase, determined mass increase and sulfide oxidation extent of polymerized samples after treatment with 30% hydrogen peroxide (H₂O₂/water) for 24 h.

sample	$\Delta m_{\text{theoretical}}$ [%]	Δm [%]	SOE [%]
TAI _{Ref., H₂O}	0	0.2	-
TAI _{H₂O₂}	16	10	63

No significant water uptake was determined for the control sample after drying. The material immersed in H₂O₂ displayed a mass increase due to the oxidation of 64% of sulfide groups; however, though stated in literature, the oxidation was not yet complete. The experiment was repeated for longer immersion times (72 h), but only a slightly higher SOE of 76% was achieved. Therefore, most probably, the oxidizing agent cannot fully penetrate the specimens, which exhibit a higher thickness (2 mm) than the samples investigated by Podgórski *et al.*³⁷¹ Therefore, this PPM is only suitable for the modification of thin objects with a thickness <2 mm.

Next, the thermomechanical properties of the samples were determined by DMTA measurements to compare the non-immersed sample (TAI_{Ref.}), the samples immersed in H₂O (TAI_{Ref., H₂O}) or H₂O₂ (TAI_{H₂O₂}).

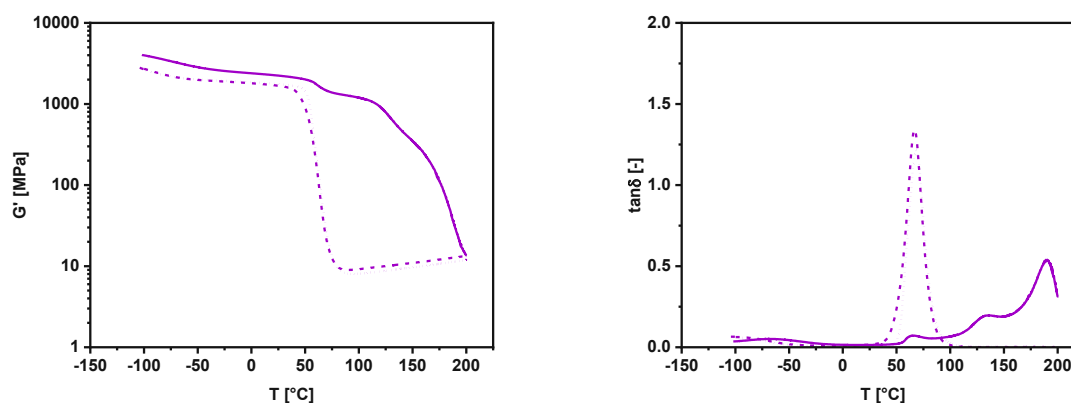


Figure 145: G' (left) and $\tan\delta$ (right) over temperature for the networks formed from the non-degradable reference TAI and the thiol TMT in an equimolar ratio of double bonds to thiol groups. TAI_{Ref.} (---); TAI_{Ref., H₂O} (---); TAI_{H₂O₂} (—).

Figure 145 shows that immersion of the sample in water does not alter the material T_g , $G'_{25^\circ\text{C}}$, or network density. Upon immersion in H₂O₂, remarkable results were obtained. The T_g of the network was increased by 122 °C to a value of 190 °C, and a drastic stiffening of the networks was observed with an increase in $G'_{25^\circ\text{C}}$ of 33% compared to the non-immersed reference. These results also corroborate the incomplete conversion (63%) to the polysulfone determined by weight, as

the $\tan\delta$ over T curve exhibits three transitions. These transitions correspond to the non-oxidized polysulfide ($\sim 65^\circ\text{C}$), the partially oxidized species at ($\sim 135^\circ\text{C}$), and the fully oxidized polysulfone (190°C), which was observed as the main transition. Therefore, upon immersion in H_2O_2 , network-reinforcing effects were observed for the material without heteroatoms. The detailed results are given in Table 43.

Table 43: Detailed results of DMTA measurements. *Could not be determined.

	T_g [$^\circ\text{C}$]	$G'_{25^\circ\text{C}}$ [MPa]	$G'_{37^\circ\text{C}}$ [MPa]	fwhm [$^\circ\text{C}$]	G'_R [MPa]
$\text{TAI}_{\text{Ref.}}$	67	1680	1550	17	13
$\text{TAI}_{\text{Ref., H}_2\text{O}}$	68	1760	1690	17	12
$\text{TAI}_{\text{H}_2\text{O}_2}$	190	2240	2150	-*	-*

Lastly, T-IR and ATR-IR spectra were recorded to confirm the formation of sulfone groups in the polymer. The results are shown in Figure 146.

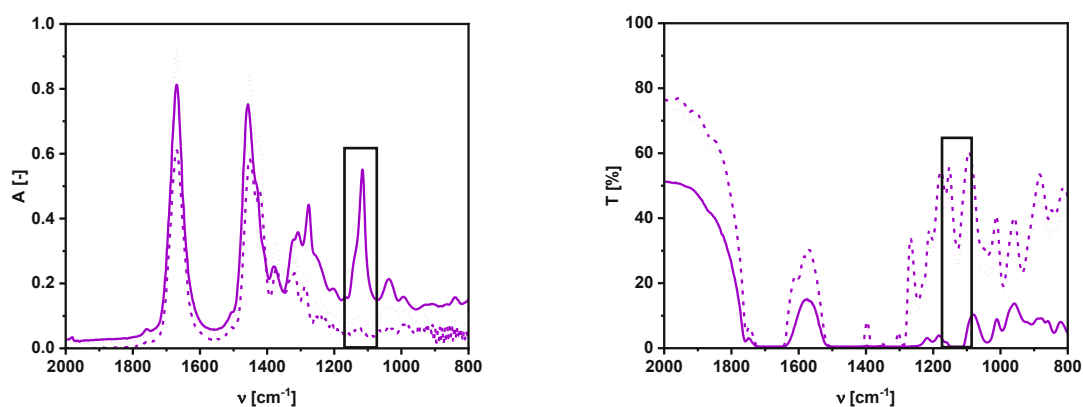
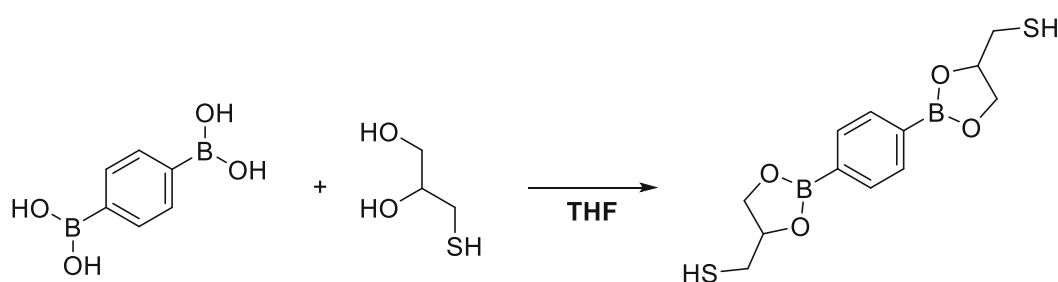


Figure 146: ATR-IR (left) and transmission spectra (right) of TAI_{Ref} (---), $\text{TAI}_{\text{Ref., H}_2\text{O}}$ (····) and $\text{TAI}_{\text{H}_2\text{O}_2}$ (—).

For both materials, ATR-IR and transmission IR spectra confirm strong absorption of the sulfone band after oxidation for 24 h with a maximum at 1114 cm^{-1} . This shows that the sulfone groups are responsible for enhanced intermolecular interactions, which lead to an increase in T_g .

4. Influence of degradable thiols

A way to further improve the degradability of the materials containing TAI, instead of non-degradable TMT, a degradable thiol might be added to the formulations. By this, every crosslinking point of the network would be degradable. As systems containing boron were shown to be most promising, the thiol 12,2'-(1,4-phenylene)-bis(4-mercaptan-1,3,2-dioxaborolane) (BDB), containing boronic ester groups, was synthesized, which is literature-known in polymers with self-healing and malleable abilities containing dynamic boronic-ester bonds.^{234,235,362,374} The synthesis was conducted according to Chen *et al.*^{234,235} and Robinson *et al.*²⁵⁶, similar to VDB and ADB (see 2.3.3.6 and 2.3.3.7).



chemicals	M [g/mol]	eq.	n [mol]	m [g]	V [mL]
benzene-1,4-diboronic acid	166.75	1.0	36	6.0	
but-3-ene-1,2-diol	108.16	2.1	74	8.0	
Na ₂ SO ₄	142.04	2.3	83	11.8	
THF					160

For the synthesis, first, thioglycerol was distilled for purification (b.p. 105 °C/3 mbar). Then, benzene-1,4-diboronic acid and 1-thioglycerol were completely dissolved in THF by stirring. To this solution, solution Na₂SO₄ was added stepwise. After stirring at rt for 16 h, the mixture was filtered, the solid was washed, and the filtrate was concentrated to obtain the product as an off-white solid.

Yield: off-white solid (92% theoretical yield).

m.p.: 92-102 °C

¹H NMR (400 MHz, CDCl₃): δ 7.81 (s, 4H, C-H_{Ar}), 4.74 (q, J = 6.2 Hz, 2H, -O-CH-), 4.50 (m, 2H, -O-CH₂-), 4.17 (m, 2H, -O-CH₂-), 2.81 (m, 4H, -CH₂-SH), 1.48 (t, J = 8.6 HZ, 2H, -CH₂-SH).

¹³C NMR (101 MHz, CDCl₃): δ 134.3 (C-H_{Ar}), 77.7 (-O-CH-), 70.0 (-O-CH₂-), 29.8. (CH₂-SH).

¹¹B-NMR (128 MHz, CDCl₃): δ 31.51.

To determine the influence of this thiol on photoreactivity, (thermo)mechanical properties, and degradation behavior, different ratios of the degradable, difunctional B-based monomer VDB in combination with non-degradable, trifunctional TAI were chosen, namely 20 mol%, 40 mol%, 60 mol%, 80 mol% VDB with respect to TAI. The amount of the B-based thiol BDB was chosen to maintain an overall ratio of double bonds to thiol groups of 1:1. As a reference, the formulation containing 0 mol% VDB (equal to 100 mol% TAI) was used, and further, it was attempted to polymerize the formulation containing only difunctional VDB and BDB (100 mol% VDB). As the B-based monomer VDB and thiol, BDB are solids at rt with respective melting points of 73-75 °C and 92-102 °C, heating for 3x10 min and vortexing was necessary to homogenize the formulations, which were then tested for their stability in regard to staying homogeneous at room temperature. Unfortunately, it was shown that all formulations require processing and curing at 100 °C, as precipitation of a solid occurs after a maximum of 30 min.

4.1 Rheology and stability of formulations

Rheological properties of all formulations were determined at 100 °C with a constant shear rate of 100 s⁻¹ analogously to 2.6.1. The results are shown in Table 44.

Table 44: Viscosity of formulations at 100 °C containing 0-100 mol% VDB with respect to non-degradable TAI and the thiol BDB in an equimolar ratio of double bonds to thiol groups, with 1 w% Ivocerin and 0.02 w% PYR.

thiol	monomer	comonomer	x_{deg} [mol%]	η [Pa·s]
BDB	VDB	TAI	0	0.772
			20	0.242
			40	0.256
			60	0.111
			80	0.113
			100	0.106

The results show that at 100 °C, low viscosities < 1 Pa·s were observed for all formulations, which is sufficiently low for 3D printing, although high temperatures would be required. Furthermore, it was shown that increasing amounts of VDB lead to a decrease in viscosity and hence better processability.

Also, stability at rt over time was assessed for the formulations and different time points t_0 , t_{1d} , t_{3d} , t_{5d} , t_{7d} , and t_{10d} . Studies were stopped before 10 d if either gelation occurred or the increase of viscosity was $\geq 100\%$ with regards to η_{t_0} . The results are shown in

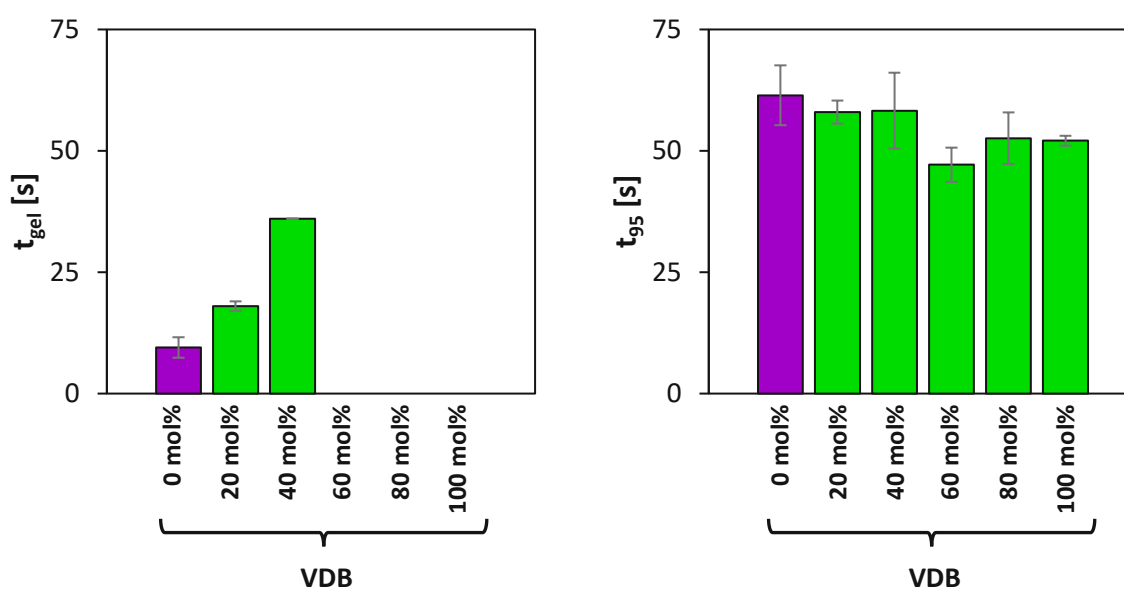
Table 45: Stability studies of formulations containing 0-100 mol% VDB with respect to non-degradable TAI and the thiol BDB in an equimolar ratio of double bonds to thiol groups via viscosity measurements at 100 °C at t_0 , t_{1d} , t_{2d} , t_{4d} , t_{5d} , and t_{7d} . *Gelation occurred.

thiol	monomer	comonomer	x_{deg} [mol%]	η [Pa·s]	$\eta_{t_{1d}}$ [Pa·s]	$\eta_{t_{2d}}$ [Pa·s]
BDB	VDB	TAI	0	0.772	0.925	3.120*
			20	0.242	0.532	5.129*
			40	0.256	0.421	2.510*
			60	0.111	0.680	3.512*
			80	0.113	0.345	6.792*
			100	0.106	0.501	8.312*

Stability studies showed that all formulations are not stable after 24 h at rt. Therefore, these formulations might not be suitable for 3D printing, as they also require high processing and printing temperatures.

4.2 Reactivity of formulations

Although preliminary results regarding formulation stability and processing temperatures were not as promising, RT-NIR photorheology measurements were still conducted with all formulations. The measurements were done analogously to 2.4.1 at 100 °C. The results are shown in Figure 147 and Figure 148.



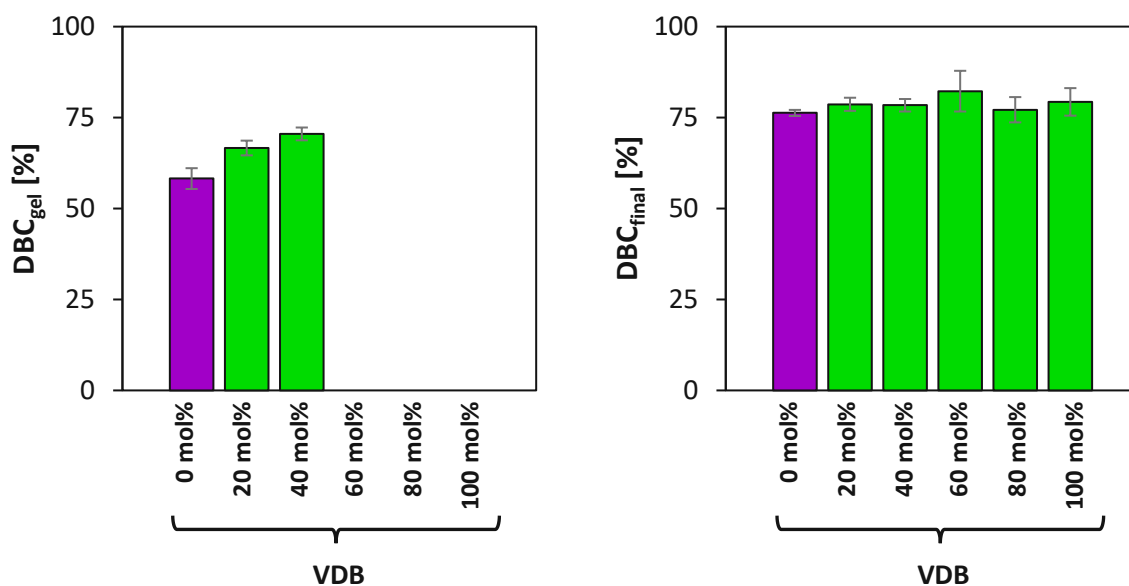


Figure 147: Results of the IR data of RT-NIR photorheology measurements: upper left: t_{gel} , upper right: t_{95} , lower left DBC_{gel} , lower right: DBC_{final} of 0 mol% VDB (equal to 100 mol% TAI) (■), 20-100 mol% VDB (■). No intersection of G' and G'' was observed for 60-100 mol% VDB specimens; hence, no t_{gel} and DBC_{gel} could be determined.

The IR data shows that the time for crosslinking increases with an increasing amount of VDB, from 9.5 s to 18 s to even 36 s for 0, 20, and 40 mol%, respectively. The same trends are visible for DBC_{gel} values, with an exceptionally high value of 71% obtained with the formulation containing 40 mol% VDB. Interestingly, no intersection of G' and G'' could be determined for the 60-100 mol% formulations, which indicates that no crosslinked network was formed. Nevertheless, solid polymer specimens were obtained for all formulations, even in the case of 100 mol% VDB, without crosslinker. This shows that starting at a content of 60 mol% of VDB, the amount of the crosslinking TAI is sufficiently low so that no network but rather a thermoplastic-like material is formed. For all formulations, similar t_{95} values ranging from 47-61 s were shown; hence fast curing is possible. Furthermore, high final double bond conversions (76-82%) can be obtained with the 0-100 mol% formulations.

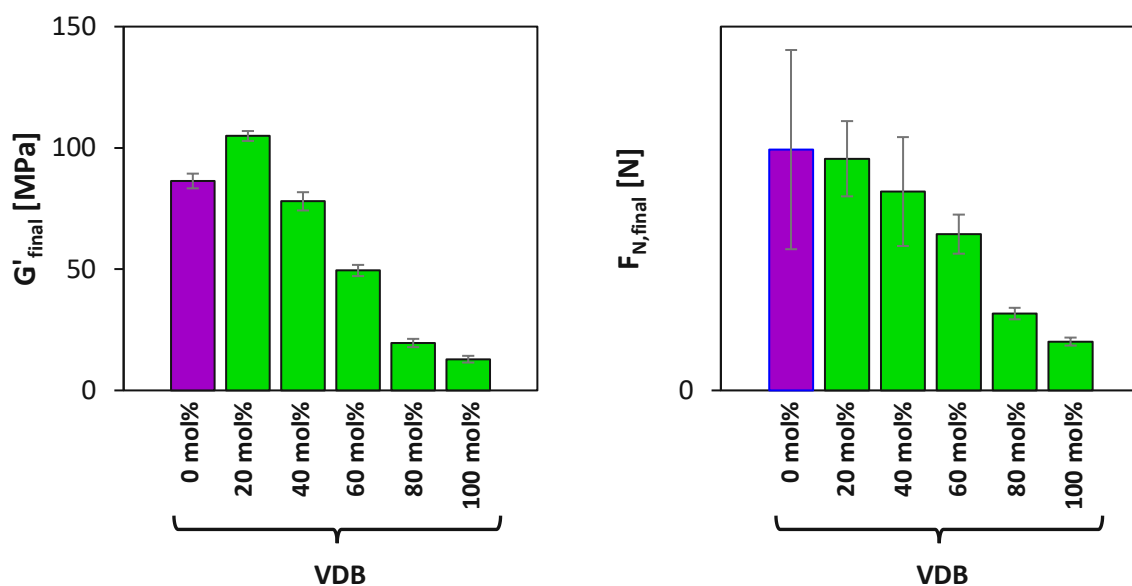


Figure 148: Results of the rheological data of RT-NIR photorheology measurements: left: G'_{final} , right: $F_{N,final}$ of 0 mol% VDB (equal to 100 mol% TAI) (■), 20-100 mol% VDB (■).

The rheology data shows that the final storage modulus decreases with an increasing amount of VDB due to the reduced crosslinking density of the network at higher boronic ester concentrations. A positive shrinkage force was determined for all formulations due to the curing conducted at 100 °C.

4.3 Mechanical properties of polymer networks

Next, the thermomechanical properties of the materials were determined via DMTA measurements, as described in 2.1.3. DMTA specimens were cured at 100 °C in a Lumamat 100 light oven with a special curing program. The results are shown in Table 46. No values could be obtained for the samples containing 80 mol% and 100 mol% VDB, as they were too brittle and broke immediately, even when clamped very carefully into the measuring device.

Table 46: Detailed results of DMTA measurements. °No results were obtained as samples were too brittle for clamping into the measuring device. *No rubber plateau, but a thermoplastic flow was observed.

thiol	monomer	comonomer	x_{deg} [mol%]	T_g [°C]	$G'_{25^\circ C}$ [MPa]	$G'_{37^\circ C}$ [MPa]	G'_R [MPa]
BDB	VDB	TAI	0	79	1640	1570	0.5
			20	85	1560	1510	0.3
			40	70	1530	1450	*
			60	68	130 β	1240	*
			80	-°	-°	-°	-°
			100	-°	-°	-°	-°

The results of the DMTA measurements show that high T_g values from 68-85 °C can be obtained with the specimens containing 0-60 mol% of degradable VDB with respect to TAI, with the best results obtained with 20 mol% VDB: Furthermore, it was shown that high storage moduli >1230 MPa at body temperature are exhibited by all materials and that a decrease of both moduli with an increasing amount of VDB occurs, due to the reduced crosslinking density of these systems. Lastly, all systems display low crosslinking density as low G'_R values of 0.5 MPa, and 0.3 MPa were measured for materials containing 0 mol% and 20 mol% VDB, and no rubber plateau, but a thermoplastic flow was observed for the polymers containing 40 mol% and 60 mol% VDB. This also corresponds with the photorheology measurements, where no t_{gel} could be determined starting at a VDB concentration of 60 mol%. As polymers containing higher amounts of VDB (80 mol% and 100 mol%) could not be measured due to high brittleness, these materials seem less promising, as tough polymers are desired as bone replacement materials.

Next, tensile test specimens of shape 5B were prepared under the same curing conditions, and testing was performed analogously to 2.4.2. The results are depicted in Figure 149.

The tests showed that good mechanical properties were achieved with 0 mol% VDB (equal to 100 mol% TAI) and 20 mol% VDB, with high strengths of 77 MPa and 73 MPa, as well as good elongations of 10% and 12%, respectively. In contrast, poor mechanical properties were observed with the other specimens. The networks containing 40 mol% VDB displayed a very brittle behavior with an elongation of break of only 1%, and the materials containing 60 mol%, 80 mol%, and 100 mol% could not even be tested due to them breaking when clamped into the testing machine. This behavior was already observed in the DMTA measurements with the specimens containing 80 mol% and 100 mol% VDB. This brittle fracture behavior might be due to the high concentration of aromatic rings in the systems. It is very likely that with decreasing amount of crosslinker and an

increasing amount of aromatic VDB, π -stacking might be enhanced, leading to very hard but also highly brittle polymers.

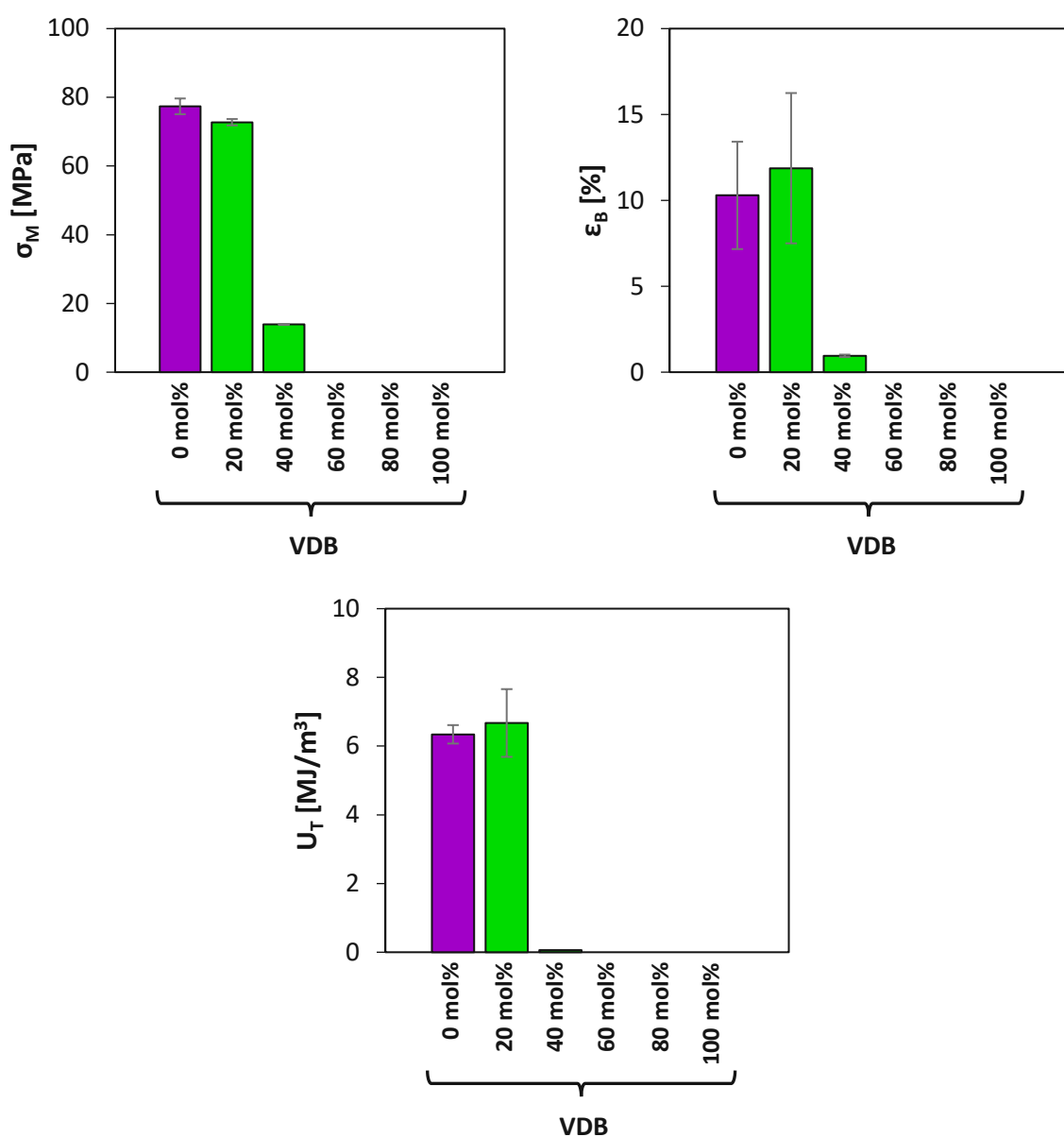


Figure 149: Results of tensile tests. Upper left: maximum strength σ_M ; upper right: elongation at break ϵ_B ; lower level: Tensile toughness U_T of 0 mol% VDB (equal to 100 mol% TAI) (■), and 20-100 mol% VDB (■). No results were obtained for materials containing 60 mol%, 80 mol%, and 100 mol% VDB, as samples were too brittle for clamping into the testing machine.

Therefore, the materials containing 40-100 mol% of VDB are unsuitable for use in BTE. Nevertheless, the 0 mol% and 20 mol% materials are quite interesting regarding their (thermo)mechanical properties. Therefore, these studies showed that a more “flexible” thiol with reduced possibility of π -stacking might be beneficial, and partial substitution of the B-based thiol BDB with previously used non-degradable TMT might be a good idea for further studies.

5. Enhanced degradation via the introduction of thioester bonds

Though comprising many advantages, one drawback of thiol-ene chemistry is the formation of thioether bonds upon crosslinking, which are not readily broken down by the body as they require the use of oxidative enzymes. Furthermore, very few naturally occurring thioethers can be found, mainly based on methionine or cysteine. On the contrary, thioester bonds can be degraded hydrolytically or enzymatically. Hence, these polymers are highly promising for use in medical applications and Tissue Engineering or drug delivery systems with the potential to degrade completely without forming unwanted, toxic products.³⁷⁵

To form these polymers, the light-initiated reaction between a thiocarboxylic acid, also referred to as thioacid or thioic acid, and a monomer comprising double bonds can be used. This method for polymer synthesis is advantageous over the formation of poly(thioesters) via condensation reaction, as no potentially toxic, low molecular weight elimination products are formed. Though thiol-ene chemistry is well researched, this photoinitiated “thioic-ene” reaction was not extensively studied (Figure 150).

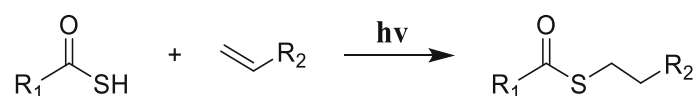


Figure 150: Mechanism of the photoinitiated “click” reaction between a thioacid and a monomer containing double bonds.

Only one patent by Dias *et al.*³⁷⁵ deals with the formation of poly(thioesters) via this reaction. It was shown that by using difunctional thioacids and enes, polymers could be synthesized, which were degradable under hydrolytic conditions due to the labile thioester bond and formed difunctional thiols and carboxylic acids upon cleavage (Figure 151).

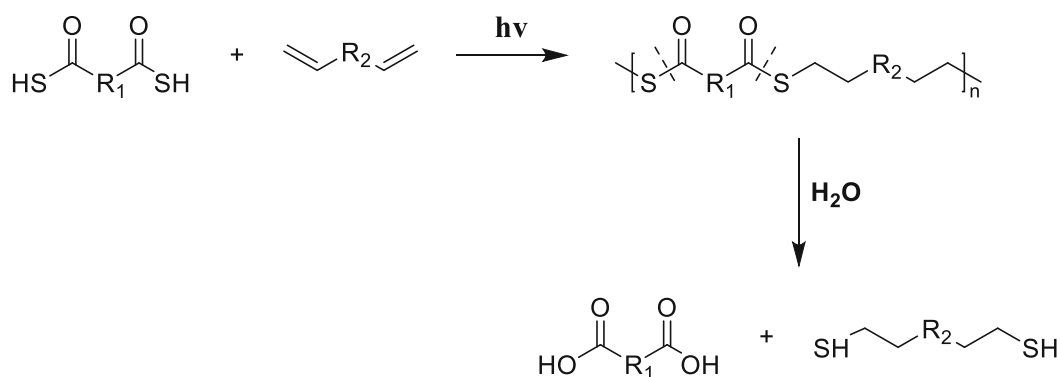


Figure 151: Synthesis of poly(thioesters) by thioic-ene photopolymerization and hydrolytic degradation to form diacids and dithiols.

Recently, it was shown that thioacids can be employed as photoinitiators by Love *et al.*³⁷⁶ and that commercially available thiobenzoic acid (TBA) and thioacetic acid (TAA) (Figure 152) are able to form radicals upon irradiation with UV light.

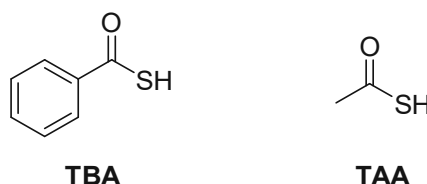


Figure 152: Chemical structures of thiobenzoic and thioacetic acid.

Only a few monofunctional thioacids, such as thiobenzoic acid and thioacetic acid, are commercially available. A reason for the limited number of compounds is the intrinsic instability of thioacids reported by literature³⁷⁶, making storage below 10 °C and careful handling (exclusion of water, oxygen, and light) necessary. Nevertheless, these compounds might be highly promising, and by the synthesis of thioacids with higher functionality, a wide variety of poly(thioesters) with tailored degradation properties might be obtained. Therefore, the goal was to synthesize difunctional thioacids. Then, poly(thioesters) should be obtained by the photoinitiated reaction of these compounds with allyl monomers. Furthermore, the potential of these compounds for self-initiation to form networks under irradiation with light should be studied, as well as the degradation behavior.

5.1 Photoinitiated thioic-ene reaction between thioacids and allyl monomers

To prove that thioacids can indeed be used as monomers in photoinitiated thioic-ene polymerizations, first, a model study was conducted with the monofunctional, commercially

available thioacids, thiobenzoic (TBA) and thioacetic acid (TAA), as well as the monofunctional allyl ester allyl hexanoate (AH) to determine, whether the formation of the product containing a thioester bond (Figure 153) occurs. All compounds used within these studies are shown in Figure 154.

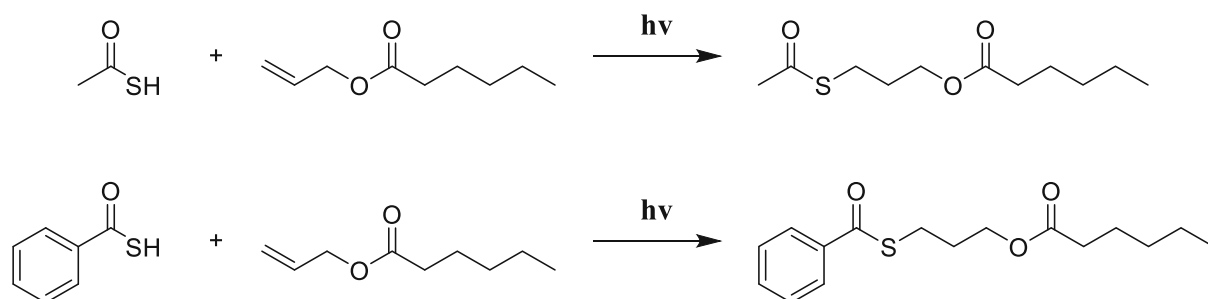


Figure 153: Photoinitiated thioic-ene polymerization of thioacetic and thiobenzoic acid with the allyl ester allyl hexanoate.

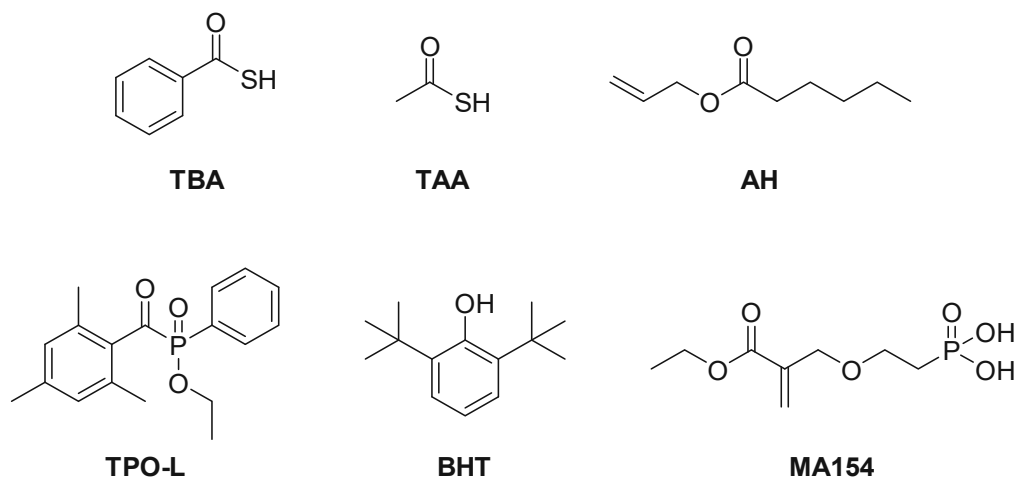


Figure 154: Chemical structures of all compounds used in the photoinitiated thioic-ene polymerization between the commercially available thioacids thiobenzoic and thioacetic acid and the ene allyl hexanoate.

For this, first, each thioacid was mixed with AH in a 1:1 molar ratio, and the formulations were added to an NMR tube. Then irradiation was conducted in a broadband UV oven at 100% intensity for 5 min. The resulting product was then quenched with CDCl_3 . As a reference, the non-irradiated formulation was dissolved in CDCl_3 as well.

In this first study, it was determined that just upon mixing each thioacid and the monomer, instant formation of the addition product occurs, even without light irradiation. Therefore, stabilizers had to be added in further studies to guarantee a controlled light-mediated reaction. Subsequently, the stabilizers BHT (90 mM) and MA154 (9 mM) depicted Figure 154 were added, which were used by Esfandiari *et al.*⁸³ as they prevent both radical formation and the formation of reactive thiolate anions.

In the second study, 1 w% of TPO-L as the photoinitiator was added to each stabilized formulation due to the enhanced solubility of this compound compared to solid PIs such as Ivocerin. The spectra of both formulations, after irradiation, are shown in Figure 155 and Figure 156. The calculated conversions are given in Table 47.

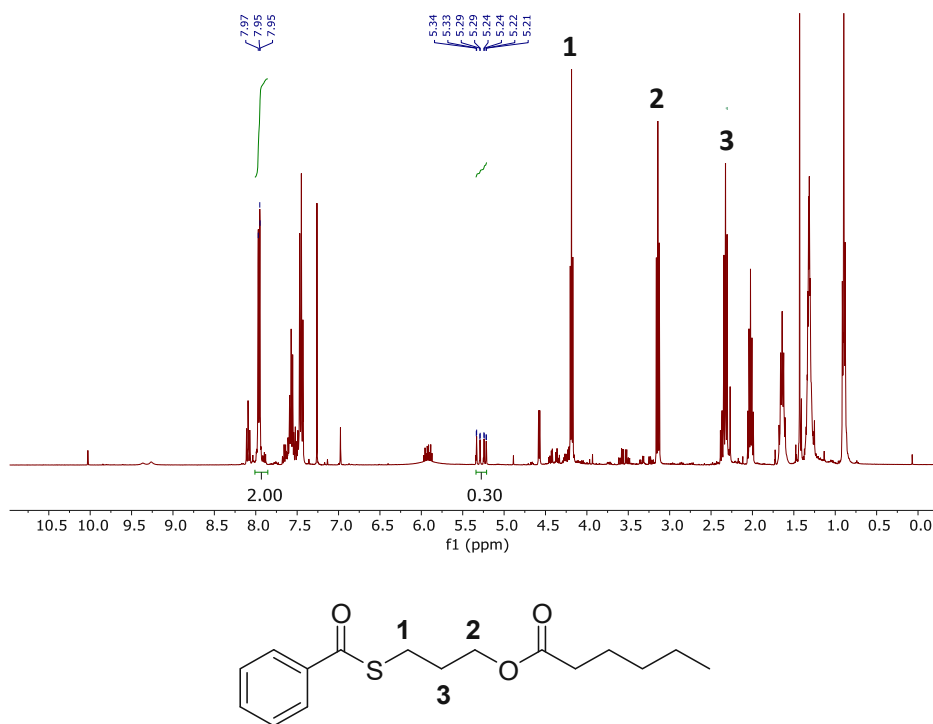


Figure 155: NMR spectra of the formulation containing TBA and AH as well as 1 w% TPO-L, 90 mM, and 9 mM of MA154 after irradiation, showing the formation of the addition product (below), with the most important peaks assigned.

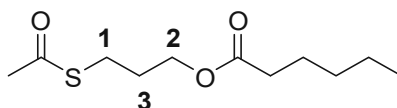
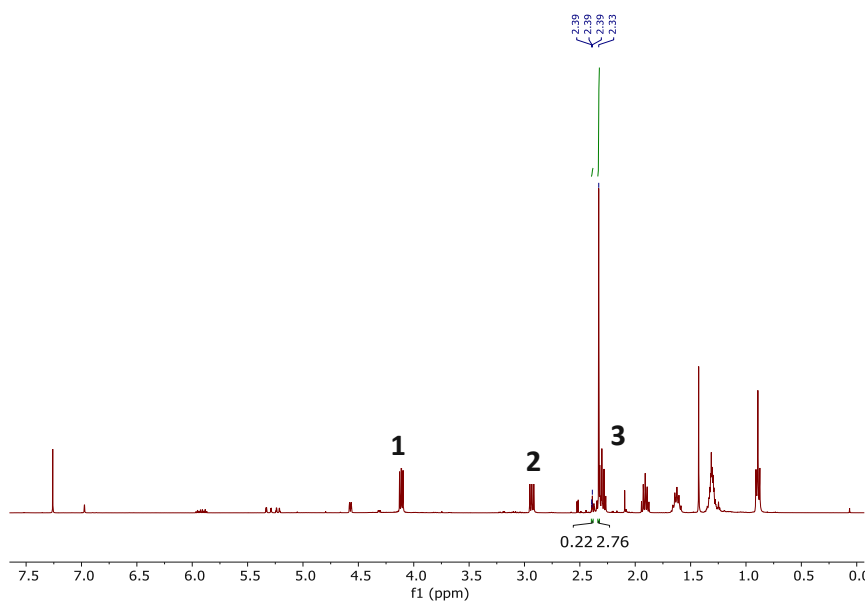


Figure 156: NMR spectra of the formulation containing TAA and AH as well as 1 w% TPO-L, 90 mM, and 9 mM of MA154 after irradiation, showing the formation of the addition product (below), with the most important peaks assigned.

Table 47: Conversions calculated by NMR after irradiation with light for the formulations containing TBA or TAA and AH in a molar ratio of 1:1, as well as 1 w% TPO-L, 90 mM, and 9 mM of MA154.

monomer	thioacid	conversion [%]
AH	TBA	84
	TAA	82

It was shown that upon the addition of stabilizers, indeed, a controlled formation of each thioester product occurs. NMR spectra proved that for each thioacid, the addition product was formed. Furthermore, it was determined that this reaction occurs with high conversions of 84% and 82% for TBA and TAA, respectively.

Since Love *et al.*³⁷⁶ state that thioacids can function as PIs, these studies were also performed without the photoinitiator TPO-L to determine the influence on conversion. Analogously to the previous study, the formulations were stabilized with BHT and MA154. The conversion is given in Table 48.

Table 48: Conversions after irradiation with light for the formulations without PI containing TBA or TAA and AH as well as 90 mM and 9 mM of MA154 calculated by NMR.

monomer	thioacid	conversion [%]
AH	TBA	19
	TAA	21

It was shown that the reaction is highly ineffective without PI, as significantly reduced conversions of 19% and 21% were determined for TBA and TAA, respectively. This shows that although some photoinitiating capacity was shown, the efficiency of these compounds is rather low compared to initiators such as TPO-L. Therefore, it is crucial to add PIs to the formulations for high monomer conversions.

To conclude, these model studies showed that the photoinitiated thioic-ene reaction between a thioacid such as thiobenzoic or thioacetic acid and a compound containing double bonds such as allyl hexanoate is indeed possible, although stabilization of these formulations is necessary to prevent a premature addition reaction and ensure a controlled light-mediated reaction. Nevertheless, it was shown that without the addition of potent PIs, low conversions are observed for this reaction. Therefore, the addition of efficient PIs to the formulations is necessary for the synthesis of poly(thioesters) with high molecular weights.

5.2 Syntheses of difunctional thioacids

As these first studies showed that the photoinitiated reaction between monofunctional thioacids and enes is successful, next, the synthesis of different difunctional thioacids, namely thioterephthalic acid (TTA) and dithioadipic acid (DTA), depicted in Figure 157, was attempted. As reference compounds without the thioacid group, 1,4-phenylenedimethane thiol (PDT), which had to be synthesized, as well as the commercially available thiol 1,6-hexane dithiol (HDT), were chosen (Figure 157).

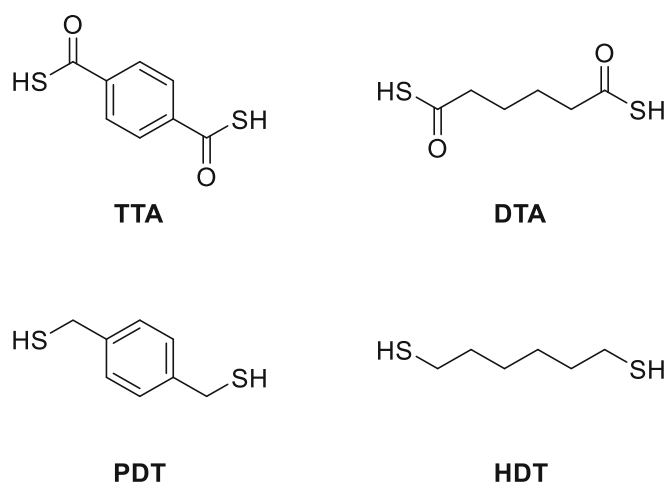
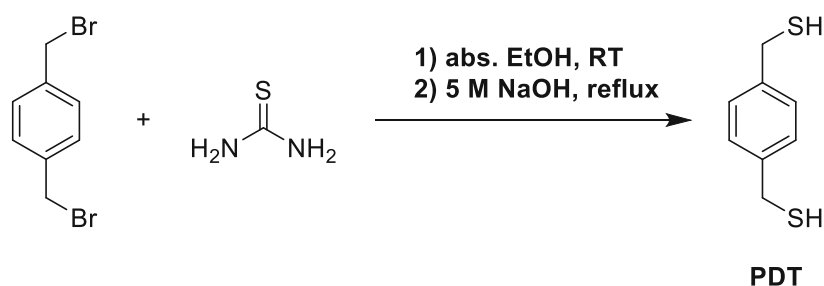


Figure 157: Chemical structures of the thioacids thioterephthalic acid (TTA), and dithioadipic acid (DTA), as well as the reference compounds 1,4 phenylenedimethane thiol (PDT), and 1,6-hexane dithiol (HDT).

5.2.1 Synthesis of 1,4-phenylenedimethane thiol (PDT)

The synthesis of the reference compound 1,4-phenylenedimethane thiol (PDT) was conducted according to Rasheed *et al.*³⁷⁷ and Riedl *et al.*³⁷⁸



chemicals	M [g/mol]	eq.	n [mol]	m [g]	V [mL]
1,4-bis(bromomethyl) benzene	263.96	1.0	100	26.4	
thiourea	76.12	2.0	200	15.2	
EtOH	46.07				270
5 M aq. NaOH	40.00				160
6 M aq. HCl	36.46				~150

Therefore, 1 eq. of 1,4-bis(bromomethyl) benzene and 2 eq. of thiourea were suspended in abs., degassed ethanol and refluxed overnight, which led to a white suspension of the resulting isothiuronium salt. The solvent was removed, the salt was suspended in aq., degassed NaOH, and heated to reflux for 22 h under argon, resulting in an orange solution. The solution was cooled to 0 °C and acidified to a pH 2 by the addition of 6 M aq. HCl and extracted with DCM. The combined organic phases were dried, and the solvent was evaporated to yield the crude product as a white

solid with brown impurities. The crude product was washed with n-hexane in order to separate the soluble product from the insoluble impurities. Evaporation *in vacuo* afforded the pure product as white crystals in a yield of 85%.

Yield: colorless to white crystals (85% theoretical yield).

R_f: 0.81 (PE:EE=1:1)

m.p.: 45-46 °C (Lit.³⁷⁹ 44-45 °C)

¹H NMR (400 MHz, CDCl₃): δ 7.28 (s, 4H, -CH_{Ar}), 3.73 (d, *J* = 7.5 Hz, 4H, -CH₂-), 1.75 (t, *J* = 7.5 Hz, 2H, -SH).

¹³C NMR-APT (101 MHz, CDCl₃): δ 140.40 (-C_{Ar}), 128.80 (-CH_{Ar}), 29.06 (-CH₂-).

5.2.2 Syntheses of thioacids

The syntheses of both thioacids were done according to by Dias *et al.*³⁷⁵, as the protocols published by Kobayashi *et al.*^{380,381} and Rao *et al.*³⁸² did not lead to product formation. Nevertheless, optimization of reaction conditions had to be conducted in penicillin vials, and studies showed that higher amounts of 1,1'-carbonyldiimidazole (CDI, 2.5 eq.) and higher dilution of the reaction compounds in pyridine (0.08 mmol diacid/mL pyridine) are necessary for product formation without significant formation of by-products.

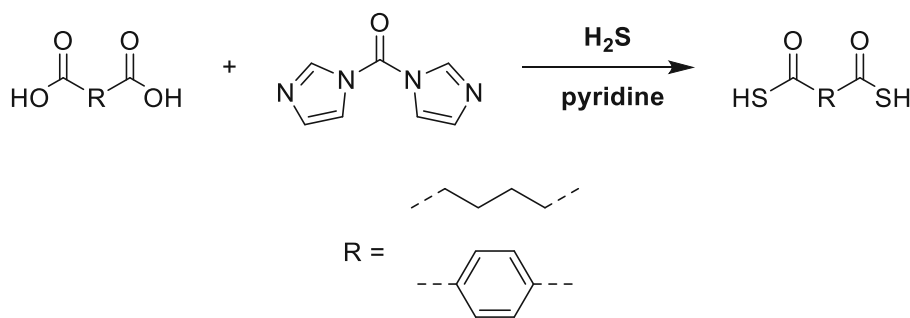
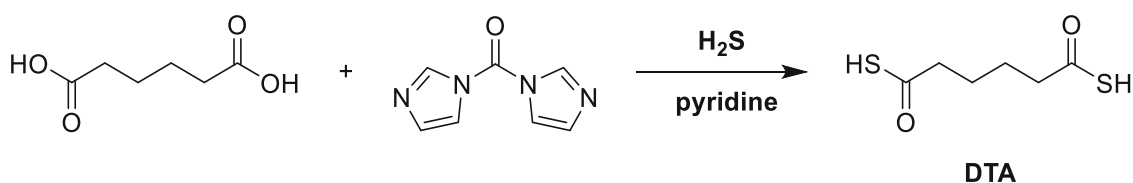


Figure 158: Syntheses of thioacids published by Dias *et al.*³⁷⁵

5.2.2.1 Synthesis of dithioadipic acid (DTA)

The synthesis of DTA was done via the previously adapted procedure described in a patent by Dias *et al.*³⁷⁵



chemicals	M [g/mol]	eq.	n [mol]	m [g]	V [mL]
adipic acid	146.14	1.0	25	3.6	
1,1'-carbonyldiimidazole	162.15	2.5	63	10.1	
H ₂ S	34.10				
pyridine	79.10				350

For the synthesis, the reaction apparatus consisted of a 500 mL three-neck round bottom flask, a reflux condenser, an Ar inlet, and a dropping funnel. The apparatus was attached to four gas wash bottles, with two of them filled with a 10% aq. solution of FeCl₂ · 4 H₂O to precipitate non-reacted H₂S as insoluble FeS. 2.5 eq. of 1,1'-carbonyldiimidazole (CDI) were dissolved in 175 mL of dry pyridine. Then, 1 eq. of adipic acid was dissolved in 175 mL pyridine and added dropwise to the reaction mixture, which led to the slow evolution of CO₂. After stirring for 1 h, a white precipitate was formed, and subsequently, H₂S was bubbled through the mixture at rt for 2 h, resulting in a clear yellow solution and full conversion according to NMR. Then 6 M HCl was added to acidify the solution to a pH of 2. The aqueous layer was extracted with CHCl₃, the organic layers were combined, dried and the solvent was evaporated to yield the crude product as a yellow to a brown oil. Purification was done by bulb tube distillation at 100-120 °C and 0.042 mbar, resulting in a yellow solid in a yield of 5%. The low yields are due to the thermal instability of this product, which was even observed at rt. As purification via column chromatography was not possible due to the decomposition of the compound, no further studies were conducted with DTA.

Yield: 0.2 g slightly yellow solid (5% theoretical yield).

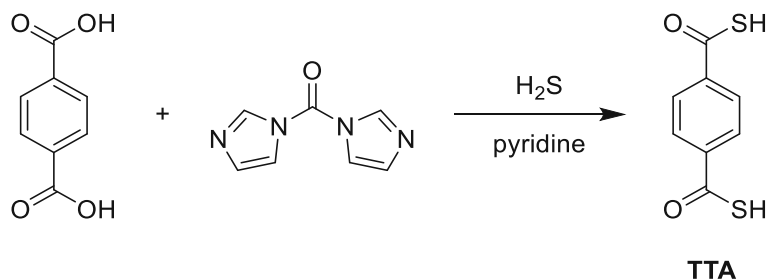
m.p.: 25-26 °C (Lit.³⁸⁰ 26-27 °C)

¹H NMR (400 MHz, CDCl₃): 3.94 (s, 2H, -SH), 2.62 (m, 4H, -CH₂-C=O), 1.67 (-CH₂-CH₂-).

¹³C NMR-APT (101 MHz, CDCl₃): 205.12 (C=O), 37.21 (-CH₂-C=O), 26.01 (-CH₂-CH₂-).

5.2.2.2 Synthesis of dithioterephthalic acid (TTA)

The synthesis of TTA was done analogously to DTA.³⁷⁵



chemicals	M [g/mol]	eq.	n [mol]	m [g]	V [mL]
terephthalic acid	166.13	1.0	50	8.3	
1,1'-carbonyldiimidazole	162.15	2.5	125	20.3	
H ₂ S	34.10				
pyridine	79.10				700

For the synthesis, the reaction apparatus consisted of a 500 mL three-neck round bottom flask, a reflux condenser, an Ar inlet, and a dropping funnel. The apparatus was attached to four gas wash bottles, with two of them filled with a 10% aq. solution of FeCl₂ · 4 H₂O to precipitate non-reacted H₂S as insoluble FeS. 2.5 eq. of 1,1'-carbonyldiimidazole (CDI) were dissolved in 350 mL of dry pyridine. Then, 1 eq. of terephthalic acid was dissolved in 350 mL pyridine and added dropwise to the reaction mixture, which led to the slow evolution of CO₂. After stirring for 1 h, a white precipitate was formed, and subsequently, H₂S was bubbled through the mixture at rt for 2 h, resulting in a clear yellow solution and full conversion according to NMR. Then 6 M HCl was added to acidify the solution to a pH of 2. The aqueous layer was extracted with DCM, the organic layers were combined, dried and the solvent was evaporated to yield the crude product as an orange precipitate in a crude yield of 90%. NMR showed that the product was formed but still contained pyridine. Therefore, 0.5 g of the crude product were dissolved in 50 mL CHCl₃, and the organic phase was washed several times (5x50 mL) with 1 M HCl and 1x50 mL brine. The pure product was obtained as a yellow solid, which displayed higher stability than DTA, probably due to its aromatic structure.

Yield: 6.6 g yellow solid (67% theoretical yield).

m.p.: 125-126 °C (Lit.³⁸⁰ 127-129 °C)

R_f: 0.6 (PE:EE=1:1)

¹H NMR (400 MHz, CDCl₃): 7.99 (s, 4H, -CH_{Ar}), 4.80 (s, 2H, -SH).

^{13}C NMR-APT (101 MHz, CDCl_3): 198.12 ($\text{C}=\text{O}$), 136.50 (C_{Ar}), 130.34 ($-\text{C}_{\text{Ar}}$).

5.3 Photoreactivity of formulations

After successful synthesis, the compound TTA was mixed with TAI in an equimolar ratio of double bonds to thiol groups and 1 w% of Ivocerin. Unfortunately, a homogeneous formulation was only obtained upon heating to 140 °C due to the high melting point of TTA. Curing was subsequently conducted in the Lumamat 100 light oven, but after 2x10 min, the formulation was still liquid and dissolved in acetone. Therefore, no crosslinked network was formed. It is presumed that the low reactivity of TTA is due to the resonance stabilization of the formed radical in the aromatic ring (Figure 159), making it unreactive toward reaction with the ene. Therefore, a different thioacid design is necessary to obtain a compound, which is thermally stable but also reactive towards thioic-ene photopolymerization.

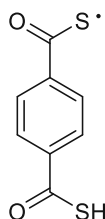


Figure 159: Radical formed from TTA.

Materials and methods

All not synthesized chemicals were purchased from respective suppliers and used as received unless otherwise noted. Solvents and reagents were purchased in a quality common for organic synthesis and purified according to common organic procedures if necessary. Commercial grade methylene chloride (CH_2Cl_2 , Donau Chemie), toluene (Donau Chemie) methanol (MeOH; Donau Chemie), tetrahydrofuran (THF, Donau Chemie), and dioxane (Donau Chemie) were dried with a PureSolvsystem (Inert, Amesbury, MA).

reagent	supplier
1-(allyloxy)-4-bromobenzene	abcr
1,3,5-triallyl-1,3,5-triazine-2,4,6-trione (TAI)	TCI
1,3,5-tris(bromomethyl)benzene	Sigma Aldrich
1,4-cyclohexanedimethanol	abcr
2,2'-(ethylenedioxy)diethanethiol (EDDT)	TCI
2,2'-azobis(2-methylpropionitrile) (AIBN)	Sigma Aldrich
2.2-dimethoxypropane	TCI
2-chloroethanol	Sigma Aldrich
2-formylphenylboronic acid	abcr
3,9-divinyl-2,4,8,10-tetraoxaspiro(5.5)undecane (VSA)	TCI
3-allyloxy-1,2-propandiol	TCI
4-bromophenol	abcr
4-carboxyphenyl boronic acid	TCI
4-dimethylaminopyridine (DMAP)	Sigma Aldrich
4-vinyl-1,3-dioxolan-2-one	TCI
acetaldehyde	Sigma Aldrich
acetonitrile	Sigma Aldrich
adiponitrile	Fisher Scientific
allyl alcohol	Sigma Aldrich
allyl bromide	TCI
allyl hexanoate	TCI
benzaldehyde	Carl Roth
benzene	Sigma Aldrich
benzene-1,4-diboronic acid	abcr
benzophenone	TCI

butylhydroxytoluene (BHT)	Sigma Aldrich
citric acid triallyl ester/triallyl citrate (CTAE)	Szabo Scancic
diallyl isocyanurate	TCI
dichlorodimethylsilane	Sigma Aldrich
diethyl ketomalonate	chemPUR
dimethyl sulfoxide	Fisher Scientific
dipentaerythritol hexa(3-mercapto-propionate) (diPETMP)	Bruno Bock
diphenyldichlorosilane	Sigma Aldrich
ethyl pyruvate	TCI
hydroquinone	Merck
bis(4-methoxybenzoyl)diethylgermanium (Ivocerin)	Ivoclar Vivadent
molecular sieve (4 Å)	Sigma Aldrich
N,N'-carbonyldiimidazole (CDI)	abcr
N,N-dimethyl formamide (DMF)	Fisher Scientific
n-BuLi (2.5 M in hexanes)	abcr
N-Ethyl-N'-(3-dimethylaminopropyl)carbodiimide hydrochloride (EDC-HCl)	abcr
palladium(II) acetate	chemPUR
paraformaldehyde	Roth
paraldehyde	Lactan
phenylhydrazine	TCI
phosgene (20 w% in toluene)	Sigma Aldrich
potassium hydroxide	Merck
p-toluenesulfonic acid	TCI
pyridine	Sigma Aldrich
pyrogallol	Merck
Quinoline Yellow	Sigma Aldrich
Sodium chloride	Carl Roth
Sodium hydride (in paraffin oil)	TCI
Sodium hydrogen carbonate	Donau Chemie
Sodium hydroxide	Acros
Sodium sulfate	VWR
tetraallyl orthosilicate (TAS)	Szabo-Scandic
tetraethyl ethylene diphosphonate	TCI
tetramethyl silicate	Sigma Aldrich
tetra-n-butylammonium bromide	Sigma Aldrich

thioacetic acid	TCI
thiobenzoic acid	TCI
thioglycerol	TCI
thionyl chloride	Sigma Aldrich
triallyl borate (TAB)	abcr
triallyl phosphate (TAP)	abcr
triethylamine	Sigma Aldrich
triisopropyl borate	abcr
trimethylol propane	Sigma Aldrich
trimethylolpropane tris(3-mercaptopropionate) (TMPMP)	Bruno Bock
trimethylsilyl chloride	abcr
tris(aminoethyl)amine	abcr
tris[2-(3-mercaptopropionyloxy)-ethyl] isocyanurate (TEMPIC)	Bruno Bock

$^1\text{H-NMR}$, $^{13}\text{C-NMR}$, $^{31}\text{P-NMR}$ and $^{11}\text{B-NMR}$ spectra were recorded with a BRUKER Avance DRX-400 FT-NMR spectrometer. The chemical shift was reported in ppm (s = singlet, d = doublet, t = triplet, q = quartet, m = multiplet). Deuterated chloroform (CDCl_3 , 99.8% deuteration), benzene (C_6D_6 , 99.5% deuteration) acetonitrile (CD_3CN , 99.8% deuteration), dimethylsulfoxide ($(\text{CD}_3)_2\text{SO}$, 99.8% deuteration) deuterium oxide (D_2O , 99.9% deuteration), methylene chloride (CD_2Cl_2 , 99.8% deuteration), purchased from Eurisotop were used as solvents. All solvents (except D_2O) were dried using 4 Å molecular sieves.

For **thin layer chromatography** (TLC), TL-aluminum foils coated with silica gel 60 F245 from Merck were used.

Column chromatography was performed on Merck silica gel 60 (0.040–0.063 mm). The silica gel chromatography was performed with a Büchi MPLC system equipped with the control unit C-620, fraction collector C-660, and UV-photometer C-635.

Melting points were determined using an Optimelt MPA100 automated melting point apparatus.

HR-MS analysis was performed from acetonitrile or methanol solutions (concentration: 10 μM) by using an HTC PAL system autosampler (CTC Analytics AG, Zwingen, Switzerland), an Agilent 1100/1200 HPLC with binary pumps, degasser, and column thermostat (Agilent Technologies, Waldbronn, Germany), and an Agilent 6230 AJS ESI-TOF mass spectrometer (Agilent Technologies, Palo Alto, CA).

ATR-IR measurements were conducted on a PerkinElmer Spectrum 65 FT-IR Spectrometer equipped with a Specac MKII Golden Gate Single Reflection ATR System.

The light-sensitive formulations were prepared in an **orange light laboratory** equipped with adhesive foils on the windows and fluorescent lamps (Osram Lumilux with chip control light color 62), with wavelengths below 480 nm filtered out.

Rheology measurements were performed with a Physica Anton Paar MCR 300 with a CP25 measuring system.

RT-NIR-Photorheology measurements were performed on an Anton Paar MCR 302 WESP rheometer, equipped with a P-PTD 200/GL Peltier glass plate and a PP25 measuring system, coupled with a Bruker Vertex 80 FTIR spectrometer.

Samples for **gel permeation chromatography (GPC)** were prepared in 1-3 mg/mL THF solutions spiked with 0.5 mg/mL butylhydroxytoluene (BHT) as a flow marker and syringe-filtered (200 nm PTFE syringe filters). Measurements were performed with a Waters GPC using three columns connected in series (Styragel HR 0.5, Styragel HR 3, and a Styragel HR 4) and a Waters 2410 RI detector.

Polymer specimens for DMTA measurements, tensile tests, and degradation studies were photocured in a light oven. In the case of broadband UV-curing, an INTELLI-RAY 600 light oven from Uvitron (irradiation power 600 W, UV-A: 125 mW cm⁻², and Vis: 125 mW cm⁻²) was used. For visible light-curing (400-500 nm), a Lumamat 100 light oven (provided by Ivoclar Vivadent AG) with 6 Osram Dulux L Blue 18 W lamps.

DMTA measurements were performed with an Anton Paar MCR 302e with a CTD 450 oven.

Tensile tests were performed on a Zwick Z050 with a maximum test force of 50 kN. The software TestXpert II was used to process and evaluate the recorded data.

Laser exposure tests and **3D printing** were conducted on a Caligma 200 UV prototype developed by Cubicure GmbH. Irradiation of samples was conducted by scanning a laser beam over a 2-dimensional plane using a Galvano scanner. An irradiation wavelength of 375 nm and a power of 70 mW/mm² were used. The diameter of the laser spot during the exposure tests was 25 μm. Writing speeds from 1000 mm/s, 500 mm/s, 200 mm/s and 100 mm/s were used.

Abbreviations

abbreviation	meaning
(M)A	(meth)acrylate
2PP	two-photon induced polymerization
AAP	2-(allyloxy)-4-((allyloxy)methyl)-1,3,2-dioxaphospholane 2-oxide
ABA	(4-(allyloxy)phenyl)boronic acid
ABB	1-(allyloxy)-4-bromobenzene
ACN	acetonitrile
ACP	4-((allyloxy)methyl)-2-chloro-1,3,2-dioxaphospholane
ADB	1,4-bis(4-((allyloxy)methyl)-1,3,2-dioxaborolan-2-yl)benzene
ADP	2,2'-(ethane-1,2-diyl)bis(4-((allyloxy)methyl)-1,3,2-dioxaphospholane-2-oxide)
AEB	allyl 4-(4-vinyl-1,3,2-dioxaborolan-2-yl)benzoate
AH	allyl hexanoate
AIBN	2,2'-azobis(2-methylpropionitrile)
AM	additive manufacturing
AMT	additive manufacturing technology
AOM	acusto-optical modulator
AVB	2-(4-(allyloxy)phenyl)-4-vinyl-1,3,2-dioxaborolane
BAB	2,6-ditertbutylphenyl diallyl borate
BAE	1,4-diallyloxybenzene
BDB	12,2'-(1,4-phenylene)-bis(4-mercaptan-1,3,2-dioxaborolane)
BE	beam expander
BE	boronic ester
BHT	butylhydroxytoluene
BP	benzophenone
BS	beam splitter
BTE	bone tissue engineering
BUD	but-3-ene-1,2-diol
CAD	computer-aided design
CAE	1,4-cyclohexanedimethanol diallyl ether
CD ₃ CN	deuterated acetonitrile
CDA	diethyl 2,2'-(carbonylbis(oxy)) diacrylate
CDCl ₃	deuterated chloroform

ABBREVIATIONS

CEA	bis(2-chloroethyl)acetal
CEB	bis(2-chloroethyl)benzal
CEE	bis(2-chloroethyl)ethanal
CEF	bis(2-chloroethyl)formal
CEK	2,2-bis(2-chloroethoxy)-1,7,7-trimethylbicyclo[2.2.1]heptane
CEM	diethyl 2,2-bis(2-chloroethoxy)malonate
CEP	bis(2-chloroethoxy)diphenylmethane
CPM	cyclopolymerizable monomer
CQ	camphorquinone
C_T	chain transfer constant
CTAE	citric acid triallyl ester
CVE	1,4-cyclohexanedimethanol divinyl ether
D₂O	deuterium oxide
DAA	activated diallyamines
DAE	ester-substituted ether dimers
DAI	diallyl isocyanurate
DAS	bis(allyloxy)diphenylsilane
DBC	double bond conversion
DBC_{final}	final double bond conversion
DBC_{gel}	double bond conversion at the gel point
DBC_{NMR}	double bond conversion determined by NMR
DCI	deuterium chloride
DCM	dichloromethane
DEVPF	diethyl vinyl phosphoformate
diPETMP	dipentaerythritol hexa(3-mercapto-propionate)
DLP-SLA	digital light processing-based stereolithography
DMAA	dimethacrylamide
DMAB	ethyl 4-(dimethylamino)benzoate
DMD	digital micro mirror device
DMEM	Dulbecco's modified eagle medium
DMF	dimethylformamide
DMSA	diethyl 2,2'-((dimethylsilanediyl)bis(oxy))diacrylate
DMSO	dimethyl sulfoxide
DMTA	dynamic mechanical thermal analysis
DTA	dithioadipic acid

ABBREVIATIONS

DVAc	divinyl acetal
DVAI	divinyl alkanal
DVB	divinyl boronic ester
DVB	divinyl benzal
DVC	divinyl carbonate
DVE	divinyl ethanal
DVF	divinyl formal
DVK	divinyl ketal
DVK	1,7,7-trimethyl-2,2-bis(vinyloxy)bicyclo[2.2.1]heptane
DVM	diethyl 2,2-bis(vinyloxy)malonate
DVP	divinyl phosphonate
DVP	divinyl silyl ether
DVP	diphenyl-bis(vinyloxy)methane
DVS	bis 2-(vinyloxy)-dimethylsilane
EC₅₀	concentration at which 50% of the cells are still viable
EDDT	2,2'-(ethylenedioxy)diethanethiol
EEP	phosphate ethylethylene phosphate
EHD	5-ethyl-5-(hydroxymethyl)-b,b-dimethyl-1,3-dioxane-2-ethanol diacrylate
EO	ethylene oxide
EPD	ethylene phosphonic dichloride
eq.	equivalent(s)
FBS	fetal bovine serum
FDM	fused deposition modeling
F_{N,max}	maximum normal force
fwhm	full width at half maximum of $\tan\delta$
G'	storage modulus
G''	loss modulus
G'_{25°C}	storage modulus at 25 °C
G'_{37°C}	storage modulus at 37 °C
G'_{final}	final storage modulus
G'_R	storage modulus at the rubber plateau
GPC	gel permeation chromatography
GS	Galvano scanner
HAP	hydroxyapatite
HDD(M)A	1,6-hexanediol di(meth)acrylate

ABBREVIATIONS

HNE	human neutrophil elastase
HOMO	highest occupied molecular orbital
IAB	(2-((E)-((2-(bis(2-((Z)-2-boronobenzylidene)amino)ethyl)amino)-ethyl)imino)methyl)phenyl)boronic acid
IAE	diallyl isosorbide
IB(M)A	isobornyl (meth)acrylate
IC	internal conversion
IGF-1	insulin-like growth factor 1
ISC	intersystem-crossing
Ivocerin	bis(4-methoxybenzoyl)diethylgermanium
KOH	potassium hydroxide
k_p	rate of propagation
k_t	rate of chain transfer
L-AMT	lithography-based additive manufacturing technology
Laser-SLA	laser-based stereolithography
LD₅₀	lethal dose, which causes death of 50% of test subjects
LUMO	lowest unoccupied molecular orbital
m₀	initial mass of sample
MA154	(2-((2-(ethoxycarbonyl)allyl)oxy)ethyl)phosphonic acid
MAA	methacrylic anhydride
m_{dry}	mass of the dry sample
MJ	material jetting
m_t	mass of the blot-dried sample at the time t
NAB	(((nitriлотris(ethane-2,1-diyl))tris(azanediyl))tris(methylene))tris(benzene-2,1-diyl))triboronic acid
NaOD	sodium deuteroxide
n_{deg}	molar amount of degradable monomer
NEt₃	triethylamine
NIPS	non-solvent induced phase separation
NVB	N1-(2-(4-vinyl-1,3,2-dioxaborolan-2-yl)benzyl)-N2,N2-bis(2-((2-(4-vinyl-1,3,2-dioxaborolan-2-yl)benzyl)amino)ethyl)ethane-1,2-di-amine
OCP	4-((allyloxy)methyl)-2-chloro-1,3,2-dioxaphospholane 2-oxide
OPEMA	2-(2-oxo-1,3,2-dioxaphospholoyloxy) ethyl methacrylate
P(M)AA	poly((meth)acrylic acid)
PCCP	poly(carboxy phenoxypropane)

ABBREVIATIONS

PCL	poly(caprolactone)
PdAc₂	palladium(II) acetate
PDI	polydispersity index
PDT	1,4-phenylenedimethane thiol
PDTRC	poly(desaminotyrosyl tyrosine ethyl ester carbonate)
PDVP	phenyl divinyl phosphate
PE	poly(ethylene)
PEEK	poly(etheretherketone)
PEG	poly(ethylene glycol)
PET	poly(ethyleneterephthalate)
PET(M)A	pentaerythritol tetra(meth)acrylate
PGA	poly(glycolic acid)
PI	photoinitiator
PLA	poly(lactic acid)
PPE	poly(phosphoester)
PPF	poly(propylene fumarate)
PSE	poly(silyl ether)
PTFE	poly(tetrafluoroethylene)
PTMC	poly(trimethylene carbonate)
pTSH	p-toluenesulfonic acid
PU	poly(urethane)
PVA	poly(vinyl alcohol)
PYR	benzene-1,2,3-triol, pyrogallol
rhBMP-2	recombinant human morphogenic protein 2
rhTGF-β1	recombinant human transforming growth factor 1
R_i[•]	radical initiating species
rt	room temperature
S	singlet state
SE	silyl ether
SLS	selective laser sintering
SOS	2,7-bis((allyloxy)methyl)-1,4,6,9-tetraoxa-5-silaspiro[4.4]-nonane
T	triplet state
t₉₅	time when 95 % of DBC is reached
TAA	thioacetic acid
TAB	triallyl borate

ABBREVIATIONS

TAI	1,3,5-triallyl-1,3,5-triazine-2,4,6-trione
tanδ	loss factor
TAP	triallyl phosphate
TAS	tetraallyl ortho silicate
TAT	1,3,5-tris(3-acetylmercaptopropyl)-1,3,5-triazine-2,4,6-trione
TBA	thiobenzoic acid
TE	tissue engineering
TEC	thiol-ene chemistry
TEMPIC	tris[2-(3-mercaptopropionyloxy)-ethyl] isocyanurate
T_g	glass transition temperature
t_{gel}	time when the gel point is reached
THF	tetrahydrofuran
TIPS	thermally-induced phase separation
TMB	benzene-1,3,5-triyltrimethanethiol
TMPMP	trimethylolpropane tris(3-mercaptopropionate)
TMPVB	2-ethyl-2-(((4-(4-vinyl-1,3,2-dioxaborolan-2-yl)-benzoyl)oxy)methyl)-propane-1,3-diyl bis(4-(4-vinyl-1,3,2-dioxaborolan-2-yl)-benzoate)
TMSA	trimethylsilanoxy ethyl acrylate
TMT	1,3,5-tris(3-mercaptopropyl)-1,3,5-triazine-2,4,6-trione
TT(M)A	trimethylolpropane tri(meth)acrylate
TTA	thioterephthalic acid
TVP	trivinyl phosphate
TVP	trivinyl phosphate
UHMWPE	ultra-high-molecular-weight poly(ethylene)
U_T	tensile toughness/deformation energy
VAB	4-(4-vinyl-1,3,2-dioxaborolan-2-yl)benzoic acid
VCF	vinyl chloroformate
VDB	1,4-bis(4-vinyl-1,3,2-dioxaborolan-2-yl)benzene
VEGF	vascular endothelial growth factor
VOTMS	vinylxy trimethylsilane
VSA	3,9-divinyl-2,4,8,10-tetraoxaspiro(5.5)undecane
WP	waveplate
x_{deg}	mol% degradable monomer
β-TCP	β -tricalcium phosphate
ϵ	tensile strain

ABBREVIATIONS

ϵ_B	elongation/strain at break
σ	tensile stress
σ_M	maximum tensile strength

References

1. Currey, J. D., *Bones: Structure and Mechanics*. Princeton University Press: 2002.
2. Henkel, J.; Woodruff, M. A.; Epari, D. R.; Steck, R.; Glatt, V.; Dickinson, I. C.; Choong, P. F.; Schuetz, M. A.; Hutmacher, D. W., Bone Regeneration Based on Tissue Engineering Conceptions - A 21st Century Perspective. *Bone Res* **2013**, *1* (3), 216-48.
3. Ethier, C. R.; Simmons, C. A., *Introductory Biomechanics: From Cells to Organisms*. Cambridge University Press: Cambridge, 2007.
4. Florencio-Silva, R.; Sasso, G. R.; Sasso-Cerri, E.; Simões, M. J.; Cerri, P. S., Biology of Bone Tissue: Structure, Function, and Factors That Influence Bone Cells. *Biomed Res Int* **2015**, *2015*, 421746.
5. 1.1 - The Skeletal System. <https://ibsehsnotes.wordpress.com/2015/05/12/1-1-the-skeletal-system/>.
6. Moszner, N.; Salz, U.; Zimmermann, J., Chemical aspects of self-etching enamel–dentin adhesives: A systematic review. *Dental Materials* **2005**, *21* (10), 895-910.
7. Boskey, A. L., Bone composition: relationship to bone fragility and antiosteoporotic drug effects. *Bonekey Rep* **2013**, *2*, 447.
8. Kini, U.; Nandeesh, B. N., Physiology of Bone Formation, Remodeling, and Metabolism. In *Radionuclide and Hybrid Bone Imaging*, Fogelman, I.; Gnanasegaran, G.; van der Wall, H., Eds. Springer Berlin Heidelberg: Berlin, Heidelberg, 2012; pp 29-57.
9. Farokhi, M.; Mottaghitalab, F.; Samani, S.; Shokrgozar, M. A.; Kundu, S. C.; Reis, R. L.; Fatahi, Y.; Kaplan, D. L., Silk fibroin/hydroxyapatite composites for bone tissue engineering. *Biotechnology Advances* **2018**, *36* (1), 68-91.
10. Olszta, M. J.; Cheng, X.; Jee, S. S.; Kumar, R.; Kim, Y.-Y.; Kaufman, M. J.; Douglas, E. P.; Gower, L. B., Bone structure and formation: A new perspective. *Materials Science and Engineering: R: Reports* **2007**, *58* (3), 77-116.
11. Liu, Y.; Luo, D.; Wang, T., Hierarchical Structures of Bone and Bioinspired Bone Tissue Engineering. *Small* **2016**, *12* (34), 4611-32.
12. Wegst, U. G. K.; Bai, H.; Saiz, E.; Tomsia, A. P.; Ritchie, R. O., Bioinspired structural materials. *Nature Materials* **2015**, *14* (1), 23-36.
13. Compston, J., Bone histomorphometry. In *Methods in Bone Biology*, Arnett, T. R.; Henderson, B., Eds. Springer US: Boston, MA, 1998; pp 177-197.
14. Kim, J. M.; Lin, C.; Stavre, Z.; Greenblatt, M. B.; Shim, J. H., Osteoblast-Osteoclast Communication and Bone Homeostasis. *Cells* **2020**, *9* (9).

REFERENCES

15. Clarke, B., Normal bone anatomy and physiology. *Clin J Am Soc Nephrol* **2008**, *3 Suppl 3* (Suppl 3), S131-9.
16. Salgado, A. J.; Coutinho, O. P.; Reis, R. L., Bone tissue engineering: state of the art and future trends. *Macromol Biosci* **2004**, *4* (8), 743-65.
17. Alghazali, K. M.; Nima, Z. A.; Hamzah, R. N.; Dhar, M. S.; Anderson, D. E.; Biris, A. S., Bone-tissue engineering: complex tunable structural and biological responses to injury, drug delivery, and cell-based therapies. *Drug Metab Rev* **2015**, *47* (4), 431-54.
18. Britannica, T. E. o. E. Osteoblast. <https://www.britannica.com/science/osteoblast>.
19. Britannica, T. E. o. E. Osteoclast. <https://www.britannica.com/science/osteoclast>.
20. Nicks, K. M.; Fowler, T. W.; Gaddy, D., Reproductive Hormones and Bone. *Current Osteoporosis Reports* **2010**, *8* (2), 60-67.
21. Buenzli, P. R.; Sims, N. A., Quantifying the osteocyte network in the human skeleton. *Bone* **2015**, *75*, 144-50.
22. Aarden, E. M.; Burger, E. H.; Nijweide, P. J., Function of osteocytes in bone. *J Cell Biochem* **1994**, *55* (3), 287-99.
23. Cullinane, D. M., The role of osteocytes in bone regulation: mineral homeostasis versus mechanoreception. *J Musculoskelet Neuronal Interact* **2002**, *2* (3), 242-4.
24. Miller, S. C.; de Saint-Georges, L.; Bowman, B. M.; Jee, W. S., Bone lining cells: structure and function. *Scanning Microsc* **1989**, *3* (3), 953-60; discussion 960-1.
25. Dobnig, H.; Turner, R. T., Evidence that intermittent treatment with parathyroid hormone increases bone formation in adult rats by activation of bone lining cells. *Endocrinology* **1995**, *136* (8), 3632-8.
26. Saunders, M.; Truesdell, S., Bone remodeling platforms: Understanding the need for multicellular lab-on-a-chip systems and predictive agent-based models. *Mathematical biosciences and engineering: MBE* **2019**, *17*, 1233-1252.
27. Sheen, J. R.; Garla, V. V., Fracture Healing Overview. In *StatPearls*, StatPearls Publishing Copyright © 2022, StatPearls Publishing LLC.: Treasure Island (FL), 2022.
28. Marsell, R.; Einhorn, T. A., The biology of fracture healing. *Injury* **2011**, *42* (6), 551-5.
29. Giannoudis, P. V.; Einhorn, T. A.; Marsh, D., Fracture healing: the diamond concept. *Injury* **2007**, *38 Suppl 4*, S3-6.
30. Perez, J. R.; Kouroupis, D.; Li, D. J.; Best, T. M.; Kaplan, L.; Correa, D., Tissue Engineering and Cell-Based Therapies for Fractures and Bone Defects. *Front Bioeng Biotechnol* **2018**, *6*, 105.
31. Lowry, J., *Bone Regeneration and Repair: Biology and Clinical Applications*. Ann R Coll Surg Engl.: 2006; Vol. 88 (3).

32. DOC, D. O. C. Strategies to Help Heal Your Broken Bones.
<https://www.directorthocare.com/strategies-to-help-heal-your-broken-bones/>.
33. Nauth, A.; Schemitsch, E.; Norris, B.; Nollin, Z.; Watson, J. T., Critical-Size Bone Defects: Is There a Consensus for Diagnosis and Treatment? *J Orthop Trauma* **2018**, *32 Suppl 1*, S7-s11.
34. Koole, R.; Bosker, H.; van der Dussen, F. N., Late secondary autogenous bone grafting in cleft patients comparing mandibular (ectomesenchymal) and iliac crest (mesenchymal) grafts. *J Craniomaxillofac Surg* **1989**, *17 Suppl 1*, 28-30.
35. Ito, M.; Liu, Y.; Yang, Z.; Nguyen, J.; Liang, F.; Morris, R. J.; Cotsarelis, G., Stem cells in the hair follicle bulge contribute to wound repair but not to homeostasis of the epidermis. *Nat Med* **2005**, *11* (12), 1351-4.
36. Jahan, K.; Tabrizian, M., Composite biopolymers for bone regeneration enhancement in bony defects. *Biomaterials Science* **2016**, *4* (1), 25-39.
37. Ratner, B. D.; Hoffman, A. S.; Schoen, F. J.; Lemons, J. E.; Editors, *Biomaterials Science, An Introduction to Materials in Medicine, 2nd Edition*. Elsevier: 2004; p 851 pp.
38. Heimann, R. B.; Lehmann, H. D., *Bioceramic Coatings for Medical Implants*. Wiley-VCH: 2012.
39. Nair, L. S.; Laurencin, C. T., Biodegradable polymers as biomaterials. *Prog. Polym. Sci.* **2007**, *32* (8-9), 762-798.
40. Baudis, S. Development and Processing of Materials for Vascular Tissue Regeneration. Dissertation, TU Wien, 2010.
41. Hench, L. L., The story of Bioglass. *J Mater Sci Mater Med* **2006**, *17* (11), 967-78.
42. Heinemann, S.; Gelinsky, M.; Worch, H.; Hanke, T., [Resorbable bone substitution materials: An overview of commercially available materials and new approaches in the field of composites]. *Orthopäde* **2011**, *40* (9), 761-73.
43. Schnürer, S. M.; Gopp, U.; Kühn, K. D.; Breusch, S. J., Knochenersatzwerkstoffe. *Der Orthopäde* **2003**, *32* (1), 2-10.
44. Felzmann, R.; Gruber, S.; Mitteramskogler, G.; Tesavibul, P.; Boccaccini, A. R.; Liska, R.; Stampfl, J., Lithography-Based Additive Manufacturing of Cellular Ceramic Structures. *Advanced Engineering Materials* **2012**, *14* (12), 1052-1058.
45. Simpson, J. P.; Hamer, A. J., How noisy are total knee and hip replacements? *J Perioper Pract* **2017**, *27* (12), 292-295.
46. Ibrahim, M. Z.; Sarhan, A. A. D.; Yusuf, F.; Hamdi, M., Biomedical materials and techniques to improve the tribological, mechanical and biomedical properties of orthopedic implants – A review article. *Journal of Alloys and Compounds* **2017**, *714*, 636-667.
47. Matassi, F.; Botti, A.; Sirleo, L.; Carulli, C.; Innocenti, M., Porous metal for orthopedics implants. *Clin Cases Miner Bone Metab* **2013**, *10* (2), 111-5.

48. Sedelnikova, M. B.; Komarova, E. G.; Sharkeev, Y. P.; Tolkacheva, T. V.; Khlusov, I. A.; Sheikin, V. V., Bioactive calcium phosphate coatings on metallic implants. *AIP Conference Proceedings* **2017**, *1882* (1), 020062.
49. Bose, S.; Roy, M.; Bandyopadhyay, A., Recent advances in bone tissue engineering scaffolds. *Trends Biotechnol* **2012**, *30* (10), 546-54.
50. Senra, M. R.; Marques, M. d. F. V., Synthetic Polymeric Materials for Bone Replacement. *Journal of Composites Science* **2020**, *4* (4), 191.
51. Davison, N. L.; Barrère-de Groot, F.; Grijpma, D. W., Degradation of Biomaterials. In *Tissue Engineering*, 2014; pp 177-215.
52. Alameda, B. M.; Palmer, T. C.; Sisemore, J. D.; Pierini, N. G.; Patton, D. L., Hydrolytically degradable poly(β -thioether ester ketal) thermosets via radical-mediated thiol-ene photopolymerization. *Polymer Chemistry* **2019**, *10* (41), 5635-5644.
53. Woodruff, M. A.; Hutmacher, D. W., The return of a forgotten polymer—Polycaprolactone in the 21st century. *Progress in Polymer Science* **2010**, *35* (10), 1217-1256.
54. Horowitz, R. A.; Leventis, M. D.; Rohrer, M. D.; Prasad, H. S., Bone grafting: history, rationale, and selection of materials and techniques. *Compend Contin Educ Dent* **2014**, *35* (4 Suppl), 1-6;quiz7.
55. Lee, S. H.; Shin, H., Matrices and scaffolds for delivery of bioactive molecules in bone and cartilage tissue engineering. *Adv Drug Deliv Rev* **2007**, *59* (4-5), 339-59.
56. Lee, S.-H.; Shin, H., Matrices and scaffolds for delivery of bioactive molecules in bone and cartilage tissue engineering. *Adv Drug Deliv Rev* **2007**, *59* (4-5), 339-59.
57. Rehmann, M. S.; Garibian, A. C.; Kloxin, A. M., Hydrolytically degradable thiol-ene hydrogels for protein release. *Macromol Symp* **2013**, *329* (1), 58-65.
58. Heller, J., *Biopolymers I. Advances in Polymer Science*, ed. Springer: 1993; Vol. 107.
59. Heller, C.; Schwentenwein, M.; Russmueller, G.; Varga, F.; Stampfl, J.; Liska, R., Vinyl esters: Low cytotoxicity monomers for the fabrication of biocompatible 3D scaffolds by lithography based additive manufacturing. *Journal of Polymer Science Part A: Polymer Chemistry* **2009**, *47* (24), 6941-6954.
60. Dellago, B.; Ricke, A.; Geyer, T.; Liska, R.; Baudis, S., Photopolymerizable precursors for degradable biomaterials based on acetal moieties. *European Polymer Journal* **2021**, *154*, 110536.
61. Chatterjee, S.; Ramakrishnan, S., Hyperbranched Polyacetals with Tunable Degradation Rates. *Macromolecules* **2011**, *44* (12), 4658-4664.
62. Ware, T.; Jennings, A. R.; Bassampour, Z. S.; Simon, D.; Son, D. Y.; Voit, W., Degradable, silyl ether thiol-ene networks. *RSC Adv.* **2014**, *4* (75), 39991-40002.

63. Li, S.; Tenon, M.; Garreau, H.; Braud, C.; Vert, M., Enzymatic degradation of stereocopolymers derived from L-, DL- and meso-lactides. *Polym. Degrad. Stab.* **1999**, *67* (1), 85-90.
64. Davis, K. A.; Burdick, J. A.; Anseth, K. S., Photoinitiated crosslinked degradable copolymer networks for tissue engineering applications. *Biomaterials* **2003**, *24* (14), 2485-2495.
65. Xiao, Y.; Yuan, M.; Zhang, J.; Yan, J.; Lang, M., Functional Poly(ϵ -caprolactone) Based Materials: Preparation, Self-assembly and Application in Drug Delivery. *Curr. Top. Med. Chem. (Sharjah, United Arab Emirates)* **2014**, *14* (6), 781-818.
66. Tangpasuthadol, V.; Pendharkar, S. M.; Kohn, J., Hydrolytic degradation of tyrosine-derived polycarbonates, a class of new biomaterials. Part I: Study of model compounds. *Biomaterials* **2000**, *21* (23), 2371-2378.
67. Heller, C.; Schwentenwein, M.; Rusmüller, G.; Koch, T.; Moser, D.; Schopper, C.; Varga, F.; Stampfl, J.; Liska, R., Vinylcarbonates and vinylcarbamates: Biocompatible monomers for radical photopolymerization. *Journal of Polymer Science Part A: Polymer Chemistry* **2011**, *49* (3), 650-661.
68. Heller, C.; Schwentenwein, M.; Varga, F.; Stampfl, J.; Liska, R., Additive Manufacturing Technologies for the 3D Fabrication of Biocompatible and Biodegradable Photopolymers. *MRS Online Proceedings Library* **2010**, *1239* (1), 805.
69. Mautner, A.; Qin, X.; Kapeller, B.; Rusmueller, G.; Koch, T.; Stampfl, J.; Liska, R., Efficient curing of vinyl carbonates by thiol-ene polymerization. *Macromol Rapid Commun* **2012**, *33* (23), 2046-52.
70. Mautner, A.; Steinbauer, B.; Rusmüller, G.; Lieber, R.; Koch, T.; Stampfl, J.; Liska, R., Vinyl carbonate photopolymers with improved mechanical properties for biomedical applications. *Designed Monomers and Polymers* **2016**, *19* (5), 437-444.
71. Katti, D. S.; Lakshmi, S.; Langer, R.; Laurencin, C. T., Toxicity, biodegradation and elimination of polyanhydrides. *Adv Drug Deliv Rev* **2002**, *54* (7), 933-61.
72. Anseth, K. S.; Shastri, V. R.; Langer, R., Photopolymerizable degradable polyanhydrides with osteocompatibility. *Nature Biotechnology* **1999**, *17* (2), 156-159.
73. Schüller-Ravoo, S.; Feijen, J.; Grijpma, D. W., Flexible, elastic and tear-resistant networks prepared by photo-crosslinking poly(trimethylene carbonate) macromers. *Acta Biomater* **2012**, *8* (10), 3576-85.
74. Peltola, S. M.; Melchels, F. P.; Grijpma, D. W.; Kellomäki, M., A review of rapid prototyping techniques for tissue engineering purposes. *Ann Med* **2008**, *40* (4), 268-80.
75. Bhushan, S.; Singh, S.; Maiti, T. K.; Sharma, C.; Dutt, D.; Sharma, S.; Li, C.; Tag Eldin, E. M., Scaffold Fabrication Techniques of Biomaterials for Bone Tissue Engineering: A Critical Review. *Bioengineering* **2022**, *9* (12), 728.

76. Ning, Z.; Xiongbiao, C., Biofabrication of Tissue Scaffolds. In *Advances in Biomaterials Science and Biomedical Applications*, Rosario, P., Ed. IntechOpen: Rijeka, 2013; p Ch. 12.
77. Sola, A.; Bertacchini, J.; D'Avella, D.; Anselmi, L.; Maraldi, T.; Marmioli, S.; Messori, M., Development of solvent-casting particulate leaching (SCPL) polymer scaffolds as improved three-dimensional supports to mimic the bone marrow niche. *Materials Science and Engineering: C* **2019**, *96*, 153-165.
78. Costantini, M.; Barbetta, A., 6 - Gas foaming technologies for 3D scaffold engineering. In *Functional 3D Tissue Engineering Scaffolds*, Deng, Y.; Kuiper, J., Eds. Woodhead Publishing: 2018; pp 127-149.
79. Gebhardt, A., *Understanding Additive Manufacturing: Rapid Prototyping, Rapid Tooling, Rapid Manufacturing*. Hanser Publishers: 2012.
80. Gebhardt, A., *Rapid Prototyping*. Hanser Publishers: 2003.
81. Srivatsan, T. S.; Sudarshan, T. S., *Additive Manufacturing: Innovations, Advances, and Applications 1st Edition*. CRC Press.: 2015.
82. Ligon, S. C.; Liska, R.; Stampfl, J.; Gurr, M.; Mülhaupt, R., Polymers for 3D Printing and Customized Additive Manufacturing. *Chemical Reviews* **2017**, *117* (15), 10212-10290.
83. Esfandiari, P.; Ligon, S. C.; Lagref, J. J.; Frantz, R.; Cherkaoui, Z.; Liska, R., Efficient stabilization of thiol-ene formulations in radical photopolymerization. *Journal of Polymer Science Part A: Polymer Chemistry* **2013**, *51* (20), 4261-4266.
84. Tumbleston, J. R.; Shirvanyants, D.; Ermoshkin, N.; Januszewicz, R.; Johnson, A. R.; Kelly, D.; Chen, K.; Pinschmidt, R.; Rolland, J. P.; Ermoshkin, A.; Samulski, E. T.; DeSimone, J. M., Additive manufacturing. Continuous liquid interface production of 3D objects. *Science* **2015**, *347* (6228), 1349-52.
85. KG, A. G. C. *AMPOWER Report 2022*; AM Power: Hamburg, Germany, 2022.
86. Hutmacher, D. W.; Schantz, T.; Zein, I.; Ng, K. W.; Teoh, S. H.; Tan, K. C., Mechanical properties and cell cultural response of polycaprolactone scaffolds designed and fabricated via fused deposition modeling. *J Biomed Mater Res* **2001**, *55* (2), 203-16.
87. Orman, S.; Hofstetter, C.; Aksu, A.; Reinauer, F.; Liska, R.; Baudis, S., Toughness enhancers for bone scaffold materials based on biocompatible photopolymers. *Journal of Polymer Science Part A: Polymer Chemistry* **2018**, *57* (2), 110-119.
88. Becker, S. T.; Bolte, H.; Krapf, O.; Seitz, H.; Douglas, T.; Sivananthan, S.; Wiltfang, J.; Sherry, E.; Warnke, P. H., Endocultivation: 3D printed customized porous scaffolds for heterotopic bone induction. *Oral Oncology* **2009**, *45* (11), e181-e188.

89. Neves, S. C.; Mota, C.; Longoni, A.; Barrias, C. C.; Granja, P. L.; Moroni, L., Additive manufactured polymeric 3D scaffolds with tailored surface topography influence mesenchymal stromal cells activity. *Biofabrication* **2016**, *8* (2), 025012.
90. Ligon, S. C.; Liska, R.; Stampfl, J.; Gurr, M.; Mulhaupt, R., Polymers for 3D Printing and Customized Additive Manufacturing. *Chem Rev* **2017**, *117* (15), 10212-10290.
91. Hatzenbichler, M.; Geppert, M.; Gruber, S.; Ipp, E.; Almedal, R.; Stampfl, J., DLP-based light engines for additive manufacturing of ceramic parts. *Proceedings of SPIE - The International Society for Optical Engineering* **2012**, *8254*, 11.
92. Bártolo, J., Paulo, *Stereolithography: Materials, Processes and Applications*. 1 ed.; Springer New York, NY: 2011.
93. Gmeiner, R.; Mitteramskogler, G.; Stampfl, J.; Boccaccini, A. R., Stereolithographic Ceramic Manufacturing of High Strength Bioactive Glass. *International Journal of Applied Ceramic Technology* **2015**, *12* (1), 38-45.
94. formlabs Guide to Stereolithography (SLA) 3D Printing. <https://formlabs.com/blog/ultimate-guide-to-stereolithography-sla-3d-printing/>.
95. Hutmacher, D. W., Scaffold-based Tissue Engineering – Design and Fabrication of Matrices Using Solid Freeform Fabrication Techniques. In *Advanced Manufacturing Technology for Medical Applications*, 2005; pp 163-189.
96. Ngo, T. D.; Kashani, A.; Imbalzano, G.; Nguyen, K. T. Q.; Hui, D., Additive manufacturing (3D printing): A review of materials, methods, applications and challenges. *Composites Part B: Engineering* **2018**, *143*, 172-196.
97. Ligon-Auer, S. C.; Schwentenwein, M.; Gorsche, C.; Stampfl, J.; Liska, R., Toughening of photo-curable polymer networks: a review. *Polymer Chemistry* **2016**, *7* (2), 257-286.
98. Mautner, A.; Steinbauer, B.; Orman, S.; Russmüller, G.; Macfelda, K.; Koch, T.; Stampfl, J.; Liska, R., Tough photopolymers based on vinyl esters for biomedical applications. *Journal of Polymer Science Part A: Polymer Chemistry* **2016**, *54* (13), 1987-1997.
99. Husár, B.; Heller, C.; Schwentenwein, M.; Mautner, A.; Varga, F.; Koch, T.; Stampfl, J.; Liska, R., Biomaterials based on low cytotoxic vinyl esters for bone replacement application. *Journal of Polymer Science Part A: Polymer Chemistry* **2011**, *49* (23), 4927-4934.
100. Stampfl, J.; Baudis, S.; Heller, C.; Liska, R.; Neumeister, A.; Kling, R.; Ostendorf, A.; Spitzbart, M., Photopolymers with tunable mechanical properties processed by laser-based high-resolution stereolithography. *Journal of Micromechanics and Microengineering* **2008**, *18*.
101. Peer, G.; Dorfinger, P.; Koch, T.; Stampfl, J.; Gorsche, C.; Liska, R., Photopolymerization of Cyclopolymerizable Monomers and Their Application in Hot Lithography. *Macromolecules* **2018**, *51* (22), 9344-9353.

102. Instruments, T. <http://www.ti.com/de-de/dlp-chip/overview.html>.
103. Laser SLA vs DLP vs Masked SLA 3D Printing Technology, . <https://theorthocosmos.com/laser-sla-vs-dlp-vs-masked-sla-3d-printing-technology-compared/>
104. Husár, B.; Hatzenbichler, M.; Mironov, V.; Liska, R.; Stampfl, J.; Ovsianikov, A., Photopolymerization-based additive manufacturing for the development of 3D porous scaffolds. *Woodhead Publ. Ser. Biomater.* **2014**, *75* (Biomaterials for Bone Regeneration), 149-201.
105. Serbin, J. O., A.; Chichkov, B., Fabrication of woodpile structures by two-photon polymerization and investigation of their optical properties. *OPTICS EXPRESS* **2004**, *12* (21), 5221-5228.
106. Gruber, P., Development of a novel wavelength-tunable high-speed 2-photon lithography setup. *PhD Thesis, Institute of Materials Science and Technology, TU Wien, 2018.*
107. Steiger, W., Investigation of multi-photon processing parameters and materials. *PhD Thesis, Institute of Materials Science and Technology, TU Wien, 2018.*
108. Arslan, A.; Steiger, W.; Roose, P.; Van den Bergen, H.; Gruber, P.; Zerobin, E.; Gantner, F.; Guillaume, O.; Ovsianikov, A.; Van Vlierberghe, S.; Dubruel, P., Polymer architecture as key to unprecedented high-resolution 3D-printing performance: The case of biodegradable hexa-functional telechelic urethane-based poly- ϵ -caprolactone. *Materials Today* **2021**, *44*, 25-39.
109. Fouassier, J.; Lalavée, J., Photoinitiators for Polymer Synthesis. Scope, Reactivity, and Efficiency. *Angew. Chem. Int. Ed.* **2013**, *52* (12), 3312-3312.
110. Fouassier, J. P.; Allonas, X.; Burget, D., Photopolymerization reactions under visible lights: principle, mechanisms and examples of applications. *Prog. Org. Coat.* **2003**, *47* (1), 16-36.
111. Kirchmayr, R.; Berner, G.; Rist, G., Photoinitiators for UV curing of paints. *Farbe Lack* **1980**, *86* (3), 224-30.
112. Mautner, A. Development of low cytotoxic Photopolymers. 2012.
113. Gauss, P. Advanced additives for radical photopolymerization. 2019.
114. Peer, G. Strategies for shrinkage stress reduction in photopolymers for dental restoratives. 2020.
115. Sandler, S. R.; Sandler, M. P.; Karo, W., *Polymer Synthesis: Volume 1*. Elsevier Science: 1992.
116. Maillard, B.; Ingold, K. U.; Scaiano, J. C., Rate constants for the reactions of free radicals with oxygen in solution. *J. Am. Chem. Soc.* **1983**, *105* (15), 5095-9.
117. Crivello, J. V., Photoinitiators for free radical cationic and anionic photopolymerisation. *Polym. Int.* **2000**, *49* (12), 1729-1729.
118. Noble, B. B.; Mater, A. C.; Smith, L. M.; Coote, M. L., The effects of Lewis acid complexation on type I radical photoinitiators and implications for pulsed laser polymerization. *Polym. Chem.* **2016**, *7* (41), 6400-6412.

REFERENCES

119. Perkampus, H.-H., *UV-VIS Spectroscopy and its Applications*. Springer Science & Business Media: 2013.
120. Gruber, H. F., Photoinitiators for free radical polymerization. *Prog. Polym. Sci.* **1992**, *17* (6), 953-1044.
121. Oldring, P. K.; Dietliker, K., *Chemistry & Technology of UV & EB Formulation for Coatings, Inks & Paints. Volume 3: Photoinitiators for Free Radical and Cationic Polymerisation*. Sita Technology: 1991.
122. Wardle, B., *Principles and applications of photochemistry*. John Wiley & Sons: 2009.
123. Fouassier, J.-P., *Photoinitiation, photopolymerization, and photocuring: fundamentals and applications*. Hanser: 1995.
124. Chatani, S.; Kloxin, C. J.; Bowman, C. N., The power of light in polymer science: photochemical processes to manipulate polymer formation, structure, and properties. *Polymer Chemistry* **2014**, *5* (7), 2187-2201.
125. Fouassier, J. P. In *Photochemistry and UV curing: a brief survey of the latest trends*, Research Signpost: 2006; pp 1-8.
126. Fouassier, J.-P.; Rabek, J. F.; Editors, *Radiation Curing in Polymer Science Technology, Vol. 2: Photoinitiating Systems*. Elsevier: 1993; p 717 pp.
127. Haslinger, C.; Leutgeb, L. P.; Haas, M.; Baudis, S.; Liska, R., Synthesis and Photochemical Investigation of Tetraacylgermanes. *ChemPhotoChem* **2022**, *6* (10), e202200108.
128. Haas, M.; Radebner, J.; Eibel, A.; Gescheidt, G.; Stueger, H., Recent Advances in Germanium-Based Photoinitiator Chemistry. *Chemistry – A European Journal* **2018**, *24* (33), 8258-8267.
129. Eibel, A.; Radebner, J.; Haas, M.; Fast, D. E.; Freissmuth, H.; Stadler, E.; Faschauner, P.; Torvisco, A.; Lamparth, I.; Moszner, N.; Stueger, H.; Gescheidt, G., From mono- to tetraacylgermanes: extending the scope of visible light photoinitiators. *Polym. Chem.* **2018**, *9* (1), 38-47.
130. Vivadent, I. I. State of the Art: Photopolymerization in dentistry. 2013.
131. Fouassier, J. P.; Ruhlmann, D.; Graff, B.; Morlet-Savary, F.; Wieder, F., Excited state processes in polymerization photoinitiators. *Prog. Org. Coat.* **1995**, *25* (3), 235-71.
132. Green, A. W., Industrial Photoinitiators: A Technical Guide. . *Chemphyschem* **2011**, *12* (7), 1389.
133. Ullrich, G.; Burtscher, P.; Salz, U.; Moszner, N.; Liska, R., Phenylglycine derivatives as coinitiators for the radical photopolymerization of acidic aqueous formulations. *J. Polym. Sci., Part A: Polym. Chem.* **2006**, *44* (1), 115-125.

134. Fouassier, J.-P., *Photoinitiation, Photopolymerization, and Photocuring: Fundamentals and Applications*. Hanser/Gardner: 1995; p 388 pp.
135. Allan, N. S.; Oldring, P. K. T., *Prepolymers & Reactive Diluents for UV & EB Curable Formulations*. SITA Technology: 1991.
136. *European Union Risk Assessment Report ACRYLIC ACID*; Institute for Health and Consumer Protection: 2002.
137. *European Union Risk Assessment Report METHACRYLIC ACID*; Institute for Health and Consumer Protection: 2002.
138. Orman, S. Toughening of Photopolymers for Additive Manufacturing of Bone Replacement. 2018.
139. Stoll, G. H.; Nimmerfall, F.; Acemoglu, M.; Bodmer, D.; Bantle, S.; Müller, I.; Mahl, A.; Kolopp, M.; Tullberg, K., Poly(ethylene carbonate)s, part II: degradation mechanisms and parenteral delivery of bioactive agents. *Journal of Controlled Release* **2001**, *76* (3), 209-225.
140. Posner, T., Beiträge zur Kenntniss der ungesättigten Verbindungen. II. Ueber die Addition von Mercaptanen an ungesättigte Kohlenwasserstoffe. *Berichte der deutschen chemischen Gesellschaft* **1905**, *38* (1), 646-657.
141. Reddy, S. K.; Cramer, N. B.; Bowman, C. N., Thiol-Vinyl Mechanisms. 1. Termination and Propagation Kinetics in Thiol-Ene Photopolymerizations. *Macromolecules* **2006**, *39* (10), 3673-3680.
142. Hoyle, C. E.; Bowman, C. N., Thiol-ene click chemistry. *Angew Chem Int Ed Engl* **2010**, *49* (9), 1540-73.
143. Seidler, K.; Griesser, M.; Kury, M.; Harikrishna, R.; Dorfinger, P.; Koch, T.; Svirikova, A.; Marchetti-Deschmann, M.; Stampfl, J.; Moszner, N.; Gorsche, C.; Liska, R., Vinyl Sulfonate Esters: Efficient Chain Transfer Agents for the 3D Printing of Tough Photopolymers without Retardation. *Angew Chem Int Ed Engl* **2018**, *57* (29), 9165-9169.
144. Gorsche, C.; Seidler, K.; Knaack, P.; Dorfinger, P.; Koch, T.; Stampfl, J.; Moszner, N.; Liska, R., Rapid formation of regulated methacrylate networks yielding tough materials for lithography-based 3D printing. *Polymer Chemistry* **2016**, *7* (11), 2009-2014.
145. Peer, G.; Eibel, A.; Gorsche, C.; Catel, Y.; Gescheidt, G.; Moszner, N.; Liska, R., Ester-Activated Vinyl Ethers as Chain Transfer Agents in Radical Photopolymerization of Methacrylates. *Macromolecules* **2019**, *52* (7), 2691-2700.
146. Gorsche, C.; Seidler, K.; Harikrishna, R.; Kury, M.; Koch, T.; Moszner, N.; Liska, R., Difunctional vinyl sulfonate esters for the fabrication of tough methacrylate-based photopolymer networks. *Polymer* **2018**, *158*, 149-157.
147. Hoyle, C. E.; Bowman, C. N., Thiol-ene click chemistry. *Angew Chem Int Ed Engl*. **2010**, *49* (9), 1540-1573.

148. Cramer, N. B.; Reddy, S. K.; O'Brien, A. K.; Bowman, C. N., Thiol–Ene Photopolymerization Mechanism and Rate Limiting Step Changes for Various Vinyl Functional Group Chemistries. *Macromolecules* **2003**, *36* (21), 7964-7969.
149. Gorsche, C. Synthesis and characterization of monomers and additives for photopolymer-based dental restoratives. TU Wien, 2015.
150. Moszner, N.; Salz, U., Recent Developments of New Components for Dental Adhesives and Composites. *Macromolecular Materials and Engineering* **2007**, *292* (3), 245-271.
151. Moszner, N.; Hirt, T., New polymer-chemical developments in clinical dental polymer materials: Enamel–dentin adhesives and restorative composites. *Journal of Polymer Science Part A: Polymer Chemistry* **2012**, *50* (21), 4369-4402.
152. Moszner, N., New Monomers for Dental Application. *Macromolecular Symposia* **2004**, *217* (1), 63-76.
153. Moszner, N.; Salz, U., New developments of polymeric dental composites. *Progress in Polymer Science* **2001**, *26* (4), 535-576.
154. Moszner, N. B., Peter Dental Materials based on low-odour thiols. 2017.
155. Bowman, C. N.; Carioscia, J. L., H.; ; Stansbury, J. W. Reactive oligomeric thiol and ene materials as dental restorative mixtures. . 2005.
156. Bowman, C. N.; Lu, H.; Stansbury, J. W. Novel photopolymerizable polymer composites with low shrinkage stress and use in dental restorative materials. 2005.
157. Stansbury, J. W.; Bowman, C. N.; Trujillo, M. Dimer acid-derived dimethacrylates and use in dental restorative compositions 2004.
158. Granskog, V.; García-Gallego, S.; von Kieseritzky, J.; Rosendahl, J.; Stenlund, P.; Zhang, Y.; Petronis, S.; Lyvén, B.; Arner, M.; Håkansson, J.; Malkoch, M., High-Performance Thiol–Ene Composites Unveil a New Era of Adhesives Suited for Bone Repair. *Advanced Functional Materials* **2018**, *28* (26), 1800372.
159. Marler, J. J.; Upton, J.; Langer, R.; Vacanti, J. P., Transplantation of cells in matrices for tissue regeneration. *Advanced Drug Delivery Reviews* **1998**, *33* (1), 165-182.
160. Seal, B. L.; Otero, T. C.; Panitch, A., Polymeric biomaterials for tissue and organ regeneration. *Materials Science and Engineering: R: Reports* **2001**, *34* (4), 147-230.
161. Pêgo, A. P.; Poot, A. A.; Grijpma, D. W.; Feijen, J., In Vitro Degradation of Trimethylene Carbonate Based (Co)polymers. *Macromolecular Bioscience* **2002**, *2* (9), 411-419.
162. Ovsianikov, A.; Schlie, S.; Ngezahayo, A.; Haverich, A.; Chichkov, B. N., Two-photon polymerization technique for microfabrication of CAD-designed 3D scaffolds from commercially available photosensitive materials. *Journal of Tissue Engineering and Regenerative Medicine* **2007**, *1* (6), 443-9.

163. Baroli, B., Photopolymerization of biomaterials: issues and potentialities in drug delivery, tissue engineering, and cell encapsulation applications. *Journal of Chemical Technology & Biotechnology* **2006**, *81* (4), 491-499.
164. Ifkovits, J. L.; Burdick, J. A., Review: Photopolymerizable and Degradable Biomaterials for Tissue Engineering Applications. *Tissue Engineering* **2007**, *13* (10), 2369-2385.
165. Rodríguez, G.; Gallardo, A.; San Román, J.; Rebuella, M.; Bermejo, P.; Buján, J.; Bellón, J. M.; Honduvilla, N. G.; Escudero, C., New resorbable polymeric systems with antithrombogenic activity. *J Mater Sci Mater Med* **1999**, *10* (12), 873-8.
166. Tessmar, J. K.; Göpferich, A. M., Customized PEG-derived copolymers for tissue-engineering applications. *Macromol Biosci* **2007**, *7* (1), 23-39.
167. Skoog, S. A.; Goering, P. L.; Narayan, R. J., Stereolithography in tissue engineering. *J Mater Sci Mater Med* **2014**, *25* (3), 845-56.
168. Burdick, J. A.; Anseth, K. S., Photoencapsulation of osteoblasts in injectable RGD-modified PEG hydrogels for bone tissue engineering. *Biomaterials* **2002**, *23* (22), 4315-23.
169. Nuttelman, C. R.; Tripodi, M. C.; Anseth, K. S., In vitro osteogenic differentiation of human mesenchymal stem cells photoencapsulated in PEG hydrogels. *J Biomed Mater Res A* **2004**, *68* (4), 773-82.
170. Cao, L.; Werkmeister, J. A.; Wang, J.; Glattauer, V.; McLean, K. M.; Liu, C., Bone regeneration using photocrosslinked hydrogel incorporating rhBMP-2 loaded 2-N, 6-O-sulfated chitosan nanoparticles. *Biomaterials* **2014**, *35* (9), 2730-42.
171. Killion, J. A.; Geever, L. M.; Devine, D. M.; Grehan, L.; Kennedy, J. E.; Higginbotham, C. L., Modulating the mechanical properties of photopolymerised polyethylene glycol–polypropylene glycol hydrogels for bone regeneration. *Journal of Materials Science* **2012**, *47* (18), 6577-6585.
172. Fisher, J. P.; Dean, D.; Mikos, A. G., Photocrosslinking characteristics and mechanical properties of diethyl fumarate/poly(propylene fumarate) biomaterials. *Biomaterials* **2002**, *23* (22), 4333-43.
173. Vehof, J. W.; Fisher, J. P.; Dean, D.; van der Waerden, J. P.; Spauwen, P. H.; Mikos, A. G.; Jansen, J. A., Bone formation in transforming growth factor beta-1-coated porous poly(propylene fumarate) scaffolds. *J Biomed Mater Res* **2002**, *60* (2), 241-51.
174. Lee, J. W.; Kang, K. S.; Lee, S. H.; Kim, J.-Y.; Lee, B.-K.; Cho, D.-W., Bone regeneration using a microstereolithography-produced customized poly(propylene fumarate)/diethyl fumarate photopolymer 3D scaffold incorporating BMP-2 loaded PLGA microspheres. *Biomaterials* **2011**, *32* (3), 744-752.

175. Rezwan, K.; Chen, Q. Z.; Blaker, J. J.; Boccaccini, A. R., Biodegradable and bioactive porous polymer/inorganic composite scaffolds for bone tissue engineering. *Biomaterials* **2006**, *27* (18), 3413-3431.
176. Matsuda, T.; Mizutani, M., Liquid acrylate-endcapped biodegradable poly(ϵ -caprolactone-co-trimethylene carbonate). II. Computer-aided stereolithographic microarchitectural surface photoconstructs. *Journal of Biomedical Materials Research* **2002**, *62* (3), 395-403.
177. Matsuda, T.; Kwon, I. K.; Kidoaki, S., Photocurable Biodegradable Liquid Copolymers: Synthesis of Acrylate-End-Capped Trimethylene Carbonate-Based Prepolymers, Photocuring, and Hydrolysis. *Biomacromolecules* **2004**, *5* (2), 295-305.
178. Declercq, H. A.; Cornelissen, M. J.; Gorskiy, T. L.; Schacht, E. H., Osteoblast behaviour on in situ photopolymerizable three-dimensional scaffolds based on D, L-lactide, ϵ -caprolactone and trimethylene carbonate. *Journal of Materials Science: Materials in Medicine* **2006**, *17* (2), 113-122.
179. Jansen, J.; Koopmans, S. A.; Los, L. I.; van der Worp, R. J.; Podt, J. G.; Hooymans, J. M.; Feijen, J.; Grijpma, D. W., Intraocular degradation behavior of crosslinked and linear poly(trimethylene carbonate) and poly(D,L-lactic acid). *Biomaterials* **2011**, *32* (22), 4994-5002.
180. Jansen, J.; Boerakker, M. J.; Heuts, J.; Feijen, J.; Grijpma, D. W., Rapid photo-crosslinking of fumaric acid monoethyl ester-functionalized poly(trimethylene carbonate) oligomers for drug delivery applications. *J Control Release* **2010**, *147* (1), 54-61.
181. Bat, E.; Kothman, B. H. M.; Higuera, G. A.; van Blitterswijk, C. A.; Feijen, J.; Grijpma, D. W., Ultraviolet light crosslinking of poly(trimethylene carbonate) for elastomeric tissue engineering scaffolds. *Biomaterials* **2010**, *31* (33), 8696-8705.
182. Zhu, C.; Kustra, S. R.; Bettinger, C. J., Photocrosslinkable biodegradable elastomers based on cinnamate-functionalized polyesters. *Acta Biomaterialia* **2013**, *9* (7), 7362-7370.
183. Guillaume, O.; Geven, M. A.; Sprecher, C. M.; Stadelmann, V. A.; Grijpma, D. W.; Tang, T. T.; Qin, L.; Lai, Y.; Alini, M.; de Bruijn, J. D.; Yuan, H.; Richards, R. G.; Eglin, D., Surface-enrichment with hydroxyapatite nanoparticles in stereolithography-fabricated composite polymer scaffolds promotes bone repair. *Acta Biomater* **2017**, *54*, 386-398.
184. Dellago, B. New cleavable moieties for biodegradable photopolymers. 2019.
185. Betz, M. W.; Modi, P. C.; Caccamese, J. F.; Coletti, D. P.; Sauk, J. J.; Fisher, J. P., Cyclic acetal hydrogel system for bone marrow stromal cell encapsulation and osteodifferentiation. *J Biomed Mater Res A* **2008**, *86* (3), 662-70.
186. Chalk, S. J., *IUPAC, Acetals. in Compendium of Chemical Terminology, 2nd ed. (the "Gold Book")*. Blackwell Scientific Publications: Oxford, 1997.
187. Chalk, S. J., *IUPAC, Ketals. in Compendium of Chemical Terminology, 2nd ed. (the "Gold Book")*. Blackwell Scientific Publications: Oxford, 1997.

188. Liu, B.; Thayumanavan, S., Substituent Effects on the pH Sensitivity of Acetals and Ketals and Their Correlation with Encapsulation Stability in Polymeric Nanogels. *J Am Chem Soc* **2017**, *139* (6), 2306-2317.
189. Tsukino, M.; Kunitake, T., The Microstructure of Poly(divinyl acetal)s as Determined by ¹³C NMR Spectroscopy. Ring Stereochemistry and Isomerization Propagation. *Polym. J.* **1979**, *11* (6), 437-447.
190. Becker, G.; Ackermann, L. M.; Schechtel, E.; Klapper, M.; Tremel, W.; Wurm, F. R., Joining Two Natural Motifs: Catechol-Containing Poly(phosphoester)s. *Biomacromolecules* **2017**, *18* (3), 767-777.
191. Marrian, S. F., The Chemical Reactions of Pentaerythritol and its Derivatives. *Chemical Reviews* **1948**, *43* (1), 149-202.
192. Bograchov, E., Exchange Reactions between Aldehydeacetals and Aldehydes. I. *Journal of the American Chemical Society* **1950**, *72* (5), 2268-2270.
193. Hufendiek, A.; Lingier, S.; Du Prez, F. E., Thermoplastic polyacetals: chemistry from the past for a sustainable future? *Polymer Chemistry* **2019**, *10* (1), 9-33.
194. Orman, S. Toughening of Photopolymers for Additive Manufacturing of Bone Replacements. 2018.
195. Shaterian, H. R.; Rigi, F., Acetalization of Carbonyl Compounds as Pentaerythritol Diacetals and Diketals in the Presence of Cellulose Sulfuric Acid as an Efficient, Biodegradable and Reusable Catalyst. *Chinese Journal of Chemistry* **2012**, *30* (3), 695-698.
196. Jin, T. S.; Zhang, F. S.; Wang, K. F.; Li, T.-S., Synthesis of pentaerythritol diacetals from aldehydes and ketones under microwave irradiation. *Chinese Journal of Organic Chemistry* **2004**, *24*, 1485-1488.
197. Jun, N.; Xiao, P.; Zhang, J. Application of cyclic polyacetal in producing visible light solidifying material for non-degradation orthopaedics renovation or reshaping beauty treatment. 2007.
198. Aurica, C.; Elena, N. L.; Diaconu Alina; Jordana, N.; Nita, T.; Vera, B. Matrix Copolymer Synthesis for Bio-medical Applications. 2015.
199. Lingier, S.; Espeel, P.; Suarez, S. S.; Türünç, O.; De Wildeman, S.; Du Prez, F. E., Renewable thermoplastic polyurethanes containing rigid spiroacetal moieties. *European Polymer Journal* **2015**, *70*, 232-239.
200. Wei, H.; Zhuo, R.-X.; Zhang, X.-Z., Design and development of polymeric micelles with cleavable links for intracellular drug delivery. *Progress in Polymer Science* **2013**, *38* (3), 503-535.
201. Gillies, E. R.; Fréchet, J. M. J., A new approach towards acid sensitive copolymer micelles for drug delivery. *Chemical Communications* **2003**, (14), 1640-1641.

202. Ulbrich, K.; Subr, V., Polymeric anticancer drugs with pH-controlled activation. *Adv Drug Deliv Rev* **2004**, *56* (7), 1023-50.
203. Shenoi, R. A.; Lai, B. F. L.; Imran ul-haq, M.; Brooks, D. E.; Kizhakkedathu, J. N., Biodegradable polyglycerols with randomly distributed ketal groups as multi-functional drug delivery systems. *Biomaterials* **2013**, *34* (25), 6068-6081.
204. Moreau, J. L.; Kesselman, D.; Fisher, J. P., Synthesis and properties of cyclic acetal biomaterials. *Journal of Biomedical Materials Research Part A* **2007**, *81A* (3), 594-602.
205. Falco, E. E.; Roth, J. S.; Fisher, J. P., EH Networks as a scaffold for skeletal muscle regeneration in abdominal wall hernia repair. *J Surg Res* **2008**, *149* (1), 76-83.
206. Patel, M.; Patel, K. J.; Caccamese, J. F.; Coletti, D. P.; Sauk, J. J.; Fisher, J. P., Characterization of cyclic acetal hydroxyapatite nanocomposites for craniofacial tissue engineering. *Journal of Biomedical Materials Research Part A* **2010**, *94A* (2), 408-418.
207. Tee, H. T.; Lieberwirth, I.; Wurm, F. R., Aliphatic Long-Chain Polypyrophosphates as Biodegradable Polyethylene Mimics. *Macromolecules* **2019**, *52* (3), 1166-1172.
208. Wolf, T.; Steinbach, T.; Wurm, F. R., A Library of Well-Defined and Water-Soluble Poly(alkyl phosphonate)s with Adjustable Hydrolysis. *Macromolecules* **2015**, *48* (12), 3853-3863.
209. Bauer, K. N.; Tee, H. T.; Velencoso, M. M.; Wurm, F. R., Main-chain poly(phosphoester)s: History, syntheses, degradation, bio- and flame-retardant applications. *Progress in Polymer Science* **2017**, *73*, 61-122.
210. Bauer, K. N.; Liu, L.; Wagner, M.; Andrienko, D.; Wurm, F. R., Mechanistic study on the hydrolytic degradation of polyphosphates. *European Polymer Journal* **2018**, *108*, 286-294.
211. Steinbach, T.; Wurm, F. R., Poly(phosphoester)s: A New Platform for Degradable Polymers. *Angew Chem Int Ed Engl* **2015**, *54* (21), 6098-108.
212. Hall, D. G., *Boronic Acids: Preparation and Applications in Organic Synthesis and Medicine*. Wiley: 2005.
213. Alexandrino, E. M.; Ritz, S.; Marsico, F.; Baier, G.; Mailänder, V.; Landfester, K.; Wurm, F. R., Paclitaxel-loaded polyphosphate nanoparticles: a potential strategy for bone cancer treatment. *Journal of Materials Chemistry B* **2014**, *2* (10), 1298-1306.
214. Becker, G.; Wurm, F. R., Breathing air as oxidant: Optimization of 2-chloro-2-oxo-1,3,2-dioxaphospholane synthesis as a precursor for phosphoryl choline derivatives and cyclic phosphate monomers. *Tetrahedron* **2017**, *73* (25), 3536-3540.
215. Markwart, J. C.; Wurm, F. R., The 2-acetylthioethyl ester group: A versatile protective group for P-OH-groups. *Tetrahedron* **2018**, *74* (52), 7426-7430.
216. Marsico, F.; Wagner, M.; Landfester, K.; Wurm, F. R., Unsaturated Polyphosphoesters via Acyclic Diene Metathesis Polymerization. *Macromolecules* **2012**, *45* (21), 8511-8518.

217. Tee, H. T.; Koynov, K.; Reichel, T.; Wurm, F. R., Noncovalent Hydrogen Bonds Tune the Mechanical Properties of Phosphoester Polyethylene Mimics. *ACS Omega* **2019**, *4* (5), 9324-9332.
218. Wolf, T.; Naß, J.; Wurm, F. R., Cyclohexyl-substituted poly(phosphonate)-copolymers with adjustable glass transition temperatures. *Polymer Chemistry* **2016**, *7* (17), 2934-2937.
219. Zheng, Y.-R.; Tee, H. T.; Wei, Y.; Wu, X.-L.; Mezger, M.; Yan, S.; Landfester, K.; Wagener, K.; Wurm, F. R.; Lieberwirth, I., Morphology and Thermal Properties of Precision Polymers: The Crystallization of Butyl Branched Polyethylene and Polyphosphoesters. *Macromolecules* **2016**, *49* (4), 1321-1330.
220. Iwasaki, Y.; Komatsu, S.; Narita, T.; Akiyoshi, K.; Ishihara, K., Biodegradable Phosphorylcholine Polymer Hydrogels Cross-Linked with Vinyl-Functionalized Polyphosphate. *Macromolecular Bioscience* **2003**, *3* (5), 238-242.
221. Wang, S.; Wan, A. C. A.; Xu, X.; Gao, S.; Mao, H.-Q.; Leong, K. W.; Yu, H., A new nerve guide conduit material composed of a biodegradable poly(phosphoester). *Biomaterials* **2001**, *22* (10), 1157-1169.
222. Leong, K. W., Polymeric Controlled Nucleic Acid Delivery. *MRS Bulletin* **2005**, *30* (9), 640-646.
223. Yang, X.-Z.; Sun, T.-M.; Dou, S.; Wu, J.; Wang, Y.-C.; Wang, J., Block Copolymer of Polyphosphoester and Poly(L-Lactic Acid) Modified Surface for Enhancing Osteoblast Adhesion, Proliferation, and Function. *Biomacromolecules* **2009**, *10* (8), 2213-2220.
224. Wen, J.; Kim, G. J. A.; Leong, K. W., Poly(d,lactide-co-ethyl ethylene phosphate)s as new drug carriers. *Journal of Controlled Release* **2003**, *92* (1), 39-48.
225. Lu, Z.-Z.; Wu, J.; Sun, T.-M.; Ji, J.; Yan, L.-F.; Wang, J., Biodegradable polycation and plasmid DNA multilayer film for prolonged gene delivery to mouse osteoblasts. *Biomaterials* **2008**, *29* (6), 733-741.
226. Du, J.-Z.; Sun, T.-M.; Weng, S.-Q.; Chen, X.-S.; Wang, J., Synthesis and Characterization of Photo-Cross-Linked Hydrogels Based on Biodegradable Polyphosphoesters and Poly(ethylene glycol) Copolymers. *Biomacromolecules* **2007**, *8* (11), 3375-3381.
227. Li, Q.; Wang, J.; Shahani, S.; Sun, D. D. N.; Sharma, B.; Elisseff, J. H.; Leong, K. W., Biodegradable and photocrosslinkable polyphosphoester hydrogel. *Biomaterials* **2006**, *27* (7), 1027-1034.
228. Zhang, Z.; Feng, X.; Mao, J.; Xiao, J.; Liu, C.; Qiu, J., In vitro cytotoxicity of a novel injectable and biodegradable alveolar bone substitute. *Biochemical and Biophysical Research Communications* **2009**, *379* (2), 557-561.
229. Parrott, M. C.; Luft, J. C.; Byrne, J. D.; Fain, J. H.; Napier, M. E.; DeSimone, J. M., Tunable Bifunctional Silyl Ether Cross-Linkers for the Design of Acid-Sensitive Biomaterials. *Journal of the American Chemical Society* **2010**, *132* (50), 17928-17932.

230. Sample, C. S.; Lee, S.-H.; Bates, M. W.; Ren, J. M.; Lawrence, J.; Lensch, V.; Gerbec, J. A.; Bates, C. M.; Li, S.; Hawker, C. J., Metal-Free Synthesis of Poly(silyl ether)s under Ambient Conditions. *Macromolecules* **2019**, *52* (5), 1993-1999.
231. Shieh, P.; Nguyen, H. V. T.; Johnson, J. A., Tailored silyl ether monomers enable backbone-degradable polynorbornene-based linear, bottlebrush and star copolymers through ROMP. *Nature Chemistry* **2019**, *11* (12), 1124-1132.
232. Wang, Y.; Fan, S.; Xiao, D.; Xie, F.; Li, W.; Zhong, W.; Zhou, X., Novel Silyl Ether-Based Acid-Cleavable Antibody-MMAE Conjugates with Appropriate Stability and Efficacy. *Cancers (Basel)* **2019**, *11* (7).
233. Bunton, C. M.; Bassampour, Z. M.; Boothby, J. M.; Smith, A. N.; Rose, J. V.; Nguyen, D. M.; Ware, T. H.; Csaky, K. G.; Lippert, A. R.; Tsarevsky, N. V.; Son, D. Y., Degradable Silyl Ether-Containing Networks from Trifunctional Thiols and Acrylates. *Macromolecules* **2020**, *53* (22), 9890-9900.
234. Chen, Y.; Tang, Z.; Liu, Y.; Wu, S.; Guo, B., Mechanically Robust, Self-Healable, and Reprocessable Elastomers Enabled by Dynamic Dual Cross-Links. *Macromolecules* **2019**, *52* (10), 3805-3812.
235. Chen, Y.; Tang, Z.; Zhang, X.; Liu, Y.; Wu, S.; Guo, B., Covalently Cross-Linked Elastomers with Self-Healing and Malleable Abilities Enabled by Boronic Ester Bonds. *ACS Appl Mater Interfaces* **2018**, *10* (28), 24224-24231.
236. Lennox, A. J. J.; Lloyd-Jones, G. C., Selection of boron reagents for Suzuki-Miyaura coupling. *Chemical Society Reviews* **2014**, *43* (1), 412-443.
237. Brooks, W. L.; Sumerlin, B. S., Synthesis and Applications of Boronic Acid-Containing Polymers: From Materials to Medicine. *Chem Rev* **2016**, *116* (3), 1375-97.
238. Bull, S. D.; Davidson, M. G.; van den Elsen, J. M. H.; Fossey, J. S.; Jenkins, A. T. A.; Jiang, Y.-B.; Kubo, Y.; Marken, F.; Sakurai, K.; Zhao, J.; James, T. D., Exploiting the Reversible Covalent Bonding of Boronic Acids: Recognition, Sensing, and Assembly. *Accounts of Chemical Research* **2013**, *46* (2), 312-326.
239. Deng, C. C.; Brooks, W. L. A.; Abboud, K. A.; Sumerlin, B. S., Boronic Acid-Based Hydrogels Undergo Self-Healing at Neutral and Acidic pH. *ACS Macro Letters* **2015**, *4* (2), 220-224.
240. Cai, B.; Luo, Y.; Guo, Q.; Zhang, X.; Wu, Z., A glucose-sensitive block glycopolymer hydrogel based on dynamic boronic ester bonds for insulin delivery. *Carbohydr Res* **2017**, *445*, 32-39.
241. Marco-Dufort, B.; Tibbitt, M. W., Design of moldable hydrogels for biomedical applications using dynamic covalent boronic esters. *Materials Today Chemistry* **2019**, *12*, 16-33.
242. Brooks, W. L. A.; Deng, C. C.; Sumerlin, B. S., Structure-Reactivity Relationships in Boronic Acid-Diol Complexation. *ACS Omega* **2018**, *3* (12), 17863-17870.

243. Röttger, M.; Domenech, T.; van der Weegen, R.; Breuillac, A.; Nicolaÿ, R.; Leibler, L., High-performance vitrimers from commodity thermoplastics through dioxaborolane metathesis. *Science* **2017**, *356* (6333), 62-65.
244. Cromwell, O. R.; Chung, J.; Guan, Z., Malleable and Self-Healing Covalent Polymer Networks through Tunable Dynamic Boronic Ester Bonds. *J Am Chem Soc* **2015**, *137* (20), 6492-5.
245. Cash, J. J.; Kubo, T.; Dobbins, D. J.; Sumerlin, B. S., Maximizing the symbiosis of static and dynamic bonds in self-healing boronic ester networks. *Polymer Chemistry* **2018**, *9* (15), 2011-2020.
246. Yesilyurt, V.; Ayoob, A. M.; Appel, E. A.; Borenstein, J. T.; Langer, R.; Anderson, D. G., Mixed Reversible Covalent Crosslink Kinetics Enable Precise, Hierarchical Mechanical Tuning of Hydrogel Networks. *Adv Mater* **2017**, *29* (19).
247. Kim, C.; Ejima, H.; Yoshie, N., Non-swellable self-healing polymer with long-term stability under seawater. *RSC Advances* **2017**, *7* (31), 19288-19295.
248. Zuo, Y.; Gou, Z.; Zhang, C.; Feng, S., Polysiloxane-Based Autonomic Self-Healing Elastomers Obtained through Dynamic Boronic Ester Bonds Prepared by Thiol-Ene "Click" Chemistry. *Macromol Rapid Commun* **2016**, *37* (13), 1052-9.
249. Cash, J. J.; Kubo, T.; Bapat, A. P.; Sumerlin, B. S., Room-Temperature Self-Healing Polymers Based on Dynamic-Covalent Boronic Esters. *Macromolecules* **2015**, *48* (7), 2098-2106.
250. He, L.; Szopinski, D.; Wu, Y.; Luinstra, G. A.; Theato, P., Toward Self-Healing Hydrogels Using One-Pot Thiol-Ene Click and Borax-Diol Chemistry. *ACS Macro Letters* **2015**, *4* (7), 673-678.
251. Bapat, A. P.; Sumerlin, B. S.; Sutti, A., Bulk network polymers with dynamic B-O bonds: healable and reprocessable materials. *Materials Horizons* **2020**, *7* (3), 694-714.
252. Wang, Y.; Yu, H.; Yang, H.; Hao, X.; Tang, Q.; Zhang, X., An Injectable Interpenetrating Polymer Network Hydrogel with Tunable Mechanical Properties and Self-Healing Abilities. *Macromolecular Chemistry and Physics* **2017**, *218* (23), 1700348.
253. Biswas, A.; Maiti, S.; Kalaskar, D. M.; Das, A. K., Redox-Active Dynamic Self-Supporting Thixotropic 3D-Printable G-Quadruplex Hydrogels. *Chemistry – An Asian Journal* **2018**, *13* (24), 3928-3934.
254. Huang, W.; Qi, C.; Gao, Y., Injectable Self-Healable Nanocomposite Hydrogels with Mussel-Inspired Adhesive Properties for 3D Printing Ink. *ACS Applied Nano Materials* **2019**, *2* (8), 5000-5008.
255. Shi, W.; Hass, B.; Kuss, M. A.; Zhang, H.; Ryu, S.; Zhang, D.; Li, T.; Li, Y.-I.; Duan, B., Fabrication of versatile dynamic hyaluronic acid-based hydrogels. *Carbohydrate Polymers* **2020**, *233*, 115803.
256. Robinson, L. L.; Self, J. L.; Fusi, A. D.; Bates, M. W.; Read de Alaniz, J.; Hawker, C. J.; Bates, C. M.; Sample, C. S., Chemical and Mechanical Tunability of 3D-Printed Dynamic Covalent Networks Based on Boronate Esters. *ACS Macro Letters* **2021**, *10* (7), 857-863.

257. Liu, Y.; Tang, Z.; Wang, D.; Wu, S.; Guo, B., Biomimetic design of elastomeric vitrimers with unparalleled mechanical properties, improved creep resistance and retained malleability by metal–ligand coordination. *Journal of Materials Chemistry A* **2019**, *7* (47), 26867-26876.
258. Li, L.; Chen, X.; Jin, K.; Torkelson, J. M., Vitrimers Designed Both To Strongly Suppress Creep and To Recover Original Cross-Link Density after Reprocessing: Quantitative Theory and Experiments. *Macromolecules* **2018**, *51* (15), 5537-5546.
259. Ruiz-Pérez, L.; Royston, G. J.; Fairclough, J. P. A.; Ryan, A. J., Toughening by nanostructure. *Polymer* **2008**, *49* (21), 4475-4488.
260. Ligon, S. C.; Seidler, K.; Gorsche, C.; Griesser, M.; Moszner, N.; Liska, R., Allyl sulfides and α -substituted acrylates as addition–fragmentation chain transfer agents for methacrylate polymer networks. *Journal of Polymer Science Part A: Polymer Chemistry* **2016**, *54* (3), 394-406.
261. Aimetti, A. A.; Machen, A. J.; Anseth, K. S., Poly(ethylene glycol) hydrogels formed by thiol-ene photopolymerization for enzyme-responsive protein delivery. *Biomaterials* **2009**, *30* (30), 6048-6054.
262. Rydholm, A. E.; Bowman, C. N.; Anseth, K. S., Degradable thiol-acrylate photopolymers: polymerization and degradation behavior of an in situ forming biomaterial. *Biomaterials* **2005**, *26* (22), 4495-4506.
263. Rydholm, A. E.; Reddy, S. K.; Anseth, K. S.; Bowman, C. N., Controlling Network Structure in Degradable Thiol–Acrylate Biomaterials to Tune Mass Loss Behavior. *Biomacromolecules* **2006**, *7* (10), 2827-2836.
264. Rydholm, A. E.; Reddy, S. K.; Anseth, K. S.; Bowman, C. N., Development and characterization of degradable thiol-allyl ether photopolymers. *Polymer* **2007**, *48* (15), 4589-4600.
265. Huang, F.; Chen, M.; Zhou, Z.; Duan, R.; Xia, F.; Willner, I., Spatiotemporal patterning of photoresponsive DNA-based hydrogels to tune local cell responses. *Nature Communications* **2021**, *12* (1), 2364.
266. Salinas, C. N.; Anseth, K. S., Mixed Mode Thiol–Acrylate Photopolymerizations for the Synthesis of PEG–Peptide Hydrogels. *Macromolecules* **2008**, *41* (16), 6019-6026.
267. Polizzotti, B. D.; Fairbanks, B. D.; Anseth, K. S., Three-Dimensional Biochemical Patterning of Click-Based Composite Hydrogels via Thiolene Photopolymerization. *Biomacromolecules* **2008**, *9* (4), 1084-1087.
268. Schreck, K. M.; Leung, D.; Bowman, C. N., Hybrid Organic/Inorganic Thiol–Ene-Based Photopolymerized Networks. *Macromolecules* **2011**, *44* (19), 7520-7529.
269. Butler, G. B.; Angelo, R. J., Preparation and Polymerization of Unsaturated Quaternary Ammonium Compounds. VIII. A Proposed Alternating Intramolecular-Intermolecular Chain Propagation. *J. Am. Chem. Soc.* **1957**, *79* (12), 3128-3131.

270. Corfield, G. C., Cyclopolymerization. *Chem. Soc. Rev.* **1972**, *1* (4), 523-552.
271. Butler, G. B., Cyclopolymerization and cyclocopolymerization. *Acc. Chem. Res.* **1982**, *15* (11), 370-378.
272. Sokolova, T. A.; Rudkovskaya, G. D., Cyclic polymerization of N-dimethacrylamides. *Journal of Polymer Science Part C: Polymer Symposia* **1967**, *16* (2), 1157-1166.
273. Gray, T. F.; Butler, G. B., The Fundamental Basis for Cyclopolymerization. X. A Systematic Study of the Cyclopolymerization of Methacrylic Anhydride. *Journal of Macromolecular Science: Part A - Chemistry* **1975**, *9* (1), 45-82.
274. Liu, Q.-Q.; Kodaira, T.; Urushisaki, M.; Hashimoto, T., Cyclopolymerization XXIII. Design of Unconjugated Dienes with High Polymerizability Using Functional Groups with No Homopolymerization Tendency and Synthesis of Completely Cyclized Polymers Therefrom: Radical Polymerizations of N-Substituted N-Allyl-2-(methoxycarbonyl)allylamines. *Polymer Journal* **1996**, *28* (11), 1000-1005.
275. Pasini, D.; Takeuchi, D., Cyclopolymerizations: Synthetic Tools for the Precision Synthesis of Macromolecular Architectures. *Chemical Reviews* **2018**, *118* (18), 8983-9057.
276. Hashimoto, T.; Takagi, H.; Hasegawa, Y.; Matsui, H.; Urushisaki, M.; Sakaguchi, T., Living/controlled cationic cyclopolymerization of divinyl ether with a cyclic acetal moiety: Synthesis of poly(vinyl ether)s with high glass transition temperature based on incorporation of cyclized main chain and cyclic side chains. *Journal of Polymer Science Part A: Polymer Chemistry* **2010**, *48* (4), 952-958.
277. Hashimoto, T.; Watanabe, K.; Kodaira, T., Cationic cyclopolymerization of 1,2-bis(2-vinyloxyethoxy)benzenes: Introduction of bulky substituents to increase cyclopolymerization tendency. *Journal of Polymer Science Part A: Polymer Chemistry* **2004**, *42* (13), 3373-3379.
278. Rahman, M. S.; Hashimoto, T.; Kodaira, T., Cationic cyclopolymerization of new divinyl ethers: The effect of ether and ester neighboring functional groups on their cyclopolymerization tendency. *Journal of Polymer Science Part A: Polymer Chemistry* **2003**, *41* (2), 281-292.
279. Hall, A. W.; Godber, M. J.; Blackwood, K. M.; Milne, P. E. Y.; Goodby, J. W., The photoinitiated cyclopolymerization of dienes in the creation of novel polymeric systems and three-dimensional networks. *Journal of Materials Chemistry* **2004**, *14* (17).
280. Kodaira, T., Structural control during the cyclopolymerization of unconjugated dienes. *Progress in Polymer Science* **2000**, *25* (5), 627-676.
281. Stansbury, J. W., Cyclopolymerizable monomers for use in dental resin composites. *J Dent Res* **1990**, *69* (3), 844-8.

282. Hall, A. W.; Blackwood, K. M.; Milne, P. E. Y.; Goodby, J. W., Novel UV cured coatings and adhesives based on the photoinitiated cyclopolymerization of derivatives of diallylamine. *Chemical Communications* **2003**, (20), 2530-2531.
283. Ruppitsch, L. A.; Peer, G.; Ehrmann, K.; Koch, T.; Liska, R., Photopolymerization of difunctional cyclopolymerizable monomers with low shrinkage behavior. *Journal of Polymer Science* **2021**, 59 (6), 519-531.
284. Arbuzova, I. A.; Rostovskiĭ, E. N., On the polymerization of polyfunctional compounds. *J. Polym. Sci.* **1961**, 52 (157), 325-330.
285. Matsoyan, Studies in Cyclic Polymerization and Copolymerization - VII. The Synthesis and Polymerization of Divinylketals. **1960**, 921.
286. Matsoyan, STUDIES IN CYCLIC POLYMERIZATION AND COPOLYMERIZATION --VI. THE SYNTHESIS AND CYCLIC POLYMERIZATION OF AROMATIC DIVINYLCETALS AND DIVINYLFURFURAL. *Vysokomo Lsoedm*, **1961**, 8 (9), 1311-1316.
287. Matsoyan, S. G., Cyclic polymerization and copolymerization of divinyl acetals. *Journal of Polymer Science* **1961**, 52 (157), 189-197.
288. Matsoyan, S. G.; Avetyan, M. G.; Voskanyan, M. G., Studies in cyclic polymerization and copolymerization—III. The synthesis and cyclic polymerization of aliphatic divinyl acetals. A new method of preparation of polyvinyl acetals. *Polymer Science U.s.s.r.* **1962**, 3, 576-585.
289. Tsukino, M.; Kunitake, T., Radical Cyclopolymerization of Divinyl Acetals—Structure Variation with Polymerization Conditions. *Polym. J.* **1985**, 17 (8), 943-951.
290. Jian, Z.; Mecking, S., Insertion Polymerization of Divinyl Formal. *Macromolecules* **2016**, 49 (12), 4395-4403.
291. Hayashi, K., Radical polymerization and copolymerization of some vinyl phosphates. *Die Makromolekulare Chemie* **1978**, 179 (7), 1753-1763.
292. Matsoyan, S. G., STUDIES IN CYCLIC POLYMERIZATION AND COPOLYMERIZATION - VII. Synthesis of divinylketals. *Vysokomil. soedin.* **1961**, 3 (9), 1317-1320.
293. Murahashi, S.; Nozakura, S. i.; Fuji, S.; Kikukawa, K., The Preparation and Polymerization of Divinyl Carbonate. *Bulletin of the Chemical Society of Japan* **1965**, 38 (11), 1905-1910.
294. Lorette, N. B.; Howard, W. L., Preparation of Ketals from 2,2-Dimethoxypropane. *The Journal of Organic Chemistry* **1960**, 25 (4), 521-525.
295. Hofecker, A.; Knaack, P.; Steinbauer, P.; Markovic, M.; Ovsianikov, A.; Liska, R., Novel synthesis routes for the preparation of low toxic vinyl ester and vinyl carbonate monomers. *Synthetic Communications* **2020**, 50 (23), 3629-3641.
296. Beak, P.; Barron, J. A., Reactions of vinyl chloroformate and oxime chloroformates with silver salts. *The Journal of Organic Chemistry* **1973**, 38 (16), 2771-2775.

297. Dworak, C.; Koch, T.; Varga, F.; Liska, R., Photopolymerization of biocompatible phosphorus-containing vinyl esters and vinyl carbamates. *Journal of Polymer Science Part A: Polymer Chemistry* **2010**, *48* (13), 2916-2924.
298. Gorsche, C.; Harikrishna, R.; Baudis, S.; Knaack, P.; Husar, B.; Laeuger, J.; Hoffmann, H.; Liska, R., Real Time-NIR/MIR-Photorheology: A Versatile Tool for the in Situ Characterization of Photopolymerization Reactions. *Anal Chem* **2017**, *89* (9), 4958-4968.
299. Sangermano, M., Advances in cationic photopolymerization. *Pure and Applied Chemistry* **2012**, *84*.
300. Yamamoto, T.; Hashimoto, T.; Urushisaki, M.; Sakaguchi, T., Synthesis of high-molecular-weight star-shaped cyclopolymers of divinyl ethers and their network membranes via controlled cationic cyclopolymerization. *Polymer Journal* **2019**, *51* (12), 1273-1285.
301. Liu, J.-H.; Wang, H.-Y., Synthesis and characterization of novel copolymers with acid-labile ketal moieties derived from camphor. *Journal of Applied Polymer Science* **2003**, *90* (11), 2969-2978.
302. Wang, L.-S.; Cheng, S.-X.; Zhuo, R.-X., Novel Biodegradable Aliphatic Polycarbonate Based on Ketal Protected Dihydroxyacetone. *Macromolecular Rapid Communications* **2004**, *25* (9), 959-963.
303. Barton, D. H. R.; Chern, C.-Y.; Jaszberenyi, J. C., The invention of radical reactions. Part XXXIV. Homologation of carboxylic acids to α -keto carboxylic acids by Barton-ester based radical chain chemistry. *Tetrahedron* **1995**, *51* (7), 1867-1886.
304. Wang, T.; Liu, T.; Ma, T.; Li, L.; Wang, Q.; Guo, C., Study on degradation of phosphorus and nitrogen composite UV-cured flame retardant coating on wood surface. *Progress in Organic Coatings* **2018**, *124*, 240-248.
305. Skarja, G.; Ragheb, A. Chromatography membranes formed by thiol-ene or thiol-yne click polymerization reactions 2019.
306. Yamamoto, T.; Yoshida, S.; Ikari, H.; Ikemori, K.; Ohtaka, K.; Ukuda, H. Anti-fogging coating material, anti-fogging coating film and anti-fogging article 1998.
307. Kim, H.-M.; Chang, Y.-R.; Kim, H. UV-curable coating compositions with self-healing capabilities, coating films, and methods of producing coating films 2012.
308. Akram, M., Citric Acid Cycle and Role of its Intermediates in Metabolism. *Cell Biochemistry and Biophysics* **2014**, *68* (3), 475-478.
309. Grellmann, W.; Seidler, S., *Kunststoffprüfung*. Carl Hanser Verlag GmbH & Co. KG: 2011; p 739.
310. Seidler, K. Photopolymer Networks with Homogeneous Polymer Architectures. 2016.
311. Reinelt, S.; Tabatabai, M.; Fischer, U. K.; Moszner, N.; Utterodt, A.; Ritter, H., Investigations of thiol-modified phenol derivatives for the use in thiol-ene photopolymerizations. *Beilstein J Org Chem* **2014**, *10*, 1733-40.

312. Reinelt, S.; Tabatabai, M.; Moszner, N.; Fischer, U. K.; Utterodt, A.; Ritter, H., Synthesis and Photopolymerization of Thiol-Modified Triazine-Based Monomers and Oligomers for the Use in Thiol-Ene-Based Dental Composites. *Macromolecular Chemistry and Physics* **2014**, *215* (14), 1415-1425.
313. Morrison, P. M.; Foley, P. J.; Warriner, S. L.; Webb, M. E., Chemical generation and modification of peptides containing multiple dehydroalanines. *Chem Commun (Camb)* **2015**, *51* (70), 13470-3.
314. Li, Z.; Kosuri, S.; Foster, H.; Cohen, J.; Jumeaux, C.; Stevens, M. M.; Chapman, R.; Gormley, A. J., A Dual Wavelength Polymerization and Bioconjugation Strategy for High Throughput Synthesis of Multivalent Ligands. *J Am Chem Soc* **2019**, *141* (50), 19823-19830.
315. Zhang, T.; Song, Z.; Chen, H.; Yu, X.; Jiang, Z., Synthesis and characterization of phosphorylcholine-capped poly(epsilon-caprolactone)-poly(ethylene oxide) di-block co-polymers and its surface modification on polyurethanes. *J Biomater Sci Polym Ed* **2008**, *19* (4), 509-24.
316. Felczak, K.; Chen, L.; Wilson, D.; Williams, J.; Vince, R.; Petrelli, R.; Jayaram, H. N.; Kusumanchi, P.; Kumar, M.; Pankiewicz, K. W., Cofactor-type inhibitors of inosine monophosphate dehydrogenase via modular approach: targeting the pyrophosphate binding sub-domain. *Bioorg Med Chem* **2011**, *19* (5), 1594-605.
317. Shan, Y.; Sun, T.; Gao, Y.; Zheng, M.; Huang, C.; Cai, Z.; Shan, W.; Liu, R. Method for preparation of fatty acid monoglyceride and nano-silica. CN109456178A, 2019.
318. Voronkov, M. G.; Romadan, Y. P.; Pestunovich, V. A.; Mazheika, I. B., STUDIES IN THE FIELD OF ALKOXYSILANES XXIII. Spirocyclic Esters of Orthosilicic Acid. *Khimiya Geterotsiklicheskikh Soedinenii* **1968**, *4* (6), 972-975.
319. Frye, C. L., Stable Silicon Heterocyclic Derivatives of Branched Alkanediols. *The Journal of Organic Chemistry* **1969**, (9), 2496-2499.
320. Jitchum, V.; Chivin, S.; Wongkasemjita, S.; Ishidab, H., Synthesis of spiro-silicates directly from silica and ethylene glycol/ethylene glycol derivatives. *Tetrahedron* **2001**, *57*, 3997-4003.
321. Spange, S.; Kempe, P.; Seifert, A.; Auer, A. A.; Ecorchard, P.; Lang, H.; Falke, M.; Hietschold, M.; Pohlers, A.; Hoyer, W.; Cox, G.; Kockrick, E.; Kaskel, S., Nanocomposites with structure domains of 0.5 to 3 nm by polymerization of silicon spiro compounds. *Angew Chem Int Ed Engl* **2009**, *48* (44), 8254-8.
322. Kemmitt, T.; Milestone, N., B., The Ring Size Influence on ²⁹Si N.M.R. Chemical Shifts of Some Spirocyclic Tetra and Penta-coordinate Diolato Silicates. *Aust. J. Chem.* **1995**, (48), 93-102.
323. Laine, R. M.; Furgal, J. C.; Doan, P.; Pan, D.; Popova, V.; Zhang, X., Avoiding Carbothermal Reduction: Distillation of Alkoxysilanes from Biogenic, Green, and Sustainable Sources. *Angew Chem Int Ed Engl* **2016**, *55* (3), 1065-9.

REFERENCES

324. Hoye, T. R.; Promo, M. A., Silicon tethered ring-closing metathesis reactions for self- and cross-coupling of alkenols. *Tetrahedron Letters* **1999**, *40* (8), 1429-1432.
325. Washburn, R. M.; Levens, E.; Albright, C. F.; Billig, F. A., Preparation, Properties, and Uses of Borate Esters. In *Metal-Organic Compounds*, 1959; pp 129-157.
326. Schörpf, S. Novel Monomers with Stress Relaxing and Shrinkage Reducing Characteristics for Dental Restorations. Dissertation, TU Wien, 2020.
327. Chardin, C.; Rouden, J.; Livi, S.; Baudoux, J., Dimethyldioxirane (DMDO) as a valuable oxidant for the synthesis of polyfunctional aromatic imidazolium monomers bearing epoxides. *Green Chem.* **2017**, *19* (21), 5054-5059.
328. Boaz, N.; Falling, S.; Moore, M., The Preparation of Enantiomerically Pure 3,4-Epoxy-1-butene and 3-Butene-1,2-diol. *Synlett* **2005**, *2005* (10), 1615-1617.
329. Schnöll, C. New low shrinkage photopolymers and additives for dental restoratives. Dissertation, TU Wien, 2020.
330. Leed, M. G.; Wolkow, N.; Pham, D. M.; Daniel, C. L.; Dunaief, J. L.; Franz, K. J., Prochelators triggered by hydrogen peroxide provide hexadentate iron coordination to impede oxidative stress. *J Inorg Biochem* **2011**, *105* (9), 1161-72.
331. Gray, C. W.; Walker, B. T.; Foley, R. A.; Houston, T. A., Boronate derivatives of bioactive amines: potential neutral receptors for anionic oligosaccharides. *Tetrahedron Letters* **2003**, *44* (16), 3309-3312.
332. Liu, Z.; Xiao, D.; Liu, G.; Xiang, H.; Rong, M.; Zhang, M., Self-healing and reprocessing of transparent UV-cured polysiloxane elastomer. *Progress in Organic Coatings* **2021**, *159*, 106450.
333. Vignollet, Y.; Maire, J. C.; Witanowski, M., Interaction between a phenyl ring and silicon atom. The nitrogen-14 nuclear magnetic resonance of nitrophenyltrimethylsilanes. *Chemical Communications (London)* **1968**, (19), 1187-1187.
334. Hagberg, E. C.; Malkoch, M.; Ling, Y.; Hawker, C. J.; Carter, K. R., Effects of Modulus and Surface Chemistry of Thiol-Ene Photopolymers in Nanoimprinting. *Nano Letters* **2007**, *7* (2), 233-237.
335. Kwon, J. S.; Park, H. W.; Kim, D. H.; Kwark, Y.-J., Solvent-Free Processable and Photo-Patternable Hybrid Gate Dielectric for Flexible Top-Gate Organic Field-Effect Transistors. *ACS Applied Materials & Interfaces* **2017**, *9* (6), 5366-5374.
336. Fahem, Z.; Bauhofer, W., Thiol-ene polymer based fast photo-curable gate insulator for organic field effect transistors. *Microelectronic Engineering* **2013**, *105*, 74-76.
337. Modjinou, T.; Versace, D.-L.; Abbad-Andallousi, S.; Bousserhine, N.; Babinot, J.; Langlois, V.; Renard, E., Antibacterial Networks Based on Isosorbide and Linalool by Photoinitiated Process. *ACS Sustainable Chemistry & Engineering* **2015**, *3* (6), 1094-1100.

338. ÇAkmakÇI, E.; ŞEn, F.; Kahraman, M. V., Isosorbide Diallyl Based Antibacterial Thiol–Ene Photocured Coatings Containing Polymerizable Fluorous Quaternary Phosphonium Salt. *ACS Sustainable Chemistry & Engineering* **2019**, *7* (12), 10605-10615.
339. Lorenzini, C.; Haider, A.; Kang, I.-K.; Sangermano, M.; Abbad-Andalloussi, S.; Mazeran, P.-E.; Lalevée, J.; Renard, E.; Langlois, V.; Versace, D.-L., Photoinduced Development of Antibacterial Materials Derived from Isosorbide Moiety. *Biomacromolecules* **2015**, *16* (3), 683-694.
340. Childress, K. K.; Alim, M. D.; Mavila, S.; Martinez, V.; Ding, Y.; Bowman, C. N.; Stansbury, J. W., Systematic Modulation and Structure–Property Relationships in Photopolymerizable Thermoplastics. *ACS Applied Polymer Materials* **2021**, *3* (2), 1171-1181.
341. Sycks, D. G.; Safranski, D. L.; Reddy, N. B.; Sun, E.; Gall, K., Tough Semicrystalline Thiol–Ene Photopolymers Incorporating Spiroacetal Alkenes. *Macromolecules* **2017**, *50* (11), 4281-4291.
342. Sycks, D. G.; Wu, T.; Park, H. S.; Gall, K., Tough, stable spiroacetal thiol-ene resin for 3D printing. *Journal of Applied Polymer Science* **2018**, *135* (22), 46259.
343. Lohse, F. Verfahren zur Herstellung von Di- und Polyallyläthern. 1981.
344. Kotha, S.; Cheekatla, S. R., Synthesis of functionalized cage propellanes and D3-Trishomocubanes via the ring-closing metathesis and acid-promoted rearrangement. *Tetrahedron* **2019**, *75* (1), 84-93.
345. Nie, J. X., Pu; Zhang, Jing Application of cyclic acetal in preparing visible light cured materials for undegraded orthopedic repair or plastic and cosmetic. 2016.
346. Chiriac, A. MATRIX COPOLYMER SYNTHESIS PROCESS FOR BIO-MEDICAL APPLICATIONS. 2016.
347. Dellago, B.; Altun, A. A.; Liska, R.; Baudis, S., Exploring the limits of toughness enhancers for 3D printed photopolymers as bone replacement materials. *Journal of Polymer Science n/a* (n/a).
348. Steinbauer, P.; Liska, R.; Baudis, S., Approaching new biomaterials: copolymerization characteristics of vinyl esters with norbornenes, allyl esters and allyl ethers. *Polymer International* **2022**, *71* (7), 790-796.
349. Pfaffinger, M., Hot Lithography – New Possibilities in Polymer 3D Printing. *Laser Technik Journal* **2018**, *15* (4), 45-47.
350. Hofstetter, C.; Orman, S.; Baudis, S.; Stampfl, J., Combining cure depth and cure degree, a new way to fully characterize novel photopolymers. *Additive Manufacturing* **2018**, *24*, 166-172.
351. Elomaa, L.; Teixeira, S.; Hakala, R.; Korhonen, H.; Grijpma, D. W.; Seppälä, J. V., Preparation of poly(ϵ -caprolactone)-based tissue engineering scaffolds by stereolithography. *Acta Biomaterialia* **2011**, *7* (11), 3850-3856.
352. Shintani, H., Ethylene Oxide Gas Sterilization of Medical Devices. *Biocontrol Sci* **2017**, *22* (1), 1-16.

353. Lambert, B. J.; Mendelson, T. A.; Craven, M. D., Radiation and ethylene oxide terminal sterilization experiences with drug eluting stent products. *AAPS PharmSciTech* **2011**, *12* (4), 1116-26.
354. Alvarado, C. J., Sterilization vs. disinfection vs. clean. *Nurs Clin North Am* **1999**, *34* (2), 483-91.
355. Harrell, C. R.; Djonov, V.; Fellabaum, C.; Volarevic, V., Risks of Using Sterilization by Gamma Radiation: The Other Side of the Coin. *Int J Med Sci* **2018**, *15* (3), 274-279.
356. *Radiation Technology in Emerging Industrial Applications*. INTERNATIONAL ATOMIC ENERGY AGENCY: Vienna, 2003.
357. Wu, A.-M.; Bisignano, C.; James, S. L.; Abady, G. G.; Abedi, A.; Abu-Gharbieh, E.; Alhassan, R. K.; Alipour, V.; Arabloo, J.; Asaad, M.; Asmare, W. N.; Awedew, A. F.; Banach, M.; Banerjee, S. K.; Bijani, A.; Birhanu, T. T. M.; Bolla, S. R.; Cámera, L. A.; Chang, J.-C.; Cho, D. Y.; Chung, M. T.; Couto, R. A. S.; Dai, X.; Dandona, L.; Dandona, R.; Farzadfar, F.; Filip, I.; Fischer, F.; Fomenkov, A. A.; Gill, T. K.; Gupta, B.; Haagsma, J. A.; Haj-Mirzaian, A.; Hamidi, S.; Hay, S. I.; Ilic, I. M.; Ilic, M. D.; Ivers, R. Q.; Jürisson, M.; Kalhor, R.; Kanchan, T.; Kavetsky, T.; Khalilov, R.; Khan, E. A.; Khan, M.; Kneib, C. J.; Krishnamoorthy, V.; Kumar, G. A.; Kumar, N.; Laloo, R.; Lasrado, S.; Lim, S. S.; Liu, Z.; Manafi, A.; Manafi, N.; Menezes, R. G.; Meretoja, T. J.; Miazgowski, B.; Miller, T. R.; Mohammad, Y.; Mohammadian-Hafshejani, A.; Mokdad, A. H.; Murray, C. J. L.; Naderi, M.; Naimzada, M. D.; Nayak, V. C.; Nguyen, C. T.; Nikbakhsh, R.; Olagunju, A. T.; Otstavnov, N.; Otstavnov, S. S.; Padubidri, J. R.; Pereira, J.; Pham, H. Q.; Pinheiro, M.; Polinder, S.; Pourchamani, H.; Rabiee, N.; Radfar, A.; Rahman, M. H. U.; Rawaf, D. L.; Rawaf, S.; Saeb, M. R.; Samy, A. M.; Sanchez Riera, L.; Schwebel, D. C.; Shahabi, S.; Shaikh, M. A.; Soheili, A.; Tabarés-Seisdedos, R.; Tovani-Palone, M. R.; Tran, B. X.; Travillian, R. S.; Valdez, P. R.; Vasankari, T. J.; Velazquez, D. Z.; Venketasubramanian, N.; Vu, G. T.; Zhang, Z.-J.; Vos, T., Global, regional, and national burden of bone fractures in 204 countries and territories, 1990–2019: a systematic analysis from the Global Burden of Disease Study 2019. *The Lancet Healthy Longevity* **2021**, *2* (9), e580-e592.
358. Klinkova, V. V.; Kozlikov, V. L.; Fedotov, N. S., The frequencies and intensities of the C = C vibrational bands in the IR absorption spectra of silicon alkenoxy derivatives. *Journal of Applied Spectroscopy* **1972**, *16* (5), 656-660.
359. Hall, H. K., Jr.; Ykman, P., Reactions of the zwitterions from trisubstituted electron-deficient ethylenes and electron-rich olefins. *Journal of the American Chemical Society* **1975**, *97* (4), 800-807.
360. Komarov, N. V.; Lisovin, E. G., Reaction of vinyloxyorganosilanes with alcohols and phenol. *Zhurnal Obshchei Khimii* **1977**, *50* (4), 854-859.
361. Sugimura, H.; Yoshida, K., A New Synthetic Method for α -Oxo- β,γ -unsaturated Esters. *Bulletin of the Chemical Society of Japan* **1992**, *65* (11), 3209-3211.

362. Tang, Z.; Huang, Q.; Liu, Y.; Chen, Y.; Guo, B.; Zhang, L., Uniaxial Stretching-Induced Alignment of Carbon Nanotubes in Cross-Linked Elastomer Enabled by Dynamic Cross-Link Reshuffling. *ACS Macro Letters* **2019**, *8* (12), 1575-1581.
363. Kohama, F., *Chemical Abstracts* **1962**, *81* (496), 170.
364. Seyferth, D., Gmelin Handbook of Inorganic Chemistry. 8th Edition. B. Boron Compounds. *Organometallics* **1984**, *3* (2), 339-339.
365. Goering, H. L.; Jacobson, R. R., A Kinetic Study of the ortho-Claisen Rearrangement¹. *Journal of the American Chemical Society* **1958**, *80* (13), 3277-3285.
366. Carpita, A.; Rossi, R., *Synthesis*. 1982; Vol. 6.
367. Chavan, S. P.; Pawar, K. P.; Praveen, C.; Patil, N. B., Chirality induction and chiron approaches to enantioselective total synthesis of α -lipoic acid. *Tetrahedron* **2015**, *71* (24), 4213-4218.
368. McConnell, R., L.; Coover, H., W. Jr.; Diallyl ethers. 1966.
369. Twibanire, J.-d. A. K.; Al-Mughaid, H.; Grindley, T. B., Synthesis of new cores and their use in the preparation of polyester dendrimers. *Tetrahedron* **2010**, *66* (50), 9602-9609.
370. Steinbauer, P. Photopolymerizable Adhesives for Bone Healing. Dissertation, TU Wien, 2021.
371. Podgórski, M.; Wang, C.; Yuan, Y.; Konetski, D.; Smalyukh, I.; Bowman, C. N., Pristine Polysulfone Networks as a Class of Polysulfide-Derived High-Performance Functional Materials. *Chemistry of Materials* **2016**, *28* (14), 5102-5109.
372. HYDROGEN PEROXIDE Concentration Determination 20-70% Technical Data Sheet. Solvay, Ed. 2019.
373. Torres, C. R.; Crastechini, E.; Feitosa, F. A.; Pucci, C. R.; Borges, A. B., Influence of pH on the effectiveness of hydrogen peroxide whitening. *Oper Dent* **2014**, *39* (6), E261-8.
374. Breuillac, A.; Kassalias, A.; Nicolaÿ, R., Polybutadiene Vitrimers Based on Dioxaborolane Chemistry and Dual Networks with Static and Dynamic Cross-links. *Macromolecules* **2019**, *52* (18), 7102-7113.
375. Dias, A. B., M. J.; Nijenhuis, A. J.; Polymers comprising thioester bonds. 2007.
376. Love, D. M.; Fairbanks, B. D.; Bowman, C. N., Evaluation of Aromatic Thiols as Photoinitiators. *Macromolecules* **2020**, *53* (13), 5237-5247.
377. Rasheed, O. K.; Bailey, P. D.; Lawrence, A.; Quayle, P.; Raftery, J., A Modular Synthesis of Multidentate S-, N- and O-Containing Meta- and Paracyclophanes. *European Journal of Organic Chemistry* **2015**, *2015* (32), 6988-6993.
378. Riedl, C. A.; Rosner, A.; Harringer, S.; Salomon, P.; Hejl, M.; Jakupec, M. A.; Kandioller, W.; Keppler, B. K., Water-soluble trithiolato-bridged dinuclear ruthenium(II) and osmium(II) arene complexes with bisphosphonate functionalized ligands as anticancer organometallics. *J Inorg Biochem* **2021**, *225*, 111618.

REFERENCES

379. Ostasz, A.; Łyszczek, R.; Mazur, L.; Tarasiuk, B., Co-crystal formation between 2-amino-4,6-dimethylpyrimidine and new p-xylylene-bis(thioacetic) acid. *CrystEngComm* **2014**, *16* (44), 10262-10272.
380. Kobayashi, J. I., K., A facile Synthesis of Thioacids by Thiolysis of acid halide/Dimethylformamide adducts. *Synthesis* **1985**, (6-7), 671-672.
381. Kobayashi, E. T., K.; Kato, M.; Aoshima S., Synthesis of New Linear Polymers Containing Thiocarbonyl Groups: Polyaddition of Dicarbothioic Acid to Diolefins. **1994**, *26* (1), 49-59.
382. Rao, Y.; Li, X.; Nagorny, P.; Hayashida, J.; Danishefsky, S. J., A simple method for the conversion of carboxylic acids into thioacids with Lawesson's reagent. *Tetrahedron Letters* **2009**, *50* (48), 6684-6686.